UCL
SCHOOL OF PHARMACY

Metabolomics Study of In Vitro Models of Hepatic Steatosis in HepG2 Cells

Maria Helena Onoufriou

Thesis submitted in accordance with the
requirements for the degree of
Doctor in Philosophy

UCL School of Pharmacy
29/39 Brunswick Square
London WC1N 1AX

September 2023

Declaration page

I, Maria Helena Onoufriou confirm that the work presented in my thesis is my own. Where information has been derived from other sources, I confirm that this has been indicated in the thesis.

Abstract

Non-alcoholic fatty liver disease (NAFLD) is one of the leading causes of liver disease with a current global prevalence of 25%. NAFLD consists of a spectrum of diseases ranging from mild steatosis to non-alcoholic steatohepatitis (NASH) and fibrosis and can be diet or drug-induced. The early stages of NAFLD and drug-induced fatty liver disease (DIFLD) are reversible. However, the symptoms of steatosis are vague and there is a lack of specific and sensitive biomarkers.

The overall aim of this project was to identify metabolite biomarkers for mild steatosis using NMR-based metabolomics; HepG2 monolayers and spheroids were used to create dietary and drug-induced *in vitro* models of mild steatosis.

To create the steatotic models HepG2 cells were dosed with various doses of either a 2:1 mixture of oleic and palmitic acid, tetracycline or valproate and incubated for 24 hours. To ensure doses were not cytotoxic MTS and LDH assays were conducted. Steatosis was confirmed using Oil Red O staining and a triglyceride assay. Cell extracts were obtained from all models and analysed by ^{1}H NMR and multivariate statistical methods.

While a mixture of oleic and palmitic acid induce an increase in lipid accumulation and upregulation of beta-oxidation, tetracycline and valproate affect lipid metabolism by reducing beta-oxidation with both eventually leading to NASH. Therefore, changes in the TCA cycle metabolites were observed as well as changes in the methylation pathways. In particular, there were changes in levels of lactate, choline, homocysteine, and arachidonic acid in all models. These metabolites could potentially be useful in a panel of biomarkers for the early detection of steatosis.

Literature has suggested that HepG2 monolayers cells have poor CYP expression compared to spheroids therefore, this study analysed CYP 2D6, 2E1 and 3A4 expression in both monolayers and spheroids. The resulting Western blots indicated changes in all CYPs in both monolayers and spheroids in response to steatosis.

The results from this project provide a good overview of the major metabolic pathways affected in steatosis, regardless of the cause. The use of HepG2 spheroids in drug-induced steatosis offers a novel *in vitro* model for biomarker research that has not been reported before in the literature.

Impact statement

Non-alcoholic fatty liver disease (NAFLD) defines a spectrum of liver diseases ranging from hepatic steatosis to non-alcoholic steatohepatitis (NASH), fibrosis and cirrhosis. NAFLD has emerged as a public health concern due to its rising global burden.

The initial stage of steatosis has long been considered a relatively benign condition; however, fatty livers are vulnerable to further injury and possible rapid progression to steatohepatitis. Data suggests that 41% of patients ultimately develop fibrosis and predicts that NAFLD may become the major cause of end stage liver disease in the coming decades. Incidence rates are set to increase by a further 18.3% in some developed countries by 2030.

Many drugs can also induce fatty liver disease (DIFLD) a specific type of drug-induced liver injury, characterised by intracellular lipid accumulation in hepatocytes. Such drugs include tetracycline, valproic acid and tamoxifen. Annual incidence rates of drug-induced liver injury were said to vary widely in population-based studies from 2.7 to 19.1 cases per 100,000 with approximately 27% of cases having some form of steatosis.

While steatosis itself is reversible the difficulty lies in diagnosis since at this stage both NAFLD and DIFLD are relatively asymptomatic. Currently liver biopsies remain the gold standard for the diagnosis and prognosis of NAFLD and DIFLD. This leaves a great unmet need for non-invasive biomarkers that can identify both NAFLD and DIFLD before they progress. The lack of biomarkers is further complicated by the fact that some patients may have pre-existing NAFLD or NASH before receiving a drug known to cause DIFLD. In addition, there is a need for specific biomarkers capable of differentiating between underlying NAFLD and DIFLD.

This project will attempt to analyse metabolite changes in both diet and drug-induced models of steatosis in HepG2 cells. There is no published comparison between diet and drug-induced models therefore this project will offer a novel insight into metabolite changes occurring in both models and could help differentiate between the two. This will potentially allow more sensitive and specific biomarkers of both diet and drug-induced steatosis to be identified.

Therapy options are scarce in part due to the lack of reliable disease models for research. There is an ongoing need for more human relevant predictive models as interspecies differences are a major drawback when extrapolating animal data to humans. Therefore, there is growing interest in *in vitro* models. This project will attempt to develop *in vitro* models of steatosis in HepG2 monolayers and spheroids. The morphology of spheroids is more reflective of the liver and will therefore provide a more reliable model for the study of steatosis. To date there are no studies in literature that have attempted to identify metabolite changes in drug-induced steatosis in HepG2 spheroids therefore this study offers novel models for the dentification of drug-induced biomarkers.

Acknowledgments

I would like to thank my supervisors Professor Mike Munday for giving me the opportunity to do this PhD and all his advice and Dr Rosemary Smyth for all her constant support, guidance and continued willingness to help over the years.

I would also like to express my gratitude to Dr Maria-Jose Martinez Bravo for teaching me how to culture cells and for willingness to answer all my questions in this regard.

To my friends Nektarios, Jumana, and Christine with whom I have shared the last four years with, you made this experience more enjoyable. Thank you for every time you kept my cells alive, I couldn't have done it without you.

Thank you to my friend Pallavi for always being there with a cup of coffee and listening.

Thank you to my work colleagues at VML for your support, particularly to Lisa Chandler for giving me the opportunity to be able to work and finish my PhD. To Dr Ursula D'Souza for always being understanding and supportive throughout this journey.

Thank you to my mum for her endless proof reading and being my biggest fan and to my dad for his support and my brothers George and Gabriel for always being there to entertain me when I had a bad day.

Table of Contents

Table of figures

List of tables

List of Abbreviations

ACC	Acetyl-CoA carboxylase
AGPAT	1-acylglycerol-3-phosphate acyltransferase
ALT	Alanine transaminase
ANOVA	Analysis of variance
ApoB 100	Apolipoprotein B 100
ARA	Arachidonic acid
AST	Aspartate transaminase
ATF4	Transcription factor 4
BHMT	Betaine-homocysteine methyltransferase
BSA	Bovine serum albumin
CD36	Cluster of differentiation
ChREBP	Carbohydrate response element binding protein
COX	Cyclooxygenase
CPS1	Carbamoylphosphate synthetase
CPT1	Carnitine palmitoyltransferase 1
CPT2	Carnitine palmitoyltransferase 2
CSSG	Cysteine-glutathione
CTL1	Choline transporter-like protein 1
CYP P450	Cytochrome P450
D_2O	Deuterium oxide
DGAT	Diacylglycerol acyltransferase
DIFLD	Drug-induced fatty liver disease
DIHS	Drug-induced hepatic steatosis
DILI	Drug-induced liver injury
DIS	Drug-induced steatosis
DISH	Drug-induced steatohepatitis
DMEM	Dulbecco's Modified Eagle high glucose medium
DMETs	Drug metabolising enzymes and transporters
DMSO	Dimethyl sulfoxide
DMT1	Divalent metal transporter 1
DNL	*De novo* lipogenesis
DTT	Dithiothreitol
EPA	Eicosapentaenoic acid
FADH2	Flavin adenine dinucleotide
FAS	Fatty acid synthetase
FBS	Fetal Bovine Serum
FABP-1	Fatty acid-binding protein 1
FDPS	Farnesyl diphosphate synthase
FID	Free induction decay
FLIP	Fatty liver inhibition of progression
ELOVL6	Elongase 6
ER	Endoplasmic reticulum
G6Pase	Glucose 6 phosphate
GGR	Gamma glutamyl transferase
GLUT	Glucose transporter
GPAT	Glycerol-3-phosphate acyltransferase
GSH	Glutathione
GSSG	Glutathione disulfide
HCl	Hydrochloric acid
HMG-CoA	3-hydroxy-3 methylglutaryl-CoA
HMGR	HMG-CoA reductase

HSCs	Hepatic stellate cells
HST	High salt tween
IL-8	Interleukin 8
IPP	Isopentenyl pyrophosphate
IRS1	Insulin receptor substrate 1
JNK	c-Jun N-terminal kinase
JRES	J-resolved
KCs	Kupffer cells
KOH	Potassium hydroxide
LC-AM/MS	Liquid chromatography and accurate mass-mass spectrometry
LDH	Lactate dehydrogenase
LOX	Lipoxygenase
MAFLD	Metabolic dysfunction-associated fatty liver disease
MAT	Methionine adenosyltransferases
$MgCl_2$	Magnesium chloride
MTS	3-(4,5-dimethylthiazol-2-yl)-5-(3-carboxymethoxyphenyl)-2-(4-sulfophenyl)-2H-tetrazolium
MTT	(3-(4,5-Dimethylthiazol-2-yl)-2,5- Diphenyltetrazolium Bromide)
MTTP	Microsomal triglyceride transfer protein
NaCl	Sodium chloride
NAFLD	Non-alcoholic fatty liver disease
NASH	Non-alcoholic steatohepatitis
NF-kb	Nuclear factor-kb
NMR	Nuclear magnetic resonance
OA	Oleic acid
OPLS	Orthogonal partial least squares
OPLS-DA	Orthogonal partial least squares discriminate analysis
OSC	Orthogonal signal correction
OTC	Ornithine transcarbamylase
OXPHOS	Oxidative phosphorylation
PBS	Phosphate-buffered saline
PC 1/2	Principal component
PC	Phosphatidylcholine
PCA	Principal component analysis
PEMT	Phosphatidylethanolamine N-methyltransferase
PEPCK	Phosphoenolpyruvate carboxykinase
PPARα	Peroxisome proliferator activated receptor alpha
PPARγ	Proliferator-activated receptor gamma
PUFA	Polyunsaturated fatty acids
ROS	Reactive oxygen species
SAF	Steatosis, activity, fibrosis
SAH	S-adenosylhomocysteine
SAM	S-adenosylmethionine
SBT1	Soybean trypsin inhibitor
SCs	Stellate cells
SCD1	Stearyl-CoA desaturase 1
SDS	Sodium dodecyl sulfate
SDS-PAGE	Sodium dodecyl sulphate polyacrylamide gel electrophoresis
SEM	Scanning electron microscopy
SHMT	Serine hydroxymethyltransferase
SOD-1	Superoxide dismutase-1
SREBP	Sterol regulatory element binding protein
TCA	Tricarboxylic acid cycle
THF	Tetrahydrofolate
TMAO	Trimethylamine N-oxide

TMS	Tetramethylsilane
TNF-α	Tumour necrosis factor
TPCK	Tosyl phenylalanyl chloromethyl ketone
TSP	3-(trimethyl-siyl) propionic acid
VIP	Variable influence of projection
VLDL	Very low-density lipoproteins
UGT	Glucuronosyltransferase
WST	Water Soluble Tetrazolium salt

Chapter One – Introduction

Chapter 1

1.1 Liver Anatomy

The liver is the largest human visceral organ in the body and contributes approximately 2-3% of the total body weight (Abdel-Misih and Bloomston, 2010). It is positioned on the right-hand side of the upper quadrant of the abdominal cavity just below the diaphragm and is protected by the ribcage. The human liver consists of four lobes: two major lobes (right and left), which are separated by the falciform ligament (Figure 1.1) and the caudate and quadrate lobes (Vernon et al., 2020). The quadrate lobe is visible on the inferior surface of the right lobe whereas the caudate lobe is located between the left and right lobes on the posterior side of the liver (Vernon et al., 2020).

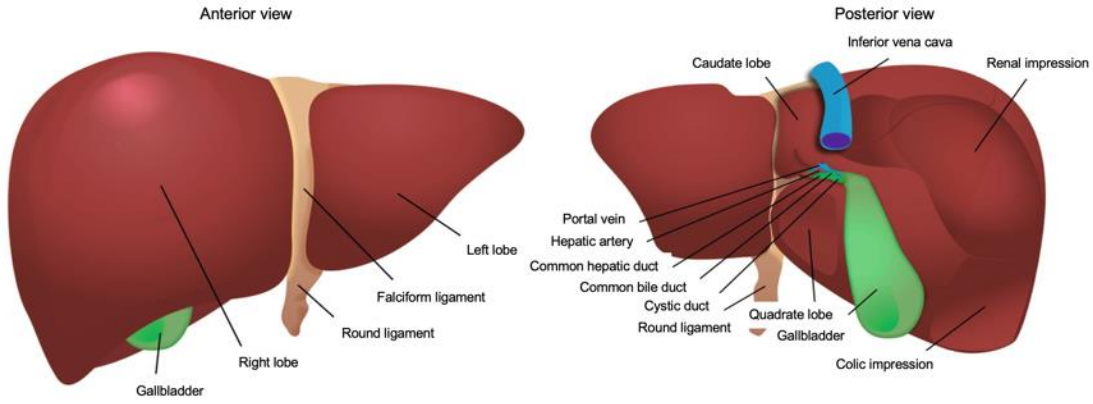

Figure 1.1 Gross anatomy of the liver. The liver is divided into the left and right lobes, separated by the falciform ligament. (Adapted from Guido et al., 2019).

1.1.1 Blood supply

The liver has a unique dual blood supply; the hepatic artery contributes approximately 25% of the blood supply while the remaining 75% comes from the hepatic portal vein (Abdel-Misih and Bloomston, 2010). The hepatic artery and portal vein enter the liver at the hilum where they are divided into the right and left branches to supply the two lobes. The hepatic artery arises from the coeliac axis and supplies the liver with oxygenated blood (Naish et al., 2009; Abdel-Misih and Bloomston, 2010). Whereas the hepatic portal vein forms at the junction of the superior mesenteric vein and the splenic vein behind the pancreas and carries nutrient-rich but deoxygenated blood

from the gut, spleen and pancreas to the liver (Naish et al., 2009). Deoxygenated blood then leaves the liver via the hepatic vein and drains into the inferior vena cava (Figure 1.2).

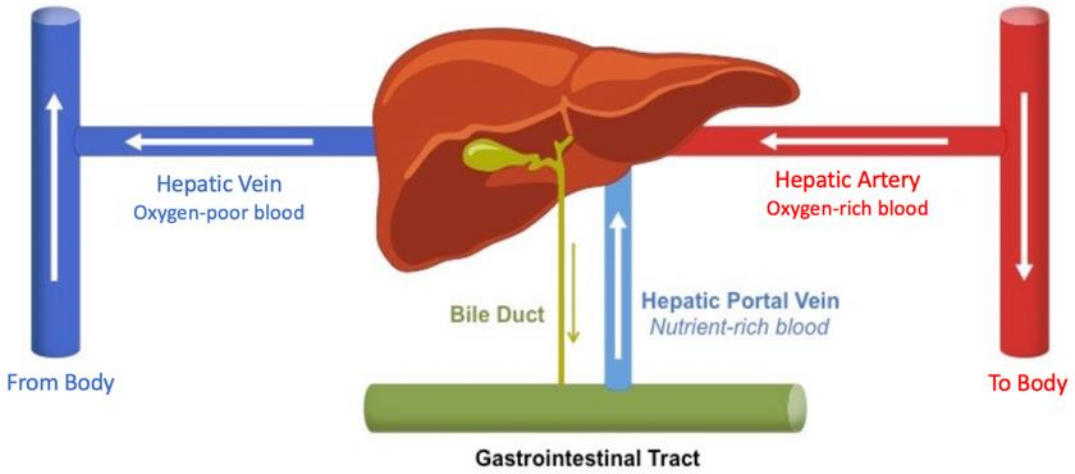

Figure 1.2 Overview of hepatic circulation. The hepatic artery supplies the liver with oxygenated blood, while the hepatic portal vein carries deoxygenated blood from the body to the liver. Deoxygenated blood then flows in the hepatic vein carries towards the inferior vena cava.

1.1.2 Microanatomy

The morphological unit of the liver is classically hexagonal in shape and is known as a lobule, with a central vein in the middle (Kietzmann, 2017). The corners of the lobule are formed by portal triads consisting of branches from the portal vein, the hepatic artery and the bile duct. Lobules are described as consisting of 3 zones; with one zone located close to the portal triads (the periportal zone), a second surrounding the central vein known as the centrilobular zone and the intermediate area between these two zones known as the midzonal regions (Krishna, 2013, Kietzmann, 2017).

While the lobule portrays the anatomical arrangement, the hepatic acinus is the term used to define the functional unit of the liver. Hepatic acini have portal triads at the centre and the terminal hepatic venule at the periphery (Dixon et al., 2013). Each acinus has 3 zones according to the distance from the arterial blood supply (Figure 1.3). Zone 1 is closest to the arterioles in the portal triads and is the most oxygenated, while zone 3 is furthest away and has the lowest supply of oxygen (Kurbel et al., 2003, Lautt, 2009).

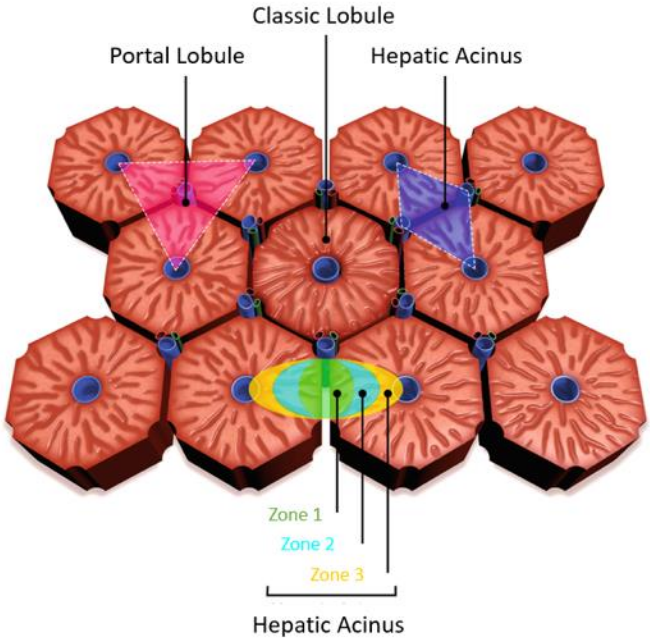

Figure 1.3 The lobular arrangement of the hepatocytes. The lobule portrays the anatomical arrangement while the acinus is the functional unit of the liver. The acini have portal triads and are separated into 3 zones. Source: (Adapted from Maronpot and Malarkey, 2019).

The main parenchymal cells of the liver are hepatocytes arranged in plates or rows 1-2 cells thick within the many hexagonal lobules (Krishna, 2013). The rows of hepatocytes have blood filled spaces known as sinusoids on each side. The sinusoidal spaces are lined with a discontinuous endothelium, in which epithelial cells are highly fenestrated allowing unimpeded flow of plasma between sinusoidal blood and the perisinusoidal space, known as the space of Disse (Haussinger and Kordes, 2019, Sanz-Garcia et al., 2020).

The space of Disse contains hepatic stellate cells (also known as Ito cells) which play a key role in fibrogenesis, the storage of vitamin A and fat and the formation of connective tissue framework made up of reticulin fibres (Dixon et al, 2013). Kupffer cells and phagocytes are also present within the sinusoids. Both form an essential part of the reticuloendothelial immune system as they are the first immune cells in the liver to encounter gut bacteria, endotoxins and microbial debris transported to the liver via the portal vein (Basit et al., 2020). Therefore, they play an essential role in host defence (Dixon et al., 2013, Nguyen-Lefebvre and Horuzsko, 2015). Kupffer cells facilitate phagocytic removal of foreign particulates and participate in the regulation of

inflammatory and repair responses via the secretion of various cytokines into the circulation and perisinusoidal space (Cullen and Stalker, 2016).

Located between the individual rows of hepatocytes are bile canaliculi which collect bile secreted by the hepatocytes. From the canaliculi bile flows towards larger collecting ducts and into the left and right hepatic ducts, which merge to form the common hepatic duct. The common bile duct then carries bile either directly to the duodenum or to the gallbladder where it is concentrated and stored (Boyer, 2013).

1.2 Liver physiology

The liver performs a wide range of vital metabolic functions including bile formation, carbohydrate, lipid and protein metabolism, drug metabolism, detoxification, and vitamin storage (Boyer, 2013, Vanputte et al., 2013, Kalra et al., 2020).

1.2.1 Carbohydrate and protein metabolism and bile formation

The human liver forms and secretes between 600-1000 mL of bile daily (Vanputte et al., 2013). Bile is composed mainly of water (95%), bile salts, bilirubin and electrolytes and is synthesised in the hepatocytes before being secreted into the bile canaliculi. Bile salts serve to emulsify fats and increase their surface area to facilitate their absorption by the intestines (Boyer, 2013). Lipophilic substances including cholesterol, bilirubin which results from the breakdown of haemoglobin, lipid soluble hormones, lecithin or lipophilic toxins are excreted from the body via bile (Vanputte et al., 2013, Hundt et al., 2020).

Carbohydrate metabolism is controlled by the liver whereby glucose is stored within hepatocytes in the form of glycogen. When blood glucose levels are elevated excess glucose is taken up by the liver cells and is used to synthesise glycogen via glycogenesis (Postic and Girard, 2004). Similarly, when blood glucose levels are depleted glycogenolysis is upregulated within the hepatocytes forming glucose from glycogen.

Proteins are synthesised from dietary amino acids in the liver. The liver is also where the synthesis and secretion of plasma proteins such as albumin and coagulation factors take place (Kalra et al., 2020).

1.2.2 Lipid metabolism

The liver is the central organ for the control of lipid metabolism via the uptake, synthesis, esterification, oxidation, and secretion of long chain fatty acids (Ding et al., 2018). Fatty acids entering the liver originate from either dietary or endogenous sources. Ingested dietary triglycerides are emulsified by bile acids in the intestinal lumen before undergoing hydrolysis primarily by pancreatic lipase, yielding sn-2-monoacylglycerols and free fatty acids (Alves-Bezerra and Cohen, 2017). Following hydrolysis, these molecules are taken up by enterocytes in the small intestine and synthesised into triglycerides. Triglycerides are then packaged into chylomicrons, which are composed of cholesterol, triglycerides and apolipoprotein B48; which are then secreted into the lymphatic system and ultimately reach the circulatory system. Most triglycerides are taken up by muscle and adipose tissue. The remainder are taken up by the liver by receptor mediated endocytosis of the chylomicron remnants (Malhi and Gore, 2008, Alves-Bezerra and Cohen, 2017, Puschel and Henkel, 2018). Thus, the rate at which fatty acids enter the liver depends on their plasma concentration levels.

The liver can also synthesise triglycerides from non-esterified fatty acids taken up from the plasma by hepatocytes or via *de novo* lipogenesis, whereby fatty acids are synthesised from carbohydrates such as glucose (Malhi and Gores, 2008). This process begins with the conversion of products from glycolysis into acetyl-CoA by pyruvate dehydrogenase in the mitochondria. It is then transferred in the cytosol as citrate followed by conversion back to acetyl-CoA by ATP-citrate lyase. Acetyl-CoA is then converted to malonyl-CoA by acetyl-CoA carboxylase (ACC). Following this fatty acid synthetase (FAS) catalyses the production of palmitic acid (a 16-carbon fatty acid). Palmitic acid can undergo elongation and desaturation by the actions of elongase 6 (ELOVL6) and stearyl-CoA desaturase 1 (SCD1) generating further mono-

unsaturated fatty acids (Ameer and Zaidi, 2014). Glycerol-3-phosphate acyltransferase (GPAT) catalyses the esterification of glycerol-3-phosphate from glycolysis by incorporating an acyl moiety at the sn-1 position of the glycerol backbone producing lysophosphatidic acid. Phosphatidic acids are then generated from lysophosphatidic acid in the presence of 1-acylglycerol-3-phosphate acyltransferase (AGPAT). The next step generates diacylglycerols via lipin 1 (Kawano and Cohen, 2013, Song et al., 2018). Triglycerides are then finally formed by the action of acyl-CoA: diacylglycerol acyltransferase (DGAT) (Figure 1.4A) (Kawano and Cohen, 2013, Ameer and Zaidi, 2014).

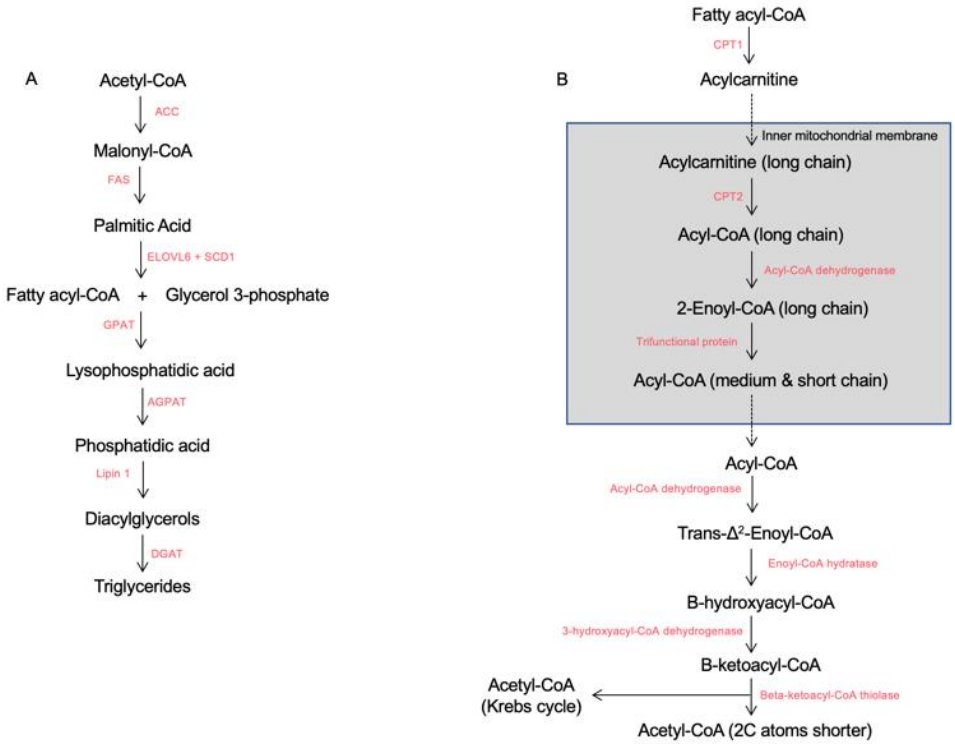

Figure 1.4 A. Overview of *de novo* lipogenesis and B. Overview of beta-oxidation**.** Excess fatty acids are degraded in the liver via beta-oxidation, while the liver can synthesise fatty acids through *de novo* lipogenesis. The enzymes that catalyse each step of these reactions are shown in red.

As well as synthesising fatty acids by *de novo* lipogenesis the liver also oxidises long chain fatty acids to produce acetyl-CoA via the process of beta-oxidation, as shown in Figure 1.4B. Beta-oxidation takes place over four steps: dehydrogenation, hydration, oxidation and thiolysis with each step catalysed by a distinct enzyme (Nelson and Cox, 2012). Prior to beta-oxidation the relatively inert fatty acids must first be activated by fatty acyl-CoA synthetase, using up one molecule of coenzyme A and one molecule of ATP producing long chain fatty acyl-CoA. The long chain acyl-CoA is then converted

to long-chain acyl-carnitine by carnitine palmitoyltransferase 1 (CPT1) allowing its transportation by a translocase across the inner mitochondrial membrane into the matrix where beta-oxidation takes place (Kumari, 2018). An inner mitochondrial membrane carnitine palmitoyltransferase 2 (CPT2) then converts the long-chain acylcarnitine back into long-chain acyl-CoA which enters the beta-oxidation pathway. Beta-oxidation begins with the oxidation of acyl-CoA by acyl CoA dehydrogenase, a double bond is formed between the second and third carbons (C2 and C3) to produce trans-Δ^2-enoyl-CoA yielding FADH2 from FAD. In the next step the double bond between C2 and C3 in trans-Δ^2-enoyl-CoA is hydrated by enoyl CoA hydratase to form β-hydroxyacyl CoA replacing the double bond with a hydroxyl group on C2. Following this the hydroxyl group is then oxidised by NAD+ in a reaction that is catalysed by 3-hydroxyacyl-CoA dehydrogenase to produce β-ketoacyl CoA and NADH+H^+ (Houten, 2010, Nelson and Cox, 2012). In the fourth and final step which is catalysed by β-ketothiolase, β-ketoacyl CoA is cleaved by a thiol group of another CoA molecule. The cleavage takes place between C2 and C3 producing acetyl CoA which enters the Krebs cycle and a 2 carbon shorter fatty acyl-CoA chain; the process repeats until the fatty acid chain has been shortened to a 2-carbon acetyl CoA (Mehta, 2013).

Under normal circumstances the liver processes large quantities of fatty acids but stores only a small amount in the form of triglycerides, typically less than 5% of the total liver volume. This homeostatic control is achieved by balancing fatty acid uptake from the plasma and *de novo* synthesis with fatty acid oxidation and secretion of triglycerides into the blood (Alves-Bezerra and Cohen, 2017). For secretion, the liver packages triglycerides into very low-density lipoproteins (VLDL) (Kawano and Cohen, 2013). VLDLs possess a hydrophobic core made up of cholesteryl esters, triglycerides and a hydrophilic coating containing a phospholipid monolayer and unesterified cholesterol (Tiwari and Siddiqi, 2012, Kawano and Cohen, 2013). Each VLDL is stabilised by a single molecule of apolipoprotein B 100 (ApoB 100), which is a key structural component (Sundaram and Yao, 2010) and contains a hydrophobic lipid binding region that participates in the assembly of lipoproteins and a hydrophilic region that interacts with the aqueous environment (Fabbrini et al., 2010). As a result, water-insoluble triglycerides are converted to a more water-soluble form as VLDLs and thus can be secreted from the hepatocytes (Kawano and Cohen, 2013). These triglycerides can then be transported to other tissues as lipoproteins for use as a source of energy

and for structural components (Ponziani et al., 2015). Triglycerides provide twice as much energy compared with carbohydrates and proteins, as the fatty acids within triacylglycerols are already in their reduced state (Mehta, 2013). The relatively small quantities of triglycerides which are stored within the liver are normally localized in cytoplasmic lipid droplets (Alves-Bezerra and Cohen, 2017).

The liver also plays a central role in cholesterol metabolism and under normal circumstances the liver is the primary site of cholesterol biosynthesis and excretion (Nemes et al., 2016, Puschel and Henkel, 2018). Cholesterol homeostasis is tightly controlled through intestinal cholesterol absorption, hepatic de-novo synthesis and cholesterol excretion from the body (Nemes et al., 2016, Malhotra et al., 2020). *De novo* synthesis begins with acetyl CoA conversion to 3-hydroxy-3 methylglutaryl-CoA (HMG-CoA) by HMG-CoA synthase which is then converted to mevalonate by HMG-CoA reductase (HMGR) (Nemes et al., 2016, Malhotra et al., 2020, Yang et al., 2020). Mevalonate undergoes a series of phosphorylation reactions followed by decarboxylation yielding isopentenyl pyrophosphate (IPP). Squalene synthase then catalyses a series of condensing reactions leading to the production of squalene (Do et al., 2008). From squalene, lanosterol, the first of the sterols is formed (Nemes et al., 2016, Malhotra et al., 2020, Yang et al., 2020). The newly synthesised cholesterol along with the cholesterol absorbed from the intestine are packaged along with triglycerides and apolipoprotein B-100 into VLDLs (Malhotra et al., 2020). As well as being the primary site of cholesterol biosynthesis the liver is also the primary site of cholesterol excretion, converting it into bile acids and removing free cholesterol and neutral sterols via biliary excretion (Nemes et al., 2016).

1.2.3 Drug metabolism

The liver is the primary site for the metabolism and detoxification of xenobiotics. The liver metabolises a wide range of drugs converting them into more water-soluble forms to aid with excretion (Vaja and Rana, 2020). Drug metabolism consists of two phases: phase I and phase II. Some drugs undergo only one phase, but for the majority of drugs both phase I and phase II metabolism occurs sequentially (Phang-Lyn and Llerena, 2020).

Phase I reactions are most commonly oxidation reactions, but reduction and hydrolysis of drugs may also take place. Oxidation reactions are predominantly catalysed by the cytochrome P450 (CYP450) enzymes and occur mainly in the smooth endoplasmic reticulum of hepatocytes (Xu et al., 2005, Schonborn, 2010). The P450 family is a gene superfamily with 57 members in the human genome, and a subset of approximately 15 P450 enzymes belonging to the CYP1, CYP2 and CYP3 gene families. Together CYP450s particularly CYP450 isoforms CYP3A4, CYP1A1, CYP2B6, CYP2C9, and CYP2E1 mediate 70-80% of all drug metabolism reactions (Zollner et al., 2010, Liu et al., 2017, Rey-Bedon et al., 2022).

Phase II metabolism involves the addition of polar groups to either the parent drug molecule or phase I metabolites via various conjugation reactions such as glucuronidation. This step increases the polarity of these compounds allowing them to be more easily excreted (Crettol et al., 2010, Schonborn, 2010). The enzymes responsible for catalysing phase II reactions are collectively known as transferases for example glucuronosyltransferase (UGT) (Liu et al., 2017).

Due to the high exposure of the liver to xenobiotics and intermediates formed during drug metabolism the liver is particularly susceptible to chemically induced liver toxicity. The intermediates formed during metabolism can cause direct injury to hepatocytes or induce the inhibition of mitochondrial respiration leading to the production of reactive oxygen species (ROS) and a depletion in ATP. This may lead to oxidative stress and subsequent inflammatory cell response by the injured hepatocytes. Increased ROS levels can directly damage DNA, proteins, enzymes and lipids in cells and induce immune-mediated liver damage thus resulting in drug-induced liver injury (DILI) (Kolaric et al., 2021).

As well as direct DILI induced by compounds or their metabolites some drugs can also cause dysregulated fat metabolism (Kolaric et al., 2021). This leads to an accumulation of lipids in liver cells resulting in drug-induced steatosis and NAFLD.

1.3 Non-alcoholic fatty liver disease

Non-alcoholic fatty liver disease (NAFLD) defines a spectrum of liver diseases ranging from hepatic steatosis (otherwise known as fatty liver), non-alcoholic steatohepatitis (NASH), fibrosis and cirrhosis (Figure 1.5) (Rabinowich and Shibolet, 2015). NAFLD is associated with excess fat deposits in the liver in the absence of excessive alcohol consumption. It is currently the most common type of liver disease globally with an estimated prevalence of about 25% in the general population (Ramos et al., 2022). Data suggests that 41% of patients ultimately develop fibrosis and predicts that NAFLD may become the major cause of end stage liver disease in the coming decades. Incidence rates are set to increase by a further 18.3% in some developed countries by 2030 due to an ever-present sedentary lifestyle and greater economic growth which could see NASH becoming the leading reason for future liver transplants (Muller and Strula, 2019, Ramos et al., 2022). There is a close association between NAFLD, diabetes, and obesity with studies reporting NAFLD as the hepatic manifestation of metabolic syndrome (Le et al., 2017). It has been suggested that individuals are 5 times more likely to develop diabetes if they already have NAFLD (Bhatt and Smith, 2015). At the time of diagnosis most patients with NAFLD already display clinical manifestations of metabolic syndrome such as diabetes, elevated plasma triglyceride, reduced high-density lipoprotein cholesterol levels, obesity and high blood pressure (Bhatt and Smith, 2015, Le et al., 2017, Sharma and John, 2020). Taking this into account hepatologists recently suggested replacing the term NAFLD with metabolic dysfunction-associated fatty liver disease (MAFLD). However currently the name remains unchanged as it might create some confusion as many clinical trials are currently specific to NASH which is not a major aspect in the MAFLD concept molecular basis (Kolaric et al., 2021, Di Pasqua et al., 2022).

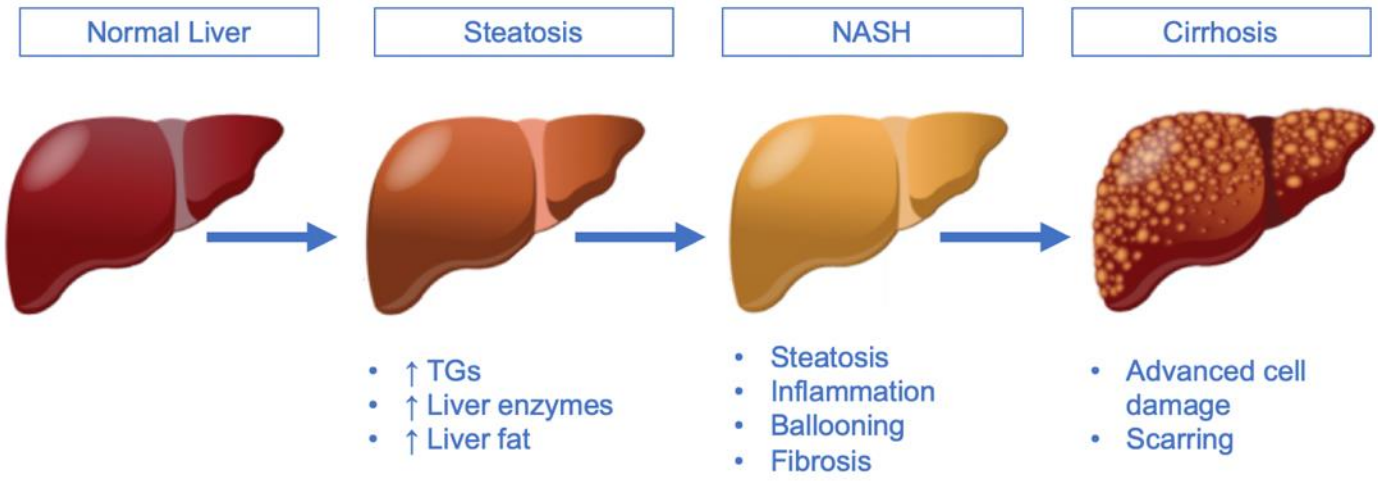

Figure 1.5 Overview of the spectrum of NAFLD. NAFLD encompasses a spectrum of disease states ranging from mild and reversible liver steatosis to more serious and irreversible liver cirrhosis. Adapted from Guo et al., 2022.

Obesity, NAFLD and diabetes are all linked to the development of insulin resistance, and are associated with increased gluconeogenesis (Gastadelli et al., 2000, Bhatt and Smith, 2015, Finck, 2018). The presence of NAFLD in obese patients is associated with adipose tissue insulin resistance and greater rates of adipose tissue lipolysis than in obese patients without NAFLD (Fabbrini et al., 2010). Excessive release of free fatty acids from adipose into circulation increases their delivery to the liver and skeletal muscle. This can simultaneously lead to increased intrahepatic triglycerides causing insulin resistance in the liver and skeletal muscle (Fabbrini et al., 2010). Skeletal muscle insulin resistance and hyperinsulinemia can further increase triglyceride accumulation in the liver by stimulating hepatic *de novo* lipogenesis and triglyceride synthesis (Fabbrini et al., 2010, Dharmalingam and Yamasandhi, 2018). *De novo* lipogenesis is further enhanced by insulin resistance as there is a reduced rate of glycogen synthesis with increased rates of gluconeogenesis in NAFLD. This increase in hepatic glucose and resultant glycolysis provides a substrate for *de novo* lipogenesis (Dharmalingam and Yamasandhi, 2018). These pathological changes occur due to the release of pro-inflammatory, procoagulant and pro-oxidant mediators and the release of fetuin-A, fibroblast growth factor-21 and retinol-binding protein-4 by the liver. Fetuin-A binds and inhibits the insulin receptor tyrosine kinase in the liver

and skeletal muscle inhibiting insulin signalling transduction resulting in systemic and hepatic insulin resistance (Dharmalingam and Yamasandhi, 2018).

NAFLD typically begins as simple steatosis, defined as when fat accounts for at least 5% of the liver weight. Steatosis results from either the dysregulated uptake of fats by the liver, excess *de novo* lipogenesis or via the suppression of beta-oxidation (Parry and Hodson, 2017, Alves-Bezerra and Cohen, 2017). This disruption to lipid metabolism results in the excessive accumulation of fats within the hepatocytes. Steatosis has long been considered a relatively benign condition; however, human studies have suggested that fatty livers are vulnerable to further injury and possible rapid progression to steatohepatitis (Kanuri and Bergheim, 2013).

The mechanism by which NAFLD is associated with increased *de novo* lipogenesis is not fully understood. However, it is thought that elevated circulating insulin and glucose activate the sterol regulatory element binding protein 1c (SREBP-1c) and carbohydrate response element binding protein (ChREBP) which transcriptionally activate genes involved in *de novo* lipogenesis (Section 1.2.2) (Smith et al., 2020).

Steatosis can manifest in two forms: macrovesicular and microvesicular steatosis. Macrovesicular steatosis is characterised by the presence of small to large droplets of fat located in the cytoplasm of the hepatocytes, which peripherally displace the nucleus and is typically caused by alcohol, diabetes or obesity (Apica and Lee, 2014, Rabinowich and Shibolet, 2015). The degree of steatosis and size of the fat droplets observed in the macrovesicular state often indicates that no further lipid accumulation is likely to occur. Whereas, in microvesicular steatosis very small fat droplets are typically observed in the cytoplasm of the hepatocytes. Microvesicular steatosis is associated with a number of conditions including acute fatty liver of pregnancy, Reye's syndrome, sodium valproate toxicity and high-dose tetracycline toxicity (Hautekeete et al., 1990). Microvesicular steatosis is also related to the severe impairment of beta-oxidation and as fatty acids are poorly oxidised by the mitochondria this leads to the esterification of triglycerides, the main lipid form that accumulates in steatosis (Satapathy et al., 2015, Kolaric et al., 2022). Consequently, microvesicular steatosis is considered the more severe form since it suggests ongoing active changes in fat

accumulation in the liver; however, unlike macrovesicular steatosis there is no peripheral displacement of the nucleus (Rabinowich and Shibolet, 2015).

The majority of patients with NAFLD suffer from simple steatosis alone but approximately 10-30% will have NASH, characterised by hepatic steatosis alongside inflammation (Dyson et al., 2013). This can progress to more serious liver diseases such as fibrosis and cirrhosis (Figure 1.5) (Feher and Lengyel, 2003).

The progression of simple steatosis to NASH is a complex process, and the mechanisms involved are not fully understood. However, it is thought to be a result of multiple parallel hits (Buzzetti et al., 2016, Kim and Lee, 2018, Tilg et al., 2020) often due to a combination of oxidative stress, hyperinsulinemia and hepatic iron and lipid accumulation (Shifflet and Wu, 2009, Sharma and John 2020). The excessive build-up of fatty acids leads to oxidative stress which in turn leads to mitochondrial dysfunction and an increase in the production of reactive oxygen species (ROS) (Nassir and Ibdah, 2014, Peng and Meex, 2018, Li et al., 2019). Mitochondrial dysfunction also leads to endoplasmic reticulum (ER) stress, uncoupling of oxidative phosphorylation and subsequently ATP depletion (Patel and Sanyal, 2013, Kim and Lee, 2018). Excess ROS can then cause direct damage to hepatocytes. Additionally, ROS may interact with polyunsaturated fatty acids in the cell membrane producing lipid peroxidation intermediates which can diffuse to neighbouring cells causing further injury. An increase in lipid peroxidation and oxidative damage to mitochondrial DNA further diminish the function of the mitochondria. This establishes a self-perpetuating vicious cycle which increases oxidative stress and mitochondrial dysfunction (Ipsen et al., 2018). Ultimately the c-Jun N-terminal kinase (JNK) signalling pathway is triggered which subsequently alters mitochondrial permeability leading to possible apoptosis and necrosis (Patel and Sanyal, 2013, Chen et al., 2015). Additionally, chronic ER stress and increased ROS production may stimulate the production of several proinflammatory molecules such as the transcription factor nuclear factor-kb (NF-kb), tumour necrosis factor (TNF)-α and interleukin (IL)-8. Immune cells such as macrophages, Kupffer cells, natural killer cells and T-cells may also be activated and release pro-inflammatory chemokines. (Patel and Sanyal, 2013, Kim and Lee, 2018). The presence of inflammation and such immune responses alongside steatosis is defined as NASH.

In obese patients with steatosis the excessive lipid accumulation and resulting inflammatory response exacerbates insulin resistance (Kitade et al., 2017, Finck, 2018). Hypertrophic adipocytes in obesity also secrete inflammatory cytokines such as TNF-α, IL-1β and IL-6. These pro-inflammatory cytokines can inhibit insulin receptor signalling resulting in reduced hepatic insulin sensitivity (Kitade et al., 2017). Thus, the activation of inflammatory pathways and recruitment of immune cells to adipose tissue, liver and skeletal muscle leads to acute inflammation, the development of insulin resistance and consequently the progression of steatosis to NASH (Kitade et al., 2017).

Another mechanism by which the progression of steatosis to NASH is thought to occur is via iron overloading. This has been reported in 30-70% of patients with NAFLD and NASH (Abe et al., 2019). It can occur because patients with NAFLD have increased iron absorption from the duodenum due to upregulation of the divalent metal transporter 1 (DMT1) due to increased mRNA levels, which begins to accumulate in the liver (Hoki et al., 2015). Studies suggest that iron can induce oxidative stress and ROS production by catalysing hydroxyl radical formation via the Fenton reaction leading to the formation of hydrogen peroxide. The induced oxidative stress leads to further lipid peroxidation, protein modification and DNA damage, thus accelerating the progression of NAFLD to NASH (Fargion et al., 2011, Nelson et al., 2011, Britton et al., 2016).

Ultimately, NASH will progress to fibrosis since the necro-inflammation that occurs in NASH triggers pathological activation of hepatic stellate cells (HSCs) located in the space of Disse. This results in differentiation of HSCs from vitamin-A storing cells to proliferating, inflammatory myofibroblasts which cause impaired collagen deposition and degradation resulting in an imbalance in fibrillar collagen in the liver and ultimately leading to cirrhosis (Bataller and Brenner, 2005, Kisseleva, 2017, Tsuchida and Friedman, 2017, Romero et al., 2020).

1.4 Drug-induced liver steatosis

Alongside NAFLD many drugs can also cause a form of fatty liver disease, known as drug-induced fatty liver disease (DIFLD). It is a specific type of drug-induced liver injury, characterised by intracellular lipid accumulation in hepatocytes. Such drugs include tetracycline, valproic acid and tamoxifen amongst others (Kolaric et al., 2021). In a recent report the annual incidence rates of drug-induced liver injury were said to vary widely in population-based studies from 2.7 to 19.1 cases per 100,000 with approximately 27% of cases having some form of steatosis (Kolaric et al., 2021). This represents a considerable number of cases of DIFLD.

DIFLD can present initially as pure microvesicular or macrovesicular steatosis or as drug-induced steatohepatitis (DISH). Drugs that cause microvesicular steatosis are often associated with acute liver injury and/or dysfunction such as Reye's syndrome (Pavlik et al., 2019). While those leading to macrovesicular steatosis and steatohepatitis are more often associated with chronic and slow progressive liver injury (Pavlik et al., 2019). Drugs linked to microvesicular steatosis include valproic acid, tetracycline, aspirin, ibuprofen and zidovudine (Satapathy et al., 2015).

The main mechanisms behind DIFLD involve the interference with mitochondrial respiration including beta-oxidation, oxidative phosphorylation and the TCA cycle (Satapathy et al., 2015, Miele et al., 2017, Di Pasqua et al., 2022). DIFLD may also be induced by the dysregulation of lipid hepatic homeostasis in terms of increased fatty acid uptake, increased *de novo* lipogenesis (DNL), and decreased transport by very low-density lipoprotein (VLDLs) as shown in Figure 1.6 (Patel and Sanyal, 2013, Pavlik et al., 2019, Di Pasqua et al., 2022). Steatogenic drugs can also lead to the inhibition of the carnitine palmitoyl shuttle and therefore prevent long chain fatty acids entering the mitochondria where beta-oxidation occurs (Patel and Sanyal, 2013, Di Pasqua et al., 2022). Drugs such as valproate can also upregulate the proliferator-activated receptor gamma (PPARγ) and cluster of differentiation 36 (CD36) which play a role in facilitating fatty acid uptake in the liver and adipose tissue in humans (Komulainen et al., 2015, Bai et al., 2017, Yan et al., 2021, Di Pasqua et al., 2022). The subsequent mitochondrial dysfunction caused by lipid accumulation leads to oxidative stress, including the release of inflammatory cytokines including TNF-alpha,

TNF-beta and IL-8 which have chemotactic, proinflammatory and profibrogenic roles (Satapathy et al., 2015, Miele et al., 2017, Pavlik et al., 2019, Di Pasqua et al., 2022). This results in stellate cells activation and the generation of reactive oxygen species (ROS) which elicits the peroxidation of fatty acids leading to further inflammation and fibrogenesis via the activation of Kupffer cells and Ito cells (Miele et al., 2017). Although drug-induced steatosis begins as a benign and reversible condition the subsequent cellular events trigger progression to the more serious condition DISH (Pavlik et al., 2019).

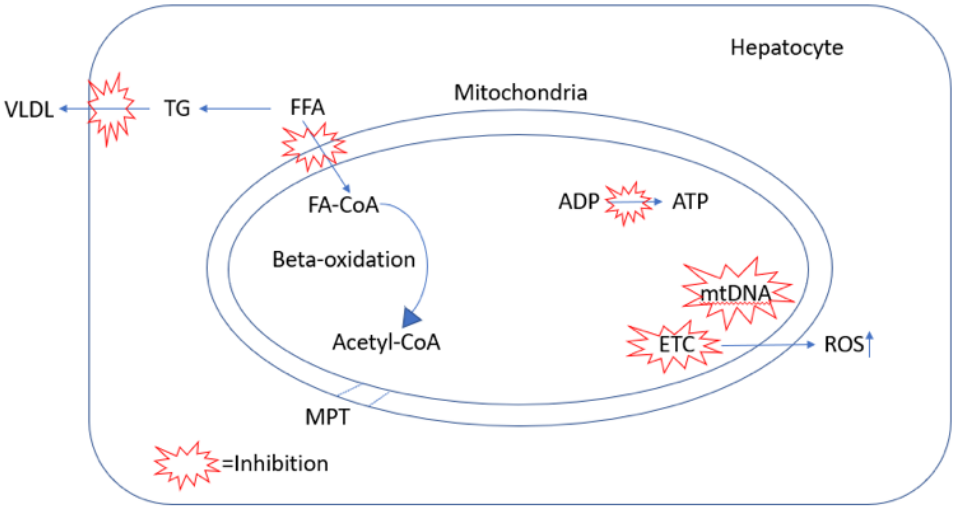

Figure 1.6 Mechanisms of drug-induced liver steatosis. Adapted from Patel and Sanyal (2013).

1.5 Tetracycline

In this project tetracycline was used to develop a drug-induced *in vitro* model of steatosis. Tetracycline belongs to a class of broad-spectrum bacteriostatic drugs usually prescribed to humans for the treatment of upper respiratory, skin and soft tissue infections (Choi et al., 2015). Tetracycline acts by inhibiting protein synthesis of bacterial cells by binding to the 30s subunit of the ribosomes and preventing aminoacyl-tRNA from binding. This prevents the addition of subsequent amino acids to the growing protein chain and therefore slows the growth of the bacterium (Patrick, 2009, Shutter and Akhondi, 2022).

Although generally considered a safe drug tetracycline induced hepatotoxicity was first described more than 50 years ago (Lewis et al., 1967, Andrade and Tulkens, 2011, Glenn and Feldman, 2011, Abdel-Gelil and Mansour, 2019). When administered in high doses (3g tetracycline administered intravenously daily for 10 days), tetracycline has been reported to induce hepatic steatosis (Robinson and Rywlin, 1970).

Tetracycline is thought to induce steatosis by inhibiting β-oxidation and the microsomal triglyceride transfer protein (MTTP) (Tagliatti and Colet, 2016). A decrease in mitochondrial β-oxidation of fatty acids and the inhibition of the microsomal triglyceride transfer protein leads to a reduction in the secretion of triglycerides and therefore accumulation of VLDLs in the liver (Tagliatti and Colet, 2016). Studies have indicated that tetracycline can downregulate genes involved in beta-oxidation including peroxisome proliferator activated receptor alpha (PPARα), carnitine palmitoyl transferase I (CPT-I), and fatty acid-binding protein 1 (FABP- 1) (Satapathy et al., 2015, AlGhamdi, 2019).

Furthermore, doxycycline and monocycline which belong to the same drug class have been shown to enhance ROS production in hepatocytes by activation of the transcription factor 4 (ATF4) which induces ROS production through the upregulation of CYP2E1 (Di Pasqua et al., 2019). This suggests that this class of drugs might be capable of inducing NASH.

1.6 Valproate

Valproate is another drug that has been shown to induce steatosis *in vitro* and was used in this study for the induction of steatosis in HepG2 cells. Valproate is a broad-spectrum antiepileptic drug which has been widely used in the treatment of convulsions, bipolar and schizoaffective disorders (Mnif et al., 2016, Bai et al., 2017, Xu et al., 2019A). Valproate is also used for the treatment of paediatric epilepsy. Pharmacologically, valproate acts as a GABA (γ-aminobutyric acid) analogue in the central nervous system, blocking voltage-gated ion channels and inhibiting histone deacetylase (Rahman and Nguyen, 2022, Allen et al., 2023).

Although valproate is generally considered safe there are a wide range of adverse effects associated with valproate treatment including hepatotoxicity (Rabinowich and Shibolet, 2015). Patients undergoing long-term treatment with valproate develop features consistent with metabolic syndrome including substantial weight gain, insulin resistance and lipid abnormalities such as inhibited beta-oxidation. (Amacher and Chalasani, 2014, Rabinowich and Shibolet, 2015, Chang et al., 2016). Approximately 61% of patients treated with valproate are diagnosed with hepatic steatosis following ultrasound examination (Bai et al., 2017). Hepatic damage is usually accompanied by elevations in serum aminotransferase and is pathologically characterised by the presence of microvesicular steatosis (Bai et al., 2017).

Despite the number of studies reporting valproate hepatotoxicity the mechanisms underlying the development of this liver injury are not fully understood (Bai et al., 2017). Earlier studies suggested that the accumulation of lipids in the liver following valproate treatment is due to an inhibition of beta-oxidation (Amacher and Chalasani, 2014, Rabinowich and Shibolet, 2015, Bai et al., 2017). Studies have also shown that valproate can upregulate the cluster of differentiation 36 (CD36), also known as fatty acid translocase, a membrane protein which plays an important role in facilitating fatty acid uptake in the liver (Chang et al., 2016, Bai et al., 2017). CD36 expression is closely associated with insulin resistance, metabolic syndrome and accelerates the development of fatty liver by increasing fatty acid uptake rates in hepatocytes (Bai et al., 2017). However, the role it plays in valproate-induced steatosis is not fully understood (Chang et al., 2016, Bai et al., 2017). It has also been proposed that the formation of valproyl-CoA causes depletion of intramitochondrial CoA affecting beta-oxidation. This leads to impaired ATP production and inhibition of carnitine palmitoyltransferase I (CPT1) which catalyses the transport of long chain fatty acid into the mitochondria for beta-oxidation (Amacher and Chalasani, 2014, Rabinowich and Shibolet, 2015, Chang et al., 2016).

1.7 Models of steatosis

NAFLD has emerged as a public health concern due to its rising global burden, yet therapy options are scarce. This is in part due to the lack of reliable disease models

for research (Kozyra et al., 2018). Thus, there is an ongoing need for more human relevant predictive models for research.

1.7.1 Animal models in steatosis

Several animal models of steatosis, NAFLD and NASH are routinely used (Boeckmans and Rodrigues, 2018). Examples include the use of genetically modified animals such as ob/ob mice which carry a spontaneous mutation in the leptin gene making them insulin resistant, hyperinsulinemic, and severely hyperglycemic (Nagarajan et al., 2012, Mohammed et al., 2017); dietary induced models such as the high fat diet and methionine-choline deficient diet as well as drug-induced models using carbon tetrachloride and sodium valproate (Gomez-Lechon et al., 2007).

However, interspecies differences can be a major drawback when extrapolating animal data to humans (Boeckmans and Rodrigues, 2018). Additionally, there is an increasing demand to reduce the number of animals used in research. This coupled with the high cost and time required for animal studies has led to growing interest in *in vitro* models of NAFLD (Grepper et al., 2019).

1.7.2 *In vitro* models of steatosis

Undoubtedly, primary hepatocytes are the “gold standard” for drug metabolism and hepatotoxicity studies (Donato et al., 2013). Primary hepatocytes are differentiated cells that can express CYP enzymes and can mimic many of the *in vivo* hepatic functions, including drug metabolism. However, they tend to be phenotypically unstable, and limitations preventing their routine use include the unavailability of continuous supplies of liver tissue for harvesting and lack of reproducibility between batches (Donato et al., 2013). This coupled with issues regarding ethics and cost greatly limits the use of primary hepatic cells (May et al., 2016).

Alternatively, cell lines derived from hepatocarcinomas present a major advantage over primary cell lines due to their easy handling, stable phenotype and unlimited

lifespan (Donato et al., 2013, Willebrords et al 2015., Alkhatabeh et al., 2016, Molinaro et al., 2020). Many hepatocellular cell lines exist, with one of the most characterised and commonly used being the HepG2 cell line (Cui et al, 2010, Garcia-Ruiz et al., 2015, Willebrords et al., 2015, Alkhatatbeh et al., 2016). This is an immortalised cell line derived from the liver tissue of a 15-year-old Caucasian male who had a well differentiated hepatocellular carcinoma.

HepG2 cells exhibit an epithelial-like morphology and are non-tumorigenic with high proliferation rates (Donato et al., 2015). In addition, HepG2 cells are reported to have the biosynthetic capabilities of normal liver parenchymal cells. Thus, these cells are highly differentiated and display many of the genotypic features of normal liver cells (Gerets et al., 2012). HepG2 cells retain many biochemical functions including the potential to secrete lipoproteins, insulin-stimulated glycogen synthesis, albumin secretion and glutathione-based detoxification making them a suitable model for studying human lipid metabolism and drug-induced liver injury (Gerets et al., 2012, Alkhatabeh et al., 2016, Sefried et al., 2018).

However, one of the main limitations of HepG2 cells is linked to their reduced metabolic capacities such as urea formation compared with primary hepatocytes (Gerets et al., 2012, Kammerer and Kupper, 2018, Sefried et al., 2018). Another disadvantage of HepG2 cells is their low level of cytochrome P450 (CYP) enzyme expression (Castell et al., 2006, Rodriguez-Antona et al., 2008, Gerets et al., 2012, Kammerer and Kupper, 2018, Sefried et al., 2018). Nevertheless, despite the low CYP enzyme expression HepG2 cells have been used in a number of toxicity and lipid metabolism studies (Cui et al., 2010, Garcia-Perez et al., 2021).

1.7.3 Steatosis models in HepG2

The induction of steatosis in HepG2 cells is most commonly achieved by the administration of saturated and/or unsaturated fatty acids (Lyall et al., 2018). Oleic and palmitic acid are the most abundant fatty acids present in the human body and have been used in many *in vitro* studies to create models of steatosis (Ricchi et al., 2009,

Lyall et al., 2018, Zeng et al., 2020). Palmitic acid has been shown to act as a greater steatogenic agent at lower concentrations of 0.25 and 0.5 mM after 24 hours whereas the steatotic effects of oleic acid are greater at higher concentrations of 0.75 and 1 mM (Cui et al., 2010, Moravcova et al., 2015, Liang et al., 2015). However, besides inducing steatosis palmitic acid has also been shown to exhibit a dose dependent cytotoxic effect associated with ROS production, apoptosis and necrosis at high doses as excess palmitic acid is poorly incorporated into triglycerides (Cui et al., 2010, Moravcova et al., 2015).

Therefore, for the development of a simple steatotic model a combination of oleic and palmitic acid is the preferred choice in the literature. A combination of the two induces steatosis at lower overall fatty acid concentrations thereby reducing the possibility of toxicity and allowing preservation of the functional capacity of cells (Moracova et al., 2015, Nemecz et al., 2019). The addition of a small amount of palmitic acid to oleic acid induces steatosis alongside minor toxic and apoptotic effects creating a benign state of chronic mild steatosis (Liang et al., 2015, Moracova et al., 2015, Dave et al., 2018). Studies have shown that a mixture of the two can induce similar dose dependent changes in HepG2 cells to those seen in hepatocytes *in vivo* (Gomez-Lechon et al., 2007, Donato et al., 2009, Cui et al, 2010). However, the overall concentration of these fatty acids and the ratio of oleic to palmitic acid is critical (Moracova et al., 2015, de Sousa et al., 2021). A study by Moracova et al., (2015) showed that oleic acid does not affect cell membrane integrity at concentrations less than 1 mM while palmitic acid enhances lactate dehydrogenase (LDH) leakage at concentrations as low as 0.25 mM. Many ratios have been tested and previous studies have used different ratios (3:1, 2:1 or 1:1) of oleic and palmitic acid to induce steatosis in HepG2 cells (Donato et al., 2009, Cui et al., 2010). In these studies, the total fatty acid concentrations varied from 0.5 to 2 mM and it was shown that the cells exhibited intracellular accumulation of lipid droplets and triglycerides (Willebrords et al., 2015). Although many ratios have been tested it is frequently reported that administering a combined concentration of 0.5 mM oleic and palmitic acid in a 2:1 molar ratio results in significant fat accumulation, insulin resistance and low-grade inflammation in HepG2 cells after 24 hours representing a mild model of steatosis (Liang et al., 2015, Dave et al., 2018).

As well as fatty acid models, several drug-induced steatosis models have been explored in HepG2 cells including the administration of tetracycline, sodium valproate, amiodarone and tamoxifen (Donato et al., 2009). Tetracycline has been commonly used and studies have demonstrated that HepG2 cells and rat primary hepatocytes treated with tetracycline show increased intracellular lipid accumulation (Donato et al., 2009, Choi et al., 2015, Garcia-Canaveras et al., 2016). Choi et al., (2015) reported that HepG2 cells treated with 100 and 200 μM tetracycline exhibited an increase in lipid accumulation after 24 hours. The literature agrees that tetracycline induces a concentration-dependent increase in steatosis up to a maximum dose of 800 μM before cytotoxicity occurs (Donato et al., 2012). Studies have also shown that single doses of valproate between 0.5-5 mM induce steatosis in various cell models (Chang et al., 2016, Bai et al., 2017, Yan et al., 2021).

1.8 3D spheroid models

Although 2D monolayer cultures are well established for creating *in vitro* NAFLD models and their low cost and easy handling make them suitable for high-throughput screening, there are some limitations with their use (Stampar et al., 2021, Ramos et al., 2022). The most important being the lack of multiple biological functions including cell-to-cell and cell-to-matrix contact which mean 2D cell cultures do not accurately mimic the natural cell microenvironment (Bialkowska et al., 2020, Stampar et al., 2021). This can result in modified cell signalling pathways and reduced expression and activities of several hepatic enzymes implicated in the metabolism of xenobiotic substances (Pingitore et al., 2019, Ingelman-Sundberg and Lauschke, 2021, Stampar et al., 2021). Furthermore, as mentioned above HepG2 cells have reduced CYP expression compared to primary hepatocytes making their use in *in vitro* models less reliable. In addition, studies have shown that CYP enzyme expression is further downregulated in HepG2 monolayer cells after 24 hours of culturing meaning they are less suitable for long term dosing studies (Mizoi et al., 2020, Stampar et al., 2020, Ingelman-Sundberg and Lauschke, 2021).

Consequently, while monolayers have been routinely used to understand the molecular mechanism of disease they do not represent the complexity of human tissues. Therefore, there is a growing need for better *in vitro* models mimicking the liver's complexity and this has led to growing interest in 3D spheroid models (Pingitore et al., 2019). 3D culture is emerging as a bridge between the easy-to-use 2D cell cultures and more complex *in vivo* models (Jensen and Teng, 2020). By maintaining hepatic cell proliferation within a controlled microenvironment 3D liver models better mimic the *in vivo* phenotype with respect to cell shape, behaviour and morphology and create an environment with tightly packed 3D multicellular aggregates providing enhanced cell-to-cell contact and extracellular matrix components (Kozyra et al., 2018, Pingitore et al., 2019, Bialkowska et al., 2020, Stampar et al., 2021, Ramos et al., 2022).

Table 1.1. Comparison of 2D and 3D cell culture methods (Adapted from: Kapalczynska et al., 2018).

Type of culture	2D	3D
Time of culture formation	24 hours	17 to 21 days
Culture quality	High performance, reproducible, easy to interpret, simple culture	Lower performance and reproducibility, cultures more difficult to carry out
In vivo imitation	Do not mimic the natural structure of the tissue	Mimic the *in vivo* environment more closely
Cell interactions	Deprived of cell to cell and cell to extracellular environment interactions	Increased cell to cell and cell to extracellular environment
Characteristics of cells	Changed morphology, loss of diverse phenotype and polarity	Preserved morphology, diverse phenotype and polarity
Access to essential compounds	Unlimited access to oxygen, nutrients and metabolites	Variable oxygen, nutrient and metabolite access
Molecular mechanisms	Changes in gene expression, mRNA splicing, topology and biochemistry of cells	Same expression of genes, splicing, topology and biochemistry of cells as *in vivo*

Since the development of the first spheroid model in the 1970s by Sutherland et al., (1971) multiple techniques have been used to establish culture systems of increasing sophistication; these include spheroids, organoids, liver-on-a-chip and bio-printed platforms (Ramos et al., 2022). Spheroids represent a very promising 3D cell model. They can be cultured under static or dynamic conditions, using many techniques, ranging from hanging drop cultures, spinner flasks, non-adhesive surfaces, micro-moulding and bioreactors (Stampar et al., 2021).

However, the most popular method of spheroid culture in NAFLD studies is by liquid overlay in which cell suspensions are cultured on ultra-low adherent surfaces allowing cell-cell adhesion rather than adherence to the flask this is shown in Figure 1.7 (Ryu et al., 2019). These 3D models have helped to elucidate the role of hepatocytes in NAFLD, the mechanism by which insulin resistance elicits *de novo* lipogenesis and lipid accumulation through the administration of monosaccharides and fatty acids as they are more reflective of the *in vivo* environment (Kozyra et al., 2018, Ramos et al., 2022).

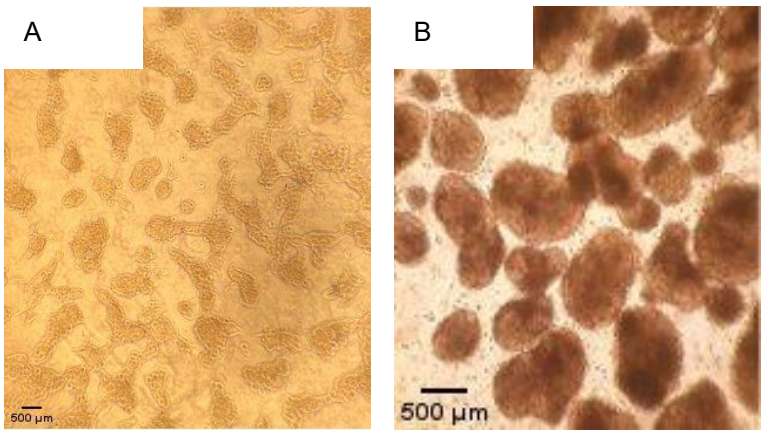

Figure 1.7 Light microscope images of HepG2 spheroids. A. HepG2 monolayer cells. B. HepG2 spheroids.

HepG2 spheroids have been reported to have higher expression of some CYP enzymes (approximately 2-fold higher) compared to monolayer models (Mizoi et al., 2020, Stampar et al., 2020 and Ingelman-Sundberg and Lauschke, 2021). They also display functional bile canaliculi, increased albumin expression and drug transporters and xenobiotic receptors that mediate induction of CYP450 enzymes (Ramaiahgari et al., 2014). Spheroids can survive up to 28 days without the need for passaging giving them an advantage over monolayers which need to be passaged every 4-5 days (Shah et al., 2017, Kozyra et al., 2018). Spheroid cultures can also be used for repeat dose studies. Furthermore, upon treatment with pathological concentrations of fatty acids, carbohydrates, or insulin, hepatic spheroids enabled induction and investigation of steatosis for up to 5 weeks offering an environment more reflective of clinical settings (Kozyra et al., 2018, Stampar et al., 2021, Ramos et al., 2022). As spheroids show greater expression of genes involved in xenobiotic metabolism, they have increased

sensitivity to hepatotoxins and compounds requiring metabolism (Edmondson et al., 2014, Shah et al., 2017, Kapalczynska et al., 2018). As there is growing interest in their use spheroids have been used in the study of NAFLD and in drug-induced liver injury where they display many *in vivo* phenomena (Kozyra et al., 2018, Lasli et al., 2019, Cox et al., 2020, Frandsen et al., 2022, Tutty et al., 2022). A study by Kozyra et al., (2018) demonstrated that 3D spheroids dosed with oleic and palmitic acid creates a steatosis model capable of demonstrating insulin resistance as well as the reversibility of steatosis. Frandsen et al., (2022) also reported that HepG2 spheroids dosed with oleic and palmitic acid displayed changes in lipid accumulation and other lipidome changes similar to those seen in vivo. These studies indicate that 3D models are well suited to the study of steatosis. Although 3D spheroid models have been used in the study of drug-induced liver injury, studies specifically looking at drug-induced steatosis in spheroids are limited.

To further improve *in vitro* studies and to create an environment that represents the complete *in vivo* phenotype there is also growing interest in co-culturing models with Kupffer or stellate cells. These models reflect the impact of cytokine signalling and demonstrate the progression to NASH as they are capable of mimicking steatosis as well as inflammation (Muller and Strula, 2019, Ouchi et al., 2019, Bialkowska et al., 2020). Such so-cultured models would provide a powerful tool to examine the effects of free fatty acid accumulation on the inflammatory process and give a better understanding of the progression of steatosis to NASH (Soret et al., 2020).

1.9 Detection and diagnosis of NAFLD

Since NAFLD exists as a spectrum of diseases, there are currently no specific and sensitive biomarkers for diagnosis (Sanal, 2015). An early diagnosis of NAFLD is dependent on the detection of steatosis (Sanal, 2015). However, steatosis and the early stages of NAFLD are typically asymptomatic which means many patients are not identified until the disease has progressed to NASH or further (Piazolla and Mangia, 2020). To date there are also no licensed pharmacological treatments for NAFLD and while bariatric surgery is effective in a small proportion of patients, diet and exercise

remain the cornerstone of disease management. This is because of evidence that suggests a 10% body weight loss allows a reversion of steatosis and inflammation (Ramos et al., 2022).

In patients with suspected NAFLD the aminotransferase enzymes, alanine transaminase (ALT) and aspartate transaminase (AST), are routinely monitored as general liver function tests to identify nonspecific hepatocellular damage (Neuman et al., 2014). However, in the absence of advanced liver disease or necrosis it is typical to observe normal or only mildly elevated levels of both enzymes (Neuman et al., 2014). In fact, approximately, 80% of patients with steatosis have normal enzyme levels making the measurement of these enzymes very unreliable and non-sensitive, they also lack specificity to NAFLD (Neuman et al., 2014).

To date, biopsy remains the “gold standard” for the diagnosis and prognosis of NAFLD (Moolla et al., 2020). This is despite the fact it is an expensive and invasive procedure with high sampling error and a risk of complications including pain, bleeding and in very rare cases death (Piazolla and Mangia, 2020). Due to poor patient acceptance of liver biopsies, there is an urgent need for reliable, accurate and non- or minimally invasive biomarkers.

In an effort to improve diagnosis of liver disease and injury several non-invasive tools, including clinical and imaging-based markers and algorithms, including the fatty liver inhibition of progression (FLIP) algorithm, have more recently been developed (Moolla et al., 2020). The FLIP algorithm is a simple histological algorithm based on a scoring system, known as the SAF score (steatosis, activity, fibrosis) intended for pathologists to reliably diagnose NASH (Bedossa, 2014, Moolla et al., 2020). The FLIP algorithm uses the presence of steatosis, grade of ballooning-change and lobular inflammation to assess the severity of NASH (Lee et al., 2020). Grade 1 or 2 ballooning change which is defined as swelling and rounding of hepatocytes and lobular inflammation are the minimum diagnostic criteria of NASH used in the FLIP algorithm. Histological scoring systems have been very successful in the evaluation of chronic liver diseases and although effective in improving diagnosis they do not provide all the information that can be conveyed by a liver biopsy and are considered as additional tools to liver biopsies (AlShaalan et al., 2015).

Alternatively, the fatty liver index comprising BMI, waist circumference serum triglyceride and gamma glutamyl transferase (GGT) levels is another algorithm used for the diagnosis of NAFLD (AlShaalan et al., 2015). However, the fatty liver index is not able to quantify lipid accumulation and does not always correlate well with the amount of fat in the liver define by magnetic resonance spectroscopy therefore its use as a quantitative biomarker of NAFLD is limited (Fedchuk et al., 2014). Inflammatory cytokines and chemokines including TNF-alpha and interleukin-6 can be used to help with the diagnosis of the inflammation associated with NASH (Neuman et al., 2014, Piazzolla and Mangi, 2020). Several other tests such as the fibrosis-4 index and the liver stiffness measure are available to help rule out the later stages of fibrosis and cirrhosis. However, these tests cannot accurately differentiate between steatosis, NASH or different severities of NASH. There is also no single test available to identify steatosis, or to predict and monitor the disease progression and these tests are best used in combination leaving the need for more reliable ways of diagnosis and staging NAFLD (Piazzolla and Mangia, 2020).

The importance of diagnosing steatosis early is highlighted by the fact that 20 – 30 percent of all NAFLD patients progress to NASH, liver fibrosis and cirrhosis and NAFLD is the second most common indication for a liver transplant (Drescher et al., 2019). Reliable non-invasive biomarkers and screening techniques to diagnose NAFLD at the earliest stages could present patients with the opportunity to reverse the disease (Drescher et al., 2019). In the majority of cases dietary and lifestyle changes can positively impact on the severity of both steatosis and NASH. Similarly, to NAFLD currently the only way to identify DIFLD is by the use of imaging methodologies or liver biopsies. Therefore, there is a great unmet need for non-invasive biomarkers that are able to identify drug-induced steatosis and steatohepatitis. Having reliable biomarkers would be especially beneficial for preclinical testing during drug development in order to determine the potential for new drugs to induce DILFD (Pavlik et al., 2019). The lack of biomarkers for both NAFLD and DIFLD is further complicated by the fact that some patients may have pre-existing NAFLD or NASH before receiving a drug known to cause DILFD. In addition, there is a need for specific biomarkers that are able to differentiate between underlying NAFLD and DILFD (Pavlik et al., 2019).

1.10 Biomarker studies

Biomarkers are unbiased differential indicators of disease onset which can help to stage disease progression and offer insights into the relative severity of disease (Neuman et al., 2014). Methods common for biomarker discovery include proteomic, genomic and metabolomic approaches (Kulasingam and Diamandis, 2006).

As explained above there is a great need for improved biomarkers for NAFLD and a number of *in vivo* and *in vitro* models of steatosis have been used in the search for potential biomarkers in NAFLD and DIFLD (Caussy et al., 2019, Masoodi et al., 2021, Nimer et al., 2021, Shao et al., 2022A).

Proteomics is typically used to investigate changes in proteins and describes the large-scale analysis of protein expression patterns, profiles and identification (Miller et al., 2021). The identification of specific proteins, either as novel biomarkers or as over/under expressed markers, can provide useful biomarkers for early diagnosis and therapy of disease and toxicity (Lim et al., 2014). The advancement of proteomics analysis tools has been taken advantage of for studying NAFLD in terms of the disease and diagnosis (Lim et al., 2014, Miller et al., 2021). This has led to changes in cytochrome P450 (CYP) enzymes being reported in the livers of patients with steatosis, and in both *in vivo* models of steatosis in experimental animals and *in vitro* models of fat-overloaded cells (Gomez-Lechon et al., 2009). These findings have suggested an association between increased lipid deposition and impaired CYP expression and activity (Fisher et al., 2009, Gomez-Lechon et al., 2009, Basaranoglu et al., 2013, Albadry et al., 2022).

However, one field of biomarker research that has become more popular is the application of metabolomic and metabonomic techniques to determine changes to the metabolome (Gowda and Raftery, 2016). The metabolome refers to the complete set of low molecular weight metabolites that are produced by cells in all metabolic pathways (Steuer et al., 2019). Metabolites serve as a direct signature of biochemical activity and are easier to correlate with phenotypes unlike genes or proteins whose functions are subject to epigenetic regulation and post translational modifications (Antcliffe and Gordon, 2016).

1.11 Metabolomics and metabonomics

The study of the metabolome focuses on the concentrations and fluxes of low molecular weight metabolites found in cells (of molecular weight <1000 Da). In doing so studies provide detailed information on metabolite patterns of change and quantification of the individual metabolites which can increase understanding of biological phenotypes and help with deciphering physiological mechanisms.

Two terms are used for metabolite profiling and quantification: metabolomics and metabonomics. Metabolomics is defined as a comprehensive and non-selective analytical chemistry approach used to identify and quantify the metabolome under a given set of conditions (O'Gorman et al., 2013). While the metabonomic approach is typically used to assess patterns of change for the quantitative measurement of metabolites in response to a stimulus, such as disease, toxicity, or a drug (Antcliffe and Gordon, 2016). Therefore, metabolomic studies can provide accurate understanding of biochemical events inside the cell and aid the identification of potential biomarkers while metabonomics provides information on pattern profiles. (Gitto et al., 2018). While both refer to separate measurements the two terms are often used interchangeably.

The study of metabolite changes may identify useful biomarkers or drug targets for disease and toxicity (Patti et al., 2012, Cui et al., 2020, Ioannou et al., 2020). As a result, metabolomics has become a common omics tool for the study of NAFLD focusing on both early detection as well as identification of altered pathways (Patti et al., 2012, Ioannou et al., 2020, Perakakis et al., 2020).

The analysis of the metabolome can be carried out using both nuclear magnetic resonance (NMR) and mass spectroscopy. Each technique has its own strengths and weaknesses highlighted in Table 1.2 with the main issue being the identification and validation of metabolites. However, when used together these techniques tend to provide complementary data (Antcliffe and Gordon, 2016). NMR spectroscopy was employed in this project due to its ability to detect many metabolites in one measurement, its reproducibility and easy sample preparation making it more suitable for larger metabolomics experiments. It was employed to identify metabolite changes

and monitor patterns of metabolite change in HepG2 cells dosed with either fatty acids, tetracycline or valproate.

Table 1.2. Comparison of NMR vs Mass spectrometry for metabolomics

	NMR	Mass spectrometry
Sensitivity	Lower but can be improved with cryo- and microprobes, higher field strength and dynamic nuclear polarisation	High and detection limit reach nanomolar
Selectivity	Generally used for nonselective analysis, however selective experiments are available such as TOCSY	Can be used for selective and nonselective analyses
Sample measurement	All metabolites that have NMR concentration level can be detected in one measurement	Usually need different chromatography techniques for difference classes of metabolites
Sample recovery	Non-destructive; samples can be recovered and stored. Therefore, several analyses can be carried out on the same sample	Destructive technique but only a small amount needed
Sample preparation	Minimal preparation required	More demanding, as columns and optimisation of ionisation conditions are needed
Reproducibility	Very high	Moderate
Target analysis	Not relevant for targeted analysis	Superior for targeted analysis

1.11.1 NMR Spectroscopy

The use of ^{1}H NMR spectroscopy enables the simultaneous analysis of low molecular weight metabolites from a variety of metabolic pathways (Nicholls et al., 2001). NMR is a non-destructive and reproducible technique giving it an advantage over other techniques when analysing biological samples, as samples can be recovered and stored meaning several analyses can be carried out on the same sample (O'Gorman et al., 2013, Emwas, 2015).

NMR spectroscopy uses the spin properties of nuclei in a strong magnetic field to analyse chemical structures. Nuclei with an odd number of protons and neutrons possess a nuclear spin meaning they can produce their own electromagnetic field (Rosen and Brady, 1983). However, the spin properties of protons and neutrons can cancel each other out giving a net spin of zero meaning nuclei with an even number will not produce an NMR signal (Koutcher and Burt, 1984). Therefore, only isotopes

such as ^{1}H, ^{13}C and ^{15}N whose spin quantum number is >1/2 are used for analysis (Shenderovich and Limbach, 2021).

When placed in the magnetic field protons within the nuclei have two spin states: one in line with the magnetic field and the other opposed to it (Antcliffe and Gordon, 2016). A radio frequency is applied which excites the nuclei from their base energy state to a higher energy state (Figure 1.8). When the radio frequency is removed the nuclei return to their base energy state, they re-emit radio wave photons which produce an interference pattern called a free induction decay (FID) (Rosen and Brady, 1983, Tognarelli et al., 2015, Antcliffe and Gordon, 2016, Esvan and Zeinyeh, 2020). The FID is converted into an NMR spectrum using a mathematical process called Fourier transformation (Rosen and Brady, 1983, Esvan and Zeinyeh, 2020). The Fourier technique transforms the function of time whereby a single proton is observed as a wave in time into a function of frequency, this generates an NMR spectrum with chemical shift shown on the x-axis and intensity on the y-axis (Esvan and Zeinyeh, 2020). Each peak or multiplet on the NMR spectrum represents a different chemical environment.

To facilitate data analysis the obtained raw NMR data must first be processed using chemical shift referencing, phase and baseline corrections. NMR spectra should be referenced against an internal chemical shift standard, this is important for correct peak alignment and future multivariate analysis (Emwas et al., 2016, Emwas et al., 2018). This reference peak is typically set at 0.00ppm when 3-(trimethyl-siyl) propionic acid (TSP) is used as the standard for aqueous samples or tetramethylsilane (TMS) for organic samples. Each spectrum is then calibrated to this internal chemical shift standard. Spectra are then phased to ensure all peaks are above the baseline maximising the absorptive character and the symmetry of all NMR peaks over all regions of the spectrum. Baseline correction is then applied to ensure any regions without peaks appear flat aiding analysis (Emwas et al., 2018). It is also important to control pH and temperature while conducting metabolomics experiments (Bhinderwala et al., 2022). Changes in pH can have an effect on metabolite stability and can lead to degradation or transformation. While temperature fluctuations can also accelerate degradation of some metabolites that are sensitive to temperature like amino acids and lipids (Trainor et al., 2020, Putko et al., 2024). Alterations in pH and temperature

can also have an effect on the chemical equilibrium of ionisable metabolites influencing their detection and quantification (Trainor et al., 2020, Putko et al., 2024). Furthermore, accurate control of pH and temperature is essential for the proper calibration of analytical instruments in NMR ensuring reliable quantification and identification of metabolites. Controlling both pH and temperature is also essential for maintaining reproducibility and standardisation between experiments (Trainor et al., 2020, Putko et al., 2024).

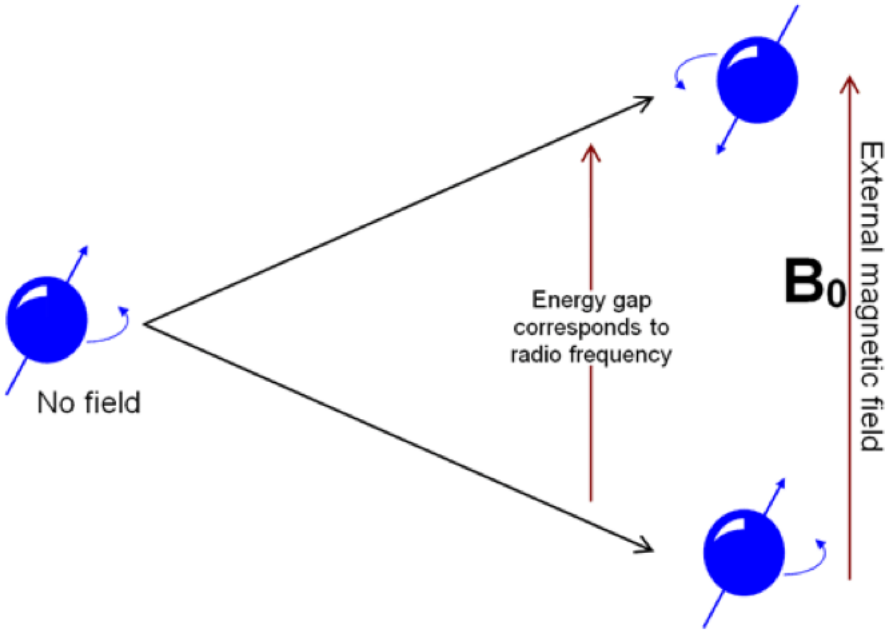

Figure 1.8 The basis of NMR. Hydrogen nuclei resonate between two spin states providing information regarding the chemical structure of molecules. Source: (NMR Lab, 2018).

Despite the ease of use one of the major limitations with using ^{1}H NMR for biological samples and biomarker identification is that large quantities of data are generated leading to spectral congestion and overlapping of peaks on the chemical shift axis making metabolite identification more difficult (de Graaf et al., 2011, Huang et al., 2015). One solution for this is the application of 2D NMR techniques including J-resolved (JRES) ^{1}H NMR spectroscopy which can yield a two-dimensional spectrum separating chemical shifts and J-couplings into different spectral dimensions aiding metabolite identification in complex metabolite mixtures (Huang et al., 2015). However, even with this, to compare the metabolite patterns in different sample spectra, it is usually necessary to apply statistical data reduction and multivariate analysis techniques (Nicholls et al., 2001).

1.11.2 Multivariate Statistical Analysis

Prior to multivariate statistical analyses further NMR spectral processing is required. The first step is known as binning whereby the individual spectra (sample observations) are divided into bins or buckets with fixed or variable widths along the x-axis. These buckets represent a chemical shift region on the NMR spectra and are sufficiently wide to include one or more NMR peaks. The intensity of all the peaks in each bucket is determined by calculating the area under the curve creating a set of integrated values for each region along the x-axis of the NMR spectra. This process is carried out for all sample spectra in the experiment. The data generated, therefore, consists of sample observations (Y) with integrated values for the different chemical shift regions (X). From this a data matrix (or bucket table) consisting of columns of spectral regions for each sample is created (Sousa et al., 2012, Emwas et al., 2018). Since the bucket regions are the same for all samples in the experiment each bucket represents a metabolic descriptor and can be compared for all samples.

Before the data can be further processed, the data must be normalised using pareto scaling to ensure that data from all samples is directly comparable with each other as some samples may have different concentrations of metabolites (Craig et al., 2006, Kohl et al., 2012). Metabolomics datasets contain a wide range of variability from one experiment to the next and can be influenced by many factors that can have an effect on metabolite concentration such as the number of cells extracted in each experiment. However, this variability can be reduced using pareto scaling. Although other scaling methods such as auto-scaling do exist pareto scaling is favoured in metabolomics as it offers a balanced approach to handling variance of metabolites with difference abundance levels (van den Berg et al., 2006). Some metabolites can have higher concentrations which can dominate the analysis masking the concentration of low-abundant metabolites. By dividing each variable by the square root of its standard deviation pareto scaling can lessen the impact of highly abundant metabolites without eliminating their variance thus balancing the influence of both high and low abundance metabolites in the analysis. Also, pareto scaling does not standardise everything to the same level, as auto-scaling does, therefore retaining some degree of biological variation within the dataset (van den Berg et al., 2006, Wheelock and Wheelock, 2013, Worley and Powers, 2013). By

reducing the dominance of high abundance metabolites Pareto scaling can also improve data visualisation in PCA plots and helps enhance performance of statistical methods making it easier to identify trends and patterns (van den Berg et al., 2006). Metabolomics data often exhibits heteroscedasticity where standard deviations can vary complicating statistical analysis and data interpretation. Pareto scaling mitigates this by applying a milder scaling factor compared to auto-scaling (van den Berg et al., 2006).

1.11.3 Principal component analysis

Following normalisation, the first step in multivariate analysis is principal component analysis (PCA). PCA is one of the oldest data reduction approaches (Ma and Dai, 2011) and is a commonly used statistical tool for metabonomic studies. PCA is an unsupervised technique used to reduce the dimensionality of the dataset, while at the same time preserving as much variability as possible (Jolliffe and Cadima, 2016). The creation of a PCA model (Figure 1.9) allows for the identification of a set of unique patterns within a data set which capture the greatest variation present in the original measurements while at the same time displaying trends and patterns. This is achieved in a PCA model by the transformation of the data into fewer dimensions whereby each spectral measurement is reduced to a single scores point (Worley and Powers, 2016). Data points are then projected onto lower dimensions called principal components (PCs).

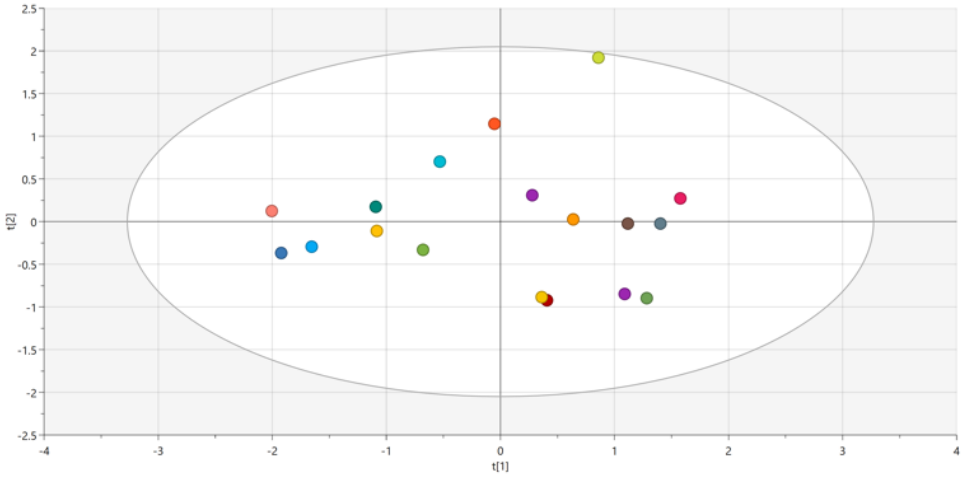

Figure 1.9 PCA Scores Plot.

For the creation of sample scores each chemical shift region in an NMR spectrum forms an axis in a k-dimensional space and the integrated values for each sample are plotted on their corresponding axis within a k-dimensional space. A linear combination of the integrated values for each sample observation is calculated, thereby reducing the data for one sample spectra to a single integrated value (score). Each original spectral sample will have its own score and all scores points can then be projected onto a plane forming a scores plot.

Principal component 1 (PC1) describes the largest variation in the dataset, while PC2 is orthogonal to PC1 and describes the next level of variation (Figure 1.10) (Jolliffe and Cadima, 2016). Each successive PC represents the maximum amount of variation possible that was not accounted for in the previous components. The goal is to find the best summary of the data using a limited numbers of PCs (Lever et al., 2017). Each component captures a certain amount of variance in the total data and this is reported in the fraction of variance. In this study the fraction of variances for the PCA plots ranged from 45-85% for PC1 and 13-21.8% for PC2. The first 2 components were chosen to be analysed in this study as they offer a simplified representation of the data while still capturing the most significant sources of variation in the dataset (Lever et al., 2017).

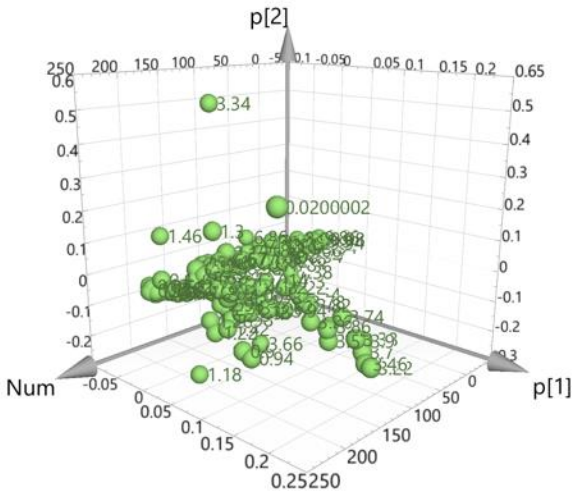

Figure 1.10 Reduction of dimensionality. PC 1 and 2 are projected onto a plane to give a scores plot, each variable has a score along each component.

Two PCs are rotated and projected onto a plane to produce a scores plot with the x-axis representing PC1 and the y-axis representing PC2 (Jolliffe and Cadima, 2016). Each sample is represented as a score along these two components which shows the location of the sample in this model and can be used to detect sample patterns, groupings, similarities or differences (Gergen and Harmanescu, 2012).

A loadings plot can then be used to further interpret the scores plot; each point on the loadings plot represents a bucket region (variable region) on the NMR spectra and reflects the extent of contribution each spectral variable region has on the complete data set (Gergen and Harmanescu, 2012). Variables close to the centre of the plot will be similar to the mean of the data set whereas those furthest away vary more from the mean and contribute most to the sample group separation. Therefore, loadings plots show the variable regions responsible for the clustering and separation of sample observations on a scores plot. Variables that have positive loadings have higher than average values for that variable, and those with a negative loadings have lower than average values.

A PCA analysis can also highlight potential sample outliers which fall outside the 95% confidence interval and are observed outside the ellipse of the scores plot. Outliers identified in a PCA model can be further analysed using the Hotelling's T^2 Range Line plot (Mashuri et al., 2021). However, only those samples which fall above the 99% confidence level on the Hotelling's plot are deemed outliers as some biological variation must be accounted for. This is the multivariate extension of student's t-test and provides a tolerance range for the data in a two-dimensional scores plot. It shows how different each individual sample spectra is from the mean of the samples. If a sample exceeds the 95% confidence level it is assumed to be an outlier and removed from further analysis (Pretzner et al., 2020).

While PCA is a powerful means of analysing spectral data, it will only reveal differences between measurements in its scores if those differences are major contributors to the total variability. Therefore, good separation between groups may not be visible. Additionally, data sets with large intragroup variation do not allow for good intergroup separation on a PCA scores plot as the subtle intergroup spectral differences are easily overwhelmed by intragroup spectral variations (Guo et al.,

2019). Consequently, it is common to use PCA to obtain an overview of the dataset and to assess for outliers before further analyses in which groups are separated according to class (Guo et al., 2019).

1.11.4 OPLS

Unlike PCA, orthogonal partial least squares (OPLS) is a supervised regression method that assesses the relationship between sample groups in the spectral dataset by assessing changes in a descriptor X variable with respect to the response Y variable. OPLS finds the variation in the X variable (NMR spectral data) that is correlated with Y (sample class) (Bylesjo et al., 2007). To generate an OPLS model, sample classes for each measurement are firstly assigned, thus prior sample class knowledge is required for constructing an OPLS model (Worley and Powers, 2016). It also displays the components that are not correlated with the Y variable (intragroup or orthogonal variation) (Wiklund, 2008). A scores plot is also produced from OPLS models. These scores plots show predictive variation between the different groups along the t[1]-discriminating component (x-axis) as well as orthogonal variation (intragroup) along the t[0]-discriminating component (y-axis).

Essentially, OPLS forces scores-space separation, because the integrated orthogonal signal correction filter removes any systematic spectral variation that does not agree with the assigned group (Worley and Powers, 2016). Therefore, separation may be visible even if it was not in the PCA.

One limitation with OPLS analysis is that data interpretation is compromised when there are more than two groups. Therefore, OPLS can be extended to allow for discriminate analysis (OPLS-DA) (Figure 1.11) when two groups are comparatively analysed at a time (Worley and Powers, 2016). OPLS-DA models are used to identify the spectral variables that define the separation between two experimental groups and can therefore enable the identification of biologically relevant changes in the metabolome (Worley and Powers, 2016).

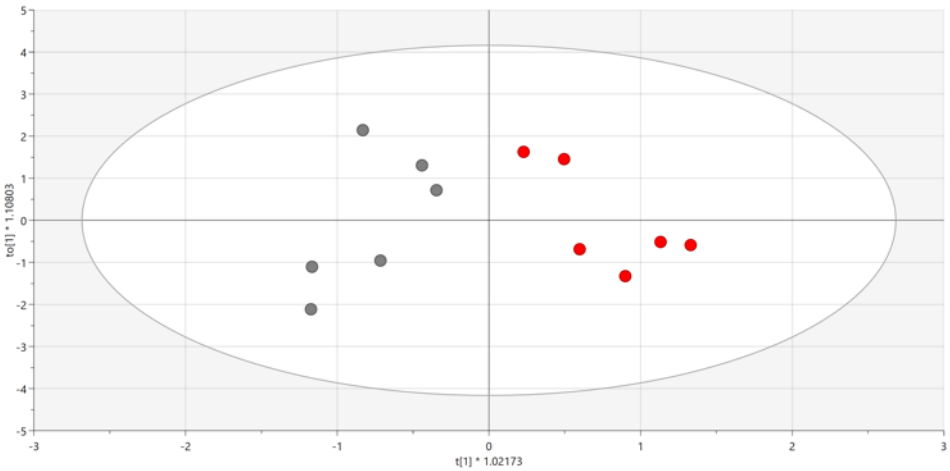

Figure 1.11 OPLS-DA scores plot.

In order to identify metabolite regions contributing to the separation between two groups in an OPLS-DA scores plot the variable influence of projection (VIP) is used. The VIP summarizes the importance of the X-variables (chemical shift regions) to sample separation on the scores plot (Galindo-Prieto, 2015). Any variable regions with a VIP value of greater than one are considered to be significant and contribute to group separation.

The variable regions can then be further visualised using S-plots which is an OPLS-DA loadings plot and combines the correlation and covariance from the OPLS-DA into a scatter plot (Wiklund, 2008). Each point on the S-plot represents a chemical shift region from the original NMR spectra. The variable regions highlighted in red, as shown in Figure 1.12, represent regions with a VIP value greater than one, the S-plot also allows an increase or decrease in these variables to be identified. Variables located in the top right-hand side of the S-plot are increased when compared to the sample group assigned 1 in analysis (e.g. a control group). In contrast variables located in the bottom left-hand side of the S-plot are decreased when compared to the primary group.

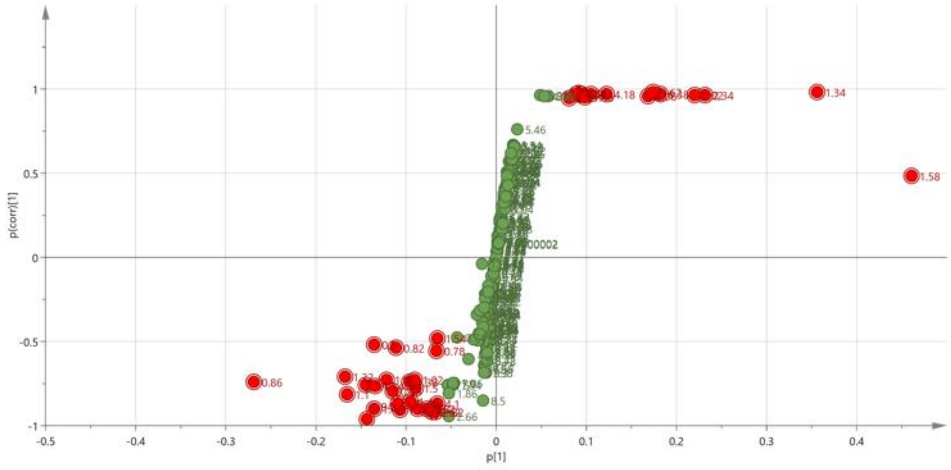

Figure 1.12 S-plot.

The chemical shift regions determined to be significant can be further validated using other statistical methods including the Kruskal-Wallis test. This rank-based nonparametric test is often used to determine whether there are statistically significant differences between two or more groups. Unlike parametric tests, non-parametric tests are based on the idea that the data does not follow normal distribution. Although parametric tests are more powerful and precise than non-parametric tests the main disadvantage of these tests are that they are sensitive to violations of the assumptions such as normality or independence. If the data does not meet the assumptions the results may be inaccurate or misleading. Non-parametric tests are more robust and flexible compared to parametric tests allowing them to handle data that is skewed, has outliers or different scales and units (Nahm, 2016). As the data in this project did not follow normal distribution and was prone to outliers it was decided that the Kruskal-Wallis test would be applied. Chemical shift regions were also assigned a p-value to assess their statistical significance. P-values are defined as the probability under the assumption of no effect or no difference of obtaining a result equal to or more extreme than what was actually observed (Dahiru, 2008). P-values can take any value between 0 and 1 where values close to 0 indicated that the difference is unlikely to be due to chance (Dahiru, 2008). Values closer to 0 are deemed to be more significant.

Once the chemical shift regions that are significantly contributing to the group separation have been determined, the corresponding metabolites can be identified based on the multiplicity of the peaks using the Human Metabolome Database

(HMDB) which stores more than 40,000 different metabolites and published literature. Metabolites can also be validated by spiking samples with metabolite standards.

1.12 CYPs and steatosis

CYP enzymes are found in all major organs but are most abundant in the liver where they are usually expressed in the centrilobular region of hepatic lobules (Albadry et al., 2022). Therefore, diseases that affect the liver and hepatotoxicants can have an impact on the expression of CYP enzymes.

CYP2E1 is perhaps one of the most studied CYP enzymes in relation to NAFLD and was the first documented as modulated in clinical fatty liver disease (Merrell and Cherrington, 2011). CYP 2E1 catalyses the biotransformation of both xenobiotics and endogenous molecules including acetone, a ketone body generated in beta-oxidation of fatty acids. It can also metabolise glycerol and different fatty acids including saturated C12 to C18 fatty acids and some polyunsaturated fatty acids such as arachidonic acid and epoxyeicosatrienoic acid (Massart et al., 2022). More recently, CYP 2E1 has been shown to potentially play a significant role in adipocyte lipid metabolism suggesting it plays a role in lipid metabolism in tissues able to accumulate lipids in normal and pathologic conditions (Massart et al., 2022). Additionally, it has been shown that CYP 2E1 could also be involved in the synthesis and metabolism of lipids by inhibiting PPARα and enhancing SREBP-1c (Wang et al., 2021). The pathogenesis of NAFLD is complex and the theory of “two hits” for progressive disease is well known. The first hit being steatosis caused by insulin resistance and the second is liver damage and inflammation caused by oxidative stress (Wang et al., 2021). The majority of studies have reported increased expression and activity of cytochrome P450 2E1 (CYP2E1) and this increase is thought to play a role in the pathogenesis of NAFLD (Merrell and Cherrington 2011, Garcia-Ruiz et al., 2015, Sukkasem et al., 2020, Wang et al., 2021). It is thought that mitochondrial dysfunction leads to abnormal activation of CYP2E1 producing reactive oxygen species (ROS) promoting oxidative stress leading to the progression of NAFLD (Wang et al., 2021). CYP2E1 is also involved in fatty acid hydroxylation capable of initiating lipid peroxidation (Bell et al., 2010). It has also been implicated as a source of nitro-oxidative stress as it is a

member of the oxidoreductase cytochrome family, oxidising a variety of small molecules including fatty acids further damaging mitochondria leading to the progression of NAFLD (Garcia-Ruiz et al., 2015).

Previous studies in rodent models, human hepatocytes and differentiated human cells have reported increases in CYP2E1 in response to fatty acid administration (Sung et al., 2004, Yao et al., 2006, Sukkasem at el., 2020). Researchers have also observed upregulation in CYP2E1 in morbidly obese patients, general steatosis and NASH due to increase lipid accumulation (Weltman et al., 1998, Emery et al., 2003, Videla et al., 2004, Kohjima et al., 2007, Baker et al., 2010, Merrell and Cherrington, 2011). In contrast a number of studies have reported a decrease in CYP2E1 expression and activity in obese and NASH mouse models potentially due to the development of hyperinsulinemia (Enriquez et al., 1999, Watson et al., 1999, Deng et al., 2005, Ito et al., 2007). As CYP 2E1 is involved in lipid metabolism and has been implicated in the pathogenesis of NAFLD it was chosen to be analysed in this study to confirm its presence in HepG2 cells.

CYP3A4 is the most abundant CYP enzyme in the liver and accounts for the metabolism of over 50% of drugs (Hewitt et al., 2007, Rey-Bedon et al., 2022). Due to its major role in drug metabolism a number of investigators have studied the impact of disease state on the expression levels of the enzymes and a decrease in expression during steatosis and NASH have been reported in rat models (Weltman et al., 1996, Zhang et al., 2007, Hanagama et al., 2008, Osabe et al., 2008). Studies have also reported decreases in CYP3A4 expression and impaired activity in NAFLD patients due to decreased mRNA expression (Weltman et al., 1998, Donato et al., 2006, Donato et al., 2007, Rey-Bedon et al., 2022). Lipid accumulation could also cause down-regulation of P450s by interfering with transcriptional activation of genes or by increasing mRNA degradation leading to decreased expression of these enzymes (Donato et al., 2007).

Although few studies have documented changes in CYP2D6 expression and activity in NAFLD a general downregulation of enzymatic activity in hepatocytes is observed (Donato et al., 2006, Merrell and Cherrington et al., 2011). Previous investigations have demonstrated a relationship between NAFLD progression and decreased activity

of CYP2D6 and CYP3A4 (Yao et al., 2006, Huang et al., 2019). Taken together the increase in CYP2E1 and decreases in CYP2D6 and CYP3A4 expression affect the progression of NAFLD via ER and mitochondrial injury (Sukkasem et al., 2020).

In this project three CYP enzymes were chosen to be investigated: CYP 2D6, 2E1 and 3A4 as increases in CYP2E1 and decreases in CYP3A4 and 2D6 are consistently reported in most NAFLD studies (Merrell and Cherrington 2011, Wang et al., 2021, Sukkasem et al., 2022, Albadry et al., 2022).

Furthermore, the majority of studies on the measurement of CYP levels in NAFLD or steatosis models have been conducted in monolayers or in *in vivo* models and there is little known about changes to CYP enzymes in 3D spheroid models.

1.13 Aims and Objectives

The overall aim of this project is to determine the metabolomic profiles of *in vitro* models of steatosis with the intention of identifying potential biomarkers for the early diagnosis of steatosis.

The major objectives are:

1. To develop three *in vitro* models of hepatic steatosis: a dietary model induced by endogenous fatty acids, and two drug-induced models using tetracycline and valproate, in HepG2 monolayers and spheroids.
2. To evaluate and compare metabolite changes in the steatotic cell models using NMR metabolomics analysis.
3. To investigate the reliability of spheroid and monolayer HepG2 cells in the investigation of steatosis by comparing metabolite changes and assessing CYP expression in all models.

In objective 1, it is known that all three treatments are toxic at high dose levels in HepG2 cells therefore the initial goal will be to identify dose levels high enough to induce mild steatosis without causing cytotoxicity. This will be determined using Oil

Red O staining and a triglyceride assay to confirm lipid accumulation and MTS and LDH assays for cytotoxicity evaluation. The results from the dose response experiments will be used to determine a suitable low and high dose to be used to induce steatosis in spheroids. This is important since it has been suggested that spheroids have greater sensitivity to hepatotoxicants.

Objective 2 will use the steatotic models developed and ^{1}H NMR spectroscopy metabolomics techniques to compare metabolite patterns and identify metabolite changes in response to steatosis in each model. Metabolite changes will be compared between the fatty acid and drug-induced models to determine any similar changes that might be occurring in both models. There is a great unmet need for markers of both diet and drug-induced steatosis, by comparing the models this would allow for biomarkers specific to each model to be identified and could help to differentiate between the two. ^{1}H NMR spectroscopy will be used for this purpose combined with multivariate analysis.

The expression levels of CYP2D6, CYP3A4 and CYP2E1 in both monolayers and spheroids treated with fatty acids, tetracycline and valproate will be determined by Western blotting. For *in vitro* models to be reliable they must be capable of reflecting physiological functions. There are claims that HepG2 monolayers have been shown to have lower CYP expression than 3D spheroids and this will be investigated as part of the validation of the models.

Chapter Two – Material and methods

Chapter 2

2.1 Materials

Methanol, absolute ethanol, isopropanol, chloroform, formalin, hexamethyldisilazane, phosphoric acid, dimethyl sulfoxide-d6 (DMSO-d6), chloroform-d, deuterium oxide (D_2O) and acetic acid were all supplied by Merck, United Kingdom. Glycerol was supplied by Fisher Scientific, United Kingdom.

For cell culture Dulbecco's Modified Eagle high glucose medium (DMEM), Fetal Bovine Serum (FBS) and penicillin/streptomycin (HycloneTM) were purchased from Thermo Fisher Scientific, Horsham, UK. Phosphate-buffered saline (PBS), trypsin HycloneTM were purchased from Merck, UK.

For cell dosing Oleic acid (C18:1), palmitic acid (C16:0), bovine serum albumin (BSA) were all from Sigma Aldrich, UK. Tetracycline hydrochloride (cell culture grade) was purchased from Affymetrix|Thermo Fisher, Horsham, UK. Sodium Valproate was obtained from mpBio, UK.

The nuView Precast Gels were supplied by Generon, Slough, UK. The PVDF Western blotting membrane was from Thermo Fisher Scientific, Horsham, UK. Extra thick blot paper and Goat Anti-Rabbit IgG (H+L) Horseradish Peroxidase Conjugate were obtained from BioRad, Watford, UK. Primary antibodies (Rabbit Polyclonal to Cytochrome P450 3A4, 2D6, 2E1) were all supplied by Abcam, Cambridge, UK. Semi skimmed milk powder, Tween 20 were purchased from VWR International LDT, Lutterworth, UK. SuperSignal™ West Pico PLUS chemiluminescent substrate was acquired from Thermo Fisher Scientific, Horsham, UK.

Coomassie blue G250 and Coomassie blue R250 were purchased from Sigma Aldrich, UK. Glycine was obtained from VWR International LDT, Lutterworth, UK. Tris and sodium chloride (NaCl) came from Thermo Fisher Scientific, Horsham, UK. 3-(trimethyl-siyl) propionic acid (TSP), potassium hydroxide (KOH), magnesium chloride ($MgCl_2$), hydrochloric acid (HCl), sodium dodecyl sulfate (SDS), bromophenol blue,

free glycerol reagent (F6428), glycerol standard (G7793), triton x-100, Oil Red O stain, dithiothreitol (DTT), soybean trypsin inhibitor (SBTI) and tosyl phenylalanyl chloromethyl ketone (TPCK) were all supplied by Sigma Aldrich, United Kingdom

Assay Kits: Triglyceride-Glo Assay Kit, Promega, Chilworth, England. MTS cell proliferation assay kit (colorimetric), lactate dehydrogenase (LDH) cytotoxicity assay kit II (ab65393) were obtained from Abcam, Cambridge, United Kingdom

2.2 HepG2 culture preparation and seeding

HepG2 cells were acquired from AddexBio supplied by Caltag Medsystems, Buckingham, UK ($3x10^6$ cells per vial, Catalog No: C0015002, Lot:0038272). Cells were thawed by gentle agitation in a 37°C water bath for 2 minutes whilst keeping the O-ring and cap out of the water to avoid contamination. The vial was then removed from the water bath and the outside of the vial decontaminated by spraying with 70 % ethanol. All operations from this point on were carried out under strict aseptic conditions.

A sterile falcon tube containing 9.0 mL of complete DMEM containing 10 % FBS and 1 % penicillin/streptomycin (complete culture media) was placed in an incubator at 37°C, 5 % CO_2 for 15 minutes prior to cell recovery to avoid excessive alkalinity. The contents of the vial were then transferred to the falcon tube and centrifuged at 125 x g for 5 minutes. After centrifugation the supernatant was discarded, and the pellet containing live cells was resuspended in 9.0 mL of complete culture media. A 20 µL aliquot of the cell suspension was removed to a fresh Eppendorf to which 20 µL of trypan blue was added for cell counting using a haemocytometer. The remainder of the cells in culture media were dispensed into a new T75 flask which was placed in an incubator at 37 °C (5 % CO_2) for 24 hours to allow the cells to attach. Cell culture media was changed every 48 hours and cells were passaged every 4 days.

For passaging, the HepG2 cell culture was removed from the incubator, media was discarded, and the attached cells washed with 8.0 mL of PBS. The PBS was

discarded, and 4.0 mL of trypsin was added to the flask for approximately 1 minute to detach the cells from the surface of the flask. Detached cells were resuspended in 20 mL of complete DMEM to stop trypsinisation and centrifuged at 400 x g for 6 minutes. After removing the supernatant, the cell pellet was resuspended in 10 mL of culture media. 20 µL of the cell suspension was then taken for counting using a haemocytometer and approximately $0.25x10^6$ cells per 1.0 mL of media were seeded into a new T75 flask.

2.3 Spheroid culture preparation

To prepare 3D spheroids in low attachment 6-well plates, HepG2 cells were seeded at a density of approximately $0.25x10^6$ cells per mL of complete DMEM; a total of 2.0 mL was added to each well ($0.5x10^6$ cells per well). For spheroid culture in 96-well plates approximately $20x10^3$ in 200 µL of media was added to each well.

For all spheroid studies the culture media was changed every second day and spheroids were grown for 17 days before dosing.

2.4 Dosing

For cell dosing of monolayers, for metabolomics and Oil Red O staining experiments HepG2 cells were seeded at a density of approximately $0.25x10^6$ cells per mL of media in 6-well plates. A total of 2.0 mL ($5x10^6$ cells per well) was added to each well and cells were allowed to attach for 24 hours prior to dosing.

Just prior to dosing HepG2 cells were removed from the incubator, media was discarded, and the cells were washed with 1.0 mL of PBS. Then 2.0 mL of complete cell culture media containing either fatty acids, tetracycline or valproate was added to the wells.

For spheroid metabolomics experiments, approximately $5x10^6$ cells in 2.0 mL of complete media were seeded in low attachment 6-well plates and incubated for 17 days. The spheroids were removed from the incubator, media was discarded and replaced with 2.0 mL of culture media containing each treatment.

In all experiments 6 replicates for each dose level of the 3 different treatment models (fatty acids, tetracycline and valproate) were prepared and the plates were incubated for 24 hours at 37°C. Each treatment model had a corresponding media only control and a media with dosing vehicle control (ethanol containing 1% BSA for the fatty acids and DMSO for tetracycline and valproate).

2.5 Preparation of cell dosing solutions

2.5.1 Fatty acid solution

A mixture of oleic and palmitic acid (2:1 combination) was used for dosing HepG2 cells. 50 mM solutions of both oleic and palmitic acid were prepared in ethanol. From these solutions a 2:1 ratio oleic acid and palmitic acid stock solution containing 1 % bovine serum albumin (BSA) was made. A serial dilution of the stock solution in complete DMEM was created to obtain final fatty acid solutions at concentrations of 0.1, 0.25, 0.5 and 1.0 mM. 5 plates in total were prepared one for each dose level and a vehicle control (media containing 2 % ethanol but no fatty acids).

2.5.2 Tetracycline solution

A 160 mM initial stock solution of tetracycline was prepared by dissolving 3.078 mg of tetracycline in 4.0 mL of DMSO. This solution was then diluted to give further stock solutions of 120, 80, 40 and 20 mM. Final dosing solutions of tetracycline at concentrations of 800, 600, 400, 200 and 100 µM tetracycline were prepared by adding 10 µL of each of the stock solutions to 1.99 mL of DMEM. Two control groups were also prepared: one containing 10 µL of DMSO only and the other consisting of media only.

2.5.3 Valproate solution

An 800 mM initial stock solution was prepared by dissolving 0.531 g of sodium valproate in 4.0 mL of DMSO. This stock solution was serially diluted using DMSO to produce solutions at 400, 200 and 100 mM. Final dosing solutions of valproate at concentrations of 0.5, 1, 2 and 4 mM were prepared by adding 75 µL of each stock to 14.925 mL of DMEM. 75 µL of DMSO was also added to 14.925 mL of DMEM to give a vehicle control and 6 wells only contained media (blank control). Plates were incubated for 24 hours at 37°C.

Monolayer HepG2 cells were dosed with all dose levels of each treatment. However, the dose levels for the spheroids were selected based on the results from Oil Red O staining and MTS viability assays. Consequently, spheroids were dosed for 24 hours at concentrations of 0.1 and 0.5 mM of fatty acid solution, 100 and 600 µM of tetracycline and 1.0 and 4.0 mM of sodium valproate.

2.6 MTS assay

Cell viability for HepG2 monolayers after dosing with the different treatments was assessed using a commercial MTS assay kit. For the assay approximately $5x10^3$ HepG2 cells in a total volume of 200 µL were seeded in a 96-well plate and allowed to attach for 48 hours to allow cells to grow to roughly 10 $x10^3$.

Cells were then dosed with either fatty acids, tetracycline or valproate as described in Section 2.5. Six replicates at each dose level were used for this assay. The viability of the controls (ethanol and DMSO) for each model was also tested. The media was removed, and the cells were washed with 100 µL of PBS before 200 µL of fresh media was added to each well. Then 20 µL of MTS reagent was added into each well and the plate was incubated at 37 ºC for 3 hours. Blank wells were prepared by adding 200 µL of fresh media and 20 µL of MTS reagent. The average absorbance from these wells was then subtracted from all test absorbance readings. The plate was shaken

briefly on a shaker and the absorbance was read at 490 nm using a plate reader. Viability was calculated as follows:

Viability (%) = (absorbance of treated cells/ absorbance of control cells) x 100.

2.7 Oil Red O staining

To confirm an increase in lipid accumulation within the monolayer cells or spheroids after dosing with the different treatment models Oil Red O staining was carried out.

To prepare the stock staining solution 60 mg of Oil Red O was dissolved in 20 mL of ethanol, mixed and allowed to rest at room temperature for 20 minutes. Three parts of the stock solution was then added to two parts distilled water and mixed at room temperature for 10 minutes before filtering.

For staining, the 6-well plates containing dosed HepG2 cells were removed from the incubator and the media was discarded from all wells. Cells were washed with 1.0 mL of PBS, which was discarded before cells were fixed in 10% phosphate buffered formalin for 15 minutes at room temperature. Cells were then washed with 60% ethanol and incubated in 2.0 mL of the Oil Red O solution for 30 minutes. Excess stain not taken up by the cells was then washed away by rinsing with distilled water several times before visualising the stained cells under a light microscope at x10 magnification.

To quantify the amount of Oil Red O taken up by the cells 1.25 mL of 100% isopropanol was added to each well to destain the cells and the plates were agitated on a shaker at room temperature for 10 minutes. The absorbance of the Oil Red O eluted from the cells was then read at 520 nm using a spectrophotometer using isopropanol as the blank.

2.8 Triglyceride Assay

A triglyceride assay was used to quantify the lipid accumulation within the cells and spheroids after dosing with either fatty acids, tetracycline or valproate using a Triglyceride-Glo™ assay kit from Promega, UK.

For the assay approximately $20x10^3$ HepG2 cells in 200 µL of DMEM media were plated in 96-well plates and incubated for 24 hours to allow attachment. For spheroid seeding approximately $20x10^3$ HepG2 cells in 200 µL of DMEM media were plated in a low attachment 96-well plate and incubated for 17 days to allow spheroids to form. Cells and spheroids were then dosed with either fatty acids, tetracycline or valproate (as described in Section 2.5) and incubated for 24 hours.

Prior to use all components of the triglyceride assay kit were thawed in a water bath at 22 °C and mixed to ensure homogeneous solutions. The Reductase Substrate, Kinetic Enhancer and Lipoprotein Lipase were then placed on ice while the assay buffers and reagents were prepared. The final volumes prepared depended on number of samples to be assayed.

To prepare the glycerol lysis solution for the assay 80 µL of Lipoprotein Lipase was added per mL of supplied glycerol lysis solution. The glycerol detection reagent for the assay was made by adding 10 µL of Reductase Substrate per mL of supplied glycerol detection solution. This detection reagent was prepared 1 hour before use and incubated at room temperature. After 1 hour 10 µL of Kinetic Enhancer per mL of glycerol detection reagent was added.

When all reagents for the assay had been prepared the treated HepG2 cells were removed from the incubator and media discarded from each well. Cells were then washed twice with 100 µL of PBS. After removing the PBS 50 µL of glycerol lysis solution containing lipoprotein lipase was added to all wells, the plate was then shaken briefly and incubated for 30 minutes at 37 °C. Following incubation, samples were transferred to an opaque white 96-well plate and 50 µL of glycerol detection reagent was added to all wells. The plate was shaken for 30-60 seconds by hand before being

incubated for 1 hour at room temperature. Luminescence was then recorded using a plate-reader.

A standard curve was created by adding 2.0 µL of the 20 mM Glycerol standard provided in the kit to 498 µL of Glycerol Lysis solution to produce an 80 µM glycerol standard and then serially diluted 2-fold by mixing 200 µL of the standard with 200 µL of Glycerol Lysis Solution to give final concentrations of 40, 20, 10, 5, 2.5 and 0 µM glycerol.

Final concentrations of triglycerides within the samples were calculated using the equation below:

$$\text{Glycerol concentration of sample} = \text{STD} \times (RLU_{sample} - RLU_{background}) / (RLU_{standard} - RLU_{background})$$

2.9 Scanning electron microscopy

Scanning electron microscopy was used to confirm that spheroids had formed and to visualise their 3D structure. Spheroids grown in both 6- and 96-well low attachment plates were gently aspirated using a 200 µL pipette tip with the end cut off. Individual spheroids were placed on a glass slide ensuring the spheroids did not get caught between the pipette and the glass slide as this may disrupt and destroy the 3D structure.

The slides were then placed in a container lined with filter paper dampened with ethanol and allowed to dry for 10-20 minutes. Slides were then coated in 1.0 mL 10% formalin and incubated for 2 hours in the tissue culture hood. To each slide 1.0 mL of PBS was briefly added before being dehydrated in a series of ethanol solutions (35, 50, 75, 95, 100% ethanol) for 10 minutes at each concentration. Slides were then placed in a fume hood and 1.0 mL of hexamethyldisilazine was added, the hexamethyldisilazine was allowed to evaporate in the fume hood. This acts as an extra drying step to remove any remaining water from the sample prior to SEM.

For SEM imaging the glass slides were attached to a self-adhesive carbon disc mounted on a 25 mm aluminium stub which was coated with 25 mm of gold using a sputter coater. The stub was then placed into an FEI Quanta 200 FEG scanning electron microscope for imaging at 5KV accelerating voltage using secondary electron detection. Spheroids were visualised and images were taken at magnifications of 100x and 500x.

2.10 Sample collection for ^{1}H-NMR analysis

In the metabonomics studies for both monolayers and spheroids sample collection was carried out 24 hours after dosing. Cell culture medium was removed from the wells, frozen and stored at -80 °C until analysis.

After removing the media, cells were washed with 1.0 mL of PBS before discarding the PBS. Cell metabolism was quenched by adding 400 µL of ice-cold methanol followed by 400 µL of ice-cold distilled water. Cells were detached from the well surface using a cell scraper to ensure that as few cells as possible remained attached to the plate and resuspended in the methanol and water mixture. The cell extracts were then transferred into a fresh Eppendorf tube containing 400 µL of chloroform at -20°C. Samples were agitated at 14,000 rpm on a tube shaker at 4°C for 20 minutes followed by 5 minutes of centrifugation at 16,000 x g.

After centrifugation, the top aqueous layer containing the more polar metabolites was removed, placed into a new Eppendorf tube and dried down in a centrifugal vacuum concentrator. The bottom organic layer was dried overnight in a fume cupboard. Both aqueous and organic extracts were stored at – 80°C until later analyses.

2.11 Sample preparation for ^{1}H-NMR-based metabolomics

Media samples were thawed and 250 µL of each sample transferred to an Eppendorf tube containing 250 µL of ice-cold methanol/water (8:1). Samples were centrifuged at

13,000 rpm for 5 minutes and 100 µL of the supernatant was placed in a new tube and dried in a rotary vacuum evaporator. The dried samples were then resuspended in 600 µL of D_2O containing 1.0 mM TSP to provide a reference peak for calibration of the NMR spectra. Samples were centrifuged at 10,000 rpm for 20 minutes and 550 µL of the supernatant was transferred into 5 mm NMR tubes.

Aqueous extract samples were resuspended in 600 µL of deuterium oxide (D_2O) containing 1.0 mM TSP. Samples were vortexed for 20 minutes followed by centrifugation for another 20 minutes at 10,000 rpm. Then 550 µL of the supernatant was transferred to a 5 mm NMR tube for NMR analysis.

The dried organic fractions were resuspended in 600 µL d-chloroform. The samples were vortexed for 20 minutes followed by a 20-minute centrifugation step at 10,000rpm. Then 550 µL of the supernatant was transferred into a 5 mm NMR tube for analysis.

2.12 ^{1}H-NMR spectroscopy

One-dimensional ^{1}H NMR spectra of cell samples were analysed at 500,000 MHz using a Bruker DRX-500 spectrometer. One-dimensional spectra were acquired using a standard pre-saturation pulse sequence for water suppression with irradiation at the water frequency during the relaxation delay of 4s. Following four dummy scans, spectra were acquired using 512 scans into 64k points with a spectral width of 10,248Hz and an acquisition time of 3.20 s. Experiments were conducted at room temperature.

Two-dimesional J-resolved (JRES) ^{1}H NMR spectra of cell extracts were measured at 500,000 MHz on a Bruker DRX-500 spectrometer. JRES spectra were acquired using standard pre-saturation pulse sequence for water suppression with irradiation at the water frequency during the relaxation delay of 4 s. Following four dummy scans, spectra were acquired using 8 scans into 8K points with a spectral width of 8,192 Hz and an acquisition time of 0.5 s.

All ^{1}H NMR spectra were phase and baseline corrected using Topspin 4.0.8 (Bruker Analytik, Rheinstetten, Germany). Data was then reduced using AMIX (Bruker Analytik, Rheinstetten, Germany) into buckets of 0.04 ppm wide corresponding to the region δ10.0-0.2 ppm giving a total of 250 buckets. The NMR region between 4.6-5.0 ppm was excluded in all aqueous samples to remove the water region from these samples as the residual solvent signal often interferes with analysis of other metabolite signals even after solvent signal suppression (Emwas et al., 2018)

The next step in data processing is known as normalisation. The area under the curve for each region of the spectra was calculated and expressed as an integral value. Then all regions of the spectra were normalised to the sum of the integrals to reduce any significant differences in concentration between individual samples.

From Amix the data was imported into Microsoft Excel and converted into bucket tables which were then transferred into SIMCA 15 (SIMCA V.15, MKS Umetics AB, Sweden). The final step in data processing known as scaling was carried out to reduce the noise in the data. This is a column operation that acts on each spectral intensity across all samples. Mean-centering scaling was applied whereby the mean of each column is subtracted from each value in the column, giving each column a mean of zero. Following this, pareto scaling was performed in which each variable was divided by the square root of its standard deviation (Craig et al., 2006).

2.13 Pattern recognition of ^{1}H NMR analysis

Using SIMCA 15 software, PCA, OPLS, and OPLS-DA analyses were performed. For all metabolomics experiments data was first analysed using principal component analysis (PCA), an unsupervised method of multivariate statistical analysis (O'Gorman et al., 2013). PCA assesses the clustering of the samples in the data set and identifies any outliers that may be present. If a sample is outside the 95% confidence ellipse on the PCA scores plot it may represent a potential outlier in the dataset which can be confirmed using a Hotelling's T2 plot. Any samples above the 99% confidence interval were excluded from further analyses.

Following PCA, orthogonal partial least square (OPLS) and orthogonal partial least square-dimensional analyses (OPLS-DA) were carried out. OPLS is a supervised method of statistical analysis which demonstrates the relationship between X variables (NMR regions on the spectra) and Y variables (sample class). It represents a more bias form of analysis since the sample class is already known. For all metabonomics experiments OPLS scores plots were constructed and used to identify separation between the sample groups along a predictive t[1] discriminating component. Intragroup (orthogonal) variation is visualised along the t[0] axis.

In each study OPLS-DA analysis was also carried out to compare two sample groups at a time. Scores plots were generated for each OPLS-DA model and used to generate variable importance of projection (VIP) predictive and S-plots. The VIP summarizes the importance of the X-variables (chemical shift regions) to sample separation on the scores plot (Galindo-Prieto, 2015). Variables with a VIP score above 1 were considered to be statistically significant and therefore thought to contribute to the sample separation on the OPLS-DA scores plot. These variables were further highlighted on an S-plot (a loadings plot). Variables located in the top right-hand side of the S-plot are increased when compared to the primary group (e.g. a control group). In contrast variables located in the bottom left-hand side of the S-plot are decreased when compared to the primary group.

2.14 Kruskal-Wallis test

The Kruskal-Wallis test is a rank based nonparametric test used to identify statistically significant differences between two or more groups of an independent variable on a continuous or ordinal dependent variable. It is an extension of the Mann-Whitney U test and allows for the comparison of more than two independent groups. The Kruskal-Wallis is also considered to be the nonparametric alternative to one-way ANOVA.

In this project the Kruskal-Wallis test was performed using SPSS statistics 26 software package to confirm statistical significance of metabolite variable regions in the bucket

tables that differ between the sample groups in OPLS-DA models. A p-value of less than 0.05 was considered to be significant.

2.15 Metabolite identification

Following multivariate analyses, the NMR spectra in each study were examined further to determine the multiplicity and chemical shifts of the statistically significant variable regions identified using the VIP plot and a Kruskal-Wallis test. The S-plot was also used to determine if the peaks in these regions were decreased or increased between two comparative sample groups. Using this information metabolites with peaks in the relevant NMR regions were then identified using the Human Metabolome database and published literature.

2.16 Protein Collection from HepG2 cells

Protein samples were collected from monolayers and spheroids 24 hours after dosing with fatty acids, tetracycline or valproate. For monolayer studies cells were cultured and dosed in 6-well plates while spheroids were grown in 96-well plates.

At 24 hours after dosing media was removed from each well and discarded. Then 1.0 mL of protein lysis buffer was added to each well. To make the protein lysis buffer 150 mM NaCl, 1% Triton X-100, 50 mM Tris pH 8 and 1.0 mM of each protease inhibitor (DTT, SBT1, TPCK) was diluted in 100 mL of water. For monolayer samples 2.0 mL of lysis buffer was added to each well while 50 µL of lysis buffer was added for the spheroid models.

Cells were scraped and then incubated for 30 minutes in the lysis buffer under constant agitation at 4 ^{o}C. Samples were then centrifuged at 12,000 rpm for 20 minutes and the supernatant was collected and frozen at -80 ^{o}C.

2.17 Bradford Assay

Protein concentration in the HepG2 monolayer and spheroid cell extracts from all treatment models were measured using the Bradford assay. Bradford reagent was prepared by dissolving 30 mg of Coomassie Blue G250 in 100 mL of absolute ethanol, and adding 55 mL of phosphoric acid, and the solution was then made up to 1.0 L with water.

To create a standard curve, firstly, a stock solution of BSA (200 µg/mL) was prepared. The stock solution of BSA was then diluted in water to produce the following concentrations of standard protein: 0 (blank), 1, 2, 3, 4, 5 6 µg/100 µL. The remaining steps were carried out in triplicate. To 100 µL of each standard sample 1.0 mL of Bradford reagent was added to all tubes, and the tubes were mixed and left for 5 minutes at room temperature. Then the absorbance for each sample was read at 595 nm using the blank sample to zero the spectrophotometer.

Protein samples extracted from dosed HepG2 monolayers and spheroids were diluted 1 in 50 with water. 100 µL of each diluted sample was added to an Eppendorf tube with 1.0 mL of Bradford reagent in triplicate and incubated for 5 minutes at room temperature. The absorbance was read at 595 nm. The BSA calibration curve was used to estimate the protein concentration in the samples taking into account the dilution factor.

2.18 One-dimensional sodium dodecyl sulphate polyacrylamide gel electrophoresis (SDS-PAGE)

SDS-PAGE describes the method of separating proteins in a gel matrix when an electric force is applied. NuView precast gels were used to separate the protein samples collected from the dosed cells.

Protein samples from all treatment models were pre-treated with SDS sample buffer. A x5 concentrated sample buffer was initially made consisting of 62.5 mM Tris HCl,

pH 6.8, 10% glycerol, 2% SDS and 0.05 mg/ml bromophenol blue. This buffer was then diluted with water to create a 2.0 mL x2 sample buffer which contained 50 µL of dithiothreitol (DTT). DTT is widely used to reduce disulphide bonds in the analysis of protein structure and function (Alliegro, 2000). Using the results from the Bradford Assay the volume of each sample equivalent to 10 µg protein was calculated and transferred to Eppendorf tubes to which an equal volume of the x2 SDS sample buffer was added and the sample mixed.

Samples were then heated to 100 ^{o}C for approximately 10 minutes and loaded into wells of the gel. A blank solution containing SDS sample buffer was loaded into any unused wells (10 µL). A protein molecular weight marker (10 µL) was also added to one well in each gel to estimate the molecular weight of the proteins of interest. The gel was placed in the tank and reservoir buffer (25 mM Tris, 0.19 M glycine and 0.1 % SDS) added. A constant voltage of 200 V was applied for 1 hour or until the dye front reached the bottom of the gel. Following this, gels were either stained in Coomassie blue or used for Western blotting.

2.19 Coomassie blue staining

Following electrophoresis proteins were visualised by Coomassie blue staining. Gels were incubated overnight in 0.4% Coomassie blue R-250 in 50% methanol and 10% acetic acid. Gels were then destained until bands were visible following several washes with destaining solution (10% acetic acid, 30% methanol). The molecular weight of the proteins present could be estimated by comparison with the standard protein molecular weight markers.

2.20 Western blotting

For Western blotting, following gel electrophoresis the gels were washed 3 times in transfer buffer (48 mM Tris, 39 mM glycine, 20 % methanol) for 5 minutes each wash to remove electrophoresis buffer salts.

PVDF membrane was cut to the size of the gel and placed in methanol for 2 seconds, followed by a brief wash in water to remove the methanol. The PVDF membrane was then equilibrated in the transfer buffer for 10 minutes. Two pieces of blotting filter pads were saturated in transfer buffer. The semi-dry transfer method was then carried out using a Trans-Blot Turbo Transfer machine. To assemble the semi-dry unit a piece of filter paper pre-soaked in transfer buffer was placed into the cassette, the equilibrated PVDF membrane was placed on top of the filter and air bubbles were removed. The gel was then placed onto the membrane followed by a second pre-soaked sheet of filter paper. The cassette was closed and placed into the machine. The gel was transferred for 30 minutes at 25 volts.

Following the transfer, the PVDF membrane was incubated in blocking solution consisting of 1 % powdered milk in high salt tween (HST) buffer (20 mM Tris HCl pH 7.4; 0.5 M NaCl; 0.5 % Tween 20) overnight at 4 ^{o}C, to prevent non-specific binding of the antibodies to the membrane proteins. The blocking solution was then removed, and membranes were then incubated in primary antibody overnight at 4 ^{o}C. The rabbit monoclonal antibodies to cytochrome 2D6 and 3A4 were diluted 1:1000 and 2E1 was diluted in 1:500 in 1% marvel HST and membranes were incubated in 20 mL of antibody solution overnight at 4 ^{o}C. Protein samples from all monolayer and spheroid models treated with fatty acids, tetracycline and valproate were tested with each antibody.

The primary antibody was removed, and membranes were then washed in HST buffer 3 times for 10 minutes. This was followed by incubation in the secondary antibody, a goat anti-rabbit IgG horseradish peroxidase conjugate antibody diluted in 1:3000 in blocking solution, for 1 hour at room temperature on an orbital shaker.

The secondary antibody was removed, and the blot membrane was washed again 5 times for 10 minutes with HST buffer. The membrane was transferred to a Syngene GeneGnome detector. A 1.0 mL SuperSignal™ West Pico PLUS Chemiluminescent Substrate detection solution was prepared using 500 µL of detection solution 1 and 500 µL of solution 2. The membrane surface was then covered in the detection solution and 5 images were taken at 1-minute intervals. Band intensities were compared using ImageJ.

2.21 LDH assay

Cell cytotoxicity was evaluated using a commercial Lactate Dehydrogenase (LDH) assay which measures LDH leakage from damaged cells. For monolayers approximately $20x10^3$ cells were seeded in 96-well adherent plates and incubated for 24 hours to allow attachment. For spheroids approximately $20x10^3$ cells were also seeded in low attachment 96-well plates and grown for 17 days to allow spheroids to form. Cells and spheroids were then dosed with the different treatments and incubated for a further 24 hours (as described in Section 2.5). After incubation the plates were gently shaken to ensure any LDH released from dosed cells into the media, due to cytotoxic effects of the treatments, was distributed evenly.

The LDH positive control powder was reconstituted by adding 100 µL of LDH assay buffer and was then aliquoted and stored at -20°C until use. The Water Soluble Tetrazolium salt (WST) Substrate Mix was reconstituted in 1.1 mL of ddH_2O and mixed thoroughly for 10 minutes. To prepare enough reaction mix for 100 assays 200 µL of WST Substrate Mix was mixed with 10 mL of LDH assay buffer.

10 µL of the media from treated cells and spheroids was removed from all wells and transferred into a fresh optically clear 96-well plate.

For the assay background control wells were prepared by adding 200 µL of cell culture medium to empty wells in triplicate, these wells allowed for the measurement of reagent and LDH background absorbance values. The value obtained for the background control was then subtracted from all other absorbance readings.

To prepare a positive control for the assay, 30 minutes before the assay was conducted 10 µL of cell lysis solution was added to 3 wells containing cells and spheroids which had been grown in media only. The cell lysis solution kills the cells releasing LDH into the media. After the 30-minute incubation 10 µL of media from these positive controls was also added in triplicate to a fresh 96-well plate.

Then 100 µL of LDH Reaction Mix was added to all wells including the background controls, the plate was mixed and then incubated for 30 minutes at room temperature.

The absorbance of all controls and samples was the read at 450 nm using a plate reader.

The data obtained from the plate reader was analysed using the following equation:

Cytotoxicity (%) = (Test Sample – Low Control) / (High Control – Low Control) X 100

2.22 LIVE/DEAD™ viability

A LIVE/DEAD assay was used to assess viability of the spheroids, the assay is a two-colour assay used to determine viability of cells based on plasma membrane integrity and esterase activity. The LIVE/DEAD assay staining solution contains a mixture of two fluorescent dyes that differentially label live and dead cells. The live cell dye labels viable cells green, it is membrane permeant and non-fluorescent until ubiquitous intracellular esterase removes an ester group producing fluorescence. The dead cell dye labels cells with compromised plasma membranes red. It cannot permeate the cell membrane and binds to DNA with high affinity. Once bound to the DNA the fluorescence increases >30 fold. A modified protocol of the commercially bought LIVE/DEAD™ viability assay (Invitrogen, UK) was used. Spheroids were grown for 16 days and dosed with either fatty acids, tetracycline or valproate and incubated for 24 hours as described in Section 2.5.

To create the cell staining solution 5 µL of calcein AM and 20 µL of ethidium homodimer-1 were mixed and added to 10 µL of PBS. Following dosing, the culture medium was removed from the spheroids and 100 µL of the staining solution was added directly to the cells. Cells were then incubated in the staining solution at room temperature for 30 minutes. Cells were observed using a Zeiss AxioLab fluorescence microscope. The LIVE/DEAD assay was used to visualise cell viable cells; therefore, cells viability was not calculated.

Chapter Three- Fatty acid-induced model of hepatic steatosis in HepG2 cells

Chapter 3

3.1 Introduction

In the present study two models of steatosis were created in HepG2 cells (monolayer and 3D spheroids) by the administration of fatty acids. Oleic and palmitic acid are the most abundant monounsaturated and saturated fatty acids present in the Western diet (Ricchi et al., 2009, Lyall et al., 2018, Zeng et al., 2020). Following intestinal absorption, both fatty acids are esterified into triglycerides and delivered to the liver in lipoproteins (Lyall et al., 2018, Eynaudi et al., 2021). Prolonged exposure to elevated levels of both oleic and palmitic acid in the diet are known to induce an increase in lipid accumulation in the liver (Ricchi et al., 2009, Lyall et al., 2018, Zeng et al., 2020). A similar accumulation of lipids has been demonstrated when both are administered to primary hepatocytes and hepatic cell lines. Therefore, it is common for both fatty acids to be used in the development of *in vitro* models of steatosis (Ricchi et al., 2009, Lyall et al., 2018, Zeng et al., 2020).

Using the newly created *in vitro* models, metabolomic and proteomic changes in the steatotic cells were investigated.

Many studies have experimented with different ratios and concentrations of oleic and palmitic acids varying from 0.5 to 2 mM. However, it has been frequently reported that the administration of a combined overall concentration of 0.5 mM oleic/palmitic acid (in a 2:1 molar ratio) to HepG2 cells results in significant fat accumulation after 24 hours (Donato et al., 2009, Cui et al., 2010, Liang et al., 2015, Willebrords et al., 2015, Dave et al., 2018).

It has also been widely suggested that the use of a 2:1 combination allows for the development of steatosis at a relatively low overall concentration of fatty acids. (Moracova et al., 2015, Nemecz et al., 2019). This is of importance since fatty acids in excess can be detrimental to cell viability and have been reported to promote ER stress and stimulate pro-inflammatory signals resulting in mitochondrial dysfunction and ROS (Mazzolini et al., 2020). Since the current study wished to create a model of

mild steatosis and avoid cytotoxicity a combination of oleic and palmitic acid at a 2:1 ratio was chosen.

However, it was important to first determine the optimum dose levels to use since too high a dose of fatty acids could result in lipotoxicity and too low a dose could be ineffective. Therefore, the first step in this study was to carry out a dose response experiment in the HepG2 monolayers to establish the optimal concentration of fatty acids that would induce steatosis without causing cytotoxicity. Dose levels of 0.1, 0.25, 0.5 and 1 mM oleic and palmitic acid (2:1 molar ratio) were evaluated. Steatosis was then confirmed using Oil Red O staining and a triglyceride assay. Based on the results a low dose capable of inducing early steatosis and a high dose level capable of inducing steatosis without cytotoxicity was chosen for the development of the 3D spheroid model.

Once the two models were developed the second objective of this study was to identify changes in the metabolome of the 2D monolayers and 3D spheroids using NMR spectroscopy and multivariate statistical analysis to find potential biomarkers of steatosis. Cytochrome P450 changes were also analysed using Western blotting.

The identification of biomarkers for early steatosis is of upmost importance since steatosis represents the first stage of NAFLD in humans and can be reversed via a change in dietary or lifestyle factors. However, there remains a great need for better non-invasive and reliable biomarkers for steatosis since none are currently available (Drescher et al., 2019 and Piazolla and Mangia, 2020).

The current study involved the development of both a monolayer and a 3D spheroid model of steatosis. Hepatic cell lines express many differentiated hepatic functions, such as synthesis and secretion of plasma proteins, cholesterol and triglyceride metabolism, bile synthesis and insulin signalling (Donato et al., 2014). However, one major limitation associated with the use of monolayer hepatic cell lines is a reduced CYP expression when compared to primary hepatocytes. In addition, studies have shown that CYP enzyme expression is further downregulated in monolayers after 24 hours of culturing. Therefore, the rationale for the development of a 3D spheroid model in this study is that it is becoming increasingly clear that monolayer cell culture models

are inadequate for reflecting the complexity of human tissues due to the loss of liver-specific functions specifically the expression of phase I and II enzymes (Pingitore et al., 2019 and Ingelman-Sundberg and Lauschke, 2021). Meanwhile 3D spheroids have been reported to show a higher expression of CYP enzymes when compared to 2D models (Mizoi et al., 2020, Stampar et al., 2020 and Ingelman-Sundberg and Lauschke, 2021). This is a result of heterogeneous cell-to-cell interactions in the 3D culture models which offers a similar micro-environment to the *in vivo* situation. Consequently, HepG2 spheroids also display functional bile canaliculi, increased albumin expression, drug transporters and xenobiotic receptors that mediate induction of CYP450 enzymes (Ramaiahgari et al., 2014). The benefits that 3D culture models offer over monolayers has led to growing interest in their use for both disease and toxicity studies (Pingitore et al., 2019, Ellero et al., 2021, Balkrishna et al., 2022).

The low CYP expression in monolayers represents a particular limitation for their use in *in vitro* studies since it has been shown that fatty liver disease can affect the expression of CYP enzymes with a resulting impact on drug metabolism (Aljomah et al., 2015, Woolsey et al., 2015, Jamwal and Barlock, 2020, Sukkasem et al., 2020, Albadry et al., 2022). For *in vitro* models to be reliable for biomarker studies and more relevant to humans they must be able to mimic all metabolic pathways.

A decrease in CYP3A4 expression has been commonly reported in NAFLD (Woolsey et al., 2015, Jamwal and Barlock, 2020, Albadry et al., 2022). Sukkasem et al (2020) also demonstrated down-regulated CYP3A4 in HepG2 cells in response to treatment with oleic acid, while in the same paper the administration of palmitic acid reduced the expression of CYP3A4 and 2D6 due to reduced mRNA expression. It has also been reported that CYP2E1 is downregulated in NALFD patients in terms of protein and mRNA expression (Albadry et al., 2022).

However, other studies reported upregulated activity and expression of CYP2E1 in NAFLD in mice (Woolsey et al., 2015, Jamwal and Barlock, 2020, Albadry et al., 2022). Increased hepatic metabolic substrates such as fatty acids and mitochondrial dysfunction can initiate the expression of CYP2E1. High concentrations of ketone bodies produced from excessive beta-oxidation can also increases CYP2E1 activity and expression (Wang et al., 2021). It is thought that CYP2E1 contributes to oxidative

stress through the production of ROS (Massart et al., 2013, Wang et al., 2021, Di Pasqua et al., 2022). CYP2E1-mediated hydroxylation of some fatty acids can generate cytotoxic lipid intermediates which can further increase ROS production (Bell et al., 2010, Aubert et al., 2011, Wang et al., 2021). The administration of oleic and palmitic acid has been shown to increase levels of CYP2E1 genes in rodents, human hepatocytes and differentiated human cells leading to ER and mitochondrial impairment (Sung et al., 2004, Sukkasem et al., 2020).

The majority of studies assessing CYPs in NAFLD or steatosis models have been conducted in monolayers but there is little known about alterations to CYP enzyme expression in 3D spheroid models. Consequently, the third objective of this study was to analyse and compare CYP expression between the monolayer and 3D models and to evaluate any dose related changes following the administration of fatty acids. CYP expression was evaluated in 2D monolayers and 3D spheroids using Western blotting for CYP antibodies.

3.2 Fatty acid study design

Monolayer HepG2 cells were plated in 6-well plates. A dose response study was carried out by administrating a mixture of 2:1 oleic and palmitic acid at dose levels of 0.1, 0.25, 0.5 and 1.0 mM to HepG2 cells followed by a 24-hour incubation. Six replicates were used for each dose level.

For the 3D spheroid model, the HepG2 cells were plated in low attachment 6-well plates and grown for 17 days before being dosed with fatty acids at concentrations of 0, 0.1 and 0.5 mM.

3.3 Results

3.3.1 Cell viability and cytotoxicity in monolayers

In this study HepG2 cell viability in response to the increasing doses of fatty acid was assessed using an MTS assay as described in Section 2.6. Cytotoxicity was also assessed using the lactate dehydrogenase (LDH) assay as described in Section 2.21.

The MTS assay results, shown in Figure 3.1, revealed no significant difference in HepG2 cell viability compared to the ethanol control at dose levels of 0.1 and 0.25 mM oleic and palmitic acid. However, when cells were dosed at 0.5 - and 1 -mM cell viability was decreased significantly ($p<0.01$ and 0.001, respectively) relative to the ethanol control. At the highest dose level cell viability had fallen to 56% compared to the control viability of 100%.

In the same study the LDH assay (Figure 3.2) results demonstrated no statistically significant increase in cell death at the lower dose levels (0.1, 0.25 and 0.5 mM) when compared to the ethanol control. At 1 mM dose level cell death was approximately 7% greater than the ethanol control values ($p<0.01$). However, this was not considered significant when compared to the positive control. Therefore, it was decided that this dose level would be acceptable for future studies.

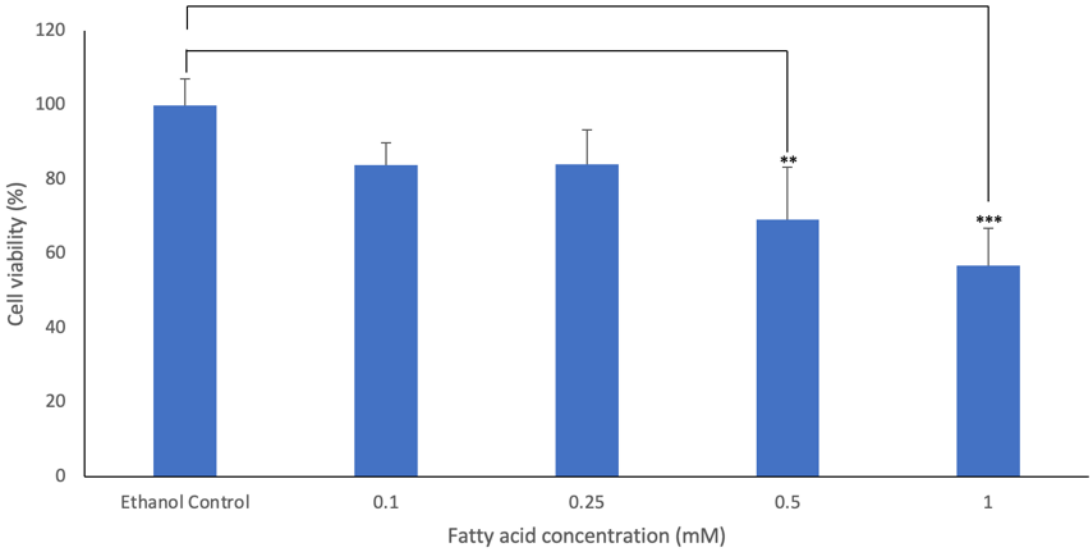

Figure 3.1 HepG2 cell viability in response to increasing fatty acid concentration as assessed by MTS assay. HepG2 cells were treated with a 2:1 mixture of oleic and palmitic acid at concentrations of 0 (ethanol control), 0.1, 0.25, 0.5 and 1 mM and incubated for 24 hours as described in Section 2.5.1. The values shown represent the mean of six replicates. The MTS assay was carried out as described in Section 2.6. Error bars represent standard deviation. Statistically significant differences compared to the ethanol control were analysed using Kruskal Wallis *(**<0.01, ***<0.001).*

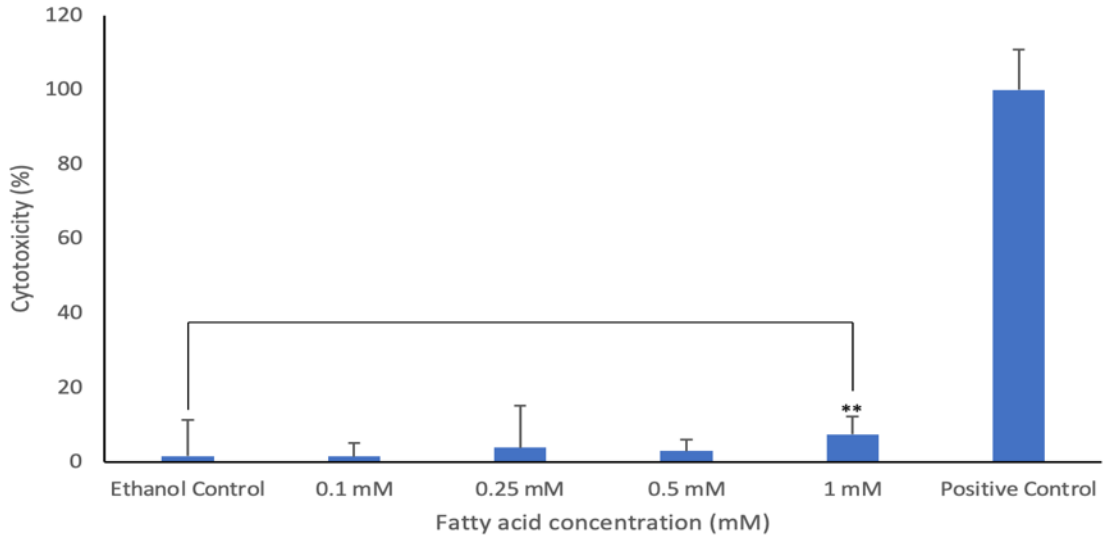

Figure 3.2 HepG2 cell death in response to increasing fatty acid concentration assessed by LDH assay. HepG2 cells were treated with a 2:1 mixture of oleic and palmitic acid at concentrations of 0 (ethanol control), 0.1, 0.25, 0.5 and 1 mM and incubated for 24 hours as described in Section 2.5.1. The value obtained for the positive control represents 100% cell death. The values shown represent the mean of six replicates. The LDH assay was carried out as described in Section 2.21. Error bars represent standard deviation. Statistically significant differences compared to the ethanol control were analysed using Kruskal Wallis *(**<0.01).*

3.3.2 Oil Red O staining of HepG2 cells

In this study to confirm that the exposure of HepG2 cell to fatty acids lead to an increase in intracellular lipid accumulation and to determine if there was a dose-related response, the cells were stained with Oil Red O stain. The Oil Red O reagent stains intracellular lipids red, therefore fat accumulation becomes clearly visible under a light microscope.

The images obtained under the light microscope (Figures 3.3 C-F) suggested a dose dependent increase in lipid accumulation in the fatty acid treated cells. This was observed as an increase in the number, size and intensity of red stained clusters in the dosed cells compared to the control, thus indicating greater stain uptake by these cells as a result of increased lipid accumulation.

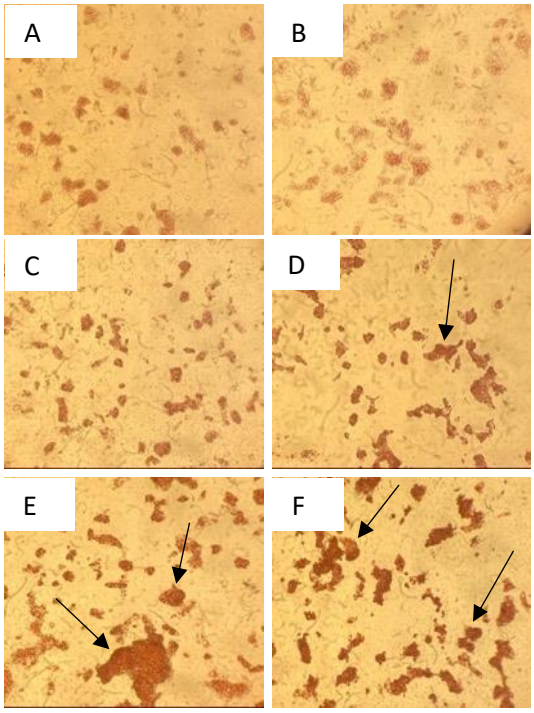

Figure 3.3 Light microscope images obtained of HepG2 cells stained with Oil Red O following treatment with fatty acids. Cells were dosed with a 2:1 mixture of oleic and palmitic acid at final concentrations of 0, 0.1, 0.25, 0.5 and 1 mM followed by a 24-hour incubation, cells incubated in media only or media dosed with ethanol (negative controls) were also included. Cells were stained using Oil Red O as described in Section 2.7. A. media only control, B. ethanol control, C. 0.1 mM, D. 0.25 mM, E. 0.5 mM and F. 1.0 mM fatty acids. The arrows indicate increased red stain uptake to lipid accumulation.

3.3.3 Triglyceride assay in the monolayer

While the Oil Red O staining offered a visual confirmation of the increase in triglyceride accumulation within the cells, it was not possible to quantify how much was present. Therefore, HepG2 cells treated with fatty acids at the different dose levels were lysed, as described in Section 2.8, and cell extracts were collected for the quantification of cellular lipids using a commercial triglyceride assay. The results showed an increase in triglyceride content in the cells collected from treated groups when compared to the ethanol control (Figure 3.4). This increase was statistically significant in the 0.25 ($p<0.05$), 0.5 ($p<0.01$) and 1 mM ($p<0.001$) sample groups when compared to the ethanol control. This would suggest that steatosis has been induced at 0.25 mM and higher.

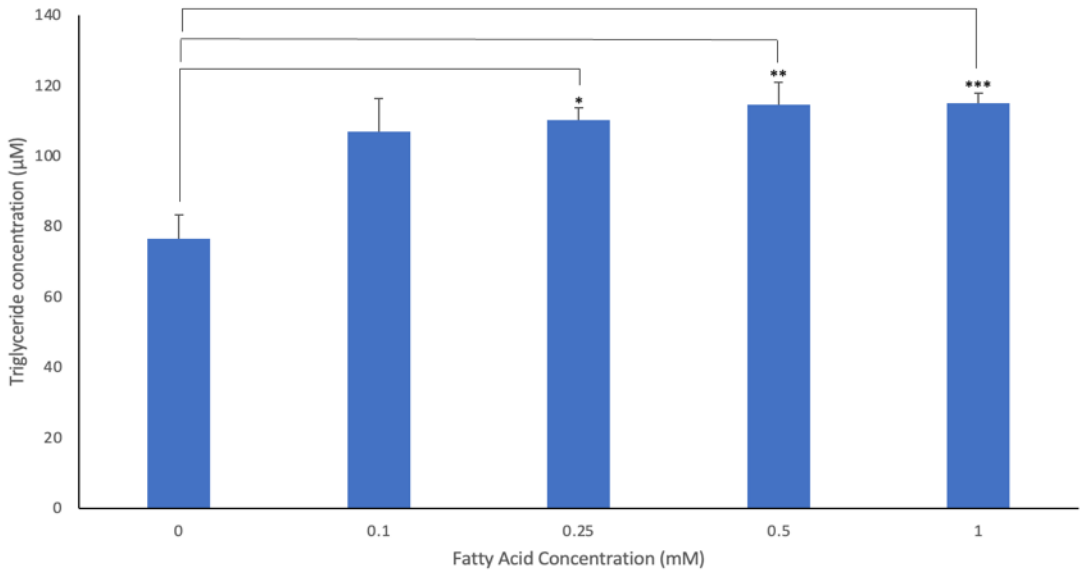

Figure 3.4 Mean triglyceride content in HepG2 cells following treatment with fatty acids. HepG2 cells were treated with a 2:1 mixture of oleic and palmitic acid at concentrations of 0 (ethanol control), 0.1, 0.25, 0.5 and 1 mM and incubated for 24 hours. A triglyceride assay was conducted as described in Section 2.8. The values shown represent the mean of six replicates. Error bars represent standard deviation. Statistically significant differences between treatment groups and controls were analysed using Kruskal Wallis *(*<0.05, **<0.01, ***<0.001).*

3.3.4 Metabolomic analysis in aqueous monolayers cell extracts

In this study HepG2 cell extract samples were also collected following a 24-hour incubation in culture media supplemented with fatty acids at different dose levels for NMR analysis. Aqueous extracts were prepared, analysed by NMR and multivariate analysis was used to determine changes in the metabolite profile in response to the fatty acids.

Visual inspection of the ^{1}H NMR spectra did not reveal obvious differences between spectra of samples from fatty acid treated cells and controls. Therefore, multivariate analysis was employed to statistically analyse metabolomic changes between the different groups. PCA, an unsupervised method of analysis, was firstly carried out and a PCA model was constructed using the NMR data from the aqueous cell extracts. The scores plot obtained (Figure 3.5) revealed some degree of separation between the different sample groups. All of the control samples, except for sample C1 were located in the top half of the scores plot, mostly in the upper right quadrant, and were therefore positive for PC2. There was large intragroup variation and one of the control samples, C5, was just outside the ellipse. To examine this sample further and to determine if it was a true outlier the Hotelling's plot was consulted. It was confirmed from the Hotelling's plot (Figure 3.6) that this sample fell just above the 95% confidence level but was below the 99 percentile. In this project only those samples that were above the 99% confidence level are considered to be outliers and excluded from analysis. Therefore, the spectrum for sample C5 was not deemed to be a true outlier and was thus included in all future analyses.

In the scores plot (Figure 3.5) the aqueous extracts from cells treated with 0.25 and 0.5 mM fatty acids were found on the left side of the plot, negative for PC1 but with some overlap between the two groups. Meanwhile the samples from cells treated at 0.1 mM were all in the lower right quadrant, while the 1 mM samples were positive for PC2 with the exception of sample 1(6).

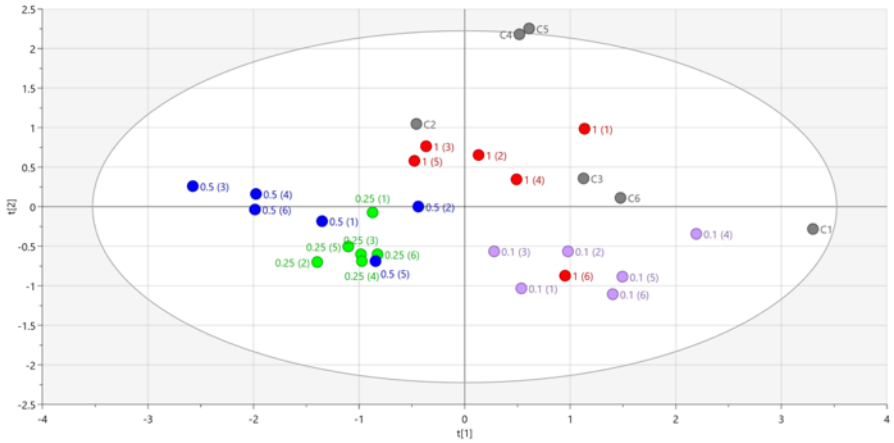

Figure 3.5 PCA scores plot derived from ^{1}H NMR spectra of aqueous extracts from HepG2 cells dosed with fatty acids at increasing dose levels. Cells were dosed with a 2:1 mixture of oleic and palmitic acid at 0, 0.1, 0.25. 0.5 and 1 mM and incubated for 24 hours. Aqueous cell extract samples were collected, and NMR analysis carried out as described in Sections 2.10 and 2.12. Each spot on the plot represents one sample. Grey = ethanol control; pink = 0.1 mM; green = 0.25 mM; dark blue = 0.5 mM; red = 1.0 mM fatty acids.

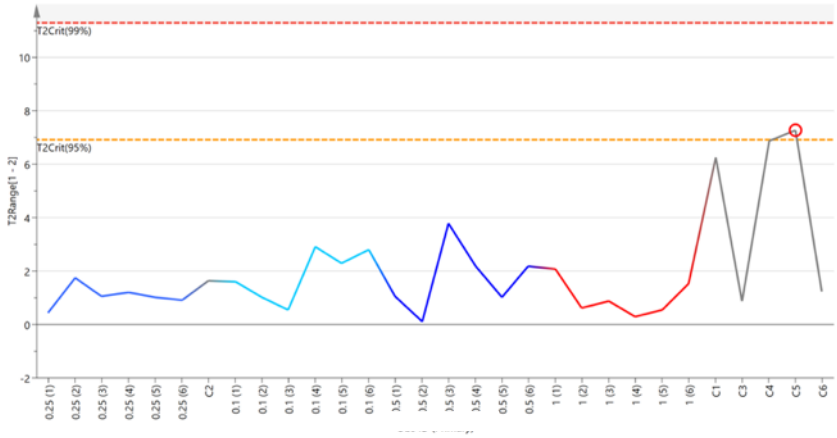

Figure 3.6 Hotelling's T2 plot created from PCA scores plot in Figure 3.5. Samples above the red line of the 99% confidence level are considered to be true outliers. Sample C5 is circled in red.

As the PCA model did not show distinct sample group separation between the treated and control groups along with much intragroup variation, the sample spectra were further analysed using OPLS. This is a supervised statistical approach, used to visualise inter- and intra-group variation based on sample class differences. The OPLS scores plot obtained for this model is shown in Figure 3.7. In general, there was better sample group separation than in the PCA scores plot with sample groups spread along the horizontal predictive t[1] axis according to class. The control samples were located on the left of the plot but showed significant intragroup variation along the orthogonal t[0] axis. Despite this, there was good clustering within the 0.1 mM treated group, and samples in this group were separate from the controls and found on the

lower left quadrant of the plot. Similar to the results seen in the PCA plot there remained some overlap between the 0.25 and 0.5 mM sample groups. This was mostly due to samples 0.5(2) and 0.25(6) being located close together on the scores plot. However, it was still possible to visualise separation between the two groups with samples from the 0.25 mM treated group mostly clustered around the centre of the scores plot while the 0.5 mM were located in the top right-hand corner. The 1 mM treated samples were found on the right lower quadrant of the plot and positive for t[1] separated from all other groups.

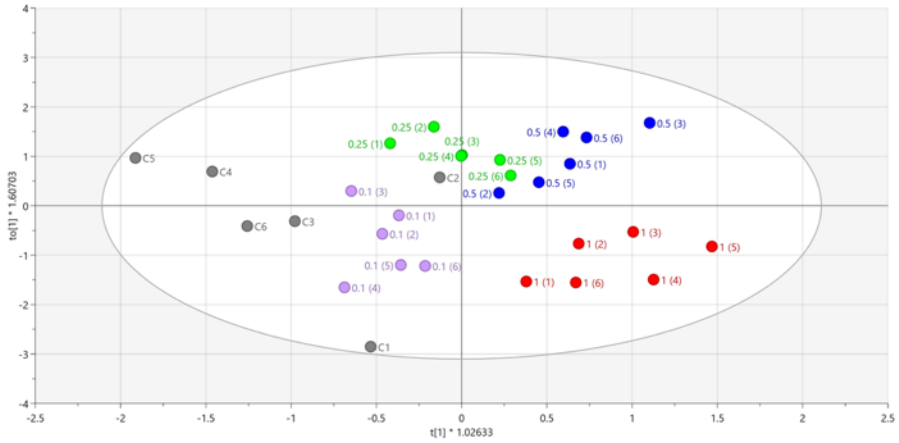

Figure 3.7 OPLS scores plot derived from NMR spectra of aqueous cell extracts from HepG2 cells treated with different dose levels of fatty acids. Cells were dosed with a 2:1 mixture of oleic acid and palmitate at 0, 0.1, 0.25, 0.5 and 1.0 mM and incubated for 24 hours. Samples were collected, and NMR analysis carried out as described in Sections 2.10 and 2.12. Each spot on the scores plot represents one sample. Grey = ethanol control; pink = 0.1 mM; green = 0.25 mM; dark blue = 0.5 mM; red = 1.0 mM fatty acids.

Following OPLS analysis each treated group was then compared directly against the control group using OPLS-DA analyses to identify changes in metabolites due to the treatment with fatty acids at each of the different dose levels. Consecutive dose level groups were also analysed using OPLS-DA to identify dose-related metabolite changes.

Each of the OPLS-DA scores plots constructed (Figure 3.8) demonstrated good separation between the ethanol control and the treated groups for each pair-wise comparison along the t[1] predictive axis. In all plots, the control sample group was located on the left side of the plot. Additionally, similar to the results obtained from the PCA and OPLS analyses there was significant intragroup variation along the

orthogonal t[0] axis for samples from the control group mainly due to control sample 1 (C1).

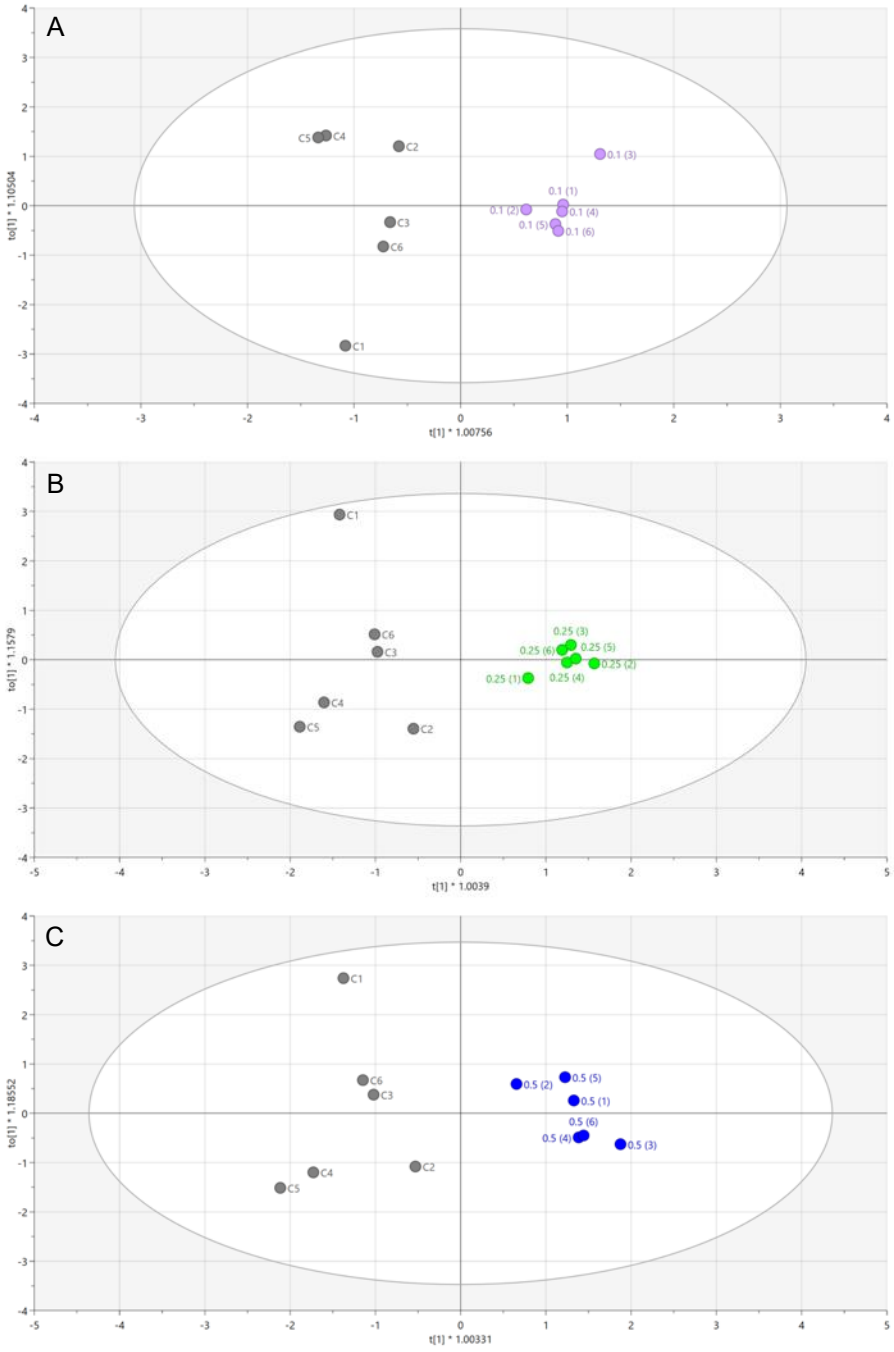

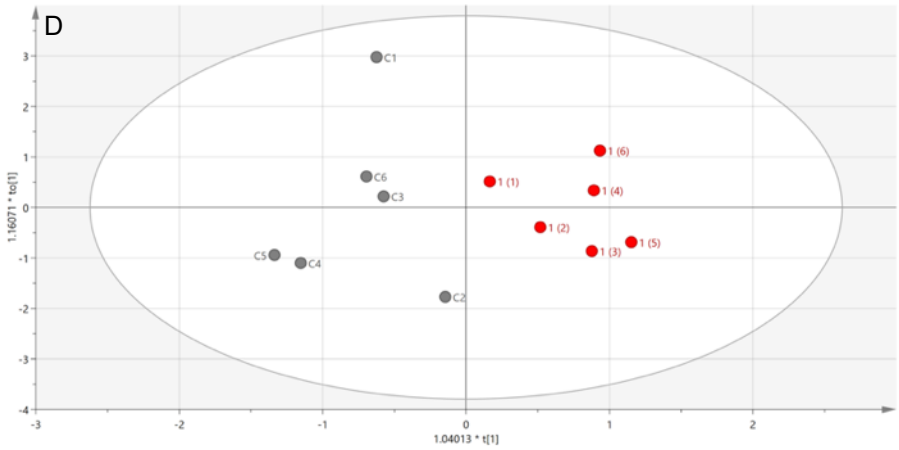

Figure 3.8 OPLS-DA scores plots derived from ^{1}H NMR spectra of aqueous extracts from HepG2 cells dosed with fatty acids at varying dose levels. Cells were dosed with a 2:1 mixture of oleic and palmitic acid at 0, 0.1, 0.25, 0.5 and 1 mM fatty acids and incubated for 24 hours. Samples were collected, and NMR analysis was carried out as described in Sections 2.10 and 2.12. Each spot on the scores plot represents one sample. A. Control vs 0.1 mM fatty acid. B. Control vs 0.25 mM fatty acid. C. Control vs 0.5 mM fatty acid. D. Control vs 1.0 mM fatty acid.

The OPLS-DA scores plots shown in Figure 3.9 demonstrated good separation between the consecutive dose level groups along the predictive t[1] axis. In each plot the lowest dose level group was set as class one in the pair-wise comparison and was located on the left-hand side of the scores plot. Significant intragroup variation was observed along the orthogonal t[0] axis particularly for the 0.1, 0.5 and 1 mM treated groups.

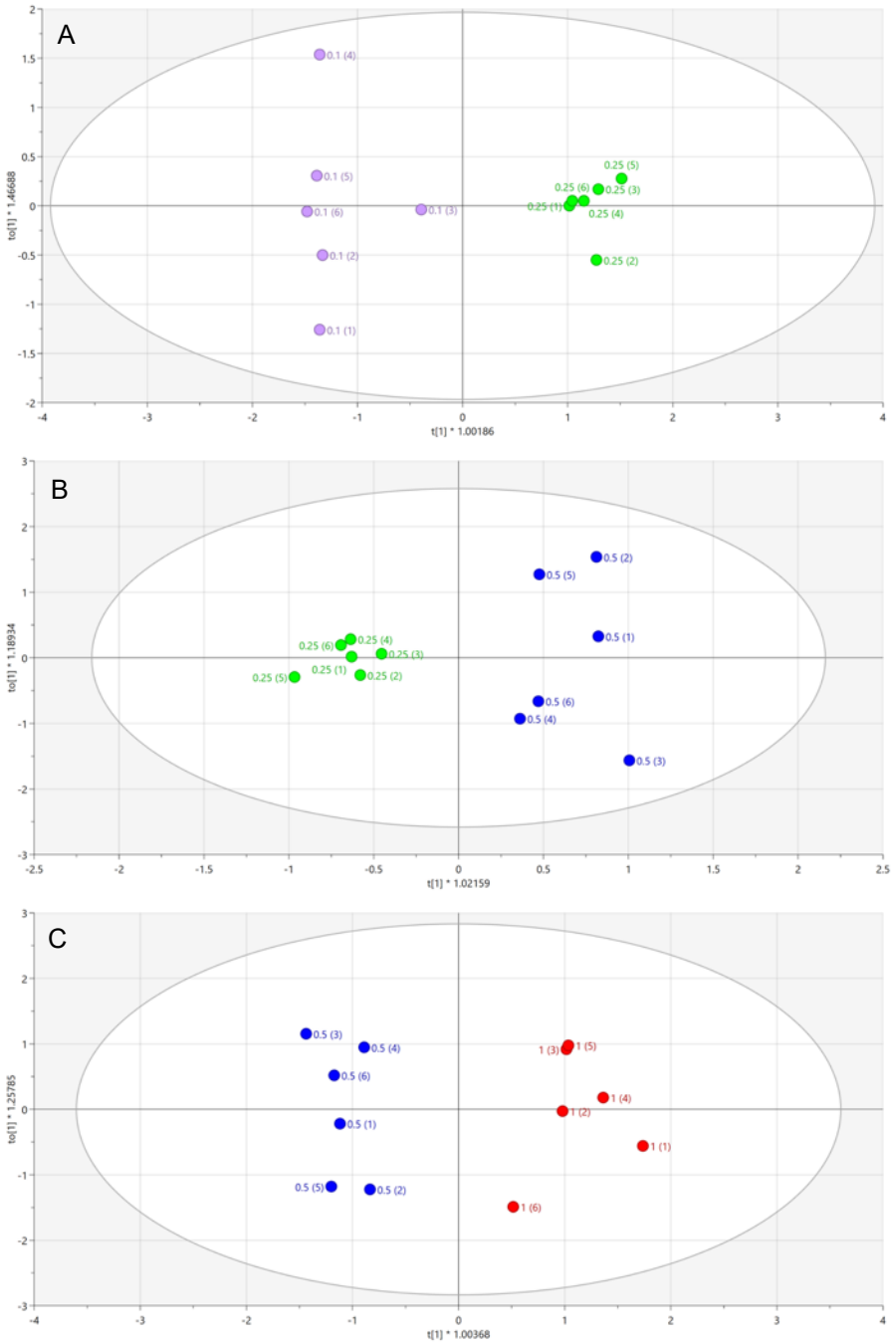

Figure 3.9 OPLS-DA scores plots derived from ^{1}H NMR spectra of aqueous extracts from HepG2 cells dosed with fatty acids at varying dose levels. Cells were dosed with a 2:1 mixture of oleic and palmitic acid at 0, 0.1, 0.25, 0.5 and 1 mM fatty acids and incubated for 24 hours. Samples were collected, and NMR analysis was carried out as described in Sections 2.10 and 2.12. Each spot on the scores plot represents one sample. A. 0.1 vs 0.25 mM. B. 0.25 vs 0.5 mM and C. 0.5 vs 1 mM. Pink = 0.1 mM, green = 0.25 mM, dark blue = 0.5 mM and red = 1.0 mM fatty acids.

Using the OPLS-DA models VIP predictive and S-plots (Figures 3.10 and 3.12) were generated to determine the metabolite regions in the NMR spectra that contributed most to the separation of the two groups in each pair-wise comparative scores plots. The VIP plots revealed NMR regions that were statistically significant and the regions

with a VIP value greater than one are highlighted in red in both the VIP and S-plots. The S-plots were then used to confirm whether peaks within these specific NMR variable regions had increased or decreased between the two groups being compared. VIP and S-plots were also constructed for consecutive dose levels and are shown in Figures 3.11 and 3.13.

Following this, the integrated spectral values were evaluated using a Kruskal-Wallis test to determine if any of the metabolite regions highlighted in the VIP were statistically significant between the groups in the pair-wise comparisons.

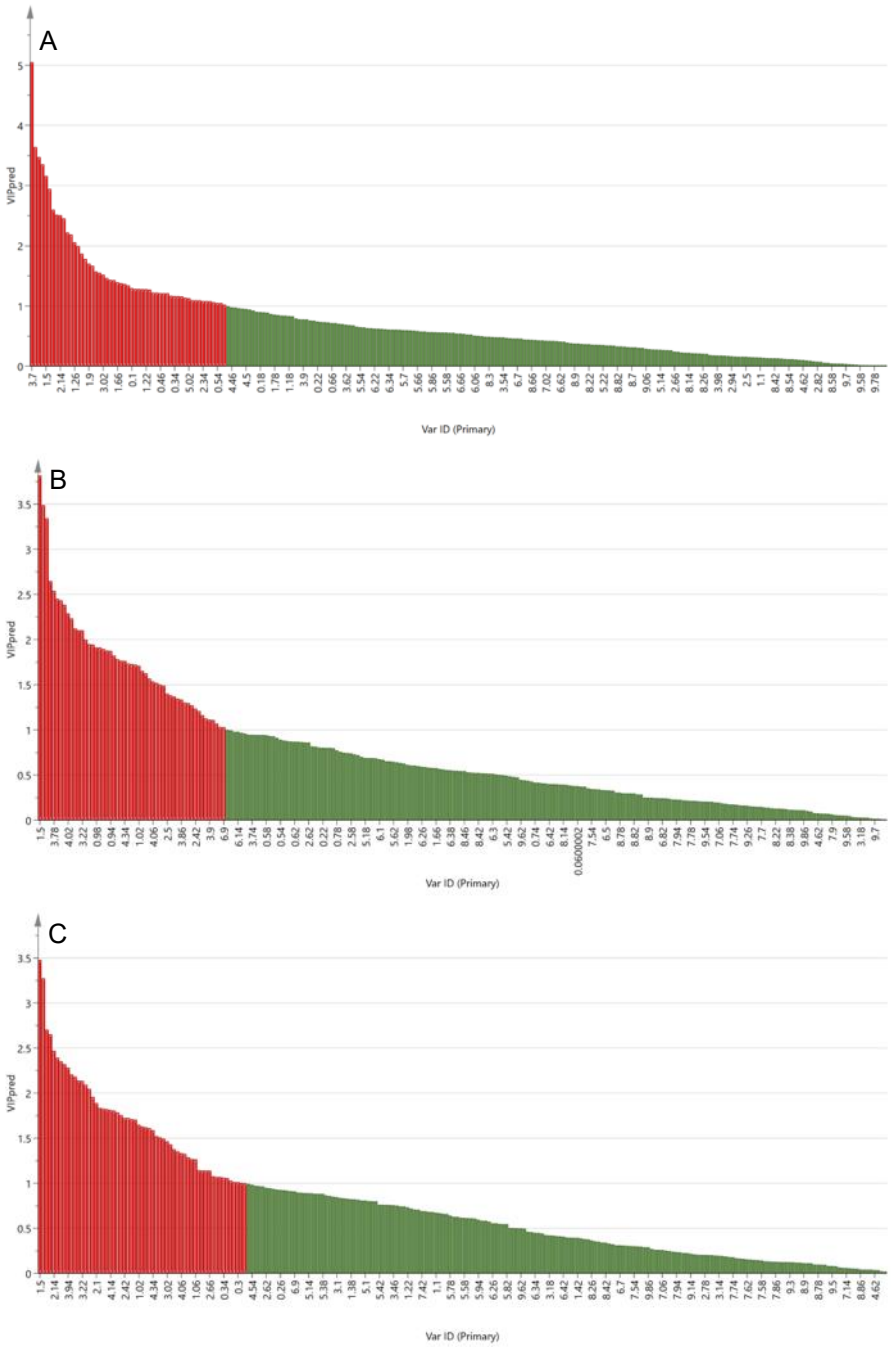

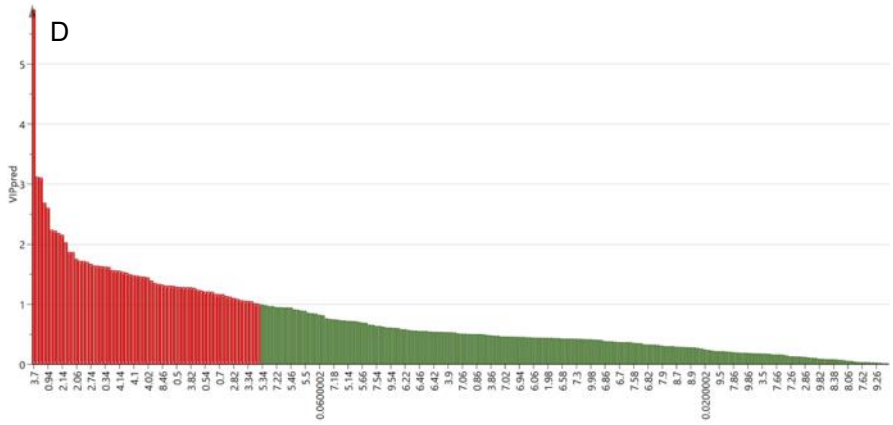

Figure 3.10 VIP predictive plots derived from OPLS-DA models of NMR spectra of aqueous extracts from HepG2 cells treated with fatty acids at different concentrations of a 2:1 mixture of oleic and palmitic acid at 0, 0.1, 0.25, 0.5 and 1 mM and incubated for 24 hour. Samples were collected, and NMR analysis was carried out as described in Sections 2.10 and 2.12. A. Control vs 0.1 mM fatty acid. B. Control vs 0.25 mM fatty acid. C. Control vs 0.5 mM fatty acid and D. Control vs 1.0 mM fatty acid. Variables with a VIPpred value above 1 were selected as significant and are highlighted in red. Variable regions are shown along the x-axis.

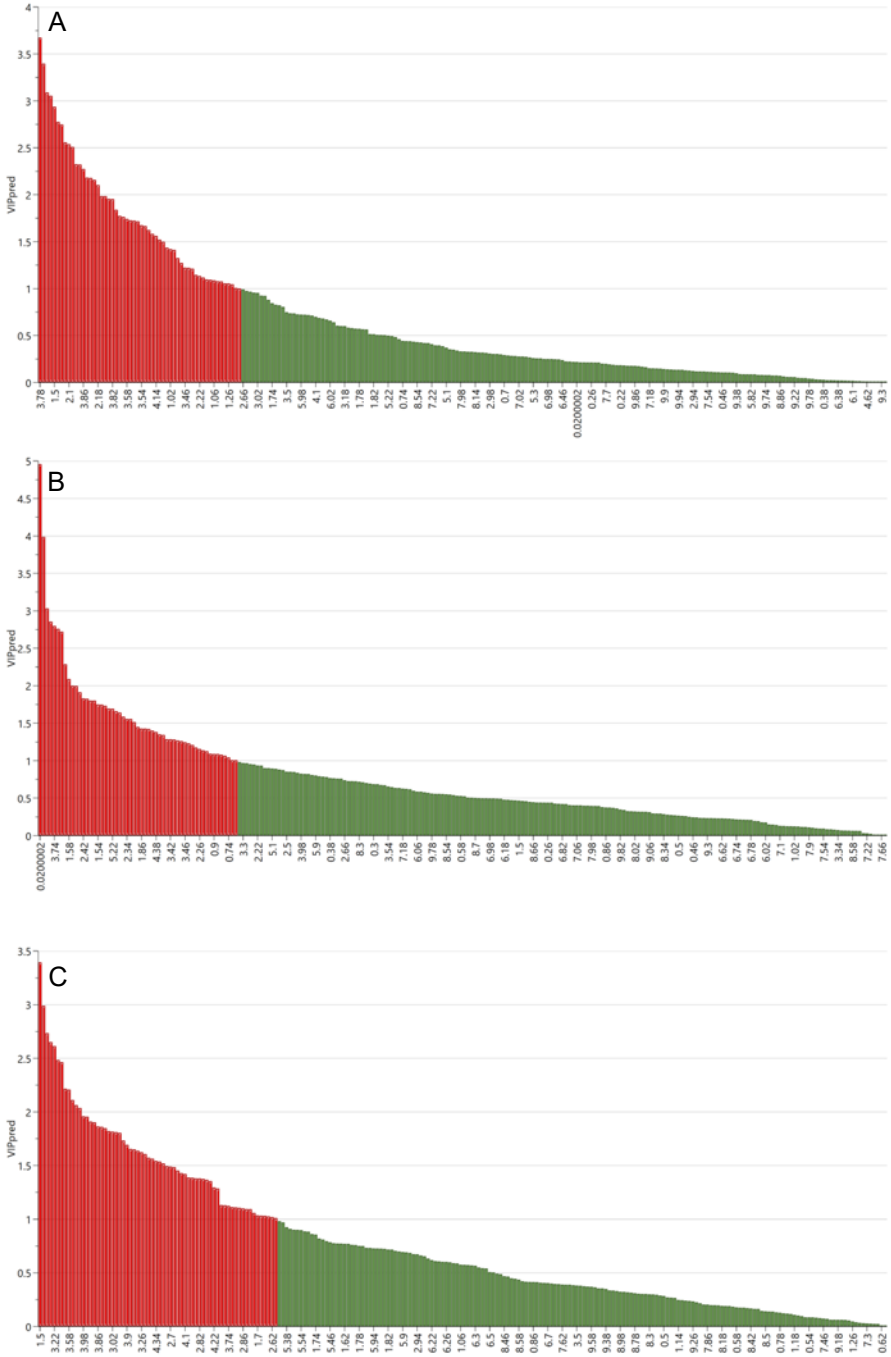

Figure 3.11 VIP predictive plots derived from OPLS-DA models of NMR spectra of aqueous extracts from HepG2 cells treated with fatty acids at different concentrations of a 2:1 mixture of oleic and palmitic acid at 0, 0.1, 0.25, 0.5 and 1 mM and incubated for 24 hour. Samples were collected, and NMR analysis was carried out as described in Sections 2.10 and 2.12. A. 0.1 vs 0.25 mM. B. 0.25 vs 0.5 mM and C. 0.5 vs 1 mM fatty acids. Variables with a VIPpred value above 1 were selected as significant and are highlighted in red. Variable regions are shown along the x-axis.

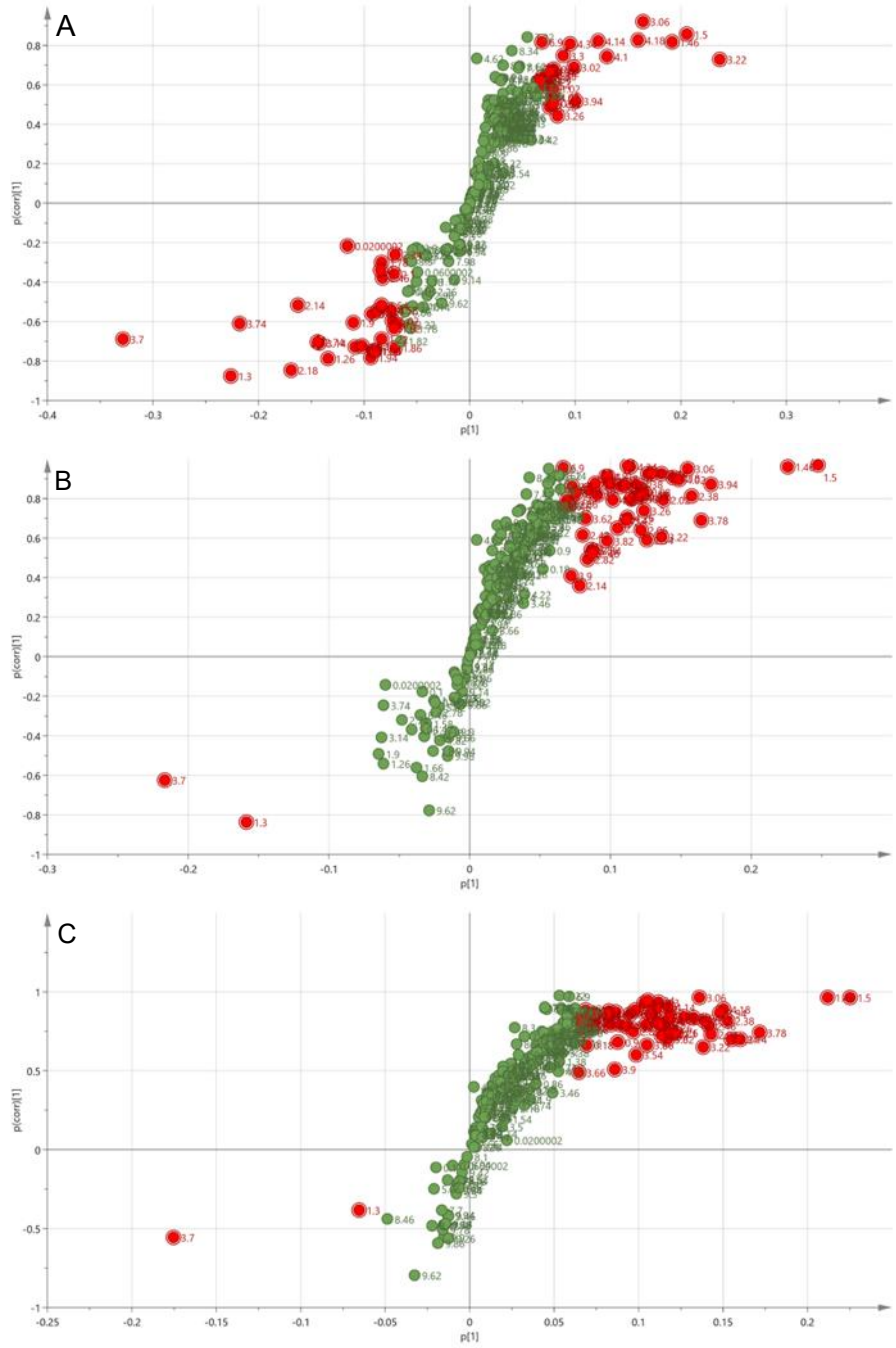
A
B
C
p[1]
p(corr)[1]

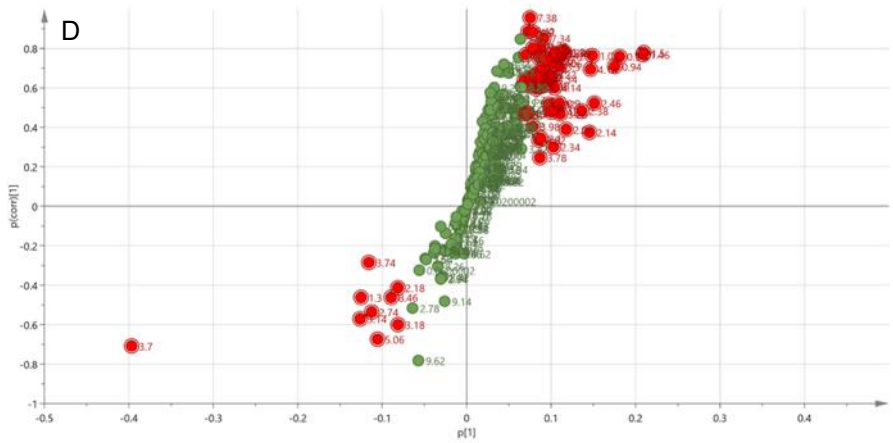

Figure 3.12 S-plots derived from OPLS-DA models of NMR spectra of aqueous extracts from HepG2 cells treated with fatty acids at different concentrations of a 2:1 mixture of oleic and palmitic acid at 0, 0.1, 0.25, 0.5 and 1 mM and incubated for 24 hours. Samples were collected, and NMR analysis was carried out as described in Sections 2.10 and 2.12. A. Control vs 0.1 mM fatty acid. B. Control vs 0.25 mM fatty acid. C. Control vs 0.5 mM fatty acid and D. Control vs 1.0 mM fatty acid.

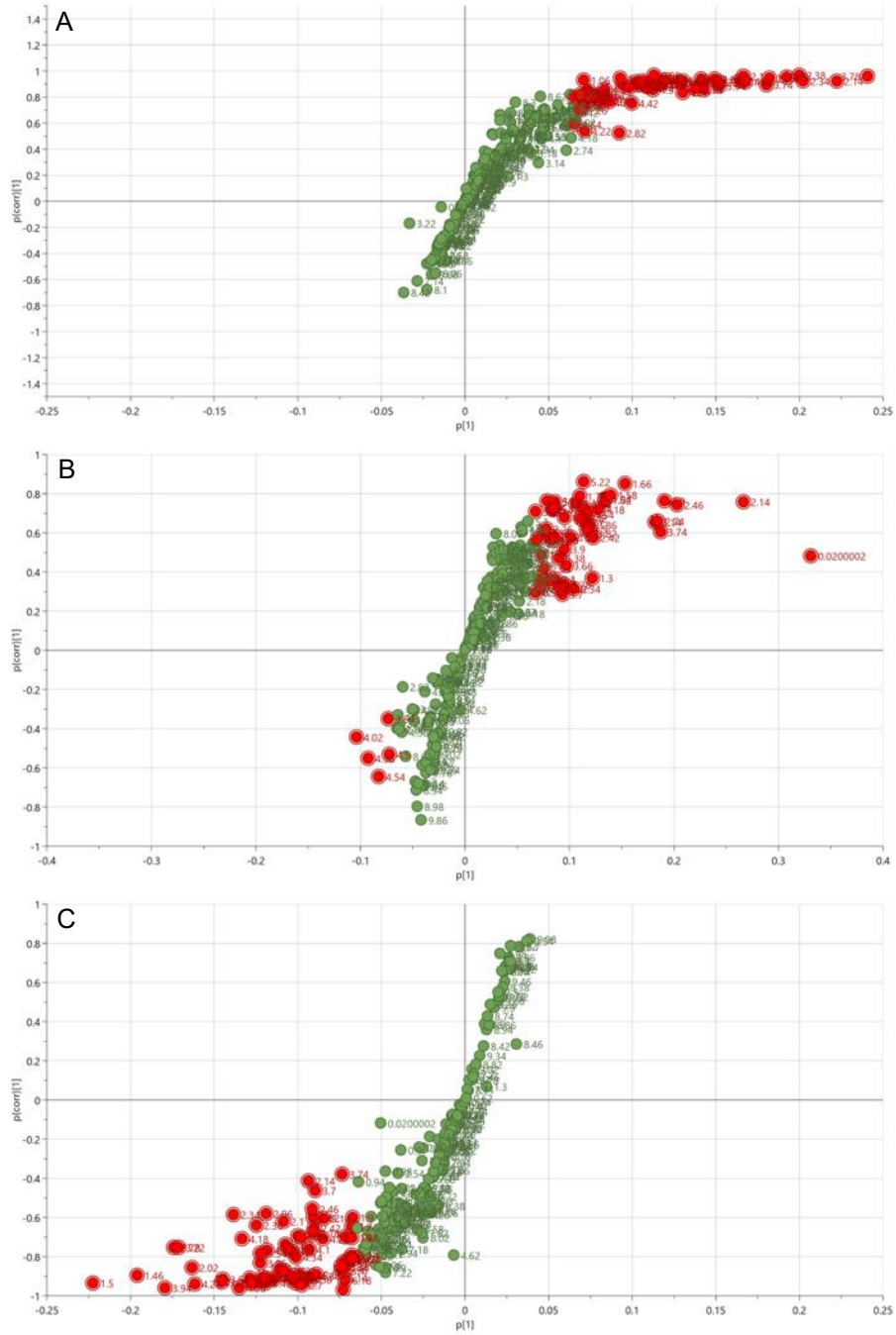

Figure 3.13 S-plots derived from OPLS-DA models of NMR spectra of aqueous extracts from HepG2 cells treated with fatty acids at different concentrations of a 2:1 mixture of oleic and palmitic acid at 0, 0.1, 0.25, 0.5 and 1 mM and incubated for 24 hours. Samples were collected, and NMR analysis was carried out as described in Sections 2.10 and 2.12. A. 0.1 vs 0.25 mM. B. 0.25 vs 0.5 mM and C. 0.5 vs 1 mM fatty acids.

NMR regions that were confirmed as being statistically different were recorded and the NMR spectra was closely examined to identify multiplicities of the peaks in these regions to aid with the identification of metabolites. Following identification of peaks using the Human Metabolome database, it was clear that there were a number of

metabolite changes including an increase ($p<0.001$) in peaks that were thought to belong to alanine and betaine in the extracts from fatty acid treated cells. There also appeared to be decreases in methylacetate ($p<0.01$) and lactate ($p<0.05$). Peaks for phosphocholine, creatine and serine were all increased in the 0.1, 0.25 and 0.5 mM treated groups but not in the 1 mM treated group.

Table 3.1 Chemical shift regions, and potential metabolites, identified as significantly different in the NMR of aqueous extracts from HepG2 cells treated with increasing concentrations of fatty acids when compared to control.

^{1}H shift ppm	Metabolite aqueous	Ctrl vs 0.1mM	Ctrl vs 0.25 mM	Ctrl vs 0.5mM	Ctrl vs 1mM	0.1 vs 0.25 mM	0.25 vs 0.5mM	0.5 vs 1mM
0.891-0.992(m)	Leucine	-	↑	↑**	↑	↑	↑	-
1.031-1.062(d)	Isoleucine	-	↑**	-	-	↑	-	-
1.31-1.35(d)	Lactate	↓*	↓	↓	↓	-	↑	-
1.467-1.501(d)	Alanine	↑	↑***	↑***	↑	↑	-	↑
1.9-1.93(s)	Acetate	↓	-	-	-	-	↑	↑
2.013-2.18(m)	Glutamate, Homocysteine	↓*	-	-	↑	↑*	↑	↑*
2.335-2.345(t of d)	Glutamate, B-hydroxybutyrate, Proline	↓	↑	↑	↑	↑	↑	↑
2.415-2.429(s)	Succinate	-	↑	↑**	↑	↑	↑	↑
2.44-2.48(m)	Glutamate	↓	↑	↑*	-	↑	↑	↑
2.72-2.74(s)	Dimethylamine	↓	-	-	↓	↑	-	↑**
2.81-2.824(s)	Aspartate	-	↑	↑*	↑	↑	-	↑
3.028(d) 3.03-3.055(s)	Creatine, Phosphocreatine, Creatinine	↑	↑**	↑	-	↑	-	↑
3.143-3.1607(s)	Choline	↓	-	-	↓	-	↑	↑
3.216-3.2301(s)	Phosphocholine	↑	↑	↑	-	-	-	↑
3.255-3.265(s)	Betaine, TMAO	↑*	↑**	↑	↑	↑	-	↑
3.535-3.55(d)	Choline	-	↑	↑	-	↑	-	↑
3.619-3.628(s)	Glycine	-	↑	-	-	↑	-	↑*
3.699-3.711(s)	Methylacetate	↓**	↓	↓	-	↑	↑	↑
3.73-3.749(s)	Citrulline	↓	-	-	↓	↑	↑	↑
3.94-3.955(m)	Serine	↑	↑**	↑	-	↑	↓	↑
4.09-4.125(d)	Proline	↑	↑**	↑*	↑	-	-	-
4.173-4.199(d)	Phosphocholine	↑	↑	↑**	-	-	-	↑
4.26-4.275(m)	Threonine	-	↑	↑	-	↑	↑	↑**

5.22-5.245(d)	Glucose	-	-	↑**	↑	-	↑	-
8.45-8.469(s)	Formate	↓	-	-	↓	-	-	-

S=singlet, d=doublet, dd=doublet of doublets, t=triplet, q=quartet, m=multiplet. An increase or decrease in the treated group was determined and these were further analysed statistically using a Kruskal-Wallis test (<0.05, **<0.01, ***<0.001)*

3.3.5 Metabolomic analysis in organic monolayers cell extracts

The NMR spectra of organic cell extracts from HepG2 cells dosed with a 2:1 mixture of oleic and palmitic acid at 0, 0.1, 0.25, 0.5 and 1.0 mM in this study were also obtained and further analysed using multivariate analysis.

From a visual inspection of the NMR spectra no differences between the control and the treated groups could be observed. Therefore, a PCA scores plot was constructed (Figure 3.14A). However, some samples, 0.5(4), 1(1) and 1(2), fell outside the 95% ellipse in the initial scores plot. The spectra for these samples were examined and re-processed to rule out experimental or analytical error. Nevertheless, analysis of the Hotelling's T2 plot shown in Figure 3.14B confirmed that sample 0.5(4) was above the 99 % confidence level and this sample was therefore excluded from further analysis. Samples 1(1) and 1(2) were found to be between the 95 % and 99 % confidence level and were not deemed to be true outliers meaning they were included in all further analyses.

After the removal of sample 0.5(4), a second PCA model was created, and the resulting PCA scores plot is shown in Figure 3.15. The figure shows the control samples were all negative for PC2 whereas the majority of the treated samples were positive for PC2, thus indicating a difference between the control and treated groups. Some separation can be seen between the 0.1, 0.25 and 0.5 mM sample groups but they are not distinctly separated from each other. Meanwhile the 1.0 mM samples were spread across the left-hand side of the PC1 axis showing great intragroup variation. Samples 1(1) and 1(2) were still located just outside the ellipse and were re-checked and remained between the 95 % and 99 % confidence level.

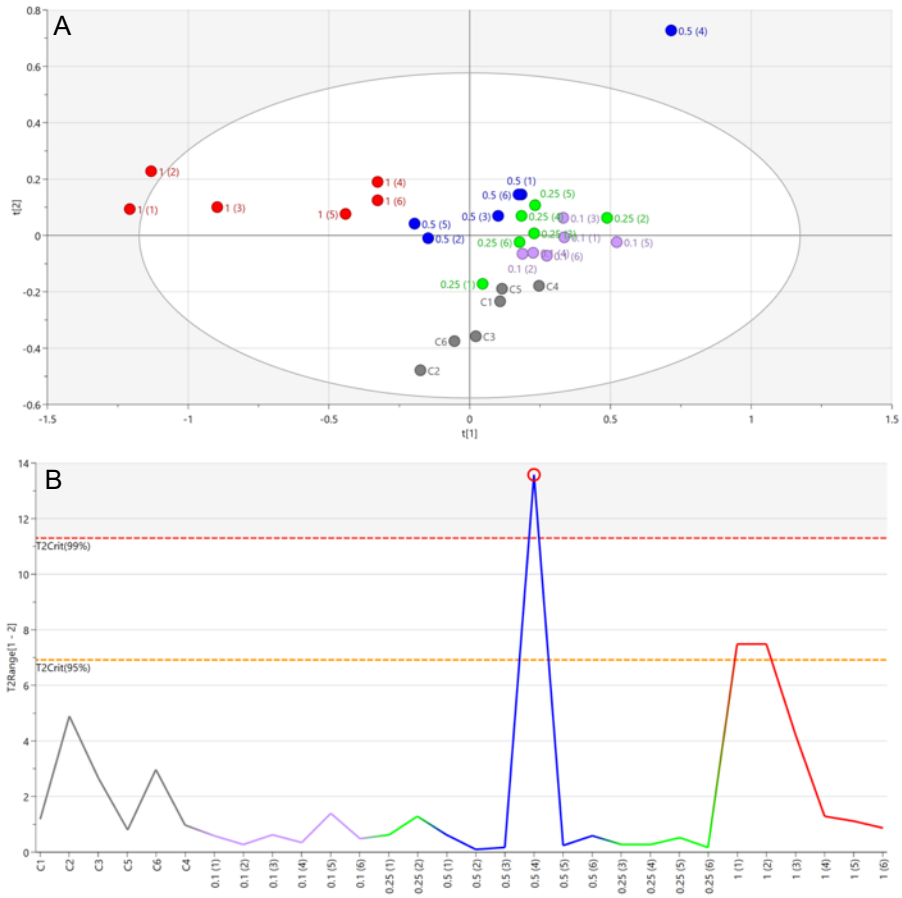

Figure 3.14 PCA scores and Hotelling's plot derived from ^{1}H NMR spectra of organic extracts from HepG2 cells dosed with fatty acids at various dose levels. A. PCA scores plot with no samples excluded. B. Hotelling's T2 plot created from PCA scores plots showing samples outside the 95 and 99% confidence levels. Cells were dosed with a 2:1 mixture of oleic and palmitic acid at 0, 0.1, 0.25. 0.5 and 1 mM and incubated for 24 hours. Samples were collected, and NMR analysis carried out as described in Sections 2.10 and 2.12. Each spot on the scores plot represent one sample. Grey = Ethanol control; pink = 0.1 mM; green = 0.25 mM; dark blue = 0.5 mM; red = 1.0 mM. In the Hotelling's plot (B) samples above the red line of the 99% confidence level are considered to be outliers.

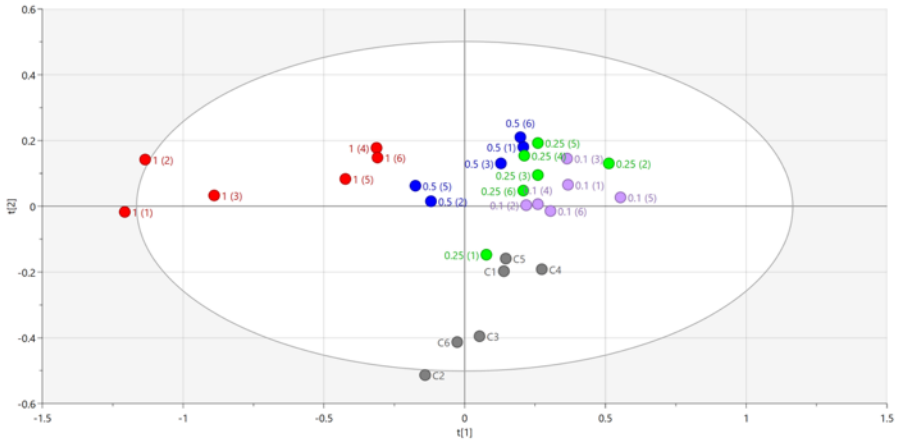

Figure 3.15 PCA scores plot derived from ^{1}H NMR spectra of organic extracts from HepG2 cells dosed with fatty acids at various dose levels. PCA scores plot with sample 0.5 (4) excluded. Cells were dosed with a 2:1 mixture of oleic and palmitic acid at 0, 0.1, 0.25. 0.5 and 1mM and incubated for 24 hours. Samples were collected, and NMR analysis carried out as described in Sections 2.10 and 2.12. Each spot on the scores plots represents one sample. Grey = Ethanol control; pink = 0.1 mM; green = 0.25 mM; dark blue = 0.5 mM; red =1.0 mM.

Since the second PCA scores plot (Figure 3.15) did not show definitive separation between the 0.1, 0.25 and 0.5 mM treated groups a OPLS analysis was conducted. The resulting OPLS scores plot (Figure 3.16) demonstrates clear separation of the control and 1 mM samples from all other groups with the control group negative for t[1] while the 1 mM samples were positive for t[1]. However, large intragroup variation along the t[0] axis was evident for samples in each of these two groups. The remaining sample groups (0.1, 0.25 and 0.5 mM) were clustered together in the lower half of the scores plot, fairly close to the centre of the plot. There was clear separation between the 0.1 and 0.5 mM samples, however the 0.25 mM samples overlap both of these groups.

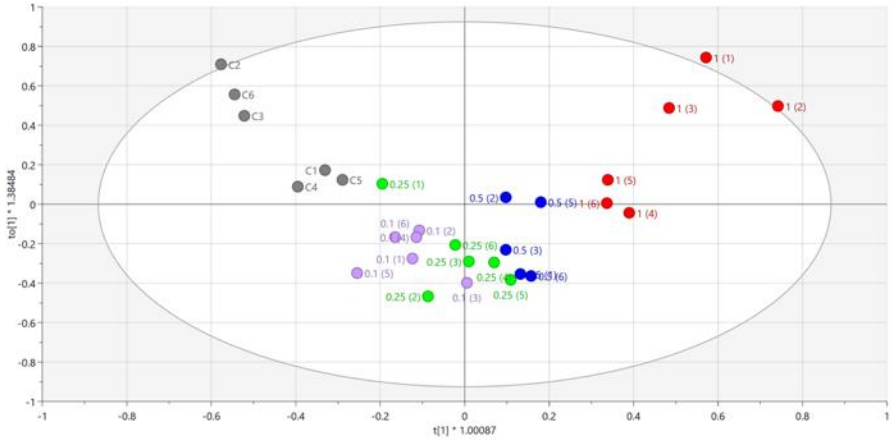

Figure 3.16 OPLS scores plot derived from ^{1}H NMR spectra of organic cell extracts from HepG2 cells treated with different dose levels of fatty acids. Cells were dosed with a 2:1 mixture of oleic acid: palmitate at 0, 0.1, 0.25, 0.5 and 1.0 mM and incubated for 24 hours. Samples were collected, and NMR analysis carried out as described in Sections 2.10 and 2.12. Each spot on the scores plot represents one sample. Grey = Ethanol control; pink = 0.1 mM; green = 0.25 mM; dark blue = 0.5 mM; red = 1.0 mM fatty acids.

Following OPLS analysis all treated groups were compared against the control group using OPLS-DA. In all OPLS-DA scores plots (Figure 3.17) the control and the treated groups were separated along the t[1] axis. Orthogonal variation within the groups along the t[0] axis were also apparent for all sample groups, particularly the control groups. This reflects similar intragroup variation seen in the PCA and OPLS models (Figures 3.15 and 3.16). For example, in the 1 mM treated group sample numbers 1,2, and 3 are separated from the other samples within the group in the PCA and OPLS scores plots with samples 1 and 2 outside the ellipse and this is clearly visible in the OPLS-DA plots.

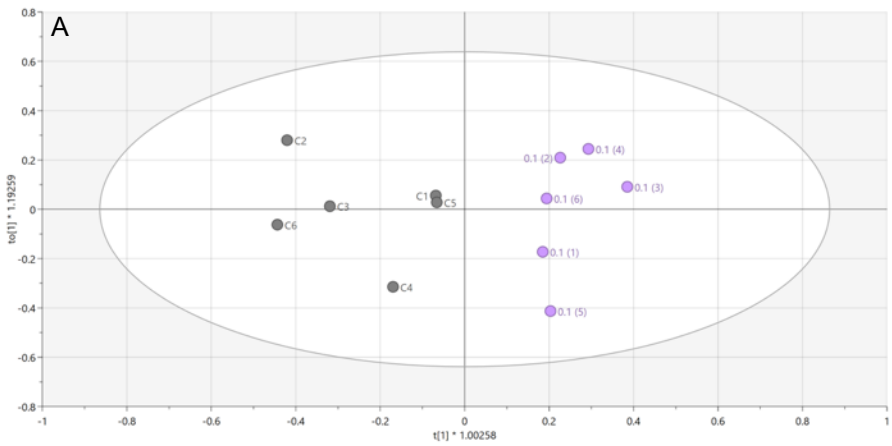

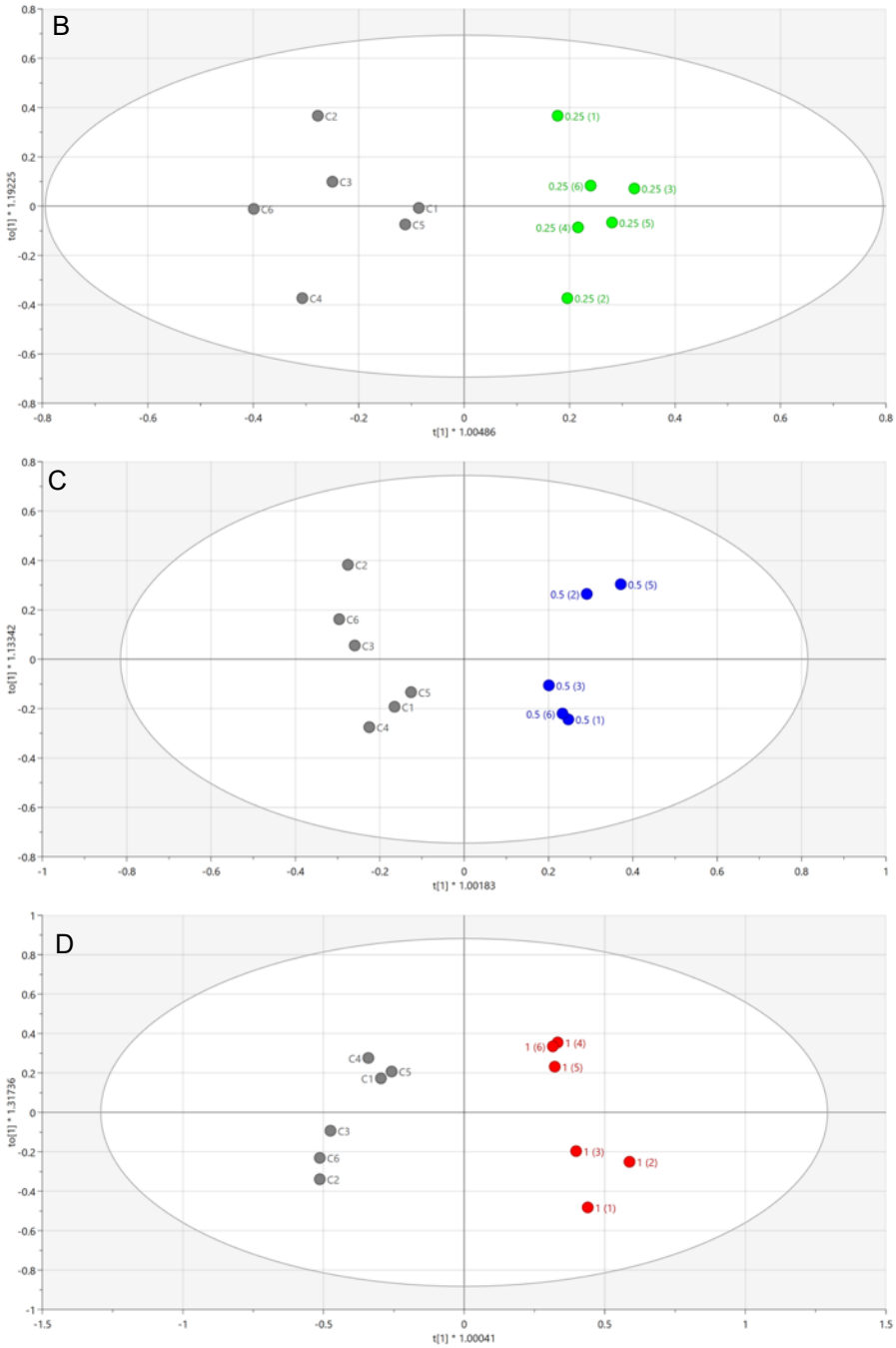

Figure 3.17 OPLS-DA scores plots derived from ^{1}H NMR spectra of organic extracts from HepG2 cells dosed with fatty acids at varying dose levels. Cells were dosed with a 2:1 mixture of oleic and palmitic acid at 0, 0.1, 0.25, 0.5 and 1 mM fatty acids and incubated for 24 hours. Samples were collected and NMR analysis was carried out as described in Sections 2.10 and 2.12. Each spot on the scores plot represents one sample. A. Control vs 0.1 mM fatty acid. B. Control vs 0.25 mM fatty acid. C. Control vs 0.5 mM fatty acid and D. Control vs 1.0 mM fatty acid. Grey = Ethanol control; pink = 0.1 mM, green = 0.25 mM, dark blue = 0.5 mM and red = 1.0 mM fatty acids.

Consecutive dose levels were also analysed using OPLS-DA analysis. In all OPLS-DA scores plots (Figure 3.18) the two groups being compared were separated along the t[1].

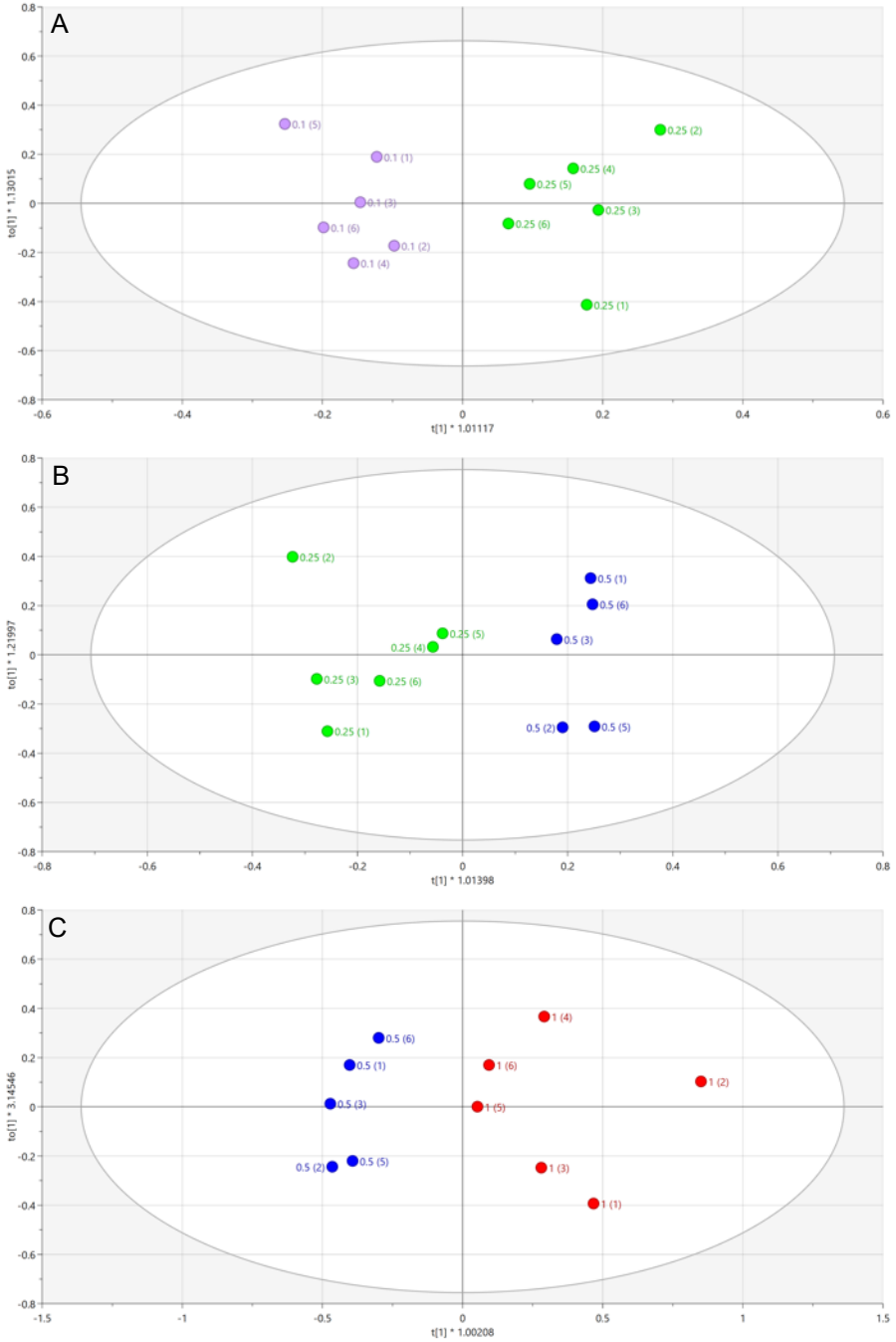

Figure 3.18 OPLS-DA scores plots derived from ^{1}H NMR spectra of organic extracts from HepG2 cells dosed with fatty acids at varying dose levels. Cells were dosed with a 2:1 mixture of oleic and palmitic acid at 0, 0.1, 0.25, 0.5 and 1 mM fatty acids and incubated for 24 hours. Samples were collected and NMR analysis was carried out as described in Sections 2.10 and 2.12. Each spot on the scores plot represents one sample. A. 0.1 vs 0.25 mM. B. 0.25 vs 0.5 mM and C. 0.5 vs 1 mM. Grey = Ethanol control; pink = 0.1 mM, green = 0.25 mM, dark blue = 0.5 mM and red = 1.0 mM fatty acids.

Following the analysis of the OPLS-DA models VIP predictive and S-plots were generated to determine the metabolite regions contributing most to the separation of the groups in the pair-wise comparison scores plots. Variable regions with a VIP value greater than one were highlighted and are shown in red in both plots. Figures 3.19 and

3.21 show changes in control versus treated groups while Figures 3.20 and 3.22 represent comparison between consecutive dose groups.

Regions of interest according to the VIP list were selected for a Kruskal Wallis analysis to test for statistical significance. The characteristics of the NMR peaks in these regions were then determined to enable identification of metabolites and compounds responsible for these peaks. Table 3.2 shows the identified compounds.

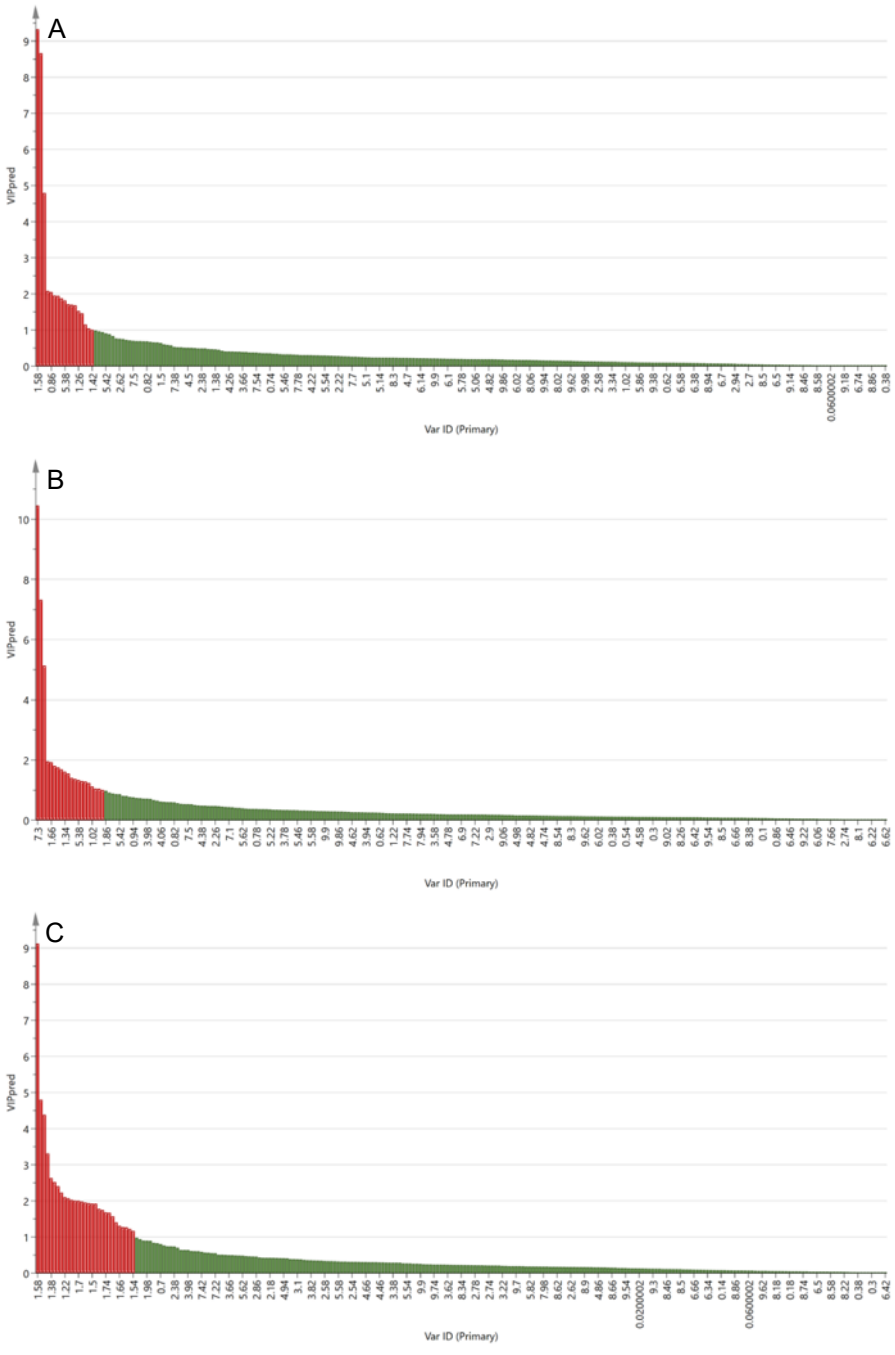

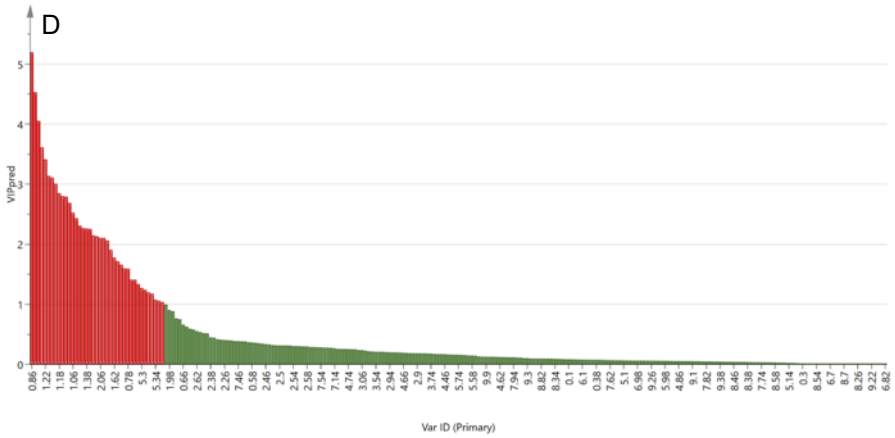

Figure 3.19 VIP predictive plots derived from OPLS-DA models of NMR spectra of organic extracts from HepG2 cells treated with fatty acids at different concentrations of a 2:1 mixture of oleic and palmitic acid at 0, 0.1, 0.25, 0.5 and 1 mM and incubated for 24 hour. Samples were collected and NMR analysis was carried out as described in Sections 2.10 and 2.12. A. Control vs 0.1 mM fatty acid. B. Control vs 0.25 mM fatty acid. C. Control vs 0.5 mM fatty acid and D. Control vs 1.0 mM. Variables with a VIPpred value above 1 were selected as significant and are highlighted in red. Variable regions are shown along the x-axis.

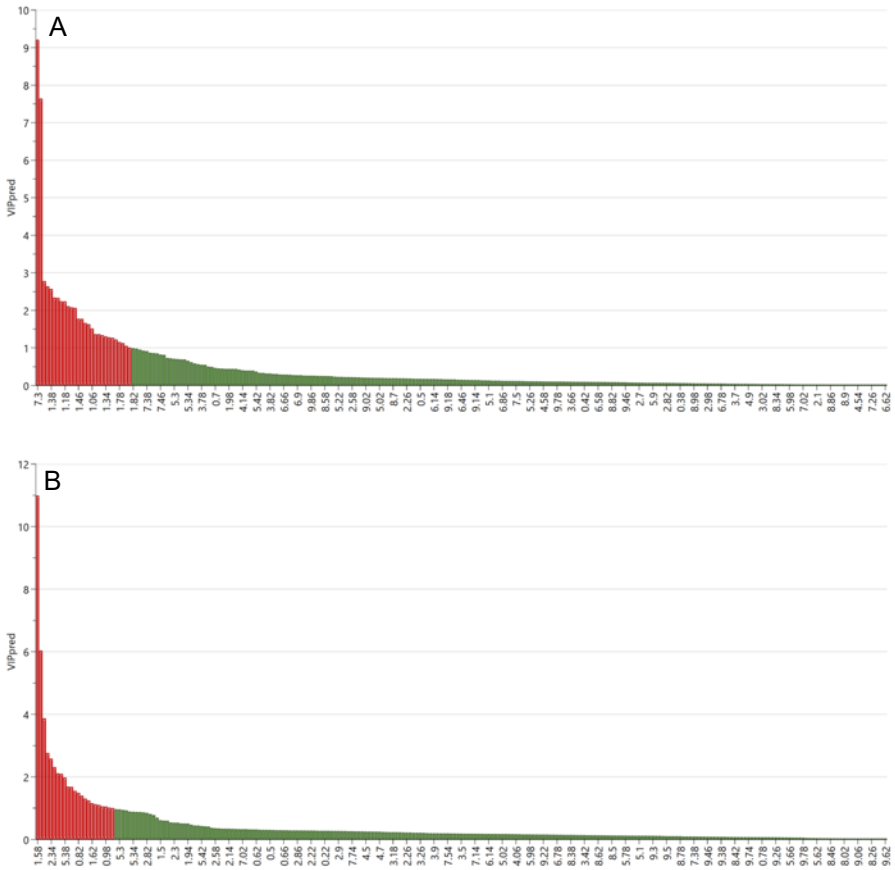

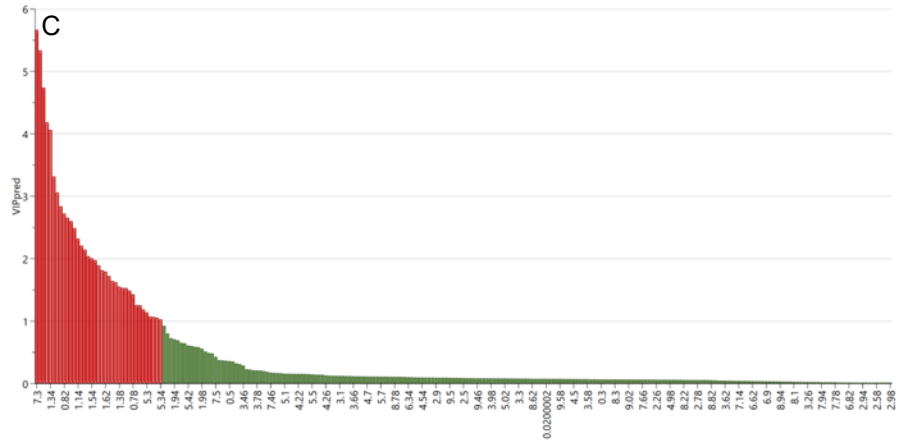

Figure 3.20 VIP predictive plots derived from OPLS-DA models of NMR spectra of organic extracts from HepG2 cells treated with fatty acids at different concentrations of a 2:1 mixture of oleic and palmitic acid at 0, 0.1, 0.25, 0.5 and 1 mM and incubated for 24 hour. Samples were collected and NMR analysis was carried out as described in Sections 2.10 and 2.12. A. 0.1 vs 0.25 mM. B. 0.25 vs 0.5 mM and C. 0.5 vs 1 mM. fatty acid. Variables with a VIPpred value above 1 were selected as significant and are highlighted in red. Variable regions are shown along the x-axis.

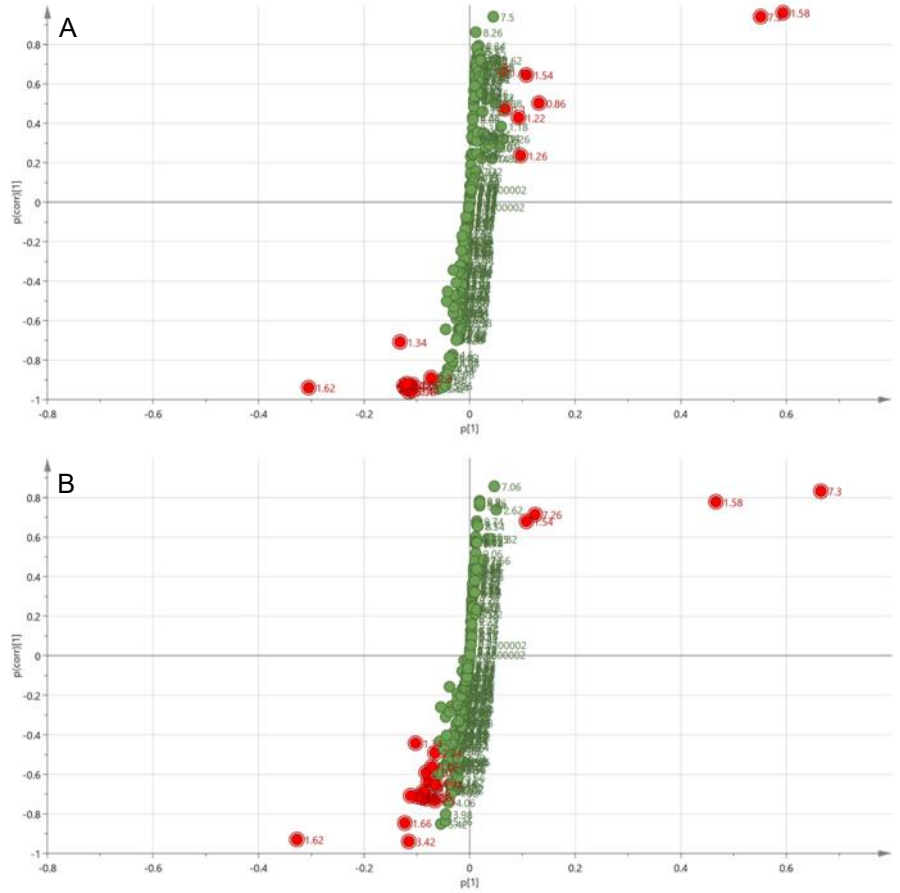

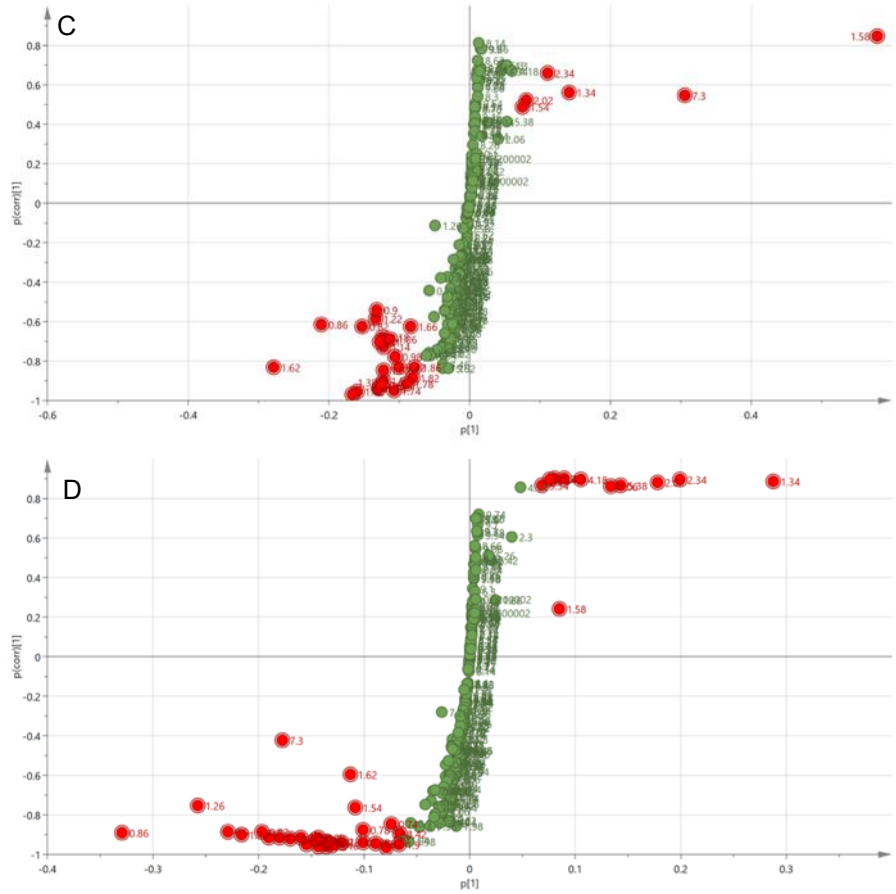

Figure 3.21 S-plot derived from OPLS-DA models of NMR spectra of organic extracts from HepG2 cells treated with fatty acids at different concentrations of a 2:1 mixture of oleic and palmitic acid at 0, 0.1, 0.25, 0.5 and 1 mM and incubated for 24 hours. Samples were collected and NMR analysis was carried out as described in Sections 2.10 and 2.12. A. Control vs 0.1 mM fatty acid. B. Control vs 0.25 mM fatty acid. C. Control vs 0.5 mM fatty acid and D. Control vs 1.0 mM.

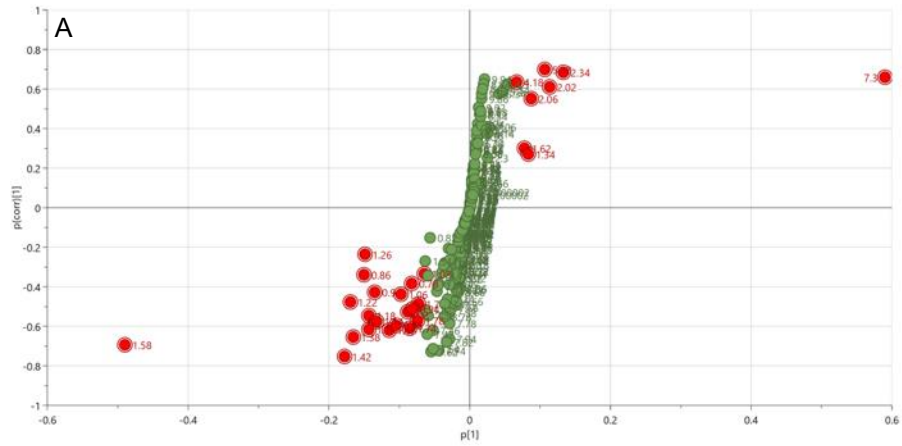

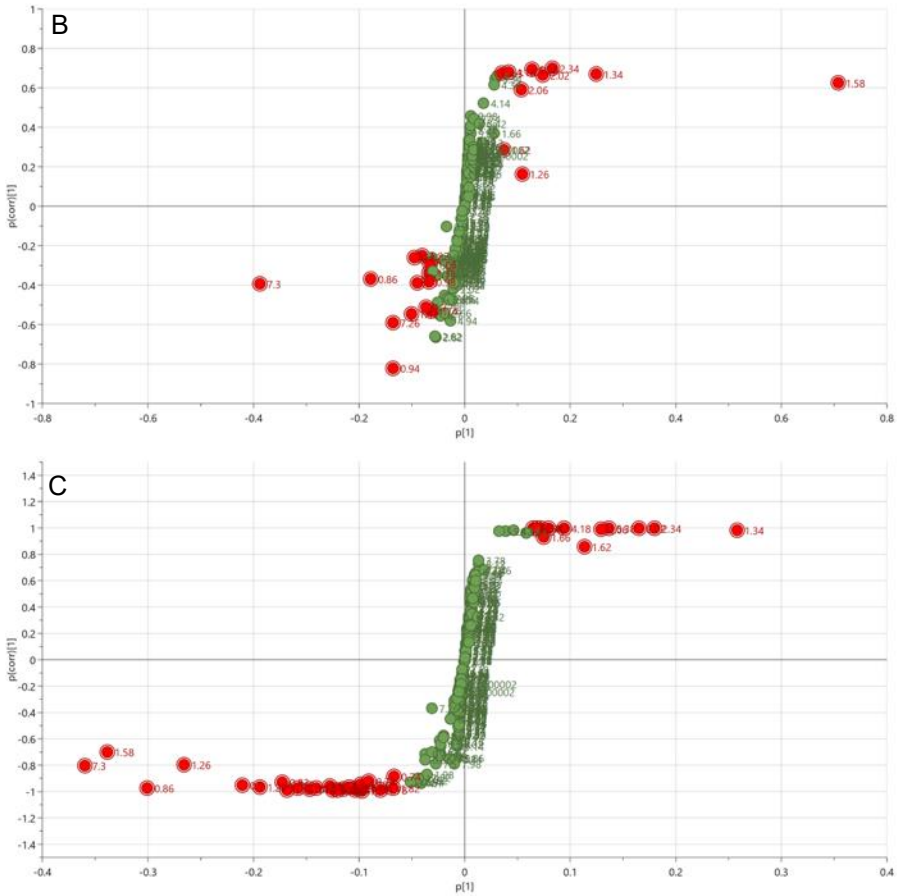

Figure 3.22 S-plot derived from OPLS-DA models of NMR spectra of organic extracts from HepG2 cells treated with fatty acids at different concentrations of a 2:1 mixture of oleic and palmitic acid at 0, 0.1, 0.25, 0.5 and 1 mM and incubated for 24 hours. Samples were collected and NMR analysis was carried out as described in Sections 2.10 and 2.12. A. 0.1 vs 0.25 mM. B. 0.25 vs 0.5 mM and C. 0.5 vs 1 mM fatty acid.

According to the Kruskal Wallis test there were no significant increases between these data sets. However significant decreases ($p<0.01$) in peaks responsible for fatty acyl groups and cholesterol ($p<0.05$) were observed in the 1 mM treated group when compared to the ethanol control. Some dose related responses could be seen between the treated and control groups, particularly in acyl groups in triglycerides which showed a decrease in the 0.1 and 0.25 mM treated groups and increases in the 0.5 and 1 mM groups.

Table 3.2 Chemical shift regions identified as significantly different in the organic extracts of HepG2 cells treated with different concentrations of fatty acids as detected by OPLS-DA analysis. The multiplicity of each peak is shown.

^{1}H shift ppm	Metabolite organic	Ctrl vs 0.1mM	Ctrl vs 0.25 mM	Ctrl vs 0.5mM	Ctrl vs 1mM	0.1 vs 0.25 mM	0.25 vs 0.5mM	0.5 vs 1mM
0.806-0.937(m)	Fatty acyl groups and Fatty acids	↑	-	↓	↓**	↓	↓	↓
1.05-1.13(m)	Cholesterol	↓	-	-	-	↓	↓	↓
1.221-1.305(s)	Cholesterol	↑	-	↓	↓*	↓	↓	↓
1.54-1.62(s)	Arachidonic acid (ARA)	↑	↑	↑	↑	↓	↑	↓
1.702-1.724(s)	Fatty acids Eicosapentaenoic acid (EPA)	-	↓	↓*	↓***	↓	↓	↓
2.008-2.062(q)	Oleic acid	↓	↓	↑	↑	↑	↑	↑
2.31-2.365(m)	Acyl groups in triglycerides	↓	↓	↑	↑	↑	↑	↑
4.145-4.203(dd)	Glyceryl group in monoglyceride	-	-	-	↑	↑	↑	↑
4.294-4.349(dd)	Glyceryl group in Triglycerides	-	-	-	↑	-	↑	↑
5.266-5.322(m)	Oleic acid	-	-	-	↑	-	-	-
5.338-5.433(m)	Fatty acids /Monounsaturated fatty acids (MUFA)	↓	-	-	↑	↑	↑	↑

S=singlet, d=doublet, dd=doublet of doublets, t=triplet, q=quartet, m=multiplet. An increase or decrease in the treated group was determined and these were further analysed statistically using a Kruskal-Wallis test (<0.05, **<0.01, ***<0.001).*

3.3.6 CYP enzyme expression levels in monolayer HepG2 cells dosed with fatty acids.

CYP expression in protein extracts from the HepG2 monolayers dosed with a 2:1 mixture of oleic and palmitic acid at different dose levels were analysed using Western blotting, as described in Section 2.20. A standard protein marker was used for all Western blots which aided the identification of target proteins (Appendix Figure 8.1). For all blots, the level constituent cell protein beta actin (Figure 3.23A) was used to ensure equal loading of different cell samples. Figures 3.23 B, C and D showed CYP2D6, CYP 3A4 and CYP2E1 expression levels, respectively at the different fatty acid concentrations. In this study the results showed no real trend for any of the CYP at the different dose levels. However, as N=1 in this study further experimentation is needed. Despite this, it is worth pointing out that all CYPs were detected in the monolayers.

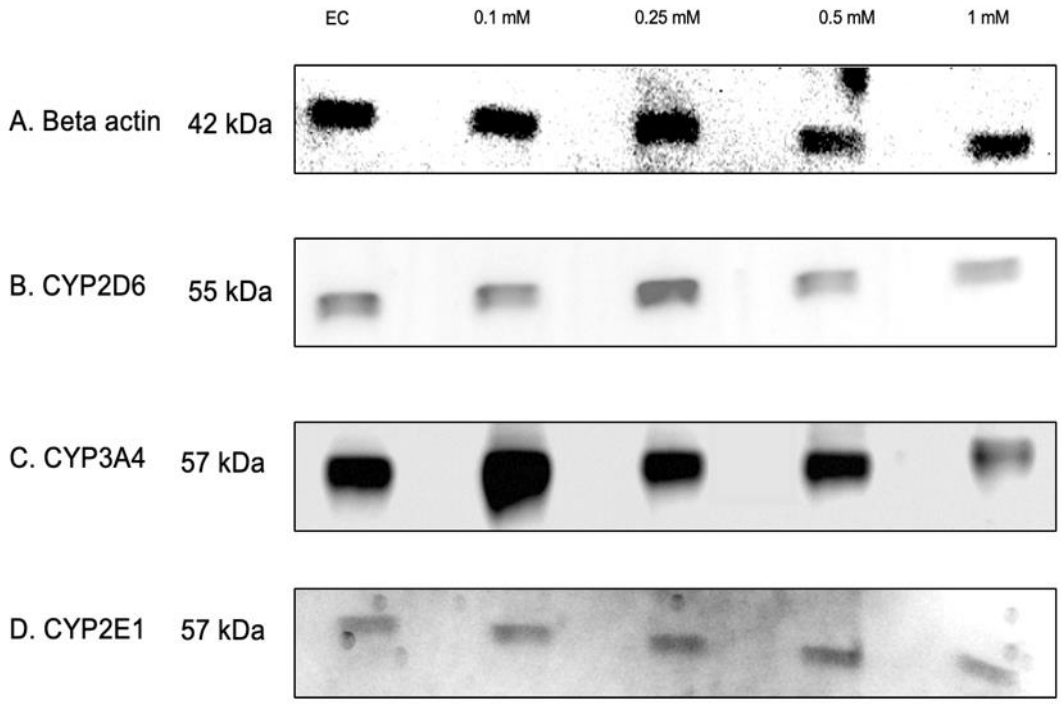

Figure 3.23 Western blot analysis of CYP enzyme expression in HepG2 monolayers dosed with fatty acids. A. Beta actin, B. CYP 2D6, C. CYP 3A4 and D. CYP2D6. Cells were dosed with a combination of oleic and palmitic acid at varying concentrations or 0, 0.1, 0.25, 0.5 and 1 mM and proteins were collected as described in Section 2.16. Western blotting was carried out as described in Section 2.20. EC: Ethanol control, 0.1 mM, 0.25 mM, 0.5 mM and 1 mM fatty acids.

Table 3.3 Raw data showing the arbitrary band intensities for CYP2D6, 3A4 and 2E1 in HepG2 monolayers dosed with fatty acids relative to the ethanol control. Cells were dosed with a combination of oleic and palmitic acid at varying concentrations or 0, 0.1, 0.25, 0.5 and 1 mM and proteins were collected as described in Section 2.16.

Fatty acid concentration (mM)	CYP2D6	CYP3A4	CYP2E1
Ethanol control	8866.73	19733.31	3437.28
0.1	8006.25	33595.34	3877.83
0.25	12146.08	17037.36	3102.69
0.5	5816.64	14519.87	4515.52
1	5650.5	7522.39	2844.05

3.3.7 3D spheroid model dosed with fatty acids

As mentioned in Section 3.1 this study was interested in the development of a 3D spheroid model of steatosis. HepG2 spheroids were grown for 17 days and dosed with a 2:1 mixture of oleic and palmitic acid at dose levels of 0.5 and 0.1 mM fatty acids to analyse changes in the metabolome and proteome when compared to control. Dose levels were chosen based on the results of the viability (Section 3.3.1) and triglyceride assays (Section 3.3.3) as conducted in the monolayers. The low dose chosen as 0.1 mM despite a lack of significance in the monolayer since spheroids are considered to be more sensitive to toxicants. The high dose was chosen as 0.5 mM to avoid any cytotoxicity.

3.3.8 Scanning electron microscopy of HepG2 spheroids

To confirm the formation of spheroids cell cultures were visualised using scanning electron microscopy. Figure 3.24 shows the scanning electron microscopy image of cultures following incubation after 14 days and confirms the presence of spheroids.

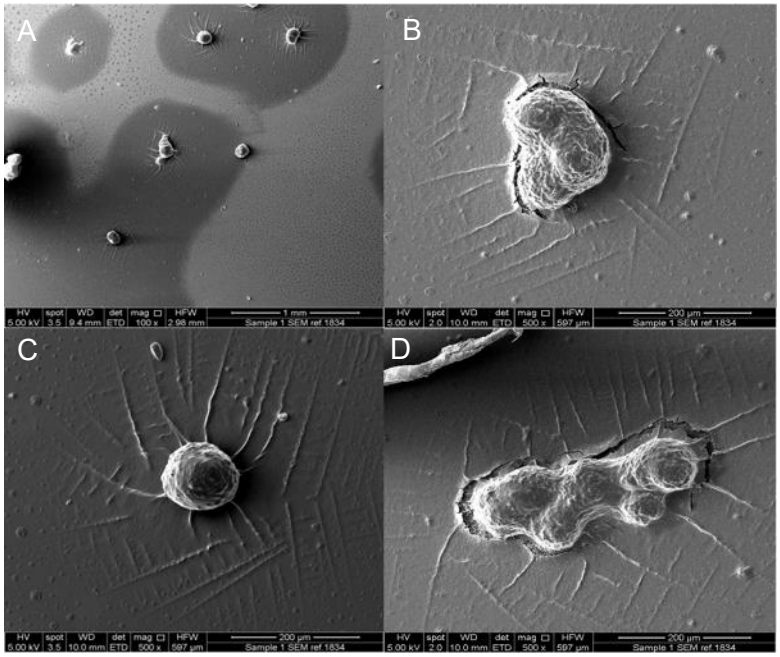

Figure 3.24 Scanning electron microscopy images following 14 days of culture. Spheroids were grown in low attachment 6-well plates as described in Section 2.3 and images were taken on day 14 of culture. A. x100 magnification, B, C and D. x500 magnification.

3.3.9 Cytotoxicity assay for spheroids dosed with fatty acid

A LIVE/DEAD assay was used to visualise viable cells in the spheroids following dosing with fatty acids at both 0.1 and 0.5 mM after 17 days of growth. The LIVE/DEAD assay stains viable cells green and non-viable cells red as described in Section 2.22. Figure 3.25 shows the confocal microscope images of control and fatty acid-treated spheroids. No red cells were apparent in either control of fatty acid-treated spheroids confirming that dosing spheroids with 0.1 and 0.5mM fatty acids (Figure 3.25 B and C) did not cause cell death.

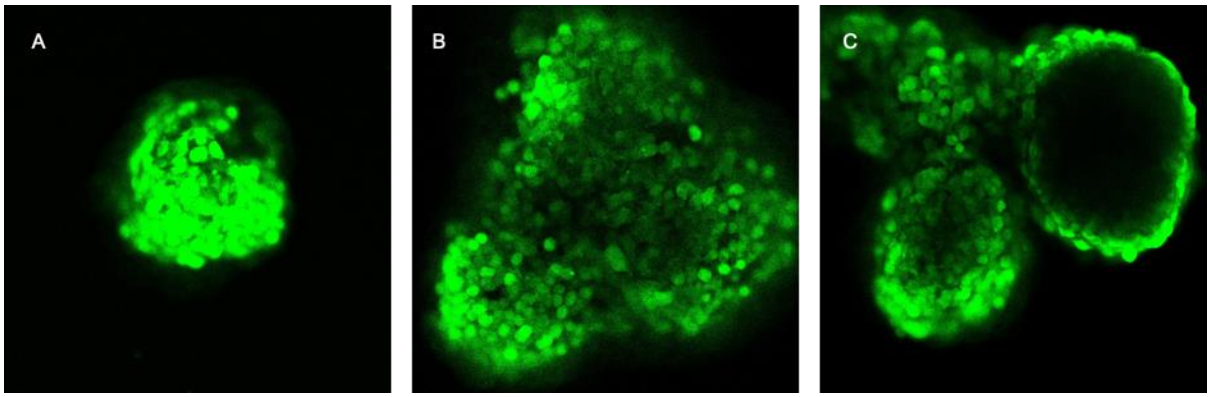

Figure 3.25 Images taken from the LIVE/DEAD assay of spheroids dosed with fatty acids. Spheroids were grown in low attachment 6-well plates as described in Section 2.3 and dosed with a 2:1 combination of oleic and palmitic acid at concentrations of 0 (ethanol control), 0.1 and 0.5 mM. The LIVE/DEAD assay was carried out as described in Section 2.22. A. Ethanol control, B. 0.1 mM fatty acids and C. 0.5 mM fatty acids.

An LDH assay was carried out to determine whether the administration of fatty acids caused LDH leakage from spheroids into the media due to cytotoxicity. Figure 3.26 confirms that dosing spheroids with fatty acids at both 0.1 and 0.5 mM did not cause cell death when compared to the ethanol control. The percentage cytotoxicity for the spheroids treated with 0.1 mM fatty acid was 0.11% while the control and 0.5 mM fatty acid-treated spheroids showed 0% cytotoxicity.

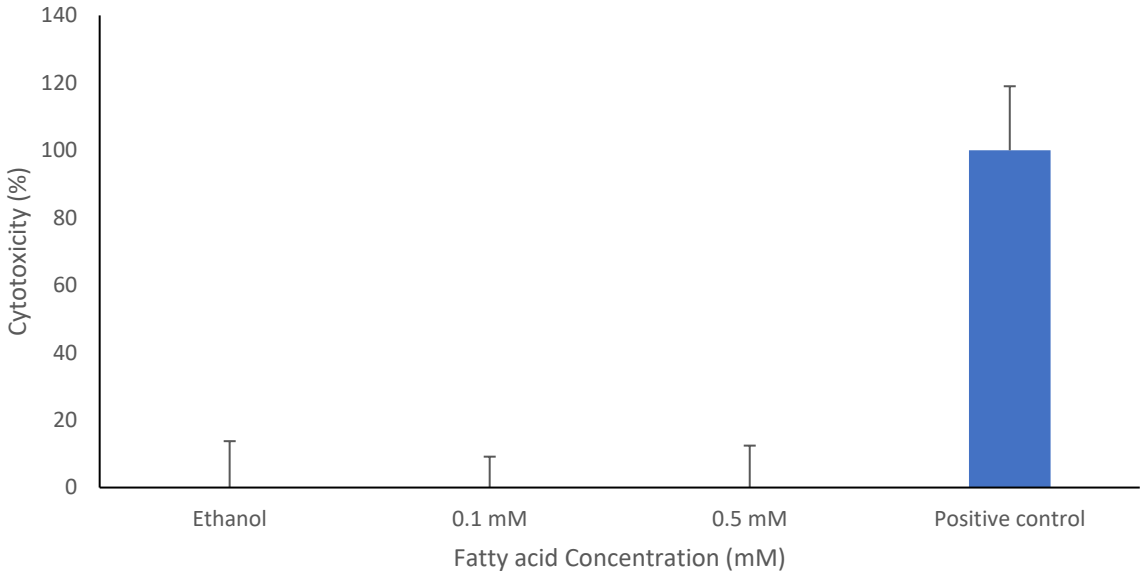

Figure 3.26 HepG2 spheroid cell death in response to increasing fatty acid concentration assessed by LDH assay. HepG2 spheroids were treated with a 2:1 mixture of oleic and palmitic acid at concentrations of 0, 0.1 and 0.5 mM and incubated for 24 hours as described in Section 2.5.1. The value obtained for the positive control represents 100% cell death. The LDH assay was carried out as described in Section 2.21. The values shown represent the mean of six replicates. Error bars represent standard deviation.

3.3.10 Triglyceride accumulation in spheroids dosed with fatty acids

Lipid accumulation was assessed in HepG2 spheroids in this study using a commercial triglyceride assay kit. The results shown in Figure 3.27 revealed no difference in triglyceride accumulation between the control and 0.1 mM fatty acid-treated groups (30.4 and 29 µg, respectively). However, there was a significant increase ($p>0.05$) to 48 µg in the 0.5 mM fatty acid-treated group.

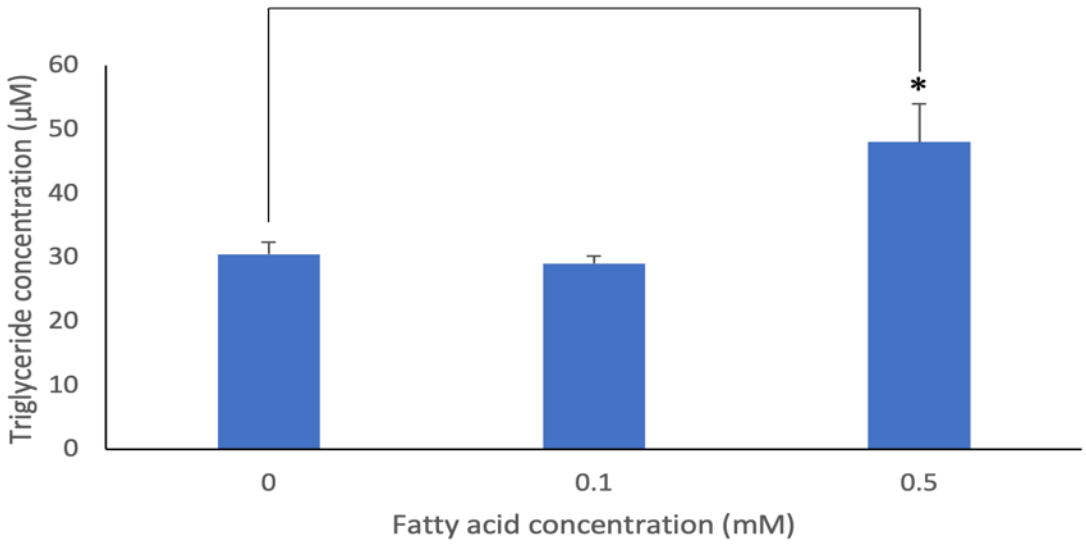

Figure 3.27 Mean triglyceride content in HepG2 spheroids following treatment with fatty acids. HepG2 cells were treated with a 2:1 mixture of oleic and palmitic acid at concentrations of 0 (ethanol control), 0.1 and 0.5 mM fatty acids and incubated for 24 hours. The triglyceride assay was carried out as described in Section 2.8. The values shown represent the mean of six replicates. Error bars represent standard deviation. Statistically significant differences were analysed using Kruskal-Wallis *(*<0.05)*.

3.3.11 Metabolomic analysis of aqueous spheroid extracts

HepG2 spheroid sample extracts were collected following a 24-hour incubation in culture media supplemented with fatty acids two different dose levels (0.1 and 0.5 mM). Aqueous extracts were prepared and analysed by NMR as described in Section 2.11. Multivariate analysis was then used to determine changes in the metabolite profile of spheroids in response to fatty acids.

Visible inspection of NMR spectra obtained from aqueous spheroid extracts did not show any differences between treated groups and the control group (data not shown). Therefore, a PCA scores plot was constructed to identify differences between the groups, as shown in Figure 3.28. The scores plot demonstrates separation between the different sample groups with all the control samples positive for PC2 and in the upper half of the plot while the majority of the treated samples were negative. However, large intragroup separation can be seen with samples from all groups spread across the PC1 axis.

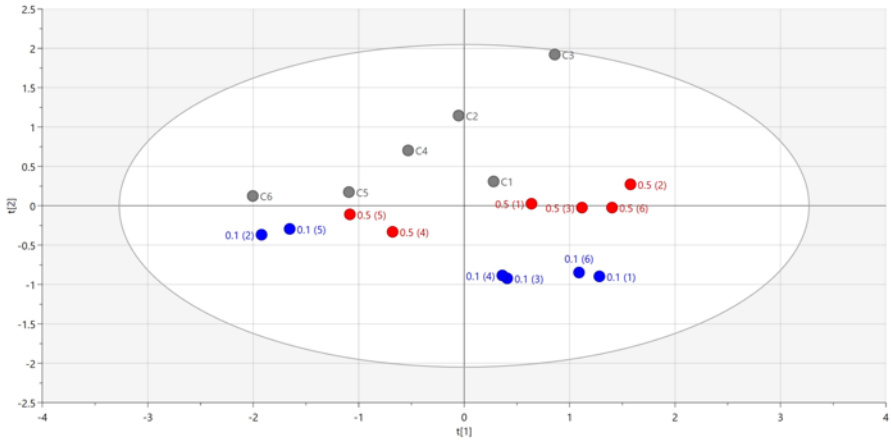

Figure 3.28 PCA scores plot derived from ^{1}H NMR spectra of aqueous extracts from HepG2 spheroids dosed with a 2:1 mixture of oleic and palmitic acid at different dose levels (0, 0.1 and 0.5 mM). Spheroids were dosed with 0, 0.1 and 0.5 mM fatty acids and incubated for 24 hours. Samples were collected and NMR analysis carried out as described in Sections 2.10 and 2.12. Each spot represents one sample. Grey = Ethanol control; blue = 0.1 mM; red = 0.5 mM.

Following on from the PCA analysis the NMR data was further analysed using OPLS analysis. The scores plot obtained, shown in Figure 3.29, revealed better inter-group separation than the PCA model. The majority of the treated samples were positive along the predictive t[1] axis. Some intragroup variation can be seen for all treated groups along the orthogonal t[0] axis with samples 0.1 mM (2 and 5) and 0.5 mM (4 and 5) being negative for t[0] while the remainder of their respective groups were positive. Large intragroup separation was also observed in the ethanol control group which has 3 samples positive for t[0] and 3 that are negative.

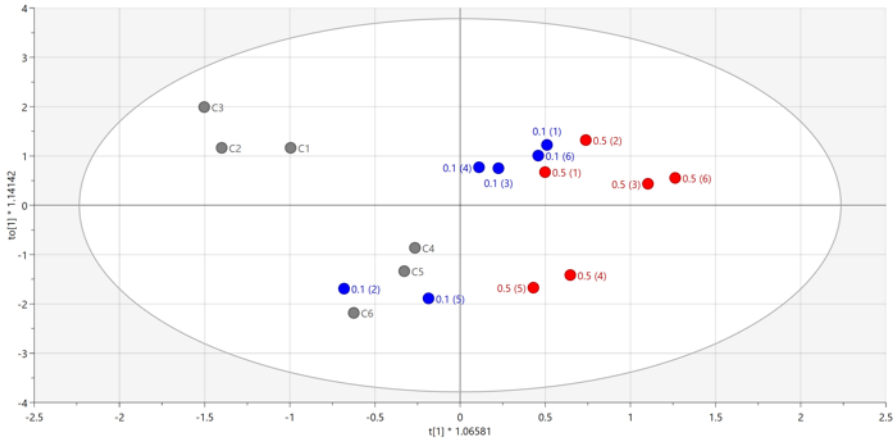

Figure 3.29 OPLS scores plot derived from ^{1}H NMR spectra of aqueous extracts from HepG2 spheroids dosed with fatty acids at different concentrations of a 2:1 mixture of oleic and palmitic acid at 0, 0.1 and 0.5 mM. Spheroids were dosed with 0, 0.1 and 0.5 mM fatty acids and incubated for 24 hours. Samples were collected and NMR analysis carried out as described in Sections 2.10 and 2.12. Each spot represents one sample. Grey = Ethanol only control; blue = 0.1 mM; red = 0.5 mM.

Further analysis of the NMR spectra in this study included the generation of OPLS-DA scores plots to carry out pair-wise comparisons of the control group versus the two treated groups as well as a direct comparison of the two treated groups. All OPLS-DA scores plots generated showed clear separation between the sample groups being compared along the t[1] axis (Figures 3.30) but orthogonal separation within each group was also visible along the t[0] axis in each plot.

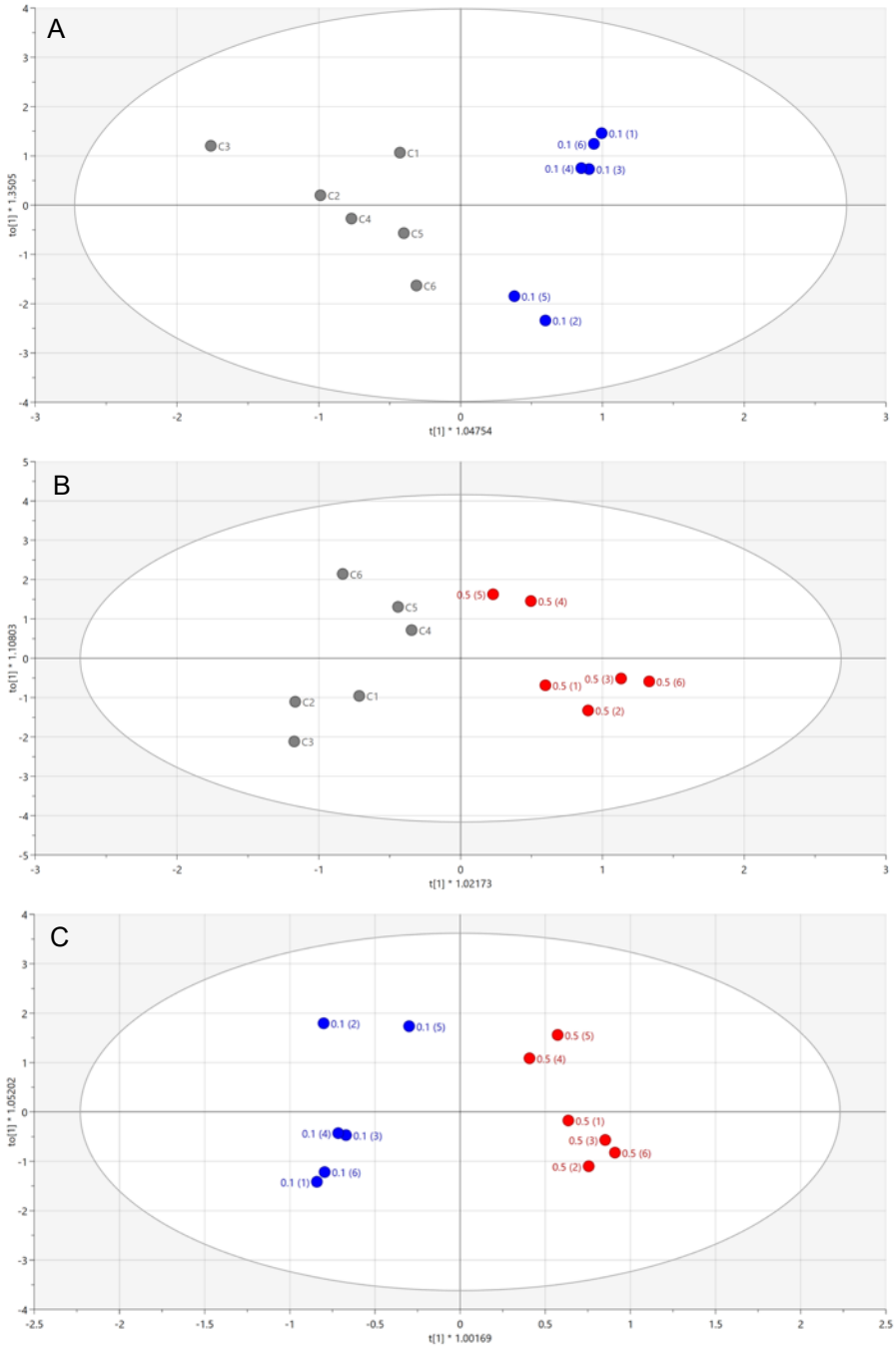

Figure 3.30 OPLS-DA scores plots derived from NMR spectra of aqueous extracts from HepG2 spheroids dosed with a 2:1 mixture of oleic and palmitic acid at varying dose levels. Spheroids were dosed with a combination of oleic and palmitic acid at 0, 0.1 and 0.5 and incubated for 24 hours. Samples were collected, and NMR analysis was carried out as described in Sections 2.10 and 2.12.

Each spot on the scores plot represents one sample. A. Control vs 0.1 mM fatty acids. B. Control vs 0.5 mM fatty acids. C. 0.1 vs 0.5 mM.

Using the OPLS-DA models VIP predictive and S-plots (Figures 3.31 and 3.32) were generated to determine the metabolite regions in the NMR spectra that contributed most to the separation of the two groups in each pair-wise comparative scores plots. The VIP plots revealed NMR regions that were statistically significant and the regions with a VIP value greater than one are highlighted in red in both the VIP and S-plots. The S-plots were then used to confirm whether peaks within these specific NMR variable regions had increased or decreased between the two groups being compared.

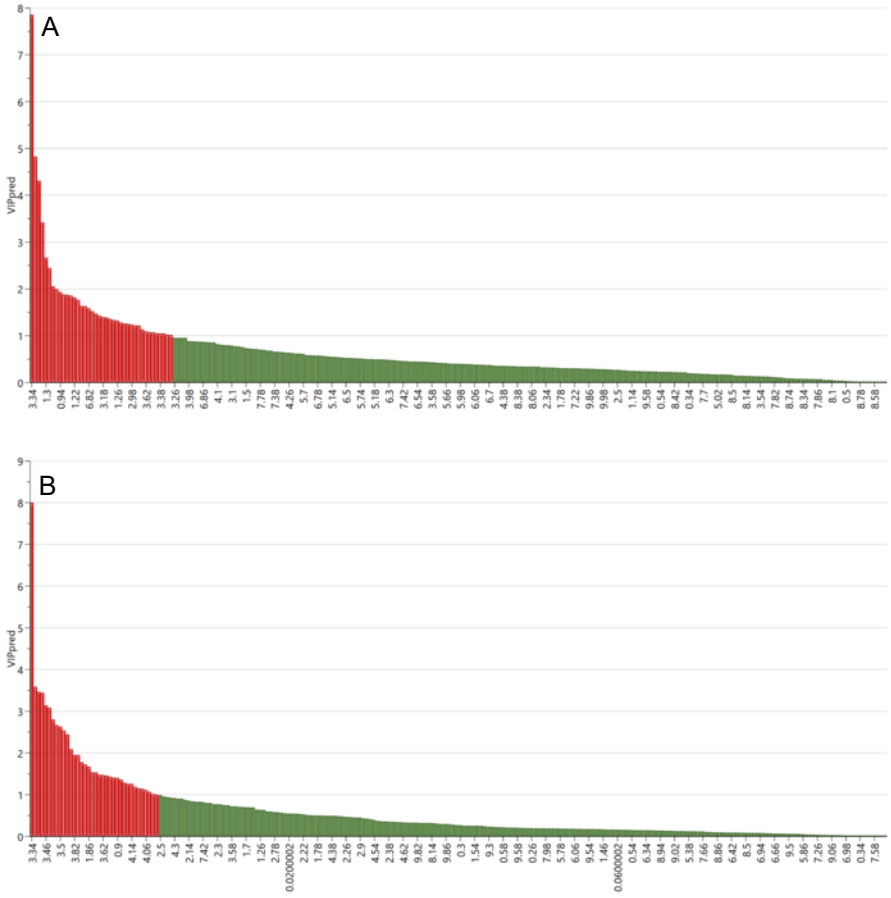

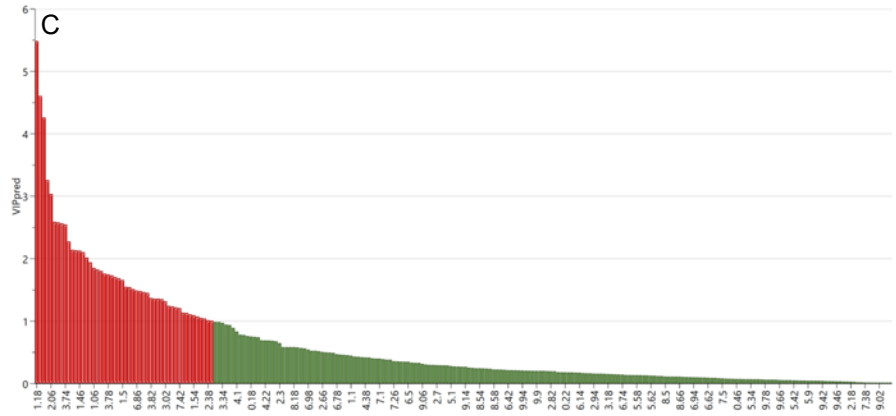

Figure 3.31 VIP predictive plots derived from OPLS-DA models of NMR spectra of aqueous extracts from HepG2 spheroids treated with a 2:1 mixture of oleic and palmitic acid at different concentrations at 0, 0.1 and 0.5 mM. Samples were collected and NMR analysis was carried out as described in Sections 2.10 and 2.12. A. Control vs 0.1 mM fatty acids. B. Control vs 0.5 fatty acids. C. 0.1 vs 0.5 mM. Variables with a VIPpred value above 1 were selected as significant and are highlighted in red. Variable regions are shown along the x-axis.

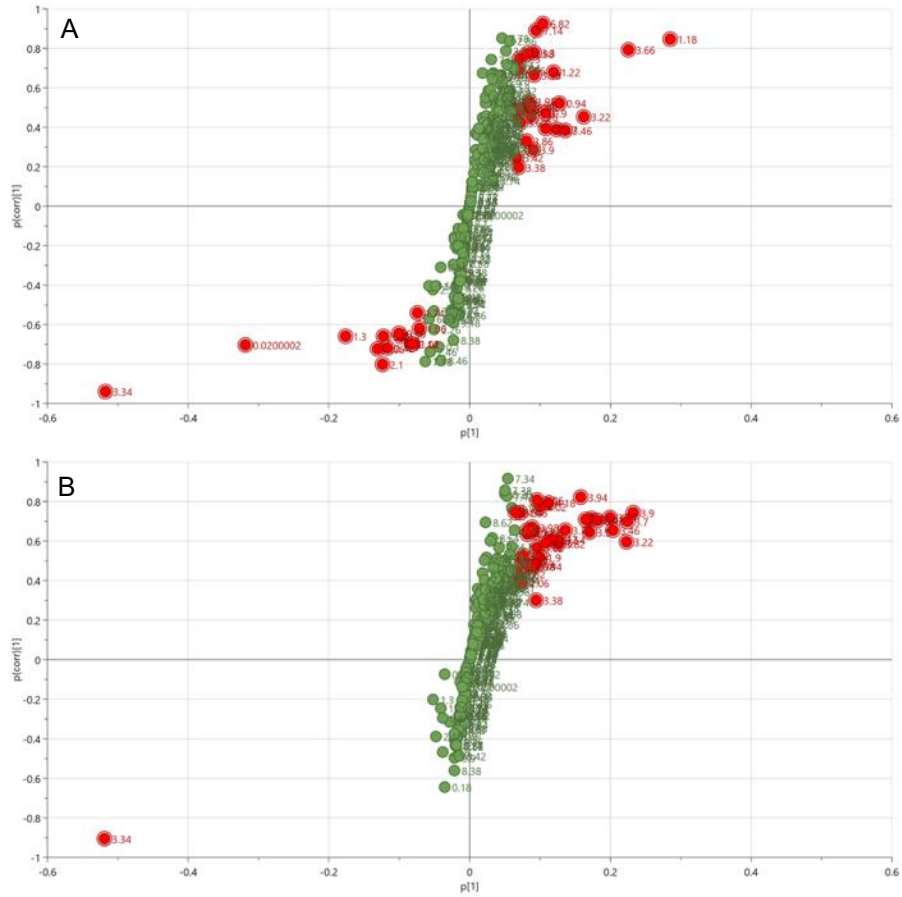

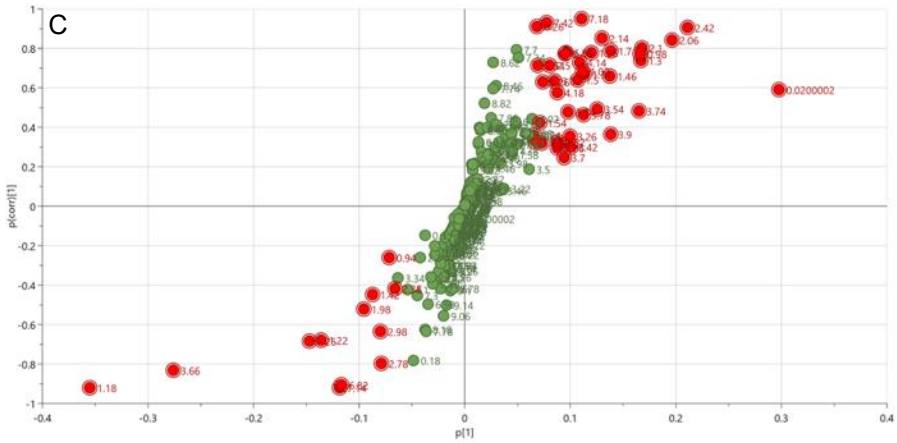

Figure 3.32 S-plot derived from OPLS-DA models of NMR spectra of aqueous extracts from HepG2 spheroids treated with a 2:1 mixture of oleic and palmitic acid at different concentrations at 0, 0.1 and 0.5 mM and incubated for 24 hours. Samples were collected and NMR analysis was carried out as described in Sections 2.10 and 2.12. A. Control vs 0.1 mM fatty acids. B. Control vs 0.5 mM fatty acids. C. 0.1 vs 0.5 mM.

Using the spectral regions highlighted in the VIP and S-plots visual inspection of the ^{1}H NMR spectra was conducted to identify the multiplicity of the peaks within these regions. A Kruskal Wallis test was also conducted to determine if there were any statistically significant differences between the regions. The Human Metabolome database and published literature were employed to identify metabolites thought to be responsible for peaks in the important VIP regions. However, it was not possible to identify all of the peaks considered significant and many remain unidentified (data not shown). Despite this, Table 3.4 shows that changes in metabolite peaks thought to belong to methionine, phosphocholine, betaine and glycine were apparent (although not statistically significant) in both treated groups when compared to the control. Succinate was significantly increased ($p<0.05$) in the 0.5 mM treated group when compared to the 0.1 mM group.

Table 3.4 Chemical shift regions identified as significantly different in the aqueous extracts of HepG2 spheroids treated with different concentrations of fatty acids as detected by OPLS-DA analysis. The multiplicity of each peak is shown.

^{1}H shift ppm	Metabolite aqueous	Ctrl + 0.1mM	Ctrl +0.5mM	0.1 + 0.5 mM
0.886-0.974 (m)	Acyl groups (CH_3)	↑	↑	↑*
1.188-1.212 (d), 1.166-1.203 (t)	B-hydroxybutyrate	↑*	-	↓
1.314-1.3458 (d)	Lactate	↓	-	↑
1.911-1.926 (s)	Acetate	-	↑	↑
1.99-2.1 (m)	Methionine, Glutamine	↑	↑	↑
2.294-2.431 (m)	Glutamate	↑	-	↑
2.415-2.431 (s)	Succinate	-	↑	↑*
3.03-3.049 (s)	Creatine	↑	-	↑
3.217-3.231(s)	Phosphocholine, Choline	↑	↑	-
3.255-3.267 (s)	Betaine/TMAO	↑	↑	↑
3.5021-3.511 (s)	Glycine	↑	↑	-
3.515-3.552 (dd)	Choline	-	↑	-
3.881-3.919 (dd)	Methionine, Homocysteine	↑	↑	↑
3.937-3.945 (s)	Creatine, Phosphocreatine	↑	↑	↑
5.22-5.245 (d)	Glucose	-	↑	-

S=singlet, d=doublet, dd=doublet of doublets, t=triplet, q=quartet, m=multiplet. An increase or decrease in the treated group was determined and these were further analysed statistically using a Kruskal-Wallis test (<0.05, **<0.01, ***<0.001).*

3.3.12 Metabolomic analysis of organic spheroid extracts

Organic extracts from HepG2 spheroids were also analysed using NMR spectroscopy. Since visual inspection of the 1D NMR spectra showed no obvious similarities between the two groups treated with fatty acids and the vehicle control multivariate analysis was carried out. Clear separation was observed in the PCA scores plot (Figure 3.33) between the vehicle control group (in grey) and the two treated groups along PC1 with the exception of sample C1. All samples in the 0.5 mM treated group apart from 0.5(5) were located in the lower quadrant of the scores plot while the majority of the 0.1 mM group were in the top right-hand except for 0.1(5) and 0.1(3). However, some intragroup variation was evident particularly for the 0.1 mM treated group. The PCA scores plot also showed a lack of complete separation between the 0.1 and 0.5 mM treatment groups.

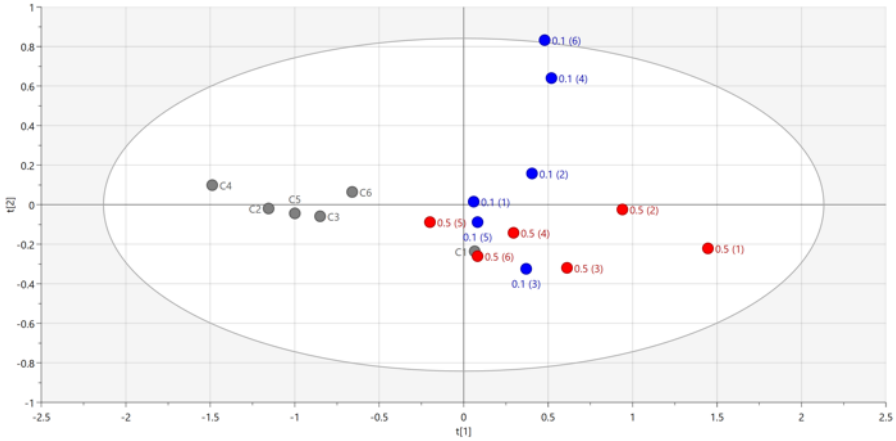

Figure 3.33 PCA scores plot derived from ^{1}H NMR spectra of organic extracts from HepG2 spheroids dosed with fatty acids at different concentrations of a 2:1 mixture of oleic and palmitic acid at 0, 0.1 and 0.5 mM. Cells were dosed with 0, 0.1 and 0.5 mM valproate and incubated for 24 hours. Samples were collected, and NMR analysis carried out as described in Sections 2.10 and 2.12. Each spot represents one sample. Grey = Ethanol control; blue = 0.1 mM; red = 0.5 mM.

As the PCA analysis failed to show clear sample group clustering an OPLS scores plot was created. However, Figure 3.34 demonstrates that the OPLS analysis revealed similar results to the PCA (Figure 3.33) with the control groups separated from the treated groups along the t[1] axis and the treated groups clustered together on the right-hand side of the scores plots. The intragroup separation within the 0.1 mM groups was also visible along the t[0] orthogonal axis.

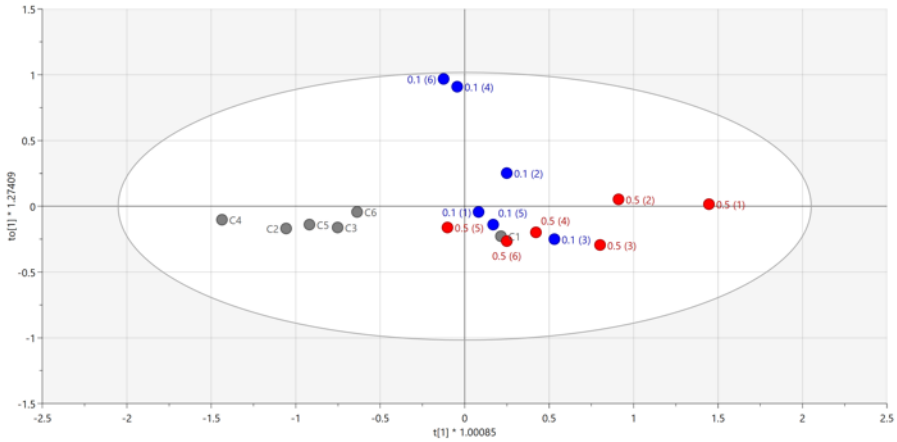

Figure 3.34 OPLS scores plot derived from ^{1}H NMR spectra of organic extracts from HepG2 spheroids dosed with fatty acids at different concentrations of a 2:1 mixture of oleic and palmitic acid at 0, 0.1 and 0.5 mM. Cells were dosed with 0, 0.1 and 0.5 mM valproate and incubated for 24 hours. Samples were collected and NMR analysis carried out as described in Sections 2.10 and 2.12. Each spot represents one sample. Grey = Ethanol control; blue = 0.1 mM; red = 0.5 mM.

To identify if there are any metabolite differences between the control and the two treatment groups and also between the 0.1 and 0.5 mM groups OPLS-DA models were created (Figure 3.35). In Figures 3.35 A and B clear separation was revealed when the control group was compared with both the 0.1 and 0.5 mM groups. For each pair-wise comparison the controls were located on the left-hand side of the scores plots with the exception of control sample 1 (C1) while the respective treated groups were on the right. Intragroup variation in the 0.1 mM group, as seen in the PCA and OPLS models, was still visible in the OPLS-DA models.

Figure 3.35 C shows the OPLS-DA scores plot constructed to directly compare the 0.1 mM group with the 0.5 mM group. As expected from the PCA and OPLS models complete separation between the treated groups along the t[1] axis was not achieved. Samples 0.1 (4 and 6) were separated from all other samples in the analyses which is likely due to the large intragroup variation within this sample group. Sample C1 was also located away from the other control samples and located on the right-hand side of the scores plot.

The OPLS-DA models were then used to identify treatment-related metabolite peak changes using the corresponding VIP and S-plots (Figure 3.36 and 3.37) NMR spectral regions with VIP values higher than 1 (shown in red) were considered to be significantly different and responsible for sample group separation and were selected for further analyses.

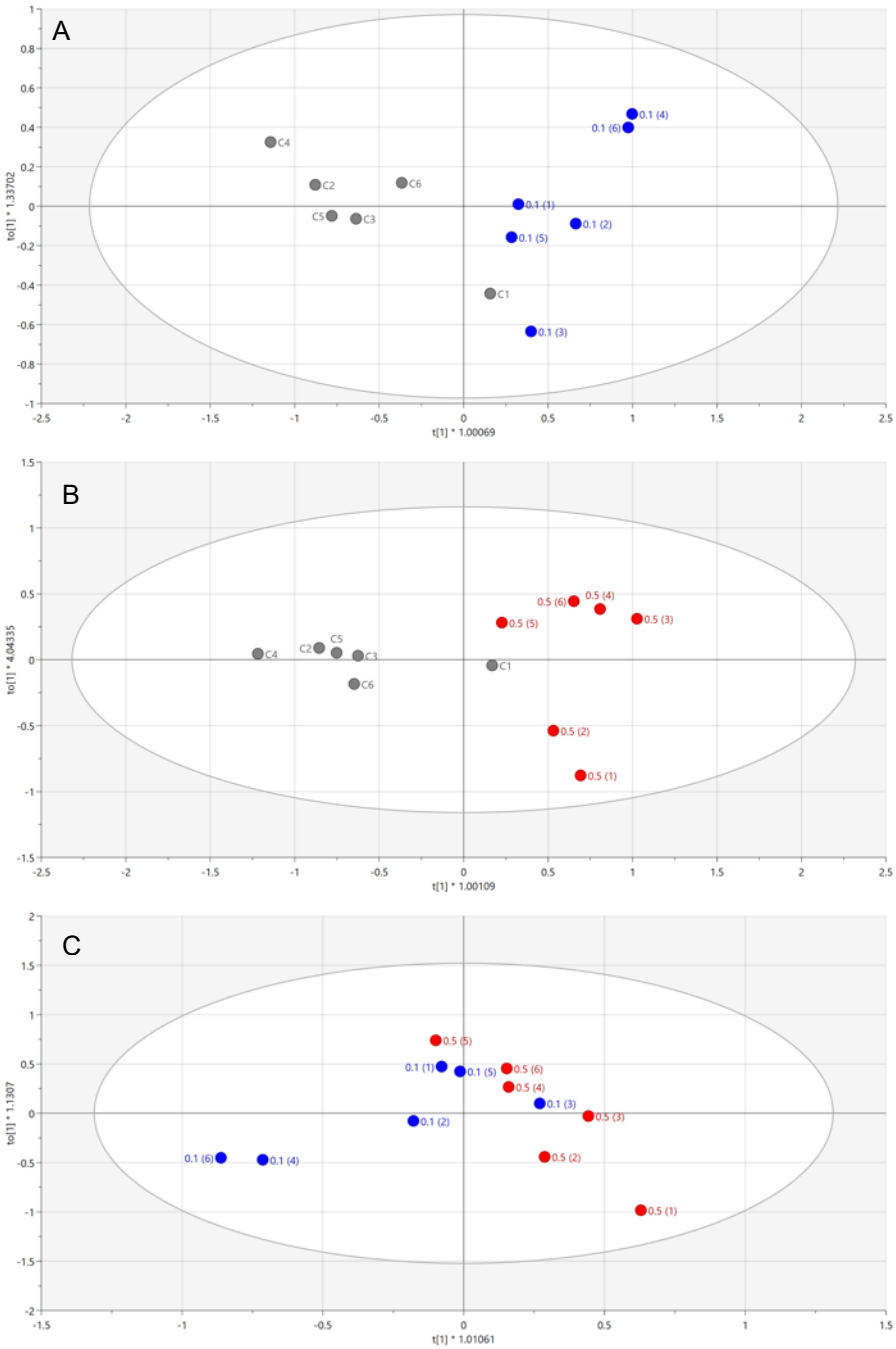

Figure 3.35 OPLS-DA scores plots derived from NMR spectra of organic extracts from HepG2 spheroids dosed with a 2:1 mixture of oleic and palmitic acid at varying dose levels. Cells were dosed a combination of oleic and palmitic acid at 0, 0.1 and 0.5 and incubated for 24 hours. Samples were collected, and NMR analysis was carried out as described in Sections 2.10 and 2.12. Each spot on the scores plot represents one sample. A. Control vs 0.1 mM fatty acids B. Control vs 0.5 mM fatty acids C. 0.1 vs 0.5 mM fatty acids.

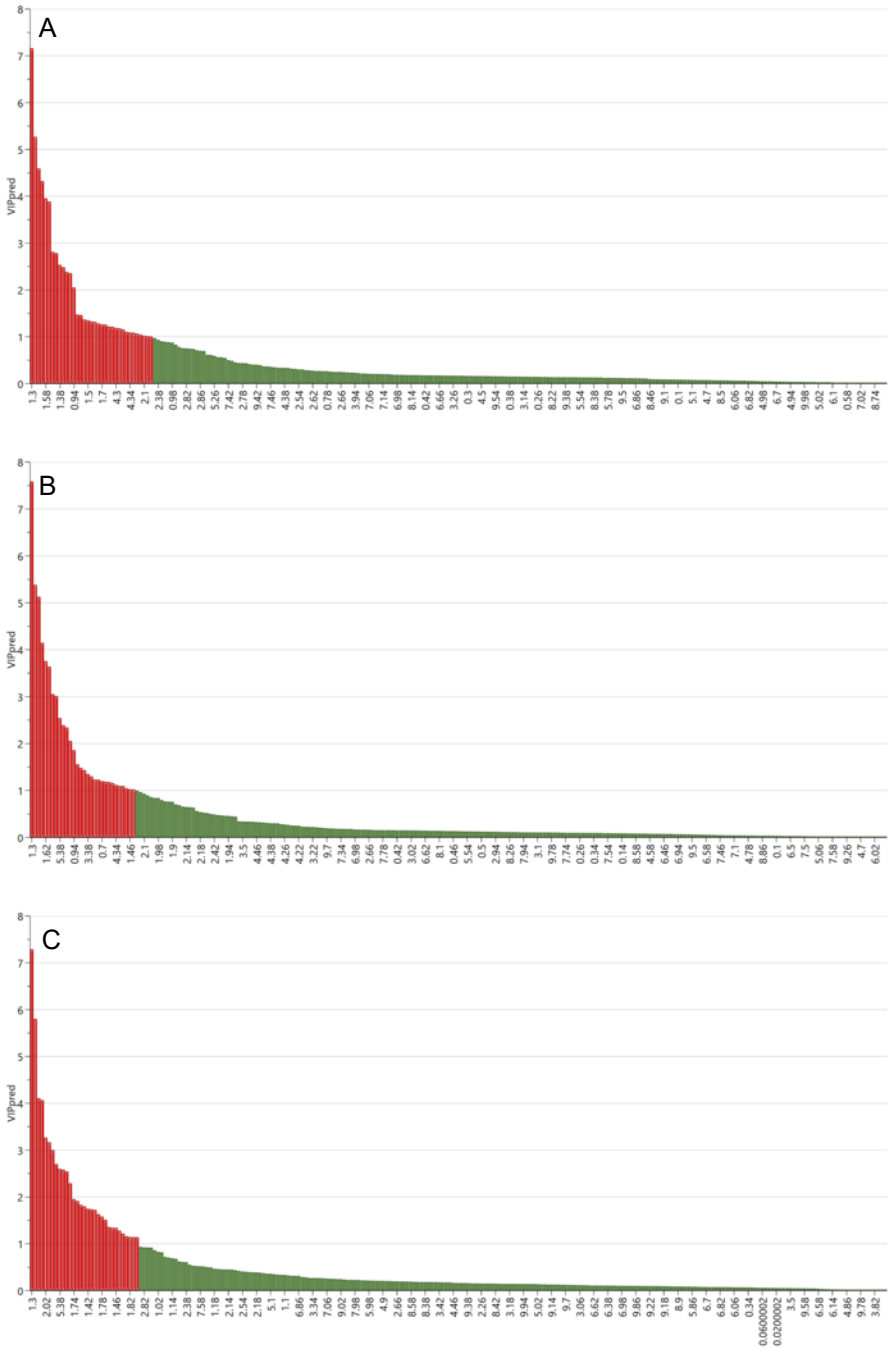

Figure 3.36 VIP predictive plots derived from OPLS-DA models of NMR spectra of organic extracts from HepG2 spheroids treated with a 2:1 mixture of oleic and palmitic acid at different concentrations at 0, 0.1 and 0.5 mM. Samples were collected and NMR analysis was carried out as described in Sections 2.10 and 2.12. A. Control vs 0.1 mM fatty acids B. Control vs 0.5 mM fatty acids C. 0.1 vs 0.5 mM fatty acids. Variables with a VIPpred value above 1 were selected as significant and are highlighted in red. Variable regions are shown along the x-axis.

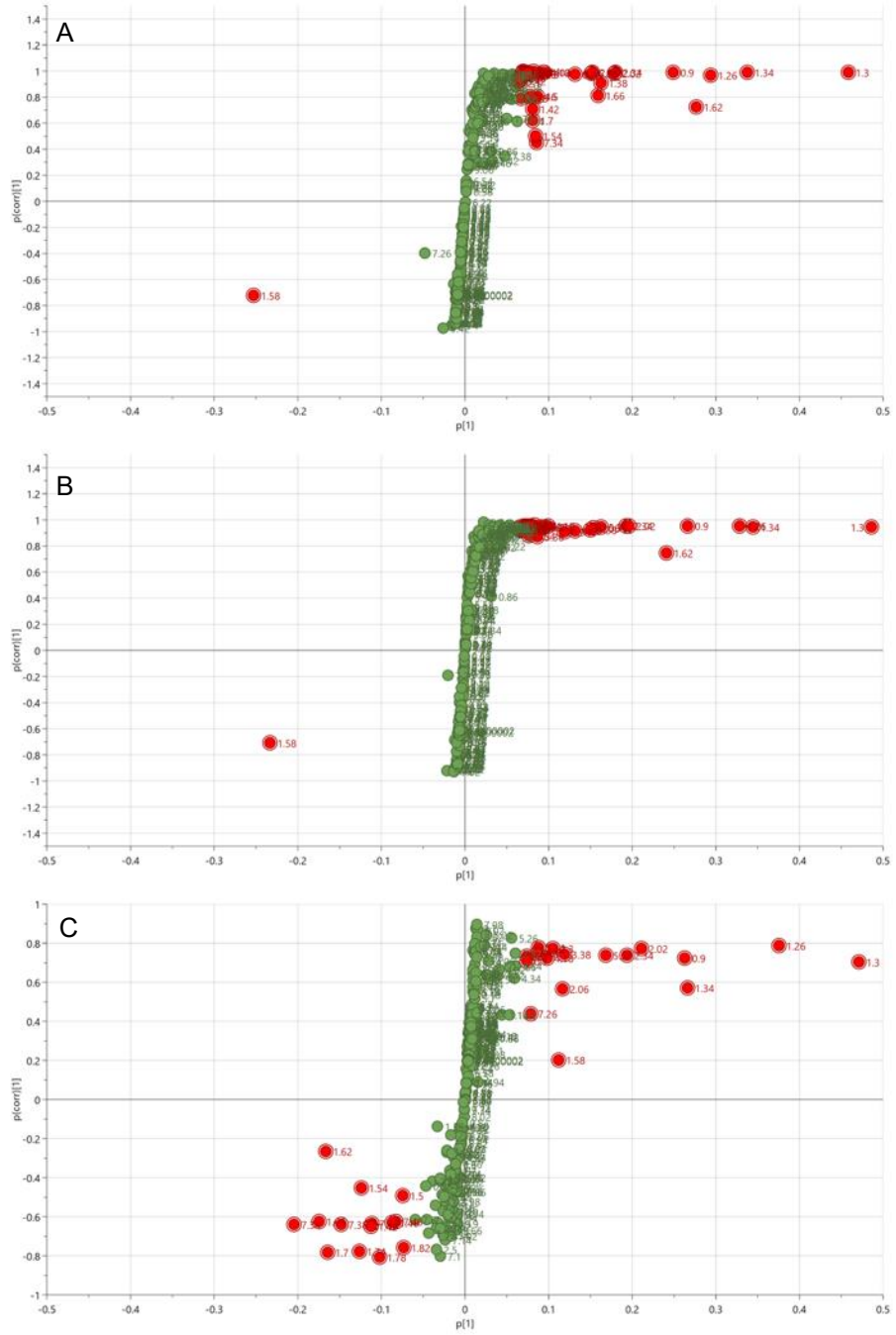

Figure 3.37 S-plot derived from OPLS-DA models of NMR spectra of organic extracts from HepG2 spheroids treated with a 2:1 mixture of oleic and palmitic acid at different concentrations at 0, 0.1 and 0.5 mM and incubated for 24 hours. Samples were collected and NMR analysis was carried out as described in Sections 2.10 and 2.12. A. Control vs 0.1 mM fatty acids B. Control vs 0.5 mM fatty acids C. 0.1 vs 0.5 mM fatty acids.

Following the identification of the spectral regions of interested from the VIP and S-plot models a visual inspection of these regions on the NMR spectra was carried out to evaluate multiplicity of the peaks within these regions (data shown in Table 3.5). Several other spectral regions were also identified as contributors to class separation; however, metabolite identification was not possible. A Kruskal Wallis test was

conducted to analyse statistically significant differences between the integral spectral values.

Significant differences between the treated groups and controls included increases ($p<0.01$) in fatty acyl groups, cholesterol and monounsaturated fatty acids in the 0.5 mM group. Arachidonic acid was the only metabolite to show a significant decrease ($p<0.01$) in both treated groups. A dose dependent response can be seen in the majority of metabolites with many of them including FA/MUFA, fatty acyl groups and cholesterol showing significant increases in the 0.5 mM but not in the 0.1 mM.

Table 3.5 Chemical shift regions identified as significantly different in the organic extracts of HepG2 spheroids treated with different concentrations of fatty acids as detected by OPLS-DA analysis. The multiplicity of each peak is shown.

^{1}H shift ppm	Metabolite aqueous	Ctrl + 0.1mM	Ctrl +0.5mM	0.1+0.5 mM
0.886-0.9262(t)	Fatty acyl groups and FA	↑	↑**	↑
1.028-1.038(s)	Cholesterol	↑	↑**	-
1.1317-1.168(m)	Multiple cholesterol protons	↑	↑**	-
1.5625-1.605(s)	Arachidonic acid (ARA)	↓**	↓**	↓
2.008-2.065(q)	Oleic acid	↑	↑**	↑
2.3129-2.365(m)	Acyl groups in triglycerides	↑	↑**	↑
4.145-4.193(dd)	Glyceryl group in monoglyceride	↑	↑**	↑
4.295-4.3404(dd)	Glyceryl group in triglycerides	↑	↑**	↑
5.267-5.315(m)	Oleic acid	↑	↑**	↑
5.327-5.414(m)	Fatty acids/Monounsaturated fatty acids MUFA	↑	↑**	↑

S=singlet, d=doublet, dd=doublet of doublets, t=triplet, q=quartet, m=multiplet. An increase or decrease in the treated group was determined and these were further analysed statistically using a Kruskal-Wallis test (<0.05, **<0.01, ***<0.001).*

3.3.13 CYP enzyme expression levels in spheroid HepG2 cells dosed with fatty acids

Western blotting of protein extracts in this experiment were performed, as described in Section 2.20, to analyse CYP expression in the HepG2 spheroids dosed with a 2:1 mixture of oleic and palmitic acid at different dose levels. For all blots, beta actin (Figure 3.38A) was used as a loading control. Figures 3.38 B, C and D showed CYP2D6, CYP 3A4 and CYP2E1 expression levels, respectively at the different fatty acid concentrations. Table 3.6 showed the relative band intensity for each target protein and revealed no significant dose related change for any of the CYPs. Similar to the Western blots for the monolayers all CYPs were detected however, no dose related responses were observed. This would suggest that spheroids do not have a higher CYP expression than monolayers.

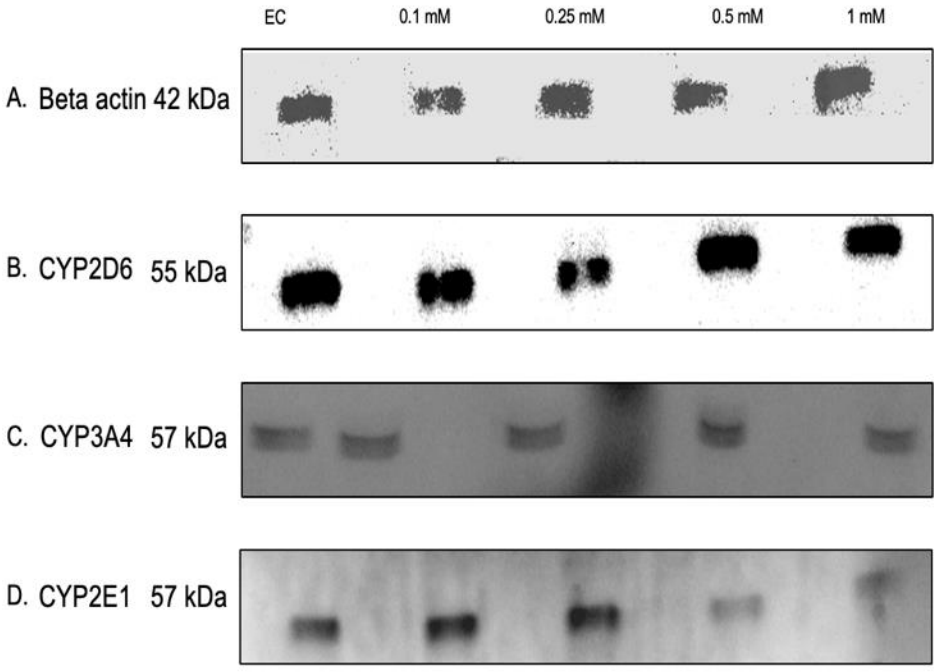

Figure 3.38 Western blot analysis of CYP enzyme expression in HepG2 spheroids dosed with fatty acids. A. Beta actin, B. CYP 2D6 and C. CYP 3A4. Spheroids were dosed with a combination of oleic and palmitic acid at varying concentrations or 0, 0.1, 0.25, 0.5 and 1 mM and proteins were collected as described in Section 2.16. Western blotting was carried as described in Section 2.20. EC: Ethanol control, 0.1 mM, 0.25 mM, 0.5 mM and 1 mM fatty acids.

Table 3.6 Raw data showing arbitrary band intensities for CYP2D6, 3A4 and 2E1 in HepG2 spheroids dosed with fatty acids. Spheroids were dosed with a combination of oleic and palmitic acid at varying concentrations or 0, 0.1, 0.25, 0.5 and 1 mM and proteins were collected as described in Section 2.16.

Fatty acid concentration (mM)	**CYP2D6**	**CYP3A4**	**CYP2E1**
Ethanol control	15003.12	9384.54	3820.28
0.1	11604.32	9945.903	5014.35
0.25	7191.71	8436.35	4501.64
0.5	15045.58	11642.34	1729.50
1	11819.44	8233.32	1588.79

3.4 Discussion

The first objective of the present study was to create *in vitro* models of steatosis in monolayer cells and 3D spheroids grown from HepG2 cells. The HepG2 cell line was chosen for this study since it has been widely used for the development of NAFLD cellular models (Dave et al., 2018, Muller and Strula, 2019, Soret et al., 2021). Many studies have used HepG2 cells for the evaluation of steatosis primarily because they can be easily treated with a combination of fatty acids and the resulting steatosis presents morphological similarities to steatotic hepatocytes *in vivo* (Cui et al., 2010, Choi et al., 2015, Dave et al., 2018, Muller and Strula, 2019, Soret et al., 2021). For this study monolayers were cultured for 24 hours to allow them to attach overnight before use. Meanwhile spheroids were grown for 17 days in DMEM media prior to dosing. Selecting the ideal number of days to grow the spheroids before dosing is vital since the expression of albumin and a number of important drug metabolizing enzymes including CYP P450 enzymes and transporters (DMETs) increases with time as the HepG2 spheroids grow (Cox et al., 2020). Many studies have analysed spheroid growth and proteomic changes at days 7, 14, 21 and 28 (Eilenberger et al., 2019, Cox et al., 2020, Ellero et al., 2021, Tutty et al., 2022, Gronert et al., 2023). Ellero et al., (2021) demonstrated that protein concentration in spheroids grown through the hanging drop method increased within the first two weeks of culture but then plateaued from days 14 to 28. While Gronert et al., (2023) demonstrated the highest albumin expression was observed in the spheroids grown by the forced floating method with a time-dependent increase up to 1257% at day 21.

Although the ability to culture for longer is an important advantage of 3D spheroids, when compared to 2D monolayers the longevity of these model systems is limited by the development of a hypoxic and necrotic core. This unwanted phenomenon due to the 3D structure of spheroids results from the accumulation of metabolic waste products and insufficient diffusion of oxygen and nutrients (Eilenberger et al., 2019, Cox et al., 2020). Development of a necrotic core, however, depends on the size of the spheroids and, therefore, is typically associated with 3D spheroids formed with proliferating cells, which become larger over time (Cox et al., 2020). Eilenberger et al., (2019) measured spheroid growth, solidity and roundness between days 3 to 5, 6 to 12 and 15 to 18 of growth. They reported an increase in the diameter of the spheroids

over the first 9 days from 746 ± 12 µm to 857 ± 19 µm which remained stable for the following days of culture with 810 ± 30 µm for day 12. At days 15 and 18 there were decreases in diameter to 766 ± 51 µm and 743 ± 10 µm, respectively indicating the start of spheroid disintegration. In their study when spheroids were visualised under the microscope both early (day 3) and mid-stage spheroids (day 6) revealed the presence of equally distributed chromatin in the nucleus as well as intact cytoplasm, thus indicating the cells were viable. In contrast, late-stage spheroids at day 18 displayed typical apoptotic characteristics with loss of integrity of the outermost lining layer (Eilenberger et al., 2019). Taking this into account, in the present study day 17 was chosen for spheroid collection as this was prior to the loss of spheroids cell viability but still maintained the highest protein expression. However, the spheroids collected throughout these experiments were different sizes meaning the necrotic core may have been bigger in some spheroid. Nevertheless, the results from the viability testing of spheroids showed that they were still viable at the time of analysis.

This study aimed to create two models of mild steatosis using fatty acids. Oleic and palmitic acid are long-chain fatty acids found in dietary sources meaning normal healthy subjects are exposed to both in the diet (Juarez-Hernandez et al., 2016, Rada et al., 2020). However, consistently high levels of dietary palmitic and oleic acid can lead to increased lipid accumulation in the liver (Ricchi et al., 2009, Lyall et al., 2018, Zeng et al., 2020) and therefore hepatic steatosis.

The use of oleic and palmitic acid for the development of *in vitro* models of steatosis have been described extensively in the literature (Gomez-Lechon et al., 2007, Ricchi et al., 2009, Mei et al., 2011, Garcia-Ruiz et al., 2015, Moracova et al., 2015 and Eynaudi et al., 2021). Studies have reported that oleic and palmitic acid can induce steatosis in primary hepatocytes and hepatoma cell lines when administered both individually and as a mixture (Gomez-Lechon et al., 2007, Ricchi et al., 2009, Mei et al., 2011, Moracova et al., 2015). However, it is known that palmitic acid at high concentrations (>250 µM) is poorly incorporated into triglycerides and leads to cellular apoptosis due to a build-up of free fatty acids (Listenberger et al., 2003, Zhang et al., 2012). Consequently, it has been shown that dosing cells with palmitic acid alone at concentrations of 0.5 mM and above increases ROS production and promotes fibrogenesis, thus creating a cell model more suitable for NASH studies (Moracova et

al., 2015, Dave et al., 2018). Meanwhile, oleic acid supplementation alone is generally well tolerated by cells and has been shown to result in a dose-dependent increase in steatosis in both HepG2 cells and primary hepatocytes (Cui et al., 2010, Moracova et al., 2015, Alkhatabeh et al., 2016, Dave et al., 2018). Studies have suggested that oleic acid can induce steatosis at doses as low as 0.1 mM (Cui et al., 2010, Alkhatabeh et al., 2016). However, high concentrations of oleic acid particularly those above 1 mM can result in a significant rise in lipid peroxides after 24 hours (Cui et al., 2010, Tie et al., 2021).

Many studies have demonstrated that treating HepG2 cells with a combination of both fatty acids is considered more effective for inducing a steatotic state that is similar to the human phenotype (Fan et al., 2013, Moracova et al., 2015, Dave et al., 2018, Boeckmans et al., 2018). The addition of a small amount of palmitic acid to the oleic acid leads to lipid accumulation alongside minor toxic and apoptotic effects. This creates a model that represents a benign state of chronic mild steatosis which is more relevant to the human form of steatosis (Liang et al., 2015, Moracova et al., 2015, Dave et al., 2018).

However, the overall concentration of these fatty acids administered to HepG2 cells and the ratio of oleic to palmitic acid is critical (Moracova et al., 2015, de Sousa et al., 2021). While studies have shown that oleic acid does not induce alterations in cell membrane integrity up to concentrations of 1 mM, palmitic acid enhances LDH leakage at concentrations of 0.25 mM and above (Moracova et al., 2015, de Sousa et al., 2021). Additionally, cells dosed with oleic acid had a 33% higher cell viability than those dosed with palmitic acid at concentrations of 0.5 mM (de Sousa et al., 2021). Therefore, the use of a dosing solution containing a higher proportion of palmitic acid (e.g., oleic acid/palmitic acid, 1:2 and 0:3 ratio) is more likely to result in reduced cell viability as the accumulation of excess palmitate can lead to lipotoxicity and cell death, thus reflecting a NASH model (Dave et al., 2018). A study using the same ratio (1:1 mixture) of the two fatty acids found a significantly lower LDH leakage from the cells, indicating reduced cell toxicity at overall fatty acid concentrations of 0.5 and 1 mM compared to when palmitic acid was administered alone (Moracova et al., 2015).

Other studies have experimented with different ratios and final concentrations of both fatty acids. For example, Gomez-Lechon et al., (2007) dosed human primary hepatocytes and HepG2 cells with different ratios of oleic/palmitic acid (3:0, 2:1, 1:1, 1:2 and 0:3) at concentrations of 0.125-2 mM for 12 and 24 hours. They reported a dose and time dependent increase in fat accumulation with maximal lipid accumulation observed at 2 mM after 24 hours of incubation. Dave et al. (2018) demonstrated using a triglyceride assay that a 2:1 oleic and palmitic acid mixture induced statistically significant increases in lipid levels without toxicity at dose levels between 0.75-1.5 mM. It has been frequently reported that a 2:1 oleic and palmitic acid mixture at a dose level of 0.5 mM induces significant fat accumulation in HepG2 cells and is only associated with very minor toxicity (Liang et al., 2015, Moracova., 2015, Dave et al., 2018).

Studies have also investigated many incubation time points including 6, 12, 16, 24 and 48 hours and all reported a maximal dose-dependent increase in lipid accumulation without causing toxicity at 24 hours (Gomez-Lechon et al., 2007, Moracova et al., 2015, Dave et al., 2018, Kahn and Kahn, 2021). Therefore, it was decided that in this study the cells would be incubated in fatty acids for 24 hours.

For this present study, in light of the literature a combination of 2:1 oleic and palmitic acid was chosen. However, since this study wished to develop models of steatosis it was important to ensure this chosen ratio of oleic to palmitic acid was not cytotoxic to the cells. Consequently, monolayer cells were dosed with 2:1 oleic and palmitic acid at concentrations of 0.1, 0.25, 0.5 and 1.0 mM and MTS and LDH assays were carried out to evaluation for any cytotoxic effects.

The results of the MTS assay (Figure 3.1) revealed a slight dose dependent decrease in cell viability at both 0.5 (56 %) and 1 mM (69 %) when compared to the ethanol control. Meanwhile the LDH assay showed a significant increase in cell death in the 1.0 mM sample group (7 %) when compared to the ethanol control. Overall, these results are reflective of the literature indicating that a 2:1 ratio of oleic acid and palmitic acid is generally well tolerated in HepG2 cells (Lechon et al., 2007, Moracova et al., 2015, Dave et al., 2018, de Sousa et al., 2021). As explained earlier the 1 mM dose level was considered acceptable for monolayer studies based on the LDH assay

results but it was decided to use 0.5 mM for future spheroid studies as this dose level displayed significant triglyceride accumulation without causing significant cytotoxicity.

Cell proliferation assays such as the MTS have two major limitations: the first being they can give false positive results as they do not actually measure the number of viable cells, but rather enzymatic activity related to cell metabolism and the second is they are unable to distinguish between an inhibition of cell proliferation and cell death (Berridge et al., 2005, Smith et al., 2011). Therefore, they basically measure the number of metabolically active cells in a sample (Berridge et al., 2005, Kroemer et al., 2009, Galluzi et al., 2009, Adan et al., 2016). This suggests that the discrepancy between the MTS and LDH assay results in the current study in which reduced cell viability values were observed for the 0.5 and 1 mM groups may be due to the steatotic state of the cells and not direct cytotoxicity. Studies have demonstrated that dosing with fatty acids results in decreased cell viability and proliferation in HepG2 cells. Plus, oleic acid has been reported to decrease cell proliferation in HepG2 cells without inducing cytotoxicity (Cui et al., 2010, Dave et al., 2018). Alternatively, the use of a LDH assay is a more reliable method of determining cell death as it measures the leakage of lactate dehydrogenase enzymes from the cell and can detect low level damage to the cell membrane (Parhamifar et al., 2012).

The next step in the study was to validate the creation of steatosis. Oil Red O staining of the HepG2 cells after 24 hours incubation with fatty acids demonstrated a clear dose dependent increase of stain uptake (Figure 3.3). The Triglyceride-Glo™ assay (Figure 3.4) showed a significant increase in triglyceride accumulation in the 0.25, 0.5 and 1 mM treated groups when compared to the control groups, with the highest increase in triglyceride concentration (114 µg) seen in the 0.5 and 1 mM groups. These results suggested that a steatotic state was created at dose levels above 0.25 mM.

In the monolayer study the rationale for using both Oil Red O staining and a triglyceride assay kit in combination to assess lipid accumulation in this study stems from limitations each have when used alone. Oil Red O staining is a simple method but does not allow for accurate quantification of cellular lipids. As a result, quantification techniques such as commercial assay kits have become increasingly popular and have been used in many studies of steatosis in HepG2 cells (Dave et al., 2017, Parra-

Vargas et al., 2018, Zhu et al., 2018, Lu et al., 2019, Tie et al., 2021). The Triglyceride-Glo™ assay kit used in this study utilises a luminescence-based chemistry allowing for better sensitivity and extended quantitative range and can detect triglyceride concentration as low as 1 µM (Wells, 2022). However, the assay kit is expensive, and several kits were required to conduct all the analyses, therefore its use in larger studies is not practical.

For the development of the spheroid model dose levels of 0.1 and 0.5 mM oleic:palmitic acid mixture (2:1) were chosen as both induced lipid accumulation in the monolayer cells and both showed no, or tolerable, cytotoxicity. HepG2 spheroids have been shown to have increased sensitivity to hepatotoxins and have considerably lower EC50 values for many different drugs when compared 2D cultures (Gaskell et al., 2016), Kammerer, 2021, Tutty et al., 2022). This would suggest that fatty acids could induce hepatoxicity at lower dose levels than in monolayers. The greater sensitivity observed in spheroids may be a result of direct cell-cell contacts, increased liver-specific functionality and structure of the spheroids allowing the hepatotoxins to exert their effect (Tutty et al., 2022).

In this study the MTS assay was also conducted on the spheroids to assess for changes to cell viability. However, the results obtained were outside the linear range of the assay; and were therefore unreliable. This was due to the high number of cells in the spheroids. The assay was repeated using lower seeding densities; however, results still fell outside the linear range. Instead of optimising and repeating it an LDH assay was performed since it is more reliable in confirming cell death in any case. The LDH assay revealed no significant cytotoxicity at both dose levels (Figure 3.26). Cytotoxicity in spheroids was also visualised in the LIVE/DEAD assay and confirmed the spheroids remained viable after 17 days growth and showed no toxic response to the fatty acid doses used (Figure 3.25). Therefore, the results from the spheroids showed no real cytotoxicity at either of the dose levels used.

Triglyceride accumulation was also assessed in the spheroids and the results from the triglyceride assay confirmed mild steatosis in spheroids (Figure 3.27) at 0.5 mM fatty acids. In the interest of time and following the positive triglyceride assay results Oil Red O staining was not performed in the spheroids.

However, staining methods and commercial triglyceride assays have been used extensively in spheroid and monolayer studies in HepG2 cells. Frandsen et al., (2022) cultured spheroids for 21 days before treatment with a mixture of 65 µM oleic acid (OA), and 45 µM palmitic acid and measured lipid content using an AdipoRed Adipogenesis assay showing a significant increase in lipid accumulation. The AdipoRed reagent is designed to specifically partition into the fat droplets of differentiated adipocytes and fluoresces at 572 nm. Pingitore et al., (2019) also dosed HepG2 spheroids with a mixture of fatty acids, palmitic acid and oleic acid at 500 µM, the same dose used in this study and used the AdipoRed assay to visualise lipid accumulation. Their results showed that the fatty acids promoted lipid accumulation and an increase in total fat content after 48 hours. Gomez-Lechon et al., (2007) dosed HepG2 cells with a combination of oleic and palmitic acid at concentrations of 0.5, 1 and 2 mM. Lipid accumulation was quantified using Nile Red staining which is a vital lipophilic dye used to label fat accumulation in the cytosol (Gomez-Lechon et al., 2007). Also, in their study the total lipid accumulation was measured using a commercial kit based on the vanillin-phosphoric acid reaction. The results showed an increase in triglyceride accumulation in HepG2 cells from 105 µg in the control to 278 µg in the treated group. A combination of both staining and an assay kit were used in this study to confirm lipid accumulation in monolayers in this study making the results more reliable.

The next objective of this current study was to analyse changes in the metabolome of cellular extracts from both models to identify potential biomarkers for the early detection of steatosis. The use of spheroids potentially allowed for identification of biomarkers in a model more reflective of the *in vivo* environment.

The first step in cell metabolomic studies is to determine how many cells are needed to obtain a good NMR signal as many papers have used different cell counts for their studies. It has been suggested that most metabolites at biological concentrations can be detected irrespective of the seeding density (Garcias-Canaveras et al., 2016, Ramirez et al., 2018, Chen et al., 2018A), but this required confirmation. Various HepG2 seeding densities have been used in the literature. One study conducted by Chen et al., (2018B) seeded $1x10^4$ cells in 96-well plates. While Garcias-Canaveras et al., (2016) and Ramirez et al., (2018) seeded $8x10^4$ cells/cm^2 and $0.45x10^6$ cells in

6-well plates, respectively. The cell count used by Ramirez et al., (2018) was similar to the one used in this study.

A preliminary metabolomics study (not presented in this thesis) tested different seeding densities in 96-well plates but the NMR signal was too low. It is likely that this is related to the methods required for metabolomics studies. A vital prerequisite for conducting reliable metabolomics experiments is the immediate quenching of the metabolic reactions at sample collection (Dettmer et al., 2011, Bi et al., 2013, Leon et al., 2013, Muschet et al., 2016). For this step, cells are detached from the surface of the well and scraped directly in ice-cold methanol/water/chloroform mixture for quenching (Teng et al., 2009, Dettmer et al., 2011, Hutschenreuther et al., 2012, Bi et al., 2013, Muschet et al., 2016). This procedure can lead to some experimental error since not all cells may be scraped from the surface which could subsequently lead to a reduced number of cells collected potentially leading to intragroup variation. Alternative methods of detaching cells from the plate include trypsinisation of the cells, however this is not considered suitable for metabolomics studies as it has been shown to cause metabolite leakage due to disruption of the cell membrane (Bi et al., 2013). Consequently, to allow for loss of cells when scraping and quenching it is generally recommended that between 1-10 million cells should be used for metabolomics samples. Based on this it was decided not to conduct metabolomics study experiments using 96-well plates as the cells would not reach a high enough confluency. In addition, scraping the cells off the bottom of the plate would be difficult and likely to lead to the loss of some of the cell extract. In the current study $0.5x10^6$ cells were seeded in six well plates for metabolomics experiments for both the monolayer and the spheroid models. This was considered suitable as HepG2 cells have a doubling time of 48 hours which means there were approximately $1x10^6$ cells by the time the samples were collected. Several preliminary studies were conducted in these studies in order to validate the methods used. The results obtained in these studies were similar to those seen in the final studies indicating that the methods used were capable of yielding reproducible results between experiments.

In this study cells metabolite changes in both monolayers and spheroids were compared. In monolayers cells attach to the flat surface of the plate. This method of cell culturing has become increasingly popular due to its simplicity and convenience

forcing cells to grow on flat surfaces limits cell-cell interaction. However, this can change the cell metabolism and functioning which could be reflected in the metabolomics data (Bialkowska et al., 2020). So, while monolayers have been routinely used to understand the molecular mechanism of disease, they do not represent the true complexity of human tissues.

3D cultures offer a similar micro-environment to the *in vivo* situation with respect to cell shape, behaviour and morphology (Pingitore et al., 2019). Therefore, the use of 3D spheroids could aid in the identification of early diagnostic biomarkers for steatosis which are more relevant to humans. Although spheroids are more relevant, their use in metabolomics studies is limited and to date there are few studies using HepG2 spheroids for the study of metabolite changes in steatosis. However, one study conducted by Kozyra et al., (2018) created a 3D steatosis model in primary hepatocytes using oleic and palmitic acid together with glucose and fructose. The result of their study indicated that 3D models have the capabilities of displaying many *in vivo* phenomena such as insulin resistance and the reversibility of steatosis through the administration of vitamin E and metformin making them suitable for the study of steatosis in biology and disease (Kozyra et al., 2018). Frandsen et al., (2022) mapped the proteome and lipidome changes in early onset NAFLD in HepG2 spheroids through the administration of oleic and palmitic acid and recorded changes similar to those *in vivo.* However, the study aimed to investigate the underlying molecular changes that occur in NAFLD rather than identify biomarkers for early detection of steatosis.

In the current study, NMR data obtained for both the spheroids and the monolayer were subject to unsupervised (PCA) and supervised (OPLS) multivariate analyses. For all statistical comparison the ethanol sample group, as the vehicle control, was used instead of the media control since fatty acids were diluted in ethanol. This was to ensure that any observed differences between the groups were due to the fatty acid treatment and not related to the ethanol vehicle (Rodríguez-Burford et al., 2003, Larsson et al., 2020). While it is necessary to use solvents such as ethanol in biological research for the dilution of therapeutic molecules especially those that are weakly soluble in water, studies have shown that ethanol can disrupt the physical structure of biological membranes and affect the growth of HepG2 cells. However, this typically

occurs at concentrations above 2.5% (Castaneda and Kinne, 2000, Ngyuyen et al., 2020). Plus, it has been proven that at concentrations between 0.3 and 2 % ethanol are well tolerated in HepG2 cells (Ngyuyen et al., 2020). Since in the current study the ethanol concentration did not exceed 2%, it is unlikely to have contributed to any cytotoxicity and this was confirmed in the MTS and LDH assays.

The PCA scores plots created for both the monolayers and spheroid studies (Figures 3.5, 3.15, 3.28 and 3.33) did not show good separation between the control and fatty acid groups at the different dose levels. This was the case for both the aqueous and organic extracts. PCA is a classical tool used to reduce the dimensionality of data and to filter noise. However, PCA assumes that biological data follow a multivariate normal distribution and decomposes data based on the maximisation of its variance (Yao et al., 2012). Clear separation may not be seen in PCA models as any differences between measurements will only be revealed if they are major contributors to the total variability in the data set (Scholz et al., 2004, Yao et al., 2012, Worley and Powers, 2016). Literature suggests that sample size in relation to the number of variables plays an important role in the separation observed in a PCA as a larger sample size reduces the probability of errors (Osborne and Costello, 2004). It has been suggested that the sample size should be larger than 5 times the number of variables while others recommend at least 100 samples (Gorsuch, 1983, Hatcher, 1994, Shaukat et al., 2016). However, these numbers would just not be feasible in cell studies as this would require a large number of cells. Therefore, for the current study 6 replicates were used since this is reflective of other studies in the literature. A study in HepG2 cells conducted by Garcia-Canaveras et al, (2016) used 6 replicates for their metabolomics study and observed clear separation between treated groups and controls. Another *in vitro* metabolomics study in HepG2 cells conducted by Ramirez et al., (2018) used between 8-20 replicates. Although there was separation between the different treatments used, dose-dependent changes for individual compounds were not easily distinguished. Another metabolomics study conducted in HepG2 cells dosed cells with 2,3,7,8-tetrachlorodibenzo-p-dioxin using 5 replicates and did observe separation between the treated groups (Ruiz-Aracama et al., 2011).

One of the major issues with the use of PCA with low sample numbers is that intragroup variation can lead to a lack of sample group clustering. It is likely this was

an issue in the present study as samples from the same groups were located in different parts of the PCA plot. In cell studies large intragroup variation can be due to inaccuracies in cell number per well and/or experimental error when collecting cell samples for NMR observed. Inaccuracies in seeding density could also have an effect on intragroup variation leading to differences in concentrations of metabolites in samples (Chen et al., 2013). Intragroup variation was a particular issue in the organic spheroids extracts as ethanol control sample 1 was located on the opposite side of the scores plot away from the rest of the samples in the group. This could potentially be due to a difference in cell seeding density when plating the spheroids which led to this sample have a different number of cells compared to the rest of the group. Additionally, outliers were also observed in all metabolomics experiments in this project possibly due to errors in sample preparation or biological response to dosing with the fatty acids. Metabolomics datasets often contain outliers because of analytical, experimental, and biological ambiguity (Kumar et al., 2018). Although clear separation was not observed for all dose levels in this chapter the control group was separate from the rest of the treated groups in all PCA plots indicating some treatment-related response due to the fatty acids. These observations are consistent with many other metabolomic studies using HepG2 cells who all reported some sample group clustering, but not clear separation (Ruiz-Aracama et al., 2011, Garcia-Canaveras et al., 2016, Ramirez et al., 2018, Martinez-Sena et al., 2023).

Due to the limitations of PCA when analysing biological samples OPLS analysis is often carried out on the spectral data and better group separation is usually expected due to the sample class input. Unlike PCA, OPLS is more likely to show separation between experimental groups because its integrated orthogonal signal correction (OSC) filter removes spectral variation that does not agree with the assigned group (Worley and Powers, 2016). Thus, this explains the better separation observed for the OPLS scores plots in this study along the sample class t[1] predictive axes with the control and the highest dose level tending to be on opposite sides of the score's plots. However, in this study the organic extracts of monolayer samples (Figure 3.16) still showed some overlap between the 0.1, 0.25 and 0.5 mM groups. Plus, the organic extracts spheroid samples (Figure 3.34) had overlapping between the two treated dose levels.

The pair-wise comparison OPLS-DA models in this Chapter allowed for the identification of many metabolite regions that differed between the treated groups and controls as well highlighting some dose related changes. However, in general, large intragroup variation along the orthogonal t[0] axis was observed for all treatment groups in the study. The intragroup variation seen in this study was more apparent in organic samples. This observation could indicate that extraction solvents fluctuate in their effectiveness in extracting metabolites from sample groups and this could explain the intragroup variation seen in this study (Andersson et al., 2019). There is a risk of losing more volatile compounds like chloroform during sample collection which would have an effect on variation within sample groups (Mushtaq et al., 2013).

In this study metabolite changes were identified using the Human Metabolome database as well as published literature. Some similarities in metabolite changes were observed in both the monolayer and spheroids (Tables 3.1, 3.2, 3.4 and 3.5) including decreases in peaks for lactate and increases in succinate, phosphocholine and betaine and creatine.

A decrease in lactate and an increase in alanine were observed in the monolayer samples dosed with fatty acids when compared to control. Changes in alanine are often related to alterations to pyruvate and lactate since the three are linked metabolically. Pyruvate can be converted to lactate by lactate dehydrogenase and alanine is produced from the transamination of pyruvate with glutamate by alanine aminotransferase producing α-ketoglutarate alongside alanine. Pyruvate is an intermediate in gluconeogenesis and plays an important role in aerobic respiration and the production of ATP since it is converted to acetyl-CoA by pyruvate dehydrogenase which then feeds into the TCA cycle (Mayr et al., 2005). In this current study an increase in alanine was observed in the fatty acid-treated monolayer samples, but not in the spheroid model. This is similar to studies in humans which reported increases in alanine concentrations in patients with metabolic syndrome and NASH when compared to healthy controls (Mannisto et al., 2014, Stechemesser et al., 2017). It has also been demonstrated that there is an increase in the ratio of alanine/pyruvate in patients with NAFLD when compared to healthy controls. In particular, the transcriptional activity of aminotransferases was reported as significantly upregulated thus increasing alanine levels (Sookoian et al., 2016). Therefore, the observed

elevation of alanine in this present study could potentially be due to an increase in transamination of pyruvate in the treated monolayer cells although changes in pyruvate were not observed. In contrast Song et al., (2013) reported a decrease in alanine in rats along with decreases in pyruvate and lactate and increases in glucose implying glycolysis was inhibited in their study.

In this current study a decrease in lactate levels was proposed due to a reduction in peak sizes in the NMR spectral region at 1.31-1.35 ppm. This decrease when compared to control was seen at all fatty acid dose levels for the monolayer cells and in the 0.1 mM dose group of the spheroid experiment. This decrease is similar to that observed by Song et al., (2013) and shows that the changes observed in the cells and spheroids are similar to those seen in rats indicating they are useful translational models of steatosis.

TCA cycle activity has been reported to increase 2-fold in patients with steatosis along with roughly a 50% increase in mitochondrial anaplerosis pathway activity predominantly pyruvate carboxylase flux (Sunny et al., 2011, Fletcher et al., 2019). The increase in TCA cycle activity is linked to an increase in beta-oxidation which would lead to elevated acetyl-CoA which feeds into the TCA cycle (Gudson et al., 2014). In this current study an increase in succinate, an intermediate in the TCA cycle, was observed in the monolayer samples and in the 0.5 mM spheroid samples. This suggests an increase in TCA activity. Ye et al., (2019) also observed significant increases in succinate in HepG2 cells when treated with liposoluble extracts. Additionally, elevated succinate has also been observed in rats fed a high fat diet (Xu et al., 2019B). Many studies have reported an increase in citrate in NAFLD patients and in mice due to excess fatty acids but changes in citrate were not observed in this study (van de Wier et al., 2013, Fontes et al., 2019, Sinton et al., 2019, Sandlers et al., 2020). Other TCA cycle metabolite levels may have been altered in this study. However, since many metabolites share similar spectral regions, individual changes may be masked by overlapping metabolite peaks.

An increase in TCA cycle activity has also been observed in spheroids in the literature. Sinton et al., (2021) observed increases in the TCA cycle intermediates caused by anaplerosis from pyruvate and lactate. Their study also reported the inhibition of the

conversion of succinate to fumarate in steatotic monolayer cells. Other studies have revealed not only changes in TCA intermediate but also higher ATP levels in fatty acid treated spheroids compared to control (Frandsen et al., 2022, Tidwell et al., 2022). In the current study changes in ATP levels were not observed in the spheroid samples, however future work could investigate this more specifically.

In this present study an increase in β-hydroxybutyrate was observed in the 0.1 mM spheroid samples and in the 0.25, 0.5 and 1 mM monolayer groups. This is likely due to excess acetyl-CoA which can be converted into ketone bodies such as β-hydroxybutyrate and acetate (Song et al., 2013, Watt et al., 2019). Studies have shown that ketogenesis disposes of as much as three-fold fat entering the liver dysregulating ketogenesis and contributing to NAFLD pathogenesis (Cotter et al., 2014, Satapati et al., 2015, Grattagliano et al., 2019, Mooli and Ramakrishnan, 2022). The increases in β-hydroxybutyrate seen in this study further confirm that beta-oxidation is increased in the cells due to the influx of fatty acids.

Increased gluconeogenesis may have occurred in the present study as an NMR spectral region at 5.22-5.245 ppm thought to correspond to glucose was increased in both the 0.5 mM and 1.0 mM fatty acid monolayer treated groups and the 0.5 mM spheroid group. However, glucose typically has a number of peaks present on ^{1}H NMR spectra and in this study the other regions were not detected as being significantly different according to the VIP plots. This may be due to the presence of other metabolites within the glucose regions which depending on their concentration could mask the glucose peaks in terms of statistical differences. Increases in beta-oxidation can also influence the progression of insulin resistance in NAFLD as the induction of lipid oxidation is required for the endergonic steps of gluconeogenesis (Sunny et al., 2011). Chronic activation of mitochondrial oxidation in the setting of lipid overload increases acetyl-CoA content exceeding the rates of mitochondrial TCA flux resulting in the activation of pyruvate carboxylase activity which stimulates gluconeogenesis (Sunny et al., 2011, Samuel and Shulman 2018).

Studies have reported that the exposure of HepG2 cells to 0.5 mM palmitic acid alone for 24 hours induces insulin resistance in the cells. As a result, palmitic acid administration has been widely used for the development of an insulin resistance

model (Gao et al., 2010, Malik et al., 2019, Zhang et al., 2019). HepG2 cells treated with palmitic acid at 0.25 mM have also been reported to have altered expression levels of insulin receptor substrate 1 (IRS1) phosphorylation and GLUT (Zhang et al., 2019, Malik et al., 2019) as well as significant increases in the protein and mRNA expression of PEPCK and G6Pase, which are key gluconeogenic enzymes (Liu et al., 2019). Fatty acids stimulate the phosphorylation of serine residues on IRS-1 and down regulate the insulin signalling pathway to cause insulin resistance (Denhez et al., 2020). Therefore, it is possible that in this study palmitic acid may be increasing gluconeogenesis. Nevertheless, it has also been reported that monounsaturated fatty acids such as oleic acid can induce gluconeogenesis in bovine hepatocytes and in humans (Mashek et al., 2002, Sarabhai et al., 2020). However, published literature has not investigated an increase in gluconeogenesis in HepG2 cells using a combination of oleic and palmitic acid, therefore future studies could attempt to analyse this.

Overall, the results in the current studies suggest an increase in beta-oxidation, changes to acetyl-CoA levels and reduced glycolysis in the monolayer and spheroid cells treated with fatty acids. This has been reported in many studies in which energy production is greater from beta-oxidation than glycolysis (Ruiz-Aracama et al., 2011, Song et al., 2013, Gudson et al., 2014). Increases in fatty acid oxidation have also been observed in obese patients in response to the excess fatty acid load (Sunny et al., 2013, Rafiei et al., 2019, Lu et al., 2021). A study in human hepatocytes co-cultured with primary human hepatic stellate cells exposed to a mixture of oleic and palmitic acid also demonstrated increased beta-oxidation (Feaver et al., 2016, Rafiei et al., 2019). Similarly, in high-fat diet fed rats upregulation of fatty acid beta-oxidation has been observed (Gusdon et al., 2014). However, in their study Gusdon et al (2014) described the accumulation of incompletely oxidised fatty acid intermediates and depleted TCA cycle intermediates resulting in exacerbated insulin resistance and the progression of NAFLD. Untreated HepG2 cells have been reported as having a high mitochondrial respiration rate, low glycolysis and low rate of lactate production and therefore they appear to be more dependent on mitochondrial OXPHOS for energy metabolism (Hsu et al., 2015). Consequently, if treatment with fatty acids affects mitochondrial respiration and induces mitochondrial oxidative stress as a result of lipotoxicity this could lead to progression of NAFLD. (Garcia-Ruiz et al., 2016). The

changes in TCA cycle metabolites and its associated anaplerotic pathways seen in this study are similar to those seen in literature and are reflective of the *in vivo* environment. This makes both spheroid and monolayer HepG2 models suitable steatosis models for the identification of biomarkers.

In this study metabolite changes related to the methyltransferase reactions were observed in both models. This included a dose dependent increase in methionine in the spheroids (Table 3.4) and in homocysteine for in both models when compared to controls. Homocysteine is a sulphur containing amino acid produced from the methylation of methionine. Under normal conditions the formation and elimination of homocysteine is strictly balanced, as it is either remethylated back to methionine or irreversibly metabolised to cystathionine in the transsulfuration pathways (Medici et al., 2010, Pacana et al., 2015, Li et al., 2020B, Werge et al., 2021).

While an increase in methionine was observed in the spheroid samples in this study there was no change detected in the monolayer, which may be a result of other peaks masking methionine on the spectra. Methionine is an essential amino acid which plays a key role in regulating several cellular functions including metabolic processes and digestive functioning in mammals (Martinez et al., 2017). Methionine is also a key intermediate in the production of s-adenosylmethionine (SAM) and glutathione, two important antioxidants (Jha et al., 2016). Demethylation of SAM converts methionine sequentially to s-adenosylhomocysteine (SAH) and homocysteine (Zhang et al., 2016, Werge, 2021). However, changes in SAH and SAM were not apparent in this study. Ye et al., (2019) also reported increases in methionine due to excess availability of methyl donors for hypermethylation in HepG2 cells exposed to liposoluble extracts suggesting an increase in methylation and oxidative stress. Elevated homocysteine and decreases in SAM have also been implicated in NAFLD (Noga et al., 2002, Craig, 2004).

Methionine has been implicated in NAFLD and several studies have indicated that rats and mice fed a methionine-supplemented diet exhibit hyperhomocysteinemia and that an excess in methionine alters hepatic lipid metabolism, induces oxidative stress and hepatocyte injury potentially leading to the progression of steatosis to NASH (Pogribny et al., 2005, Zhou et al., 2008, Song et al., 2009, Yamada et al., 2012, Aissa et al.,

2014, Yao et al., 2016). For this reason, methionine supplementation is used extensively for the development of NAFLD models (Rinella er al., 2008, Yang et al., 2018, Li et al., 2018). In contrast one of the most common models for the induction of NASH is the methionine-choline deficient diet model; this results in steatosis, fibrosis and oxidative stress (Corbin and Zeisel, 2013, Jha et al., 2014, Sherriff et al., 2015, Imbard et al., 2015). Choline is essential for the *de novo* synthesis of phosphatidylcholine which is required for the export of triglycerides via VLDL packaging meaning a deficiency in choline can cause steatosis (Rinella et al., 2008, Jha et al., 2014) while methionine can lead to oxidative stress mimicking the 'two-hit' model of NAFLD (Jha et al., 2014).

Although the full mechanism by which hyperhomocysteinemia occurs is not understood elevated levels of methionine drive the transsulfuration pathway leading to an increase in SAM and SAH and ultimately homocysteine levels (Troen et al., 2003, Aissa et al., 2014). However, it is unclear why methionine is increased in NAFLD. In humans hyperhomocysteinemia is associated with metabolic syndrome and NAFLD (Polyzos et al., 2012, Dai et al., 2016, Kumar et al., 2020). It is thought that the accumulation of homocysteine in liver cells activates a hepatic unfolded protein response ultimately leading to oxidative stress and the progression to NASH (Pancana et al., 2015, Dai et al., 2016). While many studies have investigated the effect of homocysteine in mice and humans (Hu et al., 2016, Ai et al., 2017, Yan et al., 2020) *in vitro* studies are limited. However, it has been suggested that homocysteine can induced ER stress and enhance lipid biosynthesis and uptake through the activation of the SREBPs in HepG2 cells exposed to 1 or 5 mM of homocysteine (Werstruck et al., 2001).

In this study peaks in the region between 3.255-3.265 ppm in the NMR spectra from both the spheroid and monolayer samples were revealed as being increased compared to controls. These peaks are thought to correspond to betaine according to the human metabolome database. The transmethylation reaction of betaine, a one-carbon metabolism pathway occurs principally in the mitochondria of liver and kidney cells (Zhao et al., 2018). In this reaction betaine-homocysteine methyltransferase (BHMT) catalyses the addition of a methyl group from betaine to homocysteine to form methionine (Lee et al., 2012, Garrido et al., 2018). Therefore,

an increase in betaine could also lead to an increase in homocysteine and methionine. Betaine can also be converted to dimethylglycine (Williams and Schalinske, 2007, Mailloux et al., 2016, Zhao et al., 2018). Dimethylglycine has two available methyl groups and can be degraded to sarcosine and ultimately glycine to produce creatine (Zhao et al., 2018). Increases in both glycine and creatine were seen in both models in this Chapter (Tables 3.1 and 3.4) indicating that the HepG2 cells may be converting excess betaine to dimethylglycine although changes in dimethylglycine were not observed. Human studies have shown that patients with chronic liver disease have elevated serum homocysteine levels as well as high levels of betaine due to increased activity of the BHMT (Zhao et al., 2018). In contrast to the increase in glycine seen in this study it is well established that glycine levels are reduced in NAFLD in human and rodent models (Zhou et al., 2016, Gaggini et al., 2018, Romero et al., 2020, Ghrayeb et al., 2023). Glycine plays an important role in metabolic regulation and is the rate limiting step in glutathione synthesis. In NAFLD patients increased levels of glutamate and decreases in glycine are observed due to increased transamination of glutathione by gamma-glutamyltransferase (Gaggini et al., 2018). Elevated homocysteine and decreases in SAM have also been implicated in NAFLD (Noga et al., 2002, Craig, 2004).

In the monolayer cells in this study decreased levels of formate were observed in the 0.1 and 1.0 mM groups but not in the spheroids. Formate provides carbon groups for folate metabolism resulting in the formation of tetrahydrofolate (Morrow et al., 2015, Brosnan and Brosnan, 2016). Formate is also linked to the methionine pathways via methionine synthase, a vitamin B12-dependent enzyme. (Zhao et al., 2018). In the presence of vitamin B12 methyl groups are transferred from N-methyltetrahydrofolate to homocysteine forming methionine and tetrahydrofolate in the methionine salvage pathway (Halstead et al., 2002, Froese et al., 2018). A decrease in formate levels, as seen in the 0.1 and 1.0 mM fatty acid-treated monolayer cells (Table 3.1) in this study, could indicate alterations to one-carbon metabolism and the folate cycle. Studies have shown that folate depletion can induce oxidative stress in the liver and lead to the development of more severe NAFLD (Huang et al., 2001, Radziejewska et al., 2020). Although, the main mechanism behind folate deficiency during NAFLD is not fully understood (Radziejewska et al., 2020, Vahedi et al., 2020). However, Radziejewska et al., (2020) reported a decrease in folate levels due to suppressed expression of

folate transporters in mice fed a high fat diet. Folate depletion can also lead to the utilisation of betaine and choline for homocysteine remethylation thus disrupting choline metabolism; this has been shown to increase the severity of steatosis in mice (Christensen et al., 2010, da Silva et al., 2014, Radziejewska et al., 2020). Yang et al., (2018) reported a decrease in formate in mice fed a high fat diet however this has not been investigated in any *in vitro* models dosed with fatty acids. Studies in mice have found that a decrease in folate metabolism results in increased expression of genes related to lipogenesis which in turn promotes lipid accumulation and disrupted VLDL secretion from the liver (Christensen et al., 2010, Champier et al., 2012, da Silva et al., 2014, Radziejewska et al., 2020). In the current study it is possible that the folate cycle was disrupted thus preventing the methylation of homocysteine by N-methyltetrahydrofolate (Zira et al., 2013). This could also account for the increase in homocysteine and methionine seen within the fatty acid-treated cells.

In this study organic metabolites from both the spheroids and the monolayers dosed with fatty acids were also examined (Tables 3.2 and 3.5). Metabolite changes identified included monounsaturated fatty acids, triglycerides and arachidonic acid. As the cells were dosed with fatty acids it was expected that metabolite peaks belonging to oleic and palmitic acid were present and changes in metabolite regions for oleic acid were observed in both models but not for palmitic acid.

A decrease in peaks at 1.702-1.724 ppm due to eicosapentaenoic acid (EPA) a polyunsaturated fatty acid was observed in the 0.25, 0.5 mM and 1.0 mM fatty acid treated groups. This is likely due to increased beta-oxidation and a possible accumulation of fatty acids intermediates such as lipid peroxides (Satapati et al., 2012). It has been suggested that a decrease in polyunsaturated fatty acids is observed in steatosis and NAFLD since the build-up of fatty acid intermediates are more susceptible to free radical attack as a result of their carbon-carbon double bonds and are therefore degraded (Ayala et al., 2014). Both clinical and preclinical studies have also reported decreases in polyunsaturated fatty acids due to increased oxidation, again confirming the earlier suggestions of an increase in beta-oxidation in this study (Arendt, 2015, Depner, 2013, Lytle, 2015, Jump et al., 2017).

Previous studies have also shown that excess unsaturated fatty acids induce cytochrome P450 2E1 which stimulates lipid peroxidation, subsequently promoting apoptosis and cell toxicity (Sung et al., 2004, Cui et al., 2010). This is important since CYP2E1 can metabolise polyunsaturated fatty acids such as linoleic and arachidonic acid to generate ω-hydroxylated fatty acids which are further metabolised to dicarboxylic fatty acids; these are known to be cytotoxic at high concentrations (Leung and Nieto, 2013). While many studies have reported that CYP2E1 expression and activation is increased in NAFLD the role of CYP2E1 in NAFLD progression is still under investigation (Bell et al., 2011, Leung and Nieto, 2013). However, compared to other cytochromes P450, CYP2E1 possesses a remarkably high NADPH oxidase activity, resulting in significant production of ROS. This can initiate a free radical chain reaction with unsaturated fatty acids generating toxic lipid intermediates (Hariumaki et al., 2021). Oleic acid induced steatosis is also associated with significantly decreased expression of superoxide dismutase-1 (SOD-1) enzyme, a free radical scavenger enzyme, in HepG2 cells. This demonstrated that in a steatotic state there are decreased levels of antioxidants that could protect against cellular membrane injury mediated by lipid peroxidation leading to further mitochondrial damage (Cui et al., 2010). Reduced antioxidant levels are commonly observed in NAFLD patients. Many studies have reported depleted levels of glutathione, vitamin E, vitamin C and SOD as wells as increased levels of lipid peroxidation products and oxidative stress markers eventually leading to the progression of steatosis to NASH (Garcia-Ruiz and Fernandez-Checa 2018, Ore and Akinloye 2019, Arroyave-Ospina et al., 2021).

In contrast to the decrease in EPA an increase in arachidonic acid was observed in the monolayer samples after dosing with fatty acids in this study. Arachidonic acid is an n-6 polyunsaturated fatty acid and is an important constituent of membrane phospholipids (Tallima and Ridi, 2018, Lin et al., 2022). It is metabolised by cyclooxygenases and lipoxygenases forming pro-inflammatory prostaglandins and leukotrienes. Therefore, increased metabolism of arachidonic acid in NAFLD can lead to inflammation (Puri et al., 2007, Lin et al., 2022). Sztolsztener et al., (2020) demonstrated that after 3 weeks of high-fat diet feeding in mice there was a shift in the balance between n-6 and n-3 polyunsaturated fatty acids towards n-6. Consequently, arachidonic and linoleic acid levels were increased which paralleled the development of inflammation (Sztolsztener et al., 2020). This shift in balance

between the n-6 and n-3 in a high fat diet was likely due to overnutrition particularly since a high-fat diet can serve as an exogenous source of arachidonic acid (Sztolsztener et al., 2020, Kirk et al., 2022). However, this has not been studied in HepG2 cells. This increase in arachidonic acid and the role it plays in inflammatory responses can lead to cytotoxicity and apoptosis in HepG2 cells potentially leading to NASH (Xu et al., 2003). Lin et al., (2022) reported significant changes in arachidonic acid metabolism in patients with metabolic dysfunction-associated fatty liver disease. An *in vitro* study in HepG2 cells exposed to arachidonic acid (n6) and docosahexaenoic acid (n3) ratio led to a reduction in mitochondrial activity and increased triacylglycerol accumulation (Ghazali et al., 2020) Therefore, the increase in arachidonic acid seen in this study could be contributing to the triglyceride accumulation seen in the cells as well as increasing inflammatory markers.

In the present study an increase in cholesterol was observed in the spheroid models (Table 3.5) however, a dose dependent decrease was apparent in the monolayers (Table 3.2). Cholesterol metabolism in hepatocytes is maintained via a number of metabolic pathways including cholesterol *de novo* synthesis, uptake of cholesterol in the form of LDL and chylomicron and cholesterol excretion in the form of VLDLs (Enjoji et al., 2012). However, since these pathways are disrupted in NAFLD, SREBPs act as regulators of cholesterol levels and activate genes involved in the synthesis of cholesterol and free fatty acids (Enjoji et al., 2012, Chen et al., 2022). Dosing HepG2 cells with palmitic acid has been shown to increase cholesterol levels following 12 hours of treatment as a result of the upregulation of the farnesyl diphosphate synthase (FDPS) and *ABCG1* genes due to increased SREBP-2 expression (Tarling et al., 2015, Chen et al., 2018B, Chen et al., 2022). Studies have reported that increased SREBP-2 protein levels and suppression of LDL receptor expression in HepG2 cells treated with palmitic acid result in free cholesterol accumulation. (Pal et al., 2002, Chen et al., 2022). Therefore, the increase in cholesterol seen in the spheroid model could be due to an increase in SREBP levels although the mechanism of this is not fully understood. Increases in cholesterol have been observed in humans and disturbances in cholesterol metabolism contribute to the pathophysiology of NAFLD. Increases in cholesterol synthesis and a decrease in the pathways responsible for the elimination of cholesterol lead to accumulation of free cholesterol in the liver (Malhotra et al., 2020). Increases in nuclear SREBP-2 have also been reported in humans with

NAFLD leading to an increase in HMG-CoA reductase the rate limiting step in cholesterol synthesis leading to increases in cholesterol (Kerr and Davidson, 2012). In contrast the decrease in cholesterol observed in the monolayer samples could be due to increased secretion of VLDLs from the cells. This has been proposed as oleic acid can potentially increase the packaging of triglyceride and cholesterol into VLDLs (Dashti and Wolfbauer, 1987). In addition, Dashti and Wolfbauer (1987) showed in their study that oleic acid induced VLDL secretion in HepG2 cells. Previous studies using a combination of oleic and palmitic acid have not reported decreases in cholesterol. Although the spheroids and monolayers show opposing changes in cholesterol in this study, perhaps as spheroids display a morphology more reflective of the human liver the fatty acids may be having a similar effect on cholesterol metabolism as seen *in vivo.*

Since many studies have investigated changes in other CYP enzymes in the context of steatosis CYP enzyme expression was investigated in this study. However, despite other studies suggesting that 3D spheroids have greater expression levels of CYP enzymes when compared to 2D models this was not observed in the current study (Mizoi et al., 2020, Stampar et al., 2020 and Ingelman-Sundberg and Lauschke, 2021). In general, the expression of all 3 CYP enzymes tested was similar in the monolayers and the spheroid. Similarly, when compared to controls fatty acids had no effect on CYP expression in both models.

CYP2E1 is one of the most studied CYP enzymes in relation to NAFLD and was the first documented as modulated in clinical fatty liver disease (Merrell and Cherrington, 2011). The majority of studies have reported an increase in expression and activity of CYP2E1 with the increase hypothesised to play a role in the pathogenesis of NAFLD (Merrell and Cherrington 2011, Garcia-Ruiz et al., 2015, Sukkasem et al., 2020).

Increased CYP2E1 expression and concomitant exposure to its substrate drugs can lead to severe cellular injury due to over production of radical intermediates. This further supports the findings that CYP2E1 can progress fatty liver disease whether it is induced by alcohol, or not (Sukkasem et al., 2020). CYP2E1 is a source of nitro-oxidative stress as it is a member of the oxido-reductase cytochrome family, responsible for oxidising a variety of small molecules including fatty acids further

damaging mitochondria leading to the progression of NAFLD (Garcia-Ruiz et al., 2015). Therefore, the increases in CYP2E1 seen in this study may indicate progression of steatosis. Researchers have also observed upregulation in CYP2E1 in morbidly obese patients, general steatosis and NASH (Weltman et al., 1998, Emery et al., 2003, Videla et al., 2004, Kohjima et al., 2007, Baker et al., 2010). In contrast a number of studies have reported a decrease in CYP2E1 expression and activity in mouse models potentially due to the development of hyperinsulinemia (Enriquez et al., 1999, Watson et al., 1999, Deng et al., 2005, Ito et al., 2007, Cheng et al., 2008). Few published studies document changes in CYP2D6 expression and activity during NAFLD (Merrell and Cherrington, 2011). However, a general downregulation of enzymatic activity in hepatocytes treated with fatty acids at increasing concentrations has been reported (Donato et al., 2006). Sukkasem et al., (2020) also reported a decrease in CYP2D6 expression when both palmitic acid and oleic acid were administered separately to HepG2 cells. CYP2D6 expression and activity has also been reported to be downregulated in HepG2 monolayers after 24 hours of culture whereas its expression levels increased to physiologic levels in 3D cultures (Vorrink et al., 2017, Ingelman-Sundberg and Lauschke, 2021). It has been reported that increasing concentrations (0.25-3 mM) of 2:1 oleic and palmitic acid reduce mRNA expression in primary human hepatocytes (Donato et al., 2006, Cobbina and Akhlaghi, 2017).

CYP3A4 is the most abundant CYP enzyme in the liver and accounts for over 50% of drug metabolism (Hewitt et al., 2007). Due to the importance, it plays in the metabolism of drugs a number of investigators have studied the enzymes role in NAFLD and to date a decrease in expression in steatosis and NASH have been reported in rat models (Weltman et al., 1996, Zhang et al., 2007, Hanagama et al., 2008, Osabe et al., 2008). Studies have also reported decreases in CYP3A4 in NAFLD patients (Weltman et al., 1998, Donato et al., 2006, Donato et al., 2007). It has been reported that HepG2 monolayers do not express CYP3A4 but that it is significantly upregulated in spheroids after 3 days of culture gradually reaching the highest levels at 12 days of culture (Stampar et al., 2020).

Other CYPs have been implicated as changed in NAFLD including CYP1A2, CYP2C8 and CYP2C9 (Merrell and Cherrington, 2011, Ingelman-Sundberg and Lauschke,

2021) however, these were not investigated in the present study. Future work could investigate the expression of these CYPs and their role in the progression of NAFLD.

Although both palmitic and oleic acid have been used successfully in this project and in the literature to induce steatosis other studies have evaluated different fatty acids. A study by Garcia-Ruiz et al., (2015) investigated the effects of oleic acid as well as stearic acid on OXPHOS activity in HepG2 cells in which the administration of 200 μM oleic acid to HepG2 cells did not show any significant alteration in OXPHOS complexes. However, in cells treated with the same dose level of palmitic or stearic acid there was decreased enzyme activity of OXPHOS complexes to about 67% compared to control (Garcia-Ruiz et al 2015). Future work could therefore increase the concentration and type of fatty acid administered in order to induce steatosis ranging from the relatively benign state induced by oleic acid alone to the more toxic states induced by palmitic and stearic acid. This would allow the progression of steatosis to be assessed and determine the effect on metabolite changes within the cells as steatosis progresses to NASH. Studies have also investigated many time points including 6, 12, 16, 24 and 48 hours in HepG2 cells. This would allow for the identification of metabolites which would give a broader overview of the changes that occur during the development of steatosis (Gomez-Lechon et al., 2007, Moracova et al., 2015, Dave et al., 2018, Kahn and Kahn, 2021). Future work could include the administration of different concentrations of fatty acids over different time points to further investigate the progression of steatosis to NASH.

Chapter Four – Tetracycline induced model of hepatic steatosis

Chapter 4

4.1 Introduction

In this Chapter tetracycline was used to develop two models (monolayer and 3D spheroids) of drug-induced steatosis in HepG2 cells. Tetracycline is a broad-spectrum bacteriostatic drug normally used to treat upper respiratory, skin and soft tissue infections (Choi et al., 2015). Although generally considered safe tetracycline-induced hepatotoxicity in humans was first described more than 50 years ago (Andrade and Tulkens, 2011, Glenn and Feldman, 2011, Abdel-Gelil and Mansour, 2019). While the mechanisms by which tetracycline induces steatosis are not fully understood it is thought to include the inhibition of β-oxidation and a reduced secretion of triglycerides from the liver due to an inhibition of microsomal triglyceride transfer protein (MTTP) activity (Breen et al., 1972, Letteron et al., 2003, Dash et al., 2017).

It has been reported that high dose levels of intravenous tetracycline (3g tetracycline administered daily for 10 days) can lead to increased lipid accumulation in the liver in humans and may result in severe hepatic dysfunction and acute liver failure (Robinson and Rywlin, 1970). As a result, tetracycline has been used frequently in the literature for the development of steatosis models for research especially in mice and rat models (Breen et al., 1975, Freneaux et al., 1988, Chopra and Roberts, 2001, Antherieu et al., 2011, Donato et al., 2012, Choi et al., 2015, Rabinowich and Shibolet, 2015, Garcia-Canaveras et al., 2016). The administration of tetracycline has also been shown to cause a dose dependent lipid accumulation and steatosis in HepG2 cells (Donato et al., 2013, Choi et al., 2015, Garcia-Canaveras et al., 2016).

Studies in mice suggest that tetracycline inhibits β-oxidation by downregulating genes involved in fatty acid metabolism pathways including peroxisome proliferator activated receptor alpha (PPARα), carnitine palmitoyl transferase I (CPT-I), and fatty acid-binding protein 1 (FABP- 1) (Satapathy et al., 2015, AlGhamdi, 2019, Di Pasqua et al., 2022). The impairment of fatty acid beta-oxidation is common for many steatogenic drugs and leads to increased extramitochondrial fatty acid oxidation. Thus, promoting higher rates of ROS production and lipid peroxidation leading to oxidative stress and mitochondrial dysfunction. An increase in ROS formation has been reported in HepG2

cells treated with several steatotic drugs including tetracycline confirming its mechanism as via the inhibition of beta-oxidation (Donato et al 2009). Accordingly, Garcia-Canaveras et al., (2016) demonstrated a decrease in glutathione (GSH) levels in HepG2 cells exposed to tetracycline likely to be an antioxidant response to the elevated ROS levels. In their study they also reported a decrease in GSH/glutathione disulfide (GSSG) ratio as well as an increase in cysteine-glutathione (CSSG) suggesting increased ROS formation.

There are only limited published studies using tetracycline in HepG2 cells. However, a concentration-dependent lipid accumulation has been reported following single doses of tetracycline (Donato et al., 2012). Studies by Antherieu et al., (2011) and Garcia-Canaveras et al., (2016) demonstrated that single doses of tetracycline, as low as 50 μM, lead to the induction of steatosis. In another study Choi et al., (2015) demonstrated that mild steatosis occurs 24 hours after a single dose of tetracycline at 100 μM. Meanwhile, Donato et al., (2012) observed a concentration-dependent lipid accumulation after 24 hours which was significantly different to the control at a dose level of 200 μM. In general, the literature agrees that tetracycline induces a concentration-dependent increase in lipid accumulation up to a maximum dose level of 800 μM before cytotoxicity occurs (Donato et al., 2012).

Since the literature mentions a range of dose levels and the fact there are reports of a concentration dependent increase in lipid accumulation the first step in this study was to determine the best dose levels of tetracycline to use. As mentioned above literature suggests that doses exceeding 800 μM may induce cytotoxicity. Therefore, since this study wished to develop mild steatosis, without cytotoxicity, it was decided that dose levels used would not exceed 800 μM. However, if too low a dose level was selected it could result in suboptimal lipid accumulation. Consequently, it was decided to carry out an initial dose response study in the HepG2 monolayers.

Once dose levels were confirmed this Chapter then attempted to identify changes in the metabolome in response to tetracycline as a means of determining potential steatosis biomarkers.

As mentioned in previous Chapters there is a great unmet need for non-invasive biomarkers and especially for drug-induced steatosis (DIS), (Dash et al., 2017, Lopez-Riera et al., 2017, Pavlik et al., 2019). To date, few studies have been conducted using tetracycline for the evaluation of biomarkers of drug-induced steatosis (Lopez-Riera et al., 2017, Pan et al., 2019, Pavlik et al., 2019). However, these studies looked at microRNA, protein and inflammatory biomarkers, while the current study will focus on metabolite changes. The main findings of previous studies were inhibited fatty acid beta-oxidation coupled with mitochondrial dysfunction and oxidative stress. This Chapter will build on current knowledge and develop a drug-induced 3D spheroid model. There are currently no published studies investigating tetracycline-induced steatosis in spheroids.

As described in Chapter 3 HepG2 monolayers have been reported to display lower CYP enzyme expression when compared to 3D cell cultures (Mizoi et al., 2020, Stampar et al., 2020 and Ingelman-Sundberg and Lauschke, 2021). Although dysregulation of the CYP450 enzyme family in dietary induced NAFLD has been partially characterised (Rey-Bedon et al., 2022), the effect of drug-induced steatosis on these enzymes has not yet been studied. The expression and activity of many CYP enzymes have been shown to be altered in dietary-induced steatosis, thus having an impact on metabolism of xenobiotics and bioavailability resulting in decreased pharmacotherapeutic effect and/or generation of toxic metabolites, and oxidative stress (Rey-Bedon et al., 2022).

Therefore, the third objective of this study will be to analyse and compare CYP expression following the administration of tetracycline in 2D monolayers and 3D spheroids will be evaluated using Western blotting.

4.2 Tetracycline study design

Monolayer HepG2 cells were plated in 6-well plates. A dose response study was carried out by administrating tetracycline at dose levels of 100, 200, 400, 600 and 800 μM to HepG2 cells followed by a 24-hour incubation. Six replicates were used for each dose level.

For the 3D spheroid model, the HepG2 cells were plated in low attachment 6-well plates and grown for 17 days before being dosed with fatty acids at concentrations of 0, 100 and 600 μM.

4.3 Results

4.3.1 Cell viability and cytotoxicity in HepG2 monolayers dosed with tetracycline

To ensure that cell viability was not affected by tetracycline dosing and that the concentrations used were not cytotoxic. HepG2 cell viability was assessed using an MTS assay as described in Section 2.6 and a lactate dehydrogenase (LDH) assay, as described in Section 2.21.

The MTS assay (Figure 4.1) revealed no significant difference in HepG2 cell viability at dose levels up to 600 µM tetracycline when compared to the DMSO vehicle control (0 µM). At the highest dose level viability fell to 74%, but statistical analysis revealed no significance.

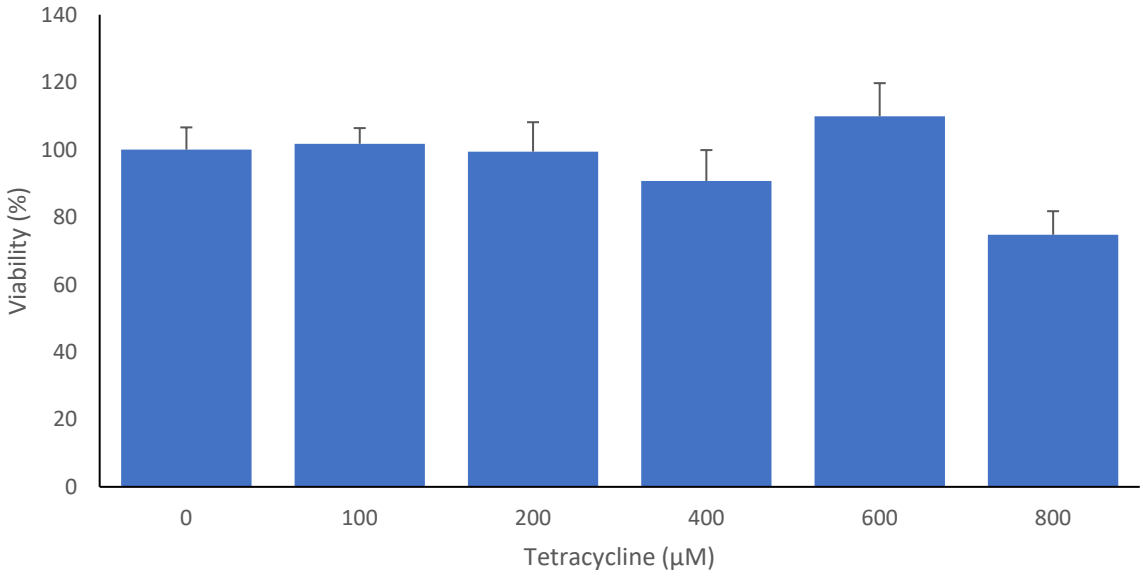

Figure 4.1 HepG2 cell viability in response to increasing tetracycline concentrations as assessed by MTS assay. HepG2 cells were treated with tetracycline at concentrations of 0 (DMSO control), 100, 200, 400, 600 and 800 µM and incubated for 24 hours as described in Section 2.5.2. The MTS assay was carried out as described in Section 2.6. The values shown represent the mean of six replicates. Error bars represent standard deviation.

The LDH assay (Figure 4.2) also demonstrated no statistically significant increases in cell death for all dose levels of tetracycline when compared to the DMSO control. A positive control was used in this experiment which represented a cytotoxicity of 100%.

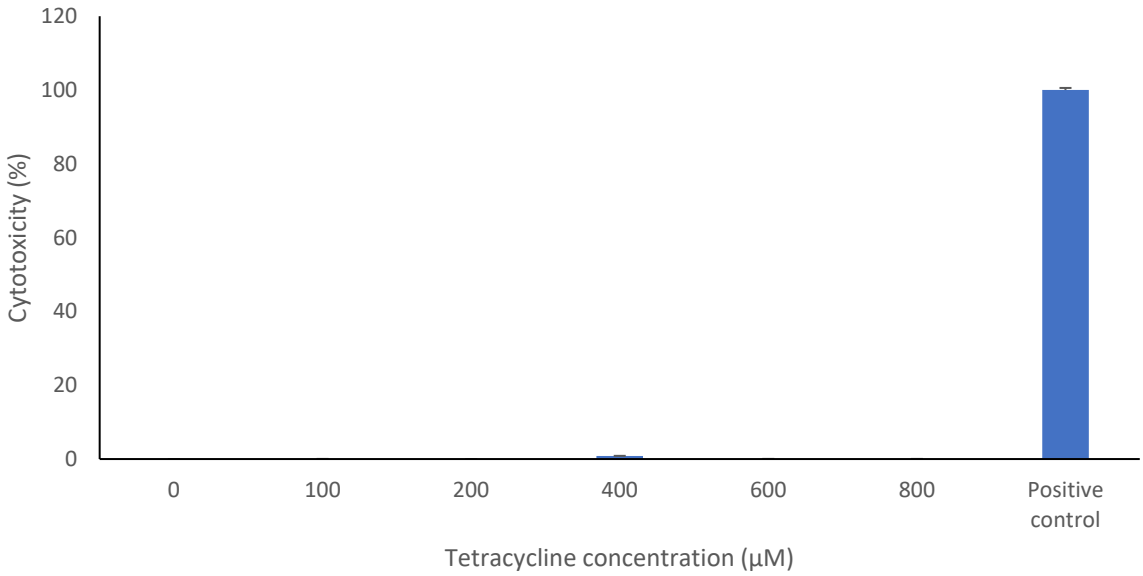

Figure 4.2 HepG2 cell death in response to increasing tetracycline concentration assessed by LDH assay. HepG2 cells were treated with tetracycline at concentrations of 0 (DMSO control), 100, 200, 400, 600 and 800 µM and incubated for 24 hours as described in Section 2.5.2. The LDH assay was carried out as described in Section 2.21. The value obtained for the positive control represents 100% cell death. The values shown represent the mean of six replicates. Error bars represent standard deviation.

4.3.2 Oil Red O staining

To confirm an increase in lipid accumulation in HepG2 cells following tetracycline administration and to determine if there was a dose-related response cells were stained with Oil Red O.

The images obtained under the light microscope suggested there was a dose-related increase in stain uptake up to a dose level of 600 µM (Figure 4.3 A-F). This was observed as an increase in the number, size and intensity of cells stained red. However, above this dose level (800 µM) the number of red stained clusters appeared to be reduced (Figure 4.3 G).

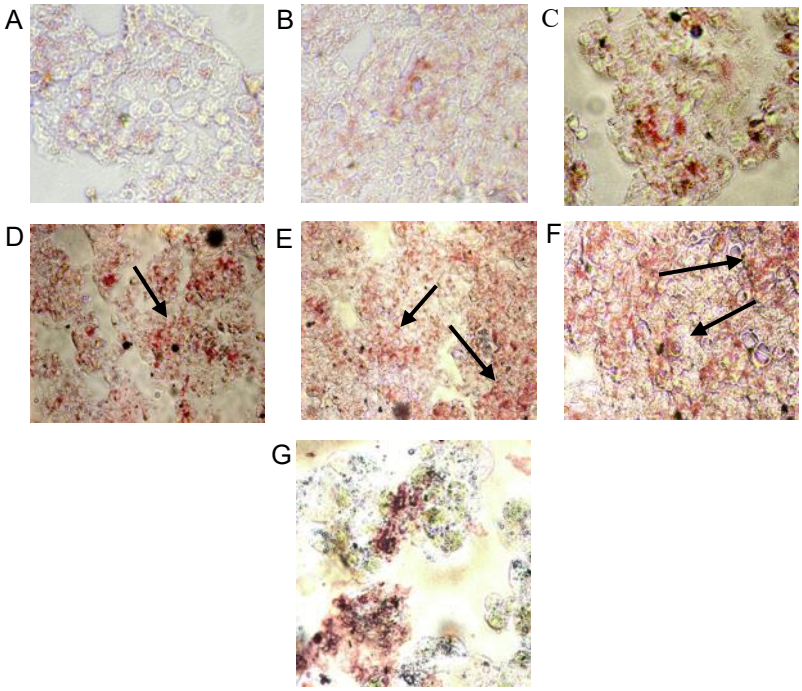

Figure 4.3 Light microscope images obtained of HepG2 cells stained with Oil Red O following treatment with tetracycline. Cells were dosed with tetracycline at final concentrations of 0 (DMSO control), 100, 200, 400, 600 and 800 µM and incubated for 24 hours. Cells were stained using Oil Red O as described in Section 2.7. A. media only control, B. DMSO control, C. 100 µM, D. 200 µM, E. 400 µM, F. 600 µM and G. 800 µM. The arrows indicated lipid accumulation.

4.3.3 Triglyceride assay in the monolayer

Oil Red O staining offered a visual representation of the triglyceride accumulation within the cell; however, it was not possible to quantify how much was present. Therefore, cell lysates from HepG2 cells treated with tetracycline at the different dose levels were analysed using a commercial Triglyceride-Glo™ assay kit to quantify triglyceride content. As shown in Figure 4.4 there was no significant change in triglyceride accumulation at any of the dose levels tested. In addition, the 400 and 800 µM treated groups had lower triglyceride content when compared to control, which could be due to the possible slight decrease in cell viability seen in Figure 4.1, although this was not statistically significant. This does correspond to the change in morphology observed in Figure 4.3 G.

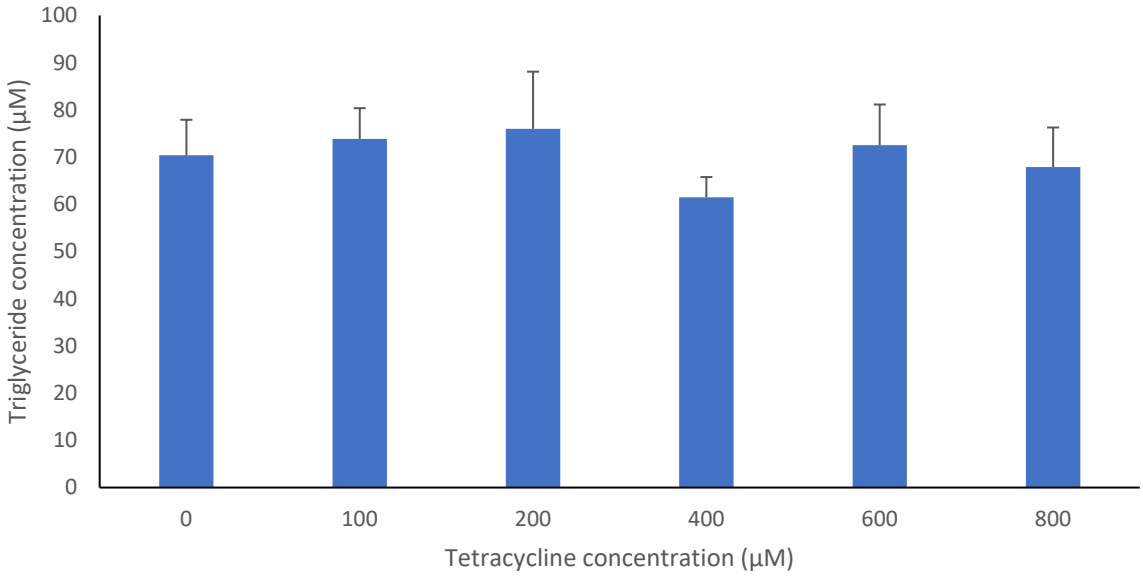

Figure 4.4 Triglyceride content in HepG2 cells following treatment with tetracycline. HepG2 cells were treated with tetracycline at concentrations of 0 (DMSO control), 100, 200, 400, 600 and 800 µM and incubated for 24 hours. The triglyceride assay was carried out as described in Section 2.8. The values shown represent the mean of six replicates. Error bars represent standard deviation.

4.3.4 Metabolomic analysis in aqueous monolayers cell extracts

In this study aqueous HepG2 cell extracts were collected following 24-hour incubation in media supplemented with tetracycline at different dose levels. NMR and multivariate analysis were used to determine changes in the metabolite profile in response to tetracycline.

Visual inspection of the ^{1}H NMR spectra did not reveal any obvious differences between sample groups (data not presented). Therefore, multivariate analysis was employed. Firstly, an unsupervised method of analysis, PCA was carried out. A PCA model was constructed and the scores plot obtained (Figure 4.5) revealed some degree of separation between the different sample groups with the low doses on the right-hand side of the scores plot and the high doses on the left. The DMSO control samples were mostly located on the right-hand side of the scores plot, although two samples from this group were separated from the rest of the group and were negative for PC1. The 400 (light blue) and 600 (blue) µM samples were clustered on the left-hand side of the scores plot with some overlap between the two groups while the 100 and 200 µM were on the right-hand side. The 800 µM samples were also mostly negative for PC1 with the exception of samples 800 µM (2 and 4). Sample 800 µM (2)

was located outside the ellipse, however upon inspection of the Hotelling's plot (Appendix Figure 8.6) it was determined that this sample was not an outlier. All samples at this dose level were positive for PC2 though.

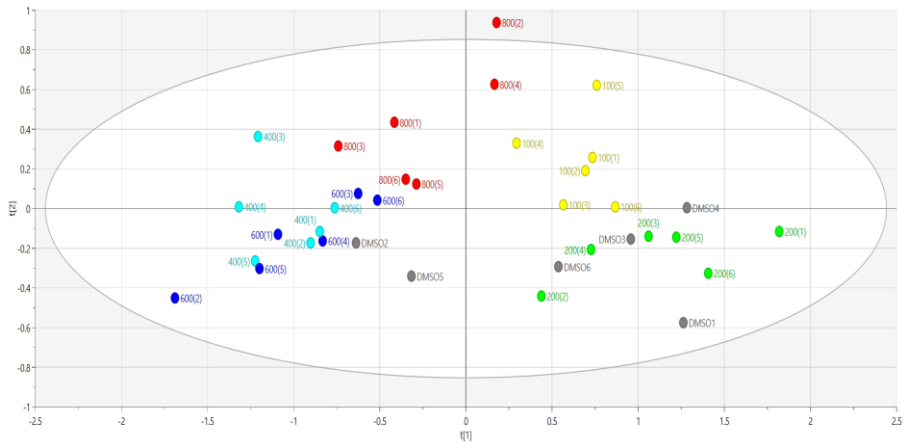

Figure 4.5 PCA scores plot derived from ^{1}H NMR spectra of aqueous extracts from HepG2 cells dosed with tetracycline at increasing dose levels. Cells were dosed with 0 (DMSO control), 100, 200, 400, 600 and 800 µM tetracycline and incubated for 24 hours. Aqueous cell extracts were collected, and NMR analysis carried out as described in Sections 2.10 and 2.12. Each spot represents one sample. Grey = DMSO only control; Yellow = 100 µM; Green = 200 µM; Light blue = 400 µM; Blue = 600 µM; Red = 800 µM.

As the PCA model did not show defined sample group separation the NMR spectra were further analysed using OPLS. The scores plot is shown in Figure 4.6. Similar to the PCA plot, the OPLS scores plot does not show clear separation between the sample groups along the predictive t[1] axis. The DMSO controls and 100 µM sample group were spread across the t[1] axis. The 200 µM sample group were found on the left-hand side of the scores plot and the 800 µM group was located on the right. However, there remains overlap between the 400 and 600 µM groups in the upper right-hand side of the quadrant. Sample 400 µM (3) was separated from the rest of the sample group. Significant intragroup variation can be seen in the DMSO control samples with all samples spread across the t[1] and t[0] axis.

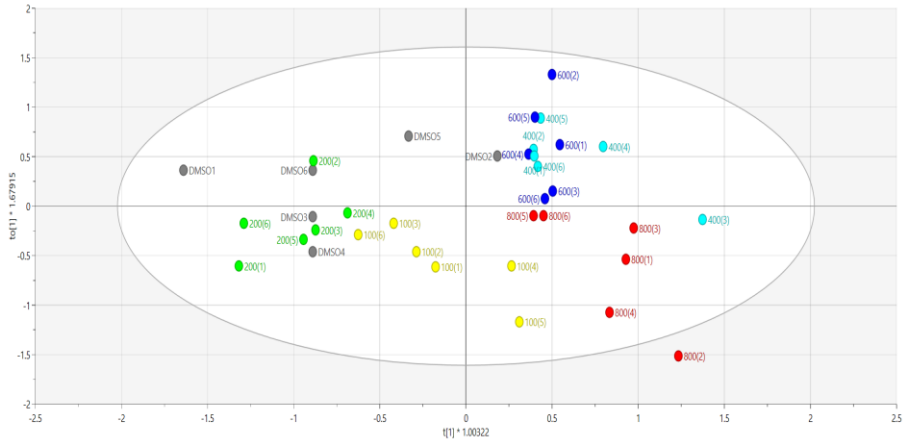

Figure 4.6 OPLS scores plot derived from NMR spectra of aqueous cell extracts from HepG2 cells treated with different dose levels of tetracycline. Cells were dosed with 0 (DMSO control), 100, 200, 400, 600 and 800 µM tetracycline and incubated for 24 hours. Aqueous cell extracts were collected, and NMR analysis carried out as described in Sections 2.10 and 2.12. Each spot on the scores plot represents one sample. Grey = DMSO only control; Yellow = 100 µM; Green = 200 µM; Light blue = 400 µM; Blue = 600 µM; Red = 800 µM.

Following OPLS analysis each treated group was then compared directly against the control group using OPLS-DA in order to compare changes in metabolites following treatment with tetracycline. Consecutive dose levels were also analysed using OPLS-DA to identify dose related metabolite changes. Each of the OPLS-DA scores plots constructed (Figure 4.7) demonstrate good separation in each pair-wise comparison along the t[1] predictive axis, with the exception of the comparison between DMSO control vs 200 µM. In this scores plot (Figure 4.7 B) DMSO sample (3) was just on the right-hand side of the scores plot although fairly central, while the rest of the group was located on the left. Otherwise, the control DMSO sample group was located on the left side of all plots. Additionally, similar to results obtained from the OPLS analyses there was significant intragroup variation along the orthogonal t[0] axis for the DMSO control sample group mainly due to control sample 4 (DMSO 4). This intragroup variation seemed to be more prominent when the control samples were compared against dose levels higher than 200 µM as well as when the treated groups were compared against each other. These samples were rephased several times and outlier analysis were conducted which confirmed no outliers were present.

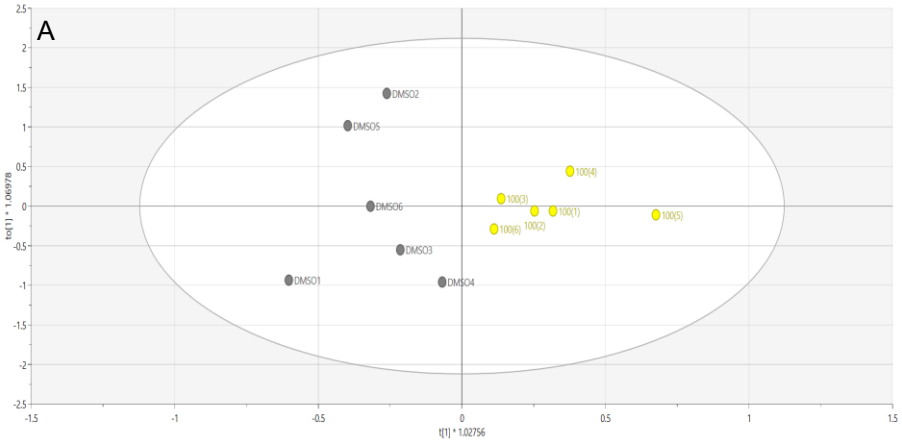
A
DMSO2
DMSO5
100(4)
100(3)
100(1)
100(5)
DMSO6
100(6)
100(2)
DMSO3
DMSO1
DMSO4
to[1] * 1.06978
t[1] * 1.02756

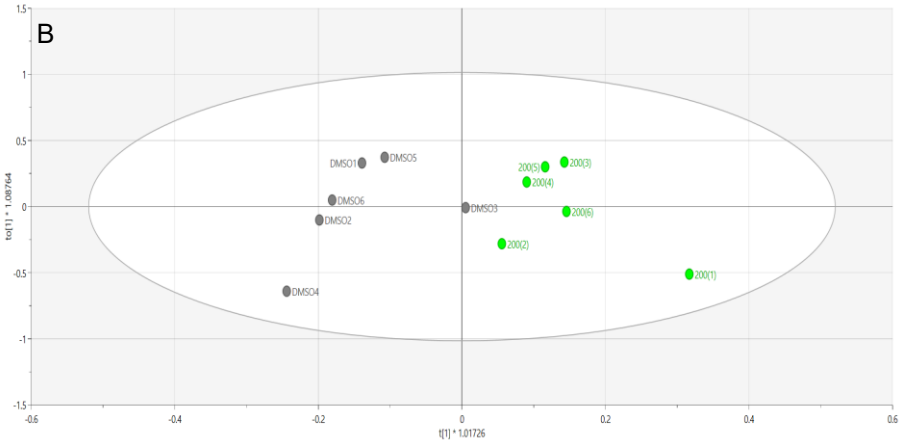
B
DMSO1
DMSO5
200(5)
200(3)
200(4)
DMSO6
DMSO3
200(6)
DMSO2
200(2)
200(1)
DMSO4
to[1] * 1.08764
t[1] * 1.01726

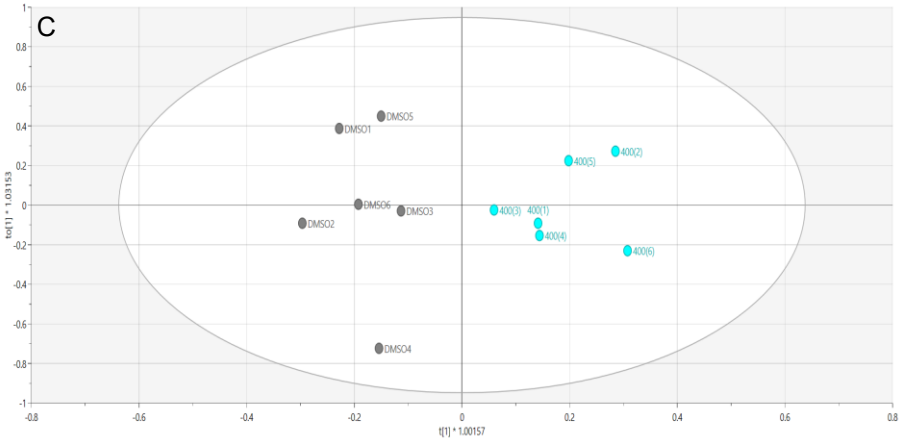
C
DMSO5
DMSO1
400(2)
400(5)
DMSO6
DMSO3
400(3)
400(1)
DMSO2
400(4)
400(6)
DMSO4
to[1] * 1.03153
t[1] * 1.00157

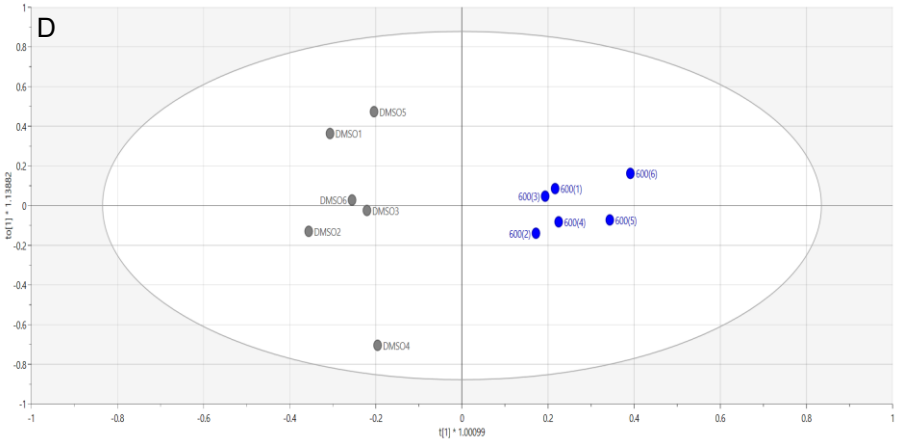
D
DMSO5
DMSO1
600(6)
600(1)
600(3)
DMSO6
DMSO3
600(4)
600(5)
DMSO2
600(2)
DMSO4
to[1] * 1.13882
t[1] * 1.00099

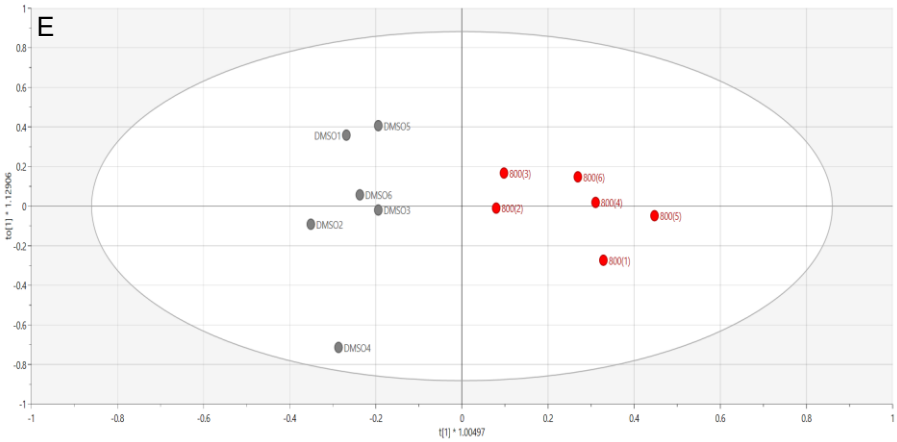
E
DMSO1
DMSO5
DMSO6
DMSO3
DMSO2
DMSO4
800(3)
800(6)
800(2)
800(4)
800(5)
800(1)
to[1] * 1.12906
t[1] * 1.00497

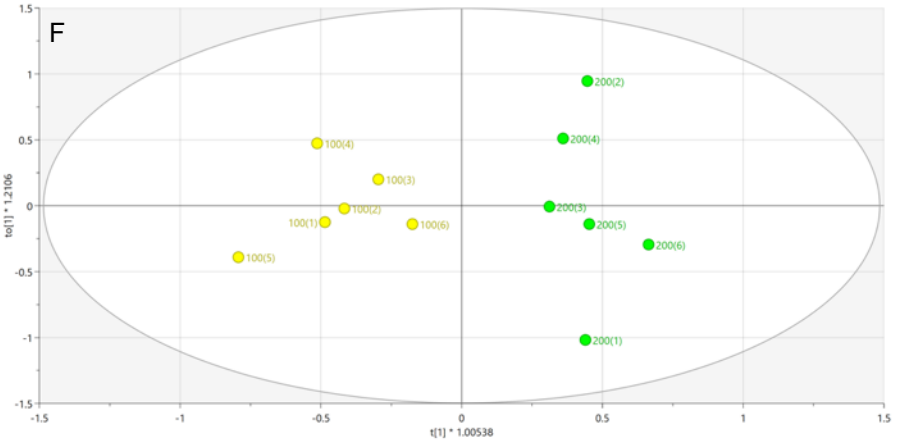
F
200(2)
100(4)
200(4)
100(3)
100(2)
200(3)
100(1)
100(6)
200(5)
200(6)
100(5)
200(1)
to[1] * 1.2106
t[1] * 1.00538

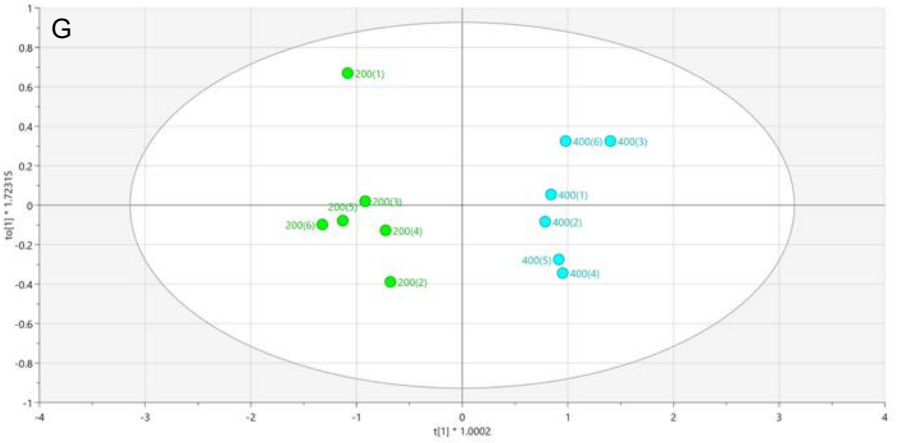
G
200(1)
400(6)
400(3)
200(5)
200(3)
400(1)
200(6)
400(2)
200(4)
400(5)
400(4)
200(2)
to[1] * 1.72315
t[1] * 1.0002

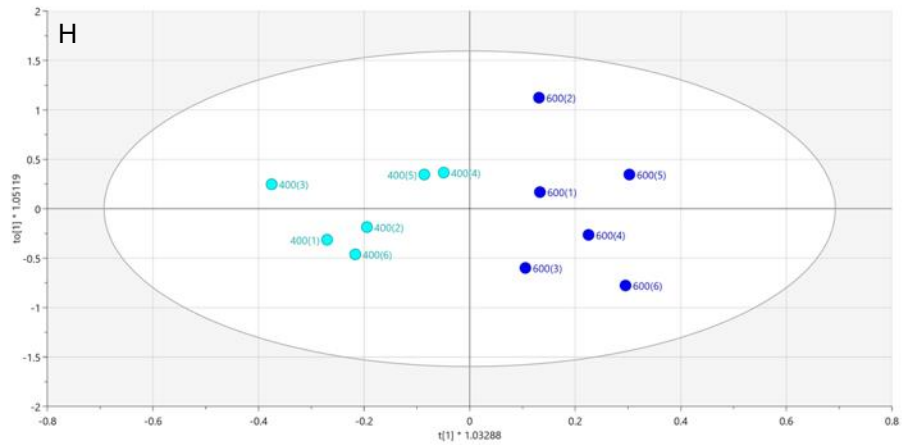
H
600(2)
400(3)
400(5)
400(4)
600(5)
600(1)
400(2)
400(1)
600(4)
400(6)
600(3)
600(6)
to[1] * 1.05119
t[1] * 1.03288

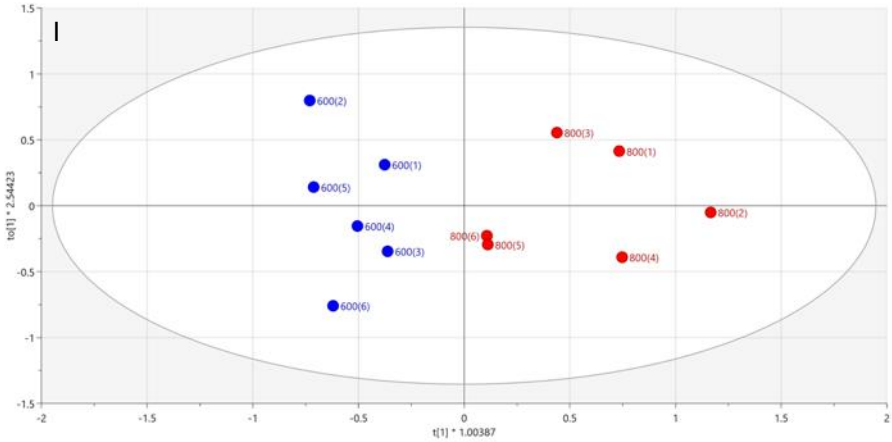

Figure 4.7 OPLS-DA scores plots derived from ^{1}H NMR spectra of aqueous extracts from HepG2 cells dosed with tetracycline at varying dose levels. Cells were dosed with tetracycline at 0, 100, 200, 400, 600 and 800 µM and incubated for 24 hours. Samples were collected, and NMR analysis was carried out as described in Sections 2.10 and 2.12. Each spot on the scores plot represents one sample. A. DMSO control vs 100 µM, B. DMSO control vs 200 µM, C. DMSO control vs 400 µM, D. DMSO control vs 600 µM, E. DMSO control vs 800 µM, F. 100 vs 200 µM, G. 200 vs 400 µM, H, 400 vs 600 µM, I. 600 vs 800 µM. Grey = DMSO only control; Yellow = 100 µM; Green = 200 µM; Light blue = 400 µM; Blue = 600 µM; Red = 800 µM.

Using the OPLS-DA models in Figure 4.7 VIP predictive and S-plots were generated (Appendix Figures 8.7 and 8.8) to determine the metabolite regions in the NMR spectra that contributed most to the separation of the two groups in each pair-wise comparative scores plot. The VIP predictive plots revealed NMR regions that were statistically significant and the regions with a VIP value greater than one are highlighted in red in both the VIP and S-plots. S-plots were used to confirm whether the peaks within the specific NMR variable regions had decreased or increased for groups in each pair-wise comparison.

Following OPLS-DA analysis, a Kruskal-Wallis test was carried out on the integral spectral values to investigate if any of the metabolite regions highlighted in the VIP were statistically significant between the groups in each pair-wise comparison.

NMR regions that were confirmed as being statistically different were recorded. The spectra were further analysed, and the multiplicities of peaks were determined in these regions to aid with the identification of metabolites. Many metabolite regions were observed to be higher in the 100 and 200 µM groups when compared to control but were then decreased at dose levels above 400 µM and significantly decreased at 600 µM. Examples of some metabolites that followed this trend include isoleucine, lactate, alanine, glutamate and homocysteine. Significant metabolite changes that were

observed when the 200 and 400 µM treated groups were compared directly included decreases lactate, choline and homocysteine ($p<0.001$). Many significant ($p<0.05$) decreases in metabolites were observed in the comparison between the DMSO and 600 µM treated group but not at other dose levels. Also, a large number of metabolite regions were revealed as significant in the VIP of DMSO versus 800 µM, but it was not possible to identify metabolite peaks in these regions.

Table 4.1 Chemical shift regions, and potential metabolites, identified as significantly different in the NMR of aqueous extracts from HepG2 cells treated with increasing concentrations of tetracycline when compared to control.

^{1}H shift ppm	Metabolite aqueous	Ctrl vs 100 µM	Ctrl vs 200 µM	Ctrl vs 400 µM	Ctrl vs 600 µM	Ctrl vs 800 µM	100 vs 200	200 vs 400	400 vs 600	600 vs 800
0.89-0.901 (m)	Acyl groups (CH_3)	↑	-	-	↓*	-	-	-	↓	-
0.925-0.9902 (m)	Isoleucine, leucine	↑	↑	↓	↓*	-	-	↓*	-	↑
0.994-1.057 (m)	Valine/Isoleucine	↑	-	↓	↓	-	-	↓*	-	↑
1.179-1.215 (t), 1.2499-1.2556 (s)	B-hydroxybutyrate	-	-	-	↓*	-	-	-	↓	↑
1.31-1.3406 (dd)	Lactate, Threonine	↑	↑	↓	↓**	↓	↓	↓***	↓	↑
1.468-1.4941 (d)	Alanine	↑	↑	↓	↓*	-	-	↓*	-	↑
1.915-1.922 (s)	Acetate	↑	-	-	-	-	-	-	↓	↑*
1.987-2.0957 (m)	Isoleucine, Glutamate, Homocysteine, SAH, Proline	↑	↑	↓	↓*	-	↑	↓**	-	-
2.0559-2.191 (m)	Glutamate, Homocysteine	↑	↑	↓	↓*	↓	↑	↓***	↓	↑
2.33-2.3819 (t of d)	Glutamate, B-hydroxybutyrate, Proline	↑	↑	↓	↓	↓	↑	↓**	-	↑

2.3847-2.3977 (s)	Succinate, Pyruvate	-	-	↓	↓*	-	-	-	-	-
2.418-2.478 (m)	Glutamine, Pantothenic acid	↑	↑	↓	↓*	↓	↑	↓***	↑	↑
2.544-2.558 (s)	Citrate	↑	↑	↓	↓*	↓	-	↓**	-	↑
2.559-2.573 (s)	GSH, GSSG	↑	↑	↓	↓*	↓	-	↓**	-	↑
2.669-2.7001 (s)	Methionine, Citrate, SAH	↑	↑	-	-	-	-	-	-	↑
2.708-2.724 (d)	Sarcosine	-	-	-	-	-	-	-	-	↑
2.9425-2.9527 (s)	Dimethylglycine	-	↑	-	-	-	-	-	-	↑
3.0331-3.0496 (d)	Creatine, Phosphocreatine, Creatinine	-	↑	↓	↓	-	↑	↓**	↑	↑
3.216-3.226 (s)	Choline, Phosphocholine, Betaine, TMAO	-	↑	↓*	↓	↓	↑	↓***	↑	↑
3.548-3.5619 (s)	Glycine, Sarcosine	↑	↑	↓	↓**	↓	-	↓*	-	↑
3.734-3.797 (m)	Leucine, Alanine, Arginine, Lysine, Glutamine, Glutamate, GSH, GSSG, Dimethylglycine, Glucose, Cysteine, Methylacetate, Citrulline	↑	↑	↓*	↓**	↓	↑	↓***	↑	↑
3.815-3.8454 (m)	Methionine, Homocysteine, (SAH), Asparagine, Glucose, Cystathionine, Serine	-	-	↓*	↓*	-	-	↓*	↑	↑
3.9276-3.9388 (s)	Creatine, Phosphocreatine, Betaine	-	-	↓	↓*	-	-	-	-	-
3.9415-3.9659 (m)	Serine	-	↑	↓*	↓	↓	↑	↓***	↑	↑
3.984-3.99 (m)	Cystathionine, Cysteine, Serine,	↑	↑	↓*	-	-	-	-	-	-

	Hippurate, Histidine, Pantothenic acid									
4.087-4.093 (s)	Creatine	↑	-	-	-	-	-	-	-	-
4.1001-4.14 (q)	B-hydroxybutyrate, Lactate	↑	-	-	-	-	-	-	-	-
4.1404-4.1909 (m)	Phosphocholine	↑	↑	↓*	↓*	↓	↑	↓***	↑	↑
4.2216-4.2698 (m)	Threonine	↓	↑	-	↓	-	↑	↓***	↑	↑

S=singlet, d=doublet, dd=doublet of doublets, t=triplet, q=quartet, m=multiplet. An increase or decrease in the treated group was determined and these were further analysed statistically using a Kruskal-Wallis test (<0.05, **<0.01, ***<0.001)*

4.3.5 Metabolomic analysis in organic monolayers cell extracts

NMR spectra of organic extracts from HepG2 cells dosed with tetracycline at 0 (DMSO control), 100, 200, 400, 600 and 800 µM in this study were also further analysed using multivariate analysis.

Initial inspection of the NMR spectra revealed no differences between the control and the treated sample groups (data not shown). Therefore, a PCA model was constructed, and the resulting PCA scores plot (Figure 4.8) showed the DMSO control sample groups on the left-hand side of the scores plot (shown in grey) and therefore negative for PC1 with the exception of sample 4 (DMSO 4) which is on the border of the ellipse. The spectra for this sample was examined and re-processed and outlier analysis was carried out to rule out any experimental or analytical error. However, this sample was not found to be an outlier and was therefore included in further analysis. The 100 and 200 µM sample groups were spread across the PC1 axis while the 600 and 800 µM sample groups were mostly clustered in the upper right-hand quadrant, with the exception of samples 800 (2 and 3). The 400 µM sample group was spread across PC1 between the other sample groups. Large intragroup variation can be seen for most sample groups.

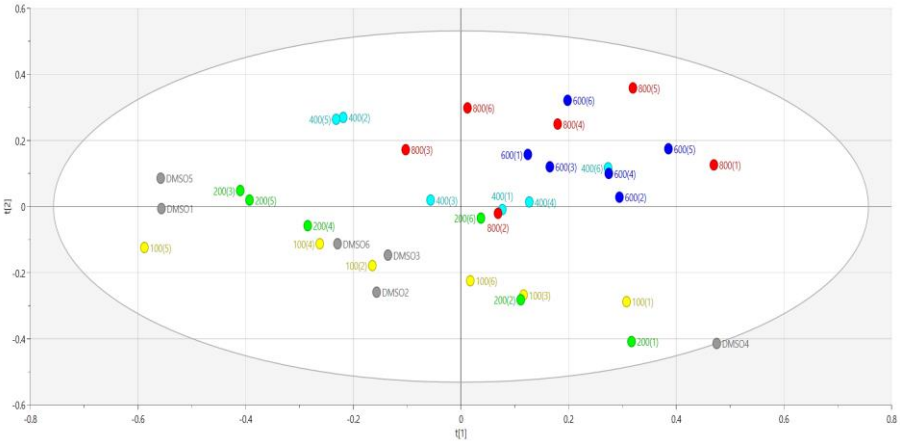

Figure 4.8 PCA scores plot derived from ^{1}H NMR spectra of organic extracts from HepG2 cells dosed with tetracycline at increasing dose levels. Cells were dosed with 0 (DMSO control), 100, 200, 400, 600 and 800 µM tetracycline and incubated for 24 hours. Organic cell extracts were collected, and NMR analysis carried out as described in Sections 2.10 and 2.12. Each spot represents one sample. Grey = DMSO only control; Yellow = 100 µM; Green = 200 µM; Light blue = 400 µM; Blue = 600 µM; Red = 800 µM.

Since the PCA scores plot showed overlap between all sample groups, OPLS models were created. The resulting OPLS scores plot (Figure 4.9) demonstrates marginally

better group separation along the predictive t[1] axis, however there is still some overlap between sample groups. Significant intragroup separation is evident for the DMSO control and the 100 and 200 µM sample groups along the orthogonal t[0] axis, with sample DMSO (4) just outside the ellipse similar to the PCA.

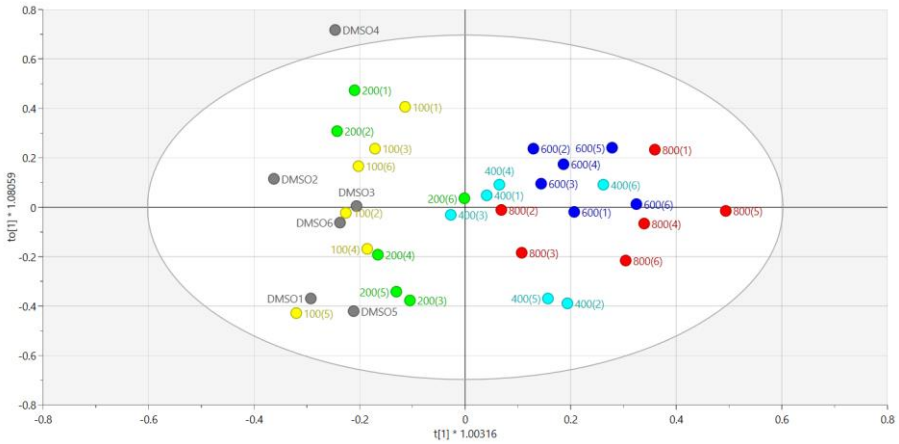

Figure 4.9 OPLS scores plot derived from NMR spectra of organic cell extracts from HepG2 cells treated with different dose levels of tetracycline. Cells were dosed with 0 (DMSO control), 100, 200, 400, 600 and 800 µM tetracycline and incubated for 24 hours. Organic cell extracts were collected, and NMR analysis carried out as described in Sections 2.10 and 2.12. Each spot on the scores plot represents one sample. Grey = DMSO only control; Yellow = 100 µM; Green = 200 µM; Light blue = 400 µM; Blue = 600 µM; Red = 800 µM.

Following OPLS analysis all treated groups were compared against the DMSO control group by constructing OPLS-DA plots. Consecutive dose levels were also analysed. Good sample group separation was observed in all scores plots along the predictive t[1] axis (Figure 4.10).

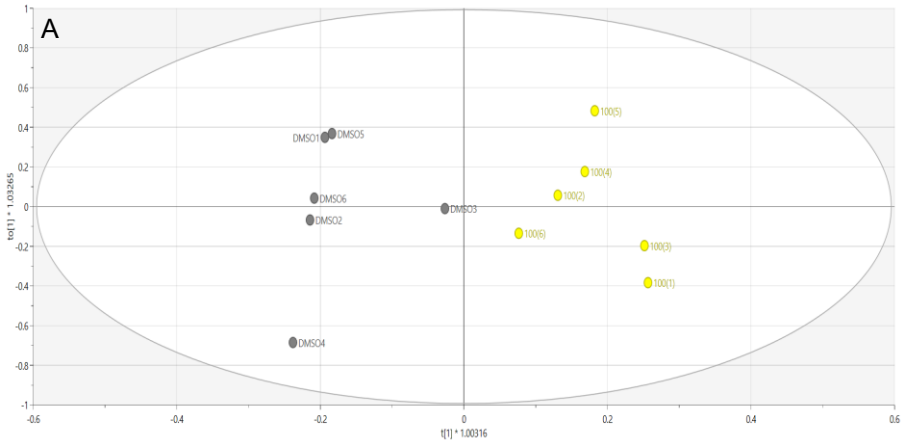
A
DMSO1
DMSO5
DMSO6
DMSO3
DMSO2
DMSO4
100(5)
100(4)
100(2)
100(6)
100(3)
100(1)
to[1] * 1.03265
t[1] * 1.00316

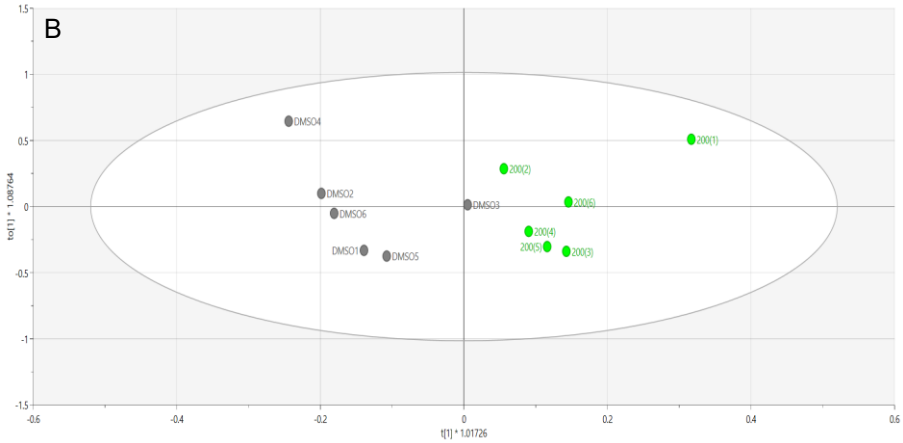
B
DMSO4
DMSO2
DMSO6
DMSO1
DMSO5
DMSO3
200(1)
200(2)
200(5)
200(4)
200(3)
to[1] * 1.08764
t[1] * 1.01726

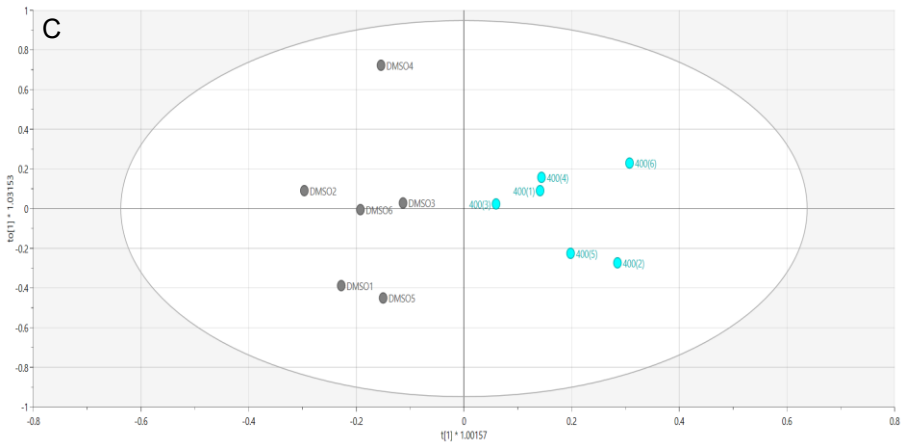
C
DMSO4
DMSO2
DMSO6
DMSO3
DMSO1
DMSO5
400(6)
400(4)
400(1)
400(3)
400(5)
400(2)
to[1] * 1.03153
t[1] * 1.00157

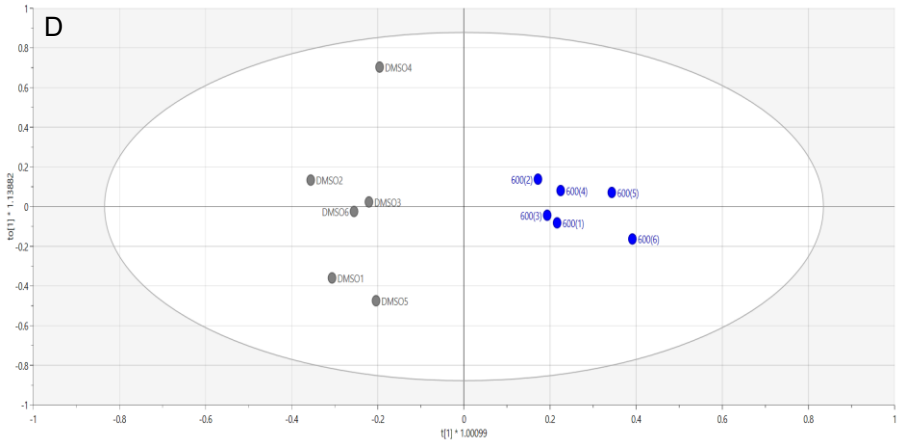
D
DMSO4
DMSO2
DMSO3
DMSO6
DMSO1
DMSO5
600(2)
600(4)
600(5)
600(3)
600(1)
600(6)
to[1] * 1.13882
t[1] * 1.00099

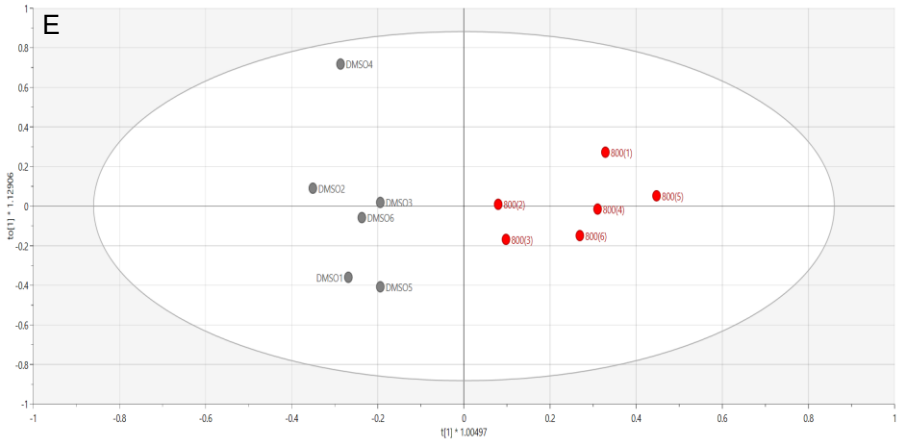
E
DMSO4
800(1)
DMSO2
DMSO3
800(2)
800(5)
800(4)
DMSO6
800(6)
800(3)
DMSO1
DMSO5
to[1] * 1.12906
t[1] * 1.00497

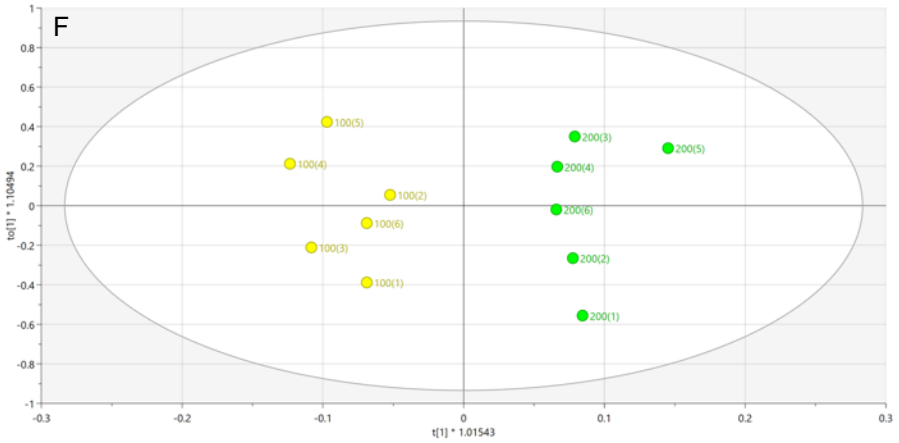
F
100(5)
200(3)
200(5)
100(4)
200(4)
100(2)
200(6)
100(6)
100(3)
200(2)
100(1)
200(1)
to[1] * 1.10494
t[1] * 1.01543

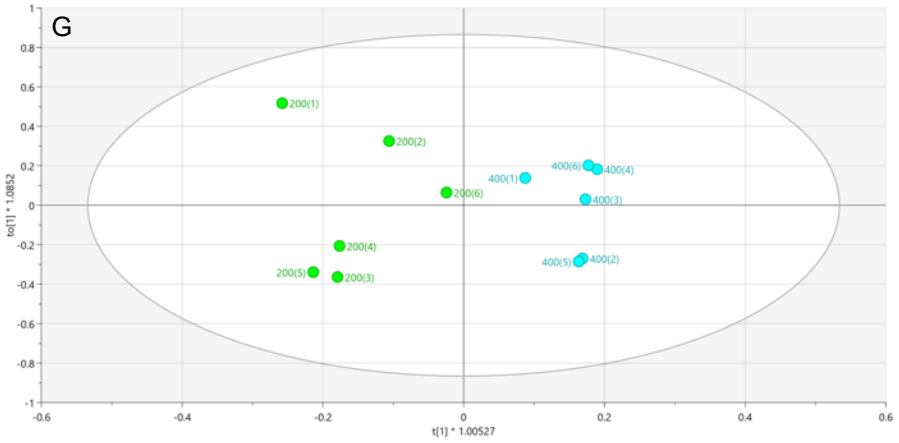
G
200(1)
200(2)
400(6)
400(4)
400(1)
200(6)
400(3)
200(4)
400(5)
400(2)
200(5)
200(3)
to[1] * 1.0852
t[1] * 1.00527

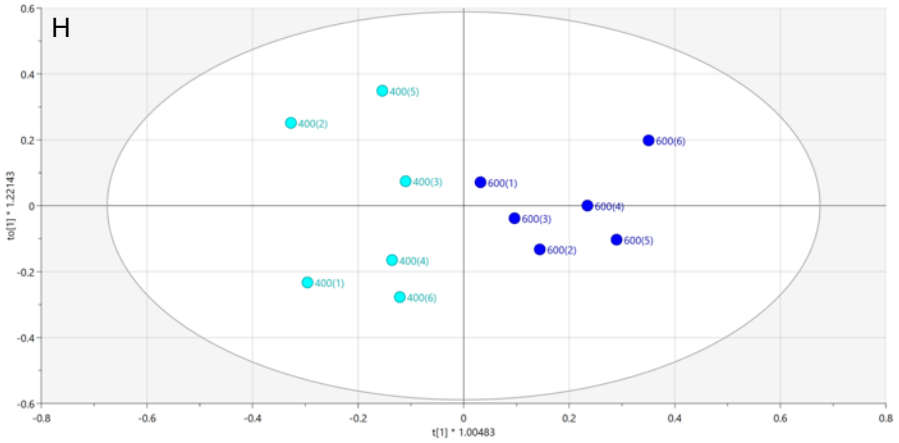
H
400(5)
400(2)
600(6)
400(3)
600(1)
600(4)
600(3)
600(5)
600(2)
400(4)
400(1)
400(6)
to[1] * 1.22143
t[1] * 1.00483

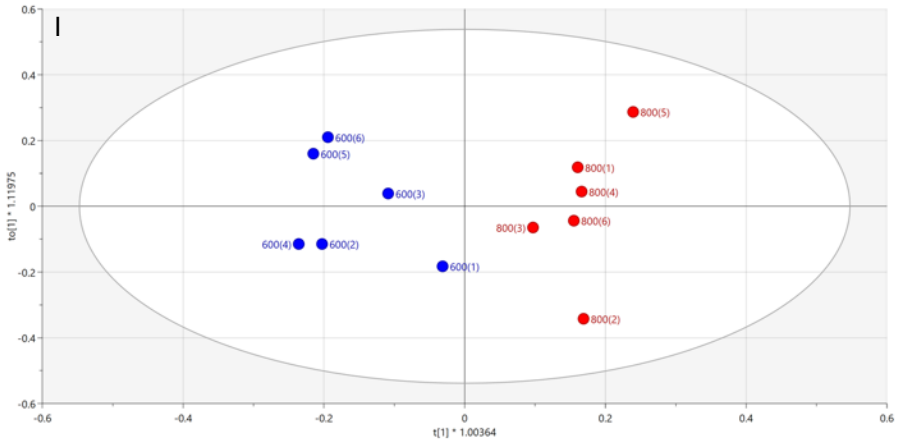

Figure 4.10 OPLS-DA scores plots derived from ^{1}H NMR spectra of organic extracts from HepG2 cells dosed with tetracycline at varying dose levels. Cells were dosed with tetracycline at 0, 100, 200, 400, 600 and 800 µM and incubated for 24 hours. Samples were collected, and NMR analysis was carried out as described in Sections 2.10 and 2.12. Each spot on the scores plot represents one sample. A. DMSO control vs 100 µM, B. DMSO control vs 200 µM, C. DMSO control vs 400 µM, D. DMSO control vs 600 µM, E. DMSO control vs 800 µM, F. 100 vs 200 µM, G. 200 vs 400 µM, H, 400 vs 600 µM, I. 600 vs 800 µM. Grey = DMSO only control; Yellow = 100 µM; Green = 200 µM; Light blue = 400 µM; Blue = 600 µM; Red = 800 µM.

Following analysis of the OPLS-DA models VIP predictive and S-plots were generated to determine the metabolite regions contributing most to separation of the groups in each pair-wise comparison scores plots (Appendix Figures 8.9 and 8.10).

Spectral regions of interest according to the VIP list were selected and further analysed using a Kruskal Wallis analysis to test for statistical significance. The characteristics of the peaks in each region were determined to enable metabolite and compound identification. Table 4.2 shows general increases in fatty acyl groups, fatty acids and cholesterol with increasing dose, however no statistically significant changes were observed. Decreases in arachidonic acid compared to the control were seen in the 100 and 200 µM treated groups but levels were then increased in doses above 400 µM. According to the Kruskal Wallis test a significant increase in arachidonic acid was observed when the 400 and 600 µM groups were compared.

Table 4.2 Chemical shift regions identified as significantly different in the organic extracts of HepG2 cells treated with different concentrations of tetracycline as detected by OPLS-DA analysis. The multiplicity of each peak is shown.

^{1}H shift ppm	Metabolite aqueous	Ctrl vs 100 µM	Ctrl vs 200 µM	Ctrl vs 400 µM	Ctrl vs 600 µM	Ctrl vs 800 µM	100 vs 200	200 vs 400	400 vs 600	600 vs 800
0.826-0.953(m)	Fatty acyl groups and FA	↑	↑	↑	↑	↑	↓	-	↑	-
1.055-1.112(m)	Cholesterol	↑	↑	↑	↑	↑	↓	-	↑	-
1.21-1.33(s)	Cholesterol	↑	↑	↑	↑	↑	↓	-	↑	↓
1.56-1.596(s)	ARA	↓*	↓	↑	↑	↑	↑	-	↑*	↓
1.7013-1.721 (s)	Fatty acids (EPA)	-	-	-	↑	-	↑	-	↑	↓
2.004-2.061 (q)	Oleic acid	-	-	-	-	-	↑	-	-	
2.298-2.365(m)	Acyl groups in triglycerides	-	-	-	-	-	↑	-	-	-
4.145-4.203 (dd)	Glyceryl group in monoglyceride	-	-	-	-	-	↑	-	-	-
4.295-4.33(dd)	Glyceryl group in Triglycerides	-	-	-	-	-	↑	-	-	-
5.348-5.38(m)	FA/MUFA	-	-	-	-	-	↑	-	-	-

S=singlet, d=doublet, dd=doublet of doublets, t=triplet, q=quartet, m=multiplet. An increase or decrease in the treated group was determined and these were further analysed statistically using a Kruskal-Wallis test (<0.05, **<0.01, ***<0.001).*

4.3.6 CYP enzyme expression levels in monolayer HepG2 cells dosed with tetracycline

In this study CYP expression in protein extracts of HepG2 cell monolayers dosed with varying concentrations of tetracycline were analysed using Western Blotting. Figure 4.11 shows the blots for CYP2D6, CYP3A4 and CYP2E1. For all blots, beta actin (Figure 4.11A) was used to ensure equal levels of cell samples were loaded. The raw data showing band intensity was shown in Table 4.3; this was determined using densitometry. A dose dependent increase in CYP2E1 was observed. CYP2D6 was also increased at all dose levels when compared to the DMSO control, although not in a dose dependent manner. CYP3A4 expression appears to be greater in the highest dose levels (600 and 800 μM). Time did not permit for repetition of these blots and therefore N= 1 which means statistical analysis was not possible.

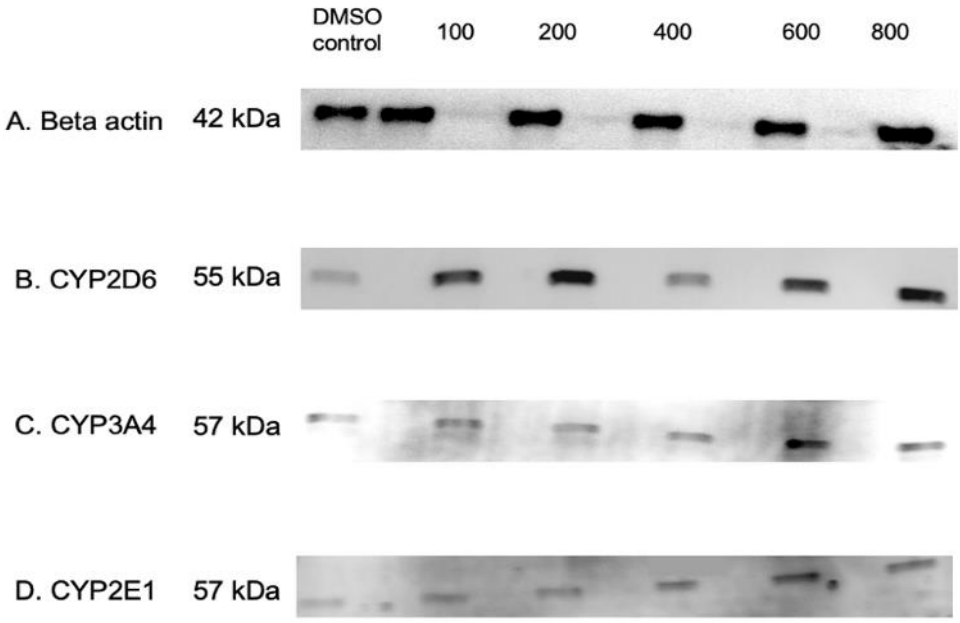

Figure 4.11 Western blot analysis of CYP enzyme expression in HepG2 monolayers dosed with tetracycline. A. Beta actin, B. CYP 2D6, C. CYP 3A4 and D. CYP2D6. Cells were dosed with tetracycline acid at varying concentrations of 100, 200, 400, 600 and 800 μM and incubated for 24 hours as described in section 2.5.2. Proteins were collected as described in Section 2.16 and analysed by Western blotting as described in Section 2.20.

Table 4.3 Raw data showing the arbitrary band intensities for CYP2D6, 3A4 and 2E1 in HepG2 monolayers dosed with tetracycline relative to the DMSO control. Cells were dosed with tetracycline at varying concentrations or 0, 100, 200, 400, 600 and 800 μM and incubated for 24 hours. Proteins were collected as described in Section 2.16 and analysed by Western blotting as described in Section 2.20.

Tetracycline concentration (μM)	CYP2D6	CYP3A4	CYP2E1
DMSO control	2244.03	3114.38	2103.49
100	9659.08	2522.45	3101.64
200	12889.54	2585.39	2284.15
400	3835.28	3342.51	3388.64
600	9519.66	4510.76	5133.54
800	11125.18	4197.03	5944.95

4.3.7 3D spheroid model dosed with tetracycline

HepG2 spheroids were grown for 17 days before being dosed with either a low or a high dose (100 and 600 μM) of tetracycline. These doses were chosen based on the results of the dose response study in the monolayers since they did not induce cytotoxicity. The purpose was to develop a spheroid model of steatosis using tetracycline and to analyse changes in the metabolome and CYP expression.

4.3.8 Cytotoxicity in spheroids treated with tetracycline

A LIVE/DEAD assay was used to visualise spheroid viability following dosing with tetracycline at both 100 and 600 μM after 17 days of growth. In the assay viable cells are stained green while non-viable cells are stained red. Figure 4.12 shows the confocal microscope images taken for the 100 and 600 μM treated spheroids and the DMSO control. No red cells were apparent confirming that spheroids dosed with 100 and 600 μM of tetracycline (Figure 4.12 B and C) did not cause cell death.

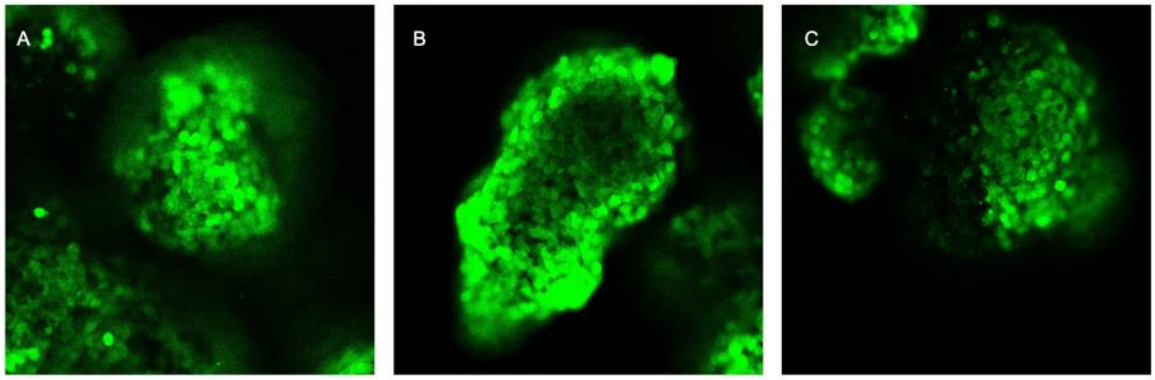

Figure 4.12 Images taken from the LIVE/DEAD assay of spheroids dosed with tetracycline. Spheroids were grown in low attachment 6-well plates as described in Section 2.3 and dosed with tetracycline at concentrations of 0 (DMSO control), 100 and 600 μM. The LIVE/DEAD assay was carried out as described in Section 2.22. A. DMSO control, B. 100 μM tetracycline and C. 600 μM tetracycline.

As the LIVE/DEAD assay only offered a visualisation of cytotoxicity it was decided that an LDH assay would be used as it gave a more quantitative measure of cytotoxicity. Figure 4.13 confirmed there was no cell death 24 hours after dosing spheroids with 100 and 600 μM of tetracycline when compared to the DMSO control. A positive control was used in this experiment, results of which represented a cytotoxicity value of 100%.

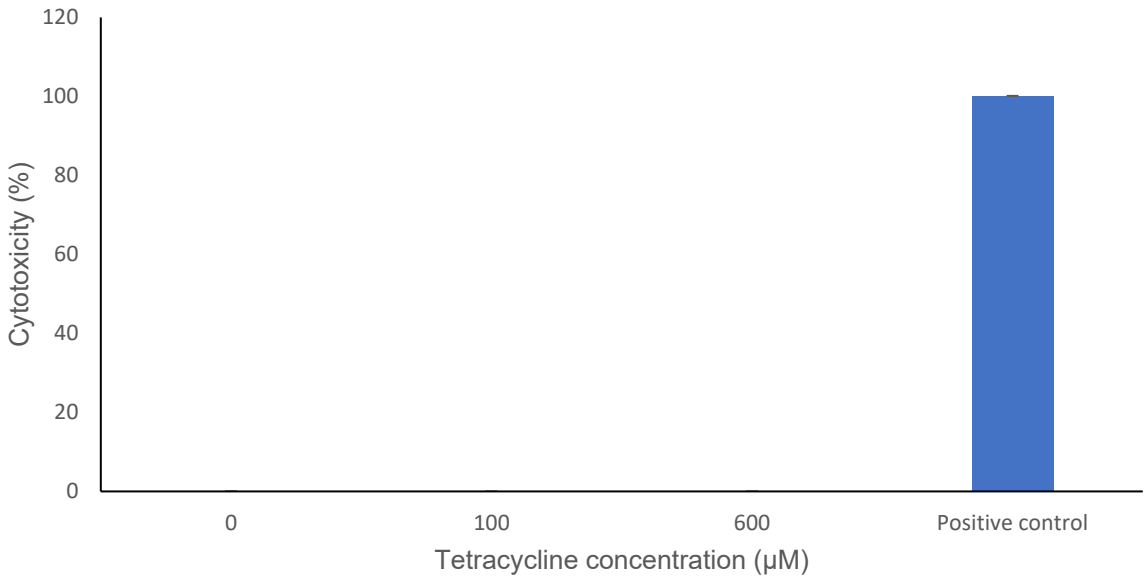

Figure 4.13 HepG2 spheroid cell death in response to increasing tetracycline concentration assessed by LDH assay. HepG2 spheroids were treated with tetracycline at concentrations of 0, 100 and 600 μM and incubated for 24 hours as described in Section 2.5.2. The LDH assay was carried out as described in Section 2.21. The value obtained for the positive control represents 100% cell death. The values shown represent the mean of six replicates. Error bars represent standard deviation.

4.3.9 Triglyceride accumulation in spheroids

Lipid accumulation was assessed in HepG2 spheroids dosed with tetracycline at dose levels of 100 and 600 μM by quantification of triglyceride content. The results shown in Figure 4.14 revealed that while there was an approximate 15% increase in triglyceride content in the two treated groups compared to the control group this was not statistically significant.

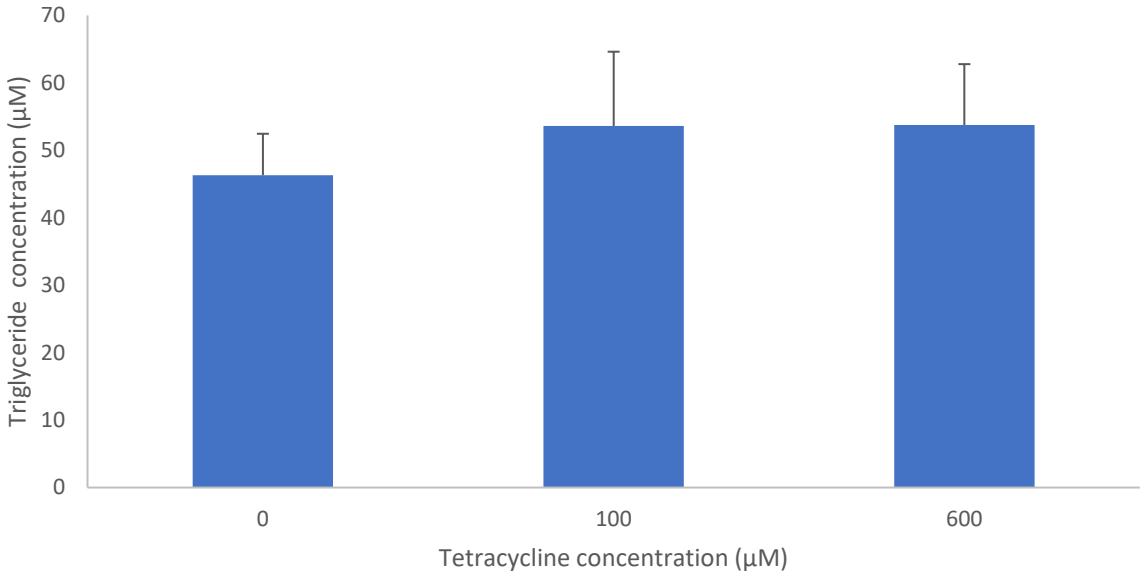

Figure 4.14 Mean triglyceride content in HepG2 spheroids following treatment with tetracycline. HepG2 spheroids were treated with tetracycline at concentrations of 0 (DMSO control), 100 and 600 µM and incubated for 24 hours as described in Section 2.5.2. The triglyceride assay was carried out as described in Section 2.8. The values shown represent the mean of six replicates. Error bars represent standard deviation.

4.3.10 Metabolomic analysis of aqueous spheroid extracts

HepG2 spheroid sample extracts were collected following a 24-hour incubation in culture media supplemented with tetracycline at the two dose levels. Aqueous extracts were prepared and analysed by NMR as described in Section 2.10. Multivariate analysis was then used to determine changes in the metabolite profile of spheroids in response to tetracycline.

Following a visual inspection of the spectra obtained from aqueous spheroid extracts, no visible difference were apparent between treated and the control groups (data not shown). Therefore, multivariate analysis was applied. An initial PCA scores plot revealed that sample 100 (4) fell outside the ellipse. Upon further inspection of the Hotelling's plot this sample was deemed an outlier and removed from further analysis. In the subsequent PCA scores plot (Figure 4.15) the DMSO 1 sample then fell outside the 95 % ellipse. However, a Hotelling's T2 plot (Appendix Figure 8.11) confirmed that the sample was below the 99 % confidence level which meant it was not an outlier and was therefore included in further analyses. The remainder of the DMSO samples were negative for PC2 while the 100 and 600 µM treated groups were positive for PC2 with the exception of 100 (3). There was slight intergroup separation along PC2.

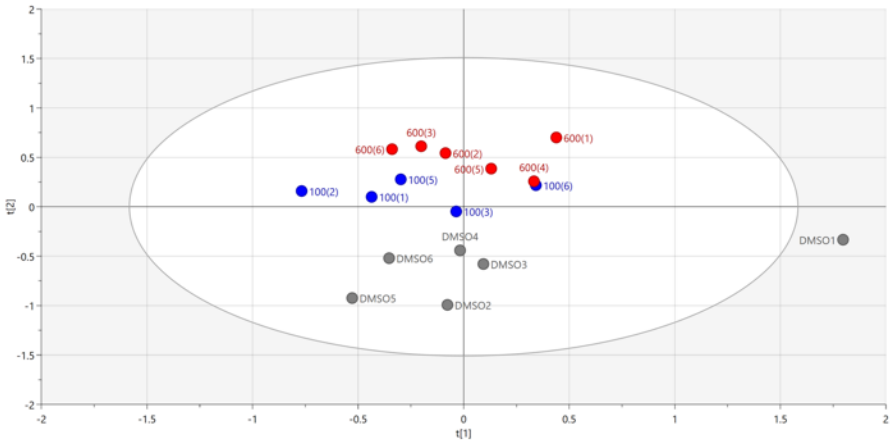

Figure 4.15 PCA scores plot derived from ^{1}H NMR spectra of aqueous extracts from HepG2 spheroids dosed with tetracycline. PCA scores plot with sample 100 (4) excluded. Cells were dosed with tetracycline at 0, 100 and 600 µM and incubated for 24 hours. Samples were collected, and NMR analysis was carried out as described in Sections 2.10 and 2.12. Each spot on the scores plot represents one sample. Grey = DMSO control, dark blue = 100 µM and red = 600 µM.

OPLS, was then used to compare between sample classes. The OPLS scores plot (Figure 4.16) demonstrated separation of the different sample groups along the predictive t[1] axis. However, some intragroup variation along the t[0] axis was evident, mostly for the DMSO control samples.

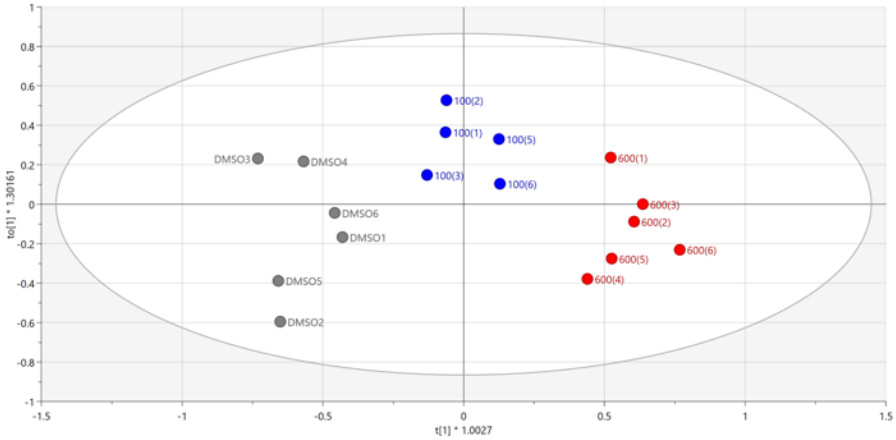

Figure 4.16 OPLS scores plot derived from ^{1}H NMR spectra of aqueous HepG2 spheroids extracts treated with different doses of tetracycline. Cells were dosed with tetracycline at 0, 100 and 600 µM and incubated for 24 hours. Samples were collected, and NMR analysis carried out as described in Sections 2.10 and 2.12. Each spot on the scores plot represents one sample. Grey = DMSO control, dark blue = 100 µM and red = 600 µM.

Following OPLS analysis OPLS-DA were created to assess pairwise differences between the individual treated groups and the DMSO control as well as between the low and high dose groups. In all OPLS-DA scores plots (Figure 4.17) the control and

the treated groups were separated along the t[1] axis. Good separation was also observed between the two treated groups (Figure 4.17 C). Orthogonal variation along the t[0] axis was apparent in the DMSO control group.

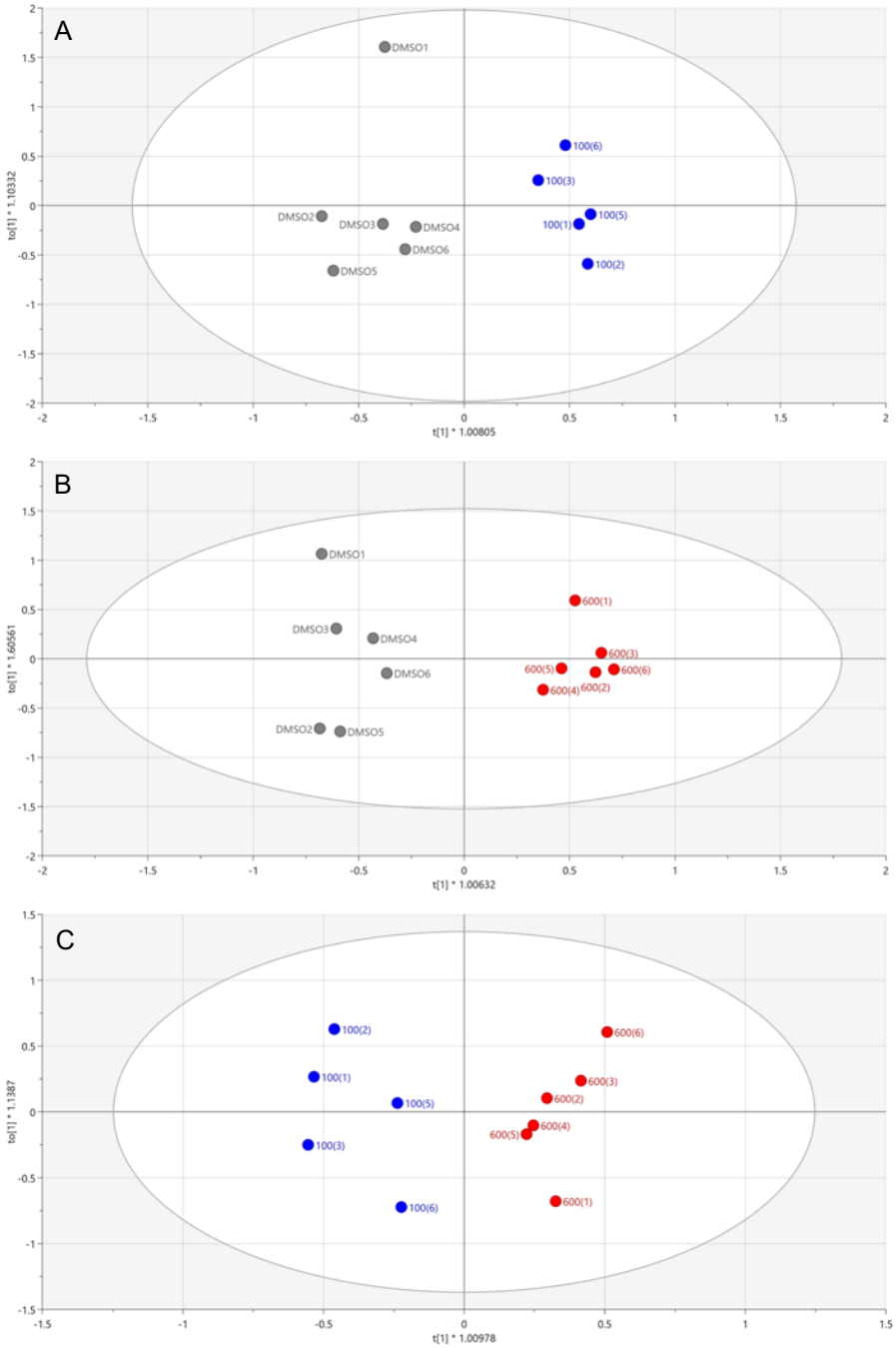

Figure 4.17 OPLS-DA scores plots derived from NMR spectra of aqueous extracts from HepG2 spheroids dosed with tetracycline. Spheroids were dosed with tetracycline at 0, 100 and 600 µM and incubated for 24 hours. Samples were collected, and NMR analysis was carried out as described in Sections 2.10 and 2.12. Each spot on the scores plot represents one sample. Grey = DMSO control, dark blue = 100 µM and red = 600 µM. A. Control vs 100 µM tetracycline. B. Control vs 600 µM tetracycline. C. 100 vs 600 µM tetracycline.

VIP predictive and S-plots (Appendix Figures 8.12 and 8.13) were generated from the OPLS-DA models and were used to determine the NMR regions contributing most to the separation of the groups in the OPLS-DA scores plots.

The spectral regions highlighted in the VIP and S-plots were visually inspected on the ^{1}H NMR spectra to identify the multiplicity of the peaks within these regions. The Human Metabolome Database and published literature were used to identify metabolites thought to be within these regions. However, it was not possible to identify metabolites for all the regions considered to be significant by the VIP and many peaks remained unidentified (data not shown). Spectral regions were further analysed using a Kruskal Wallis test to determine any statistical significance.

Table 4.4 shows significant increases in many metabolite regions were observed in the 600 μM treated group when compared to the DMSO control. These included metabolite changes in alanine, glutamate and β-hydroxybutyrate. Decreases in lactate were also seen in both treated groups with a significant decrease ($p<0.05$) seen in the 600 μM when compared to the DMSO control. Decreases in creatine, phosphocreatine and creatinine were also seen in both the 100 and 600 μM treatment groups. Dose dependent changes were apparent when comparing the treated groups with the control with many of the changes becoming statistically significant with increasing dose. For example, decreases in isoleucine and succinate were observed in the treated groups; this was significant only in the higher dose group of 600 μM ($p<0.001$).

Table 4.4 Chemical shift regions identified as significantly different in the aqueous extracts of HepG2 spheroids treated with different concentrations of tetracycline as detected by OPLS-DA analysis. The multiplicity of each peak is shown.

^{1}H shift ppm	Metabolite aqueous	Ctrl + 100uM	Ctrl +600uM	100 +600uM
0.886-0.974 (m)	Acyl groups (CH_3)	↑	↓***	↓
0.982-1.05 (m)	Valine, Isoleucine	↓	↓***	↓
1.07-1.074(s)	Isoleucine	↑	-	-
1.186-1.214(d)	Lysine, Citrulline	-	-	↓
1.314-1.479 (d)	Lactate, Threonine	↓	↓*	↓
1.43-1.47(d)	Alanine	↑	↑***	↑
1.805-1.903(m)	Lysine, Citrulline	↑*	-	↓
1.912-1.927(s)	Acetate	↑	-	↓
1.978-2.107(m)	Isoleucine, Glutamate, Homocysteine, SAH, Proline	↑*	↓**	↓
2.115-2.137(m)	Methionine, Glutamine, GSH, GSSG, Homocysteine, Cystathionine	↓	↓*	↓
2.23.245(s)	Valine	↑**	-	↓
2.307-2.3815(m)	B-hydroxybutyrate, Glutamate, Proline	↓	↑*	↓
2.416-2.428(s)	Pyruvate, Succinate	↓	↓***	↓
2.48-2.545(m)	Citrate	-	↓*	↓
3.034-3.049(s)	Creatine, Phosphocreatine, Creatinine	↓	↓**	↓
3.218-3.231(s)	Choline, Phosphocholine, Betaine, TMAO	↑	↓	↓
3.257-3.265(m)	Arginine, Taurine, Histidine	-	↓	↓
3.34-3.35(s)	Glucose, Hypotaurine, Pantothenic acid	↑	-	↓
3.4602-3.494(m)	Proline, Taurine, Pantothenic acid	↑	↑	-
3.515-3.552 (dd)	Glucose, Pantothenic acid	↑	↓	-
3.617-3.629(m)	Phosphocholine	-	↓	-

3.688-3.79 (m)	Leucine, Alanine, Arginine, Lysine, Glutamine, Glutamate, GSH, GSSG, Dimethylglycine, Glucose, Cysteine, Methylacetate, Citrulline	↑	↓	↓
3.815-3.8454 (m)	SAH, Asparagine, Glucose, Cystathionine, Serine	-	↓*	↓
3.881-3.9205(m)	Homocysteine, Methionine, SAH, Cystathionine	↑	↓	↓
3.947-3.959(s)	Creatine, Phosphocreatine, Betaine	-	-	↓
3.9628-3.991(m)	Cystathionine, Cysteine, Serine, Hippurate, Histidine, Pantothenic acid	-	↓	-
4.085-4.137 (q)	B-hydroxybutyrate, Lactate,	↓	↓	↓
4.14-4.198(m)	Phosphocholine	-	↓**	↓
6.036-6.06(m)	NAD	-	-	↑

S=singlet, d=doublet, dd=doublet of doublets, t=triplet, q=quartet, m=multiplet. An increase or decrease in the treated group was determined and these were further analysed statistically using a Kruskal-Wallis test (<0.05, **<0.01, ***<0.001).*

4.3.11 Metabolomic analysis of organic spheroid extracts

Organic extracts from HepG2 spheroids were analysed using ^{1}H NMR spectroscopy. Visual inspection of the 1D ^{1}H NMR spectra was conducted prior to multivariate analysis. In the PCA model (Figure 4.18) sample 100 (3) was located just outside the ellipse, but the corresponding Hotelling's plot confirmed (Appendix Figure 8.14) this sample was within the 95 % confidence level and it was therefore included in further analyses. The PCA shows many samples were spread across the scores plot with no distinct intergroup separation. Large intragroup variation was observed particularly in the 600 µM group.

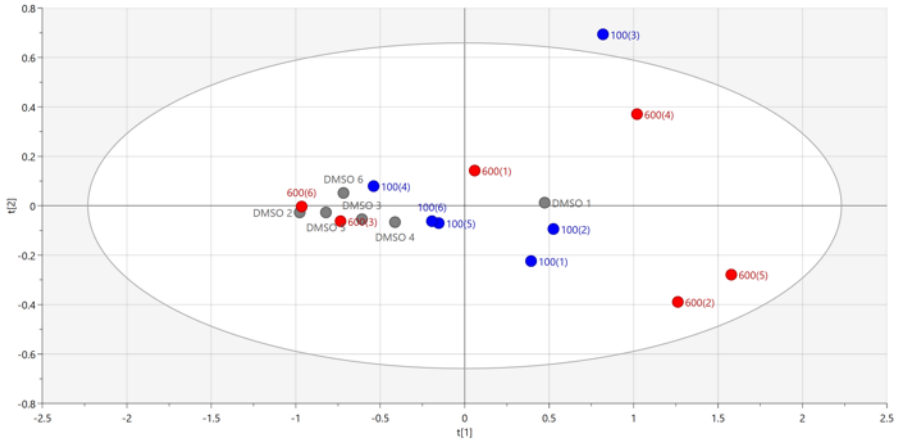

Figure 4.18 PCA scores plot derived from ^{1}H NMR spectra of organic extracts from HepG2 spheroids treated with tetracycline. Spheroids were dosed at 0 (DMSO control), 100 and 600 µM and incubated for 24 hours. Samples were collected, and NMR analysis carried out as described in Sections 2.10 and 2.12. Each spot represents one sample. Grey = DMSO control, dark blue = 100 µM and red = 600 µM.

OPLS analysis was applied to examine sample class separation. The scores plot (Figure 4.19) shows the DMSO control samples were on the left-hand side of the plot with some orthogonal separation along the t[0] axis. However, clear group separation was not observed as both the 100 and 600 µM treated groups were spread across the predictive t[1] axis with large intragroup separation for both groups and intergroup overlapping.

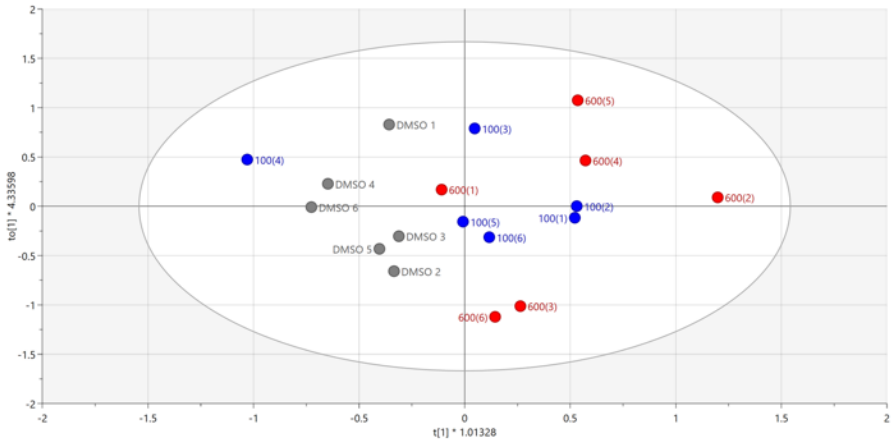

Figure 4.19 OPLS scores plot derived from ^{1}H NMR spectra of organic HepG2 spheroids extracts treated with tetracycline. Cells were dosed with tetracycline at 0, 100 and 600 µM and incubated for 24 hours. Samples were collected, and NMR analysis carried out as described in Sections 2.10 and 2.12. Each spot on the scores plot represents one sample. Grey = DMSO control, dark blue = 100 µM and red = 600 µM.

OPLS-DA was carried out to evaluate pair-wise comparisons. The scores plots in Figure 4.20 A and B revealed separation between the DMSO control and each of the two treatment groups along the predictive t[1] axis. However, large intragroup variation is evident for both treatment groups along the orthogonal t[0] axis. For each pair-wise comparison the controls were on the left-hand side of the scores plot while each respective treatment group was on the right.

Figure 4.20 C shows the OPLS-DA scores plot constructed to compare the two treated groups. Samples 100 (1) and 600 (1) were located on opposite sides of the scores plot from their respective sample groups. This meant the separation between the two groups along the predictive axis was not distinct. This was also visible in the PCA scores plot.

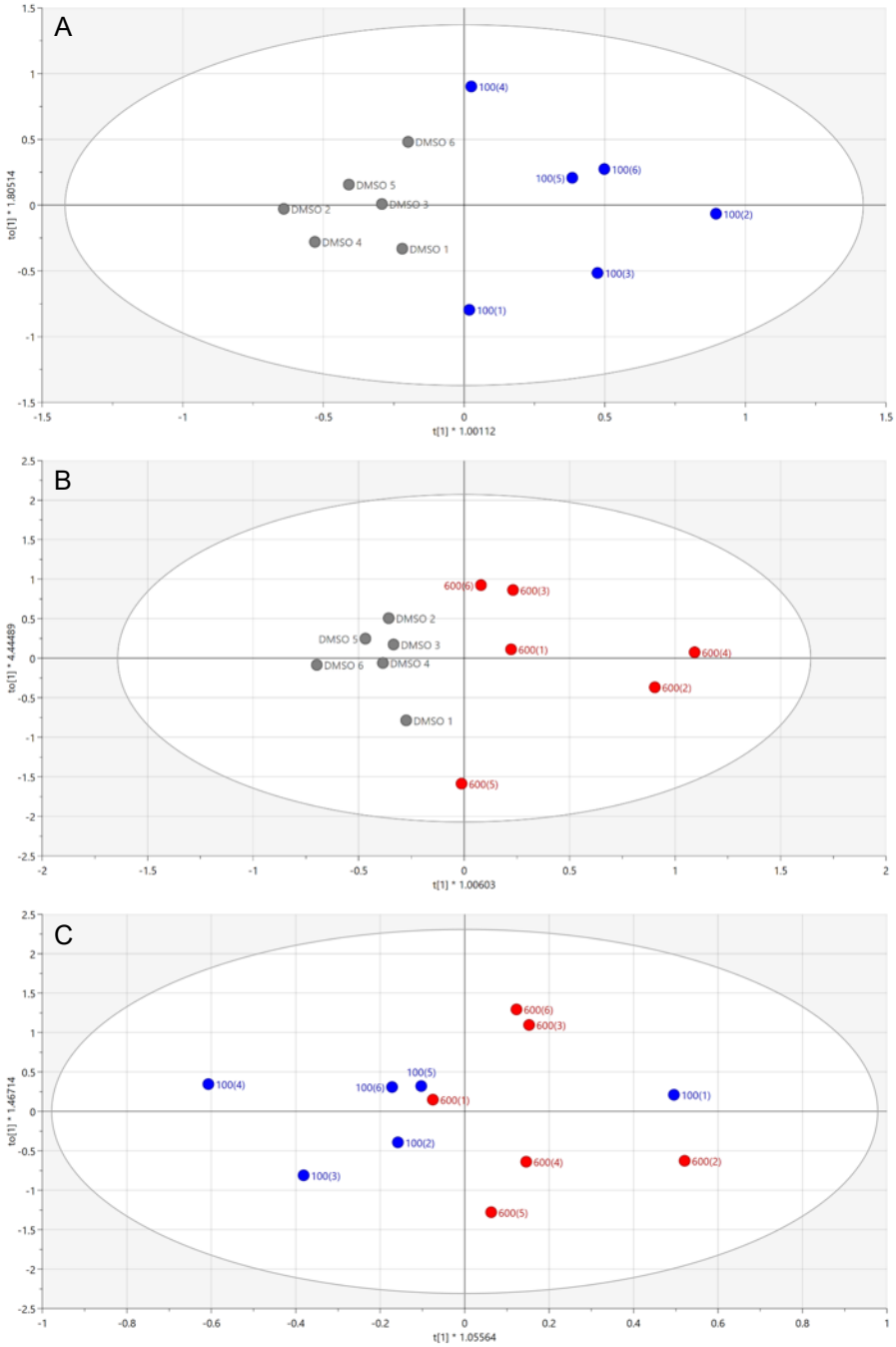

Figure 4.20 OPLS-DA scores plots derived from NMR spectra of organic extracts from HepG2 spheroids dosed with tetracycline. Spheroids were dosed with tetracycline at 0, 100 and 600 µM and incubated for 24 hours. Samples were collected, and NMR analysis was carried out as described in Sections 2.10 and 2.12. Each spot on the scores plot represents one sample. Grey = DMSO control, dark blue = 100 µM and red = 600 µM. A. Control vs 100 µM tetracycline. B. Control vs 600 µM tetracycline. C. 100 vs 600 µM tetracycline.

The OPLS-DA models were then used to identify treatment-related metabolite changes using the corresponding VIP and S-plots (Appendix Figures 8.15 and 8.16) Spectral regions with a VIP predictive value greater than 1 were highlighted and

considered to be significantly different and responsible for the sample separation. These variable regions are also highlighted in red in the S-plots.

Following identification of the spectral regions of interest from the VIP and S-plot models a visual inspection of these regions on the spectra was conducted to identify the multiplicities of the peaks within each region. Using this information metabolites were identified using the Human Metabolome Database along with published literature and assigned metabolites and compounds are shown in Table 4.5. A Kruskal Wallis test was carried out to observe any statistical significance, however, no significance was observed for any of the NMR regions in this study. Despite the lack of significance, increases in cholesterol were apparent in both treated groups as well as decreases in arachidonic acid. Many other metabolite regions were also highlighted in the VIP plots, but metabolite identification was not possible.

Table 4.5 Chemical shift regions identified as significantly different in the organic extracts of HepG2 spheroids treated with different concentrations of tetracycline as detected by OPLS-DA analysis. The multiplicity of each peak is shown.

^{1}H shift ppm	Metabolite aqueous	Ctrl + 100 µM	Ctrl +600 µM	100+600 µM
0.826-0.953(m)	Fatty acyl groups and FA	↑	↑	-
1.114-1.131(s)	Cholesterol	↑	-	-
1.2651-1.285(s)	Cholesterol	↑	↑	↑
1.5625-1.605(s)	ARA	↓	↓	↓
2.008-2.065(q)	Oleic acid	↑	↑	-
2.3129-2.365(m)	Acyl groups in triglycerides	↑	↑	↑
4.145-4.193(dd)	Glyceryl group in monoglyceride	↑	-	-
5.327-5.414(m)	FA/MUFA	↑	↑	-

S=singlet, d=doublet, dd=doublet of doublets, t=triplet, q=quartet, m=multiplet. An increase or decrease in the treated group was determined and these were further analysed statistically using a Kruskal-Wallis test (<0.05, **<0.01, ***<0.001).*

4.3.12 CYP enzyme expression levels in HepG2 spheroids dosed with tetracycline

Western blotting was used to analyse CYP enzyme expression in HepG2 spheroids dosed with tetracycline in this study. Figure 4.21 shows the blots from CYP2D6, CYP3A4 and CYP2E1 with beta actin used as the level constituent cell protein to ensure equal loading levels of samples. The results in Table 4.6 show the raw data of arbitrary units for all enzymes. The results show an increase in CYP2D6 expression in the 600 and 800 µM samples. Increased CYP3A4 expression was also observed in all dose levels compared to the control. However, CYP2E1 levels were decreased in all dose levels when compared to the DMSO control with the lowest expression being in the 800 µM samples. However, as N=1 further analysis is required.

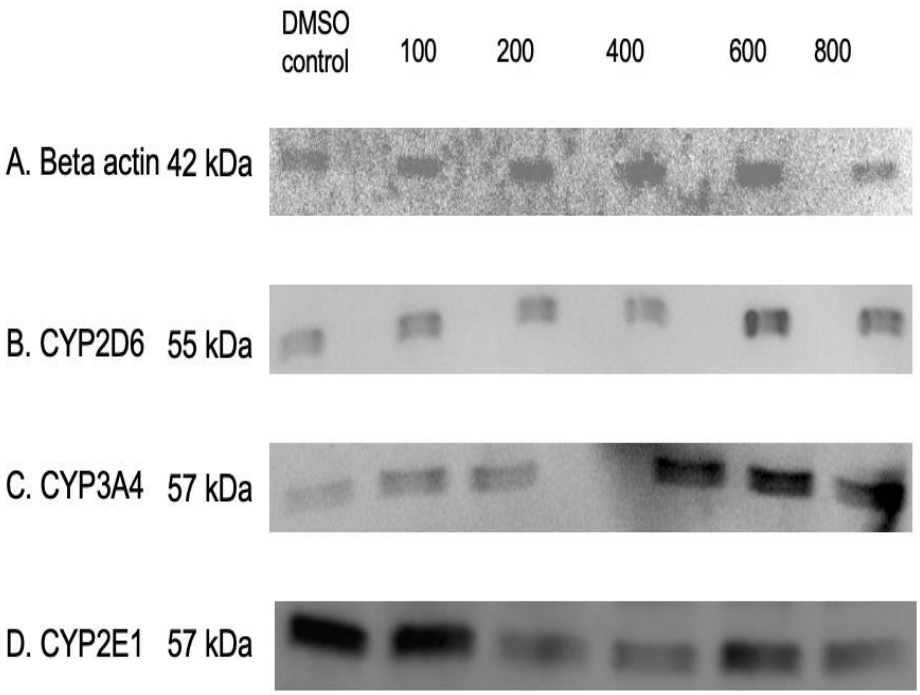

Figure 4.21 Western blot analysis of CYP enzyme expression in HepG2 spheroids dosed with tetracycline. A. Beta actin, B. CYP 2D6, C. CYP 3A4 and D. CYP2D6. Spheroids were dosed with tetracycline at varying concentrations of 100, 200, 400, 600 and 800 µM as described in Section 2.5.2. Proteins were collected as described in Section 2.16 and analysed by Western blotting as described in Section 2.20.

Table 4.6 Raw data showing arbitrary band intensities for CYP2D6, 3A4 and 2E1 in HepG2 spheroids dosed with tetracycline relative to the DMSO control. Spheroids were dosed with tetracycline at varying concentrations or 0, 100, 200, 400, 600 and 800 μM as described in Section 2.5.2. Proteins were collected as described in Section 2.16.

Tetracycline concentration (μM)	CYP2D6	CYP3A4	CYP2E1
DMSO control	4160.86	1563.13	16744.02
100	5817.05	3104.45	14621.86
200	4856.64	2676.33	6099.49
400	3899.91	7559.89	5308.83
600	11747.88	9282.66	11821.02
800	7766.76	6389.83	6456.85

4.4 Discussion

The first objective of this present study was to create *in vitro* models of tetracycline-induced steatosis in monolayer HepG2 cells and 3D spheroids. While the majority of steatosis and steatohepatitis cases result from dietary causes, it is estimated that around 2% of cases are related to drug-induced side effects (Rabinowich et al., 2015, Di Pasqua et al., 2022). This form is known as drug-induced hepatic steatosis (DIHS). Many drugs have been demonstrated to cause DIHS, including antiarrhythmic drugs, anti-epileptic drugs and antibiotics such valproate and tetracycline (Muller and Strula, 2019, Soret, et al., 2020, Di Pasqua et al., 2022). DIHS has been described as a chronic disorder associated with long term exposure to the offending drug (Di Pasqua et al., 2022). While there is no data on the exact incidence rates for drug-induced steatosis the annual incidences of drug-induced liver injury vary in population-based studies from 2.7 to 19.1 cases per 100,000 with approximately 27% of all cases presenting with some form of steatosis (Kolaric et al., 2021).

DIHS presents as either microvesicular or macrovesicular steatosis or as drug-induced steatohepatitis. Drugs such as methotrexate, tamoxifen and cisplatin which are associated with macrovesicular steatosis are more often associated with chronic and slowly progressive liver injury which is likely to progress to NASH (Pavlik et al., 2019). However, tetracycline is known to result in microvesicular steatosis; the form of steatosis linked with acute liver injury and/or dysfunction such as Reye's syndrome. Microvesicular steatosis is also related to the severe impairment of beta-oxidation and as fatty acids are poorly oxidised by the mitochondria this leads to the esterification of triglycerides the main lipid form that accumulates in steatosis (Satapathy et al., 2015, Kolaric et al., 2022).

To date there are no definitive guidelines for the management of patients with drug-induced fatty liver disease (DIFLD) (Patel and Sanyal, 2013). There are also no specific therapeutic drugs for treating the condition with the only option being the discontinuation of the offending drug (Patel and Sanyal, 2013, Blohm et al., 2017). In addition, the only way to reliably identify DIFLD is via imaging methodologies or liver biopsies, which, as previously discussed, can result in delayed detection. Consequently, there is a great unmet need for non-invasive biomarkers that can identify drug-induced steatosis and steatohepatitis in clinics as well as during drug

development (Pavlik et al., 2019). Therefore, this current study wished to create two *in vitro* drug-induced models of steatosis using tetracycline and identify drug-induced biomarkers of steatosis.

Tetracycline is a broad-spectrum antibiotic belonging to the tetracycline family, which also includes doxycycline, methacycline and minocycline. As mentioned above the tetracycline family has been shown to induce various types of hepatic injury including cholestasis, microvesicular steatosis and necrosis (Fromenty et al., 2020). Although the number of drugs associated with liver lipotoxicity is large and these include amiodarone, methotrexate, tamoxifen and CCl_4 the tetracycline model for steatosis research has advantages such as lower cost and mild toxicity, thus creating mild steatosis (Szalowska et al., 2014, Zhong et al., 2019). Since tetracyclines are widely used for the treatment of human and animal infections due to their activity against gram-positive and gram-negative bacteria a tetracycline-induced steatotic model is relevant to the clinical setting (Willebrords et al., 2015).

Tetracycline induced steatosis was first described over 50 years ago as one of the first drugs reported to induce microvesicular steatosis (Willebrords et al., 2015). In humans it has been reported that high doses of intravenous tetracycline (3 g tetracycline daily for 10 days) can induce fatty liver disease resulting in hepatic dysfunction; however, this is reversible once treatment is stopped (Robinson and Rywlin, 1970, Andrade and Tulkens, 2011, Glenn and Feldman, 2011, Abdel-Gelil and Mansour, 2019). Tetracycline is thought to induce microvesicular steatosis through the inhibition of genes involved in fatty acid oxidation such as PPARα, CPT1 and fatty acid binding protein 1, thus leading to impaired beta-oxidation (Freneaux et al., 1988, Fromenty et al., 1995, Szalowska et al., 2014, Fromenty et al., 2019). Studies have also suggested that tetracycline influences many genes associated with fatty acid transport and esterification including the fatty acid transporter CD36 and diacylglycerol acyltransferase 2 (DGAT2) in HepG2 cells and primary rat hepatocytes (Yin et al., 2006, Antherieu et al., 2011, Choi et al., 2015, Di Pasqua et al., 2022). Tetracycline has also been shown to activate transcription factor 4 (ATF4) and induce ROS production via the upregulation of CYP2E1 (Bruning et al., 2014, Di Pasqua et al., 2022).

In the literature tetracycline has been used extensively for the development of steatosis models, particularly in rodents (Breen et al., 1975, Freneaux et al., 1988, Chopra and Roberts, 2001, Antherieu et al., 2011, Donato et al., 2012, Chou et al., 2015, Rabinowich and Shibolet, 2015, Garcia-Canaveras et al., 2016). Dose levels up to 50 mg/kg in mice have been reported as inducing hepatic steatosis by inhibition of beta-oxidation (Breen et al., 1975, Freneaux et al., 1988, Chopra and Roberts, 2001, Choi et al., 2015).

Previous studies have also confirmed that tetracycline administration induces dose dependent lipid accumulation and steatosis in HepG2 cells (Donato et al., 2013, Choi et al., 2015, Garcia-Canaveras et al., 2016). This is also thought to be due to impairment of fatty acid oxidation and has been linked to increased extramitochondrial fatty acid oxidation, thus promoting higher rates of ROS production and lipid peroxidation (Donato et al., 2009, Choi et al, 2015, Garcia-Canaveras et al., 2016).

In their studies, Donato et al., (2009) and Garcia-Canaveras et al., (2016) confirmed the induction of steatosis in HepG2 cells using a triglyceride assay kit. They demonstrated that tetracycline causes concentration-dependent lipid accumulation from a dose level of 50 µM. Both studies also demonstrated via a MTT assay that a decrease in cell viability occurs at 800 µM and higher. Donato et al., (2012) reported significant increases in ROS production at dose levels of 400 and 800 µM following single dosing for 24 hours representing a more steatohepatitis model, which ideally would be avoided in this study. Nevertheless, studies have tested single doses of 100 µM tetracycline and reported mild steatosis after 24 hours (Donato et., 2009, Antherieu et al., 2011, Choi et al., 2015, Garcia-Canaveras et al., 2016). In summary, doses below 400 µM are considered to be well tolerated by HepG2 cells and induce benign lipid accumulation (Donato et al., 2012, Choi et al., 2015, Garcia-Canaveras et al., 2016). As cellular models are often much simpler than whole organisms it is necessary to dose them with high drug concentrations to observed the desired effects. It has been reported that the toxic concentration of tetracycline in humans in above 10 µg/ml (22µM) which is around 36 times lower than the toxic concentration in cells (800 µM) (Chopra and Roberts, 2001).

In this project since various dose levels have been reported to be effective in the literature a preliminary tetracycline dose response study (data not shown) was conducted to identify dose levels that could induce mild steatosis for a second larger metabonomic study. In this preliminary study dose levels of 50, 100, 200 and 400 μM were used. Oil Red O staining revealed no difference in lipid accumulation in tetracycline treated HepG2 cells (data not presented). The study did confirm that the NMR metabolomic techniques were able to detect metabolite changes and that cells remained viable. However, PCA and OPLS scores plots showed an overlap between the 50 μM treated group and the controls indicating very little difference at this dose level. This lack of separation between the 50 μM treated group and the control in the metabolomics data indicated that this dose level was perhaps too low to induce lipid accumulation and therefore, it was decided not to test dose levels below 100 μM in future studies. Some overlap between the 100, 200 and 400 μM treated groups was also observed reflecting the results seen in the Oil Red O staining. This preliminary metabolomics study showed overlap between all the dose levels results suggesting that higher dose levels may be needed to see a difference between control and treated. Consequently, in the second dose response study (results presented in this Chapter) tetracycline was administered at concentrations of 0, 100, 200, 400, 600 and 800 μM. 100 μM and 200 μM were included as the low dose groups and dose levels of 600 and 800 μM were included even though they are greater than the reported tolerable dose of 400 μM (Donato et al., 2012, Garcia-Canaveras et al., 2016).

Since the current study wished to develop models of mild steatosis it was important to ensure that the tetracycline dose levels used were not cytotoxic since this was not tested in the preliminary study. It was expected that doses of 100 and 200 μM would be generally well tolerated by the cells (Choi et al., 2015, Garcia-Canaveras et al., 2016). Donato et al., (2009) reported that 200 μM was the minimum effective concentration for cytotoxicity before significant effects on the cell membrane were induced and that 600 μM was the concentration at which there was significant ROS generation.

The MTS assay (Figure 4.1) revealed slight decreases in cell viability at 400 μM tetracycline from 100% to 96%, however this was not statistically significant. In the 800 μM treated group cell viability was 75% of control, although this was also not

statistically significant. Studies have demonstrated using MTT assays that tetracycline has an IC10 of around 800 μM and an IC50 of 1350 μM in HepG2 cells following a 24-hour incubation (Donato et al., 2009, Garcia-Canaveras et al., 2016). Therefore, some decrease in cell viability was expected in the current study at 800 μM. The LDH assay revealed no significant cytotoxicity for treated cells compared to the DMSO control at all dose levels (Figure 4.2). This confirmed that the doses used were well tolerated by HepG2 cells and could be used for future studies. As described in Chapter 3 the discrepancy between the results of the MTS and the LDH assay for the 800 μM dose is likely because cell proliferation assays such as the MTS cannot differentiate between cell proliferation and cell death (Smith et al., 2011).

Oil Red O staining of the HepG2 monolayers after 24-hour incubation in tetracycline demonstrated a clear dose-dependent accumulation of lipid up to 600 μM (Figure 4.3). However, the number of red clusters were reduced in the 800 μM treated group, this was potentially due to possible reduced cell viability as seen in the MTS assay, albeit with no significance. Despite the staining results, the triglyceride assay demonstrated no significant differences in triglyceride accumulation when the treated groups were compared to the control (Figure 4.4). Increased lipid accumulation was expected at the dose levels used based on results from other published work. However, as discussed in Chapter 3 Oil Red O is a fat-soluble dye used to stain neutral lipids, cholesteryl esters and lipoproteins, therefore it is taken up by all lipids. Meanwhile the assay only measures free glycerol released from the hydrolysis of extracted triglycerides within the samples. For this reason, as discussed in Chapter 3 there are limitations with both staining techniques and assay kits meaning a combination of both gives a more accurate picture of lipid accumulation. Therefore, the discrepancy seen between the Oil Red O staining and the triglyceride assay could be due to the fact the Oil Red O staining allows for the visualisation of all lipids in the samples, not just triglycerides.

To move forward, the results of the Oil Red O stain were considered as validation of the model but since there was not a great increase in lipid accumulation it was concluded that the model developed was of mild steatosis. The results of the monolayer study were then used to determine appropriate dose levels for the spheroid study. The 600 μM dose level was chosen as a high dose due to the reduced cell

viability seen in the 800 µM treatment groups and it was decided to avoid this as the increased cell-to-cell contact in spheroids is thought to make them more sensitive. As 100 µM tetracycline displayed some increase in lipid accumulation in the monolayer Oil Red O staining it was chosen as the low dose for spheroids.

In this study an MTS assay was conducted on the spheroid samples however, the absorbance values were outside the linear range of the assay potentially due to the higher cell number in the spheroids as cells continued to proliferate for 17 days. The optimum seeding density for the assay as stated in the protocol was between 5000-10000 cells but HepG2 cells have a doubling time of around 48 hours. A study by Chang and Hughes-Fulford (2009) reported that the rate of cell proliferation in 2D and 3D cultures was not significantly different and reported higher cell numbers in spheroids at early time points. However, the rate of cell proliferation decreased over time with cell numbers becoming lower and equivalent to those in monolayers by 72 hours and 6 days, respectively. Over time cell proliferation decreases in HepG2 spheroids since they consist of three main zones: an outer proliferating rim, a quiescent viable zone, and an inner necrotic core (Stampar et al., 2020). Cell proliferation is also determined by seeding density with lower initial seeding densities having higher proliferation rates (Chang and Hughes-Fulford, 2009, Stampar et al., 2022). Stampar et al., (2022) reported spheroid proliferation rates of 82% after 3 days, which decreased to approximately 68%, 54%, and 13% after 5, 7, and 18 days. At a higher initial seeding density cell proliferation decreased to 65.5% after 24 hours (Stampar et al., 2022). The current study tested various initial seeding densities from 5000 cells per well to 40,000. However, following 17 days of growth, regardless of the initial cell number, the spheroid cultures continued to grow and therefore exceeded the optimum cell number for the MTS assay. Consequently, it was decided to use the LDH assay for confirming cell cytotoxicity since it is not limited by cell density and is more reliable for measuring cell death. The LDH assay showed zero cytotoxicity at both dose levels in the spheroid samples when compared to the DMSO control (Figure 4.13). Cell viability was also visualised in spheroids using a LIVE/DEAD assay and the images taken from this assay also revealed no cytotoxicity (Figure 4.12). These results confirm the spheroid models are stable enough to be treated with tetracycline at the dose levels used. Following a 24-hour incubation of spheroids in tetracycline with both dose levels demonstrated a slightly higher accumulation of triglycerides

(approximately 15% in both) when compared to the DMSO control, although these were not significantly different (Figure 4.14). Despite this lack of statistical significance this could suggest very mild steatosis.

Although rodent models of tetracycline induced steatosis are well established there is a lack of *in vitro* models and more specifically for drug-induced steatosis or steatosis in HepG2 spheroids. Tetracycline-induced steatosis has been investigated in HepG2 monolayers and has been previously administered to 3D primary hepatocytes and HepaRG spheroid models to investigate cholestasis and identify the underlying mechanism of drug-induced liver injury (Hendriks et al., 2016). It has also been used in co-culture models with primary hepatocytes, functionally active Kupffer cells (KCs), stellate cells (SCs), and liver sinusoidal endothelial cells to assess drug-induced liver diseases including steatosis (Li et al., 2020A, Nudischer et al., 2020). Despite the wide-spread use in research there are yet no studies describing its effects in HepG2 spheroids. Therefore, this current study offers a novel model for the discovery of early biomarkers of tetracycline-induced steatosis which could aid diagnosis before progression to NASH. In this study the spheroid and monolayer experiments demonstrated mild tetracycline-induced steatosis and lack of cytotoxicity, thus making these models suitable for biomarker studies.

The subsequent experiments described in this Chapter were designed to analyse changes in the metabolome of cellular extracts from both the monolayer and spheroids as means of detecting potential biomarkers. The PCA scores plots created for both the aqueous and organic monolayers (Figures 4.5 and 4.8) did not show clear separation between the sample groups. However, there was better group PCA separation for the spheroids (Figures 4.15 and 4.18) which could suggest tetracycline was having a greater dose-related response in spheroids. OPLS scores plots for spheroids further improved the group separation along the t[1] axis. However, while the OPLS scores plots for the monolayers (Figures 4.6 and 4.9) showed better group separation than the PCA scores plot there was still some overlap. This would suggest a lack of dose-related response in the monolayers.

Also, in the monolayer analysis large intragroup variation was observed for the control, 100 and 200 µM treated groups along the orthogonal t[0] axis in both the organic and

aqueous extracts. However, intragroup variation was observed in all models across this project which was expected as cell cultures are affected by biological factors (Badrick, 2021, Frank, 2021, Reddin et al., 2023). For example, every time cells divide there is a risk that factors such as random mutations or transcription errors occur, although this is rare (Frank, 2021). In addition, small sample sizes were used in these experiments which even with strict parameters regarding cell numbers for assays, absence of contamination and sourcing of reagents data variability is still likely to occur if there is slightly unequal cell count in each well (Badrick, 2021, Reddin et al., 2023). This may occur since seeding is conducted manually. The use of small sample sizes is common for metabolomics studies, due to the scale of the experiments, despite some studies recommending the use of 100 samples (Gorsuch, 1983, Hatcher, 1994, Shaukat et al., 2016). However, this number would not be feasible in terms of culture time, facilities and collecting samples.

In the current study, regardless of the lack of dose response in the monolayers, and the large intragroup variation, group separation was observed along the predictive t[1] axis in the OPLS-DA models. Therefore, metabolite peaks contributing to these separations were identified. Both the monolayer and spheroids displayed changes in the same metabolites following incubation with tetracycline (Tables 4.1, 4.2, 4.4 and 4.5) including increases in cholesterol and fatty acyl groups, again suggesting possible steatosis. Decreases were also observed for TCA cycle metabolites such as citrate at dose levels above 400 μM. Decreases in choline, phosphocholine and betaine were also observed in both models. Changes in these metabolites are implicated in the progression of steatosis indicating lipid accumulation in the monolayers. This supports the Oil Red O assessment of lipid accumulation and casts further doubt on the triglyceride assay results.

As observed in the fatty acid study described in Chapter 3 metabolite changes related to the methyltransferase reactions were noted in both models (Tables 4.1 and 4.4). These included dose dependent decreases in choline and phosphocholine in the spheroid samples. Choline is an important precursor of phosphatidylcholine (PC) in the phosphatidylethanolamine N-methyltransferase (PEMT) pathway (Piras et al., 2022). PC is an essential component in the synthesis of VLDLs and is therefore vital for the secretion of triglycerides from the liver. The process begins with the hydrolysis

of PC to produce phosphocholine and diacylglycerol with diacylglycerol undergoing acylation to produce triglycerides utilising choline. Therefore, depletion of both in the presence of increased fatty acids could explain the decreases in choline and phosphocholine seen in this study (Van der Veen et al., 2012, Payne et al., 2014, Sherriff et al., 2016). Studies in animals have confirmed that choline deficiency in animals significantly impairs the production and secretion of VLDLs from the liver by inhibiting the synthesis of phosphatidylcholine (Vance et al., 2008, Rinella et al., 2008, Lee et al., 2019, Alves-Bezerra and Cohen, 2017, Piras et al., 2022). In the absence of phosphatidylcholine fat droplets accumulate in the liver (Jha et al., 2014, Chiba et al., 2016, Piras et al., 2022). However, to date there are no studies looking at choline in drug-induced steatosis, making it difficult to determine why choline is decreased in this study.

The PEMT pathway plays a very important role in the development of steatosis. Studies have demonstrated that *PEMT*$^{-/-}$ knockout mice fed a diet high in fat and sucrose rapidly develop hepatic steatosis, inflammation, and fibrosis (Zhu et al., 2003, Waite et al., 2002, Piras et al., 2022). In humans inhibition of the PEMT pathway impairs phosphatidylcholine synthesis and is associated with increased risk of NAFLD (Song et al 2005, Bale et al., 2019, Piras et al., 2022). Under normal conditions, the PEMT pathway produces 30% of the total PC in the liver while the remainder is synthesized via the Kennedy (CDP-choline) pathway in the presence of choline (Gibellini and Smith, 2010). However, when dietary choline supply is limited the PEMT pathway becomes critical since it is the sole source of endogenous choline for maintaining sufficient supply of PC in the liver (Payne et al., 2014, Sherriff et al., 2016). In the *in vitro* experimental situation choline is provided in cell culture media therefore, there should be sufficient supply for the cells. However, choline uptake may be decreased in the cells due to tetracycline treatment. Although the literature has not commented on this in drug-induced models a study by O'Dwyer et al (2020) reported that HepG2 cells treated with a mixture of fatty acids display a decrease in choline uptake along with a decrease in total protein content of the choline transporter-like protein 1 (CTL1), the reduction of other choline transporters and other CDP-choline pathway enzymes. Therefore, it is possible tetracycline is having an effect on choline transporters, thus reducing choline uptake by the cells. Although, decreases in choline have not been previously reported in tetracycline induced *in vitro* models.

Reduced PEMT expression may also contribute to the progression of NAFLD to NASH, particularly in individuals who are not meeting their daily dietary choline needs as a result of the increased accumulation of fatty acids in the liver (Piras et al., 2022). Since choline plays a major role in mitochondrial membrane integrity, decreased choline levels can lead to impaired mitochondrial bioenergetics and altered beta-oxidation. This has been observed in rats fed a methionine-choline deficient diet (Teodoro et al., 2008, Serviddio et al., 2011, Corbin and Zeisel, 2012, Li et al., 2017, Lee et al., 2019) which is one of the most common models used to study NASH (Corbin and Zeisel, 2013, Jha et al., 2014, Sherriff et al., 2015, Imbard et al., 2015). Methionine plays a crucial role in the synthesis of SAM and glutathione, two important antioxidants (Lu, 2000, Rinella et at., 2008, Lee et al., 2019).

Despite the relatively mild steatosis caused by tetracycline in the current models, significant decreases ($p<0.05$) in methionine in the 400 and 600 μM treated groups in the monolayer (Table 4.1) and in the 600 μM spheroid group were recorded (Table 4.4). Therefore, both methionine and choline were decreased in this study and the effects of this could be reflective of a methionine-choline deficiency.

There were also decreases in peaks thought to be s-adenosylhomocysteine (SAH). SAH is produced from the demethylation of SAM converting methionine to SAH and homocysteine (Zhang et al., 2016, Werge 2021). It has been reported that some drugs such as methotrexate can affect methylene tetrahydrofolate reductase, the enzyme which catalyses the generation of methionine to homocysteine thus decreasing methionine levels (Desouza et al., 2002, Pandit et al., 2017). This results in a decrease in methionine and SAH and subsequently an increase in homocysteine is observed due to decreased utilisation in the cycle (Pacana et al., 2015, Pandit et al., 2017). An increase in homocysteine was not observed in this study; but this could be because it shares spectral regions with several other metabolites including glutamine, glutathione and cystathionine. To confirm the absence or presence of homocysteine in this study future work could spike samples with a homocysteine standard.

In this present study metabolites associated with the TCA cycle and glycolysis including lactate, alanine, citrate and succinate were altered (Tables 4.1 and 4.4). Peaks for these metabolites were elevated in the 100 and 200 μM treated groups in

the monolayer samples when compared to control but were lower at doses of 400 µM and above. In the spheroid model a decrease in peaks thought to be succinate and lactate was observed at both dose levels which was significant ($p<0.001$ and $p<0.05$ respectively) at the high dose. Alanine appeared to be increased at both dose levels but was only significant ($p<0.001$) in the 600 µM treated group. Alanine levels are closely related to glucose utilisation and the changes observed in this study suggest that glycolysis and glycogenolysis are upregulated. As tetracycline is a known inhibitor of beta-oxidation an increase in the levels of these metabolites observed in the monolayers at low dose levels and spheroids could indicate an increase in glycolytic activity within the cells. Studies conducted in mice have suggested that the administration of drugs including methapyrilene, acetaminophen and CCl_4 can lead to an increase in glycolysis and glycogenolysis due to mitochondrial dysfunction and disrupted beta-oxidation (Craig et al., 2003, Zira et al., 2013, Dargue et al., 2020). Additionally, a study by Chen et al., (2018A) reported that emodin, a naturally occurring anthraquinone derivative, increased glycolytic activity and reduced gluconeogenesis in HepG2 cells. This also backs up the hypothesis that cells switch to glycolysis in times of oxidative stress as a protective process to compensate for the loss of ATP coming from beta-oxidation (Chan et al., 2018, Dargue et al., 2020). However, an increase in glycolysis has not been specifically reported in HepG2 cells treated with tetracycline.

In this current study although the metabolomics analyses indicate an increase in glycolytic activity in the cells at the lower dose levels, lactate, alanine and other TCA cycle metabolites are lower than control at doses of 400 µM and above. Although these specific metabolite changes have not been mentioned in previous studies the decreases observed could be related to increased oxidative stress since this has been reported at dose levels above 400 µM (Donato et al., 2009, Donato et al., 2012). Although not significant the slight decreases in cell viability seen in the MTS assay at 400 and 800 µM monolayer samples could back up this proposed hypothesis.

Drugs that induce steatosis and steatohepatitis primarily interfere with mitochondrial respiration, beta-oxidation or both. As the two pathways are metabolically interlinked, drugs affecting one pathway invariably affect the other. Thus, when hepatic mitochondrial β-oxidation is severely inhibited, fatty acyl-CoA β-oxidation is impaired

leading to increases in fatty acyl-CoA and non-esterified fatty acids, which are converted into triglycerides (Satapathy et al., 2015, Kolaric et al., 2022).

This effect was observed in the current study in organic cell extracts whereby increases in peak regions corresponding to acyl groups of triglycerides were evident in both models (Tables 4.2 and 4.5). A study by Donato et al., (2009) reported that treatment of HepG2 cells with tetracycline does induce mitochondrial membrane depolarisation. Such mitochondrial dysfunction can lead to an impairment of the respiratory chain with decreased ATP levels and increased oxidative stress. This in turn could potentially lead to a decrease in metabolites associated with aerobic respiration and may explain why metabolites such as succinate, lactate and citrate were decreased at higher dose levels. All of this points to some degree of mitochondrial dysfunction and oxidative stress at these dose levels.

It has also been suggested that tetracycline plays a role in the progression of steatosis by enhancing oxidative stress through activating the transcription factor 4 (ATF4) and inducing ROS generation via CYP2E1 upregulation (Di Pasqua et al., 2022). The Western blots in this study do suggest an increase in CYP2E1 expression with increasing dose level in the monolayers but a decrease was observed in the spheroids (Tables 4.3 and 4.6).

A further indicator of oxidative stress in this study was the decreased levels of GSH and GSSG in both models at doses above 400 µM. Whereas, the 100 and 200 µM groups in the monolayer appeared to have increased levels of these metabolites. In animal studies glutathione levels initially increase as steatosis is developing before a progressive decrease and depletion is observed as the disease worsens (Yang et al., 2000, Grattagliano et al., 2008, Vairetti et al., 2021). The initial increase in glutathione in rats is likely an antioxidant response for the prevention of lipid and protein oxidation. It has also been shown that gene expression associated with glutathione is enhanced at early stages (Lee et al., 2008, Vairetti et al., 2021). In addition, a disruption in redox homeostasis is a common effect in many drug-induced models of steatosis. The ratio of glutathione to reduced glutathione (GSH/GSSG) is the principal redox buffer within cells and changes to this ratio are associated with early oxidative damage (Yuan et al., 2009, Carretero et al., 2014, Garcia-Canaveras et al., 2016). Garcia-Canaveras et

al., (2016) observed a dose-dependent decrease in GSH/GSSG ratio in HepG2 cells dosed with hepatotoxic drugs including tetracycline. Decreases in these metabolites may have occurred in both models however, these metabolites share spectral regions with several others and therefore definitive identification was not possible. Future work could include spiking samples with metabolite standard to confirm their presence and determine a possible decrease in ATP levels using a commercial assay kit.

In this study many NMR regions from the aqueous extracts thought to be important for sample group separation remain unidentified. Future work could implement the use of mass spectroscopy to help with identification. Nevertheless, the aqueous metabolite changes that have been identified indicate changes between controls and treated groups potentially due to steatotic changes in the cells.

Organic metabolites from both the monolayer and the spheroid models dosed with tetracycline were also examined in this study (Tables 4.2 and 4.4). Similar metabolite changes to those seen in the fatty acid-induced model (Chapter 3) were observed. These included changes in cholesterol, fatty acyl groups and arachidonic acid.

A decrease in peaks at 1.5625-1.605 ppm due to arachidonic acid (ARA) a polyunsaturated fatty acid was observed in the 100 and 200 μM treated group in the monolayer and in both spheroid groups. Wang et al., (2011) also reported a decrease in polyunsaturated fatty acids (PUFA) including arachidonic acid in mice fed both a high fat diet and CCl_4. They also suggested that the decrease in PUFA could be a compensatory response to progressing NAFLD. Fatty acids are precursors for eicosanoids which are oxidised derivatives of PUFAs formed by the cyclooxygenase (COX), lipoxygenase (LOX) and cytochrome P450 pathways. They play a role in the amelioration of hepatotoxicity by decreasing inflammation but can also have pro-inflammatory effects (Nebert et al., 2008, Wang et al., 2011, Calder, 2020, Shoieb et al., 2020). Arachidonic acid is released from membrane phospholipids by phospholipase A2 and from phosphatidylinositol bisphosphate by phospholipase C. It is then converted to prostaglandins by cyclooxygenase which may act as an integral mediator in inflammatory reactions and in the pathogenesis of several conditions such as cardiovascular and liver diseases (Di Marzo, 1995, Das et al., 2006, Wang et al.,

2011, Shoieb et al., 2020). It is possible that increased utilisation of arachidonic acid contributes to the decrease in levels seen in NAFLD (Wang et al., 2011).

Similar to the fatty acid-induced model (Chapter 3) increases in cholesterol were observed in all treated groups in this study (Table 4.2 and 4.5), as would be expected in a steatotic model. In a previous study the administration of tetracycline to rats for 7 days significantly increased triglycerides and LDL-cholesterol by 186.1 % and 81.3%, respectively when compared to the control group (Santhosh et al., 2006, Shabana et al., 2012). Increases in cholesterol have been reported for other steatosis inducing drugs including tamoxifen and amiodarone as a result of decreased VLDL secretion (Antherieu et al., 2011, Rabinowich and Shibolet, 2015). Increases in cholesterol have also been observed in animal models treated with amiodarone and tetracycline (Choi et al., 2015, Rabinowich and Shibolet, 2015, Di Pasqua et al., 2022). Antherieu et al., (2011) also demonstrated increases in lanosterol synthase, an intermediate in cholesterol biosynthesis, in HepaRG cells treated with tetracycline for 14 days representing an indirect mechanism of phospholipidosis. Several metabolite regions were also observed as significant in the metabolomic analysis of organic extracts; however, metabolite identification was not possible.

In this Chapter CYP2D6, CYP2E1 and CYP3A4 expression levels were also analysed in protein extracts obtained from monolayer and spheroids dosed with tetracycline. The purpose was to observe the effects of tetracycline on CYP expression levels with increasing dose and to compare expression in spheroids to monolayers. Many previous studies have observed lower CYP expression in HepG2 monolayers compared to spheroids (Mizoi et al., 2020, Stampar et al., 2020 and Ingelman-Sundberg and Lauschke, 2021). However, the results from this study suggest that CYP enzyme expression was similar in monolayers and spheroids possibly negating the argument that monolayers are less relevant to the *in vivo* state.

Alterations in CYP expression have been well documented during NAFLD *in vivo* and *in vitro* with studies generally reporting increased CYP2E1 along with decreases in CYP3A4 and CYP2D6 (Sukkasem et al., 2020). Few published studies have documented the effects of tetracycline on CYP expression. Despite N equalling 1 in the present study expression was generally higher in the treated compared to the

DMSO control in both the spheroids and the monolayer samples. However, such changes have not been reported in the literature.

Members of the P450 enzyme family participate in the generation of oxidative changes in drug-induced fatty liver via increased production of the free oxygen radical H_2O_2. In the context of hepatic steatosis, CYP2E1 and CYP3A4 are involved in the metabolism of long chain fatty acids (Satapathy et al., 2015). As discussed in Chapter 3 CYP2E1 is a source of nitro-oxidative stress and is responsible for oxidising a variety of small molecules including fatty acids and thereby initiate lipid peroxidation. In this study a dose dependent increase in CYP2E1 was observed in the monolayer cells while, decreases were observed in the spheroid samples. Therefore, it is unclear what effect tetracycline is having on CYP2E1 expression and further work is needed to validate this.

In this study CYP3A4 expression was decreased in the 100 and 200 μM monolayer samples when compared to control but then increased in the higher doses which could mean higher doses of tetracycline increase CYP3A4 expression. CYP3A4 is controlled by the transcription factor PPARα which governs gene expression and is involved in intracellular fatty acid disposal (Kersten et al., 1999). Alterations of PPARα play an important role in the development of steatohepatitis and in a decrease of CYP3A4 expression. Tetracycline is known to inhibit beta-oxidation by downregulating genes involved in the pathway including PPARα (Satapathy et al., 2015, AlGhamdi, 2019, Di Pasqua et al., 2022), thus potentially decreasing CYP3A4 expression. Yasuda et al., (2015) demonstrated that tetracyclines at concentrations of 10 and 50 μM induce significant increases in CYP3A4 mRNA which could increase expression. General increases in CYP3A4 were also observed in the spheroid models. The Western blot results in this study are not entirely consistent with the literature. Also, no repeat blots were completed due to time constraints of the project. Therefore, further work is needed to fully understand the effect of tetracycline on CYP expression in both monolayers and spheroids.

Chapter Five- Valproate induced steatosis in HepG2 cells

Chapter 5

5.1 Introduction

In the previous Chapter (Chapter 4) tetracycline was administered to monolayer HepG2 cells and 3D spheroids to create *in vitro* models of drug-induced steatosis. The data presented in Chapter 4 agreed with published work that tetracycline caused some steatosis. However, there are many drugs reported to induce steatosis via different mechanisms. Thus, evaluating multiple drug-induced models for the identification of biomarkers of steatosis would provide greater specificity and sensitivity for the detection of early stages of NAFLD.

In this current Chapter two models of hepatic steatosis (monolayers and 3D spheroids) in HepG2 cells were developed using valproate. Valproate (VPA) is a broad-spectrum anti-epileptic drug which has been widely prescribed to humans for the treatment of convulsions, migraines and bipolar disorders (Chateauvieux et al., 2010, Bai et al., 2017, Rahman and Nguyen, 2021). It has been a first-line therapy in the treatment of epilepsy for more than 30 years. However, valproate is linked to various adverse drug reactions, including hepatotoxicity, obesity and bone marrow suppression (Tsiropoulos et al., 2009, Bai et al., 2017, Xu et al., 2019A). Consequently, there has been widespread global concern surrounding the regular exposure to the drug (Zhang et al., 2014).

Valproate is known to induce mild steatosis (Szalowska et al., 2014) but has a delayed onset in humans ranging from weeks to months and in some cases years following the initial exposure, and is also dose dependent (Mnif et al., 2016, Pirozzi et al., 2019). Studies that report valproate-induced steatosis following prolonged exposure times claim that this makes it harder to predict in patients (Luef et al., 2009, Farinelli et al., 2015, Mnif et al., 2016, Pirozzi et al., 2019). However, the liver injury is frequently resolved with dose reduction or drug discontinuation. Approximately 61% of patients treated with valproate have been diagnosed with hepatic steatosis mostly by ultrasound examination and nearly 25% of patients show progression which increases the risk of NASH and cirrhosis (Luef et al., 2009, Zhang et al., 2014, Farinelli et al.,

2015). Increased lipid accumulation in liver was reported by Luef et al., (2009) in a population who had been taking valproate for at least 2 years, and by Xu et al., (2019) in patients who had been taking valproate for at least 2 months. In rodent models it has also been reported that after dosing with 100, 150, 250 and 500 mg/kg per day valproate caused significant lipid accumulation (Zhang et al., 2014, Jutric et al., 2022).

The mechanisms behind valproate-induced hepatotoxicity have been studied for many years but are not yet fully understood (Zhang et al., 2014, Komulainen et al., 2015, Bai et al., 2017, Gai et al., 2020, Yan et al., 2021). However, it is known that all types of valproate related hepatotoxicity feature mitochondrial injury, oxidative stress, and microvesicular steatosis with varying degrees of inflammation and cholestasis (Gai et al., 2020). Microvesicular hepatosteatosis is typical and it has been suggested that impairment of fatty acid beta-oxidation plays a central role in the accumulation of triglycerides and the development of lactic acidosis (Pirozzi et al., 2019, Yan et al., 2021). However, it is not clear whether mitochondrial injury and oxidative stress are secondary to the lipid accumulation or are primary events in the onset of the liver injury. In addition, upregulation of the proliferator-activated receptor gamma (PPARγ) and cluster of differentiation 36 (CD36) dependent lipid uptake in response to valproate in primary hepatocytes have also been demonstrated (Komulainen et al., 2015, Bai et al., 2017, Yan et al., 2021).

Valproic acid is metabolized by both phase-I and phase-II enzyme systems as well as fatty acid β-oxidation. Cytochrome P450 enzymes including CYP2A6, CYP2B6, CYP2C9, and CYP3A5 are involved as well as UDP-glucuronyltransferase enzymes (Bennett and Shad, 2021). The main metabolite formed, valproyl-CoA, can inhibit hepatic carnitine palmitoyl-transferase (CPT) 1A, a pivotal enzyme in mitochondrial fatty acid beta-oxidation *in vivo* and *in vitro* (Mnif et al., 2016, Pirozzi et al., 2019). Valproyl-CoA can also cause depletion of intra mitochondrial CoA affecting fatty acid β-oxidation and lead to reduced ATP production (Mnif et al., 2016). Although both valproate and tetracycline affect fatty acid beta-oxidation the mechanisms through which they cause lipid accumulation are slightly different. While tetracycline downregulates genes involved in beta-oxidation, valproate has an effect on enzymes associated with beta-oxidation and upregulates proteins associated with lipid accumulation. Therefore, the evaluation of valproate alongside the tetracycline model

in Chapter 4 enables comparison of differing mechanisms of drug-induced steatosis (DIHS) and their impact on metabolites.

Single doses between 0.5-5 mM of valproate have been previously used for development of *in vitro* models of steatosis using HepG2 cells and FL83B cells (Chang et al., 2016, Bai et al., 2017, Yan et al., 2021). Yan et al., (2021) demonstrated using Oil Red O staining and a triglyceride assay kit increased lipid accumulation in HepG2 cells following a single dose of valproate at 2 mM after a 24-hour incubation period. They also reported a significant increase in lipid accumulation in cells dosed at 1 and 2 mM after 48 hours, this was greater than in the 24 hours however, cell viability decreased. In another study, Bai et al., (2017) confirmed that incubating HepG2 cells in 1, 2.5 and 5-mM valproate for 24 hours resulted in a concentration-dependent increase in intracellular lipids, and this was further enhanced when the incubation time was extended to 48 hours. Other studies in HepG2 cells have reported 2 mM as the highest dose level before mitochondrial activity is affected by the drug (Komulainen et al., 2015, Pirozzi et al., 2019, Yan et al., 2021). Thus, the literature shows quite a wide range of dosing concentrations following a single dose but does confirm that valproate is useful for *in vitro* studies of steatosis.

In this Chapter the objective was to create two valproate-induced steatosis models: in HepG2 monolayer and 3D spheroids. An initial dose response study ranging from 0.5-4 mM in the monolayer cells was conducted to test efficacy in creating mild steatosis and cytotoxicity.

In the literature *in vivo* and *in vitro* studies have used omics techniques to assess mechanisms of valproate induced steatosis and to measure various lipid biomarkers (Tong et al., 2005, Cuykx et al., 2018A, Xu et al., 2019A, Shnayder et al., 2023). Cuykx et al., (2018A) used liquid chromatography and accurate mass-mass spectrometry (LC-AM/MS) metabolomics to profile steatosis progression through toxicological fingerprinting in HepaRG cells. Xu et al., (2019) conducted lipidomic profiling in children treated with valproate for at least two months and found increased hepatic triglyceride accumulation and disrupted hepatic gene expressions involved in lipid metabolism and the Akt-PPARγ pathway. Tong et al., (2005) investigated lipid peroxidation biomarkers in rats and found decreases in beta-oxidation metabolites as

well as increases in lipid peroxidation markers indicating that valproate treatment can induce oxidative stress. However, there are no studies focussing specifically on biomarkers of mild steatosis and no NMR metabolomics studies of HepG2 monolayer or spheroid cells dosed with valproate. Therefore, the current study will identify changes in the metabolome of both models using NMR spectroscopy and multivariate statistical analysis in search of potential biomarkers of steatosis. CYP enzyme expression will also be assessed in both monolayers and spheroids as it has been suggested CYP expression is higher in spheroids.

5.2 Valproate study design

Monolayer HepG2 cells were plated in 6-well plates. A dose response study was carried out by administrating tetracycline at dose levels of 0.5, 1, 2 and 4 mM to HepG2 cells followed by a 24-hour incubation. Six replicates were used for each dose level.

For the 3D spheroid model, the HepG2 cells were plated in low attachment 6-well plates and grown for 17 days before being dosed with fatty acids at concentrations of 0, 1 and 4 mM.

5.3 Results

5.3.1 Cell viability and cytotoxicity in monolayers

In this study cytotoxicity was assessed using MTS and LDH assays.

The MTS assay results (Figure 5.1) revealed a slight decrease in cell viability with increasing dose of valproate when compared to the DMSO control. The 4 mM dose demonstrated the lowest viability (88%) when compared to control. However, there was no statistically significant change at any dose level when compared to the DMSO control.

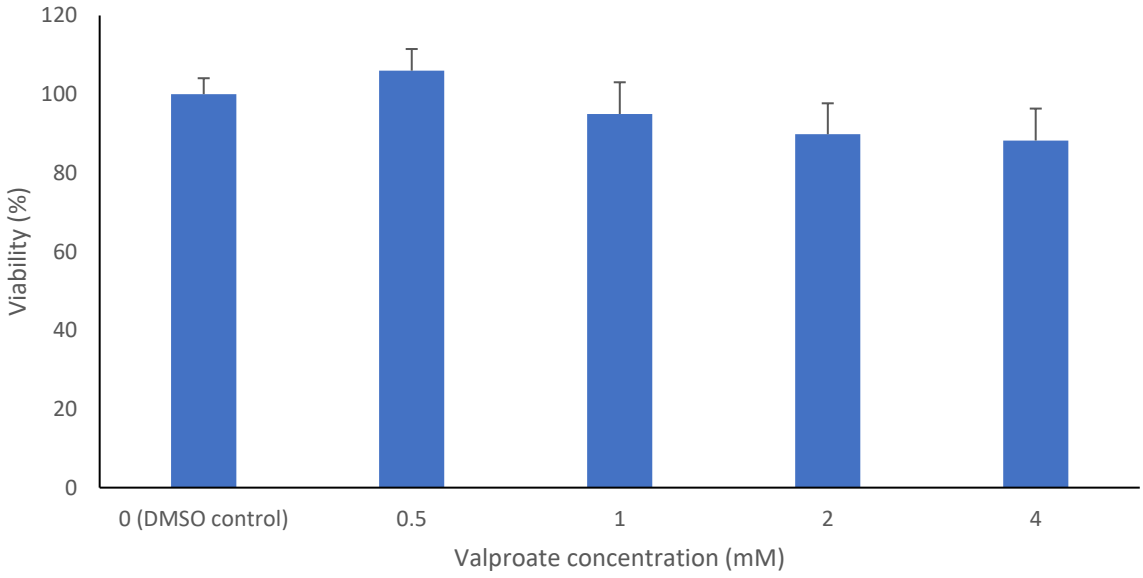

Figure 5.1 HepG2 cell viability in response to increasing valproate concentration as assessed by MTS assay. HepG2 cells were treated with valproate at concentrations of 0 (DMSO control), 0.5, 1, 2 and 4 mM and incubated for 24 hours as described in Section 2.5.3. The MTS assay was carried out as described in Section 2.6. The values shown represent the mean of six replicates. Error bars represent standard deviation.

In the same study the LDH assay (Figure 5.2) suggested no significant cell death at any of the dose levels used (0.5, 1, 2 and 4 mM) when compared to the DMSO control or to the positive control.

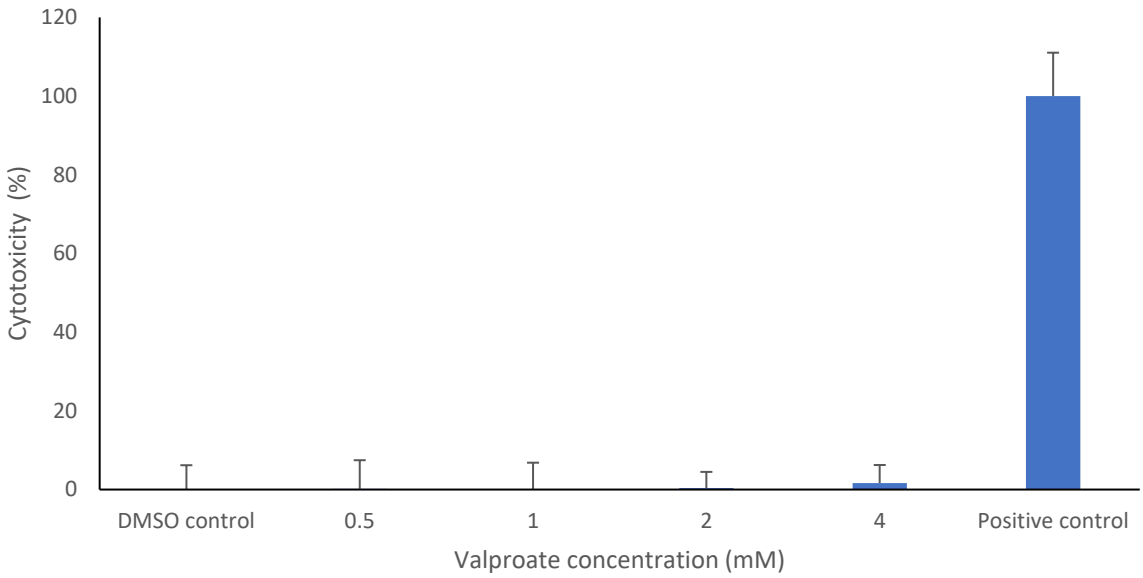

Figure 5.2 HepG2 cell death in response to increasing valproate concentration assessed by LDH assay. HepG2 cells were treated with valproate at concentrations of 0 (DMSO control), 0.5, 1, 2 and 4 mM and incubated for 24 hours as described in Section 2.5.3. The value obtained for the positive control represents 100% cell death. The LDH assay was carried out as described in Section 2.21. The values shown represent the mean of six replicates. Error bars represent standard deviation.

5.3.2 Oil Red O staining

To confirm a dose-related increase in intracellular lipid accumulation, the cells were stained with Oil Red O. The images obtained under the light microscope as shown in Figure 5.3 suggest a dose dependent increase in lipid accumulation in the treated groups (Figures 5.3 C-F) compared to DMSO control (Figure 5.3B). An increase in the number, size and intensity of the red clusters indicated a greater stain uptake by these cells is shown by the arrows.

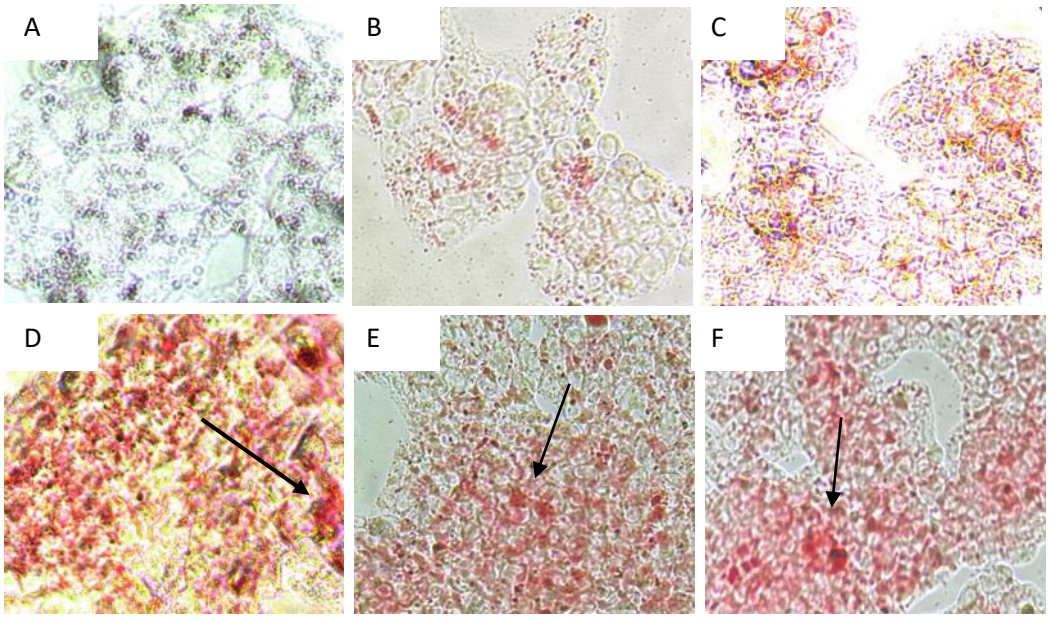

Figure 5.3 Light microscopy images obtained of HepG2 cells treated with valproate and stained with Oil Red O. Cells were dosed with valproate at final concentrations of 0 (DMSO controls), 0.5, 1, 2 and 4 mM followed by a 24-hour incubation as described in Section 5.2.3, cells incubated in media only were also stained and visualised to act as negative controls. Cells were stained using Oil Red O as described in Section 2.7. A. Media only control, B. DMSO control, C. 0.5 mM, D. 1 mM, E. 2 mM and F. 4 mM.

5.3.3 Triglyceride assay in the monolayer

To quantify the triglyceride accumulation HepG2 cells treated with valproate were lysed and cell lysate samples were collected for triglyceride quantification using a commercial assay. Although a clear dose dependent response was not observed (Figure 5.4) the triglyceride content in the treated cells did appear to be greater than in the DMSO control at all dose levels. However, no statistical significance was observed at any dose level. Despite this there was around a 25% increase in lipid accumulation at 1 and 2 mM when compared to the DMSO control, but this is not as obvious as the results from the Oil Red O staining.

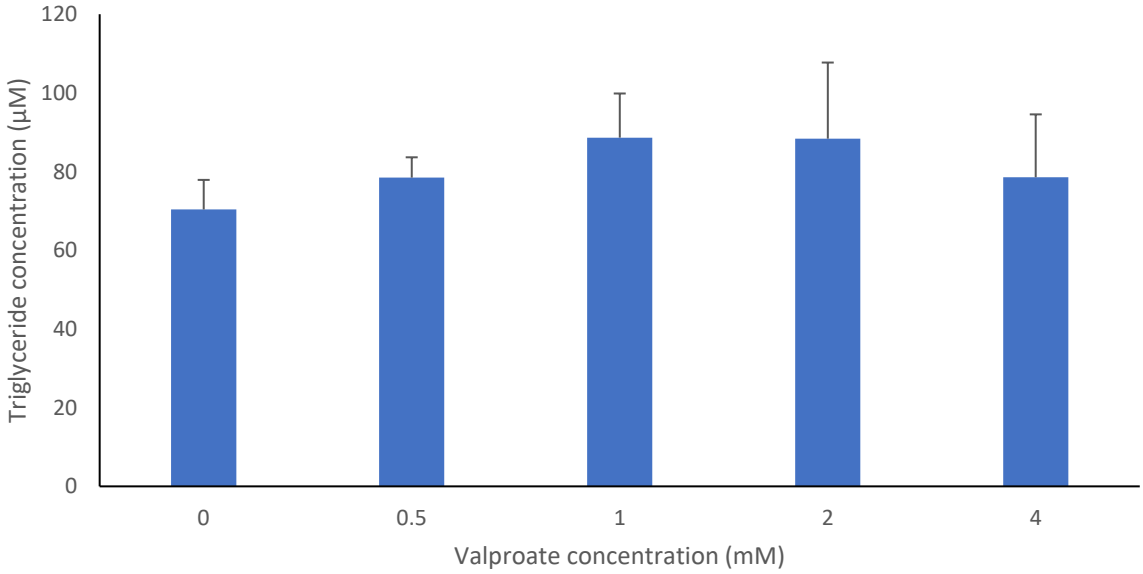

Figure 5.4 Mean triglyceride content in HepG2 cells following treatment with valproate. HepG2 cells were treated with valproate at concentrations of 0 (DMSO control), 0.5, 1, 2 and 4 mM and incubated for 24 hours as described in Section 5.2.3. The triglyceride assay was carried out as described in Section 2.8. The values shown represent the mean of six replicates. Error bars represent standard deviation.

5.3.4 Metabolomic analysis of aqueous monolayer cell extracts

Upon confirmation of no cytotoxicity and slight increases in lipid content within the cells, suggesting possible mild steatosis, the metabolomic profile of the valproate model was investigated.

^{1}H NMR spectra of aqueous extracts were visually inspected but no obvious differences between sample groups were observed (data not shown). Consequently, multivariate analysis was employed to statistically analyse metabolomic differences between the groups. An initial PCA scores plot was created but sample 0.5 mM (1) was located outside the ellipse (Appendix Figure 8.17). The spectra for this sample was reanalysed and following inspection of the Hotelling's plot (Appendix Figure 8.18) it was determined that this sample was a true outlier and was excluded from analysis. A second PCA scores plot was created (Figure 5.5). Some degree of sample group separation was observed, albeit with intragroup variation. The DMSO control samples were located on the top right-hand side of the scores plot and were therefore positive for PC1 with the exception of sample DMSO (5) which was negative. The 1 mM treated group was located on the left side of the scores plot and was therefore negative for

PC1, while the 4 mM sample group was clustered together and positive for PC1. The 4 mM group was marginally separated from the other treated groups along the PC2 axis. In the scores plot sample 4 mM (6) was located outside the ellipse but further analysis of the spectra revealed it was not an outlier (Appendix Figure 8.19).

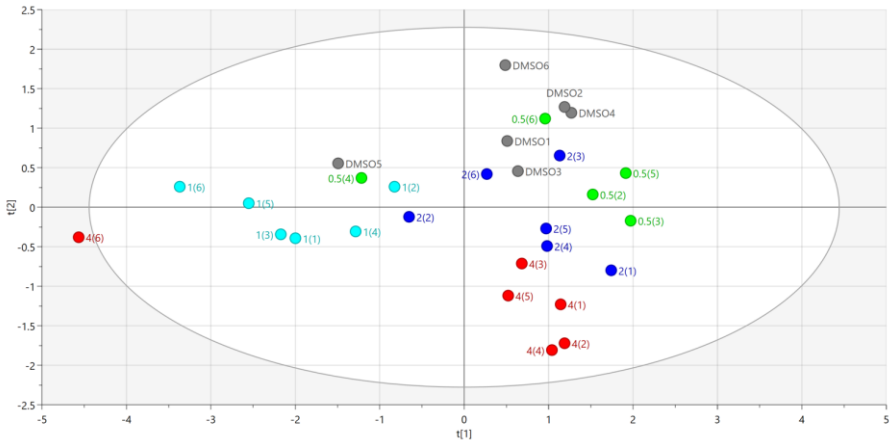

Figure 5.5 PCA scores plot derived from ^{1}H NMR spectra of aqueous extracts from HepG2 cells dosed with valproate at various dose levels. Cells were dosed with DMSO, 0.5, 1, 2 and 4 mM valproate and incubated for 24 hours. Aqueous cell extract samples were collected, and NMR analysis carried out as described in Sections 2.10 and 2.12. Each spot on the plot represents one sample. Grey = DMSO only control; green = 0.5 mM; light blue = 1 mM; blue = 2 mM; red = 4 mM.

Sample spectra were then further analysed using OPLS, in order to visualise inter- and intra-group variation based on class differences. The OPLS scores plot revealed better class separation than the PCA between the treated groups along the predictive t[1] axis with a little overlap between groups. The DMSO controls and the 0.5 mM treated group were located on the left-hand side of the scores plot. The 1 mM treated group was clustered around the centre of the scores plot while the 4 mM treated group was located in the bottom right quadrant of the scores plot. Some intragroup variation was also observed for the majority of the sample groups along the orthogonal t[0] axis (Figure 5.6).

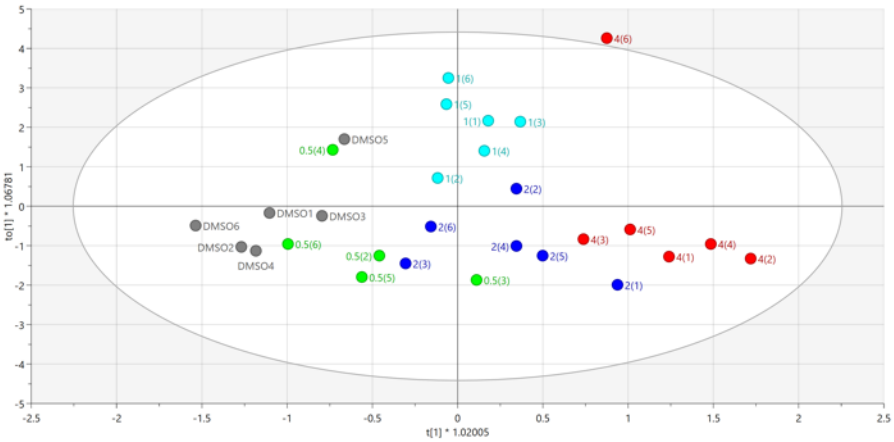

Figure 5.6 OPLS scores plot derived from NMR spectra of aqueous cell extracts from HepG2 cells treated with different dose levels of valproate. Cells were dosed with DMSO, 0.5, 1, 2 and 4 mM valproate and incubated for 24 hours. Aqueous cell extract samples were collected, and NMR analysis carried out as described in Sections 2.10 and 2.12. Each spot on the plot represents one sample. Grey = DMSO only control; green = 0.5 mM; light blue = 1 mM; blue = 2 mM; red = 4 mM.

OPLS-DA was then carried out in order to identify changes in metabolites following treatment with valproate at the different dose levels when compared to the DMSO controls. Consecutive dose levels were also analysed to determine dose-related differences.

All OPLS-DA scores plots shown in Figure 5.7 demonstrated good separation between the control and the treated groups as well as for consecutive dose groups for each pair-wise comparison along the predictive t[1] axis. In all scores plots the DMSO control group was located on the left-hand side of the scores plot when compared against the treated groups while the treated groups were on the right. Significant intragroup variation was observed in all sample groups along the orthogonal t[0] axis but, in particular, for the 0.5 and 4 mM treated groups with samples 0.5 (4) and 4 (6) being separated from the rest of the group.

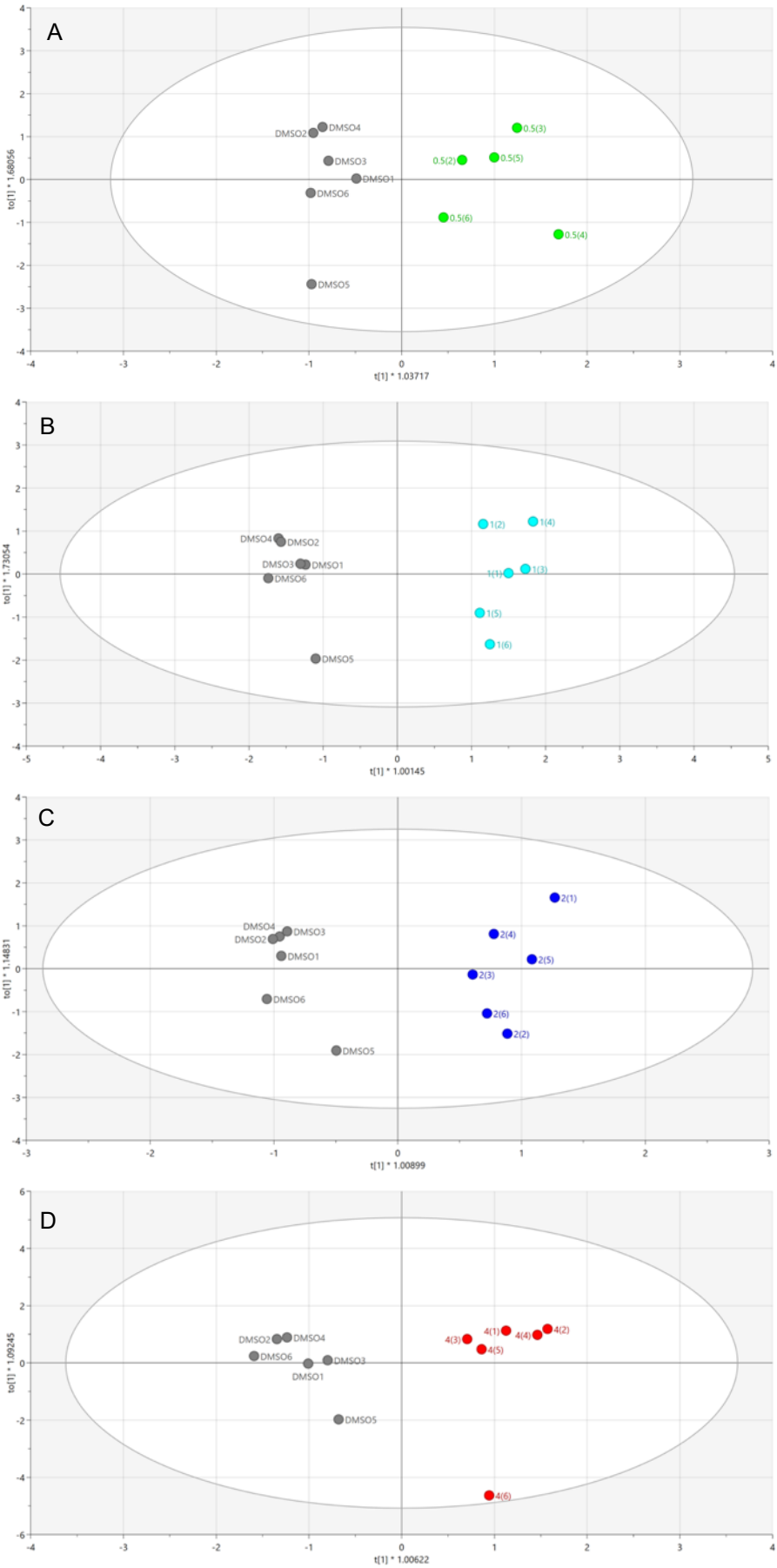
A
DMSO2
DMSO4
DMSO3
DMSO1
DMSO6
DMSO5
0.5(3)
0.5(2)
0.5(5)
0.5(6)
0.5(4)
to[1] * 1.68056
t[1] * 1.03717
B
DMSO4
DMSO2
DMSO3
DMSO1
DMSO6
DMSO5
1(2)
1(4)
1(1)
1(3)
1(5)
1(6)
to[1] * 1.73054
t[1] * 1.00145
C
DMSO4
DMSO2
DMSO3
DMSO1
DMSO6
DMSO5
2(1)
2(4)
2(5)
2(3)
2(6)
2(2)
to[1] * 1.14831
t[1] * 1.00899
D
DMSO2
DMSO4
DMSO6
DMSO3
DMSO1
DMSO5
4(1)
4(4)
4(2)
4(3)
4(5)
4(6)
to[1] * 1.09245
t[1] * 1.00622

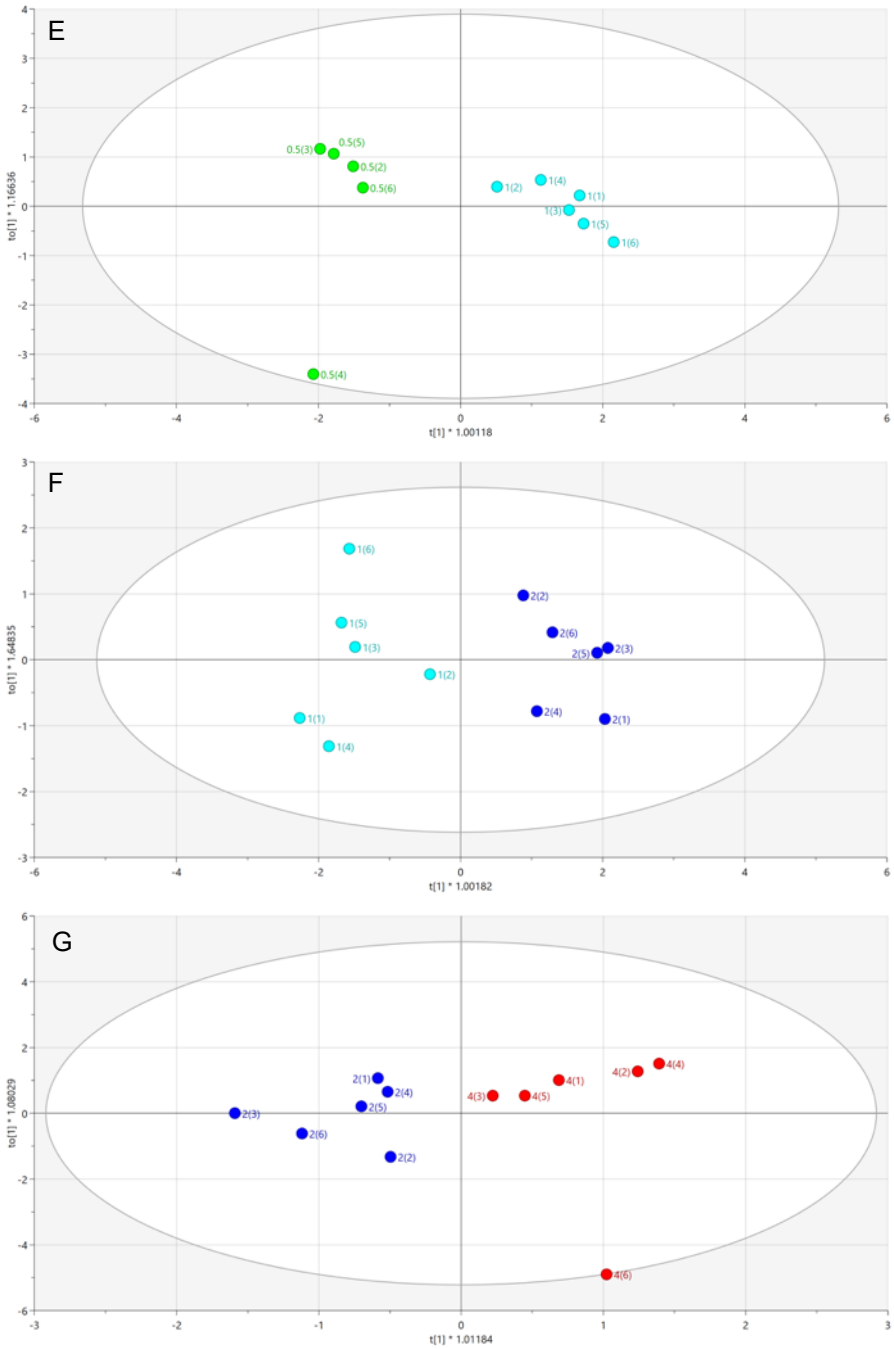

Figure 5.7 OPLS-DA scores plots derived from NMR spectra of aqueous extracts from HepG2 cells dosed with valproate at varying dose levels. Cells were dosed with valproate at 0, 0.5, 1, 2 and 4 mM and incubated for 24 hours. Samples were collected, and NMR analysis was carried out as described in Sections 2.10 and 2.12. Each spot on the plot represents one sample. A. Control vs 0.5 mM valproate B. Control vs 1 mM valproate C. Control vs 2 mM valproate. D. control vs 4 mM valproate. E. 0.5 vs 1 mM valproate. F. 1 vs 2 mM valproate. G. 2 vs 4 mM valproate. Grey = DMSO only control; green = 0.5 mM; light blue = 1 mM; blue = 2 mM; red = 4 mM.

VIP and S-plots were generated to determine the metabolite regions in the NMR spectra contributing to the separation of the groups in each pair-wise comparative scores plot. Spectral regions with a VIP value greater than one are highlighted in red in both the VIP and S-plots. S-plots were then used to confirm whether peaks within

these specific NMR regions had increased or decreased between the groups. (Appendix Figures 8.20 and 8.21).

Following multivariate analysis, the integrated spectral values for each region were evaluated using a Kruskal-Walls test to determine if any of the metabolite regions highlighted in the VIP were statistically significant in each pair-wise comparison.

NMR regions that were confirmed as being statistically different were closely examined to identify metabolite peaks in these regions to aid the identification of metabolites. These identifications were also confirmed by checking other peak regions for each metabolite. Following identification, metabolites were identified as shown in Table 5.1. Decreases were observed for many metabolites including leucine, glutathione, homocysteine and methionine. Significant increases ($p<0.001$) in acetate were observed in the 4 mM treated groups compared to the DMSO control. Many other metabolite regions were also significant however metabolite identification was not possible.

Table 5.1 Chemical shift regions with potential metabolite identifications, determined to be significantly different in the NMR of aqueous extracts from HepG2 cells treated with increasing concentrations of valproate when compared to control.

^{1}H shift ppm	Metabolite aqueous	Ctrl vs 0.5 mM	Ctrl vs 1 mM	Ctrl vs 2 mM	Ctrl vs 4 mM	0.5 vs 1 mM	1 vs 2m M	2 vs 4m M
0.857-0.902(t)	Acyl groups (CH_3)	↓	-	-	-	↓*	↑*	-
0.948-0.969(m)	Leucine, Isoleucine	-	↓*	-	-	↓	↑	-
1.015-1.027(s)	Valine, Isoleucine	-	↓	-	-	-	↑*	-
1.237-1.297(m)	B-hydroxybutyrate	↓	-	-	-	↓*	↑*	-
1.306-1.347(d)	Lactate, Threonine	↑	↓**	↑	↑	↓	↑	↓
1.459-1.498(d)	Alanine	↓	↓	↑	↑	-	-	-
1.913-1.923(s)	Acetate	↑	-	↑*	↑***	-	↑	↑

2.025-2.086(m)	Isoleucine, Glutamate, Homocysteine, SAH, Proline	↑	↓	-	-	↓*	↑	-
2.105-2.194(m)	Methionine, Glutamine, GSH, GSSG, Homocysteine, Cystathionine	↓	↓	↓	↓**	↓	↑	↓
2.327-2.382(tofd)	Glutamate, B-hydroxybutyrate, Proline	-	↓*	↓	↓	↓*	↑	↓
2.385-2.395(s)	Succinate, Pyruvate	-	-	-	↓	-	-	-
2.426-2.477(m)	Glutamine, Pantothenic acid	↑	↓*	↑	-	↓	↑*	↓
2.508-2.575(q)	Citrate, GSH, GSSG	↑	↓*	↑	-	↓**	↑	-
2.671-2.699(m)	Methionine, Citrate, SAH	↑	-	↑	-	↓	↑	-
2.707-2.723(d)	Sarcosine	↑	-	↑	-	↓	↑*	-
2.791-2.812(d)	Homocysteine, Asparagine	↑	-	↑	↑**	-	-	↑
2.989-3.005(s)	SAH, GSH, GSSG, Cysteine	-	↓**	-	-	↓*	↑	-
3.02-3.05(d)	Creatine, Phosphocreatine, Creatinine	↑	↓	↑	-	↓*	↑*	↓
3.214-3.23(s)	Choline, Phosphocholine, Betaine, TMAO	↑	↓	↑	↑	↓	↑*	↓
3.252-3.278(m)	Arginine, Proline, Taurine, TMAO, Histidine	-	↓	↑	-	-	-	-
3.291-3.338(2xd)	Arginine, Proline, Taurine, TMAO, Histidine	-	↓**	↓	↓	↓	↑*	↓
3.734-3.797(m)	Leucine, Alanine, Arginine, Lysine, Glutamine, Glutamate, GSH, GSSG, Dimethylglycine, Glucose, Cysteine, Citrulline	↓	↓**	↓	↓*	↓*	↑	↓

3.813-3.86(m)	SAH, Asparagine, Glucose, Cystathionine, Serine	↑	↓	-	↓	↓*	↑	-
3.879-3.919(dd)	Homocysteine, Methionine, SAH, Cystathionine	-	↓*	-	-	↓**	↑	↓
3.926-3.9402(s)	Creatine, Phosphocreatine, Betaine	-	↓	-	-	↓	↑	
3.983-3.992(m)	Cystathionine, Cysteine, Serine, Hippurate, Histidine	↑	↓	↑	-	↓	↑	-
8.529-8.587(s)	ATP	-	↓*	-	-	↓***	-	-

S=singlet, d=doublet, dd=doublet of doublets, t=triplet, q=quartet, m=multiplet. An increase or decrease in the treated group was determined and these were further analysed statistically using a Kruskal-Wallis test (<0.05, **<0.01, ***<0.001)*

5.3.5 Metabolomic analysis of organic monolayer cell extracts

In this study the organic extracts from HepG2 cells were also analysed.

Visual inspection of the NMR spectra showed no difference between the treated and control groups (data not shown). Therefore, a PCA scores plot was constructed as shown in Figure 5.8. Sample 2 (4) was located outside the ellipse however, the Hotelling's plot (Appendix Figure 8.22) revealed it was below the 99% confidence level and it was therefore included in further analysis. The resulting scores plot did not demonstrate good separation between the control and the two treated groups with much overlap observed on the right side of the plot. However, the majority of the 2 and 4 mM samples were located on the left side of the scores plot separated from the other treatment groups with the exception of samples 4 mM (2) and 4 mM (3).

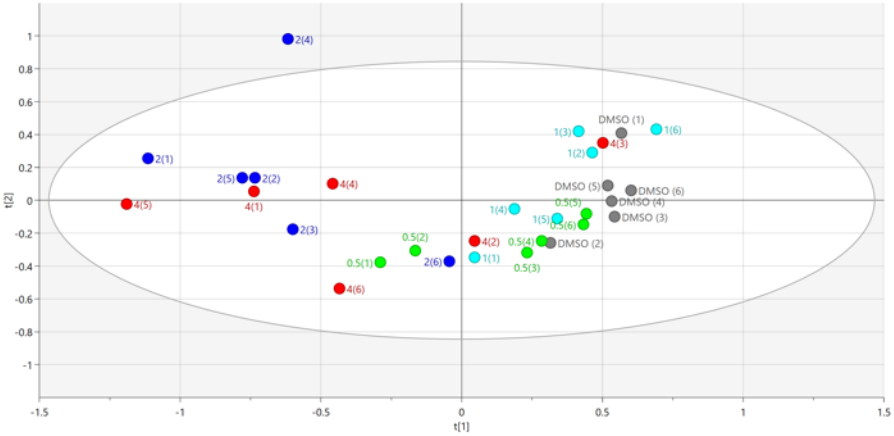

Figure 5.8 PCA scores plot derived from ^{1}H NMR spectra of organic extracts from HepG2 cells dosed with valproate at various dose levels. Cells were dosed with DMSO, 0.5, 1, 2 and 4 mM valproate and incubated for 24 hours. Organic cell extract samples were collected, and NMR analysis carried out as described in Sections 2.10 and 2.12. Each spot on the plot represents one sample. Grey = DMSO only control; green = 0.5 mM; light blue = 1 mM; blue = 2 mM; red = 4 mM.

As the PCA score plot failed to show distinct group separation an OPLS scores plot was constructed. Figure 5.9 shows slightly better clustering within each group along the predictive t[1] axis with the DMSO and the majority of the 0.5 mM treated group on the left-hand side of the scores plot and the 1 mM treated group close to the centre. Large intragroup variation was observed for all groups along the orthogonal t[0] axis with the exception of the 1 mM treated group.

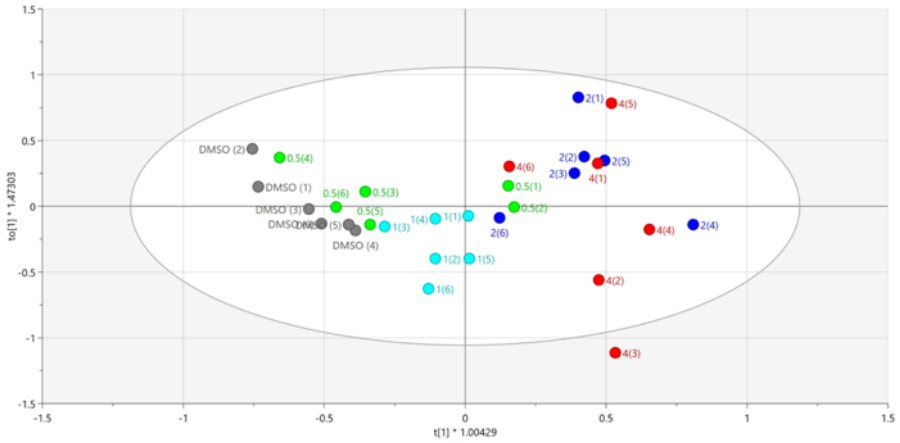

Figure 5.9 OPLS scores plot derived from NMR spectra of organic cell extracts from HepG2 cells treated with different dose levels of valproate. Cells were dosed with DMSO, 0.5, 1, 2 and 4 mM valproate and incubated for 24 hours. Organic cell extract samples were collected, and NMR analysis carried out as described in Sections 2.10 and 2.12. Each spot on the plot represents one sample. Grey = DMSO only control; green = 0.5 mM; light blue = 1 mM; blue = 2 mM; red = 4 mM.

Following OPLS analysis OPLS-DA scores plots were constructed to identify metabolite changes between treated groups and the DMSO control and dose-dependent changes. Figure 5.10 shows that in each scores plot the two groups being compared are separated along the predictive t[1] axis with the exception of the 2 and 4 mM groups where some overlap is observed. However, large intragroup variation was observed in all treated groups along the orthogonal t[0] axis.

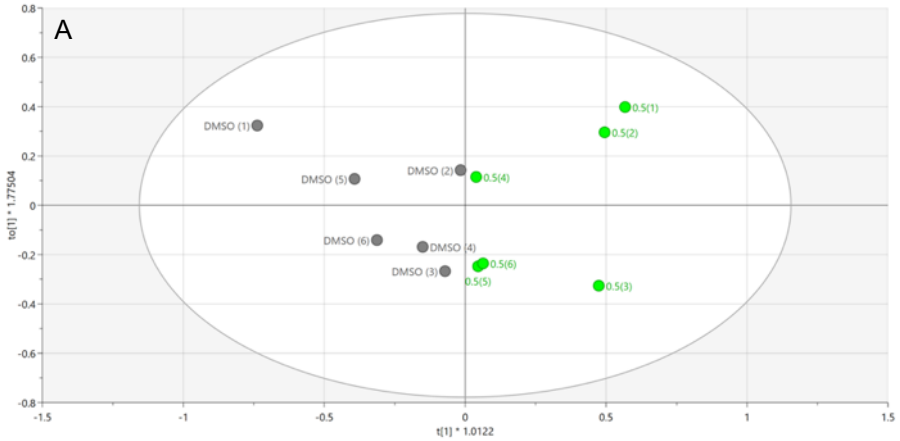

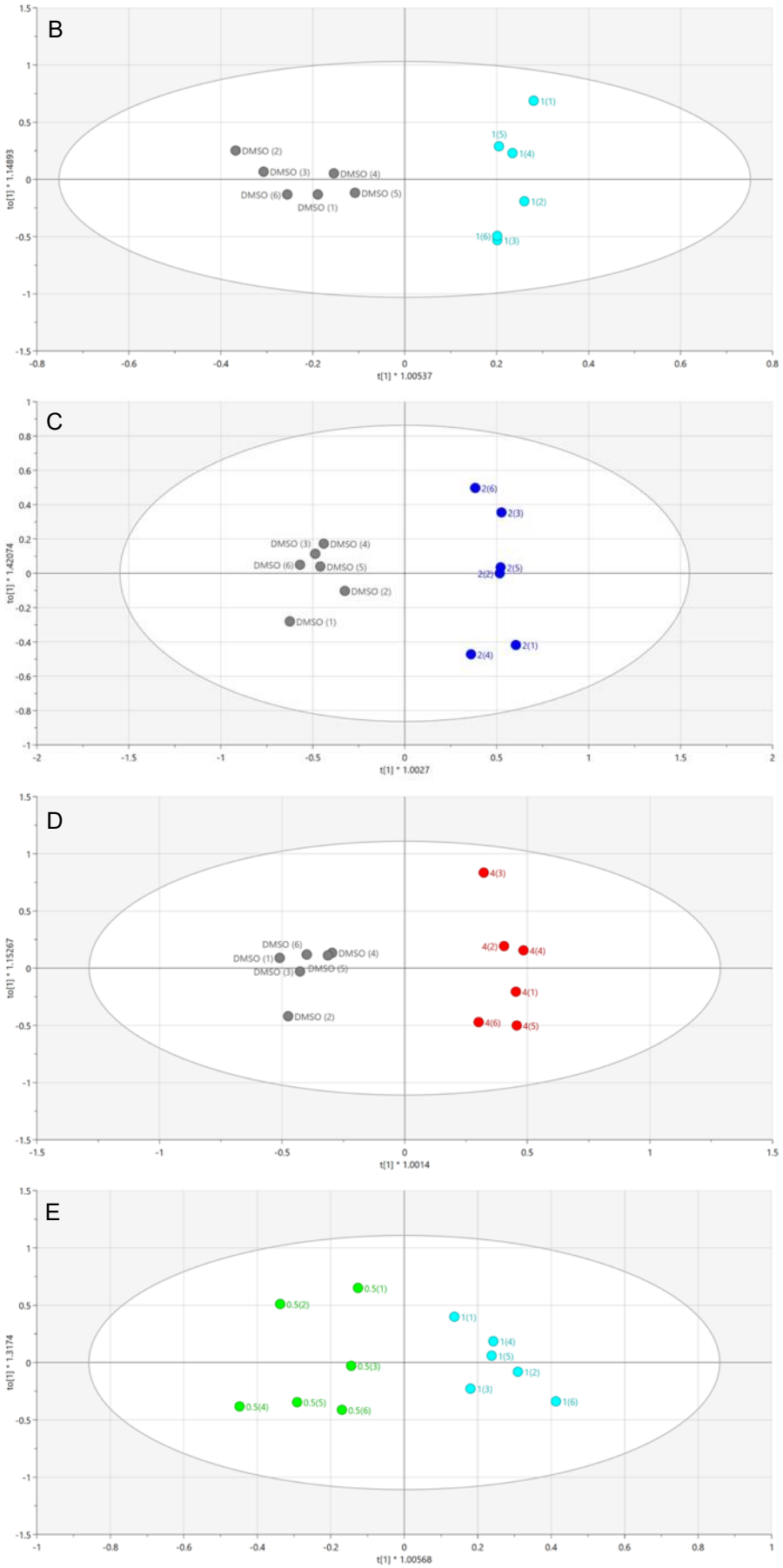
B
1(1)
1(5)
1(4)
DMSO (2)
DMSO (3)
DMSO (4)
DMSO (6)
DMSO (5)
DMSO (1)
1(2)
1(6)
1(3)
to[1] * 1.14893
t[1] * 1.00537
C
2(6)
2(3)
DMSO (3)
DMSO (4)
DMSO (6)
DMSO (5)
2(2)
2(5)
DMSO (2)
DMSO (1)
2(1)
2(4)
to[1] * 1.42074
t[1] * 1.0027
D
4(3)
DMSO (6)
DMSO (1)
DMSO (4)
DMSO (3)
DMSO (5)
4(2)
4(4)
4(1)
DMSO (2)
4(6)
4(5)
to[1] * 1.15267
t[1] * 1.0014
E
0.5(1)
0.5(2)
1(1)
1(4)
1(5)
0.5(3)
1(2)
1(3)
1(6)
0.5(4)
0.5(5)
0.5(6)
to[1] * 1.3174
t[1] * 1.00568

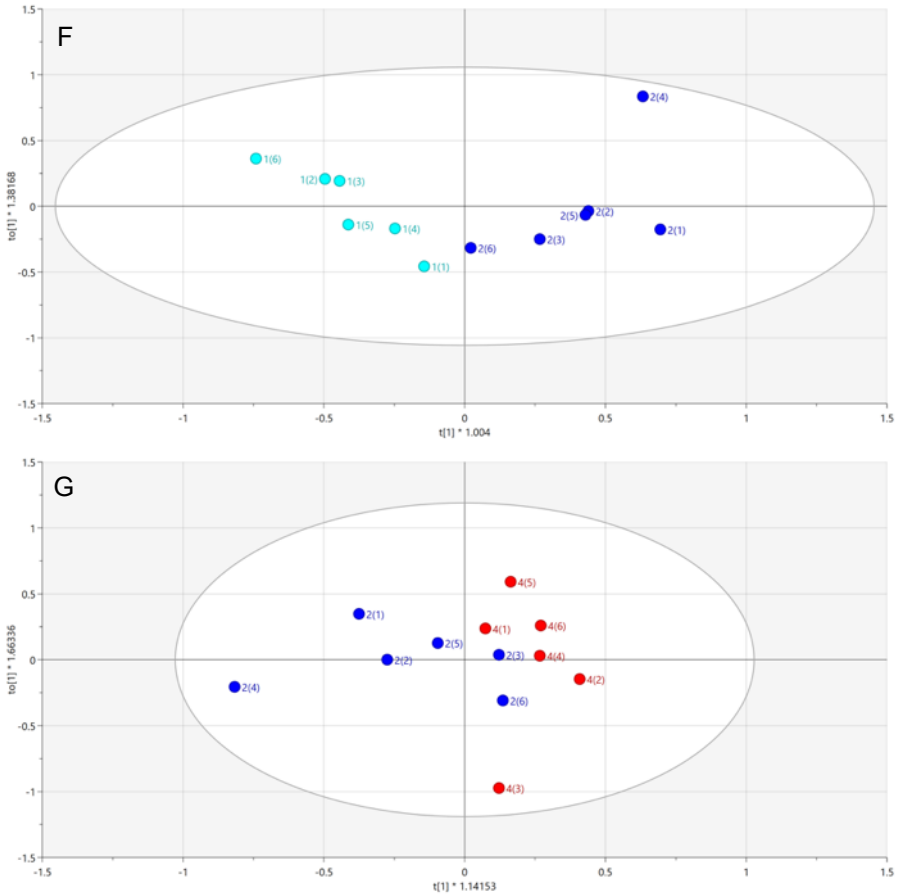

Figure 5.10 OPLS-DA scores plots derived from NMR spectra of organic extracts from HepG2 cells dosed with valproate at varying dose levels. Cells were dosed with valproate at 0, 0.5, 1, 2 and 4 mM and incubated for 24 hours. Samples were collected, and NMR analysis was carried out as described in Sections 2.10 and 2.12. Each spot on the plot represents one sample. A. Control vs 0.5 mM valproate B. Control vs 1 mM valproate C. Control vs 2 mM valproate. D. Control vs 4 mM valproate. E. 0.5 vs 1 mM valproate. F. 1 vs 2 mM valproate. G. 2 vs 4 mM valproate. Grey = DMSO only control; green = 0.5 mM; light blue = 1 mM; blue = 2 mM; red = 4 mM.

Following OPLS-DA analysis VIP predictive and S-plots were generated and variable regions with a VIP value greater than one were highlighted in red in both plots (Appendix Figures 8.23 and 8.24).

Following multivariate analysis, the NMR spectra were further analysed to determine the multiplicity of the significant spectral regions highlighted in the VIP to aid metabolite identification. Significant changes in metabolites observed in this study included decreases in cholesterol in the 0.5, 2 and 4 mM treated groups. Dose-dependent increases in arachidonic acid were observed in all dose levels and these increases were significant at the higher doses (2 mM, $p<0.001$, 4 mM $p<0.01$). Similar to the aqueous samples many NMR regions were highlighted in the VIP plot, but metabolite

identification was not possible. A Kruskal Wallis test was then conducted to determine statistical significance of variable regions, as shown in Table 5.2.

Table 5.2 Chemical shift regions identified as significantly different in the organic extracts of HepG2 cells treated with different concentrations of valproate as detected by OPLS-DA analysis. The multiplicity of each peak is shown.

^{1}H shift ppm	Metabolite aqueous	Ctrl vs 0.5 mM	Ctrl vs 1 mM	Ctrl vs 2 mM	Ctrl vs 4 mM	0.5 vs 1 mM	1 vs 2m M	2 vs 4m M
0.875-0.895(m)	Fatty acyl groups, fatty acids	-	-	↓		↑	↓	↑
1.093-1.189(m)	Cholesterol	↓	-	↓*		↑	↓*	
1.259-1.286(s)	Cholesterol	↓	↑	↓	↓	↑	↓	↑
1.546-1.617(s)	ARA	↑	↑	↑**	↑**	↑	↑	↓
2.29-2.362(m)	Acyl groups in triglycerides	↓		↓*	↓	↑		
3.744-3.809(m)	Unidentified			↓*				
5.344-5.412(m)	FA/MUFA	↓		↓*	↓	↑	↓*	

S=singlet, d=doublet, dd=doublet of doublets, t=triplet, q=quartet, m=multiplet. An increase or decrease in the treated group was determined and these were further analysed statistically using a Kruskal-Wallis test (<0.05, **<0.01, ***<0.001).*

5.3.6 CYP enzyme expression levels in HepG2 monolayers dosed with valproate

CYP enzyme expression in HepG2 cells treated with valproate was evaluated by Western blotting. Figure 5.11 shows the blots for CYP2D6, CYP3A4 and CYP2E1 with the level constituent cell protein beta actin (Figure 5.11A) ensuring equal loading of different cell samples. Table 5.3 displays the raw data of band intensities for each CYP. Levels of CYP2D6 were lower at all valproate dose levels when compared to the DMSO control but there was no dose-related trend. There was a decrease in CYP2E1 levels when compared to the DMSO control. While increases in CYP3A4 levels were observed at all dose levels. However, there appeared to be no dose-related trends in CYP expression in response to valproate. Also, as N=1 in this study further experiments would be needed to confirm these changes.

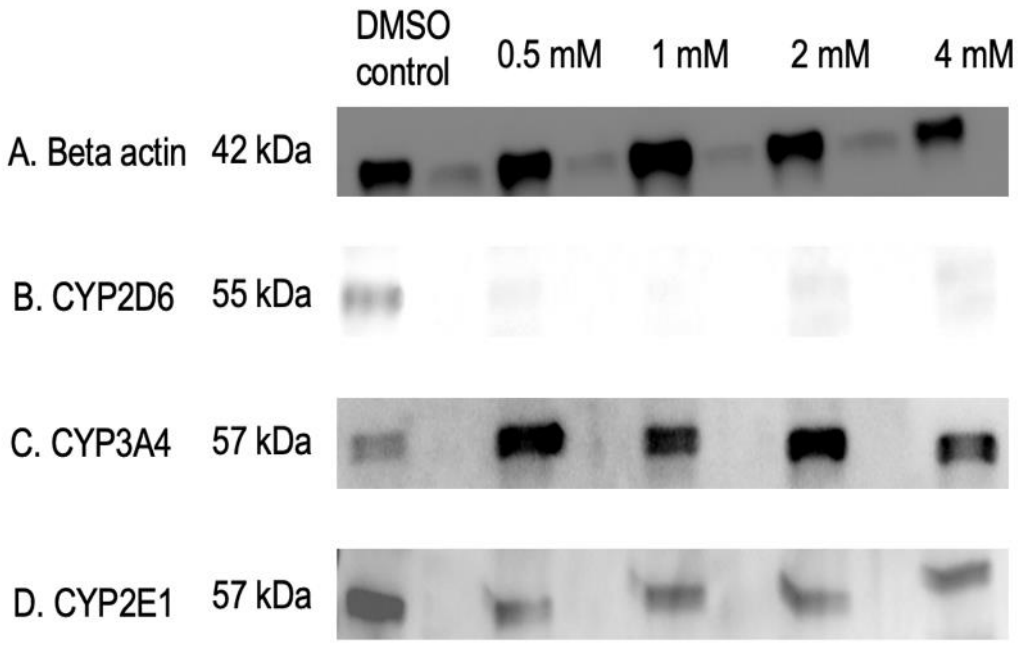

Figure 5.11 Western blot analysis of CYP enzyme expression in HepG2 cells dosed with valproate. A. Beta actin, B. CYP 2D6, C. CYP 3A4 and D. CYP2D6. Monolayers were dosed with valproate at varying concentrations of 0, 0.5, 1, 2 and 4 and proteins were collected as described in Section 2.16. Western blotting was carried out as described in Section 2.20.

Table 5.3 Raw data showing the arbitrary band intensities for CYP2D6, 3A4 and 2E1 in HepG2 monolayers dosed with valproate relative to the DMSO control. Monolayers were dosed with valproate at varying concentrations or 0, 0.5, 1, 2 and 4 mM and proteins were collected as described in Section 2.16.

Valproate concentration (mM)	**CYP2D6**	**CYP3A4**	**CYP2E1**
DMSO control	16572.46	2395.08	10487.1
0.5	1728.55	9856.08	6473.68
1	410.09	5384.71	8488.29
2	1732.67	9409.25	7985.48
4	1266.55	7522.78	8868.56

5.3.7 3D spheroid model dosed with valproate

HepG2 spheroids were grown for 17 days before being dosed with valproate at dose levels of 1 and 4 mM and incubated for 24 hours. Changes in the metabolome following dosing were analysed. Changes in CYP enzyme expression were also analysed using Western blotting.

5.3.8 Cytotoxicity in HepG2 spheroids dosed with valproate

Cytotoxicity in spheroids dosed with 1 and 4 mM valproate was visualised using the LIVE/DEAD assay. The images taken from the assay are shown in Figure 5.12 and revealed no observed cytotoxicity at either dose level. The LIVE/DEAD assay stains viable cells green and non-viable cells red.

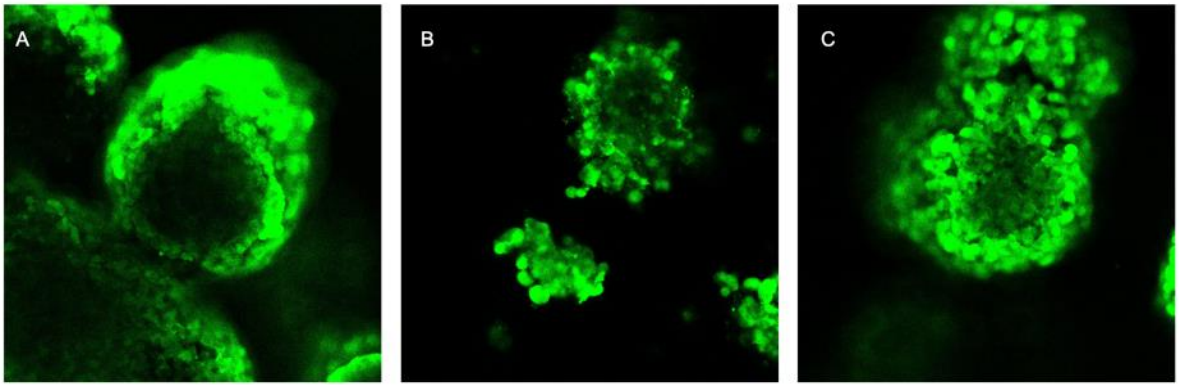

Figure 5.12 Images taken from the LIVE/DEAD assay of spheroids dosed with valproate. Spheroids were grown in low attachment 6-well plates as described in Section 2.3 and dosed with valproate at concentrations of 0 (DMSO control), 1 and 4 mM. The LIVE/DEAD assay was carried out as described in Section 2.22. A. DMSO control, B. 1 mM valproate and C. 4 mM valproate.

Cytotoxicity in this study was assessed using an LDH assay. Figure 5.13 confirmed there was no cell death at either dose levels. While the positive control used in the assay had a cytotoxicity value of 100%, the cytotoxicity value for the 1 and 4 mM groups was 0%.

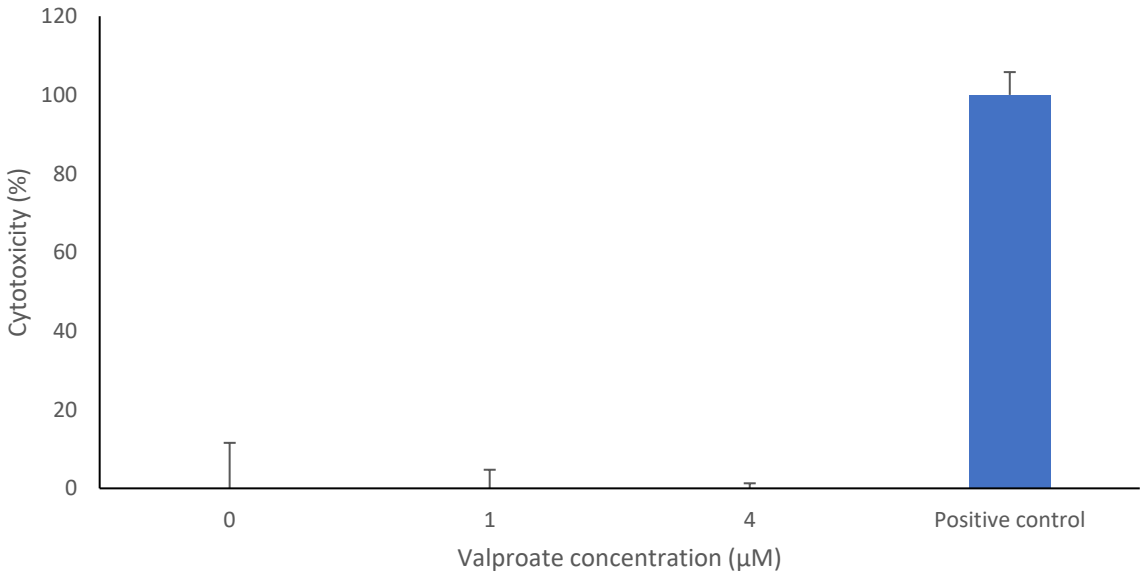

Figure 5.13 HepG2 spheroid cell death in response to increasing valproate concentration assessed by LDH assay. HepG2 spheroids were treated with valproate at concentrations of 0, 1 and 4 mM and incubated for 24 hours as described in Section 2.5.3. The LDH assay was carried out as described in Section 2.21. The value obtained for the positive control represents 100% cell death. The values shown represent the mean of six replicates. Error bars represent standard deviation.

5.3.9 Triglyceride accumulation

Triglyceride accumulation was assessed in the HepG2 spheroids. The results shown in Figure 5.14 revealed an increase in triglyceride accumulation in both treated groups when compared to the DMSO control. There was a significant increase (39%) in triglyceride accumulation in the 1 mM treated group when compared to the DMSO control.

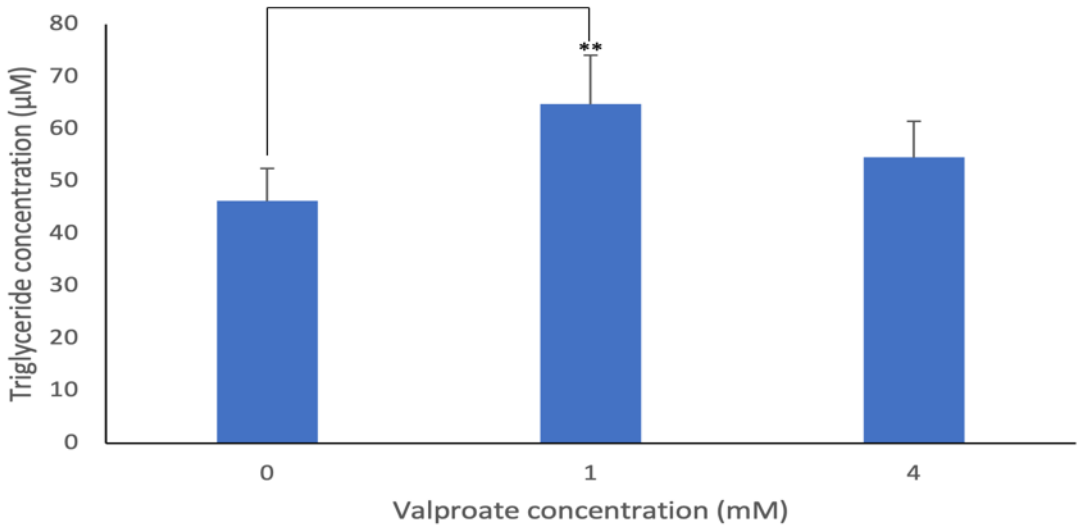

Figure 5.14 Mean triglyceride content in HepG2 spheroids following treatment with valproate. HepG2 cells were treated with valproate at concentrations of 0 (DMSO control), 1 and 4 mM valproate and incubated for 24 hours as described in Section 5.2.3. The values shown represent the mean of six replicates. Error bars represent standard deviation. The triglyceride assay was carried out as described in Section 2.8. Statistically significant differences were analysed using Kruskal-Wallis *(**<0.01).*

5.3.10 Metabolomic analysis of aqueous spheroid extracts

NMR spectra from aqueous spheroid extracts were visually examined but no differences were observed (data not presented). Therefore, a PCA scores plot was created as shown in Figure 5.15. In the scores plot good separation is apparent between the 3 groups with the DMSO control group located on the right-hand side of the scores plot and therefore positive for PC1, while the 4 mM treated group was negative. The 1 mM treated group was located between the DMSO control and the 4 mM group.

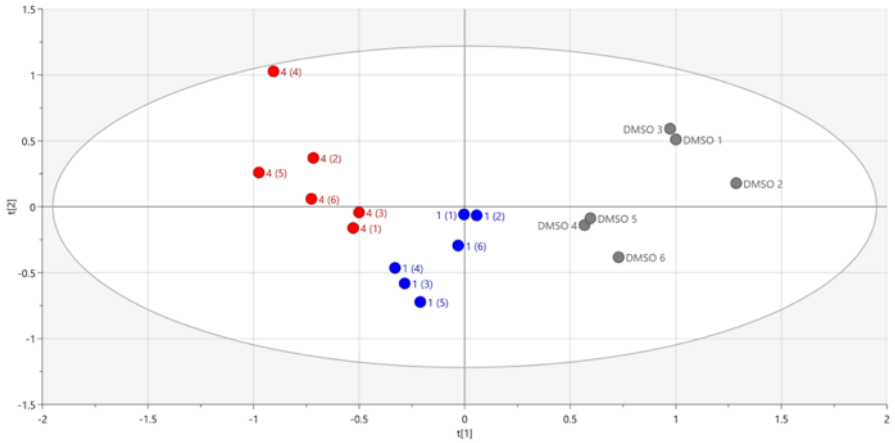

Figure 5.15 PCA scores plot derived from ^{1}H NMR spectra of aqueous extracts from HepG2 spheroids dosed with valproate at different dose levels (0, 1 and 4 mM). Spheroids were dosed with 0, 1 and 4 mM valproate and incubated for 24 hours as described in Section 5.2.3. Samples were collected and NMR analysis carried out as described in Sections 2.10 and 2.12. Each spot represents one sample. Grey=DMSO control; Blue=1 mM; Red=4 mM valproate.

Spectra were further analysed using OPLS. The resulting scores plot shown in Figure 5.16 demonstrated good separation between the groups along the predictive t[1] axis, with the DMSO group located on the left side of the scores plot and the 4 mM on the right.

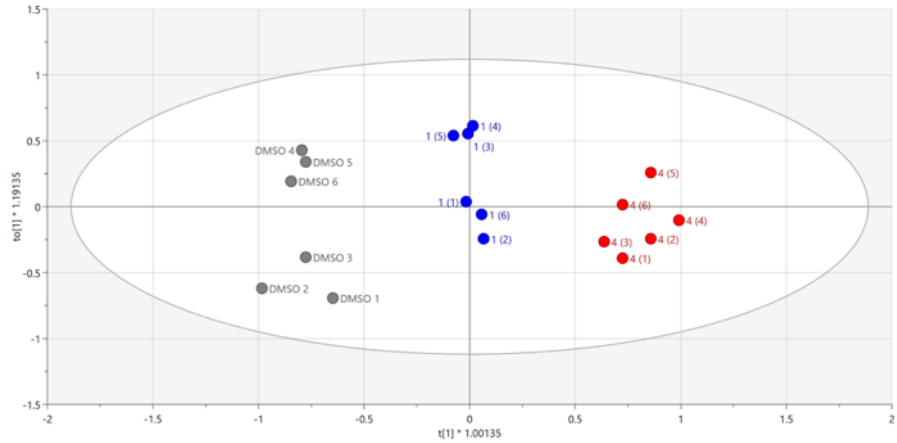

Figure 5.16 OPLS scores plot derived from ^{1}H NMR spectra of aqueous extracts from HepG2 spheroids dosed with valproate at different concentrations. Spheroids were dosed with 0, 1 and 4 mM valproate and incubated for 24 hours as described in Section 5.2.3. Samples were collected and NMR analysis carried out as described in Sections 2.10 and 2.12. Each spot represents one sample. Grey=DMSO control; Blue=1 mM; Red=4 mM valproate.

OPLS-DA analysis was conducted for pair-wise comparisons of the control against each of the two treated groups as well as a direct comparison of the two treated groups. All OPLS-DA scores plots generated showed clear separation along the t[1]

axis, intragroup variation was also observed along the orthogonal t[0] axis in all scores plots (Figure 5.17).

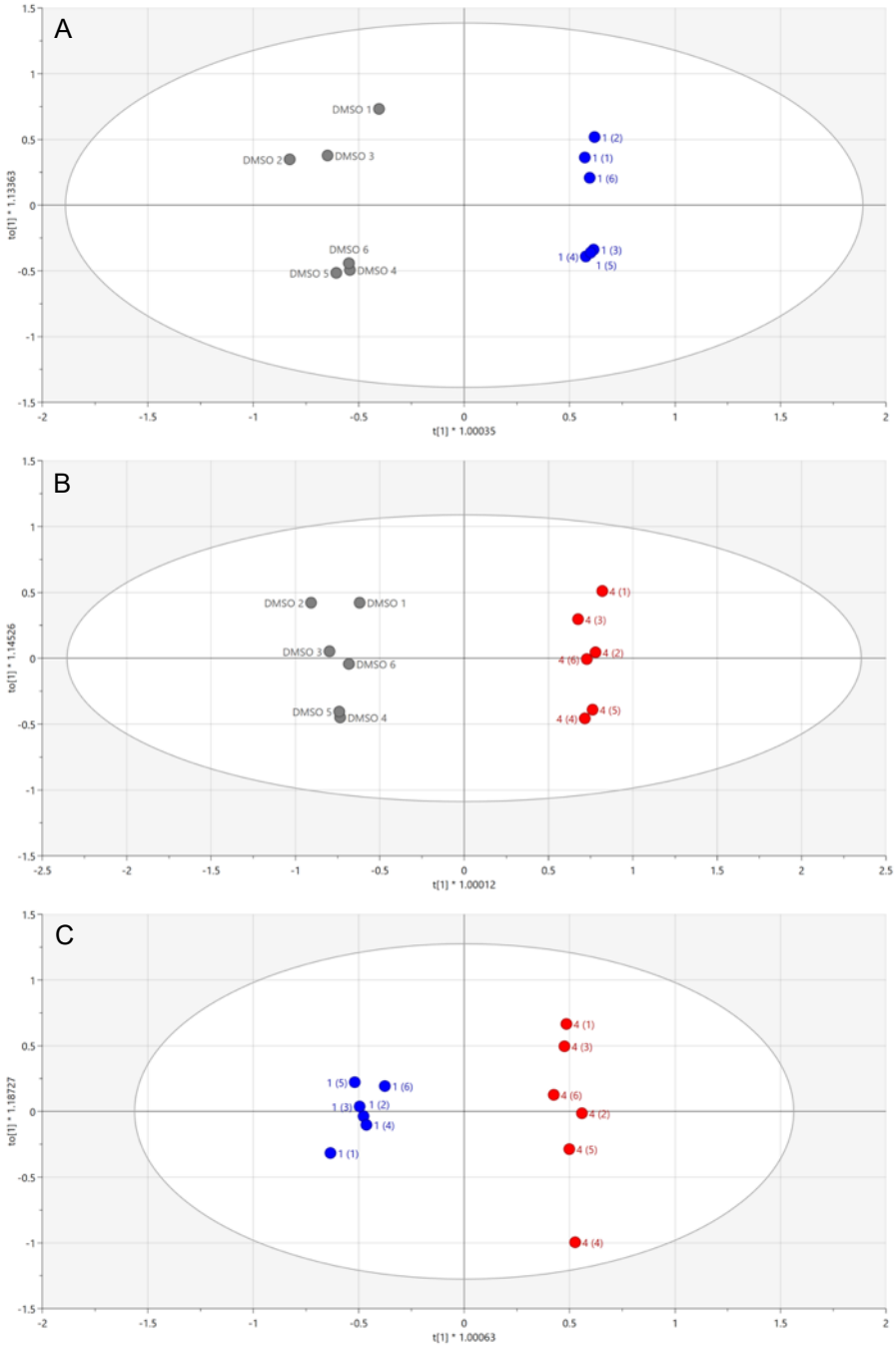

Figure 5.17 OPLS-DA scores plots derived from NMR spectra of aqueous extracts from HepG2 spheroids dosed with valproate at varying dose levels. Spheroids were dosed with valproate at 0, 1 and 4 mM and incubated for 24 hours as described in Section 5.2.3. Spheroids were collected and NMR analysis was carried out as described in Sections 2.10 and 2.12. Each spot on the scores plot represents one sample. Grey=DMSO control; Blue=1 mM; Red=4 mM valproate. A. Control vs 1 mM valproate; B. Control vs 4 mM valproate; C. 1 vs 4 mM valproate.

VIP predictive and S-plots (Appendix Figures 8.25 and 8.26) were generated from the OPLS-DA models and variable regions with a VIP greater than one were highlighted and shown in red in both models.

Following NMR analysis, the integrated spectral values were evaluated using a Kruskal-Wallis test to determine any statistically significant variable regions. The NMR spectra were then closely examined to identify metabolite peaks in these regions to aid the identification of metabolites. This revealed that significant decreases in essential amino acids including leucine, isoleucine and valine were observed in the treated groups, as well as significant decreases in succinate, glycine, acetate and choline. Alanine was significantly ($p<0.05$) increased in both treated groups. A significant increase ($p<0.01$) in β-hydroxybutyrate was also observed. Again, there were a large number of unidentified regions not shown in table.

Table 5.4 Chemical shift regions, and potential metabolites, identified as significantly different in the NMR of aqueous extracts from HepG2 spheroids treated with increasing concentrations of valproate when compared to control.

^{1}H shift ppm	Metabolite aqueous	Ctrl vs 1mM	Ctrl vs 4mM	1 vs 4mM
0.857-0.901(t)	Acyl groups (CH_3)	↑	↑***	↑
0.9125-1.0467(m)	Leucine, isoleucine, Valine	↓**	↓***	↓*
1.236-1.296(m)	B-hydroxybutyrate	-	↑**	-
1.3107-1.3505(d)	Lactate, threonine	-	↑**	↑*
1.4207-1.479(d)	Alanine	↑*	↑*	-
1.806-1.851(m)	Lysine, Citrulline	-	↓**	↓
1.912-1.927(s)	Acetate	↓**	↓*	-
1.978-2.107(m)	Isoleucine, Glutamate, Homocysteine, SAH, proline	↓***	↓	↑
2.3818-2.3975(d)	B-hydroxybutyrate, Glutamate, Proline	↓***	↓	↑
2.416-2.428(s)	Succinate	↓*	↓**	-
3.034-3.049(s)	Creatine	↓**	-	↑
3.218-3.231(s)	Choline, Phosphocholine	↓*	↓*	-

3.257-3.265(s)	Betaine, TMAO	↓*	↓**	-
3.34-3.35(s)	Glucose, Hypotaurine, Pantothenic acid	↓	↓**	↓
3.388-3.395(s)	Betaine	-	↓**	-
3.459-3.495(m)	Glucose, Pantothenic acid	-	↓***	↓
3.502-3.5113(s)	Glycine	↓*	↓**	↓
3.536-3.552(dd)	Choline	↓*	↓**	-
3.688-3.748 (m)	Isoleucine, Valine, Threonine, Choline	↓	↓***	↓
3.881-3.9204(s)	Creatine	↓**	↓***	↓
3.947-3.955(s)	Creatine, Phosphocreatine, Betaine	↓	↓*	↓
4.085-4.137 (q)	B-hydroxybutyrate, Lactate,	↓	-	↑
6.81-6.863(d)	4-hydroxybenzoic acid	-	-	↓

S=singlet, d=doublet, dd=doublet of doublets, t=triplet, q=quartet, m=multiplet. An increase or decrease in the treated group was determined and these were further analysed statistically using a Kruskal-Wallis test (<0.05, **<0.01, ***<0.001)*

5.3.11 Metabolomic analysis of organic spheroid extracts

Organic extracts from HepG2 spheroids were analysed using ^{1}H NMR. A PCA scores plot shown in Figure 5.18 did not show clear separation between the two treated groups, while samples from the DMSO control group were spread across the plot. The DMSO 1 sample was located just outside the ellipse, but this was determined not to be an outlier and therefore it was included in further analysis (Appendix Figure 8.27).

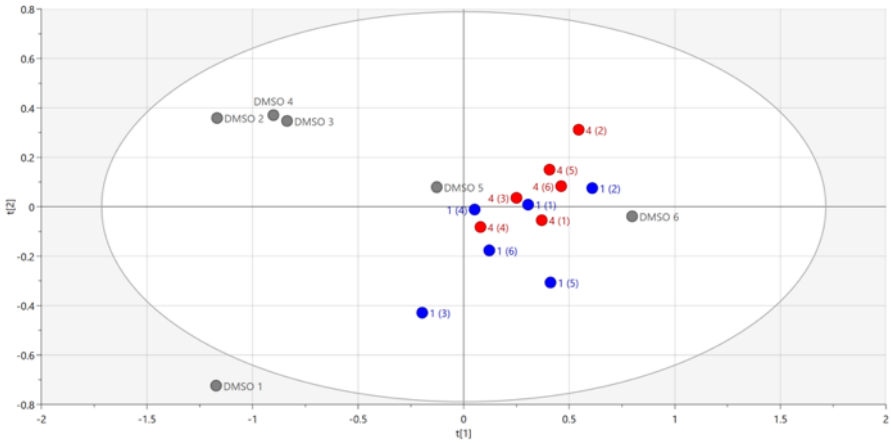

Figure 5.18 PCA scores plot derived from ^{1}H NMR spectra of organic extracts from HepG2 spheroids dosed with valproate at different dose levels (0, 1 and 4 mM). Spheroids were dosed with 0, 1 and 4 mM valproate and incubated for 24 hours as described in Section 2.5.3. Samples were collected and NMR analysis carried out as described in Section 2.10 and 2.12. Each spot represents one sample. Grey=DMSO control; Blue=1 mM; Red=4 mM valproate.

The OPLS scores plot (Figure 5.19) also failed to show clear separation between the two treated groups along the predictive t[1] axis. While large intragroup variation could be seen in the DMSO control group, with sample DMSO 6 located just outside the ellipse (Appendix Figure 8.28).

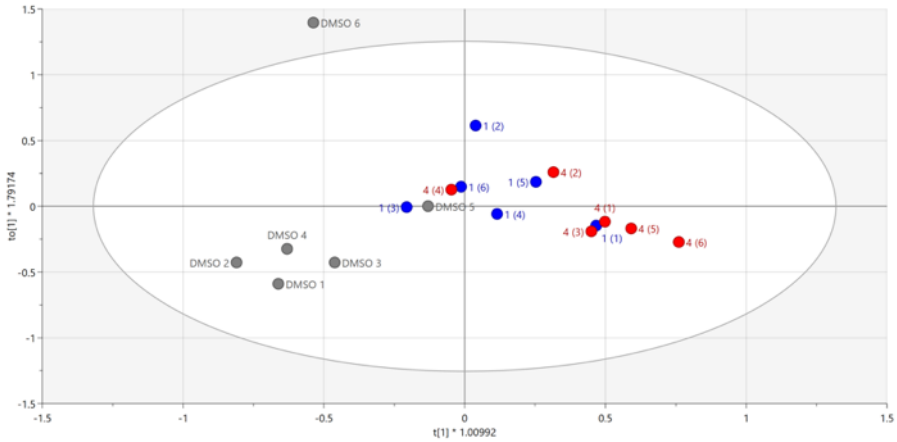

Figure 5.19 OPLS scores plot derived from ^{1}H NMR spectra of organic extracts from HepG2 spheroids dosed with valproate at different concentrations. Spheroids were dosed with 0, 1 and 4 mM valproate and incubated for 24 hours as described in Section 2.5.3. Samples were collected and NMR analysis carried out as described in Section 2.10 and 2.12. Each spot represents one sample. Grey=DMSO control; Blue=1 mM; Red=4 mM valproate.

Pair-wise comparisons between the treated and control groups and the two treated groups was also conducted. The resulting OPLS-DA scores plots shown in Figure 5.20 did produce separation of the groups along the t[1] axis with the DMSO control group located on the left side of the plots in Figure 5.20 A and B. However, large intragroup variation could be seen across the orthogonal t[0] axis between treated groups in Figure 5.20 C and between the DMSO control and treated (Figure 5.20 A and B).

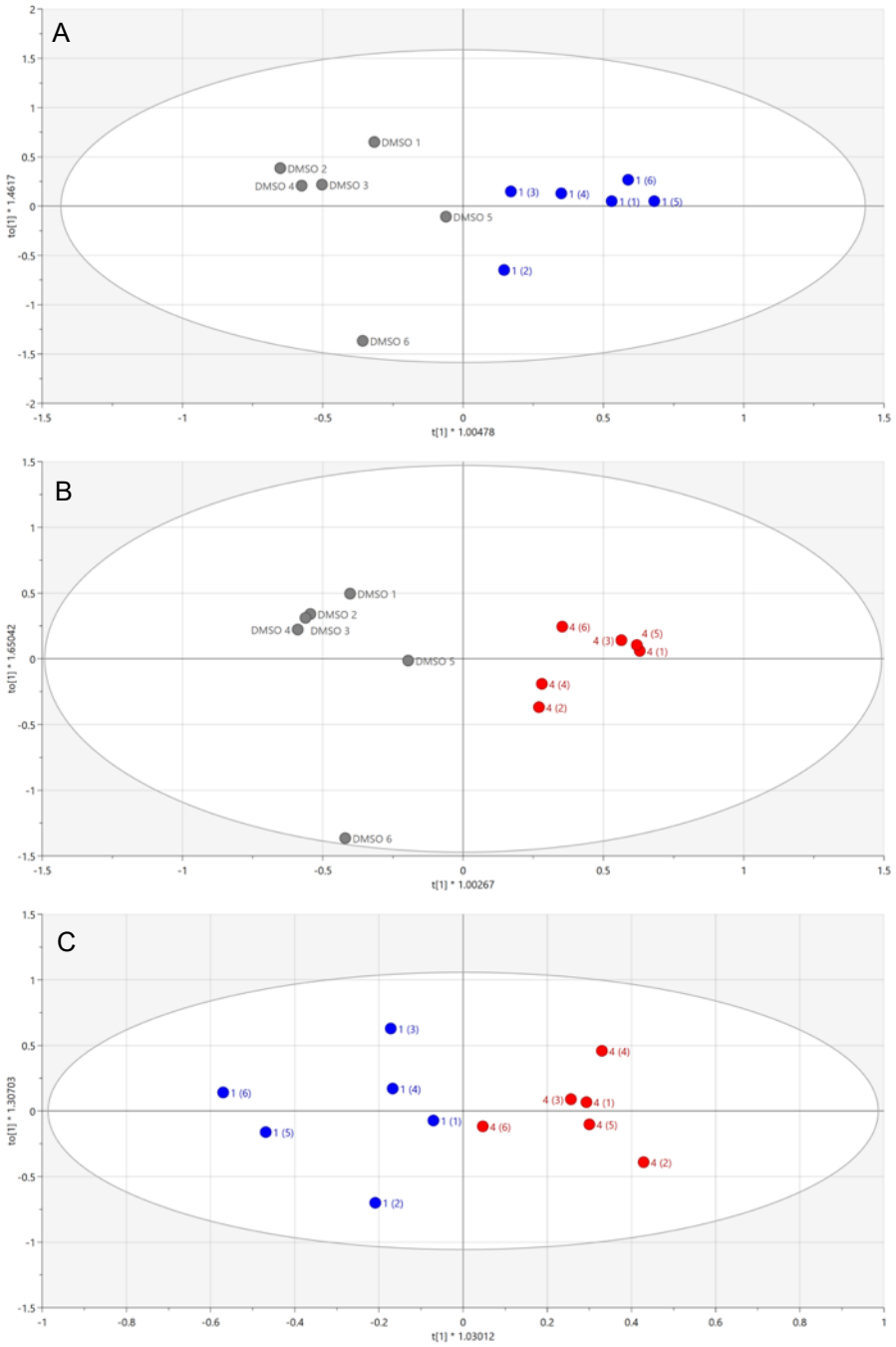

Figure 5.20 OPLS-DA scores plots derived from NMR spectra of organic extracts from HepG2 spheroids dosed with valproate at varying dose levels. Spheroids were dosed with valproate at 0, 1 and 4 mM and incubated for 24 hours as described in Section 2.5.3. Spheroids were collected and NMR analysis was carried out as described in Sections 2.10 and 2.12. Each spot on the scores plot represents one sample. Grey=DMSO control; Blue=1 mM; Red=4 mM valproate. A. Control vs 1 mM valproate; B. Control vs 4 mM valproate; C. 1 vs 4 mM valproate.

VIP and S-plots were generated from the OPLS-DA models and regions with VIP predictive value greater than 1 were highlighted and can be seen in red in Appendix Figures 8.29 and 8.30.

Spectral regions highlighted in the VIP were examined to determine the peak characteristics in order to aid metabolite identification using the Human Metabolome database. Kruskal-Wallis was used performed to determine if any statistically significant changes were apparent.

Following identification, increases in fatty acyl groups were observed at both dose levels as well as increases in arachidonic acid. However, the Kruskal-Wallis only revealed two regions at 0.886-0.9262 and 1.5625-1.605 ppm which were significant. Furthermore, many other NMR regions were highlighted as contributing to group separation in the VIP plots but identification of the metabolites in these regions was not possible.

Table 5.5 Chemical shift regions identified as significantly different in the organic extracts of HepG2 spheroids treated with different concentrations of valproate as detected by OPLS-DA analysis. The multiplicity of each peak is shown.

^{1}H shift ppm	Metabolite aqueous	Ctrl vs 1 mM	Ctrl vs 4 mM	1 vs 4 mM
0.692-0.7127(s)	Unidentified	-	-	↓
0.886-0.9262(t)	Fatty acyl groups, fatty acids	↑	↑	↓**
1.25-1.377(d/s)	Cholesterol	-	↓	↓
1.5625-1.605(s)	ARA	↑*	↑	↓
2.008-2.065(q)	Oleic acid	-	-	↓
2.3129-2.365(m)	Acyl groups in triglycerides	-	-	↓
4.145-4.193(dd)	Glyceryl groups in monoglycerides		-	-
5.327-5.414(m)	FA/MUFA	-	-	↓

S=singlet, d=doublet, dd=doublet of doublets, t=triplet, q=quartet, m=multiplet. An increase or decrease in the treated group was determined and these were further analysed statistically using a Kruskal-Wallis test (<0.05, **<0.01, ***<0.001).*

5.3.12 CYP enzyme expression levels in HepG2 spheroids dosed with valproate

CYP expression in HepG2 spheroids treated with valproate was analysed using Western blotting. Blots for CYP2D6, CYP3A4 and CYP2E1 are shown in Figure 5.21 with the constituent cell protein beta actin ensuring that equal amounts of protein sample was loaded for each treated group.

The results in Table 5.6 shows the raw data of band intensity from the blots for each CYP. Although n=1 some changes in CYP expression was observed. Overall expression of CYP2D6 appeared to be lower in the treated groups relative to the DMSO control. Levels of CYP3A4 tended to be greater in all treated groups than the DMSO control. CYP2E1 expression appeared to be increased in the 1 mM treated groups but was lower in the other treated groups when compared to the DMSO control.

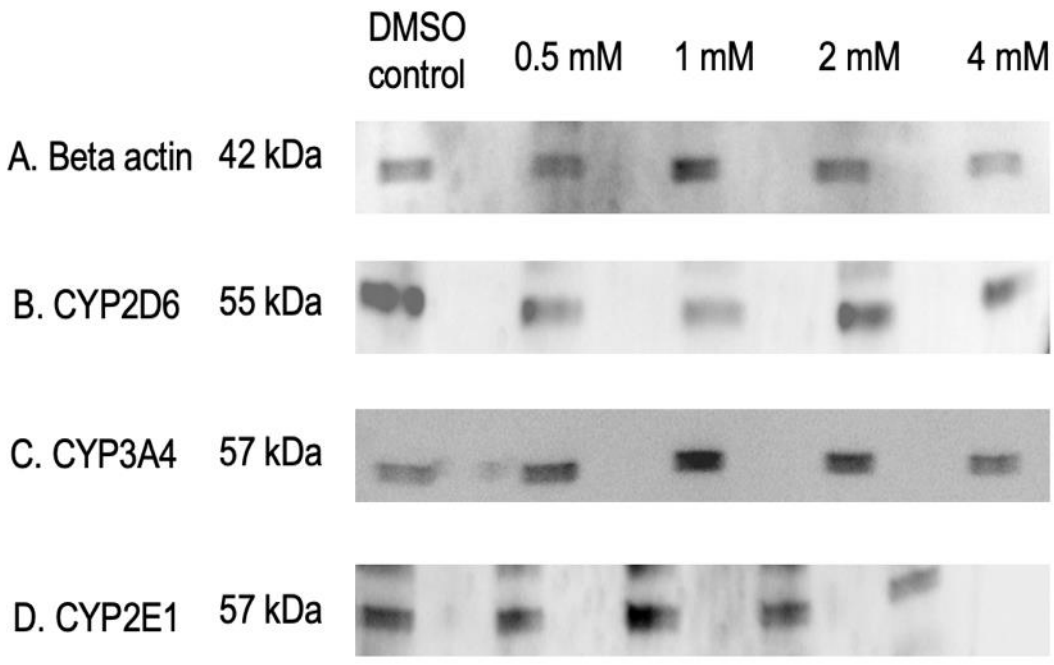

Figure 5.21 Western blot analysis of CYP enzyme band intensities in HepG2 spheroids dosed with valproate. Spheroids were dosed with valproate at varying concentrations of 1 and 4 mM and proteins were collected as described in Section 2.16. Western blotting was carried out as described in Section 2.20. A. Beta actin, B. CYP 2D6, C. CYP 3A4 and D. CYP2D6.

Table 5.6 Raw data showing the arbitrary band intensities for CYP2D6, 3A4 and 2E1 in HepG2 spheroid dosed with valproate relative to the DMSO control. Spheroids were dosed with valproate at varying concentrations or 0, 0.5, 1, 2 and 4 mM and proteins were collected as described in Section 2.16.

Valproate concentration (mM)	**CYP2D6**	**CYP3A4**	**CYP2E1**
DMSO control	15012.92	6284.13	9972.49
0.5	8303.37	9230.25	9051.903
1	6409.44	12368.37	13325.27
2	11289.56	9730.004	8206.73
4	7614.38	6358.29	5032.12

5.4 Discussion

Studies suggest that following prolonged treatment with valproate, around 61% of patient's treated are diagnosed with hepatic steatosis (Luef et al., 2009, Zhang et al., 2014, Farinelli et al., 2015). Valproate is also associated with weight gain, with the frequency of developing obesity in children treated with valproate ranging from 10-70%, thereby increasing the risk of developing NAFLD given the link between the two (Farinelli et al., 2015).

The exact mechanism for valproate induced hepatotoxicity remains unclear and is likely multifactorial (Farinelli et al., 2015, Komulainen et al., 2015, Yan et al., 2021). However, many *in vivo* and *in vitro* studies have reported that valproate-induced liver injury is associated with microvesicular steatosis, mitochondrial injury and oxidative stress (Tsiropoulos et al., 2009, Gai et al., 2014, Komulainen et al., 2015, Bai et al., 2017, Yan et al., 2021). It has been reported that valproate upregulates the cluster differentiation 36 (CD36) protein, which plays an important role in facilitating fatty acid uptake in the liver and adipose tissue in humans (Chang et al., 2016, Bai et al., 2017, Yan et al., 2021). This is supported by Bai et al., (2017) who reported a dose-dependent increase in CD36 expression in mice treated with valproate at 100, 250 and 500 mg/kg for 14 days with a 2-fold increase at the highest dose level. Their study also demonstrated a similar pattern in HepG2 cells exposed to valproate (1, 2.5 and 5 mM) for 24 hours. An *in vitro* study by Chang et al., (2016) in mouse FL83B cells also indicated an increase in CD36 expression following 24-hour dosing with 1 mM valproate.

Various *in vitro* studies have demonstrated a concentration-dependent increase in hepatic lipid accumulation in HepG2 cells in response to valproate treatment (0.5-5 mM) for up to 48 hours. Rodent models have also used different valproate concentrations (100 – 750 mg/kg) to induce steatosis over a wide range of exposure times (Lewis et al., 1982, Kesterson et al., 1984, Zhang et al., 2014, Bai et al., 2017). Lewis et al., (1982) reported that 750 mg/kg valproate produced substantial microvesicular steatosis after 48 hours in rats. While Bai et al., (2017) demonstrated a significant increase in VLDL in mouse liver following consecutive intragastric valproate administrations of 500 mg/kg for 14 days. Incubating HepG2 cells with

valproate for 24 hours has previously resulted in an increase in lipid accumulation (Bai et al., 2017, Yan et al., 2021), therefore, the exposure time chosen in this study was 24 hours.

Valproate is generally well tolerated in HepG2 cells and studies using dose levels up to 5 mM have not demonstrated cytotoxicity (Bai et al., 2017), whereas others have reported impaired mitochondrial activity following 24 hour dosing with 2 mM valproate (Komulainen et al., 2015, Pirozzi et al., 2019, Yan et al., 2021). Despite this Yan et al., (2021) assessed the viability at different concentrations (0.5, 1 and 2 mM) of valproate for 24 and 48 hours in HepG2 cells using an MTT assay and only observed decreased viability at 2 mM after 48 hours. Chang et al., (2016) reported significant cytotoxicity at high doses of 5 and 10 mM due to lipotoxicity and suggest these dose levels are more suited to the creation of NASH models. As discussed in Chapter 4 the cells must be dosed with higher concentrations of drugs to observe the desired effects, therefore toxic concentrations of valproate in humans are around 5 times less than (150 µg/ml, 1050 µM) compared to those in cells (> 5-10 mM) (Twiesselmann et al., 2008).

Consequently, the current study examined dose levels of 0.5, 1, 2 and 4 mM valproate to induce mild steatosis but avoid cytotoxicity. Neither the MTS or LDH assay (Figures 5.1 and 5.2) revealed significant changes to cell viability or cytotoxicity, respectively after 24 hours.

Oil Red O staining of the monolayer revealed a dose dependent increase in lipid accumulation (Figure 5.3). However, the Triglyceride-Glo assay did not show a corresponding significant increase in triglyceride accumulation in the treated groups. Nevertheless, triglyceride content was slightly greater in the treated groups compared to the control with a 25% increase in lipid accumulation observed at 1 and 2 mM. Yan et al., (2021), using a triglyceride assay kit, did find that triglyceride accumulation was increased following dosing with 2 mM valproate after 24 hours and following dosing with 1 and 2 mM valproate after 48 hours. Similar to the present study Bai et al., (2017), using Oil Red O staining observed a concentration-dependent increase in lipid content in HepG2 cells following a 24-hour incubation with valproate at doses of 1, 2.5 and 5 mM. They observed a further increase when the incubation time was extended to 48

hours. The studies by Yan et al., (2021) and Bai et al., (2017) dosed for 24 and 48 hours and reported greater lipid accumulation at the later time point (Bai et al., 2017, Yan et al., 2021). However, valproate is rapidly metabolised and has a half-life of 9-16 hours *in vitro* (Van Breda et al., 2018), therefore, to conduct prolonged exposure studies, repeated dosing is necessary. A study by Van Breda et al., (2018) exposed primary hepatocytes to repeated doses of valproate every 24 hours for 3 and 5 days to test mechanisms of steatosis and demonstrated possible inhibition of β-oxidation and increased uptake of fatty acids due to increased expression of the CD36 transporter. However, HepG2 cells have a doubling time of 48 hours and would become too confluent if grown for longer periods of time. Studies that have dosed for longer used different cells lines including primary hepatocytes and FL83B cells which may be more suited to longer exposure time (Chang et al., 2016, Van Breda et al., 2018). A study by Katsura et al., (2002) maintained primary hepatocytes for more than 56 days. Nevertheless, on the basis of the Oil Red O staining and the apparent increases in triglycerides though not significant, it does appear that a mild state of steatosis was induced indicating valproate can be used as a model of mild steatosis in monolayer HepG2 cells and is suitable for potential biomarker study.

In the literature HepG2 spheroid steatotic models using valproate have not been previously reported. In this Chapter 1 and 4 mM valproate were chosen as the low and high dose levels. The 4 mM dose level was chosen since it did not induce any cytotoxicity in the monolayers. The 1 mM dose level was chosen as the low dose for spheroids because the 0.5 mM dose level was too similar to controls in the metabolomics analysis of monolayers.

To assess cytotoxicity, an MTS assay was conducted for the spheroid experiment as for the monolayers; However, the results were not reliable as the absorbance readings were outside the linear range for the assay. This was due to the high cell count in the spheroids after 17 days of growth. The assay was repeated using different cell seeding densities starting as low as $1x10^3$ cells however, after 17 days of culture the cell count still exceeded that of the linear range of the assay. The LDH assay revealed zero cytotoxicity when compared to the DMSO control indicating both doses were well tolerated. The LIVE/DEAD assay confirmed a lack of cytotoxicity in the spheroids (Figure 5.12).

Following a 24-hour incubation in valproate spheroids dosed with both levels of valproate had greater triglyceride content when compared to the DMSO control as assessed by the triglyceride assay. The 1 mM treated group had the highest triglyceride content and was significantly increased ($p<0.01$) when compared to control. However, there was no statistical significance for the increase seen in the 4 mM treated group. This lower triglyceride content in the 4 mM group than for the 1 mM may be due to decreased cell viability at this dose level as was seen in the monolayers. It is known that spheroids are more susceptible to hepatotoxicants due to their increased cell-to-cell contact (Stampar et al., 2020 and Ingelman-Sundberg and Lauschke, 2021). This was not reflected in the LDH assay but as mentioned above it was not possible to obtain results for cell proliferation in the MTS assay. As mentioned in previous Chapters one of the main issues with spheroids is that the core may become necrotic due to a lack of nutrients in that region; this could have an effect on cell viability. Additionally, as spheroids continue to grow cell proliferation is slowed (Stampar et al., 2022). These phenomena could be the reason for the difference seen in lipid accumulation between the two dose levels.

The increases in triglyceride content in the spheroid groups (Figure 5.14) along with slight increases in lipid accumulation for the monolayers (Figure 5.4) confirms valproate can successfully create HepG2 monolayers and spheroid models of mild steatosis.

Using these models, this Chapter investigated changes in the metabolome of monolayer and spheroid cellular extracts. The monolayers PCA scores plots for both the aqueous and organic extracts (Figures 5.5 and 5.8) did not show clear separation between the sample groups. Whereas there was separation between the two treated groups in relation to the DMSO control in the aqueous spheroid sample PCA scores plot (Figure 5.15), but not for the organic extracts (Figure 5.18).

In general, all OPLS scores plots showed better separation between the groups but there was still some overlap for the 0.5 mM and DMSO control groups in the monolayers (Figures 5.6 and 5.9). This suggests that the 0.5 mM valproate dose was not influencing the cell metabolome and the dose level was too low. Some intragroup variation was also observed in all groups along the orthogonal t[0] axis. As discussed

in Chapter 4 cell cultures are more susceptible to intragroup variation due to biological factors so this was expected (Badrick, 2021, Frank, 2021, Reddin et al., 2023). The overlap between dose groups and lack of separation observed in some plots may also be due to the small sample size. Additionally, some samples fell outside the ellipse which would have likely skewed the average of the data set causing other samples to overlap. This was observed in the organic spheroid model with two of the DMSO control samples (1 and 6) falling outside the ellipse in the OPLS and PCA, respectively. It is common to use 6 replicates in metabolomics studies, but some suggest using larger sample sizes to improve separation and statistical analysis (Gorsuch, 1983, Hatcher, 1994, Shaukat et al., 2016). However, as previously discussed it is not feasible to use a large number of cell samples for metabolomics studies. Also, it is possible that the lack of sample separation seen in the score's plots could be due to sampling errors when collecting samples and inaccuracies in counting cell numbers per well. While haemocytometers are an integral part of cell culture their use is not free from error as they require manual counting meaning human error is inevitable at various stages. Any error in cell count would affect the number of cells in each well and could give rise to intragroup variation. Intragroup variation was similar across spheroid and monolayer samples indicating that both models are susceptible to sampling errors.

The pair-wise comparisons in the OPLS-DA scores plots revealed good separation in all sample group comparisons with the exception of the 2 and 4 mM treated organic monolayer samples (Figure 5.10 G) which showed some overlap between the two groups.

In this study metabolite peaks responsible for separation of the different groups in OPLS-DA models were identified with similar metabolite changes revealed for both the monolayer and spheroid models (Tables 5.1, 5.2, 5.4 and 5.5). These changes include increases in lactate and alanine and decreases in methionine and glutamine. As well as decreases in cholesterol and increases in arachidonic acid. The similar findings for both models further confirm the reliability of spheroids for *in vitro* hepatotoxicity studies. This is important since most research is focused on the development of better in vitro models, but little progress has been made on using 3D

spheroids. To date no studies have used HepG2 spheroids dosed with valproate to investigate biomarkers.

For both the spheroid and monolayer treated cell extracts in this study glucose levels were decreased following valproate treatment, indicating a potential increase in glycolysis within the cells. Many drugs including valproate have been shown to inhibit mitochondrial beta-oxidation. Therefore, it has been suggested that glycolysis is upregulated in drug-induced steatosis to compensate for reduced production of ATP from beta-oxidation (Chan et al., 2018, Dargue et al., 2020). In a previous study decreased ATP levels were observed in HepG2 cells cultured in galactose medium in response to valproate (Komulainen et al., 2015). However, in the same study cells grown in glucose medium had higher ATP levels indicating an increase in ATP production from glycolysis.

Valproate has been reported to have an impact on mitochondrial metabolism through inhibition of α-ketoglutarate dehydrogenase, a key enzyme in the TCA cycle leading to a decrease in the TCA cycle and ATP production (Salsaa et al., 2020). It is also known to decrease carnitine levels which transports fatty acids to the mitochondria for oxidation (Luder et al., 1990, El Hage et al., 2012, Salsaa et al., 2020). In a study conducted by Zhang et al., (2014) it was observed that valproate treated rats displayed decreased levels of citrate, a key TCA metabolite. A change in citrate could not be confirmed in this study however, significant decreases in succinate, another TCA cycle metabolite ($p<0.05$ and 0.01) were observed in both treated groups in the spheroid samples. Therefore, the current study and evidence from the literature suggest an increase in glycolysis may be occurring in our models to compensate for the inhibition of mitochondrial bioenergetics. Salsaa et al., (2020) reported that yeast cells dosed with 0.6 mM valproate for either 5 or 10 hours fermented pyruvate, the end-product of glycolysis, into ethanol in response to valproate. Studies in humans have also reported increases in glycolysis following daily valproate administration for at least 2 months (Huo et al., 2014, Xu et al., 2019A). Enhanced glycolysis leads to increased production of acetyl-CoA which cannot enter the TCA cycle due to reduced TCA activity. This can result in an accumulation of acetyl-CoA which is then converted to ketone bodies. In a study by Huo et al., (2014) an increase in acetate was reported in humans following valproate administration indicating the presence of increased ketone bodies since

acetyl-CoA can be hydrolysed to acetate by acetyl-CoA hydrolase. In this current study significant increases in acetate were observed in the 2 and 4 mM treated groups in the monolayers which could confirm a possible increase in glycolysis.

An increase in glycolysis and glycogenolysis has been observed for other drugs including methapyrilene, acetaminophen and CCl_4 that induce mitochondrial dysfunction in mice (Craig et al., 2003, Zira et al., 2013, Dargue et al., 2020). Chen et al., (2018) reported that emodin, a naturally occurring anthraquinone derivative, increased glycolytic activity and reduced gluconeogenesis in HepG2 cells via mitochondrial dysfunction.

Significant increases in lactate and alanine were also identified in the current study in the high dose spheroid samples (Table 5.4) as well as increases in the 2 and 4 mM monolayer samples (Table 5.1). This is consistent with a number of previous studies reporting impaired beta-oxidation in drug-induced steatosis in HepG2 cells and mice models (Donato et al., 2009, Begriche et al., 2010, Choi et al., 2015, Garcia-Canaveras et al., 2016, Fromenty, 2019, Salsaa et al., 2020). A metabolomics study conducted by Huo et al., (2014) assessing hepatotoxicity in epileptic patients also demonstrated increases in lactate and alanine following dosing with valproate. In the literature lactate and alanine are the most commonly reported metabolite changes when it comes to hepatoxicity with lactic acidosis being frequently described in drug-induced steatosis (Cuykx et al., 2018A, Lee and Kim, 2019, Dargue et al., 2020). Thus, the changes in lactate for both models are in agreement with changes observed in literature confirming the use of spheroids as a model of steatosis and again suggests a potential switch to glycolysis in these cells.

The present study revealed significant decreases in essential amino acids including leucine, isoleucine and valine in both treated spheroid groups and in the 1 mM monolayer groups (Table 5.1). Amino acids can be utilised in hepatocytes for the production of ATP as an adaptive response to compensate for the loss of ATP when beta-oxidation is impaired (Rui et al., 2014, Zhang et al., 2014). Therefore, these findings are in agreement with valproate inhibition of beta-oxidation and the use of amino acids as an alternative source of ATP production. Decreases in leucine and isoleucine were demonstrated in a study by Zhang et al., (2014) in which rats were

treated with valproate for 8 weeks. Previous studies have also reported decreases in amino acids such as leucine in CCl_4 drug-induced liver injury due to the downregulation of energy metabolism in HepG2 cells and in rats (Li et al., 2014, Oh et al., 2022). As the liver plays a major role in amino acid metabolism disturbances to amino acid levels are well documented and play an important role in the pathological process of drug-induced liver injury (Nicholson et al., 2003, Kaspar et al., 2009, Yu et al., 2017, An et al., 2020).

In the monolayer study (Table 5.1) a metabolite region at 2.105-2.194 ppm was decreased in all treated groups when compared to control. According to databases this region may contain peaks belonging to many metabolites, including methionine and glutathione. As described in Chapter 4 methionine is an essential amino acid and is a key intermediate in transsulfuration pathway for the production of s-adenosylmethionine (SAM) and glutathione, two important antioxidants (Jha et al., 2016). It is unclear whether SAM levels were affected in this current study as no metabolite regions for this were identified. Since SAM levels are dependent on the availability of methionine obtained from the diet and its production by *de novo* synthesis in the presence of methyl-tetrahydrofolate and vitamin B12, any decreases in methionine are likely to decrease SAM (Ornoy et al., 2020). SAM is a methyl donor for nearly all methylation reactions in the body and is converted to S-adenosylhomocysteine (SAH) through the donation of active methyl groups in the methylation pathway (Shrubsole et al., 2015, Zhang et al., 2016, Ornoy et al., 2020, Werge, 2021). Any changes in methionine would also have an effect on homocysteine as it is formed in methionine recycling by the conversion of SAH to homocysteine adenosine by SAH hydrolase. Significant decreases ($p<0.001$) in homocysteine were seen in the 1 mM spheroid group (Table 5.4) as well as decreases in all monolayer groups (Table 5.1) in this study. Nearly 50% of the homocysteine formed is then further converted to cysteine by the transsulfuration pathway for further glutathione formation.

In the current study peaks in many regions potentially corresponding to cysteine and cystathionine, intermediates in the transsulfuration pathway were also decreased. This was observed in the monolayer samples; however, these metabolite identifications could not be validated since many metabolites have peaks in the same spectral regions. Studies have reported that a deficiency in methionine results in post-

transcriptional down-regulation of cystathionine β-synthase, the first enzyme involved in the transsulfuration of homocysteine to cystathionine. This would then lead to an accumulation of homocysteine (Jhee and Kruger, 2005, Tang et al., 2009, Caballero et al., 2010). A decrease in methionine can therefore contribute to greater levels of homocysteine due to decreased utilisation of homocysteine leading to oxidative stress and progression to NASH (Pacana et al., 2015). Consequently, studies have shown that mice and rats fed a methionine deficient diet also exhibit hyperhomocysteinemia which can lead to oxidative stress and consequently NASH (Tang et al., 2009, Caballero et al., 2010, Aissa et al., 2014, Pacana et al., 2015). However, in this study it appears that homocysteine was decreased in all models although this decrease cannot be confirmed as homocysteine shares its metabolite regions with other metabolite peaks. Future work could spike standard samples with homocysteine to confirm. The decrease in many methyltransferase pathways metabolites seen in this study are indicative of disruption in the methylation pathway but this requires future work for confirmation.

Many studies have reported that valproate can cause an impairment in the methionine cycle (Alonso-Aperte et al., 1999, Ubeda et al., 2002, Chateauvieux et al., 2010, Chen et al., 2014, Ornoy et al., 2020). Plus, it has been suggested that alterations in the methionine cycle could be the common mechanism underlying the hepatotoxic, teratogenic and antifolate effects of valproate (Alonso-Aperte et al., 1999, Chateauvieux et al., 2010, Chen et al., 2014). It has been demonstrated that valproate can lead to a reduction in methionine adenosyltransferases (MAT), the enzyme responsible for the production of methionine from SAM. In one study Ubeda et al., (2002) noted a 56% reduction in MAT activity after 1 hour in rats treated with 400 kg/mg valproate. The reduced MAT activity is concomitant with decreased cellular levels of glutathione with glutathione depletion seemingly a direct consequence of valproate treatment in rats following single dosing due to increased glutathione S-transferase activity (Ubeda et al., 2002). Therefore, a reduction in MAT activity could be related to oxidative stress. However, it is still unclear whether the first insult is glutathione depletion that leads to decreased MAT activity or the other way round (Ubeda et al., 2002). In this study peaks potentially belonging to glutathione were observed as decreased in all treated monolayer groups and were significantly ($p<0.05$) decreased in the 4 mM group compared to the DMSO control (Table 5.1). This could

be linked to decreases in MAT activity. However, despite similarities for many metabolite changes in this study between monolayer and spheroids changes in glutathione were not observed in the spheroids.

The link between valproate treatment and decreased levels of glutathione (GSH) are considered to be due to exhaustion of GSH stores and a consequent increase in oxidative stress further leading to depletion of GSH. Sokmen et al., (2012) reported depleted GSH levels in a rat study indicating valproate-induced tissue injury was associated with oxidative stress. Other studies have also reported that valproate leads to an increased generation of free radicals and oxidative stress (Tong et al., 2005, Kiang et al., 2011). As this study wished to create a model of mild steatosis these changes in glutathione and homocysteine highlight the importance of choosing dose levels that do not cause significant oxidative stress. This could be confirmed in future studies using assay kits such as the Comet assay which measures DNA damage due to oxidative stress.

Valproate has been reported to have an effect on vitamin B6 in a study by Ubeda el al., (2002), where they observed a 54% decrease in plasma B6 concentrations in rats. It is thought that chronic treatment with anticonvulsant drugs in humans may induce vitamin B6 deficiency and impair homocysteine/methionine metabolism (Schwaninger et al., 1999). However, Ubeda et al., (2002) administered a single dose of valproate to rats and still observed decreases in vitamin B6 suggesting the decrease in B6 was the result of dysregulation of the methionine cycle. The balance between methionine, folate and B12 regulates the activity of the folate and methionine cycles which are mechanistically co-dependent. The folate cycle converts tetrahydrofolate (THF) into 5,10-methyleneTHF by serine hydroxymethyltransferase (SHMT), a reaction that is coupled with the hydroxylation of serine to glycine and requires B6 as a cofactor. Vitamin B6 is also a cofactor for the conversion of homocysteine to cysteine via transsulfuration for use in glutathione synthesis (Lyon et al., 2020). This could mean that decreases in vitamin B6 could lead to reduced glutathione and cause increases in serine. Changes in serine were not observed in either of the two models in this current study. However significant decreases in glycine ($p<0.05$ and 0.01) were observed in the low and high dose of the spheroid samples indicating a potential decrease in B6 activity. Decreased levels of glycine have been linked with insulin

resistance and the progression of NAFLD to fibrosis (Hasegawa et al., 2020), however further research is needed to confirm changes in glycine levels in valproate induced steatosis.

The remethylation of methionine can take place via two independent pathways one being the 5,10-methyleneTHF dependent pathway and the other the betaine-dependent remethylation pathway, if homocysteine is present. The latter is catalysed by betaine-homocysteine methyltransferase (BHMT) which utilises a methyl group from betaine to form dimethylglycine and methionine (Chen et al., 2014). It has been shown that BHMT expression is downregulated in HepG2 cells treated with valproate in part by inducing NFxB a repressor for the human BHMT gene (Chen et al., 2014). In the present study a significant decrease in betaine was observed in spheroids treated with valproate at both doses indicating a potential decrease in BHMT expression in the spheroids but not in the monolayer samples.

In this study many changes in the methyltransferase pathways were reported which agree with the literature. However, there are only a few studies highlighting these changes in HepG2 cells and none specifically looking at valproate induced steatosis in spheroids. Therefore, this valproate study offers an insight into a novel model of steatosis in HepG2 spheroids and shows their suitability for *in vitro* studies. However, a limitation of this study was that it was not possible to validate all metabolite changes involved in the methyltransferase pathways as many of the metabolite peaks overlap in similar spectral regions. Despite the overlapping peaks the metabolites in these regions are all linked to the methyltransferase pathways supporting the hypothesis that valproate is having an effect on the pathway as a whole meaning this pathway could be useful in a panel of biomarkers of steatosis.

In the organic extracts, increases in arachidonic acid were noted in both the spheroid and the monolayer valproate-treated groups with significant increases ($p<0.01$) observed in both the 2 and 4 mM treated groups. This increase in arachidonic acid could be due to the activation of the arachidonic acid metabolism pathway due to the inhibition of beta-oxidation induced by valproate (Cuykx et al., 2018A). Arachidonic acid is known to be a precursor of inflammatory molecules, such as the prostaglandins. Increased arachidonic acid has also been documented in humans

and mice and is linked to inflammation and increased oxidative stress (Ma et al., 2016, Wells et al., 2016).

Decreases in cholesterol peaks were observed in the monolayer samples and in the 4 mM spheroid treated groups in this study. Studies have reported that valproate can reduce cholesterol levels in rats and humans due to decreased levels of acetyl-CoA (Zhang et al., 2014, Kusumastuti and Jaeri, 2020). There were also many metabolite regions determined to be important for group separation in the organic samples, but it was not possible to identify the individual lipid molecules in this project. This is because organic metabolites mainly consist of fatty acid groups of different chain lengths and it is hard to differentiate them using NMR-based metabolomics. Future studies could employ the use of mass spectroscopy in an attempt to elucidate some of the structures of the fatty acids in an attempt to identify more of the organic metabolites.

In this Chapter Western blotting was used to analyse CYP expression levels in the steatotic HepG2 monolayers and spheroids following dosing with valproate. As mentioned in the previous Chapters changes to CYP expression levels in NAFLD are well established with the most documented changes being increases in CYP2E1 and decreases in CYP3A4 and CYP2D6 (Satapathy et al., 2015, Sukkasem et al., 2020, Di Pasqua et al., 2022). However, to date, studies reporting the effects of valproate on CYP expression in HepG2 cells in the context of steatosis are limited. HepG2 monolayers are thought in general to have lower CYP expression than spheroids. But this would require confirmation especially in the context of steatosis and therefore in this study CYP expression was evaluated in both monolayers and spheroids.

Although N=1 increased CYP3A4 levels were observed in both models at all tested doses when compared to the DMSO control however no dose dependent patterns were observed (Tables 5.3 and 5.6). Valproate has been reported to significantly upregulate CYP3A4 mRNA in primary hepatocytes and increase gene expression of CYP3A4 genes in primary hepatocytes and HepG2 cells via the activation of the pregnane X receptor (PXR) (Cerveny et al., 2007, Yan et al., 2021). Most studies in the literature report a decrease in CYP3A4 expression and activity in humans and cells in dietary-induced NAFLD (Hanagama et al., 2008, Osabe et al., 2008, Sukkasem et

al., 2020). Despite this a study by Huang et al., (2019) observed an increase in CYP3A4 expression in LO2 cells dosed with fatty acids due to increased miRNA expression indicating that CYP3A4 is induced by steatosis.

CYP2D6 expression levels were demonstrated to be lower than the DMSO controls in both models in this study (Tables 5.3 and 5.6). In general, CYP2D6 levels are thought to be decreased in steatosis due to reduced mRNA expression and this has been observed in HepG2 cells dosed with fatty acids (Sukkasem et al., 2020). However, as this was a single experiment with no repeats it is difficult to make any firm conclusions. The effect of valproate on CYP2D6 expression have not been well documented. However, a study by Wen et al., (2001) demonstrated that concentrations ranging from 50 to 1000 μM valproate showed minimal inhibitory effects on CYP2D6 activity in human liver microsomes.

Although only single experiments were conducted in this study a decrease in CYP2E1 expression levels was observed in the monolayers (Table 5.3) and in the 0.5, 2 and 4 mM spheroid groups (Table 5.6) while increases were seen in the 1 mM spheroid groups. Studies in the literature have mainly demonstrated an increase in expression and activity of CYP2E1 in response to lipid accumulation with the increase hypothesised to play a role in the progression of NAFLD (Merrell and Cherrington 2011, Garcia-Ruiz et al., 2015, Sukkasem et al., 2020). Although the effect of valproate on CYP2E1 expression in the context of steatosis has not previously been investigated. Nevertheless, studies in rat hepatocytes have also reported that valproate-induced oxidative stress and mitochondrial dysfunction is a result of metabolic activation of CYP2E1 and have shown that ROS formation was prevented by CYP2E1 inhibitors (Zhu et al., 2017, Meseguer et al., 2021, Shnayder et al., 2023).

Although there are few studies reporting the effect of valproate on CYP expression in HepG2 cells in the context of steatosis the results in this study suggest that CYP expression in both monolayers and spheroids is similar. It is clear that valproate does affect CYP expression levels. However, future work could include repeated experimentation to validate these changes.

Chapter Six- Conclusions and future work

Chapter 6

6.1 Conclusions

6.1.1 Steatosis

The aim of this project was to firstly develop models of dietary and drug-induced hepatic steatosis in HepG2 monolayers and spheroids and then to use the models for the evaluation of metabolite pathways that change in steatosis. This project wished to compare metabolite changes in both dietary and drug-induced steatosis to find common biomarkers for early steatosis. Steatotic models were created using either a combination of oleic and palmitic acid, tetracycline or valproate since these are the most commonly used models in the literature (Donato et al., 2009, Cui et al., 2010, Choi et al., 2015, Garcia-Canaveras et al., 2016, Bai et al., 2017, Yan et al., 2021). While the mechanisms by which tetracycline, valproate and fatty acids induce steatosis in cells have been reviewed in literature (Cui et al., 2010, Choi et al, 2015, Garcia-Canaveras et al., 2016) a direct comparison of metabolite changes has not been previously conducted. Overlap between metabolites or related biochemical pathways could allow for the identification of reliable markers for steatosis that are common across all mechanisms leading to NAFLD. This could potentially contribute to biomarker panels to increase sensitivity and specificity for diagnosis.

While monolayers have been routinely used to study the molecular mechanism of disease and for the development of *in vitro* models of steatosis, they do not represent the true complexity and physiology of human tissues (Bialkowska et al., 2020). 3D cultures offer a micro-environment more representative of the *in vivo* phenotype (Pingitore et al., 2019). Therefore, the use of 3D spheroids could potentially aid in the search for early diagnostic biomarkers for steatosis which are more relevant to the *in vivo* situation.

In this project the three models were validated in terms of lipid accumulation and steatotic state using Oil Red O staining and a commercial triglyceride assay kit. In Chapter 3 dose-dependent increases in triglyceride accumulation were revealed in the triglyceride assay for the fatty acid treated groups. These increases were statistically

significant in the 0.25 ($p<0.05$), 0.5 ($p<0.01$) and 1 mM ($p<0.001$) sample groups when compared to the ethanol control (Figure 3.4) confirming steatosis in these groups. However, Chapter 4 only revealed slight increases in lipid accumulation which were not significant using the triglyceride assay for the tetracycline treated groups compared to the DMSO controls. The highest percentage increase (approximately 7%) was observed in the 200 µM group (Figure 4.4). Chapter 5 demonstrated increases in lipid accumulation in the 0.5, 1 and 2 mM valproate treated groups. Although not significant, there was around a 25% increase in triglycerides at 1 and 2 mM when compared to the DMSO control (Figure 5.4). Despite the lack of significance seen in the tetracycline and valproate models the Oil Red O staining in all Chapters (Figure 3.3, 4.3 and 5.3) allowed the validation of the models as these results confirmed dose-dependent increases in lipid accumulation in the treated monolayers.

A major goal for the project was to develop 3D spheroid models of steatosis. Spheroids are considered more reflective of the *in vivo* environment and would therefore provide a potential improvement to the use of monolayers in *in vitro* studies. We successfully created steatotic spheroid models for each of the three treatment types: fatty acids (0.1 and 0.5 mM), tetracycline (100 and 600 µM) and valproate (1 and 4 mM). The LDH assay confirmed a lack of cytotoxicity in all models. Significant increases in triglyceride accumulation (57%) were observed in the 0.5 mM fatty acid treatment groups (Chapter 3) and the 1 mM valproate treatment groups (39%) (Chapter 5) indicating mild steatosis in these spheroid models. This is in contrast to the non-significant increases in triglyceride in the fatty acid- and valproate-treated monolayers. This could suggest that the spheroid model more readily develops steatosis, potentially due to the increased cell-to-cell contact. Increases in triglyceride were observed in the tetracycline treated spheroids (Chapter 4) using the triglyceride assay, however these were not significant.

Despite the lack of statistical significance for some of the increases in triglyceride levels determined by the triglyceride assay in some of the models; it was concluded that the dose levels chosen induce mild steatosis, without cytotoxicity in both monolayers and spheroids using the Oil Red O staining.

6.1.2 Metabolomics

A number of studies in the literature have used metabolomic techniques in humans and in rodent models to show alterations in metabolic pathways in NAFLD/NASH with the most common alterations observed involving changes to amino acid, bile and lipid metabolism (Caussy et al., 2019, Masoodi et al., 2021, Nimer et al., 2021, Shao et al., 2022B). However, few *in vitro* metabolomics studies have been conducted with fatty acids, tetracycline and valproate (Garcias-Canaveras et al., 2016, Chang et al., 2016, Ramirez et al., 2017) and to date no studies have investigated metabolite changes in steatosis induced by tetracycline or valproate in HepG2 spheroids.

The results from the metabolomics studies in Chapters 3,4 and 5 provided an insight into the mechanisms through which steatosis is achieved in each model. While a mixture of oleic and palmitic acid induce an increase in lipid accumulation and upregulation of beta-oxidation, tetracycline and valproate reduce beta-oxidation with both eventually leading to NASH (Cui et al., 2010, Choi et al, 2015, Garcia-Canaveras et al., 2016). These changes in metabolites could become part of a panel of possible biomarkers for the early diagnosis of steatosis. Following this, pathway analysis was completed for low and high dose groups in both monolayers and spheroids from all three models. These metabolites changes were then compared using a heatmap to identify pathways and metabolites that would increase sensitivity and specificity when diagnosing steatosis.

Figures 6.1, 6.2 and 6.3 show changes in metabolites from both monolayers and spheroids at a low and high dose for each treatment. The doses are colour coded and increases in metabolites are represented as solid boxed lines while decreases are dashed.

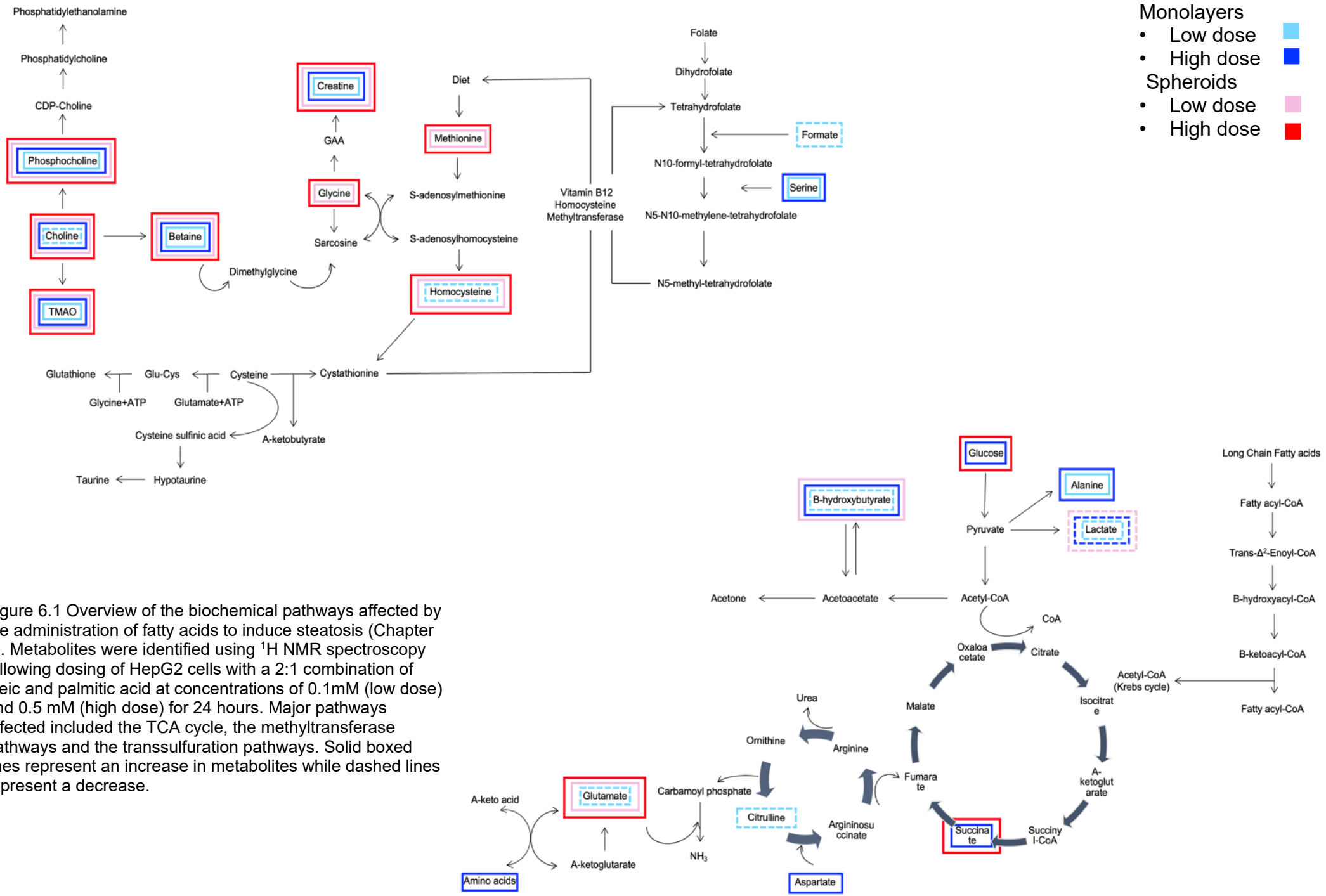

Figure 6.1 Overview of the biochemical pathways affected by the administration of fatty acids to induce steatosis (Chapter 3). Metabolites were identified using ^{1}H NMR spectroscopy following dosing of HepG2 cells with a 2:1 combination of oleic and palmitic acid at concentrations of 0.1mM (low dose) and 0.5 mM (high dose) for 24 hours. Major pathways affected included the TCA cycle, the methyltransferase pathways and the transsulfuration pathways. Solid boxed lines represent an increase in metabolites while dashed lines represent a decrease.

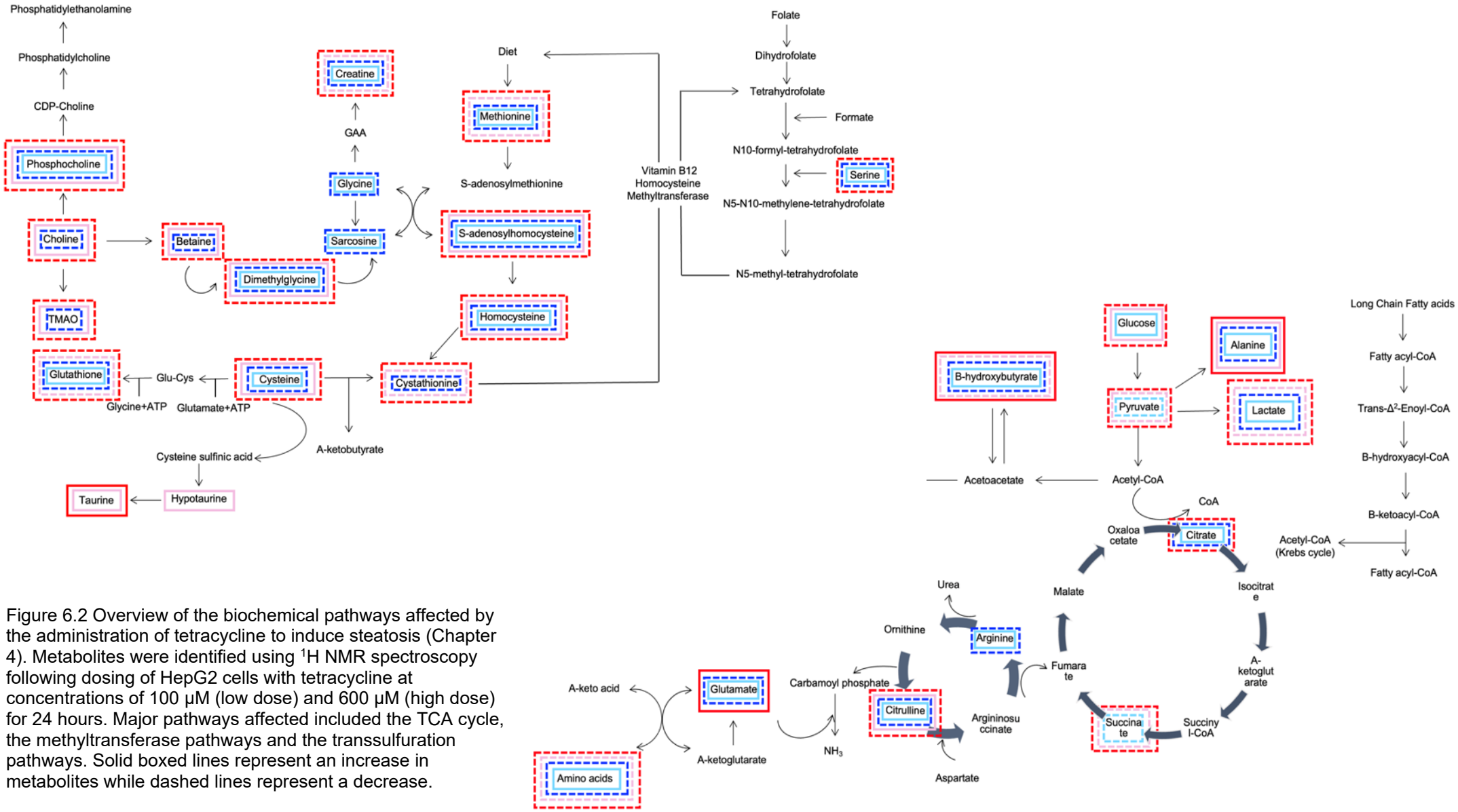

Figure 6.2 Overview of the biochemical pathways affected by the administration of tetracycline to induce steatosis (Chapter 4). Metabolites were identified using ^{1}H NMR spectroscopy following dosing of HepG2 cells with tetracycline at concentrations of 100 µM (low dose) and 600 µM (high dose) for 24 hours. Major pathways affected included the TCA cycle, the methyltransferase pathways and the transsulfuration pathways. Solid boxed lines represent an increase in metabolites while dashed lines represent a decrease.

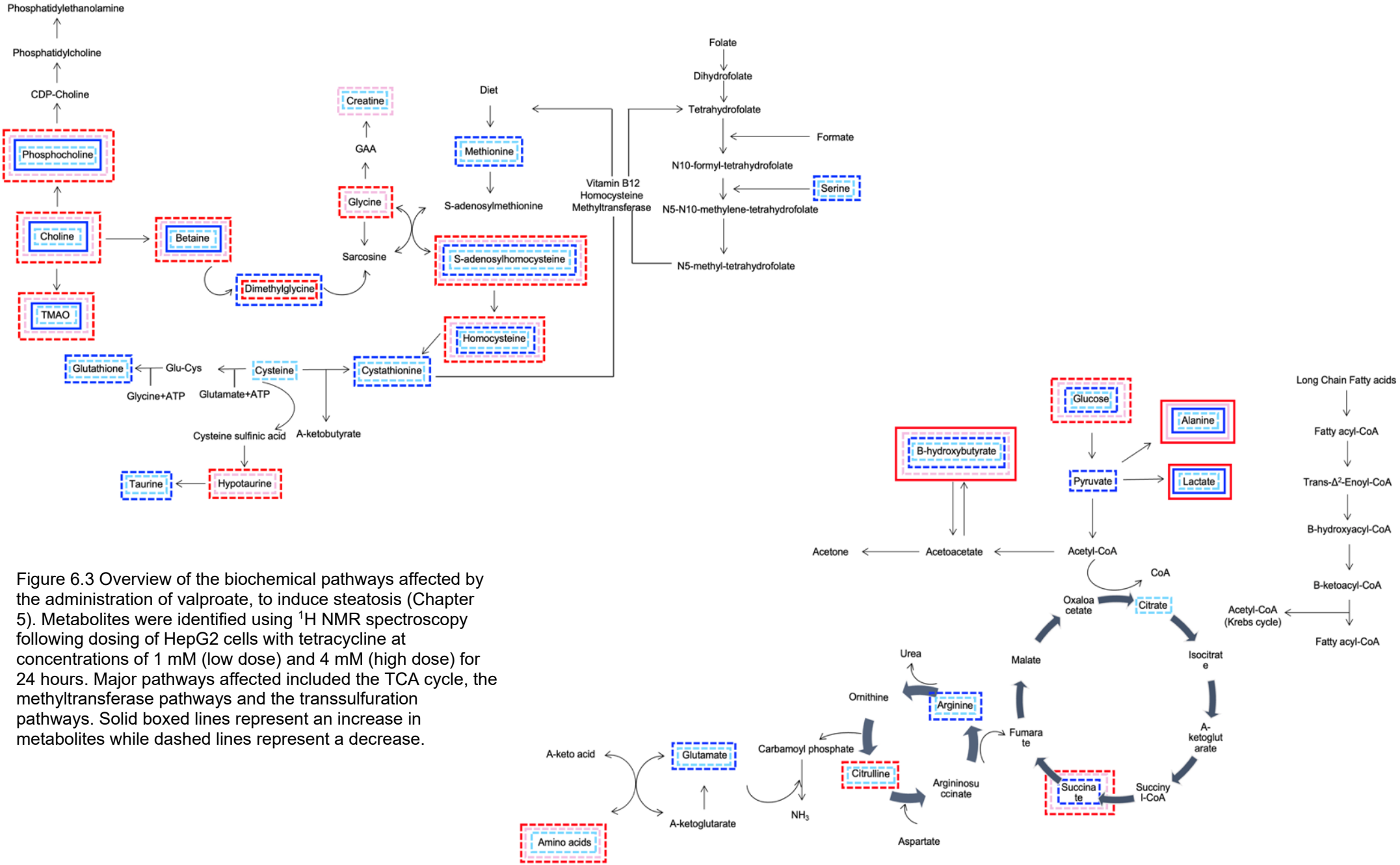

Figure 6.3 Overview of the biochemical pathways affected by the administration of valproate, to induce steatosis (Chapter 5). Metabolites were identified using ^{1}H NMR spectroscopy following dosing of HepG2 cells with tetracycline at concentrations of 1 mM (low dose) and 4 mM (high dose) for 24 hours. Major pathways affected included the TCA cycle, the methyltransferase pathways and the transsulfuration pathways. Solid boxed lines represent an increase in metabolites while dashed lines represent a decrease.

Metabolite changes observed in the pathway analysis in the figures above were grouped according to their respective pathways to identify the pathways most affected by each treatment. Increases in metabolites are shown in red while decreases are shown in blue.

Pathway	Treatment	Fatty acids				Tetracycline				Valproate			
	Model	Monolayer		Spheroid		Monolayer		Spheroid		Monolayer		Spheroid	
	Dose	L	H	L	H	L	H	L	H	L	H	L	H
CDP-choline	Phosphocholine												
	Choline												
	TMAO												
BHMT-betaine methylation	Betaine												
	Dimethylglycine												
	Sarcosine												
	Glycine												
	Creatine												
Methionine cycle	Methionine												
	S-adenosyl homocysteine												
	Homocysteine												
Trassulfuration	Cystathionine												
	Cysteine												
	Glutathione												
	Hypotaurine												
	Taurine												
Folate cycle	Formate												
	Serine												
Glycolysis	Glucose												
	Alanine												
	Lactate												
TCA cycle	Pyruvate												
	Citrate												
	Succinate												
Ketogenesis	B-hydroxybutyrate												
Urea cycle	Arginine												
	Aspartate												
	Citrulline												
Amino acid metabolism	Glutamate												
	Amino acids												

Figure 6.4 Heatmap showing metabolites changes across the three treatment groups. A low and high dose for each monolayer and spheroid models was analysed for each treatment. Each metabolite was grouped to their respective pathway. Increases= red, decreases=blue.

Figure 6.4 shows common metabolites in the metabolic pathways (Figures 6.1, 6.2, 6.3) that were altered across the three models of steatosis. The pathway with the most metabolites affected across all three models was the CDP-choline pathway and the most affected metabolite was phosphocholine which showed changes across all treated groups. The methionine cycle also had many altered metabolites including homocysteine and methionine.

Methionine may be useful for distinguishing between drug-induced and fatty acid-induced steatosis since it was decreased in the monolayer valproate groups and in the high dose monolayer and both spheroid groups in the tetracycline models demonstrating this is perhaps a common change in drug-induced steatosis. Whereas, in contrast an increase in methionine was observed in the fatty acid spheroid models, but not the monolayers.

In this project changes in homocysteine levels were observed in all models. Decreases in all valproate-treated groups were observed as well as in the tetracycline high dose groups. While homocysteine increased in the low dose tetracycline groups, this may have been due to other peaks in this region creating conflicting results. A decrease in the fatty acid monolayer occurred while increases in both spheroid groups were seen, this could be related to the increase in methionine seen in the spheroids. However, it may also be due to the metabolite regions containing peaks from other metabolites. Alterations to homocysteine levels in NAFLD are conflicting in the literature. Some studies in humans have found that circulating homocysteine is increased in NAFLD compared to controls while others have observed decreases (Gulsen et al., 2005, De Carvalho et al., 2013, Pastore et al., 2014, Jia et al., 2015). Therefore, the conflicting changes seen in these models are not different from the literature. However, it is important to highlight homocysteine as a potential biomarker of NAFLD since levels do change in response to both fatty acids and drugs and other studies have also reported the link between homocysteine and the disease mechanisms.

Homocysteine is formed during methionine turn-over by the conversion of s-adenosylhomocysteine (SAH) to homocysteine and adenosine by SAH hydrolase. In this project decreases in SAH were seen in both valproate models and in the high doses of both monolayer and spheroids in the tetracycline. As changes in SAH as well

as other methyltransferase metabolites were only observed in the high doses of the tetracycline model this could indicate that tetracycline could be inducing a more mild form of steatosis as determined in the triglyceride assay results. Changes in SAH were not apparent in the fatty acid model at all despite being expected as alterations to methionine and homocysteine were observed. The changes to SAH and homocystine could indicate that the two drugs were having an effect on methylene tetrahydrofolate reductase thereby decreasing methionine levels and could represent potential biomarkers for drug-induced steatosis.

In both drug-induced models alterations to metabolites associated with the transsulfuration pathways (TSP) were observed with decreases in cystathione and glutathione in the monolayer treated groups of both valproate and tetracycline and in the spheroid treated groups of the tetracycline. However, changes in the TSP were not observed in either of the fatty acid models in this study. Studies associated with fatty acid induced steatosis have also not commented on changes in the TSP. Nevertheless, the TSP could be a pathway of interest in drug-induced steatosis and its metabolites could potentially be part of a panel of biomarkers.

The decreases in methionine seen in the drug-induced models could result in post-transcriptional down-regulation of cystathionine β-synthase, the first enzyme in the transsulfuration of homocysteine to cystathionine, leading to decreases in glutathione (Jhee and Kruger, 2005, Tang et al., 2009, Caballero et al., 2010). Homocysteine is also involved in the TSP where it is converted to cysteine via the intermediate cystathionine and plays a key role in sulfur metabolism and the redox environment of cells (Werge et al., 2021). Nearly 50% of the homocysteine formed is further converted to cysteine by the transsulfuration pathway for further glutathione formation therefore, any decreases in homocysteine could cause decreases in TSP metabolites (Werge et al., 2021). As increases in methionine and homocysteine were seen in the fatty acid spheroid model and would be readily available for use in the TSP this may be why changes in glutathione and other TSP metabolites were not observed in this model.

In this study elevated betaine levels were observed in both the fatty acid models while general decreases were seen in the tetracycline and valproate models once again highlighting the different mechanisms inducing steatosis in these models. The

decrease in betaine seen in the drug-induced models could potentially be due to increased SAM which in turn inhibits BHMT activity (Ji et al., 2007). Overaccumulation of SAM has also been reported to downregulate BHMT expression in HepG2 cells treated with valproate in part by inducing NFxB a repressor for the human BHMT gene as discussed in Chapter 5 (Chen et al., 2014). Although betaine levels in HepG2 cells treated with tetracycline have not been described in the literature the decrease in betaine seen in the 600 µM treated groups of the spheroids and monolayers may be due to the same mechanisms. The differences in betaine levels between the drug-induced models and the fatty acids model was expected. Nevertheless, both an increase and a decrease change in betaine levels can be linked to NAFLD, therefore, betaine is a possible metabolite biomarker of interest. The differentiation between increased or decreased levels could help determine the cause of steatosis.

In this study decreases in the CDP-pathway metabolites including choline and phosphocholine were observed in the high doses of the tetracycline models, the valproate, spheroid models and the low dose monolayer. A decrease in choline was also observed in the 0.1 mM monolayer fatty acid samples indicating similar changes in both models. It has been hypothesised that tetracycline has an effect on choline metabolism subsequently leading to fatty liver (Gwee,1982). But little research has been conducted to explore this and there are no previous studies investigating the effect of valproate on choline. Figure 6.4 shows that the metabolites most affected in terms of score belong to the CDP-choline pathway as they were changed in all three treatment groups. This suggests that monitoring changes to the CDP-choline pathway could prove to be a very effective means of detecting early steatosis.

This project also revealed changes to TCA intermediates in all three models as summarised in Figures 6.1, 6.2 and 6.3. In the fatty acid model increases in succinate were observed in the two high dose groups for the spheroid and monolayer models. In contrast citrate and succinate were decreased in both drug-induced models. This is easily explained by the mechanisms by which steatosis is induced by the different treatment types. In NAFLD induced by high fat diet mitochondrial beta-oxidation is upregulated driving an increase in TCA cycle activity (Sunny et al., 2011, Fabbrini and Magkos, 2015, Fletcher et al., 2019). In contrast, tetracycline and valproate are known inhibitors of fatty acid oxidation (Miele et al., 2017). In order to make up for the loss of

acetyl-CoA from beta-oxidation it is hypothesised that glycolysis is upregulated in drug-induced steatosis (Chan et al., 2018, Dargue et al., 2020). This current study also suggests this occurs since decreases in glucose were observed in both valproate models and in the 600 µM monolayer tetracycline group. Meanwhile in the fatty acid model glucose was increased in both high doses of the spheroid and monolayers potentially indicating upregulated beta-oxidation. Thus, the measurement of TCA cycle metabolites could represent potential markers for beta-oxidation and the presence of steatosis.

In this study decreases in lactate occurred in both fatty acid models as well as in the high dose monolayer tetracycline and the spheroid model. Decreases in lactate are usually coupled with decreases in alanine and are associated with hyperlipidaemia and reduced pyruvate. However, increases in alanine were seen in the monolayer fatty acid groups but not the spheroids and also in the 4 mM monolayer group and both spheroid valproate treated groups. It is unclear why conflicting results were observed. Elevated alanine levels are potentially related to an increase in transamination of pyruvate. According to literature lactic acidosis is common in drug-induced steatosis and therefore an increase in lactate was expected in the drug-induced models (Cuykx et al., 2018B, Lee and Kim, 2019, Dargue et al., 2020). As it was increases in lactate were observed the high dose valproate models were observed. Lactic acidosis is caused by TCA cycle inhibition, and this is shown in the valproate model with the decreases in TCA cycle intermediates (Massart et al., 2013). Decreases in TCA cycle metabolites also occurred in the tetracycline model despite the decreases in lactate. Regardless, the conflicting changes in lactate, alanine and glucose were all altered in the three treatment models which suggests they may be important for the detection of early steatosis.

Figure 6.4 revealed changes in metabolites associated with the urea cycle in all three models, in particular decreases in citrulline in the 0.1 mM monolayer fatty acid, both spheroid and monolayer 600 µM tetracycline and in the 1 mM monolayer and 4 mM spheroid valproate groups. Again, like many other metabolites identified in this study, the changes in urea cycle metabolites only occurred in some groups and it is unclear why. Nevertheless, these results demonstrate that all treatments were affecting citrulline levels but cannot be confirmed as the changes were not consistent across all

groups. It has been previously suggested that the genes for urea cycle enzymes carbamoylphosphate synthetase (CPS1) and ornithine transcarbamylase (OTC) are modified in NAFLD due to mitochondrial injury leading to reduced expression and function and ultimately hyperammonaemia (De Chiara et al., 2018, Gallego-Duran et al., 2022, Thomesen et al., 2023). OTC catalyses the reaction between carbamoyl phosphate and ornithine to form citrulline and phosphate. Thus, the decreases seen in citrulline in this study may indicate that OTC gene expression is reduced in HepG2 cells although this remains to be confirmed. As decreases in citrulline were common in all treatment groups this would indicate citrulline has potential as a biomarker regardless of the steatotic cause.

Alterations in amino acids were also observed in this study with increases in the 0.5 mM monolayer of the fatty acid model, however, decreases were apparent in the high dose monolayer and both dose levels for the spheroids in the tetracycline and valproate models. Increased amino acids, seen in the fatty acid model, have been previously reported in NAFLD (Kalhan et al., 2011). In contrast, Zhang et al., (2014) demonstrated decreases in leucine and isoleucine in rats treated with valproate potentially due to an adaptive response by hepatocytes to compensate for the loss of ATP produced from beta-oxidation. Increases in branched-chain amino acids and glutamate have been implicated in insulin resistance and in obese patients with NAFLD. However, their role in NAFLD is yet to be elucidated and it remains unclear whether the change in serum amino acid levels in subjects with NAFLD and NASH is the result of altered hepatic metabolism or insulin resistance (Hasegawa et al., 2020). Although as the models present in this study represent mild steatosis insulin resistance is unlikely. Nevertheless, amino acid levels are of interest for the detection of NAFLD and could be useful for distinguishing between drug-induced steatosis and diet induced.

Organic metabolites were also identified in this project with the main metabolite changes across the three groups being in arachidonic acid, cholesterol and in multiple fatty acyl groups. Changes in cholesterol and fatty acyl groups were expected due to the increased lipid accumulation in the cells which would also confirm steatosis. Arachidonic acid has been implicated in NAFLD and is associated with increased

inflammation and the production of pro-inflammatory prostaglandins and leukotrienes which play a role in the progression of steatosis.

In summary in this project many metabolite changes were observed, and some similarities were identified between the different models. Furthermore, the metabolomics studies revealed similar changes in spheroids when compared to the monolayers which indicates they are useful *in vitro* models for the study of steatosis.

6.1.3 CYP enzyme expression

In this project 3D HepG2 spheroids models of steatosis were developed to determine if they represent a more advanced *in vitro* model than monolayers. For *in vitro* models to be reliable in biomarker studies and relevant to humans they should mimic all metabolic pathways. Spheroids are thought to have increased CYP enzyme expression compared to monolayers. This is important since CYP enzymes play a role in the development and progression of NAFLD (Aljomah et al., 2015, Woolsey et al., 2015, Jamwal and Barlock, 2020, Sukkasem et al., 2020, Albadry et al., 2022). In each Chapter in this thesis the expression levels of CYP 2D6, 3A4 and 2E1 were determined in all models using Western blotting. However, the blots suggested no real difference in CYP expression when monolayers and spheroids were compared and for all blots N=1. Therefore, it cannot be confirmed whether CYP expression in spheroids was better than monolayers as this would require repeated blots and statistical analysis in future work.

Nevertheless, the use of HepG2 spheroids particularly in the drug-induced models have offered a novel insight into metabolite changes in an *in vitro* model which is considered more reflective of the *in vivo* environment in terms of architecture and physiology due to increased cell-to-cell contact.

6.2 Limitations and future work

This project had some limitations including the lack of validation for the metabolites identified. Peak identification was mostly reliant on one-dimensional NMR spectroscopy; this was supplemented using J-RES spectroscopy but not all peaks could be confirmed using J-RES due to overlapping peaks. Although NMR is a non-destructive reproducible method of analysing metabolites there are some issues with metabolite identification as NMR techniques have low to moderate sensitivity when compared to other techniques (Alexandri et al., 2017, Williamson and Hatzakis, 2017, Emwas et al., 2019). ^{1}H NMR spectroscopy is also restricted by relatively small chemical shift windows meaning there is a greater likelihood of overlapping peaks

particularly in complex biological samples (Hughes et al., 2015, Alexandri et al., 2017, Emwas et al., 2019). Overlapping of peaks can lead to greater ambiguity in metabolite identification particularly when identifying lipids as many fatty acids share the same spectral regions and biomolecules have complex structures and often switch between different conformations. (Hughes et al., 2015, Alexandri et al., 2017, Emwas et al., 2019). Therefore, although many metabolite changes were identified in the metabolomics analysis in this study, it was not possible to identify all the metabolites particularly those in organic extracts. Nevertheless, to ensure that the metabolites identified in this experiment were as accurate as possible, metabolite peaks were only assigned if all peaks for each metabolite were present in the NMR spectra regardless of their significance in the VIP lists. Also, JRES was used to decipher overlapping peaks where assigning multiplicity was more difficult in order to give the most accurate identification possible. Future work could focus more on 2D NMR methods including J-resolved (JRES) NMR spectroscopy and also employ the use of mass spectrometry to help identify some of the unidentified metabolites. Metabolite identification could also be validated by spiking samples with known metabolite standards.

It is important to phase and baseline correct spectra to ensure peaks are in their absorptive mode and to remove noise, artefacts and baseline drifts allowing for accurate identification and quantification of signals (Emwas et al., 2018). Phasing also improves the resolution of closely spaced peaks, which is crucial when trying to distinguish between different chemical environments particularly in complex biological samples. Errors in phasing can result in shifts in peak position particularly in crowded regions of the spectrum resulting in incorrect chemical shift assignments and mistakes in metabolite identification. Spectra were manually phased, and baseline corrected in this study which allows for fine-tuning of peak shapes particularly when phasing spectra with overlapping peaks and crowded regions (Ernst et al., 1990, Claridge, 2016, Emwas et al., 2018). Although this process is time consuming and automatic phasing is possible, automatic phasing relies on algorithms which can struggle with complex spectra and overlapping peaks. Manual baseline correction allows for tailored adjustments of the baseline which can be particularly useful for complex spectra and can allow the user to address noise spikes and artefacts that automatic correction may miss (Ernst et al., 1990, Claridge, 2016, Emwas et al., 2018). However, automatic spectra can consistently apply the same phasing procedure across multiple spectra

reducing variability. Although spectra were manually phased and baseline in the same way there was potential for human error which could have introduced errors in peak shapes leading to incorrect metabolite identification or outliers.

Additionally, metabolite peaks were identified solely based on literature and the Human Metabolome database. While the Human Metabolome Database (HMDB) is perhaps the most extensive public metabolomic spectral database to date and stores more than 40,000 different metabolites the physical diversities of metabolites make them difficult to identify (Xiao et al., 2012, Alonso et al., 2015). The development of innovative computational strategies has been a major driver in overcoming some of the challenges with metabolite identification (Johnson et al., 2016). There are now online tools available including MetaboHunter which matches the reference peak positions against a list of detected peak positions automatically. FOCUS is an algorithm that follows the same metabolite identification approach but with the added advantage that it can discriminate between partially overlapping metabolites (Alonso et al., 2013, Alonso et al., 2015). These online tools could be implemented in future work to validate metabolite identification.

The metabolite changes that were observed are connected to the onset and progression of steatosis but are also associated with general liver injury including oxidative stress and cholestasis (Martinez-Sena et al., 2023). Therefore, identifying changes in these metabolites alone would not give an accurate diagnosis of steatosis. But could be useful in a panel of biomarkers. The *in vitro* models described in this project could also be improved by 3D co-culturing HepG2 cells with Kupffer or stellate cells as this would provide a better representation of the complete *in vivo* phenotype. Co-cultured models also demonstrate the impact of cytokine signalling and would allow for the progression of steatosis to NASH and fibrosis to be assessed (Muller and Strula, 2019, Ouchi et al., 2019, Bialkowska et al., 2020). Although studies have demonstrated the use of HepG2 cells in 3D spheroid co-culturing none have conducted metabolomics studies to find potential biomarkers of steatosis. This would be of great interest for future work as metabolite changes identified in co-cultured models would have greater sensitivity and have greater specificity to the different stages of NAFLD. Additionally, steatosis is usually associated with prolonged and repeated exposure particularly when it is drug-induced as patients take repeated

doses for long periods of time. Future work could include repeat dosing studies using tetracycline and valproate in 3D spheroids. This would allow for more accurate metabolite analysis which were more reflective of clinical settings and would identify more sensitive biomarkers for drug-induced steatosis. Also, to validate the current models as mild models of steatosis in the cells it would be necessary to test for oxidative stress markers as more severe forms of steatosis are associated with increased ROS production and oxidative stress (Donato et al., 2009). This could be measured using assays that measure DNA/RNA damage, lipid peroxidation and protein oxidation/nitration as well as levels of ATP.

The techniques used in this study could also be applied to clinical research in patients taking the drugs used in this study particularly valproate. As valproate treatment is usually long term NMR metabolomics and multivariate analysis of blood and urine samples could offer a non-invasive technique to assess the development and or progression of steatosis in patients.

Despite the limitations this thesis has provided a novel overview of the major metabolite pathways affected in mild steatosis regardless of how it has been induced and this will aid the future search for sensitive biomarkers for the early detection of steatosis.

Chapter Seven- References

Chapter 7

7.1 References

Abdel-Gelil, O.E.A. and Mansour, S.R. (2019). Tetracycline and toxicity induced. Gastroenterology & Hepatology: Open Access, 10 (4), 177-179.

Abdel-Misih, S.R.Z. and Bloomston, M. (2010). Liver Anatomy. Surgical Clinics of North America, 90 (4), 643-653.

Abdi, H. and Williams, L.J. (2010). Principal component analysis. Wiley Interdisciplinary Reviews, 2 (4), 433-459.

Abe, N., Tsuchida, T., Yasuda, S.I. and Oka, K. (2019). Dietary iron restriction leads to a reduction in hepatic fibrosis in a rat model of non-alcoholic steatohepatitis. Biology Open, 8, 1-9.

Adan, A., Kiraz, Y. and Baran, Y. (2016). Cell Proliferation and Cytotoxicity Assays. Curr. Pharm. Biotechnol, 17 (14), 1213-1221.

Ai, Y., Sun, Z., Peng, C., Liu, L., Xiao, X. and Li, J. (2017). Homocysteine Induces Hepatic Steatosis Involving ER Stress Response in High Methionine Diet-Fed Mice. Nutrients, 9 (4), 346).

Aissa, A.F., Tryndyak, V., de Conti, A., Melnyk, S., Gomes, T..D..U.H., Bianchi, M.L.P., James, J., Beland, F.A., Antunes, M.G. and Pogribny, P. (2014). Effect of methionine-deficient and methionine-supplemented diets on the hepatic one-carbon and lipid metabolism in mice. Molecular Nutrition, 58 (7), 1502-1512.

Albadry, M., Hopfl, S., Ehteshamzad, N., Konig, M., Bottcher, M., Neumann, J., Lupp, A., Dirsch, O., Radde, N., Christ, B., Christ, M, Schwen, L.O., Laue, H., Klopfleisch, R. and Dahmen, U. (2022). Periportal steatosis in mice affects distinct parameters of pericentral drug metabolism. Scientific Reports, 12 (21825).

Alexandri, E., Ahmed, R., Siddiqui, H., Choudhary, M.I., Tsiafoulis, C.G. and Gerothanassis, I.P. (2017). High Resolution NMR Spectroscopy as a Structural and Analytical Tool for Unsaturated Lipids in Solution. Molecules, 22 (10), 1663.

AlGhamdi, S. (2019). Drug-Induced Fatty Liver. International Journal of Pharmaceutical Research & Allied Sciences, 8 (4), 82-90.

Aljomah, G., Baker, S.S., Liu, W., Kozielski, R., Oluwole, J., Lupu, B., Baker, R.D. and Zhu, L. (2015). Induction of CYP2E1 in non-alcoholic fatty liver disease. Exp Mol Pathol, 99 (3), 677-681.

Alkhatatbeh, M.J., Lincz, L.F. and Thorne, R.F. (2016). Low simvastatin concentrations reduce oleic acid-induced steatosis in HepG2 cells: An in vitro model of non-alcoholic fatty liver disease. Experimental And Therapeutic Medicine, 11 (4), 1487-1492.

Allard, J., Bucher, S., Massart, J., Ferron, P.J., Guillou, D.L., Loyant, R., Daniel, Y., Launay, Y., Buron, N., Begriche, K., Borgne-Sanchez, A. and Fromenty, B. (2020). Drug-induced hepati steatosis in absence of severe mitochondrial dysfunction in HepaRG cells: proof of multiple mechanism-based toxicity. Cell Biology and Toxicology, 37, 151-175.

Allen, M.J., Sabir, S. and Sharma, S. (2023). GABA Receptor. StatPearls Publishing. Available from: https://www.ncbi.nlm.nih.gov/books/NBK526124/

Alonso-Aperte, E., Ubeda, N., Achon, M., Perez-Miguelsanz, J. and Varela-Moreiras, G. (1999). Impaired methionine synthesis and hypomethylation in rats exposed to valproate during gestation. Neurology, 52 (4), 750-6.

Alonso, A., Rodriguez, M.A., Vinaixa, M., Tortosa, R., Correig, X., Julia, A. and Marsal, S. (2014). Focus: A Robust Workflow for One-Dimensional NMR Spectral Analysis. Anal Chem, 86 (2), 1160-1169.

Alonso, A., Marsal, S. and Julia, A. (2015). Analytical methods in untargeted metabolomics: state of the art in 2015. Frontiers in Bioengineering and Biotechnology, 3.

Alshaalan, R., Ajiffry, M., Al-Busafi, S., Metrakos, P and Hassanain, M. (2015). Nonalcoholic Fatty Liver Disease: Noninvasive Methods of Diagnosing Hepatic Steatosis. The Saudi Journal of Gastroenterology, 21 (2), 64-70.

Alves-Bezerra, M. and Cohen, D.E. (2017). Triglyceride metabolism in the liver. Comprehensive Physiology, 8 (1), 1-8.

Alves, S., Paris, A. and Rathahao-Paris, E. (2020). Chapter Four- Mass spectrometry-based metabolomics for an in-depth questioning of human health. Advances in Clinical Chemistry, 99, 147-191.

Amacher, D.E. and Chalasani, N. (2014). Drug-Induced Hepatic Steatosis. Seminars in Liver Disease, 34 (02), 205-214.

Ameer, F. and Zaidi, N. (2014). De novo lipogenesis in health and disease. Metabolism, 63 (7), 895-902.

Amoresano, A. and Pucci, P. (2022). Chapter 40- Mass spectrometry in metabolomics. Metabolomics Perspectives, 109-147.

An, Z., Hu, T., Lv, Y., Li, P. and Liu, L. (2020). Targeted amino acid and related amines analysis based on iTRAQ®-LC-MS/MS for discovering potential hepatotoxicity biomarkers. Journal of Pharmaceutical and Biomedical Analysis, 178, 112812.

Andersson, E.R., Day, R.D., Loewenstein, J.M., Woodley, C.M. and Schock, T.B. (2019). Evaluation of Sample Preparation Methods for the Analysis of Reef-Building Corals Using ^{1}H-NMR-Based Metabolomics. Metabolites, 9 (2), 32.

Andrade R.J. and Tulkens, P.M. (2011). Hepatic safety of antibiotics used in primary care. Journal of Antimicrobial Chemotherapy, 66 (1), 1431-1446.

Antcliffe, D. and Gordon, A.C. (2016). Metabonomics and intensive care. Critical Ca, 20 (68), 1-7. Arguello, G., Balboa, E., Arrese, M. and Zanlungo, S. (2015), Recent insights on the role of cholesterol alcoholic fatty liver disease. Biochimica et Biophysica Acta- Molecular Basis of Disease, 1852 (9), 1765-1778.

Antherieu, S., Rogue, A., Fromentry, B., Guillouzo, A. and Robin, M.A. (2011). Induction of vesicular steatosis by amiodarone and tetracycline is associated with up-regulation of lipogenic genes in heparg cells. AASLD, 53 (6), 1895-1905.

Apica, B.S. and Lee, W.M. (2014). Drug-Induced Liver Injury. Pathobiology of Human Disease, 1825-1837.

Arendt, B.M., Comelli, E.M., Ma, D.W., Lou, W., Teterina, A., Kim, T., Fung, D.K.H., McGilvray, I., Fischer, S.E. and Allard, J.P. (2015). Altered hepatic gene expression in non-alcoholic fatty liver disease is associated with lower n-3 and n-6 polyunsaturated fatty acids. Hepatology, 61, 1565–1578.

Arroyave-Ospina, J.C., Wu, Z., Geng, Y. and Moshage, H. (2021). Role of Oxidative Stress in the Pathogenesis of Non-Alcoholic Fatty Liver Disease: Implications for Prevention and Therapy. Antioxidants, 10 (2), 174.

Atienzar, F.A., Novik, E.I., Gerets, H.H., Parkeh, A., Delatour, C., Cardenas, A., MacDonald, J., Yarmush, M.L. and Dhalluin, S. (2014). Predictivity of dog co-culutre model, primary human hepatocytes and HepG2 cells for the detection of hepatotoxic drugs in humans. Toxicology and Applied Pharmacology, 257 (1), 44-61.

Aubert, J., Begriche, K., Knockaert, L., Robin, M.A. and Fromenty, B. (2011). Increased expression of cytochrome P450 2E1 in nonalcoholic fatty liver disease: Mechanisms and pathophysiological role. Clinics and Research in Hepatology and Gastroenterology, 35 (10), 630-637.

Ayala, A., Munoz, M.F. and Arguelles, S. (2014). Lipid Peroxidation: Production, Metabolism, and Signalling Mechanisms of Malondialdehyde and 4-hydroxy-2-Nonenal. Oxidative Medicine and Cellular Longevity, 360438, 1-31.

Badrick, T. (2021). Biological variation: Understanding why it is so important? Pract Lab Med, 23, e00199.

Baker, S.S., Baker, R.D., Liu, W., Nowak, N.J. and Zhu, L. (2010). Role of alcohol metabolism in non-alcoholic steatohepatitis. PLoS One, 5, e9570.

Bai, X., Hong, W., Cai, P., Chen, Y., Xu, C., Cao, D., Yu, W., Zhao, Z., Huang, Min. and Jin, J. (2017). Valproate induced hepatic steatosis by enhanced fatty acid uptake and triglyceride synthesis. Toxicology and Applied Pharmacology, 324, 12-25.

Bai, X.P., Dong, F., Yang, G.H. and Zhang, L. (2019). Influences of sterol regulatory element binding protein-1c silencing on glucose production in HepG2 cells treated with free fatty acid.

Bale, G., Vishnubhotla, R.V., Mitnala, S., Sharma, M., Padaki, R.N., Pawar, S.C. and Duvvur, R.N. (2019). Whole-Exome Sequencing Identifies a Variant in Phosphatidylethanolamine N-Methyltransferase Gene to be Associated With Lean-Nonalcoholic Fatty Liver Disease. J. Clin. Exp. Hepatol, 9, 561–568.

Balkrishna, A., Gohel, V., Kumari, P., Manik, M., Bhattacharya, K., Dev, R. and Varshney, A. (2022). Livogrit Prevents Methionine-Cysteine Deficiency Induced Nonalcoholic Steatohepatitis by Modulation of Steatosis and Oxidative Stress in Human Hepatocyte-Derived Spheroid and in Primary Rat Hepatocytes, Bioengineered, 13 (4), 10811-108261.

Basaranoglu, M., Basaranoglu, G. and Senturk, H. (2013). From fatty liver to fibrosis: A tale of “second hit” World Journal of Gastroenterology, 19 (8), 1158-1165.

Basit, H., Tan, M.L. and Webster, D.R. (2020). Histology, Kupffer Cell. StatPearls. Treasure Island (FL).

Bataller, R. and Brenner, D.A. (2005). Liver Fibrosis. J Clinc Invest, 115 (2), 209-218.

Bedossa, P. (2014). Utility and appropriateness of the fatty liver inhibition of progression (FLIP) algorithm and steatosis, activity, and fibrosis (SAF) score in the evaluation of biopsies of nonalcoholic fatty liver disease. Hepatology, 60 (2), 565-575.

Begriche, K., Massart, J., Robin, M.A., Borgne-Sanchez, A. and Fromenty, B. (2010). Drug-induced toxicity on mitochondria and lipid metabolism: mechanistic diversity and deleterious consequences for the liver. J Hepatol, 54 (4), 773-94.

Bell, C.C., Hendriks, D.F.G., Moro, S.M.L., Ellis, E., Walsh, J., Renblom, A., Fredriksson Puigvert, L., Dankers, A.C.A., Jacobs, F., Snoeys, J., Sison-Young, R.L., Jenkins, R.E., Nordling, A., Mkrtchian, S., Park, B.K., Kitteringham, N.R. Goldring, C.E.P., Lauschke, V.M. and Ingelman-Sundberg, M. (2016). Characterization of primary human hepatocyte spheroids as a model system for drug-induced liver injury, liver function and disease. Scientific reports, 6 (25187).

Bell, L.N., Temm, C.J., Saxena, R., Vuppalanchi, R., Schauer, P., Rabinovitz, M., Krasinskas, A., Chalasani, N. and Mattar, S.G. (2010). Bariatric Surgery-Induced Weight
Loss Reduces Hepatic Lipid Peroxidation Levels and Affects Hepatic Cytochrome P-450 Protein Content. Ann Surg, 251 (6), 1041-1048.

Bell, L.N., Molleston, J.P., Morton, M.J., Klipsch, A., Saxena, R., Vuppalanchi, R. and Chalasani, N. (2011). Hepatic Lipid Peroxidation and Cytochrome P-450 2E1 in Pediatric Nonalcoholic Fatty Liver Disease and its Subtypes, 45 (9), 800-807.

Bennett, S. and Shad, M.U. (2021). Valproic acid autoinduction: a case-based review. International Journal of Bipolar Disorders, 9 (27).

Berridge, M.V., Herst, P.M. and Tan, A.S. (2005) Tetrazolium dyes as tools in cell biology: new insights into their cellular reduction. Biotechnol Annu Rev, 11 (1), 127–152.

Bhatt, H.B. and Smith, R.J. (2015). Fatty liver disease in diabetes mellitus. Hepatobiliary Surgery and Nutrition, 4 (2), 101-108.

Bhinderwala, F., Roth, H.E., Noel, H., Feng, D. and Powers, R. (2022). Chemical shift variations in common metabolites. Journal of Magnetic Resonance, 345.

Bi, H., Krausz, K.W., Manna, S.K., Li, F., Johnson, C.H. and Gonzalez, F.J. (2013). Optimization of harvesting, extraction, and analytical protocols for UPLC-ESI-MS-based metabolomic analysis of adherent mammalian cancer cells. Anal Bioanal Chem, 405 (15), 5279-5289.

Bialkowska, K., Komorowski, P., Bryszewska, M. and Milowska, K. (2020). Spheroids as a Type of Three-Dimensional Cell Cultures-Examples of Methods of Preparation and the Most Important Application. Int J Mol Sci, 21 (17), 6225.

Blohm, E., Lai, J. Neavyn, M. (2017). Drug-induced hyperlactatemia. Clin Toxicol, 55 (8), 869-878.

Boeckmans, J. and Rodrigues, R.M. (2018). Human-based systems: Mechanistic NASH modelling just around the cornoer? Pharmacological Research, 134, 257-267.

Boyer, J.L. (2013). Bile Formation and Secretion. Comprehensive Physiology, 3 (3), 1035-1078.

Breen, K., Schenker, S. and Heimberg M. (1972). The effect of tetracycline on the hepatic secretion of triglyceride. Biochim. Biophys, 270, 74–80.

Breen, K.J., Schenker, S. and Heimberg, M. (1975). Fatty Liver Induced By Tetracycline In The Rat. Gastroenterology, 69 (3), 714-723.

Britton, L.J., Subramaniam, V.N. and Crawford, D.H.G. (2016). Iron and non-alcoholic fatty liver disease. World J Gastroenterol, 22 (36), 8112-8122.

Brosnan, M.E. and Brosnan, J.T. (2016). Formate: The Neglected Member of One-Carbon Metabolism. Annual Review of Nutrition, 36, 369-399.

Brüning, A., Brem, G.J., Vogel, M. and Mylonas, I. (2014). Tetracyclines cause cell stress-dependent ATF4 activation and mTOR inhibition. Exp. Cell Res, 320, 281–289.

Buzzetti, E., Pinzani, M. and Tsochatzis, E.A. (2016). The multiple-hit pathogenesis of non-alcoholic fatty liver disease (NAFLD). Metabolism, 65 (8), 1038-48.

Bylesjo, M., Rantalainen, M., Cloarec, O., Nicholson, J.K., Holmes, E. and Trygg, J. (2007). OPLS discriminant analysis: combining the strengths of PLS-DA and SIMCA classification. Journal of Chemometrics, 20 (8-10), 341-351.

Caballero, F., Fernandez, A., Matias, N., Martinez, L., Fucho, R., Elena, M., Caballeria, J., Morales, A. and Fernandez-Checa. (2010). Specific contribution of methionine and choline in nutritional nonalcoholic steatohepatitis: impact on mitochondrial S-adenosyl-L-methionine and glutathione. Lipids, 285, (24), 18528-18536.

Calder, P.C. (2020). Eicosanoids. Essays Biochem, 64 (3), 423-441.

Carretero, A., Leon, Z., Garcia-Canaveras, J.C., Zaragoza, A., Gomez-Lechon, M.J., Donato, M.T. and Lahoz, A. (2014). In vitro/in vivo screening of oxidative homeostasis and damage to DNA, protein, and lipids using UPLC/MS-MS. Anal Bioanal Chem, 406 (22), 5465-76.

Castaneda, F. and Kinne, R.K. (2000). Short exposure to millimolar concentrations of ethanol induces apoptotic cell death in multicellular HepG2 spheroids. J Cancer Res Clin Oncol. 126 (6), 305-10.

Castell, J., Jover, R., Martinez-Jimnez, C.P. and Gomez-Lechon, M.J. (2006). Hepatocyte cell lines: their use, scope and limitations in drug metabolism studies. Expert Opinion on Drug Metabolism &Toxicology, 2 (2).

Caussy, C., Hsu, C., Singh, S., Bassirian, S., Kolar, J., Faulkner, C., Sinha, N., Bettencourt, R., Gara, N., Valasek, M.A., Schnabl, B., Richards, L., Brenner, D.A., Hofmann, A.F. and Loomba, R. (2019). Serum bile acid patterns are associated with the presence of NAFLD in twins, and dose-dependent changes with increase in fibrosis stage in patients with biopsy-proven NAFLD. Aliment. Pharmacol. Ther. 49 (2), 183–193.

Cerveny, L., Svecova, L., Anzenbacherova, E., Vrzal, R., Staud, F., Dvorak, Z., Ulrichova, J., Anzenbacher, P. and Pavek. (2007). Valproic Acid Induces CYP3A4 and MDR1 Gene Expression by Activation of Constitutive Androstane Receptor and Pregnane X Receptor Pathways. Drug Metabolism and Disposition, 35 (7), 1032-1041.

Champier, J., Claustrat, F., Nazaret, N., Montange, M.F. and Claustrat, B. (2012). Folate depletion changes gene expression of fatty acid metabolism, DNA synthesis and circadian cycle in male mice. Nutrition Research, 32, 2, 124-132.

Chan, T.S., Cassim, S., Raymond, V.A., Gottschalk, S., Merlem, G., Zwingmann, C., Lapierre, P., Darby, P., Mazer, C.D. and Bilodeau, M. (2018). Upregulation of Krebs cycle and anaerobic glycolysis activity early after onset of liver ischemia. PLoS One, 13 (6), e0199177.

Chang, T.T. and Hughes-Fulford, M. (2009). Monolayer and Spheroid Culture of Human Liver Hepatocellular Carcinoma Cell Line Cells Demonstrate Distinct Global Gene Expression Patterns and Functional Phentotypes. Tissue Engineering, 559-567.

Chang, R., Chou, M.C., Hung, L.Y., Wang, M.E., Hsu, M.C. and Chiu, C.H. (2016). Study of Valproic Acid-Enhanced Hepatocyte Steatosis. Drug-Induced Liver Injury, 9576503, 1-11.

Chateauvieux, S., Morceau, F., Dicato, M. and Diederich, M. (2010). Molecular and therapeutic potential and toxicity of valproic acid. J Biomed Biotechnol.

Chen, C., Gao, J., Wang, T.S., Guo, C., Yan, Y.J., Mao, C.Y., Gu, L.W., Yang, Y., Li, Z.F. and Liu, A. (2018A). NMR-based Metabolomic Techniques Identify the Toxicity of Emodin in HepG2 Cells. Scientific Reports, 8 (9379).

Chen, M., Suzuki, A., Borlak J., Andrade, R.J. and Lucena, I. (2015). Drug-induced liver injury: Interactions between drug properties and host factors. Journal of Hepatology, 63 (2), 503-514.

Chen, J., Liu, Y., Luo, H., Chen, G., Zheng, Z., Wang, T., Hu, X., Zhao, Y., Tang, J., Su, C. and Zha, L. (2022). Inflammation Induced by Lipopolysaccharide and Palmitic Acid Increases Cholesterol Accumulation via Enhancing Myeloid Differentiation Factor 88 Expression in HepG2 Cells. Pharmaceuticals, 15 (5), 813.

Chen, X., Li, L., Liu, X., Luo, R., Liao, G., Li, L., Liu, J., Cheng, J., Lu, Y. and Chen, Y. (2018B). Oleic acid protects saturated fatty acid mediated lipotoxicity in hepatocytes and rat of non-alcoholic steatohepatitis. Life Sci, 203, 291–304.

Chen, Y., Shen, G., Zhang, R., He, J., Zhang, Y., Xu, J., Yang, W., Chen, X., Song, Y. and Abliz, Z. (2013). Combination of injection volume calibration by creatinine and MS signals' normalization to overcome urine variability in LC-MS-based metabolomics studies. Anal Chem, 85 (16), 7659-65.

Chen, Y., Lin, P.X., Hsieh, C.L., Peng, C.C. and Peng, R.Y. (2014). The Proteomic and Genomic Teratogenicity Elicited by Valproic Acid Is Preventable with Resveratrol and α-Tocopherol. PLOS ONE, 9 (12).

Chiba, T., Suzuki, S., Sato, Y., Itoh. T. and Umegaki, K. (2016). Evaluation of Methionine Content in a High-Fat and Choline-Deficient Diet on Body Weight Gain and the Development of Non-Alcoholic Steatohepatitis in Mice. PLOS One, 11 (10), 1-17.

Choi, Y.J., Lee, C.H., Lee, K.Y., Jung, S.H. and Lee, B.H. (2015). Increased Hepatic Fatty Acid Uptake and Esterification Contribute to Tetracycline-Induces Steatosis in Mice. Toxicological Sciences, 145 (2), 273-282.

Chopra, I. and Roberts, M. (2001). Tetracycline Antibiotics: Mode of Action, Applications, Molecular Biology, and Epidemiology of Bacterial Resistance. Microbiology and Molecular Biology Reviews, 65 (2).

Christensen, K.E., Wu, Q., Wang, X., Deng, L., Caudill, M.A. and Rozen, R. (2010). Steatosis in Mice Is Associated with Gender, Folate Intake, and Expression of Genes of One-Carbon Metabolism. The Journal of Nutrition, 140 (10), 1736-1741.

Claridge, T.D.W. (2016). High-resolution NMR techniques in organic chemistry. Elsevier, Amsterdam 3rd Edition.

Cobbina, E. and Akhlaghi, F. (2016). Non-alcoholic fatty liver disease (NAFLD)- pathogenesis, classification, and effect on drug metabolizing enzymes and transporters. Drug Metabolism Reviews, 49 (2), 197-211.

Corbin, K.D. and Zeisel, S.H. (2012). Choline Metabolism Provides Novel Insights into Non-alcoholic Fatty Liver Disease and its Progression. Current Opinions In Gastroenterology, 28 (2), 159-165.

Cotter, D.G., Ercal, B., Huang, X., Leid, J.M., d'Avignon, D.A., Graham, M.J., et al. (2014). Ketogenesis Prevents Diet-Induced Fatty Liver Injury and Hyperglycemia. J Clin Invest, 124, 5175-5190.

Cox, C.R., Lynch, S., Goldring, C. and Sharma, P. (2020). Current Perspective: 3D Spheroid Models Utilizing Human-Based Cells for Investigating Metabolism-Dependent Drug-Induced Liver Injury. Front. Med. Technol, 2 (611913).

Craig, A., Cloarec, O., Holmes, E., Nicholson, J.K. and Lindon, J.C. (2006). Scaling and Normalization Effects in NMR Spectroscopy Metabonomic Data Sets. Analytical Chemistry, 78 (7), 2262-2267.

Craig, S.A.S. (2004). Betaine in human nutrition. The American Journal of Clinical Nutrition, 80 (3), 539-549.

Crettol, S., Petrovic, N. and Murray, M. (2010). Pharmacogenetics of phase I and phase II drug metabolism. Curr Pharm Des, 16 (2), 204-219.

Cui, H., Li, Y., Cao, M., Liao, J., Liu, X., Miao, J., Fu, H., Song, R., Wen, W., Zhang, Z. and Wang, H. (2020). Untargeted Metabolomic Analysis of the Effects and Mechanism of Nuciferine Treatment on Rats with Nonalcoholic Fatty Liver Disease. Frontiers in Pharmacology, 11 (858).

Cui, W., Chen, S.L. and Hu, K.H. (2010). Quantification and mechanisms of oleic acid-induced steatosis in HepG2 cells. American Journal of Translational Research, 2 (1), 95-104.

Cullen, J.M. and Stalker, M.J. (2016). Liver and Biliary System. Jubb. Kennedy & Palmer's Pathology of Domestic Animals, 2, 258-352.

Cuykx, M., Claes, L., Rodrigues, R.M., Vanhaecke, T. and Covaci, A. (2018A). Metabolomics profiling steatosis progression in HepaRG cells using sodium valproate. Toxicology Letters, 286, 22-30

Cuykx, M., Rodriigues, R.M., Laukens, K., Vanhaecke, T. and Covaci, A. (2018B). In vitro assessment of hepatotoxicity by metabolomics: a review. Arch Toxicol, 92 (10), 3007-3029.

Da Silva, R.P., Kelly, K.B., Rajabi, A.A. and Jacobs, R.L. (2014). Novel insights on interaction between folate and lipid metabolism. BioFactors, 40 (3), 277-283.

Dahiru, T. (2008). *P*-VALUE, A TURE TEST OF STATISTICAL SIGNIFICANCE? A CAUTIONARY NOTE. Ann Ib Postgrad Med, 6 (1), 21-26.

Dai, H., Wang, W., Tang, X., Chen, R., Chen, Z., Lu, Y. and Yuan, H. (2016). Association between homocysteine and non-alcoholic fatty liver disease in Chinese adults: a cross-sectional study. Nutrition Journal, 15 (102), 1-7.

Dargue, R., Zia, R., Lau, C., Nicholls, A.W., O Dare, T., Lee, K., Jalan, R., Coen, M. and Wilson, I.D. (2020). Metabolism and Effects on Endogenous Metabolism of Paracetamol (Acetaminophen) in a Porcine Model of Liver Failure. Toxicological Sciences, 175 (1), 87-89.

Das U.N. (2006). Essential fatty acids: Biochemistry, Physiological and Pathology. Biotechnol J, 1, 420-439.

Dash, A., Figler, R.A., Sanyal, A.J. and Wamhoff, B.R. (2020). Drug-induced steatohepatitis. Expert Opin Drug Metab Toxicol, 13 (2), 193-204.

Dashti, N and Wolfbauer, G. (1987). Secretion of lipids, apolipoproteins, and lipoproteins by human hepatoma cell line, HepG2: effects of oleic acid and insulin. Journal of Lipid Research, 28 (4), 423-436.

Dave, T., Tilles, A.W. and Vemula, M. (2018). A Cell-Based Assay to Investigate Hypolipidemic Effects on Nonalcoholic Fatty Liver Disease Therapeutics. SLAS Discovery, 23 (3), 274-282.

De Carvalho, S.C.R., Muniz, M.T.C., Siqueira, M.D.V., Siqueira, E.R.F., Gomes, A.V., Silva, K.A., Bezerra, L.C.L., D'Almeida, V., De Oliveira, C.P.M.S. and Pereira, L.M.M.B. (2013). Plasmatic higher levels of homocysteine in Non-alcoholic fatty liver disease (NAFLD). Nutr. J, 12, 37.

De Chiara, F., Heeboll, S., Marrone, G., Montoliu, C., Hamilton-Dutoit, S., Ferrandez, A., Andreola, F., Rombouts, K., Gronbaek, H., Felipo, V., Gracia-Sancho, J., Mookerjee, R.P., Vilstrup, H., Jalan, R. and Thomsen, K.L. (2018). Urea cycle dysfunction in non-alcoholic fatty liver disease. Journal of Hepatology, 69 (4), 905-915.

De Graaf, R.A., Prinsen, H., Giannini, C., Caprio, S. and Herzog, R.I. (2015). Quantification of ^{1}H NMR Spectra from Human Plasma. Metabolomics, 11 (6), 1702-1707.

Deng, Q.G., She, H., Cheng, J.H., French, S.W., Koop, D.R., Xiong, S. and Tsukamoto, H. (2005). Steatohepatitis induced by intragastric overfeeding in mice. Hepatology, 42, 905–914.

Denhaz, B., Rousseau, M., Spino, C., Dancosst, D.A., Dumas, M.E., Guay, A., Lizotte, F. and Geraldes, P. (2020). Saturated fatty acids induce insulin resistance in podocytes through inhibition of IRS1 via activation of both IKKβ and mTORC1. Scientific Reports, 21628.

Depner, C.M., Philbrick, K.A. and Jump, D.B. (2013). Docosahexaenoic acid attenuates hepatic inflammation, oxidative stress, and fibrosis without decreasing hepatosteatosis in a Ldlr(−/−) mouse model of western diet-induced nonalcoholic steatohepatitis. J Nutr, 143, 315–323.

De Sousa, J., Prom, C.M. and Lock, A.L. (2021). Altering the ratio of dietary palmitic acid and oleic acids affects production responses during the immediate postpartum and carryover periods in dairy cows. Journal of Diary Science, 104 (3), 2896-2909.

Desouza, C., Keebler, M., Namara, D.B. and Fonseca V. (2002). Drugs affecting homocysteine metabolism: impact on cardiovascular risk. Drugs, 62: 605–616.

Dettmer, K., Nürnberger, N., Kaspar, H., Gruber, M. A., Almstetter, M. F., and Oefner, P. J. (2011). Metabolite extraction from adherently growing mammalian cells for metabolomics studies: optimization of harvesting and extraction protocols. *Analytical and Bioanalytical Chemistry, 399*, 1127–1139.

Dharmalingham, M. and Yamasandhi, P.G. (2018). Nonalcoholic Fatty Liver Diseaseand Type 2 Diabetes Mellitus. Indian J Endocrinol Metab, 22 (3), 421-428.

Di Marzo, V. (1995). Arachidonic acid and eicosanoids as targets and effectors in second messenger interactions. Prostag Leukotr Ess, 53, 239-254.

Di Mauro, S., Alessandra, S., Filipello, A., Di Pino, A., Scicali, R., Malaguarnera, R., Purrello, F. and Piro, S. (2021). Clinical and Molecular Biomarkers for Diagnosis and Staging of NAFLD. International Journal of Molecular Sciences, 22 (2), 11905.

Ding, H.R., Wang, H.Z. and Shi, X.L. (2018). Lipometabolism and Glycometabolism in Liver Disease. BioMed Research International, 1, 1-7.

Di Pasqua, L.G., Cagna, M., Berardo, C., Vairetti, M. and Ferrigno. (2022). Detailed Molecular Mechanisms Involved in Drug-Induced Non-Alcoholic Fatty Liver Disease and Non-Alcoholic Steatohepatitis: An Update. Biomedicines, 10 (1), 194.

Dixon, L.J., Barnes, M., Tang, H., Pritchard, M.T. and Nagy, L.E. (2013). Kupffer Cells in the Liver. Comprehensive Physiology, 3 (2), 785-797. Cells, 8 (845), 1-23.

Do, r., Kiss, R.S., Gaudet, D. and Engert, J. (2008). Squalene synthase: a critical enzyme in the cholesterol biosynthesis pathway. Clinical Genetics, 75 (1), 19-29.

Donato, M. T., Lahoz, A., Jimenez, N., Perez, G., Serralta, A., Mir, J., Castell, J.V. and Gomez-Lechon, M.J. (2006). Potential impact of steatosis on cytochrome P450 enzymes of human hepatocytes isolated from fatty liver grafts. Drug Metab Dispos, 34, 1556–1562.

Donato, M.T., Jimenez, N., Serralta, A., Mir, J., Castell, J. V. and Gomez-Lechon, M.J. (2007). Effects of steatosis on drug-metabolizing capability of primary human hepatocytes. Toxicol In Vitro, 21, 271–276.

Donato, M.T., Martinez-Romero, A., Jimenez, N., Negro, A., Herrera, G., Castell, J.V., O'Connor, J.E. and Gomez-Lechon, M.J. (2009). Cytometric analysis for drug-induced steatosis in HepG2 cells. Chemico-Biological Interactions, 181 (3), 417-423.

Donato, M.T., Tolosa, L., Jimenez, N., Castell, J.V. and Gomez-Lechon, M.J. (2012). High-Content Imaging Technology for the Evaluation of Drug-Induced Steatosis Using a Multiparametric Cell-Based Assay. SLAS Discovery, 17 (3), 394-400.

Donato, M.T., Jover, R. and Gomez-Lechon, M.J. (2013). Hepatic Cell Lines for Drug Hepatotoxicity Testing: Limitations and Strategies to Upgrade their Metabolic Competence by Gene Engineering. Current Drug Metabolism, 14, 946-968.

Donato, M.T., Tolosa, L., Gomez-Lechon, M.J. (2014). Culture and Functional Characterization of Human Hepatoma HepG2 Cells. Methods Mol Biol, 1250, 77-93.

Donato, M.T., Gallego-Ferrer, G. and Tolosa, L. (2022). In Vitro Models for Studying Chronic Drug-Induced Liver Injury. International Journal of Molecular Sciences, 23 (19), 11428.

Drescher, H.K., Weiskirchen, S. and Weiskirchen, R. (2019). Current Status in Testing for Nonalcoholic Fatty Liver Disease (NAFLD) and Nonalcoholic Steatohepatitis (NASH).

Dyson, J.K., Anstee, Q.M. and McPherson, S. (2013). Non-alcoholic fatty liver disease: a practical approach to treatment. Postgraduate Medical Journal, 91 (1072), 92-101.

Edmondson, R., Jenkins Broglie, J., Adcock, A.F. and Yang, L. (2014). Three-Dimensional Cell Culture Systems and Their Applications in Drug Discovery and Cell-Based Biosensors. Assay Drug Dev Technol, 12 (4), 207-218.

Eilenberger, C., Rothbauer, M., Ehmoser, E.K., Ertl, P. and Kupcu, S. (2019). Effect of Spheroidal Age on Sorafenib Diffusivity and Toxicity in a 3D HepG2 Spheroid Model. Scientific reports, 9 (4863).

El Hage, M., Baverel, G. and Martin, G. (2012). Effects of valproate on glutamate metabolism in rat brain slices: a 13C NMR study. Epilepsy Res, 99, 94-100.

Ellero, A.A., Van den Bout, I., Cromarty, A.D. and Hurrell, T. (2021). Continual proteomic divergence of HepG2 cells as a consequence of long-term spheroid culture. Scientific reports, 11 (10917).

Emery, M.G., Fisher, J. M., Chien, J.Y., Kharasch, E.D., Dellinger, E.P., Kowdley, K.V., Thummel, K.E. (2003). CYP2E1 activity before and after weight loss in morbidly obese subjects with nonalcoholic fatty liver disease. Hepatology, 38, 428–435.

Emwas, A.H. (2015). The Strengths and Weaknesses of NMR Spectroscopy and Mass Spectroscopy with Particular Focus on Metabolomics Research. Metabonomics, (1277), 161-193.

Emwas., A.H., Roy, R., McKay, R.T., Ryan, D., Brennan, L., Tenori, L., Luchinat, C., Gao, X., Zeri, A.C., Gowda, G.A.N., Raftery, D., Steinbeck, C., Salek, R.M. and Wishart, D.S. (2016). Recommendations and Standardization of Biomarker Quantification Using NMR-Based Metabolomics with Particular Focus on Urinary Analysis. Journal of proteome, 15 (2), 360-373.

Emwas, A.H., Saccenti, E., Gao, X., McKay, R.T., Martins dos Santos, V.A.P., Roy, R. and Wishart, D.S. (2018). Recommended strategies for spectral processing and post-processing of 1D ^{1}H-NMR data of biofluids with a particular focus on urine. Metabolomics, 14 (31).

Enjoji, M., Yasutake, K., Kohjima, M. and Nakamuta, M. (2011). Nutrition and Nonalcoholic Fatty Liver Disease: The Significance of Cholesterol. Hindawi, 925807, 1-6.

Enriquez, A., Leclercq, I., Farrell, G. C. and Robertson, G. (1999). Altered expression of hepatic CYP2E1 and CYP4A in obese, diabetic ob/ob mice, and fa/fa Zucker rats. Biochem Biophys Res Commun, 255, 300–306.

Ernst, R.R., Bodenhausen, G. and Wokaun, A. (1990). Principles of Nuclear Magnetic Resonance in One and Two Dimensions. Oxford science pulications, Clarendon Press.

Esvan, Y.J. and Zeinyeh, W. (2020). Basics of Fourier Transform Applied to NMR Spectroscopy: An Interactive Open-Source Web Application. Journal of Chemical Education, 97, 263-264.

Eynaudi, A., Diaz-Castro, F., Borquez, J.C., Bravo-Sagua, R., Parra, V. and Troncoso, R. (2021). Differential Effects of Oleic and Palmitic Acids on Lipid Droplet-Mitochondria Interaction in the Hepatic Cell Line HepG2. Food Chemistry, 8, 1-12.

Fabbrini, E., Sullivan, S. and Klein, S. (2010). Obesity and Non-alcoholic Fatty Liver Disease: Biochemical Metabolic and Clinical Implications. Hepatology, 51 (2), 679-689.

Fabbrini, E. and Magkos, F. (2015). Hepatic Steatosis as a Marker of Metabolic Dysfunction. Nutrients, 7 (6), 4995-5019.

Fan, H., Chen, Y.Y., Bei, W.J., Wang, L.Y., Chen, B.T. and Guo, J. (2013). In Vitro Screening for Antihepatic Steatosis Active Components within Coptidis Rhizoma Alkaloids Extract Using Liver Cell Extraction with HPLC Analysis and Free Fatty Acid-Induced Hepatic Steatosis HepG2 Cell Assay. Evidence-Based Complementary and Alternative Medicine.

Farinelli, E., Giampaoli, D., Cenciarini, A., Cercado, E. and Verrotti, A. (2015). Valproic acid and Nonalcoholic fatty liver disease: A possible association? World Journal of Hepatology, 7 (9), 1251-1257.

Fargion, S., Valenti, L. and Fracanzani, A.L. (2011). Beyond heredity hemochromatosis: new insights into the relationship between iron overload and chronic liver diseases. Digestive and Liver Disease, 43 (2), 89-95.

Feaver, R.E., Cole, B.K., Lawson, M.J., Hoang, S.A., Marukian, S., Blackman, B.R., Figler, R.A., Sanyal, A.J., Wamhoff, B.R. and Dash, A. (2016). Development of an in vitro human liver system for interrogation nonalcoholic steatohepatitis. JCI Insights, 1 (20).

Fedchuk, L., Nascimbeni, F., Pais, R., Charlotte, F., Housset, C. and Ratziu, V. (2014). Performance and limitations of steatosis biomarkers in patients with nonalcoholic fatty liver disease. Alimentary Pharmacology and Therapeutics, 40 (1), 1209-1222.

Feher, J. and Lengyel, G. (2003). A New Approach to Drug Therapy in Non-alcoholic Steatohepatitis (NASH). The Journal of International Medical Research, 31 (1), 537-551.

Finck, B.N. (2018). Targeting Metabolism, Insulin Resistance, and Diabetes to Treat Nonalcoholic Steatohepatitis. Diabetes, 67 (12), 2485-2493.

Fisher, C.D., Lickteig, A.J., Augustine, L.M., Ranger-Moore, J., Jackson, J.P., Ferguson, S.S. and Cherrington, N.J. (2009). Hepatic Cytochrome P450 Enzyme Alterations in Humans with Progressive Stages of Nonalcoholic Fatty Liver Disease. Drug Metabolism and Disposition, 37 (10), 2087-2094.

Fletcher, J.A., Deja, S., Satapati, S., Fu, X., Burgess, S.C. and Browning, J.D. (2019). Impaired ketogenesis and increased acetyl-CoA oxidation promote hyperglycemia in human fatty liver. JCI Insights, 4 (11).

Fontes, A., Alemany-Pages, M., Oliveira, P.J., Ramalho-Santos, J., Zischka, H. and Azul, A.M. (2019). Antioxidant Versus Pro-Apoptotic Effects of Mushroom-Enriched Diets on Mitochondria in Liver Disease. Int. J. Mol. Sci, 20 (16), 3987.

Frandsen, H.S., Vej-Nielsen, J.M., Smith, L.E., Sun, L., Mikkelsen, K.L., Thulesen, A.P., Hagensen, C.E., Yang, F. and Rogowska-Wrzesinska, A. (2022). Mapping Proteome and Lipidome Changes in Early-Onset Non-Alcoholic Fatty Liver Disease Using Hepatic 3D Spheroids. Cells, 11 (20), 3216.
Frank, M. (2021). An introduction to cell culture techniques and challenges. Cell culture, blog. Available from https://www.integra-biosciences.com/united-kingdom/en/blog/article/introduction-cell-culture-techniques-and-challenges

Freneaux, E., Labbe, G., Letteron, P., Le Dinh, T., Degott, C., Geneve, J., Larrey, D. and Pessayre, D. (1988). Inhibition of the Mitochondrial Oxidation of Fatty Acids by Tetracycline in Mice and in Man: Possible Role in Microvesicular Steatosis Induced by This Antibiotic, 8 (5), 1056-1062.

Froese, D.S., Fowler, B. and Baumgartner, M.R. (2018). Vitamin B12, folate and the methionine remethylation cycle- biochemistry, pathways and regulation. Journal of Inherited Metabolic Disease, 42 (4), 673-685.

Fromenty, B. and Pessayre, D. (1995). Inhibition of mitochondrial beta-oxidation as a mechanism of hepatotoxicity. Pharmacol. Ther.

Fromenty, B. (2019). Inhibition of mitochondrial fatty acid oxidation ion drug-induced hepatic steatosis, 3, 157-169.

Fromenty, B. (2020). Alteration of mitochondrial DNA homeostasis in drug-induced liver injury. Food Chem. Toxicol, 135, 110916.

Gaggini, M., Carli, F., Rosso, C., Buzzigoli, E., Marietti, M., Della Latta, V., Ciociaro, D., Abate, M.L., Gambino, R., Cassader, M., Bugianesi, E. and Gastaldelli, A. (2018). Altered Amino Acid Concentrations in NAFLD: Impact of Obesity and Insulin Resistance. Hepatology, 67, 1, 145-158.

Gai, Z., Krajnc, E., Samodelov, S.L., Visentin, M, and Kullak-Ublick, G.A. (2020). Obeticholic Acid Ameliorates Valproic Acid-Induced Hepatic Steatosis and Oxidative Stress. Molecular Pharmacology, 97 (5), 314-323.

Gallego-Duran, R., Ampuero, J., Pastor-Ramirez, H., Alvarez-Amor, L., del Campo, J.A., Maya-Miles, D., Montero-Vallejo, R., Cardenas-Garcia, A., et al., (2022). Liver injury in non-alcoholic fatty liver disease is associated with urea cycle enzyme dysregulation. Scientific Reports, 12, 3418.

Galindo-Prieto, B., Eriksson, L. and Trygg, J. (2015). Variable influence on projection (VIP) for OPLS models and its applicability in multivariate time series analysis. Chemometrics and Intelligent Laboratory Systems, 146, 297-304.

Galluzzi, L., Aaronson, S.A., Abrams, J., Alnemri, E.S., Andrews, D.W., Baehrecke, E.H., Bazan, N.G., Blagosklonny, M.V., Blomgren, K., Borner, C., Bredesen, D.E., Brenner, C., Castedo, M., Cidlowski, J.A., Ciechanover, A., Cohen, G.M. et al. (2009). Guidelines for the use and interpretation of assays for monitoring cell death in higher eukaryotes. Cell Death Differ, 16 (1), 1093–1107.

Gao, D., Nong, S., Huang, X., Wang, S. and Yang, J. (2010). The Effects of Palmitate on Hepatic Insulin Resistance Are Mediated by NADPH Oxidase 3-derived Reactive Oxygen Species through JNK and $p38^{MAPK}$ Pathways. Journal of Biological Chemistry, 285 (39), 29965-29973.

Garcia-Canaveras, J., Castell, J.V., Donato, M.T. and Lahoz, A. (2016). A metabolomics cell-based approach for anticipating and investigating drug-induced liver injury. Scientific Reports, 6, 27239.

Garcia-Ruiz, C. and Fernandez-Checa, J.C. (2018). Mitochondrial Oxidative Stress and Antioxidants Balance in Fatty liver Disease. Hepatology Communications, 2 (12), 1425-1439.

Garcia-Ruiz, I., Solis-Munoz, P., Fernandez-Moreira, D., Munoz-Yague, T. and Solis-Herruzo, J.A. (2015). *In Vitro* treatment of HepG2 cells with saturated fatty acids reproduces mitochondrial dysfunctional found in Nonalcoholic steatohepatitis. Disease Models & Mechanisms, 8 (2), 183-191.

Garcia-Perez, E., Ryu, D., Lee, C. and Lee, H.J. (2021). Ochratoxin A Induces Oxidative Stress in HepG2 Cells by Impairing the Gene Expression of Antioxidant Enzymes. Toxins, 13 (271), 1-12.

Garrido, F., Pacheco, M., Vargas-Martinez, R., Velasco-Garcia, R., Jorge, I., Serrano, H., Portillo, F., Vazquez, J. and Pajares, M.A. (2018). Identification of hepatic protein-protein interaction targets for betaine homocysteine S-methyltransferase. PLOS ONE, 13 (6).

Gaskell, H., Sharma, P., Colley, H.E., Murdoch, C. and Williams, D.P., Webb, S.D. (2016). Characterization of a functional C3A liver spheroid model. Toxicol. Res, 5, 1053–1065.

Gastadelli, A., Baldi, S., Pettiti, M., Toschi, E., Camastra, S., Natali, A., Landau, B.R. and Ferrannini, E. (2000). Influence of Obesity and Type 2 Diabetes on Gluconeogenesis and Glucose Output in Humans. Diabetes, 49, 1367-1373.

Gerets, H.H.J., Tilmant, K., Gerin, B., Chanteux, H., Depelchin, B.O., Dhalluin, S. and Atienzar, F.A. (2012). Characterization of primary human hepatocytes,l HepG2 cells and HepaRG cells at the mRNA level and CYP activity in response to inducers and their predictivity for the detection of human hepatotoxins. Cell Biology and Toxicology, 28 (2), 69-87.

Gergen, I. and Harmanescu, M. (2012). Application of principal component analysis in the pollution assessment with heavy metals of vegetable food chain in the old mining areas. Chemistry Central Journal, 6 (156), 1-13.

Ghazali, R., Mehta, K.J., Bligh, S.A., Tewfik, I., Clemens, D. and Patel, V.B. (2020). High omega arachidonic acid/docosahexaenoic acid ratio induces mitochondrial dysfunction and altered lipid metabolism in human hepatoma cells
World J Hepatol, 12, 84-98.

Ghrayeb, A., Agranovich, B., Peled, D., Finney, A.C., Abramovich, I., Garcia, J.F., Traylor, J., Drucker, S., Fernandes, S.I., Weissman, N., Chen, Y.E., Rom, O., Mor, I. and Gottlieb, E. (2023). Fatty liver-mediated glycine restriction impairs glutathione synthesis and causes hypersensitization to acetaminophen. BioRxiv.

Gibellini F. and Smith T. K. (2010). The Kennedy pathway–De novo synthesis of phosphatidylethanolamine and phosphatidylcholine. IUBMB Life **62**, 414–428.

Gitto, S., Schepis., Andreone, P. and Villa, E. (2018). Study of the Serum Metabolomic Profile in Nonalcoholic Fatty Liver Disease: Research and Clinical Perspectives. Metabolites, 8 (1), 17.

Glenn, C. and Feldman, S.R. (2011). Tetracycline-induced hepatotoxicity. Dermatology Online Journal, 17 (12), 14.

Gomez-Lechon, M.J., Donato, M.T., Martinez-Romero, A., Jimenez, N, Castell, J.V. and O'Connor J.E. (2007). A human hepatocellular in vitro model to investigate steatosis. Chemico-Biological Interactions, 165 (2), 106-116.

Gorsuch, R.L. (1983). Factor analysis. Hillsdale NJ: Lawrence Erlbaum Associates.

Gowda, G.A.N. and Raftery, D. (2016). Biomarker Discovery and Translation in Metabolomics. Curr Metabolomics, 1 (3), 227-240.

Grattagliano, I., Caraceni, P., Calamita, G., Ferri, D., Gargano, I., Palasciano, G. and Portincasa, P. (2008). Severe liver steatosis correlates with nitrosative and oxidative stress in rats. Eur. J. Clin. Investig, 38, 523–530

Grattagliano, I., Montezinho, L.P., Oliveira, P.J., Fruhbeck, G., Gomez-Ambrosi, J., Montecucco, F., et al. (2019). Targeting Mitochondria to Oppose the Progression of Nonalcoholic Fatty Liver Disease. Biochem Pharmacol, 160, 34-45.

Grepper, S., Kostadinove, R., Thoma, E. and Wolf, A. (2019). Evolving Models for NASH Drug Discovery: Tools for stemming a silent epidemic. Drug Discovery World.

Gronert, A., Zierau, O., Thieme, D., Keiler, A.M. (2023). Effect of HepG2 cell 3D cultivation on the metabolism of the anabolic androgenic steroid methandienone. Drug Testing and Analysis, 1-10.

Guido, M., Sarcognato, S., Sacchi, D. and Ludwig, K. (2019). The Anatomy and Histology of the Liver and Biliary Tract. Pediatric Hepatology and Liver Transplantation, 41-55.

Gulsen, M., Yesilova, Z., Bagci, S., Uygun, A., Ozcan, A., Ercin, C.N., Erdil, A., Sanisoglu, S.Y., Cakir, E., Ates, Y., Kemal Erbil, M., Karaeren, N. and Dagalp, K. (2005). Elevated plasma homocysteine concentrations as a predictor of steatohepatitis in patients with non-alcoholic fatty liver disease. J. Gastroenterol. Hepatol, 20, 1448–1455.

Guo, S., Rosch, P., Popp, J. and Bocklitz, T. (2019). Modified PCA and PLS: Towards a better classification in Raman spectroscopy-based biological applications. Journal of Chemometrics, 34 (4).

Guo, X., Yin, X., Liu, Z. and Wang, J. (2022). Non-Alcoholic Fatty Liver Disease (NAFLD) Pathogenesis and Natural Products for Prevention and Treatment. Int J Mol Sci, 23 (24), 15489.

Gusdon, A.M., Song, K.X. and Qu, S. (2014). Nonalcoholic Fatty Liver Disease: Pathogenesis and Therapeutics from a Mitochondria-Centric Perspective. Oxid Med Cell Longev, 637027, 1-20.

Gwee, M.C. (1982). Can tetracycline-induced fatty liver in pregnancy be attributed to choline deficiency? Med Hypotheses, 9 (2), 157-62.

Hanagama, M., Inoue, H., Kamiya, M., Shinone, K., Nata, M. (2008). Gene expression on liver toxicity induced by administration of haloperidol in rats with severe fatty liver. Leg Med (Tokyo), 10, 177–184.

Harjumaki, R., Pridgreon, C.S. and Ingelman-Sundberg, M. (2021). CYP2E1 in Alcoholic and Non-Alcoholic Liver Injury. Roles of ROS, Reactive Intermediates and Lipid Overload. International Journal of Molecular Science, 22 (15), 8221.

Hasegawa, T., Lino, C., Endo, T., Mikami, K., Kimura, M., Sawada, N., Nakaji, S. Fukuda, S. (2020). Changed Amino Acids in NAFLD and Liver Fibrosis: A Large Cross-Sectional Study without Influence of Insulin Resistance. Nutrients, 12 (5), 1450.

Hatcher, L. (1994). A step-by-step approach to using the SAS system for factor analysis and structural equation modeling. Cary: SAS Institute.

Haussinger, D. and Kordes, C. (2019). Space of Disse: a stem cell niche in the liver. Biol Chem, 401 (1), 81-95.

Hautekeete, M.L., Degott, C. and Benhamou, J.P. (1990). Microvesicular steatosis of the liver. Acta Clin Belg, 45 (5), 311-26.

Hendriks, D.F.G., Puigvert, L.F., Messner, S., Mortiz, W. and Ingelman-Sundberg. (2016). Hepatic 3D spheroid models for the detection and study of compounds cholestatic liability. Scientific Reports, 6 (35434).

Hewitt, N.J., Lechon, M.J., Houston, J.B., Hallifax, D., Brown, H.S., Maurel, P., Kenna, J.G., Gustavsson, L., Lohmann, C., Skonberg, C., Guillouzo, A., Tuschl, G., Li, A.P., LeCluyse, E., Groothuis, G.M.M. and Hengstler, J.G. (2007). Primary hepatocytes: current understanding of the regulation of metabolic enzymes and transporter proteins, and pharmaceutical practice for the use of hepatocytes in metabolism, enzyme induction, transporter, clearance, and hepatotoxicity studies. Drug Metab Rev, 39, 159–234.

Hoki, T., Miyanishi, K., Tanaka, S., Takada, K., Kawano, Y., Sakurada, A., Sato, M., Kubo, T., Sato, T., Sato, Y., Takimoto, R., Kobune, M. and Kato, J. (2015). Increased duodenal iron absorption through up-regulation of divalent metal transporter 1 from enhancement of iron regulatory protein 1 activity in patients with nonalcoholic steatohepatitis. Hepatology, 62 (3), 751-61.

Houten, S.M. and Wander, R.J.A. (2010). A general introduction to the biochemistry of mitochondrial fatty acid β-oxidation. Journal of Inherited Metabolic Disease, 33 (5), 469-477.

Hsu, C.C., W, L.C., Hsia, C.Y., Yin, P.H., Chi, C.W., Yeh, T.S. and Lee, H.C. (2015). Energy metabolism determines the sensitivity of human hepatocellular carcinoma cells to mitochondrial inhibitors and biguanide drugs. Oncology Reports, 34, 1620-1628.

Hu, Y., Liu, J., Dong, X., Xu, Y., Leng, S. and Wang, G. (2016). Clinical Study of Serum Homocysteine and Non-Alcoholic Fatty Liver Disease in Euglycemic Patients. Medical Science Monitor, 22, 4146-4151.

Huang, R.F.S., Hsu, Y.C., Lin, H.S. and Yang, F.L. (2001). Folate Depletion and Elevation Plasma Homocysteine Promote Oxidative Stress in Rat Livers. The Journal of Nutrition, 131 (1), 33-38.

Huang, Y., Zhang, Z., Chen, H., Feng, J., Cai, S. and Chen, Z. (2015). A high-resolution 2D J-resolved NMR detection technique for metabolite analyses of biological samples. Scientific Reports, 5 (8390).

Huang, Z., Wang, M., Liu, L., Peng, J., Guo, C., Chen, X., Huang, L., Tan, J. and Yang, G. (2019) Transcriptional repression of CYP3A4 by increased miR-200a-3p and miR-150-5p promotes steatosis in vitro. Front Genet, 10, 484.

Hughes, T.S., Wilson, H.D., de Vera, I.M.S. and Kojetin, D.J. (2015). Deconvolution of Complex 1D NMR Spectra Using Objective Model Selection. PLOS One, 10 (8), 1-16.

Hundt, M., Basit, H. and John, S. (2020). Physiology, Bile Secretion. StatPearls. StatPearls Publishing, Treasure Island (FL).

Huo, T., Chen, X., Lu, X., Qu, L., Liu, Y. and Cai, S. (2014). An effective assessment of valproate sodium-induced hepatotoxicity with UPLC-MS and ^{1}HNMR-based metabonomics approach. Journal of Chromatography B, 696, 109-116.

Hutschenreuther, A., Kiontke, A., Birkenmeier, G., & Birkemeyer, C. (2012). Comparison of extraction conditions and normalization approaches for cellular metabolomics of adherent growing cells with GC-MS. *Analytical Methods, 4*, 1953.

Imbard, A., Benoist, J.F., Esse, R., Gupta, S., Lebon, S., de Vriese, A.S., Ogier de Baulny, H., Kruger, W., Schiff, M. and Blom, H.J. (2015). High homocysteine induces betaine depletion. Biosci Rep, 28;35 (4).

Ingelman-Sundberg, M. and Lauschke, V.M. (2021). 3D human liver spheroids for translational pharmacology and toxicology. Basic & Clinical Pharmacology & Toxicology, 130 (51), 5-15.

Ioannou, G.N., Gowda, G.A.N., Djukovic, D. and Raferty, D. (2020). Distinguishing NASH Histological Severity Using a Multiplatform Metabolomics Approach. Metabolites, 10 (168), 1-15.

Ipsen, D.H., Lykkesfeldt, J. and Tveden-Nyborg, P. (2018). Molecular Mechanisms of hepatic lipid accumulation in non-alcoholic fatty liver disease. Cell Mol Life Sci, 75 (18), 3313-3327.

Ito, M., Suzuki, J., Tsujioka, S., Sasaki, M., Gomori, A., Shirakura, T., Hirose, H., Ito, M., Ishihara, A., Iwaasa, H. and Kanatani, A. (2007). Longitudinal analysis of murine steatohepatitis model induced by chronic exposure to high-fat diet. Hepatol Res, 37, 50–57.

Jamwal, R. and Barlock, B.J. (2020). Nonalcoholic Fatty Liver Disease (NAFLD) and Hepatic Cytochrome P450 (CYP) Enzymes. Pharmaceuticals, 13 (9), 222.

Jensen, C. and Teng, Y. (2020). Is It Time to Start Transitioning From 2D to 3D Cell Culture? Front. Mol. Biosci, 7.

Jha, P., Knopf, A., Koefeler, H., Mueller, M., Lackner, C., Hoefler, G., Claudel, T. and Trauner, M. (2014). Role of adipose tissue in methionine-choline-deficient model of non-alcoholic steatoheptitis (NASH). Biochemica et Biophysica Acta, 1842 (7), 959-970.

Jhee, K.H. and Kruger, W.D. (2005). The role of cystathionine beta-synthase in homocysteine metabolism. Anitoxid Redox Signal, 7 (5-6), 813-22.

Jia, G., Di, F., Wang, Q., Shao, J., Gao, L., Wang, L., Li, Q. and Li N. (2015). Non-Alcoholic Fatty Liver Disease Is a Risk Factor for the Development of Diabetic Nephropathy in Patients with Type 2 Diabetes Mellitus. PLoS ONE, 10.

Ji, C., Shinohara, M., Kuhlenkamp, J., Chan, C. and Kaplowitz, N. (2007). Mechanisms of Protection by the Betaine-Homocysteine Methyltransferase/Betaine System in HepG2 Cells and Primary Mouse Hepatocytes. Hepatology, 46 (5), 1586-1596.

Jolliffe, I.T. and Cadima, J. (2016). Principal component analysis: a review and recent developments. Philosophical Transactions, 375 (2065), 1-16.

Johnson, C.H., Ivanisevic, J. and Siuzdak, G. (2016). Metabolomics: beyond biomarkers and towards mechanisms. Nature Reviews Molecular Cell Biology, 17, 451-459.

Jones, I., Yelhekar, T.D., Wiberg, R., Kingham, P.J., Johansson, S., Wiberg, M. and Carlsson, L. (2018). Development and validation of an *in vitro* model system to study peripheral sensory neuron development and injury. Scientific reports, 8 (15961).

Jorge, T.F., Mata, A.T. and Antonio, C. (2016). Mass spectrometry as a quantitative tool in plant metabolomics. Philosophical Transactions of The Royal Society A Mathematical, Physical and Engineering Sciences, 374, 2079.

Juarez-Hernandez, E., Chavez-Tapia, N.C., Uribe, M. and Barbero-Becerra, V.J. (2016). Role of bioactive fatty acids in nonalcoholic fatty liver disease. Nutrition Journal, 17 (72).

Jump, D.B., Lytle, K.A., Depner, C.M. and Tripathy, S. (2017). Omega-3 Polyunsaturated Fatty Acids as a Treatment Strategy for Nonalcoholic Fatty Liver Disease. Pharmacol Ther, 181, 108-125.

Jutric, D., Dikic, D., Boros, A., Odeh, D., Drozdek, S.D., Gracan, R., Dragicevic, P., Crnic, I. and Jurcevic, I.L. (2022). Effects of Naringin and Valproate Interaction on Liver Steatosis and Dyslipidaemia Parameters in Male C57BL6 Mice. Archives of Industrial Hygiene and Toxicology, 73 (1), 71-82.

Kahn, S.U. and Kahn, M.U. (2022). Molecular developments in cell models of fatty liver disease. Life Science Dysona, 3 (1), 16-29.

Kalhan, S.C., Guo, L., Edmison, J., Dasarathy, S., McCullogh, A.J., Hanson, R.W. and Milburn, M. (2011). Plasma metabolomic profile in nonalcoholic fatty liver disease. Metabolism Clinical and Experimental, 60, 404-413.

Kalra, A., Yetiskul, E., Wehrle, C.J. and Tuma, F. (2020). Physiology, Liver. StatPearls.

Kamalian, L., Chadwick, A.E., Bayliss, M., French, N.S., Monshouwer, M., Snoeys, J. and Park, B.K. (2015). The utility of HepG2 cells to identify direct mitochondrial dysfunction in the absence of cell death. Toxicology in Vitro, 29 (4), 732-740.

Kammerer, S. and Kupper, J.H. (2018). Human hepatocyte systems for in vitro toxicology analysis. Journal of Cellular Biotechnology, 3 (2), 85-93.

Kanuri, G. and Bergheim, I. (2013). In Vitro and in Vivo Models of Non-Alcoholic Fatty Liver Disease (NAFLD). International Journal of Molecular Sciences, 14 (6), 11963-11980.

Kaspar, H., Dettmer, K., Gronwald, W. and Oefner, P.J. (2008). Advances in amino acid analysis. Analytical and Bioanalytical Chemistry, 393, 445-452.

Katsura, N., Ikai, I., Mitaka, T., Shiotani, T., Yamanokuchi, S., Sugimoto, S., Kanazawa, A., Terajima, H, Mochizuki, Y. and Yamaoka, Y. (2002). Long-term culture of primary human hepatocytes with preservation of proliferative capacity and differentiated functions. J Surg Res, 106 (1), 115-23.

Kapalczynska, M., Kolenda, T., Przybyla, W., Zajaczkowska, M., Teresiak, A., Filas, V., Ibbs, M., Blizniak, R., Luczewski, L. and Lamperska, K. (2018). 2D and 3D cell culture- a comparison of different types of cancer cell culutures. Archives of Medical Science, 14 (4), 910-919.

Kawano, Y. and Cohen, D.E. (2013). Mechanisms of hepatic triglyceride accumulation in nonalcoholic fatty liver disease. Journal of Gastroenterology, 48 (4), 434-441.

Kesterson, J.W., Granneman, G.R. and Machinist, J.M. (1984). The Hepatotoxicity of Valproic Acid and Its Metabolites in Rats. I. Toxicologic, Biochemical and Histopathologic Studies. Hepatology, 4 (6), 1143-1152.

Kerr, T.A. and Davidson, N.O. (2012). Cholesterol and NAFLD: Renewed focus on an old villain. Hepatology, 56 (5), 1995-1998.

Kersten, S., Seydoux, J., Peters, J.M., Gonzalez, F.J., Desvergne, B. and Wahli, W. (1999). Peroxisome proliferator-activated receptor alpha mediates the adaptive response to fasting. J Clin Invest, 1489-1498.

Kiang, T.K.L., Teng, X.W., Surendradoss, J., Karagiozov, S., Abbott, F.S. and Chang, T.K.H. (2011). Glutathione depletion by valproic acid in sandwich-cultured rat hepatocytes: Role of biotransformation and temporal relationship with onset of toxicity. Toxicology and Applied Pharmacology, 252 (3), 318-324.

Kietzmann, T. (2017). Metabolic zonation of the liver: The oxygen gradient revisited. Redox Biology, 11, 622-630.

Kim, K.H. and Lee, M.S. (2018). Pathogenesis of Nonalcoholic Steatohepatitis and Hormone-Based Therapeutic Approaches. Frontiers in Endocrinology, 9, 1-14.

Kirk, L.M., Waits, C.M.K., Bashore, A.C., Dosso, B., Meyers, A.K., Renaldo, A.C., DePalma, T.J., Simms, K.N., Hauser, N., Chuang Key, C.C., McCall, C.E., Parks, J.S., Sergeant, S., Langefeld, C.D., Skardal. A. and Rahbar, E. (2022). Exploiting three-dimensional human hepatic constructs to investigate the impact of *rs174537* On fatty acid metabolism. PLOS ONE, 17 (1).

Kisseleva, T. (2017). The Origin of Fibrogenic Myofibroblasts in Fibrotic Liver. Hepatology, 65 (3), 1039-1043.

Kitade, H., Chen, G., Ni, Y. and Ota, T. (2017). Nonalcoholic Fatty Liver Disease and Insulin Resistance: New Insights and Potential New Treatments. Nutrients, 9 (4), 387.

Kohjima, M., Enjoji, M., Higuchi, N., Kato, M., Kotoh, K., Yoshimoto, T., Fujino, T., Yada, M., Yada, R., Harada, N., Takayanagi, R. and Nakamuta, M. (2007). Re-evaluation of fatty acid metabolism-related gene expression in nonalcoholic fatty liver disease. Int J Mol Med, 20, 351–358.

Kohl S.M., Klein, M.S., Hochrein, J., Oefner, P.J., Spang, R. and Gronwald, W. (2012). State-of-the art normalization methods improve NMR-based metabolomic analysis. Metabolomics, 8 (1), 146-160.

Kolaric, T.O., Nincevic, V., Kuna, L., Duspara, K., Bojanic, K., Vukadin, S., Raguz-Lucic, N., Wu, G.Y. and Smolic, M. (2021). Drug-induced Fatty Liver Disease: Pathogenesis and Treatment. Journal of Clinical and Translational Hepatology, 9 (5), 731-737.

Komulainen, T., Lodge, T., Hinttala, R., Bolszak, M., Pietila, M., Koivunen, P., Hakkola, J., Poulton, J., Morten, K.J. and Uusimaa, J. (2015). Sodium valproate induces mitochondrial respiration dysfunction in HepG2 *in vitro* cell model. Toxicology, 331, 47-56.

Koutcher, J.A. and Burt, T. (1984). Principles of Nuclear Magnetic Resonance. Journal of Nuclear Medicine, 25, 101-111.

Kozyra, M., Johansson, I., Nordling, A., Ullah, S., Lauschke, V.M. and Ingelman-Sundberg, M. (2018). Human hepatic 3D spheroids as a model for steatosis and insulin resistance. Scientific Reports, 8 (14297).

Krishna, M. (2013). Microscopic anatomy of the liver. Clinical Liver Disease, 2 (1), 4-7.

Kroemer, G., Galluzzi, L., Vandenabeele, P., Abrams, J., Alnemri, E.S., Baehrecke, E.H., Blagosklonny, M.V., El-Deiry, W.S., Golstein, P., Green, D.R., Hengartner, M., Knight, R.A.,

Kumar, S., Lipton, S.A., Malorni, W., Nunez, G., Peter, M.E., Tschopp, J., Yuan, J., Piacentini, M., Zhivotovsky, B. and Melino, G. (2009) Classification of cell death: recommendations of the Nomenclature Committee on Cell Death 2009. Cell Death Differ, 16 (1), 3–11.

Kulasingam, V. and Diamandis, E.P. (2006). Proteomic and Genomic Technologies for Biomarker Discovery. Clinical Proteomics, 2. 5-12.

Kumar, N., Hoque, M.A. and Sugimoto, M. (2018). Robust volcano plot: identification of differential metabolites in the presence of outliers. BMC Bioinformatics, 19 (128).

Kumar, S., Alam, S.F. and Ganguly, P.K. (2020). Obesity-Induced Non-alcoholic Fatty Liver Disease (NAFLD): Role of Hyperhomocysteinemia. Pathophysiology of Obesity-Induced Health Complications, 19, 181-192.

Kumari, A. (2018). Beta-oxidation of Fatty Acids. Sweet Biochemistry. London: Elsevier, 17-19.

Kurbel, S., Kurbel, B., Vcev, A., Loncar, B., Vegar-Brozvic, V. and Cavcic, J. (2003). A model of dual circulation in liver acini with hypoxia regulated adenosine secretion. Med Hypotheses, 60 (4), 515-519.

Kusumastuti, K. and Jaeri, S. (2020). The effect of long-term valproic acid treatment in the level of total cholesterol among adult. Indian J Pharmacol, 52 (2), 134-137.

Larsson, P., Engqvist, H., Biermann, J., Werner Ronnerman, E., Forssell-Aronsson, E., Kovacs, A., Karlsson, P., Helou, K. and Parris, T.Z. (2020). Optimization of cell viability assays to improve replicability and reproducibility of cancer drug sensitivity screens. Scientific Reports, 10 (5798), 1-12.

Lasli, S., Kim, H.J., Lee, K., Suurmond, C.A.E., Goudie, M., Bandaru, P., Sun, W., Zhang, S., Zhang, Niyuan, Z., Ahadian, S., Dokmeci, M.R., Lee, J. and Khademhosseini, A. (2020). A human liver-on-a-chip platform for modelling non-alcoholic fatty liver disease. Adv Biosyst, 3 (8).

Lautt, W.W. (2009) Hepatic Circulation: Physiology and Pathophysiology. Chapter 2. Morgan & Claypool Life Sciences, San Rafael (CA).

Le, M.H., Devaki, P., Ha, N.B., Won Jun, D., Te, H.S., Cheung, R.C. and Nguyen, M.H. (2017). Prevalence of non-alcoholic fatty liver disease and risk factors for advanced fibrosis and mortality in the United States. PLOS, 12 (3), 1-13.

Lee, K., Jung, E.S., Yu, E., Kang, Y.K., Cho, M.Y., Kim, J.M., Moon, W.S., Jeong, J.S., Park, C.K., Park, J.B., Kang, D.Y., Sohn, J.H. and Jin, S.Y. (2020). A scoring system for the

diagnosis of non-alcoholic steatohepatitis from liver biopsy. Journal of Pathology and Translational Medicine, 54(3): 228-236.

Lee, M.B., Kooistra, M., Zhang, B., Slow, S., Fortier, A.L., Garrow, T.A., Lever, M., Trasler, J.A. and Baltz, J.M. (2012). Betaine Homocysteine Methyltransferase Is Active in the Mouse Blastocyst and Promotes Inner Cell Mass Development. Journal of Biological Chemistry, 287 (39), 33094-33103.

Lee, S., Kwak, J.H., Kim, S.H., Jeong, T.B., Won Son, S., Kim, J.H., Lim, Y., Cho, J.Y., Hwang, D.Y., Kim, K.S. and Jung, Y.S. (2019). Comparative study of liver injury induced by high-fat methionine- and choline- deficient diet in ICR mice originating from three different sources. Laboratory Animal Research, 35 (15), 1-7.

León, Z., García-Cañaveras, J. C., Donato, M. T., & Lahoz, A. (2013). Mammalian cell metabolomics: experimental design and sample preparation. *Electrophoresis, 34*, 2762–2775.

Lettéron, P., Sutton, A., Mansouri, A., Fromenty, B. and Pessayre, D. (2003). Inhibition of microsomal triglyceride transfer protein: Another mechanism for drug-induced steatosis in mice. Hepatology38, 133–140.

Leung, T.M. and Nieto, N. (2013). CYP2EI and oxidant stress in alcoholic and non-alcoholic fatty liver disease. Journal of Hepatology, 58 (2), 395-398.

Lever, J., Krzywinski, M. and Altman, N. (2017). Principal component analysis. Springer Nature, 14 (7), 641-642.

Lewis, M., Schenker, S. and Combes, B. (1967). Studies on the pathogenesis of tetracycline-induced fatty liver. The American Journal of Digestive Diseases, 12, 429-438.

Lewis, J, H., Zimmerman, H.J., Garrett, C.T., Rosenberg, E. (1982). Valproate-induced hepatic steatogenesis in rats. Hepatology, 2 (6), 870-3.

Li, H., Toth, E. and Cherrington, N.J. (2018). Asking the Right Questions With Animal Models: Methionine- and Choline- Deficient Model in Predicting Adverse Drug Reactions in Human NASH. Toxicological Sciences, 161 (1), 23-33.

Li, F., Cao, L., Parikh, S. Zuo, R. (2020A). Three-Dimensional Spheroids With Primary Human Liver Cells and Differential Roles of Kupffer Cells in Drug-Induced Liver Injury. Journal of Pharmaceutical Sciences, 109 (6), 1912-1923.

Li, X., Zhang, F., Wang, D., Li, Z., Qin, X. and Du, G, (2014). NMR-based metabolomic and quantitative real-time PCR in the profiling of metabolic changes in carbon tetrachloride-induced rat liver injury. Journal of Pharmaceutical and Biomedical Analysis, 89, 42-49.

Li, Z., Li, L., Yang, Z., Xue, W., Tian, X. and Zhang, X. (2017). ^{1}H-NMR Based Serum Metabolomics Study to Investigate Hepatoprotective Effect of Qin-Jiao on Carbon Tetrachloride-Induced Acute Hepatotoxicity in Rats. Evidence-Based Complementary and Alternative Medicine, 1-11.

Li, Z., Li, Y., Z, H.X., G, J.R., L, C.W.K., W, C.Y. and Z, W. (2019). Mitochondria-Mediated Pathogenesis and Therapeutics for Non-Alcoholic Fatty Liver Disease. Molecular Nutrition & Food Research, 63 (16).

Li, Z., Wang, F., Liang, B., Su, Y., Sun, S., Xia, S., Shao, J., Zhang, Z., Hong, Zhang, F. and Zheng, S. (2020B). Methionine metabolism in chronic liver diseases: and update on molecular mechanism and therapeutic implication. Signal Transduction and Targeted Therapy, 5 (280).

Liang, H., Zhang, L., Wang, H., Tang, J., Yang, J., Wu, C. and Chen, S. (2015). Inhibitory Effect of Gardenoside on Fatty Acid-Induced Steatosis in HepG2 Hepatocytes. Int. J. Mol. Sci, 16 (11), 27749-27756.

Lim, J.W., Dillon, J. and Miller, M. (2014). Proteomic and genomic studies of non-alcoholic fatty liver disease- clues in the pathogenesis. World Journal of Gastroenterology, 20 (26), 8325-8340.

Lin, X., Liu, X., Triba, M.N., Bouchemal, N., Liu, Z., Walker, D.I., Palama, T., Le Moyec, L., Ziol, M., Helmy, N., Vons, C., Xu, G., Prip-Buus, C. and Savarin, P. (2022). Plasma Metabolomic and Lipidomic Profiling of Metabolic Dysfunction-Associated Fatty Liver Disease in Humans Using an Untargeted Multiplatform Approach. Metabolites, 12 (1081).

Listenberger, L.L., Han, X., Lewis, S.E., Cases, S., Farese, R.V., Ory, D.S. and Schaffer, J.E. (2003). Triglyceride accumulation protects against fatty acid-induced lipotoxicity. PNAS, 100 (6), 3077-3082.

Liu, J.Y., Zhang, Y.C., Song, L.N., Yang, F.Y., Zhu, X.R., Cheng, Z.Q., Cao, X. and Yang, J.K. (2019). Nifuroxazide ameliorates lipid and glucose metabolism in palmitate-induced HepG2 cells. RSC Advances, 67 (9), 39394-39404.

Liu, X., Wang, H. and Roberts, M.S. (2017). Chapter 30-Hepatic Metabolism in Liver Health and Disease. Liver Pathophysiology, 391-400.

Lopez-Riera, M., Conde, I., Tolosa, L., Zaragoza, A., Castell, J.V., Gomez-Lechon, M. and Jover, R. (2017). New microRNA Biomarkers for Drug-Induced Steatosis and Their Potential to Predict the Contribution of Drugs to Non-alcoholic Fatty Liver Disease. Frontiers in Pharmacology, 8 (3), 1-12.

Lu, S.C. (2000). S-Adenosylmethionine. The International Journal of Biochemistry & Cell Biology, 32 (4), 391-396.

Lu, Q., Tian, X., Wu, H., Huang, J., Li, M., Mei, Z., Zhou, L., Xie, H. and Zheng, S. (2021). Metabolic Changes of Hepatocytes in NAFLD. Front Physiol, 12 (710420).

Lu, X., Zhong, R., Sun, H., Zheng, B., Chen, L., Miao, S. and Liang, P. (2019). Inhibition Effect of Triglyceride Accumulation by Large Yellow Croacker Roa DHA-PC in HepG2 Cells. Mar Drugs, 17 (9), 485.

Luder, A.S., Parks, J.K., Frerman, F. and Parker Jr, W.D. (1990). Inactivation of beef brain alpha-ketoglutarate dehydrogenase complex by valproic acid and valproic acid metabolites. Possible mechanism of anticonvulsant and toxic actions. J Clin Invest, 86 (5), 1574-81.

Luef, G., Rauchenzauner, M., Waldmann, M., Sturm, W., Sandhofer, A., Seppi, K., Trinka, E., Unterberger, I., Ebenbichler, C.F., Joannides, M., Walser, G., Bauer, G., Hoppichler, F. and Lechleitner, M. (2009). Non-alcoholic fatty liver disease (NAFLD), insulin resistance and lipid profile in antiepileptic drug treatment. Epilepsy Research, 86 (1), 42-47.

Lyall, M.J., Cartier, J., Thomson, J.P., Cameron, K., Meseguer-Ripolles, J., O'Duibhir, E., Szkolnicka, D., Lucendo Villarin, B., Wang, Y., Rodriguez Blanco, G., Dunn, W.B., Meehan,

R.R., Hay, D.C. and Drake, A.J. (2018). Modelling non-alcoholic fatty liver disease in human hepatocyte-like cells. Philosophical Transactions of the Royal Society B, 5 (373), 1750.

Lyon, P., Strippoli, V., Fang, B. and Cimming, L. (2020). B Vitamins and One-Carbon Metabolism: Implications in Human Health and Disease. 12 (9), 2867.

Lytle, K.A., Depner, C.M., Wong, C.P. and Jump, D.B. (2015). Docosahexaenoic acid attenuates western diet induced hepatic fibrosis in Ldlr−/− mice by targeting the TGF-beta-Smad pathway. J Lipid Res, 56, 1936–1946.

Ma, D.W.L., Ardent, B.M., Hillyer, L.M., Fung, S.K., McGilvray, I., Guindi, M. and Allard, J.P. (2016). Plasma phospholipids and fatty acid composition differ between liver biopsy-proven nonalcoholic fatty liver disease and healthy subjects. Nutrition & Diabetes, 6, 1-7.

Ma, S. and Dai, Y. (2011). Principal component analysis-based methods in bioinformatics studies. Briefings in Bioinformatics, 12 (6), 714-722.

Mahadevan, V. (2014). Anatomy of the Liver. Surgery, 1-5.

Malhi, H., Bronk, S.F. and Werneburg, N.W. (2006). Free Fatty Acids Induce JNK-dependent Hepatocyte Lipoapoptosis. Journal of Biological Chemistry, 281 (17), 12093-12101.

Malhi, H. and Gore, G.J. (2008). Molecular Mechanism of Lipotoxicity in Nonalcoholic Fatty Liver Disease. Seminars in Liver Disease, 28 (4), 360-369.

Mailioux, R.J., Young, A., Chalker, J., Gardiner, D., O'Brien, M., Slade, L. and Brosnan, J.T. (2016). Choline and dimethylglycine produce superoxide/hydrogen peroxide from the electron transport chain in liver mitochondria. FEBS Letters, 590, 431804328.

Malhotra, P., Gill, R.K., Saksena, S. and Alrefai, W.A. (2020). Disturbances in Cholesterol Homeostasis and Non-alcoholic Fatty Liver Diseases. Frontiers in Medicine Gastroenterology, 7 (467).

Malik, S.A., Acharya, J.D., Mehendale, N.K., Kamat, S.S. and Ghaskadbi, S.S. (2019). Pterostilbene reverses palmitic acid mediated insulin resistance in HepG2 cells by reducing oxidative stress and triglyceride accumulation. Free Radic Res, 53 (7), 815-827.

Mannisto, V.T., Simonen, M., Hyysalo, J., Soininen, P., Kangas, A.J., Kaminska, D., Matte, A.K., Venesmaa, S., Kakela, P., Karja, V., Arola, J., Gylling, H., Cederberg, H., Kuusisto, M., Yki-Jarvinen, Ala-Korpela, M., Pihlajamaki, J. (2014). Ketone body production is differentially altered in steatosis and non-alcoholic steatohepatitis in obese humans. Liver International, 35 (7), 1853-1861.

Maronpot, R.R, and Malarkey, D.E. (2019). Pathology of the Liver and Gallbladder. Toxicology Pathology for Non-Pathologists. Humana, New York.

Martinez, Y., Li, X., Liu, G., Bin, P., Yan, W., Mas, D., Valdivie, M., Hu, C.A.A., Ren, W. and Yin, Y. (2017). The role of methionine on metabolism oxidative stress, and disease. Amino Acids, 49 (12), 2091-2098.

Martinez-Sena, T., Moro, E., Moreno-Torres, M., Quintas, G., Hengstler, J. and Castell, J.V. (2023). Metabolomics-based strategy to assess drug hepatotoxicity and uncover the mechanisms of hepatotoxicity involved. Archives of Toxicology.

Mashek, D.G., Bertics, S.J. and Grummer, R.R. (2001). Metabolic Fate of Long-Chain Unsaturated Fatty Acids and Their Effects on Palmitic Acid Metabolism and Gluconeogenesis in Bovine Hepatocytes. Journal of Dairy Science, 85 (9), 2283-2289.
Mahuri, M., Ahsan, M, Lee, M.H., Prastyo, D.D. and Wibawati. (2021). PCA-based Hotelling's T^2 chart with fast minimum covariance determinant (FMCD) estimator and kernel density estimation (KDE) for network intrusion detection. Computers & Industrial Engineering, 158, 107447.

Masoodi, M., Gastaldelli, A., Hyötyläinen, T., Arretxe, E., Alonso, C., Gaggini, M., Brosnan, J., Anstee, Q.M., Millet, O., Ortiz, P., Mato, J.M., Dufour, J.F. and Oresic, M. (2021). Metabolomics and lipidomics in NAFLD: Biomarkers and non-invasive diagnostic tests. Nat. Rev. Gastroenterol. Hepatol. 18 (12), 835–856.

Massart, J., Begriche, K., Buron, N., Porceddu, M., Borgne-Sanchez, A. and Fromenty, B. (2013). Drug-Induced Inhibition of Mitochondrial Fatty Acid Oxidation and Steatosis. Current Pathobiology Reports, 1, 147-157.

Massart, J., Begriche, K., Hartman, J.H. and Fromenty, B. (2022). Role of Mitochondrial Cytochrome P450 2E1 in Healthy and Diseased Liver. Cells, 11 (2), 288.

May, J.E., Xu, J., Morse, H.R., Avent, N.D. and Donaldson, C. (2016). Toxicity testing: the search for an in vitro alternative to animal testing. British Journal of Biomedical Science, 66 (3), 160-165.

Mayr, M., Chung, Y.L., Mayr, U., Yin, X., Ly, Lucy., Troy, H., Fredericks, S., Hu, Y., Griffiths, J.R. and Xu, Q. (2005). Proteomic and Metabolomic Analyses of Atherosclerotic Vessels From Apolipoprotein E-Deficient Mice Reveal Alterations in Inflammation, Oxidative Stress, and Energy Metabolism. Atherosclerosis, Thrombosis and Vascular Biology, 25, 2135-2142.

Mazzolini, G.M., Sowa, J.P., Atorrasagasti, C., Kucukoglu, O., Syn, W.K. and Canbay, A. (2020). Significance of Simple Steatosis: An Update on the Clinical and Molecular Evidence. Cells, 9 (11), 2458.

Medici, V., Peerson, J.M., Stabler, S.P., French, S.W., Gregory III, J.F., Virata, M.C., Albanese, A., Bowlus, C.L., Devaraj. S., Panacek, E.A., Rahim, N., Richards, J.R., Rossaro, L. and Halsted, C.H. (2010). IMPAIRED HOMOCYSTEINE IS AN INDICATOR OF ALCOHOLIC LIVER DISEASE. J Hepatol, 53 (3), 551-557.

Mehta, S. (2013). Oxidation of Fatty Acids. Pharma Change, 11 October. Available from https://pharmaxchange.info/2013/10/oxidation-of-fatty-acids/

MEI, S., NI, H.M., MANLEY, S., BOCKUS, A., KASSEL, K.M., LUYENDYK, J.P, COPPLE, B.L. and DING, W.X. (2011). Differential roles of unsaturated and saturated fatty acids on autophagy and apoptosis in hepatocytes. J Pharmacol Exp Ther 339 (2), 487-498.

Merrell, M.D. and Cherrington, N.J. (2011). Drug metabolism alterations in nonalcoholic fatty liver disease. Drug Metab Rev, 43 (3), 317-334.

Meseguer, E.S., Elizalde, M.U., Borobia, A.M. and Ramirez, E. (2021). Valproic Acid-Induced Liver Injury: A Case-Control Study from a Prospective Pharmacovigilance Program in a Tertiary Hospital. Journal of Clinical Medicine, 10 (6), 1153.

Miele, L., Liguori, A., Marrone, G., Biolato, M., Araneo, C., Vaccaro, F.G., Gasbarrini, A. and Grieco, A. (2017). Fatty liver and drugs: the two sides of the same coin. European Review for Medical and Pharmacological Sciences, 21 (1), 86-94.

Miller, M.H., Ferguson, M.A.J. and Dillon, J.F. (2011). Systematic review of performance of non-invasive biomarkers in the evaluation of non-alcoholic fatty liver disease. Liver International, 31 (4), 461-473.

Mitra, V. and Metcalf, J. Functional anatomy and blood supply of the liver. Anaesthesia and Intensive Care Medicine, 13 (2), 52-53.

Mizoi, K., Arakawa, H., Yano, K., Koyama, S., Kojima, H. and Ogihara, T. (2020). Utility of Three-Dimensional Cultures of Primary Human Hepatocytes (Spheroids) as Pharmacokinetic Models. Biomedicines, 8 (10), 374.

Mnif, L., Sellami, R. and Masmoudi, J. (2016). Valproic Acid and Hepatic Steatosis: A Possible Link? About a Case Report. Psychopharmacol Bull, 46 (2), 59-62.
Rui, L. (2014). Energy Metabolism in the Liver. Compr Physiol, 4 (1), 177-197.

Mohammed-Ali, Z., Carlisle, R.E., Nademi, S. and Dickhout, J.G. (2017). Chapter 16- Animal Models of Kidney Disease. Animal Models for the Study of Human Disease (Second Edition), 379-417.

Molinaro, A., Becattini, B. and Solinas, G. (2020). Insulin signalling and glucose metabolism in different hepatoma cell lines deviate from hepatocyte physiology toward a convergent aberrant phenotype. Scientific reports, 10, 12031.

Moola, A., de Boer., Pavlov, D., Amin, A., Taylor., Gilligan, L., Hughes, B., Ryan, J., Barnes, E., Hassan-Smith, Z., Grove, J., Aithal, G.P., Verrijken, A., Francque, S., Van Gaal, L., Armstrong, M.J., Newsome, P.N., Cobbold, J.F., Arlt, W., Biehl, M. and Tomlinson, J.W. (2020). Accurate non-invasive diagnosis and staging of non-alcoholic fatty liver disease using the urinary steroid metabolome. Alimentary Pharmacology & Therapeutics, 51 (11), 1188-1197.

Mooli, R.G.R., and Ramakrishnan, S.K. (2022). Emerging Role of Hepatic Ketogenesis in Fatty Liver Disease. Frontiers in Physiology, 13, 946474.

Moravcova, A., Cervinkova, Z., Kucera, O., Mezera, V. and Rychtrmoc, D. (2015). The Effect of Oleic and Palmitic Acid on Induction of Steatosis and Cytotoxicity on Rat Hepatocytes in Primary Culture. Physiol Res, 64 (5), 627-636.

Morrow, G.P., MacMillan, L., Lamarre, S.G., Young, S.K., Macfarlane, A.J., Brosnan, M.E. and Brosnan, J.T. (2015). In Vivo Kinetics of Formate Metabolism in Folate-deficient and Folate-replete Rats. Journal of Biological Chemistry, 290 (4), 2244-2250.

Morvan, D. and Demidem, A. (2007). Metabolomics by proton nuclear magnetic resonance spectroscopy of the response to chloroethylmitrosourea reveals drug efficacy and tumor adaptive metabolic pathways. Cancer Res, 67 (5), 2150-9.

Muller, F.A. and Strula, S.J. (2019). Human in vitro models of nonalcoholic fatty liver disease. Current Opinion in Toxicology, 16, 9-16.

Muschet, C., Moller, G., Prehn, C., de Angelis, M.H., Adamski, J. and Tokarz, J. (2016). Removing the bottlenecks of cell culture metabolomics: fast normalization procedure, correlation of metabolites to cell number, and impact of the cell harvesting method. Metabolomics, 12 (151).

Mushtaq, M.Y., Choi, Y.H., Verpoorte, R. and Wilson, E.G. (2014). Extraction for Metabolomics: Access to The Metabolome. Phytochemical Analysis, 25 (4), 291-306.

Nahm, F.S. (2016). Nonparametric statistical tests for the continuous data: the basic concept and the practical use. Korean J Anesthesiol. 69 (1), 8-14.

Naish, J., Revest, P. and Syndercombe Court, D. (2009). Medical Sciences. London: Elsevier.

Nagarajan, P., Kumar, M.J.M., Venkatesan, R., Majundar, S.S. and Juyal, R.C. (2012). Genetically modified mouse models for the study of nonalcoholic fatty liver disease. World journal of Gastroenterology, 21 (18), 1141-1153.

Nassir, F. and Ibdah, J.A. (2014). Role of Mitochondria in Nonalcoholic Fatty Liver Disease. Int J Mol Sci, 15 (5), 8713-8742.

Nebert, D.W. and Karp, C.L. (2008). Endogenous functions of aryl hydrocarbon receptor (AHR): intersection of cytochrome P450-1 (CYP1)- metabolized eisocanoids and AHR biology. J Biol Chem, 283, 36061-36065.

Nelson, D.L. and Cox, M.M. (2012). Lehninger Principles of Biochemistry. 6th Edition. New York: W.H. Freeman.

Nelson, J.E., Klintworth, H. and Kowdley, K.V. (2011). Iron Metabolism in Nonalcoholic Fatty Liver Disease. Current Gastroenterology Reports, 14, 8-16.

Nelson, L.J., Navarro, M., Treskes, P., Samuel, K., Tura-Ceide, O., Morely, S.., Hayes, P.C, and Plevris, J.N. (2015). Acetaminophen cytotoxicity is ameliorated in a human liver organotypic co-culture model. Scientific Reports, 5 (17455).

Nemecz, M., Constantin, A., Dumitrescu, M., Alexandru, N., Filippi, A., Tanko, G. and Georgescu, A. (2019). The Distinct Effects of Palmitic and Oleic Acid on Pancreatic Beta Cell Function: The Elucidation of Associated Mechanisms and Effector Molecules. Frontiers in Pharmacology, 9 (1554).

Nemes, K., Aberg, F., Gylling, H. and Isoniemi, H. (2016). Cholesterol metabolism in cholestatic liver disease and liver transplantation: From molecular mechanisms to clinical implications World Journal of Hepatology, 8 (88), 924-932.

Neuman, M.G., Cohen, L.B. and Nanau, R.M. (2014). Biomarkers in non-alcoholic fatty liver disease. Canadian Journal of Gastroenterology and Hepatology, 28 (11), 607-618.

Nguyen, S.T., Nguyen, H.T.L. and Truong, K.D. (2020). Comparative cytotoxic effects of methanol, ethanol and DMSO on human cancer cell lines. Biomedical Research and Therapy, 7 (7), 3855-3859.

Nguyen-Lefebvre, A.T. and Horuzsko, A. (2015). Kupffer Cell Metabolism and Function. Journal of Enzymology and Metabolism, 1 (1), 101.

Nicholls, A.W., Holmes, E., Lindon, J.C., Shockcor, J.P., Duncan Farrant, R., Haselden, J., Damment, S.J.P., Waterfield, C.J. and Nicholson, J.K. (2001). Metabonomic Investigations into Hydrazine Toxicity in the Rat. Chemical Research in Toxicology, 14 (8), 975-987.

Nicholson, J.K. and Wilson, I.D. (2003). Understanding 'Global' Systems Biology: Metabonomics and the Continuum of Metabolism, 2, 668-676.

Nimer, N., Choucair, I., Wang, Z., Nemet, I., Li, L., Gukasyan, J., Weeks, T.L., Alkhouri, N., Zein, N., Wilson Tang, W.H., Fischbach, M.A., Brown, J.M., Allayee, H., Dasarathy, S., Gogonea, V. and Hazen, S.L. (2021). Bile acids profile, histopathological indices and genetic variants for non-alcoholic fatty liver disease progression. Metabolism. 116, 154457.

NMR Lab. (2018). The basis of NMR [image]. Available from http://chem.ch.huji.ac.il/nmr/whatisnmr/whatisnmr.html [Accessed 30 August].

Noga, A.A., Zhao, Y. and Vance, D.E. (2002). An unexpected requirement for phosphatidylethanolamine N-methyltransferase in the secretion of very low density lipoproteins. J Biol Chem, 277 (44), 42358-65.

Nudischer, R., Renggli, K., Hierlemann, A., Roth, A.B. and Bertinetti-Lapatki, C. (2020). Characterization of a long-term mouse primary liver 3D tissue model recapitulating innate-immune responses and drug-induced liver toxicity. PLOS ONE, 15 (7).

O'Dwyer, C., Yaworski, R., Katsumura, S., Ghorbani, P., Gobeil Odai, K., Nunes, J.R.C., LeBlond, N.D., Sanjana, S., Smith, T.T.K., Han, S., Margison, K.D., Alain, T., Morita, M. and Fullerton, M.D. (2020). Hepatic Choline Transport Is Inhibited During Fatty Acid-Induced Lipotoxicity and Obesity. Hepatology Communications, 4 (6), 876-889.

O'Gorman, A., Gibbons, H. and Brennan, L. (2013). Metabolomics in the Identification of Biomarkers of Dietary Intake. Computational and Structural Biotechnology Journal, 4 (5), 1-7.

Oh, H.A., Kim, Y.J., Moon, K.S., Seo, J.W., Jung, B.H. and Woo, D.H. (2022). Identification of integrative hepatotoxicity induced by lysosomal phospholipase A2 inhibition of cationic amphiphilic drugs via metabolomics. Biochemical and Biophysical Research Communications, 607, 1-8.

Ore, A. and Akinloya, O.A. (2019). Oxidative Stress and Antioxidant Biomarkers in Clinical and Experimental Models of Non-Alcoholic Fatty Liver Disease, Medicina, 55 (2), 26.

Ornoy, A., Becker, M., Weinstein-Fudim, L. and Ergaz, Z. (2020). S-Adenosine Methionine (SAMe) and Valproic Acid (VPA) as Epigenetic Modulators: Special Emphasis on their Interactions Affecting Nervous Tissue during Pregnancy. International Journal of Molecular Sciences, 21 (1).

Osabe, M., Sugatani, J., Fukuyama, T., Ikushiro, S., Ikari, A., Miwa, M. (2008). Expression of hepatic UDP-glucuronosyltransferase 1A1 and 1A6 correlated with increased expression of the nuclear constitutive androstane receptor and peroxisome proliferator-activated receptor alpha in male rats fed a high-fat and high sucrose diet. Drug Metab Dispos, 36, 294-302.

Osborne, J.W. and Costello, A.B. (2004). Sample size and subject to item ration in principle component analysis. Practical Assessment, Research, and Evaluation, 9 (11).

Ouchi, R., Togo, S., Limura, M., Yoshikawa, H.Y., Wells, J.M. and Takebe, T. (2019). Modelling Steatohepatitis in Humans with Pluripotent Stem Cell-Derived Organoids. Cell Metabolosim, 30, 374-384.

Pacana, T., Cazanave, S., Verdianelli, A., Patel, V., Min, H.K., Mirshahi, F., Quinlivna, E. and Sanyal, A.J. (2015). Dysregulated Hepatic Methionine Metabolism Drives Homocysteine Elevation in Diet-Induced Nonalcoholic Fatty Liver Disease. PLOS One, 10 (8).

Padberg, F., Hering, H., Luch, A. and Zellmer, S. (2020). Indirect co-cultivation of HepG2 with differentiated THP-1 cells induces AHR signalling and release of pro-inflammatory cytokines. Toxicology in Vitro, 68 (104957).

Pal, S., Thomson, A.M., Bottema, C.D.K. and Roach, P.D. (2002). Polyunsaturated fatty acids downregulate the low density lipoprotein receptor of human HepG2 cells. The Journal of Nutritional Biochemistry, 13 (1), 55-63.

Pan, Y., Cao, M., You, D. and Qin, G. (2019). Research Progress on the Animal Models of Drug-Induced Liver Injury: Current Status and Further Perspectives. BioMed Research International, (1283824), 1-12.

Pandit, A., Sachdeva, T. and Bafna, P. (2012). Drug-induced Hepatotoxicity: A review. Journal of Applied Pharmaceutical Science, 2 (5), 233-243.

Parhamifar, L., Andersen, H. and Moghimi, S.M. (2012). Lactate Dehydrogenase Assay for Assessment of Polycation Cytotoxicity. Nanotechnology for Nucleic Acid Delivery, 948, 13-22.

Parra-Vargas, M., Sandoval-Rodriguez, A., Rodriguez-Echevarria, R., Dominguez-Rosales, J.A., Santos-Garcia, A. and Armendariz-Borunda, J. (2018). Nutrients, 10 (8).

Parry, S.A. and Hodson, L. (2017). Influence of dietary macronutrients on liver fat accumulation and metabolism. Journal of Investigative medicine, 65 (8).

Pastore, A., Alisi, A., Di Giovamberardino, G., Crudele, A., Ceccarelli, S., Panera, N., Dionisi-Vici, C. and Nobili, V. (2014). Plasma Levels of Homocysteine and Cysteine Increased in Pediatric NAFLD and Strongly Correlated with Severity of Liver Damage. Int. J. Mol. Sci, 15.

Patel, V. and Sanyal, A.J. (2013). Drug-Induced Steatohepatitis. Clinical Liver Disease, 17 (4), 533546.

Patrick, G.L. (2009). An Introduction to Medical Chemistry, 4th ed. Oxford: Oxford University Press.

Patti, G.J., Yanes, O. and Siuzdak, G. (2012). Metabolomics: the apogee of the omics trilogy. Nature reviews, 13, 263-269.

Pavlik, L., Regev, A., Ardayfio, P. and Chalasani, N.P. (2019). Drug-Induced Steatosis and Steatohepatitis: The Search for Novel Serum Biomarkers Among Potential Biomarkers for Non-Alcoholic Fatty Liver Disease and Non Alcoholic Steatohepatitis. Toxicology and Drug Experience, 42 (6), 701-711.

Payne, F., Lim, K., Girousse, A., Brown, R.J., Kory, N., Robbins, A., Xue, Y., Sleigh, A., Cochran, E., Adams, C., Borman, A.D., Russel-Jones, D., Gorden, P., Semple, R.K., Saudek, V., O'Rahilly, S., Walther, T.C., Barroso, I. and Savage, D.B. (2014). Mutations disrupting the Kennedy phosphatidylcholine pathway in humans with congenital lipodystrophy and fatty liver disease.

Peng, K.Y. and Meex, R.C.R. (2018). Mitochondrial dysfunction-related lipid changes occur in nonalcoholic fatty liver disease progression. Journal of Lipid Research, 59 (10), 1977-1986.

Perakakis, N., Stefanakis, K. and Mantzoros, C.S. (2020). The role of omics in the pathophysiology, diagnosis and treatment of non-alcoholic fatty liver disease. Metabolism, 11, 1-24.

Petrini, L., Pennati, G. and Fotiadis, D. (2022). Editorial: Verification and Validation of in *silico* Models for Biomedical Implantable Devices. Frontiers in Medical Technology, 4.

Phang-Lyn, S. and Llerena, V.A. (2020). Biochemistry, Biotransformation. StatPearls. Treasure Island (FL).

Piazzolla, V.A. and Mangia, A. (2020). Noninvasive Diagnosis of NAFLD and NASH. Cells, 9 (1005), 1-17.

Pingitore, P., Sasidharan, K., Ekstrand, M., Prill, S., Linden, D. and Romeo, S. (2019). Human Multilineage 3D Spheroids as a Model of Liver Steatosis and Fibrosis. International Journal of Molecular Sciences, 20 (7), 1629.

Piras, I.S., Raju, A., Don, J., Schork, N.J., Gerhard, G.S. and DiStefano, J.K. (2022). Hepatic PEMT Expression Decreases with Increasing NAFLD Severity. Int J Mol Sci, 23 (1), 9296.

Pirozzi, C., Lama, A., Annunziata, C., Cavaliere, G., De Caro, C., Citraro, R., Russo, E., Tallarico, M., Iannone, M., Ferrante, M.C., Mollica, M.P., Raso, G.M., De Sarro, G., Calignano, A. and Meli, R. (2019). Butyrate prevents valproate-induced liver injury: In vitro and in vivo evidence. The FASEB Journal, 34, 676-690.

Pogribny, I.P., Prizimirska, T.V., Kulik, G.I., Lutsiuk, M.B., Pentiuk, O.O., Postovitenko, K.P., Artemchuk, M.A., Poirier, L.A. and Chekhun, V.F. (2005). Age-related effects of methionine-enriched diet on plasma homocysteine concentration and methylation of hepatic DNA in rats. Ukr Biokhim Zh, 77, 114-119.

Polyzos, S.A., Kountouras, J., Patsiaoura, K., Katsiki, E., Zafeiriadou, E., Deretzi, G., Zavos, C., Gavalas, E., Katsinelos, P., Mane, V. and Slavakis, A. (2012). Serum homocysteine levels in patients with nonalcoholic fatty liver disease. Annals of Hepatology, 11 (1), 68-76.

Ponziani, F., Pecere, S., Gasbarrini, A. and Ojetti, V. (2015). Physiology and pathophysiology of liver lipid metabolism. Expert Review of Gastroenterology, 9, 1055-1067.

Postic, C. and Girard, D.J. (2004). Role of the liver in the control of carbohydrate and lipid homeostasis, Diabetes and Metabolism, 30 (5), 389-408.

Powell, N.R., Liang, T., Ipe, J., Cao, S, Skaar, T.C., Desta, Z., Qian, H.R., Ebert, P.J., Chen, Y., Thomes, M.K. Chalasani, N. (2023). Clinically important alterations in pharmacogene expression in histologically severe nonalcoholic fatty liver disease. Nat Commun, 14, 1474.

Pretzner, B., Taylor, C., Dorozinski, F., Denker, M., Liebminger, A. and Herwig, C. (2020). Multivariate Monitoring Workflow for Formulation Fill and Finish Processes. Bioengineering, 7 (50), 1-16.

Puri, P., Baillie, R.A., Wiest, M.M., Mirshahi, F., Choudhury, J., Cheung, O., Sargeant, C., Contos, M.J and Sanyal, A.J. (2007). A lipidomic Analysis of Nonalcoholic Fatty Liver Disease. Hepatology, 46 (4), 1081-1090.

Puschel, G.P. and Henkel, J. (2018). Dietary cholesterol does not break your heart but kills your liver. Porto Biomedical Journal, 3 (1), 12.

Putko, P., Romero, J.A. and Kazimierczuk, K. (2024). A pH-enhanced resolution in benchtop NMR spectroscopy. Analyst, 149, 1998-2003.

Rabinowich, L. and Shibolet, O. (2015). Drug-induced Steatohepatitis: An Uncommon Culprit of a Common Disease. BioMed Research International, 1 (1), 1-14.

Rada, P., Gonzalez-Rodriguez, A., Garcia-Monzon, C. and Valverde, A.M. (2020). Understanding lipotoxicity in NAFLD pathogenesis: is CD36 a key driver? Cell Death & Disease, 11 (802).

Radziejewska, A., Muzsik, A., Milagro, F.I., Martinez, J.A. and Chmurzynska, A. (2020). One-Carbon Metabolism and Nonalcoholic Fatty Liver Disease: The Crosstalk between Nutrients, Microbiota, and Genetics. Lifestyle Genomics, 13, 53-63.

Rafiei, H., Omidian, K. and Bandy, B. (2019). Dietary Polyphenols Protect Against Oleic Acid-Induced Steatosis in an in Vitro Model of NAFLD by Modulating Lipid Metabolism and Improving Mitochondrial Function. Nutrients, 11 (3), 541.

Rahman, M and Nguyen, H. (2022). Valproic Acid. StatPearls, Treasure Island. Available from: https://www.ncbi.nlm.nih.gov/books/NBK559112/

Ramaiahgari, S.C., den Braver, M.W., Herpers, B., Terpstra, V., Commandeur, J.N.M., van de Water, B. and Price, L.S. (2014). A 3D in vitro model of differentiated HepG2 cell spheroids with improved liver-like properties for repeated dose high-throughput toxicity studies. Archives of Toxicology, 88, 1083-1095.

Ramirez, T., Strigun, A., Verlohner, A., Huener, H.A., Peter, E., Herold, M., Bordag, N., Mellert, W., Walk, T., Spitzer, M., Jiang, X., Sperber, S., Hofmann, T., Hartung, T., Kamp, H. and van Ravenzwaay, B. (2018). Prediction of liver toxicity and mode of action using metabolomics in vitro in HepG2 cells. Arch Toxicol, 92 (2), 893-906.

Ramos, M.J., Bandiera, L., Menolascina, F. and Fallowfield, J.A. (2022). *In vitro* models of non-alcoholic fatty liver disease: Emerging platforms and their applications. iScience, 25 (1), 103549.

Reddin, I.G., Fenton, T.R., Wass, M.N. and Michaelis, M. (2023). Large inherent variability in data derived from highly standardised cell culture experiments, Pharmacol Res. 188:106671.

Ren, J.L., Zhang, A.H., Kong, L. and Wang, X.J. (2018). Advances in mass spectrometry-based metabolomics for investigation of metabolites. RSC Advances, 40.

Rey-Bedon, C., Banik, P., Gokaltun, A., Hofheinz, O., Yarmush, M.L., Uygun, M.K. and Usta, O.B. (2022). CYP450 drug inducibility in NAFLD via an in vitro hepatic model: Understanding drug-drug interactions in the fatty liver. Biomedicine & Pharmacotherapy, 146, 112377.

Ricchi, M., Odoardi, M.R., Carulli, L., Anzivino, C., Ballestri, S., Pinetti, A, Fantoni L.I., Marra, F., Bertolotti, M., Banni, S.,Lonardo, A., Carulli, N. and Loria, P. (2009). Differential effect of oleic and palmitic acid on lipid accumulation and apoptosis in cultured hepatocytes. Gastroenterology, 24, 830-840.

Rinella, M.E., Elias, M.S., Smolak, R.R., Fu, T., Borensztajn, J. and Green, R.M. (2008). Mechanisms of hepatic steatosis in mice fed a lipogenic methionine choline-deficient diet. J Lipid Res, 49 (5), 1068-76.

Robinson, M.J. and Rywlin, A.M. (1970). Tetracycline-associated fatty liver in the male. Report of an autopsied case. Am J Dig Dis, 15 (9), 857-62.

Rodriguez-Antona, C., Donato, M.T., Boobis, A., Edwards, R.J., Watts, P.S., Vicente Castell, J. and Gomez-Lechon, M.J. (2008). Cytochrome P450 expression in human hepatocytes and hepatoma cell lines: molecular mechanisms that determine lower expression in cultured cells. Xenobiotica, 32 (6), 505-520.

Rodriguez-Burford, C., Oelschlager, D.K., Talley, L.I., Barnes, M.N., Partiridge, E.E. and Grizzle, W.E. (2003). The use of dimethylsulfoxide as a vehicle in cell culuture experiments using ovarian carcinoma cell lines. Biotechnic & Histochemistry, 78 (1), 17-21.

Romero, F.A., Jones, C.T., Xu, Y., Fenaux, M. and Halcomb, R.L. (2020). The Race to Bash NASH: Emerging Targets and Drug Development in a Complex Liver Disease.Journal of Medicinal Chemistry, 63 (10), 5031-5073.

Romualdo, G.R., Da Silva, T.C., De Albuquerque Landi, M.F., Morais, J.A., Barbisan, L.F., Vinken, M., Oliveira, C.P. and Cogliati, B. (2020). Sorafenib reduces steatosis-induced fibrogenesis in a human 3D co-culture model of non-alcoholic fatty liver disease. Environmental Toxicology, 36, 168-176.

Rosen, B.R. and Brady, T.J. (1983). Principles of nuclear magnetic resonance for medical application. Semin Nucl Med, 13 (4), 308-318.

Ruiz-Aracama, A., Peijnenburg, A., Kleinjans, J., Jennen, D., van Delft., J., Hellfrisch, C. and Lommen, A. (2011). An untargeted multi-technique metabolomics approach to studying intracellular metabolites of HepG2 cells exposed to 2,3,7.8-tetrachlorodibenzo-p-dioxin. BMC, 12 (251).

Ryu, N.E. Lee, S.H. and Park, H. (2019). Spheroid Culture System Methods and Applications for Mesenchymal Stem Cells. Cells, 8 (12), 1620.

Salsaa, M., Pereira, B., Liu, J., Yu, W., Jadhav, S., Huttermann,, M. and Greenberg, M.L. (2020). Valproate inhibits mitochondrial bioenergetics and increases glycolysis in *Saccharomyces cerevisiae.* Scientific Reports, 10 (11785).

Samuel, V.T. and Shulman, G.I. (2018). Nonalcoholic Fatty Liver Disease as a Nexus of Metabolic and Hepatic Diseases. Cell Metabolism, 27 (1), 22-41

Sanal, G.M. (2015). Biomarkers in non-alcoholic fatty liver diseases- the emperor has no clothes? World Journal of Gastroenterology, 21 (11), 3223-3231.

Sandlers, Y., Shah, R.R., Pearce, R.W., Dasarathy, J. and McCullough, A.J. (2020). Plasma Krebs Cycle Intermediates in Nonalcoholic Fatty Liver Disease. Journal of Clinical Medicine, 9 (2), 314.

Santhosh, S., Sini, T.K., Anandan, R. and Mathew, P.T. (2006). Effect of chitosan supplementation on antitubercular drugs-induced hepatotoxicity in rats. Toxicology, 219 (1-3), 53-59.

Sanyal, A.J. (2019). Past, present and future perspectives in nonalcoholic fatty liver disease. Nat. Rev. Gastroenterol. Hepatol, 16 (6), 377–386.

Sanz-Garcia, C., Fernandez-Iglesias, A., Gracia-Sancho, J., Arraez-Aybar, L.A., Nevzorova, Y.A. and Cubero, F.J. (2020). The Space of Disse: The Liver Hub in Health and Disease. Liver, 1, 3-26.

Sarabhai, T., Kahl, S., Szendroedi, J., Markgraf, D.F., Zaharia, O.P., Barosa, C., Herder, C., Wickrath, F., Bobrov, P., Hwang, J.H., Jones, J.G. and Roden, M. (2020). Monounsaturated fat rapidly induces hepatic gluconeogenesis and whole-body insulin resistance. JCI Insights, 5 (10).

Satapati, S., Sunny, N.E., Kucejova, B., Fu, X., Teng He, T., Mendez-Lucas, A., Shelton, J.M., Perales, J.C., Browning, J.D. and Burgess, S.C. (2012). Elevated TCA cycle function in the pathology of diet-induced hepatic insulin resistance and fatty liver. Journal of Lipid Research, 56 (6), 1080-1092.

Satapathy, S.K., Kuwakima, V., Nadelson, J., Atiq, O. and Sanyal, A.J. (2015). Drug-induced fatty liver disease: An overview of pathogenesis and management. Annals of Hepatology, 14 (6), 789-806.

Scholz, M., Gatzek, S., Sterling, A., Fiehn, O. and Selbig, J. (2004). Metabolite fingerprinting: detecting biological features by independent component analysis. Bioinformatics, 12 (20), 2447-54.

Schonborn, J.L. (2010). The Role of The Liver in Drug Metabolism Anaesthesia Tutorial of the Week 179.

Schwaninger, M., Ringleb, P., Winter, R., Kohl, B., Fiehn, W., Rieser, P.A. and Walter Sack, I. (1999). Elevated plasma concentrations of homocysteine in antiepileptic drug treatment. Epilepsia, 40, 345-350.

Sefried, S., Haring, H.U., Weigert, C. and Eckstein, S.S. (2018). Suitability of hepatocyte cell lines HepG2, AML12 and THLE-2 for investigation of insulin signalling and hepatokine gene expression. Open Biology, 8 (10).

Serviddio, G., Giudetti, A.M., Bellanti, F, et al. (2011). Palmitoyl Transferase-I (CPT-I) Impairs Fatty Acid Beta-Oxidation in Rats Fed a Methionine-Choline Deficient Diet. PLoS One, e24084.

Shabana, M.B., Ibrahim, H.M., Khadre, S.E.M. and Elemam, M.G. (2012). Influence of rifampicin and tetracycline administration on some biochemical and histological parameters in albino rats. The Journal of Basic & Applied Zoology, 65 (5), 299-308.

Sharma, B. and Savio, J. (2021). Nonalcoholic Steatohepatitis. StatPearls.

Shah, U.K., de Oliviera Mallia, J., Singh, N., Chapman, K.E., Doak, S.H. and Jenkins, G.J.S. (2017). A three-dimensional in vitro HepG2 cells liver spheroid model for genotoxicity studies. Mutat Res Genet Toxicol Environ Mutagen, 825, 51-58.

Shambaugh, G.E. (1977). Urea biosynthesis I. The urea cycle and relationships to the citric cycle. Am J Clin Nutr, 12, 2083-7.

Shao, C., Ye, J., Li, X., Lin, Y., Feng, S., Liao, B., Wang, W., Gong, X. and Zhong, B. (2022A). Discrepancies between Nonalcoholic and Metabolic-associated Fatty Liver Disease by Multiple Steatosis Assessment. J Clin Transl Hepatol, 10 (6), 1013-1026.

Shao, M., Lu, Y., Xiang, H., Wang, J., Ji, G. and Wu, T. (2022B). Application of metabolomics in the diagnosis of non-alcoholic fatty liver disease and the treatment of traditional Chinese medicine. Frontiers of Pharmacology and Drug Discovery, 13.

Shaukat, S.S., Rao, T.A. and Khan, M.A. (2016). Impact of sample size on principle component analysis ordination of an environmental data set: effects on eigenstructure. Ekologia, 35 (2), 173-190.

Shenderovich, I.G. and Limbach, H.H. (2021). Solid State NMR for Nonexperts: An Overview of Simple but General Practice Methods. Solids, 2, 139-154.

Sherriff, J.L., O'Sullivan, T.A., Properzi, C., Oddo, J.L. and Adams, L.A. (2016). Choline, Its Potential Role in Nonalcoholic Fatty Liver Disease, and the Case for Human and Bacterial Genes. Advances in Nutrition, 7 (1), 5-13.

Shifflet, A. and Wu, G.Y. (2009). Non-alcoholic Steatohepatitis: An Overview. Journal of the Formosan Medical Association, 108 (1), 4-12.
Smyth, R., (2018). Metabolomics and translation to clinic. Biomarkers. [Accessed 3 August 2018].

Shnayder, N.A., Grechkina, V.V., Trefilova, V.V., Efremov, I.S., Dontceva, E.A., Narodova, E.A., Petrova, M.M., Soloveva, I.A. et al., (2023). Valproate-Induced Metabolic Syndrome. Biomedicines, 11 (5), 1499.

Shoieb, S.M., El-Ghiaty, M.A., Alqahtani, M.A. and El-Kadi, A.O.S. (2020). Cytochrome P450-derived eicosanoids and inflammation in liver diseases. Prostaglandins & Other Lipid Mediators, 147, 106400.

Shrubsole, M.J., Wagner, C., Zhu, X., Hou, L., Loukachevitch, L.V., Ness, R.M and Zhang, W. (2015). Associations between S-adenosylmethionine, S-adenosylhomocysteine, and colorectal adenoma risk are modified by sex.

Shutter, M.C. and Akhondi, H. (2022). Tetracycline. StatPearls Publishing. Available from: https://www.ncbi.nlm.nih.gov/books/NBK549905/#

Sinton, M.C., Meseguer-Ripolles, J., Lucendo-Villarin, B., Tennant, D.A., Hay, D.C. and Drake, A.J. (2021). A human pluripotent stem cell model for the analysis of metabolic dysfunction in hepatic steatosis. iSceince, 24, 101931.

Smith, S.M., Wunder, M.A., Norris, D.A. and Shellman, Y.G. (2011). A Simple Protocol for using a LDH-Based Cytotoxicity Assay to Assess the Effects of Death and Growth Inhibition at the Same Time. PLOS ONE, 6 (11).

Smith, G.I., Shankaran, M., Yoshino, M., Schweitzer, G.G., Chondronikola, M., Beals, J.W., Okunade, A.L., Patterson, B.W., Nyangau, E., Field, T., Sirlin, C.B., Talukdar, S., Hellerstein, M.K. and Klein, S. (2020). Insulin resistance drives hepatic de novo lipogenesis in nonalcoholic fatty liver disease. The Journal of Clinical Investigation, 130 (3), 1453-1460.

Sokmen, B.B., Tunali, S. and Yanardag, R. (2012). Effects on vitamin U (S-methyl methionine sulphonium chloride) on valproic acid induced injury in rats. Food Chem Toxicol, 50 (1), 3562.

Song, J., da Costa, K.A., Fischer, L.M., Kohlmeier, M., Kwock, L., Wang, S. and Zeisel, S.H. (2005). Polymorphism of the PEMT gene and susceptibility to nonalcoholic fatty liver disease (NAFLD). FASEB J, 19, 1266–1271.

Song, X., Wang, J., Wang, P., Tian, N., Yang, M. and Kong, L. (2013). ^{1}H NMR-based metabolomics approach to evaluate the effect of Xue-Fu-Zhu-Yu decoction on hyperlipidemia rats induced by high fat diet. Journal of Pharmaceutical and Biomedical Analysis, 78 (79), 202-210.

Song, Y., Cho, M., Cho, C. and Rosenfeld, M.E. (2009). Methionine-induced hyperhomocysteinemia modulates lipoprotein profile and oxidative stress but not progression of atherosclerosis in aged apolipoprotein E knockout mice. J Med Food, 12 (1), 137-44.

Song, Z., Xiaoli, A.M. and Yangm F. (2018). Regulation and Metabolic Significance of *De Novo* Lipogenesis in Adipose Tissues. Nutrients, 10 (10), 1383.

Sookoian, S., Castaño, G.O., Scian, R., Fernández Gianotti, T., Dopazo, H., Rohr, C., Gaj, G., San Martino, J., Sevic, I., Flichman, D. and Pirola, C.J. (2016) Serum aminotransferases in nonalcoholic fatty liver disease are a signature of liver metabolic perturbations at the amino acid and Krebs cycle level. Am. J. Clin. Nutr, 103, 422–434.

Soret, P.A., Magusto, J., Housset, C. and Gautheron, J. (2020). In Vitro and In Vivo Models of Non-Alcoholic Fatty Liver Disease: A Critical Appraisal. Journal of Clinical Medicine, 10 (36),1-18.

Sousa, S.A.A., Magalhaes, A. and Ferreira, M.M.C. (2013). Optimized bucketing for NMR spectra: Three case studies. Chemometrics and Intelligent Laboratory Systems, 122, 93-102.

Stampar, M., Breznik, B., Filipic, M. and Zegura, B. (2020). Characterization of In Vitro 3D Cell Model Developed from Human Hepatocellular Carcinoma (HepG2) Cell Line. Cells, 9 (12), 2557.

Stechemesser, L., Eder, S.K., Wagner, A., Patsch, W., Feldman, A., Strasser, M., Auer, S., Niederseer, D., Huber-Schönauer, U., Paulweber, B., Zandanell, S., Ruhaltinger, S., Weghuber, D., Haschke-Becher, E., Grabmer, C., Rohde, E., Datz, C., Felder, T.K. and Aigner, E. (2016). Metabolomic profiling identifies potential pathways involved in the interaction of iron homeostasis with glucose metabolism. Mol Metab 6 (1), 38–47.

Steuer, A.E., Brockbals, L. and Kraemer, T. (2019). Metabolomic Strategies in Biomarker Research-New Approach for Indirect Identification of Drug Consumption and Sample Manipulation in Clinical and Forensic Toxicology? Frontiers in Chemistry, 7 (319).

Sukkasem, N., Chatuphonpraser, W. and Jarukamjorn, K. (2020). Cytochrome P450 expression-associated multiple-hit pathogenesis of non-alcoholic fatty liver disease (NAFLD) in HepG2 cells. Tropical Journal of Pharmaceutical Research, 19 (4), 707-714.

Sundaram, M. and Yao, Z. (2010). Recent progress in understanding protein and lipid factors affecting hepatic VLDL assembly and secretion. Nutrition & Metabolism, 7 (35).

Sung, M., Kim, I., Park., Whang, Y. and Lee, M. (2004). Differential effects of dietary fatty acids on the regulation of CYP2E1 and protein kinase C in human hepatoma HepG2 cells. J Med Food, 7 (2), 197-203.

Sunny, N.E., Parks, E.J., Browning, J.D. and Burgess, S.C. (2011). Excessive Hepatic Mitochondrial TCA Cycle and Gluconeogenesis in Humans with Nonalcoholic Fatty Liver Disease. Cell Metab, 14 (6), 804-810.

Sutherland, R.M., McCredie, J.A. and Inch, W.R. (1971). Growth of multicell spheroids in tissues culture as a model of nodular carcinomas. J Natl Cancer Inst, 46 (1), 113-20.

Szalowska, E., van der Burg, B., Man, H. Y., Hendriksen, P.J.M. and Peijnenburg, A.A.C.M. (2014). Model Steatogenic Compounds (Amiodarone, Valproic Acid, and Tetracycline) Alter Lipid Metabolism by Different Mechanisms in Mouse Liver Slices. PLoS ONE, 9.

Sztolsztener, K., Chabowski, A., Harasim-Symbor, E., Bielawiec, P. and Konstantynowicz-Nowicka, K. (2020). Arachidonic Acid as an Early Indicator of Inflammation during Non-Alcoholic Fatty Liver Disease Development. Biomolecules, 10 (8), 1-15.

Tagliatti, V. and Colet, J.M. (2016). Drug-Induced Impairment of Mitochondrial Fatty Acid BetaOxidation: A Metabonomic Evaluation in Rats. HSOA Journal of Medical Genomics and Biomarkers, 3 (005), 1-7.

Tallima, H., and El Ridi, R. (2018). Arachidonic acid: Physiological roles and potential health benefits- A review. Journal of Advanced Research, 11, 33-41.

Tang, B., Mustafa, A., Gupta, S., Melnyk, S., James, S.J. and Kruger, W.D. (2011). Methionine-deficient diet induces post-transcriptional down-regulation of Cystathionine β-Synthase. Nutrition, 26 (11-12), 1170-1175.

Tarling, E.J., Ahn, H. and de Aguiar, V.T. (2015). The nuclear receptor FXR uncouples the actions of miR-33 from SREBP-2. Arterioscler. Thromb. Vasc. Biol, 35, 787–795.

Teng, Q., Huang, W., Collette, T. W., Ekman, D. R., & Tan, C. (2009). A direct cell quenching method for cell-culture based metabolomics. *Metabolomics, 5*, 199–208.

Teodoro, J.S., Rolo, A.P., Duarte, F.V., Simoes, A.M. and Palmeira, C.M. (2008). Differential alterations in mitochondrial functions induced by a choline-deficient diet: Understanding fatty liver disease progression. (2008). Mitochondrion, 8 (5-6), 367-376.

Thomsen, K.L., Eriksen, P.L., Kerbert, A.J.C., De Chiara, F., Jalan, R. Vilstrup, H. (2023). Role of Ammonia in NAFLD: An Unusual Suspect. Med Hypotheses, 113, 91-97.

Tidwell, T.R., Rosland, G.V., Tronstad, K.J., Soreide, K. and Hagland, H.R. (2022). Metabolic flux analysis of 3D spheroids reveals significant differences in glucose metabolism from matched 2D cultures of colorectal cancer and pancreatic ductal adenocarcinoma cell lines. Cancer & Metabolism, 10 (9).

Tie, F., Ding, J., Hu, N., Dong, Q., Chen, Z. and Wang, H. (2021). Kaempferol and Kaempferide Attenuate Oleic Acid-Induced Lipid Accumulation and Oxidative Stress in HepG2 Cells. International Journal of Molecular Science, 22 (16).

Tilg, H., Adolph, T.E. and Moschen, A.R. (2020). Multiple Parallel Hits Hypothesis in Nonalcoholic Fatty liver Disease: Revisited After a Decade. AASLD, 73 (2), 833-842.

Tiwari, S. and Siddiqi, S.A. (2012). Intracellular Trafficking and Secretion of Very Low Density Lipoproteins. Arterioscler Thromb Vasc Biol, 32 (5), 1079-1086.

Tognarelli, J.M., Dawood, M., Shariff, M.I., Grover, V.PB., Crossey, M.M.E., Cox, I.J., Taylor-Robinson, S.D. and McPhail, M.J.W. (2015). Magnetic Resonance Spectroscopy: Princliples and Techniques: Lessons for Clinicians. J Clin Exp Hepatol, 5 (4), 320-328.

Tong, V., Teng, X.W., Chang, T.K.H. and Abbott, F.S. (2005). Valproic Acid I: Time Course of Lipid Peroxidation Biomarkers, Liver Toxicity, and Valproic Acid Metabolite Levels in Rats. Toxicological Sciences, 86 (2), 427-435.

Trainor, K., Palumbo, J.A., Mackenzie, D.W.S. and Meiering, E.M. (2020). Temperature dependence of NMR chemical shifts: Tracking and statistical analysis. Protein Science, 29 (1), 306-314.

Troen, A.M., Lutgens, E., Smith, D.E., Rosenberg, I.H. and Selhub, J. (2003). The atherogenic effect of excess methionine intake. Proceedings of the National Academy of Sciences of the United States of America, 100 (25), 15089-15094.

Tsiropoulos, I., Andersen, M. and Hallas, J. (2009). Adverse events with use of antiepileptic drugs: a prescription and event symmetry analysis. Pharmacoepidemiology and Drug Safety, 18 (6), 483-491.

Tsuchida, T. and Friedman, S.L. (2017). Mechanisms of hepatic stellate cell activation. Nature Reviews Gastroenterology & Hepatology, 14, 397-411.

Tutty, M.A, Vella, G. and Prina-Mello, A. (2022). Pre-clinical 2D and 3D toxicity response to a panel of nanomaterials; comparative assessment of NBM-induced liver toxicity. Drug Deliv Transl Res, 12 (9), 2157-2177.

Twiesselmann, C., Blasig, I.E. and Smollich, M. (2008). Valproic acid: Therapeutic ranges, efficacy, and monitoring. Therapeutic Drug Monitoring, 30 (5), 498-505.

Ubeda, N., Alonso-Aperte, E. and Gregorio, V.M. (2002). Acute Valproate Administration Impairs Methionine Metabolism in Rats. The Journal of Nutrition, 132 (9), 2737-2742.

Vairetti, M., Di Pasqua, L.G., Cagna, M., Richelmi, P., Ferrigno, A. and Berardo, C. (2021). Changes in Glutathione Content in Liver Diseases: An Update. Antioxidants, 10 (3), 364.

Vaja, R. and Rana, M. (2020). Drugs and the liver. Anaesthesia and Intensive Care Medicine, 21 (10), 517-523.

Vance, D. (2008). Role of phosphatidylcholine biosynthesis in the regulation of lipoprotein homeostasis. Lipid Metabolism, 19 (3), 229-234.

Van Breda, S.G.J., Claessen, S.M.H., van Herwijnen, M., Theunissen, D.H.J., Jennen, D.G.J., de Kok, T.M.C.M. and Kleinjans, J.C.S. (2018). Integrative omics data analyses of repeated dose toxicity of valproic acid *in vitro* reveal new mechanisms of steatosis induction. Toxicology, 393, 160-170.

Van der Vreen, J.N., Lingrell, S. and Vance, D.E. (2012). The Membrane Lipid Phosphatidylcholine is an Unexpected Source of Triacylglycerol in the Liver. Journal of Biological Chemistry, 287 (28), 23418-23426.

Van de Wier, B., Balk, J.M., Haenen, G.R.M.M., Giamouridis, D., Bakker, J.A., Bast, B.C., den Hartog, G.J.M., Koek, G.H. and Bast, A. (2013). Elevated citrate levels in non-alcoholic fatty liver disease: The Potential of citrate to promote radical production. FEBS Letters, 587 (15), 2461-2466.

Vanputte, C., Regan, J. and Russo, A.F. (2013). Seeley's Anatomy and Physiology, 10th ed. New York: McGraw Hill.

Vernon, H., Wehrle, C.J. and Kasi, A. (2020). Anatomy, Abdomen and Pelvis, Liver. StatPearls.

Videla, L.A., Rodrigo, R., Orellana, M., Fernandez, V., Tapia, G., Quinones, L., Varela, L.A., Contreras, J., Lazarte, R., Csendes, A., Rojas, J., Maluenda, F., Burdiles, P., Diaz, J.C., Smok, G., Thielemann, L. and Poniachik, J. (2004). Oxidative stress-related parameters in the liver of non-alcoholic fatty liver disease patients. Clin Sci (Lond), 106, 261–268.

Vorrink, S.U., Ullah, S., Schmidt, S., Nandania, J., Velagapudi, V., Beck, O., Ingelman-Sundberg, M. and Lauschke, V.M. (2017). Endogenous and xenobiotic metabolic stability of primary human hepatocytes in long-term 3D spheroid cultures revealed by a combination of targeted and untargeted metabolomics. The FASEB Journal, 31 (6), 2696-2708.

Waite, K.A., Cabilio, N.R. and Vance, D.E. (2002). Choline deficiency-induced liver damage is reversible in Pemt(-/-) mice. J. Nutr, 132, 68–71.

Wang, K., Tan, W., Liu, X., Deng, L., Huang, L., Wang, X. and Gao, X. (2021). New insights and potential therapy for NAFLD: CYP2E1 and flavonoids. Biomedicine & Pharmacotherapy, 137, 111326.

Wang, X., Cao, Y., Fu, Y., Guo, G. and Zhang, X. (2011). Liver fatty acid composition in mice with or without nonalcoholic fatty liver disease. Lipids in Healthy and Disease, 10 (234).

Watson, A.M., Poloyac, S.M., Howard, G., Blouin, R. A. (1999). Effect of leptin on cytochrome P-450, conjugation, and antioxidant enzymes in the ob/ob mouse. Drug Metab Dispos, 27, 695–700.

Watt, M.J., Miotto, P.M., De Nardo, W. and Montgomery, M.K. (2019). The Liver as an Endocrine Organ-Linking NAFLD and Insulin Resistance. Endocrine Reviews, 40 (5), 1367-1393.

Wells, F. (2022). Comparing the Triglyceride-Glo™ Assay to Oil Red O Staining to Assess Adipogenesis. Promega Corporation.

Wells, M.A., Vendrov, K.C., Edin, M.L., Ferslew, B.C., Zha, W., Nguyen, B.K.H., Church, R.J., Lih, F.B., DeGraff, L.M., Brouwer, K.L.R., Barrit IV, A.S., Zeldin, D.C. and Lee, C.R. (2016). Characterization of the Cytochrome P450 epoxyeicosanoid pathway in non-alcoholic steatohepatitis. Prostaglandins & Other Lipid Mediators, 125, 19-29.

Weltman, M.D., Farrell, G.C., Liddle, C. (1996). Increased hepatocyte CYP2E1 expression in a rat nutritional model of hepatic steatosis with inflammation. Gastroenterology, 111, 1645–1653.

Weltman, M.D., Farrell, G.C., Hall, P., Ingelman-Sundberg, M., Liddle, C. (1998). Hepatic cytochrome P450 2E1 is increased in patients with nonalcoholic steatohepatitis. Hepatology, 27, 128–133.

Wen, X., Wang, J.S., Kivisto, K.T., Neuvonen, P.J. and Backman, J.T. (2001). *In vitro* evaluation of valproic acid as an inhibitor of human cytochrome P450 isoforms: preferential inhibition of cytochrome P45 2C9 (CYP2C9). British Journal of Clinical Pharmacology, 52 (5), 547-553.

Werge, M.P., McCann, A., Douglas Galsgaard, E., Holst, D., Bugge, A., Wewer Albrechtsen, N.J. and Gludd, L.L. (2020). The Role of the Transsulfuration Pathway in Non-Alcoholic Fatty Liver Disease. Journal of Clinical Medicine, 10 (1081), 1-20.

Werstuck, G.H., Lentz, S.R., Dayal, S., Hossain, G.S., Sood, S.K., Shi, Y.Y., Zhou, J., Maeda, N., Krisans, S.K., Malinow, M.R. and Austin, R.C. (2011). Homocysteine-induced endoplasmic reticulum stress causes dysregulation of the cholesterol and triglyceride biosynthetic pathways. The Journal of Clinical Investigation, 107 (10), 1263-1273.

Wheelock, A.M. and Wheelock, C.E. (2013). Trials and tribulations of 'omics data analysis: assessing quality of SIMCA-based multivariate models using examples from pulmonary medicine. Molecular BioSystems, 11 (9), 2589-2596.

Wiklund, S., (2008). Multivariate Data Analysis for Omics. Umetrics – an MKS Company, IID 1062.

Willebrords, J., Pereira, I.V.A., Maes, M., Crespo Yanguas, S., Colle, I., Van Den Bossche, B., Da Silva, T.C., Oliveira, C.P., Andraus, W., Avancini Ferreira Alves, V., Cogliati, B. and Vinken, M. (2015). Strategies, models and biomarkers in experimental non-alcoholic fatty liver disease research. Progress in Lipid Research, 59, 106-125.

Williams, K.T. and Schlinske, K.L. (2007). New Insights into the Regulation of Methyl Group and Homocysteine Metabolism. The Journal of Nutrition, 137 (2), 311-314.

Williamson, K. and Hatzakis, E. (2017). NMR Spectroscopy as a Robust Tool for the Rapid Evaluation of the Lipid Profile of Fish Oil Supplements. J Vis Exp, 123, 55547.

Worley, B. and Powers, R. (2016). PCA as a practical indicator of OPLS-DA model reliability. Current Metabolomics, 4 (2), 97-103.

Woolsey, S.J., Mansell, S.E., Kim, R.B., Tirona, R.G. and Beaton, M.D. (2015). CYP3A Activity and Expression in Nonalcoholic Fatty Liver Disease. Drug Metabolism and Disposition, 43 (10).

Xiao F.J., Zhou, B, and Ressom, H.W. (2012). Metabolite identification and quantitation in LC-MS/MS-based metabolomics. Trends Analyt Chem, 32, 1-14.

Xu, C., Li, C.Y.T. and Kong, AN.T. (2005). Induction of phase I, II and III drug metabolism/transport by xenobiotics. Arch Pharm Res, 28 (3), 249-68.

Xu, Y., Leo., M.A. and Lieber, C.S. (2003). Lycopene attenuates arachidonic acid toxicity in HepG2 cells overexpressing CYP2E1. Biochemical and Biophysical Research Communications, 303 (3), 745-750.

Xu, S., Chen, Y., Ma, Y., Liu, T., Zhao, M., Wang, Z. and Zhao, L. (2019A). Lipidomic Profiling Reveals Disruption of Lipid Metabolism in Valproic Acid-Induced Hepatotoxicity. Frontiers in Pharmacology, 10.

Xu, Y., Han, J., Dong, J., Fan, X., Cai, Y., Li, J., Wang, T., Zhou, J. and Shang, J. (2019B). Metabolomics Characterizes the Effects and Mechanisms of Quercetin in Nonalcoholic Fatty Liver Disease Development. Int J Mol Sci, 20 (5), 1220.

Yamada, H., Akahoshi, N., Kamata, S., Hagiya, Y., Hishiki, T., Nagahata, Y., Matsuura, T., Takano, N., Mori, M., Ishizaki, Y., Izumi, T., Kumagai, Y., Kasahara, T., Suematsu, M. and Ishii, I. (2012). Methionine excess in diet induces acute lethal hepatitis in mice lacking cystathionine y-lyase, an animal model of cystathioninuria. Free Radic Biol Med, 52 (9), 1716-26.

Yan, L., Yang, K., Wang, S., Xie, Y., Zhang, L and Tian, X. (2021). PXR-mediated expression of FABP4 promotes valproate-induced lipid accumulation in HepG2 cells. Toxicology Letters, 346, 47-56.

Yan, X., Liu, P., Xu., J., Wang, Z., Ding, L., et al., (2022). Targeted metabolomics profiles serum fatty acids by HFD induced non-alcoholic fatty liver in mice based on GC-MS. J Pharm Biomed Anal, 211 (114620).

Yan, Y., Wu, X., Wang, P., Zhang, S., Sun, L., Zhao, Y., Zeng, GY., Liu, B., Xu, G., Liu, H., Wang, L., Wang, X. and Jiang, C. (2020). Homocysteine promotes hepatic steatosis by activating the adipocytes lipolysis in a HIFIα-ERO1α-dependent oxidative stress manner. Redox Biology, 37, 101742.

Yang, J., Wang, L. and Jia, R. (2020). Role of de novo cholesterol synthesis enzymes in cancer. Journal of Cancer, 11 (7), 1761-1767.

Yang, S., Zhu, H., Li, Y., Lin,H., Gabrielson, K., Trush, M.A. and Diehl, A.M. (2000). Mitochondrial adaptations to obesity-related oxidant stress. Arch. Biochem. Biophys, 378, 259–268.

Yang, Y., Wang, Y., Sun, J., Zhang, J., Guo, H., Shi, Y., Cheng, X., Tang, X. and Le, G. (2018). Dietary methionine restriction reduces hepatic steatosis and oxidative stress in high-fat-fed mice by promoting H_2S production. Food & Function, 10 (1), 61-77.

Yao, H.T., Chang, Y.W., Lan, S.J., Chen, C.T., Hsu, J.T.A. and Yeh, T.K. (2006). The inhibitory effect of polyunsaturated fatty acids on human CYP enzymes. Life Sci, 79(26), 2432- 2440.

Yao, F., Coquery, J., Le Cao, K.A., (2012). Independent Principal Component Analysis for biologically meaningful dimension reduction of large biological data sets. BMC Bioinformatics, 13 (24), 1-15.

Yao, L., Wang, C., Zhang, X., Peng, L., Liu, W., Zhang, X., Liu, Y., He, J., Jiang, C., Ai, D. and Zhu, Y. (2016). Hyperhomocysteinemia activates the aryl hydrocarbon receptor/CD36 pathway to promote hepatic steatosis in mice. Hepatology, 64 (1), 92-105.

Yasuda, K., Ranade, A., Venkataramanan, R., Strom, S., Chupka, J., Ekins, S., Schuetz, E. and Bachmann, K. (2015). A Comprehensive *in vitro* and *in silico* Analysis of Antibiotics that Activate PXR and Induce CYP3A4 in Liver and Intestine. Drug Metab Dispos, 36 (8), 1689-1697.

Ye, G., Ding, D., Gao, H., Chi, Y., Chen, J., Wu, Z., Lin, Y. and Dong, S. (2019). Comprehensive metabolic responses of HepG2 cells to fine particulate matter exposure: Insights from an untargeted metabolomics. Science of The Total Environment, 691, 874-884.

Yin, H.Q., Kim, M., Kim, J.H., Kong, G., Lee, M.O., Kang, K.S., Yoon, B.I.L., Kim, H.L. and Lee, B.H. (2006). Hepatic gene expression profiling and lipid homeostasis in mice exposed to steatogenic drug, tetracycline. Toxicol. Sci, 94, 206–216.

Yu, M., Zhu, Y., Cong, Q. and Wu, C. (2017). Metabolomics Research Progress on Liver Diseases. Canadian Journal of Gastroenterology and Hepatology, 8467192, 1-10.

Yuan, L. and Kaplowitz, N. (2009). Glutathione in liver diseases and hepatotoxicity. Mol Aspects Med 30, 29–41.

Zeng, X., Zhu, M., Liu, X., Chen, X., Yuan, Y., Li, L., Liu, J., Lu, Y., Cheng, J. and Chen, Y. (2020). Oleic acid ameliorates palmitic acid induced hepatocellular lipotoxicity by inhibition of ER stress and pyroptosis. Nutrition and Metabolism, 17 (11).

Zhang, H., Liu, Z., Ma, S., Zhange, H., Kong, F., He, Y., Yang, X., Wang, Y., Xu, H., Yang, A., Tian, J., Zhang, M., Cao, J., Jiang, Y., Guo, X. (2016). Ratio of S-adenosylmethionine to S-adenosylhomocysteine as a sensitive indicator of atherosclerosis. Molecular Medicine Reports, 14 (1), 289-300.

Zhang, L.F., Liu, L.S., Chu, X.M., Xie, H., Cao, L.J., Guo, C., A, J.Y., Cao, B, Li, M.J., Wang, G.J. and Hao. H.P. (2014). Combined effects of a high-fat diet and chronic valproic acid treatment on hepatic steatosis and hepatotoxicity in rats. Acta Pharmacologica Sinica, 35, 363-372.

Zhang, W.V., Ramzan, I., Murray, M. (2007). Impaired microsomal oxidation of the atypical antipsychotic agent clozapine in hepatic steatosis. J Pharmacol Exp Ther, 322, 770–777.

Zhang, X., Xue, X.C., Wang, Y., Cao, F.F., You, J., Uzan, G., Peng, B. and Zhang, D.H. (2019). Celastrol Reverses Palmitic Acid-Induced Insulin Resistance in HepG2 Cells via Restoring the miR-23 and GLUT4 Pathway, Canadian Journal of Diabetes, 43 (3), 165-172

Zhang, Y., Xue, R., Zhang, Z., Yang, X. and Shi, H. (2012). Palmitic and linoleic acids induce ER stress and apoptosis in hepatoma cells. Lipids health and Disease, 11 (1), 1-8.

Zhao, G., He, F., Wu., Li, P., Li, N., Deng, J., Zhu, g., Ren, W. and Peng, Y. (2018). Betaine in Inflammation: Mechanistic Aspects and Applications. Frontiers in Immunology, 9 (1070).

Zhong, F., Zhou, X., Xu, J. and Gao, L. (2019). Rodent Models of Nonalcoholic Fatty Liver Disease. Karger, 101 (5).

Zhou, J., Werstuck, G.H., Lhotak, S., Shi, Y.S., Tedesco, V., Trigatti, B., Dickhout, J., Majors, A.K., Dibello, P.A., Jacobsen, D.W. and Austine, R.C. (2008). Hyperhomocysteinemia induced by methionine supplementation does not independently cause atherosclerosis in C57BL/6J mice. FASEB J, 22 (7), 2569-78.

Zhou, X., Han, D., Xu, R., Wu, H., Qu, C., Wang, F., Wang, X. and Zhao, Y. (2016). Glycine protects against high sucrose and high fat-induced non-alcoholic steatohepatitis in rats. Oncotarget, 7, 80223-80237.

Zhu, X., Song, J., Mar, M.H., Edwards, L. and Zeisel, S.H. (2003). Phosphatidylethanolamine N-methyltransferase (PEMT) knockout mice have hepatic steatosis and abnormal hepatic choline metabolite concentrations despite ingesting a recommended dietary intake of choline. Biochem. J, 370, 987–993.

Zhu, M.M., Li, H.L., Shi, L.H., Chen, X.P., Luo, J. and Zhang, Z.L. (2017). The pharmacogenomics of valproic acid. Journal of Human Genetics, 62, 1009-1014.

Zhu, X., Yan, H., Xia, M., Chang, X., Xu, X., Wang, L., Sun, X., Lu, Y., Bian, H., Li, X. and Gao, X. (2018). Metformin attenuates triglyceride accumulation in HepG2 cells through decreasing stearyl-coenzyme A desaturase 1 expression. Lipids in Health and Disease, 17 (114).

Zira, A., Kostidis, S., Theocharis, S., Sigala, F., Engelsen, S.B., Andreadou, I. and Mikros, E. (2013). ^{1}H NMR-based metabonomics approach in a rat model of acute liver injury and regeneration induced by CCl_4 administration. Toxicology, 303 (7), 115-124.

Zollner, A., Buchheit, D., Meyer, M.R., Maurer, H.H., Peter, F.T. and Bureik, M. (2010). Production of human phase 1 and 2 metabolites by whole-cell biotransformation with recombinant microbes. Bioanalysis, 2 (7), 1277-90.

Chapter Eight- Appendices

Chapter 8

8.1 Appendix

Protein marker used for all Western blots to help identify size of target protein.

Figure 8.1 Protein marker displaying molecular weight of proteins used in Western blotting

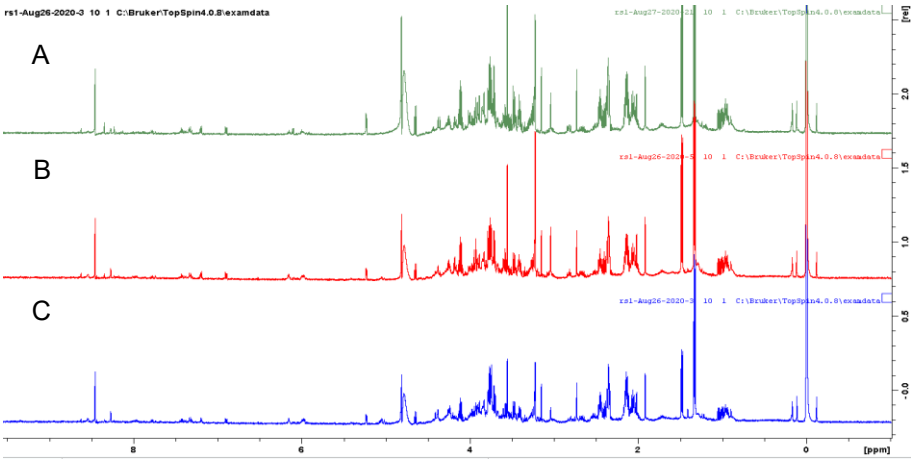

Figure 8.2 Representative ^{1}H NMR spectra of aqueous cell extracts from HepG2 cells. Cells were seeded in 6-well plates and allowed to attach for 24 hour before dosing. A. Control, B. 0.1 mM fatty acid, C. 0.5 mM fatty acid.

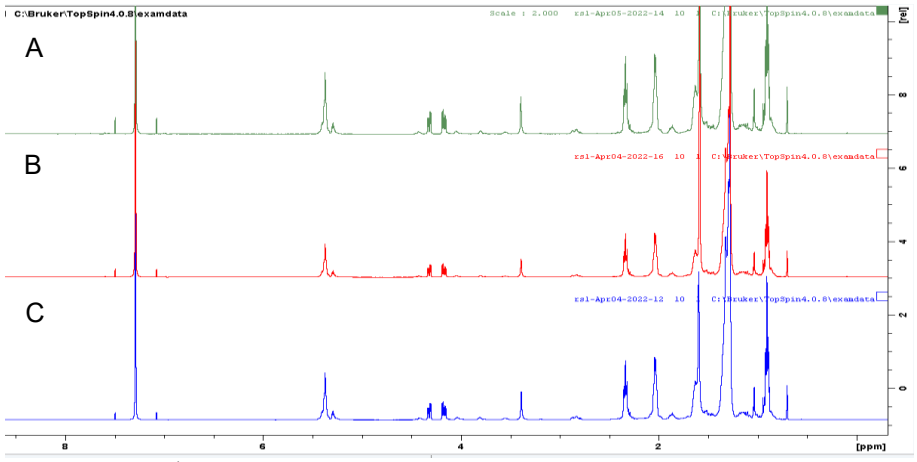

Figure 8.3 Representative ^{1}H NMR spectra of organic cell extracts from HepG2 cells. Cells were seeded in 6-well plates and allowed to attach for 24 hour before dosing. A. Control, B. 0.1 mM fatty acid, C. 0.5 mM fatty acid.

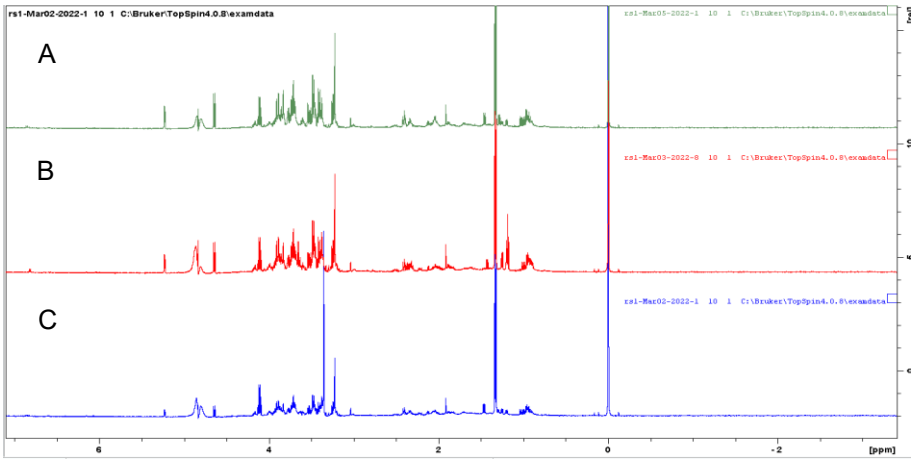

Figure 8.4 Representative ^{1}H NMR spectra of aqueous spheroid extracts from HepG2 cells. Spheroids were seeded in low attachment 6-well plates and allowed to grow for 17 days before dosing. A. Control, B. 0.5 mM valproate, C. 4 mM valproate.

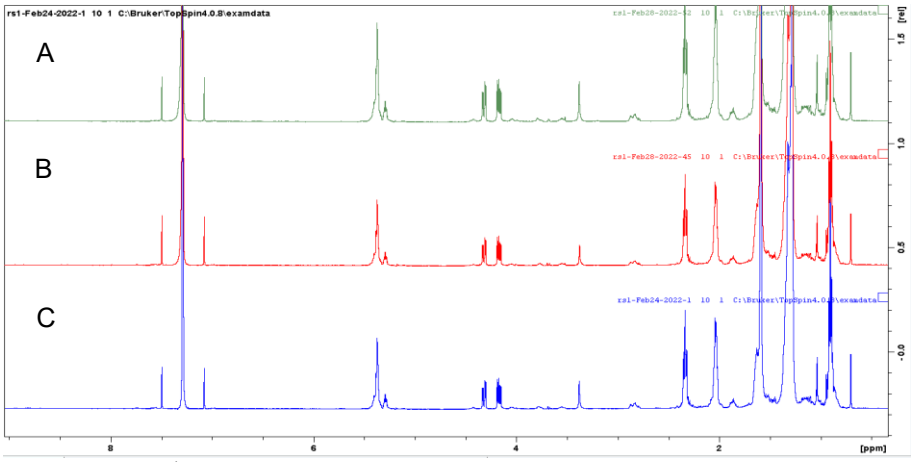

Figure 8.5 Representative ^{1}H NMR spectra of organic spheroid extracts from HepG2 cells. Spheroids were seeded in low attachment 6-well plates and allowed to grow for 17 days before dosing. A. Control, B 100 µM tetracycline, C. 800 µM tetracycline.

8.1.2 Metabolomic analysis of aqueous monolayer extracts dosed with tetracycline

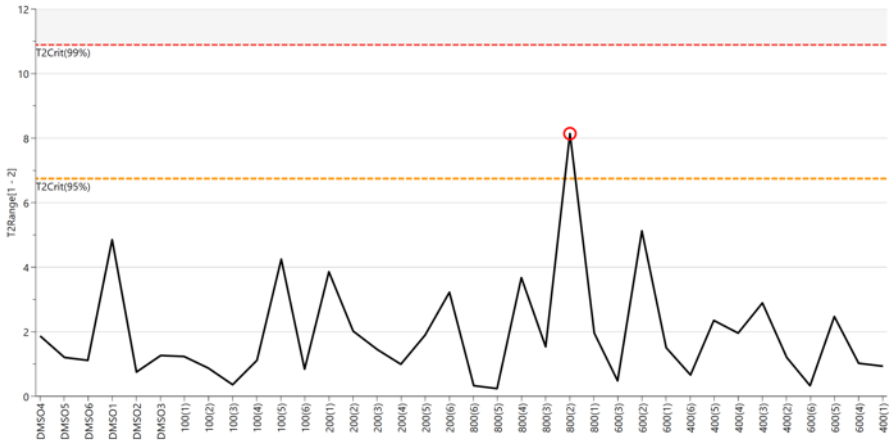

Figure 8.6 Hotelling's T2 plot created from PCA scores plot in Figure 4.5. Samples above the red line of the 99% confidence level are considered to be true outliers. Sample 800(2) is circled in red.

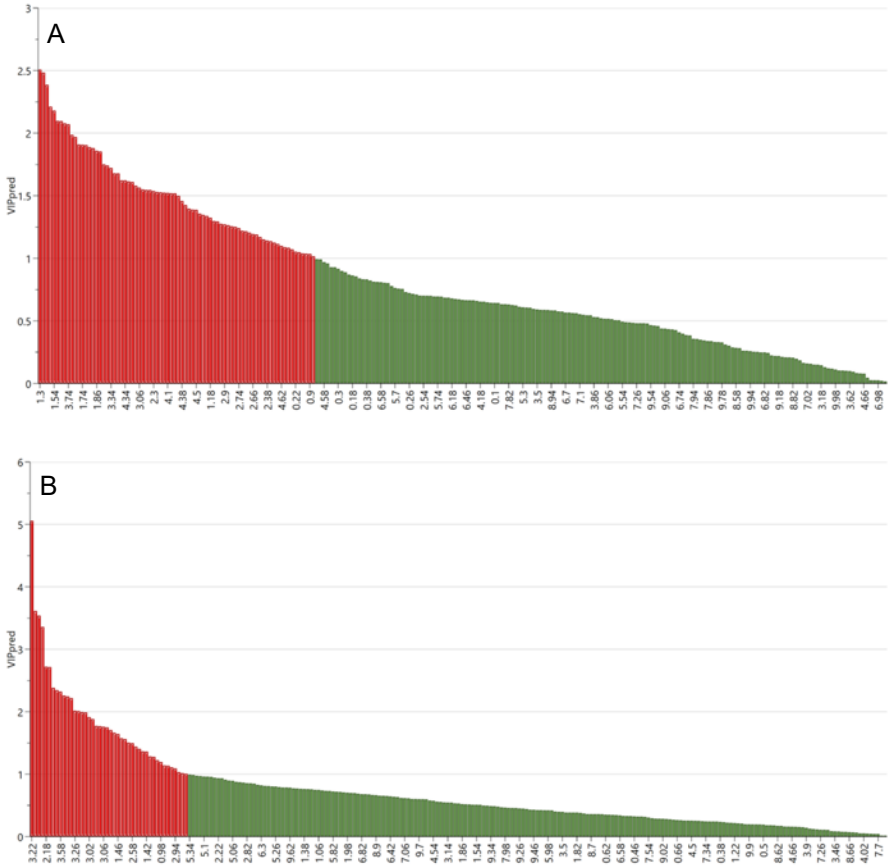

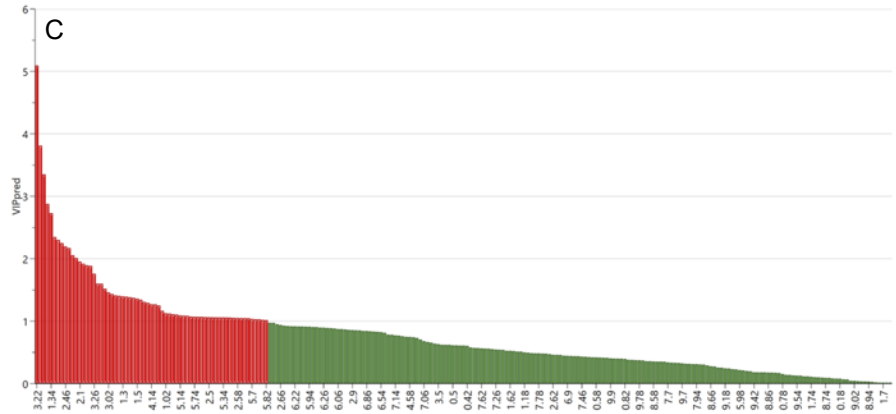
C
VIPpred

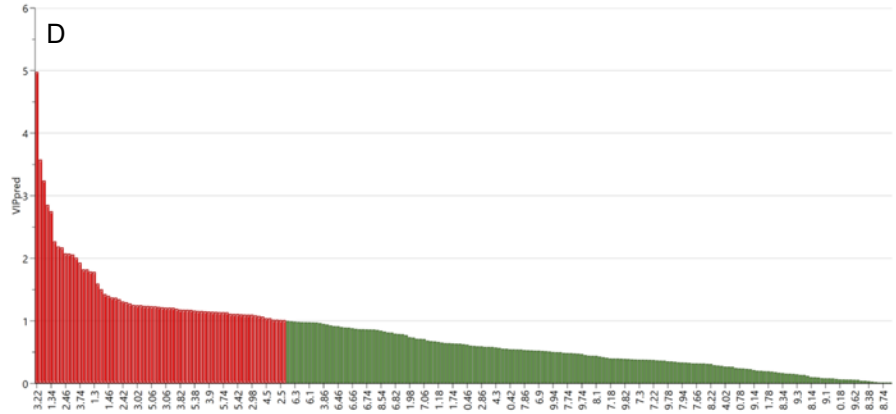
D
VIPpred

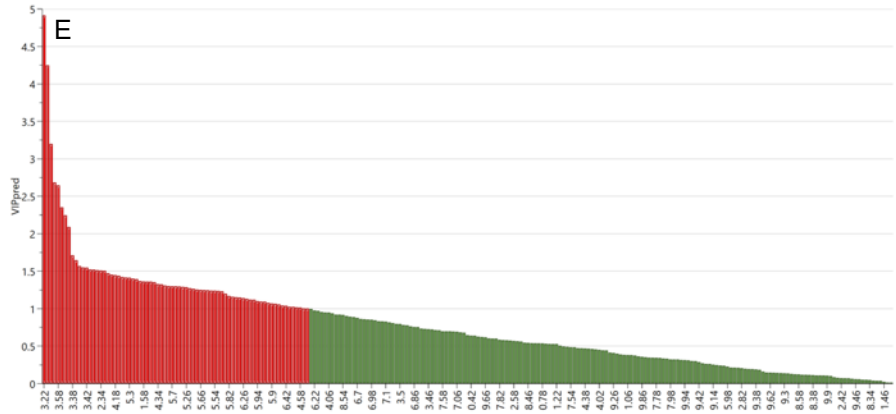
E
VIPpred

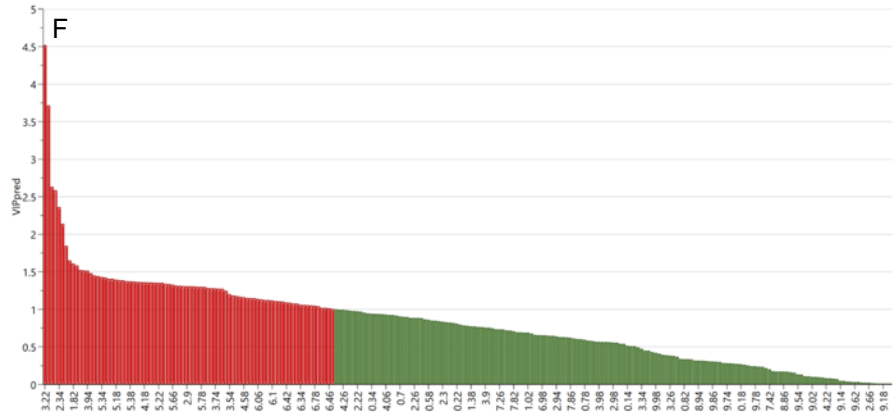
F
VIPpred

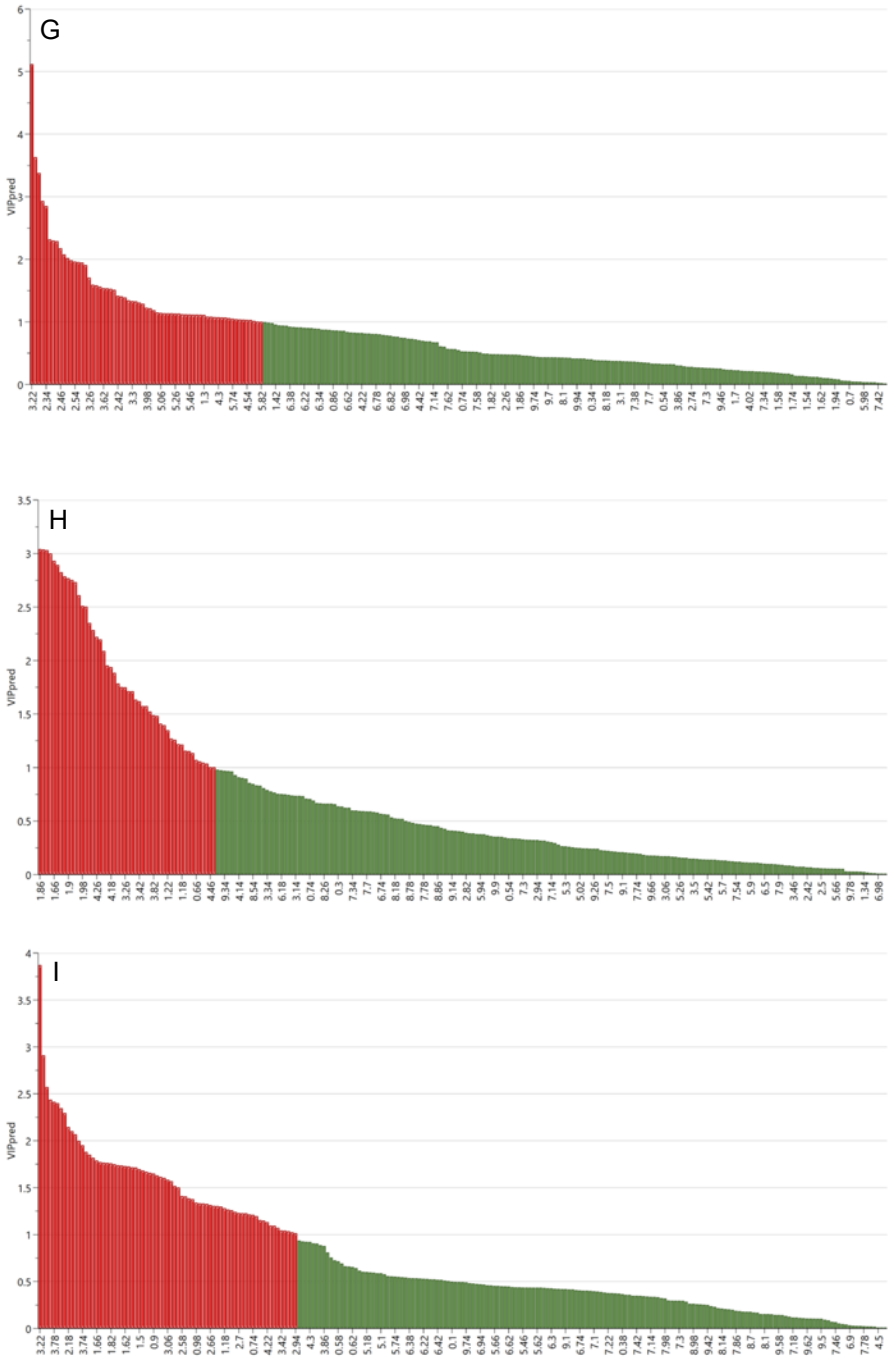

Figure 8.7 VIP predictive plots derived from OPLS-DA models of NMR spectra of aqueous extracts of HepG2 cells treated with tetracycline at different concentrations. Cells were dosed at final concentrations of 0 (DMSO control), 100, 200, 400, 600 and 800 µM and incubated for 24 hours. Samples were collected and NMR analysis was carried out as described in Sections 2.10 and 2.13. A. DMSO control vs 100 µM, B. DMSO control vs 200 µM, C. DMSO control vs 400 µM, D. DMSO control vs 600 µM, E. DMSO control vs 800 µM, F. 100 vs 200 µM, G. 200 vs 400 µM, H, 400 vs 600 µM, I. 600 vs 800 µM.

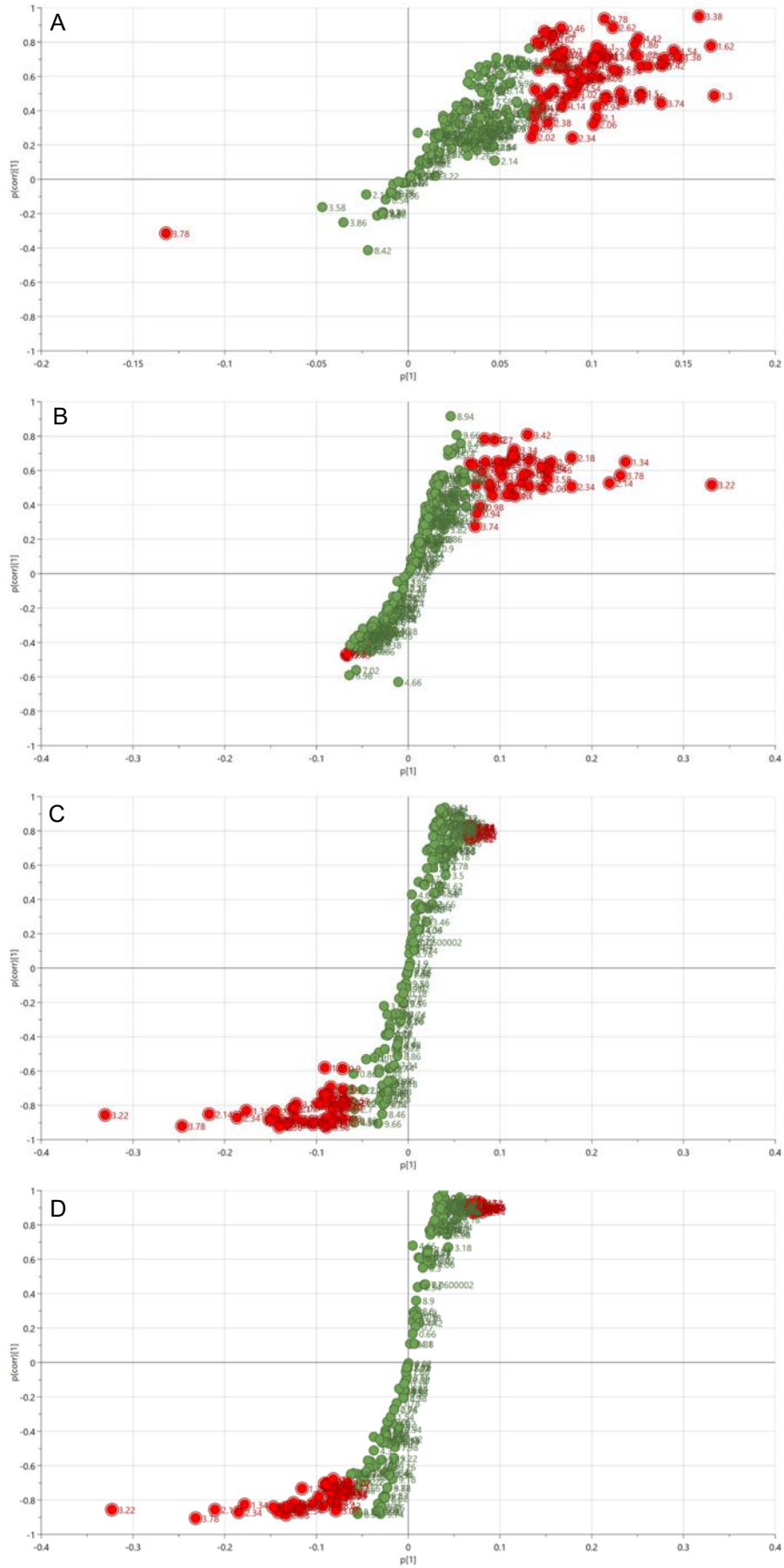
A
B
C
D
p[1]
p(corr)[1]

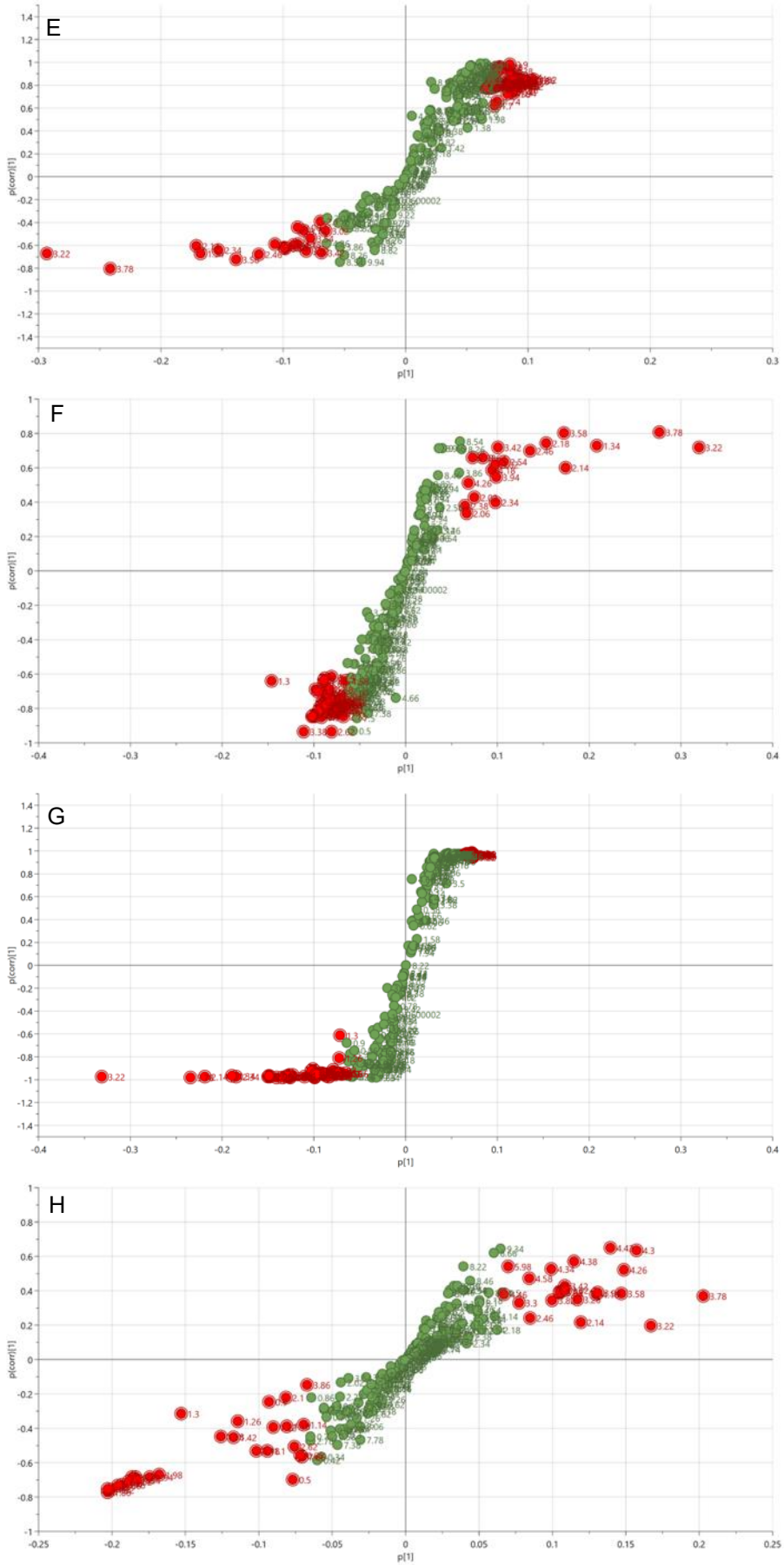
E
F
G
H
p[1]
p(corr)[1]

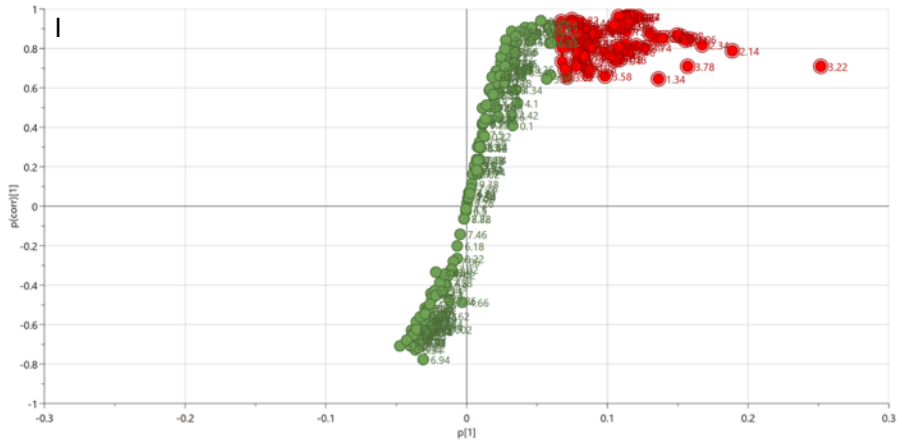

Figure 8.8 S-plot derived from OPLS-DA models of NMR spectra of aqueous extracts from HepG2 cells treated with tetracycline at different concentrations. Samples were collected, and NMR analysis was carried out as described in Sections 2.10 and 2.13. A. DMSO control vs 100 μM, B. DMSO control vs 200 μM, C. DMSO control vs 400 μM, D. DMSO control vs 600 μM, E. DMSO control vs 800 μM, F. 100 vs 200 μM, G. 200 vs 400 μM, H, 400 vs 600 μM, I. 600 vs 800 μM.

8.1.3 Metabolomic analysis of organic monolayer extracts dosed with tetracycline

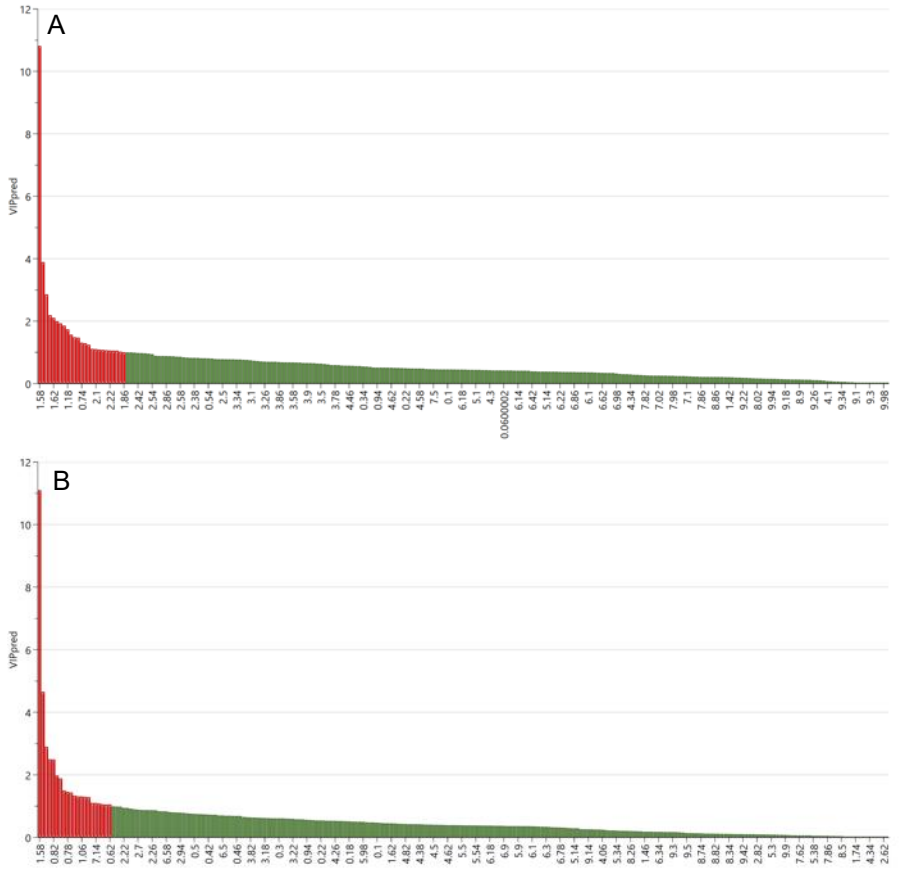

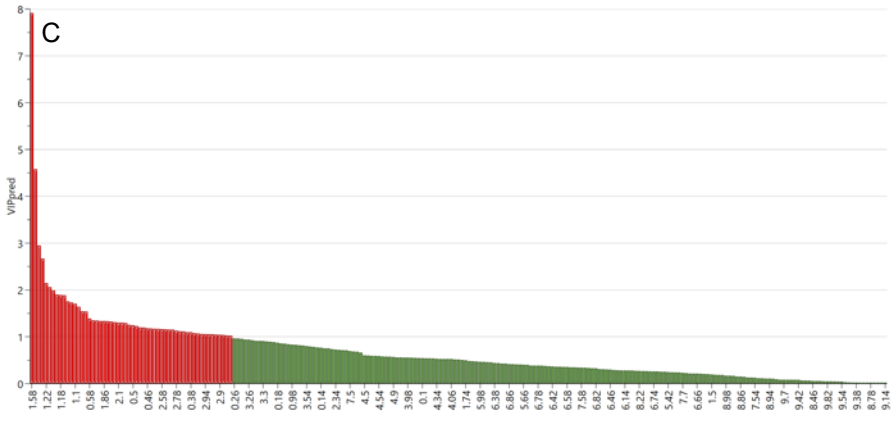
C
VIPpred

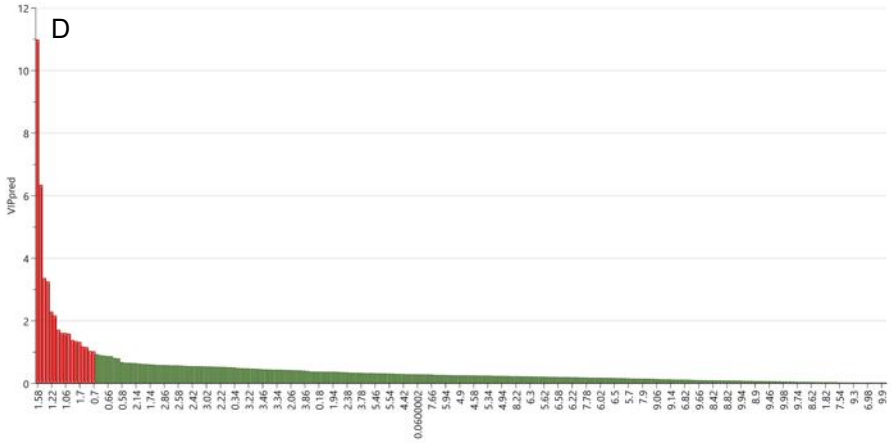
D
VIPpred

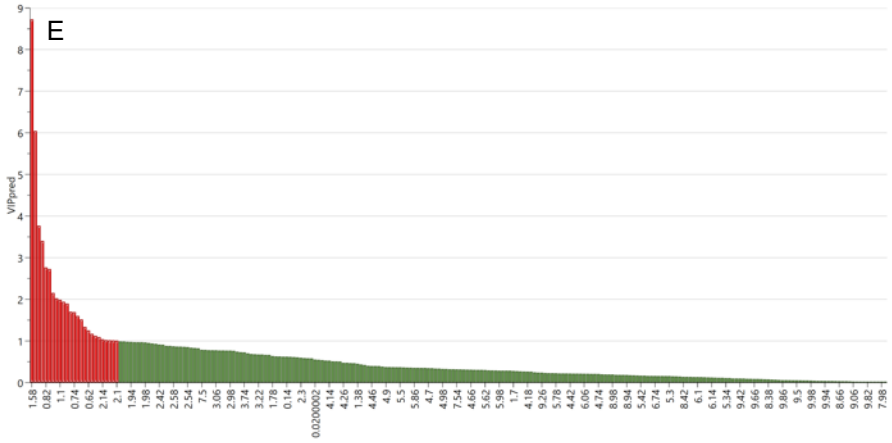
E
VIPpred

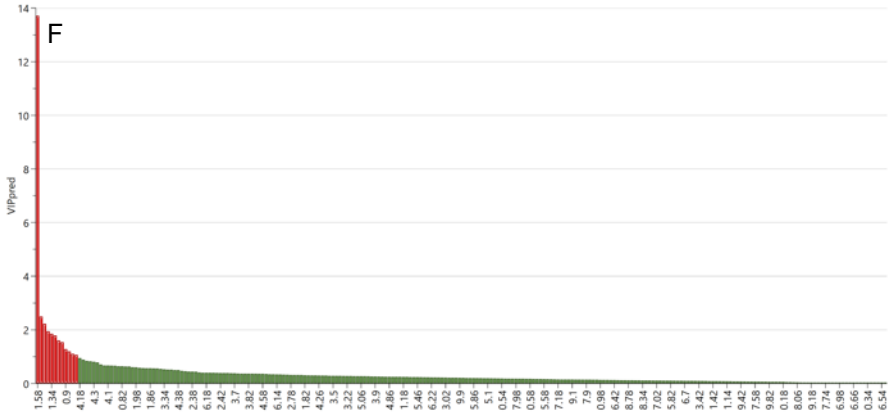
F
VIPpred

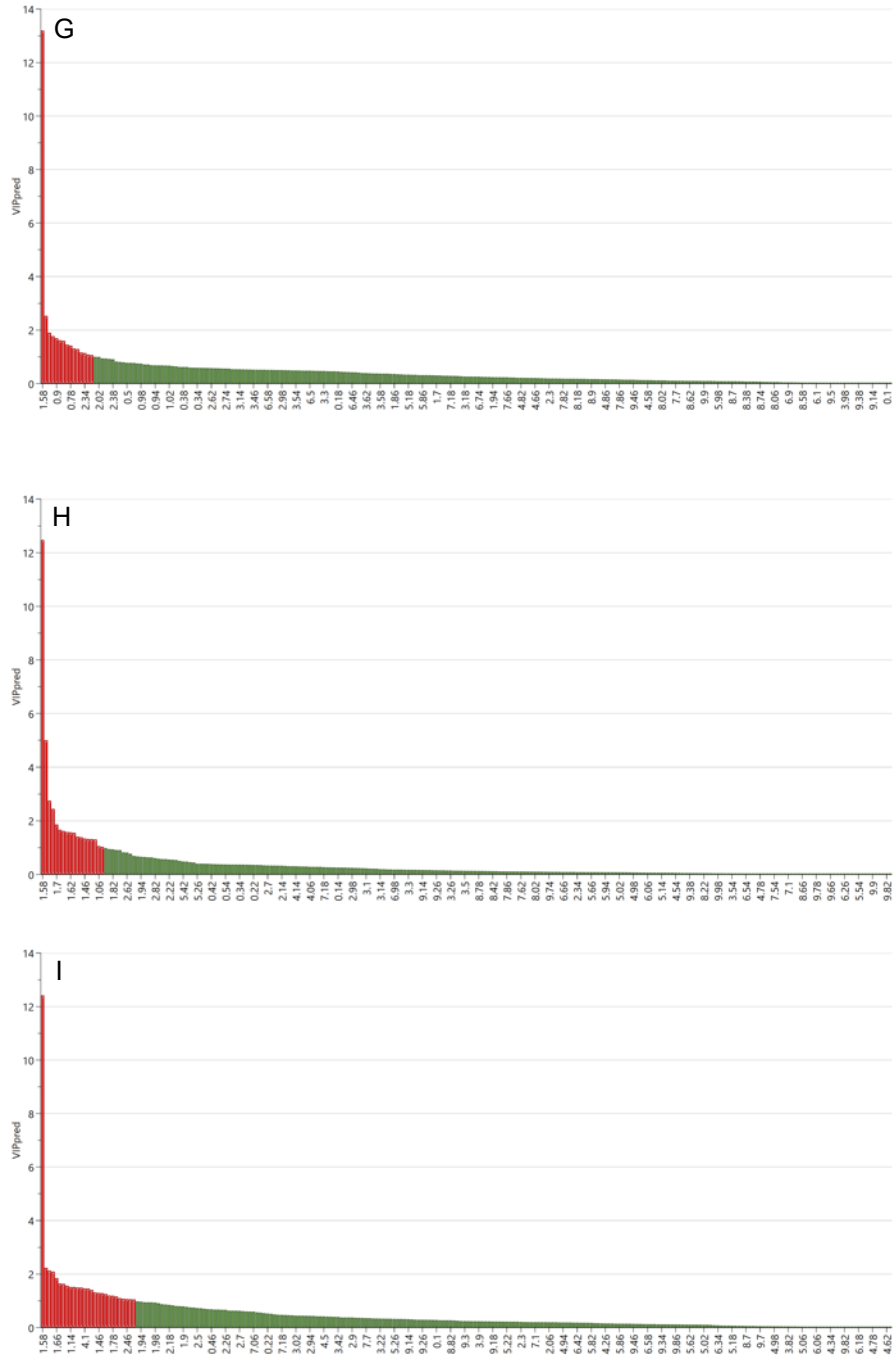

Figure 8.9 VIP predictive plots derived from OPLS-DA models of NMR spectra of organic extracts of HepG2 cells treated with tetracycline at different concentrations. Cells were dosed at final concentrations of 0 (DMSO control), 100, 200, 400, 600 and 800 µM and incubated for 24 hours. Samples were collected and NMR analysis was carried out as described in Sections 2.10 and 2.13. A. DMSO control vs 100 µM, B. DMSO control vs 200 µM, C. DMSO control vs 400 µM, D. DMSO control vs 600 µM, E. DMSO control vs 800 µM, F. 100 vs 200 µM, G. 200 vs 400 µM, H. 400 vs 600 µM, I. 600 vs 800 µM.

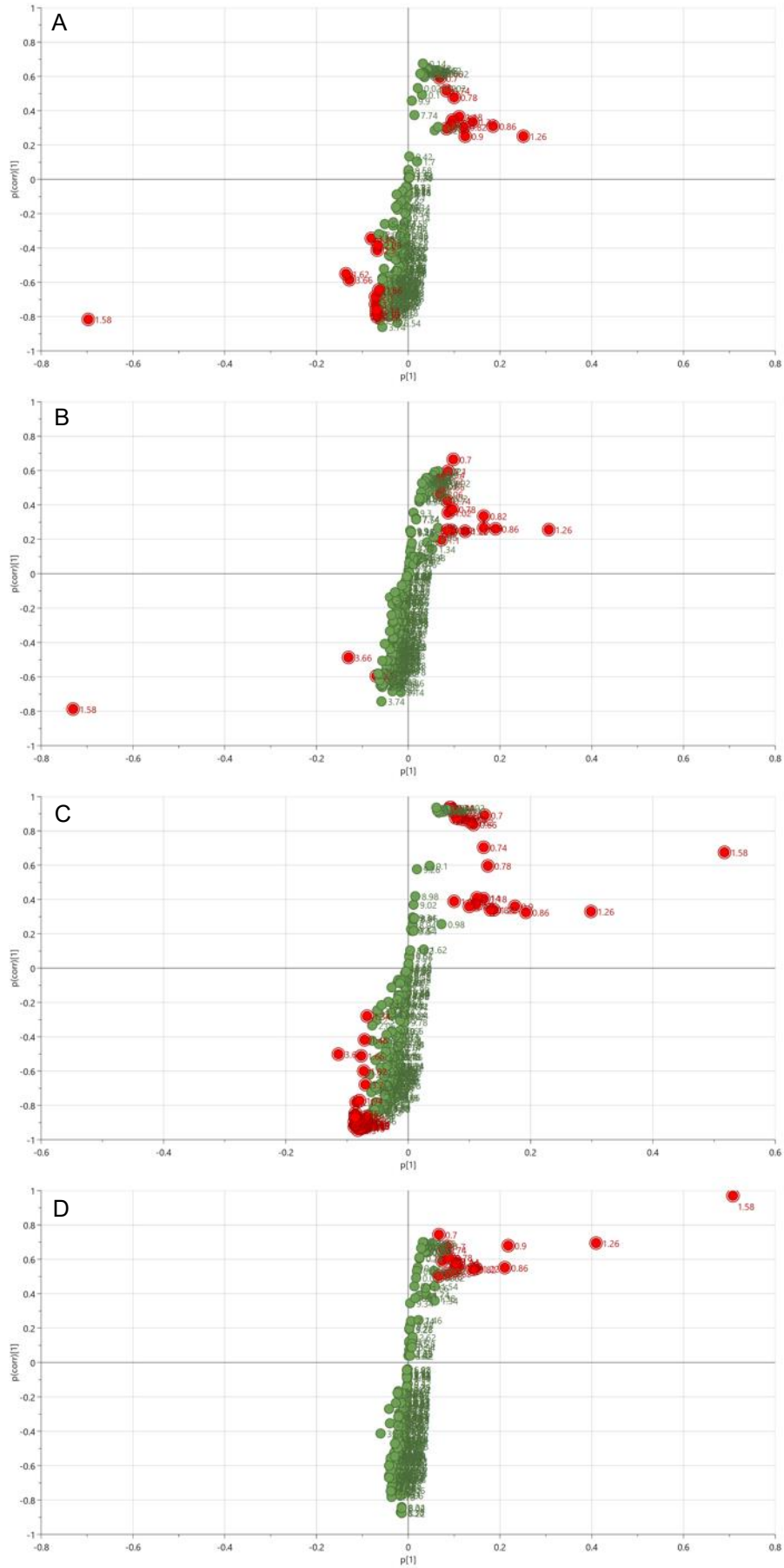
A
B
C
D
p[1]
p(corr)[1]

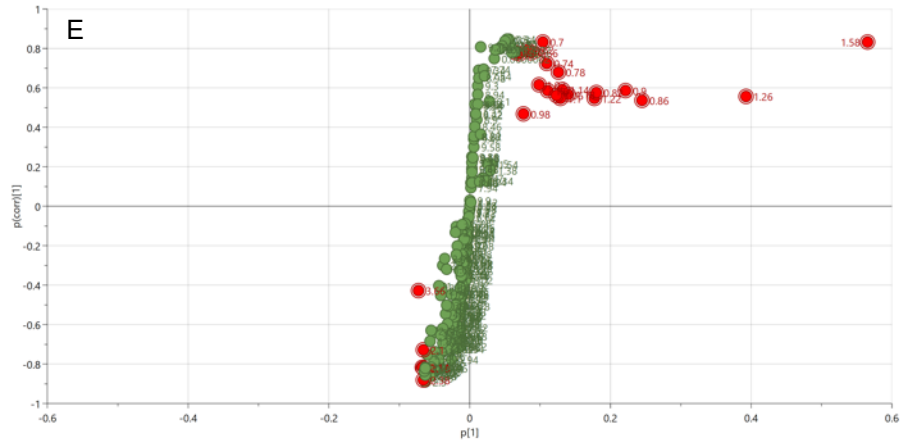
E
p(corr)[1]
p[1]
1.58
1.26
0.98
0.86
0.78
0.74
0.7

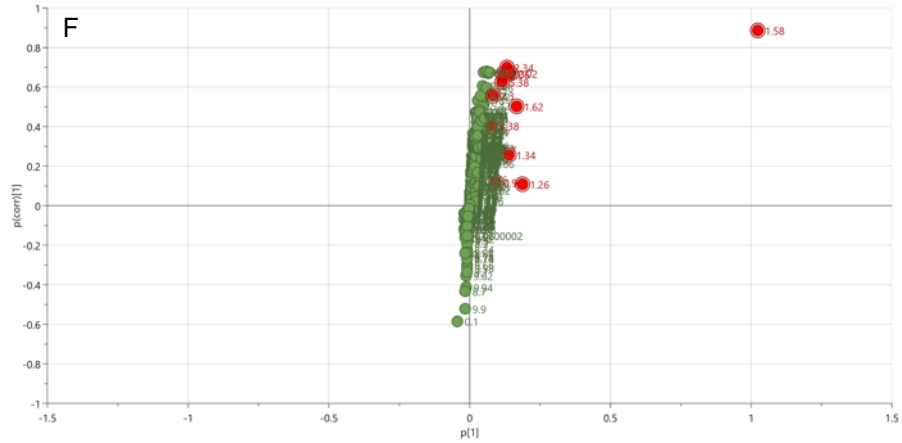
F
p(corr)[1]
p[1]
1.58
1.62
1.34
1.26
9.9
0.1

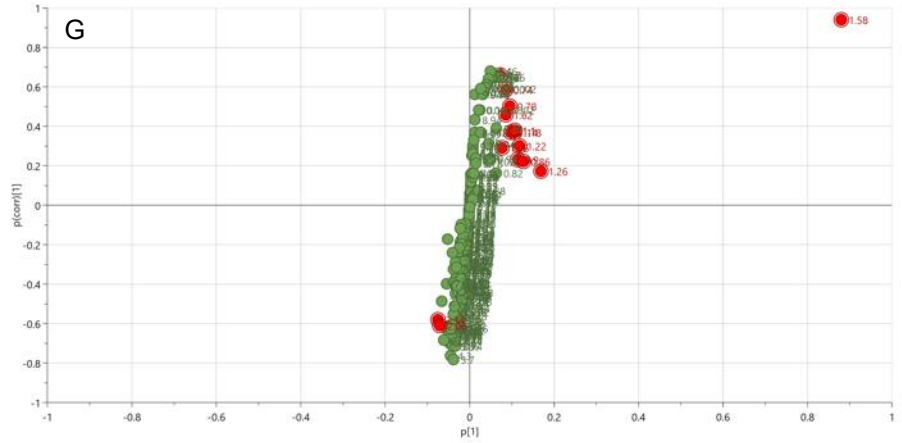
G
p(corr)[1]
p[1]
1.58
1.26
0.82

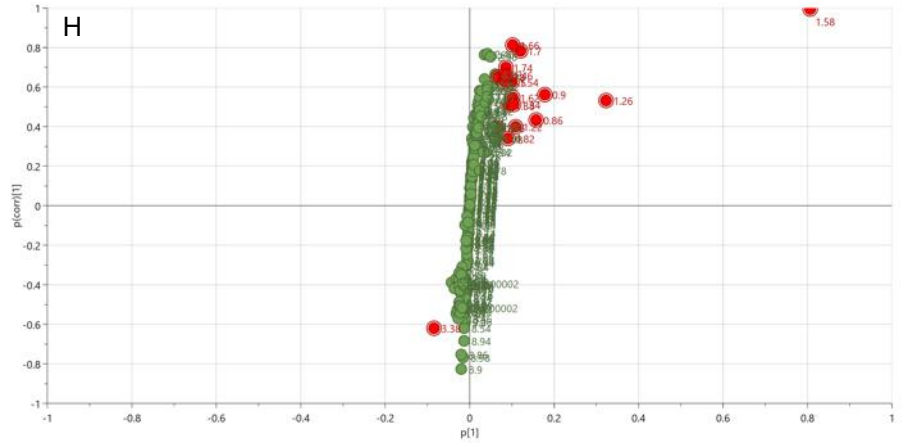
H
p(corr)[1]
p[1]
1.58
1.26
0.9
0.86
0.82
8.94
5.9

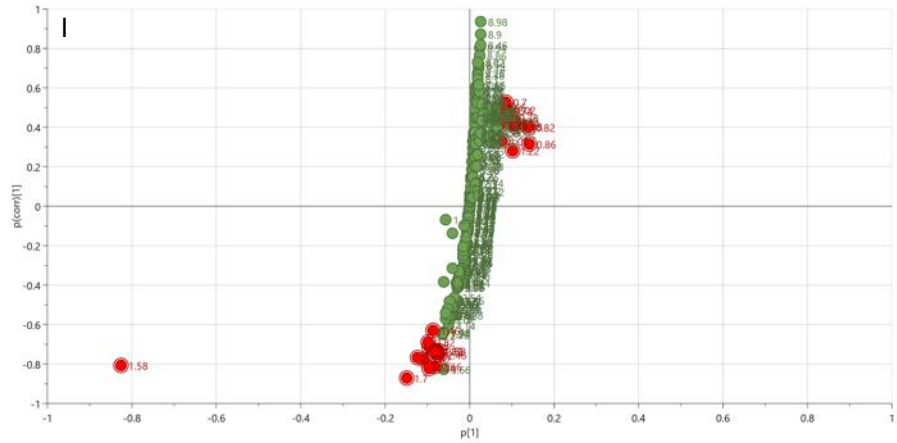

Figure 8.10 S-plot derived from OPLS-DA models of NMR spectra of organic extracts from HepG2 cells treated with tetracycline at different concentrations. Samples were collected, and NMR analysis was carried out as described in Sections 2.10 and 2.13. A. DMSO control vs 100 μM, B. DMSO control vs 200 μM, C. DMSO control vs 400 μM, D. DMSO control vs 600 μM, E. DMSO control vs 800 μM, F. 100 vs 200 μM, G. 200 vs 400 μM, H, 400 vs 600 μM, I. 600 vs 800 μM.

8.1.4 Metabolomic analysis of aqueous spheroid extracts dosed with tetracycline

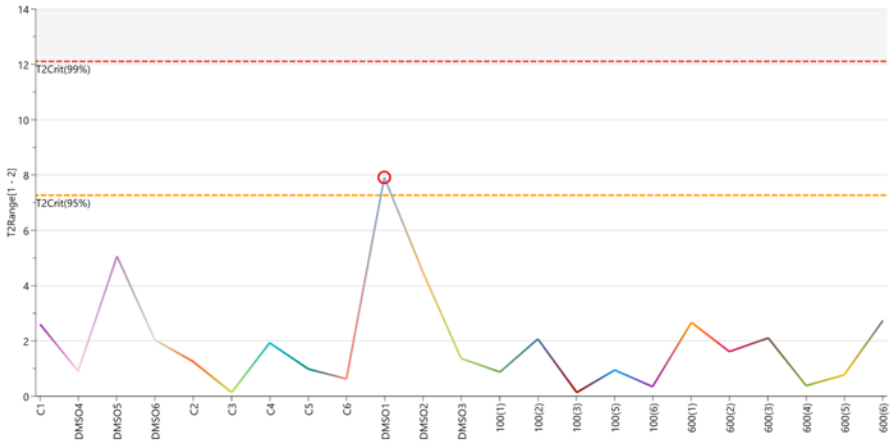

Figure 8.11 Hotelling's T2 plot created from PCA scores plot shown in Figure 4.15. Samples above the red line of the 99 % confidence level are considered to be outliers. Sample DMSO (1) is circled in red.

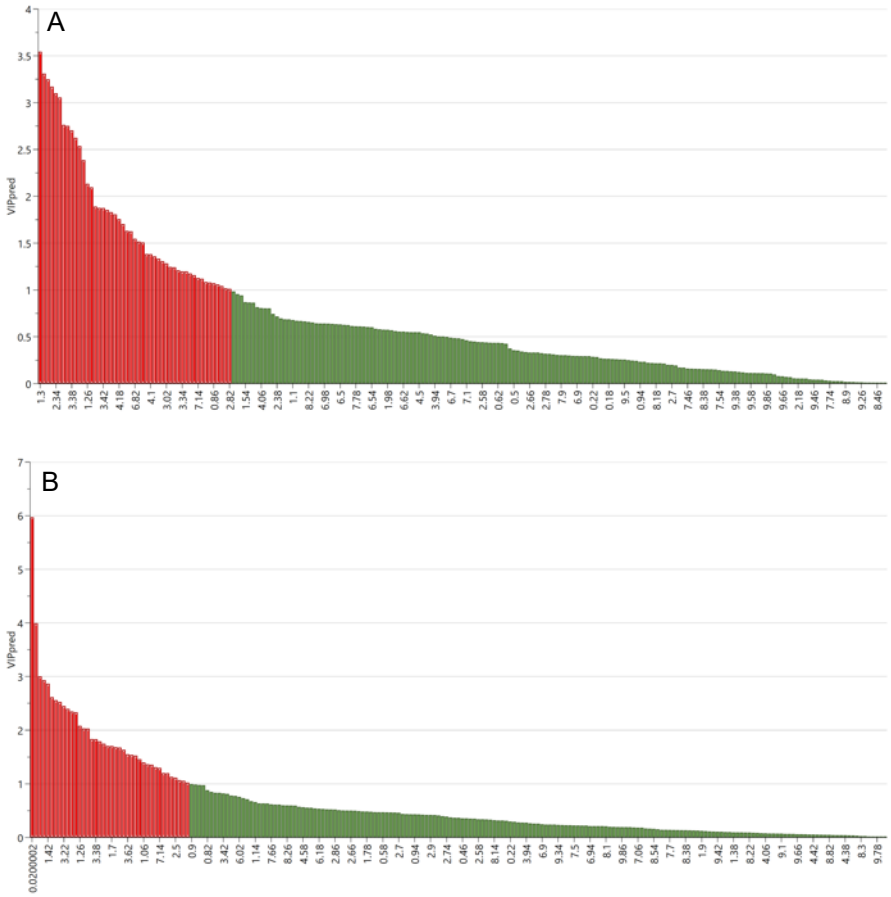

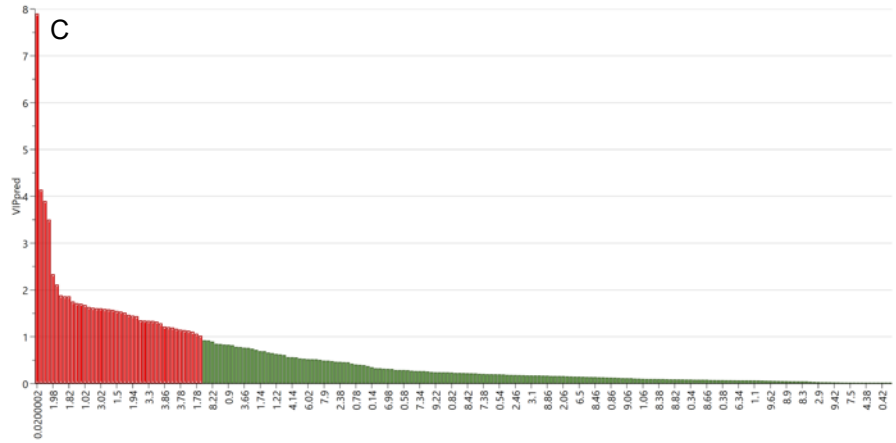

Figure 8.12 VIP predictive plots derived from OPLS-DA models of NMR spectra of aqueous extracts from HepG2 spheroids dosed with tetracycline at different concentrations. Spheroids were treated with either 0 (DMSO control), 100 or 600 μM tetracycline. Samples were collected and NMR analysis was carried out as described in Sections 2.10 and 2.12. A. Control vs 100 μM tetracycline. B. Control vs 600 μM tetracycline. C. 100 vs 600 μM tetracycline. Variables with a VIPpred value above 1 were selected as significant and were highlighted in red.

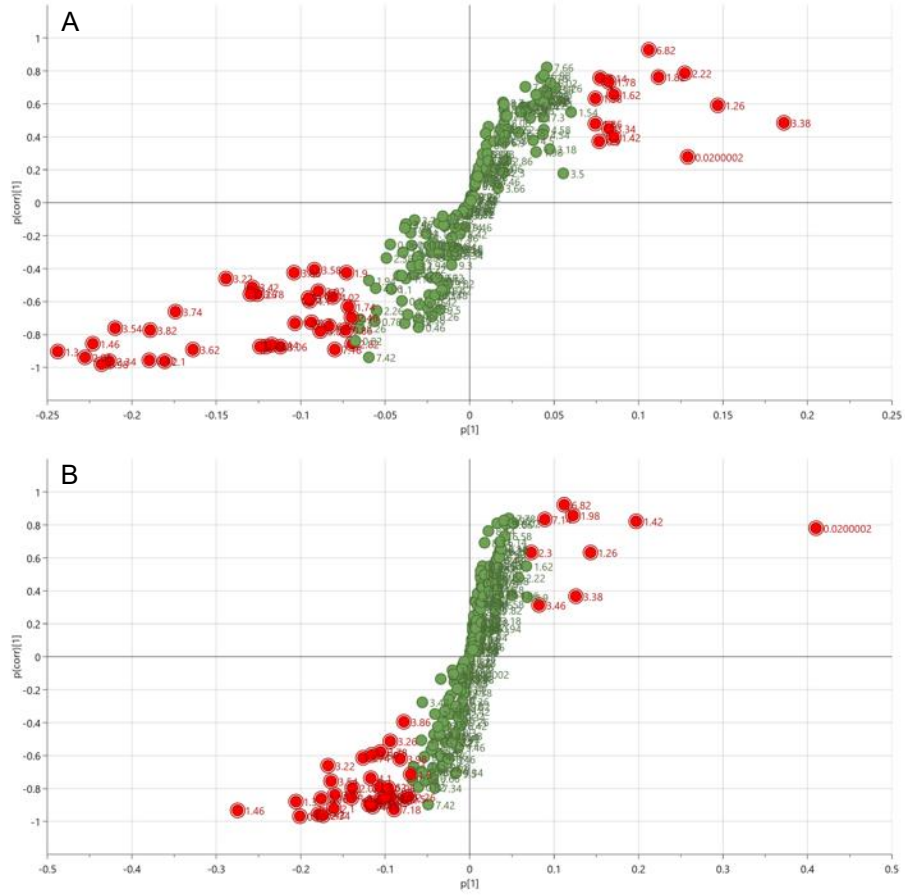

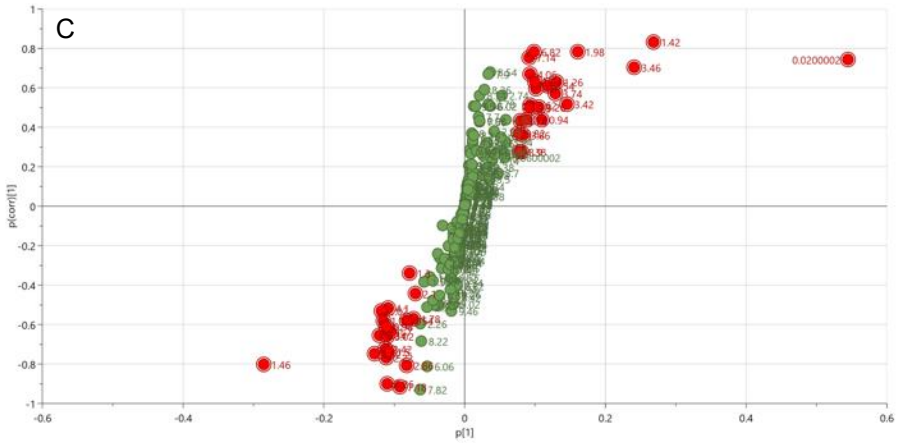

Figure 8.13 S-plots derived from OPLS-DA models of NMR spectra of aqueous extracts from HepG2 spheroids treated with tetracycline at different concentrations. Spheroids were treated with either 0 (DMSO control), 100 or 600 μM tetracycline. Samples were collected and NMR analysis was carried out as described in Sections 2.10 and 2.13. A. Control vs 100 μM tetracycline. B. Control vs 600 μM tetracycline. C. 100 vs 600 μM tetracycline.

8.1.5 Metabolomic analysis of organic spheroid extracts dosed with tetracycline

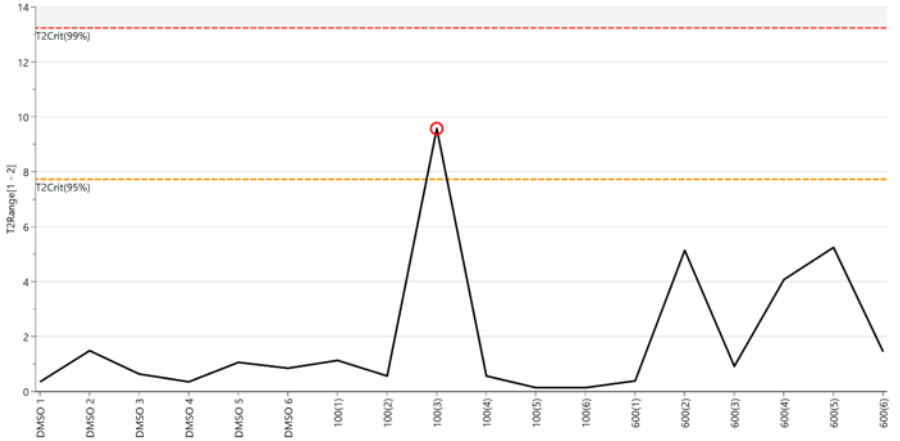

Figure 8.14 Hotelling's T2 plot created from PCA scores plot in Figure 4.18. Samples above the red line of the 99% confidence level are considered to be true outliers. Sample 100 (3) is circled in red.

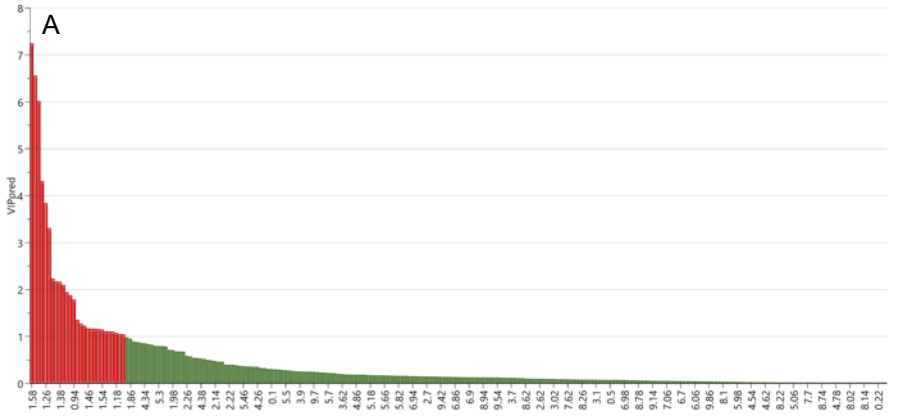

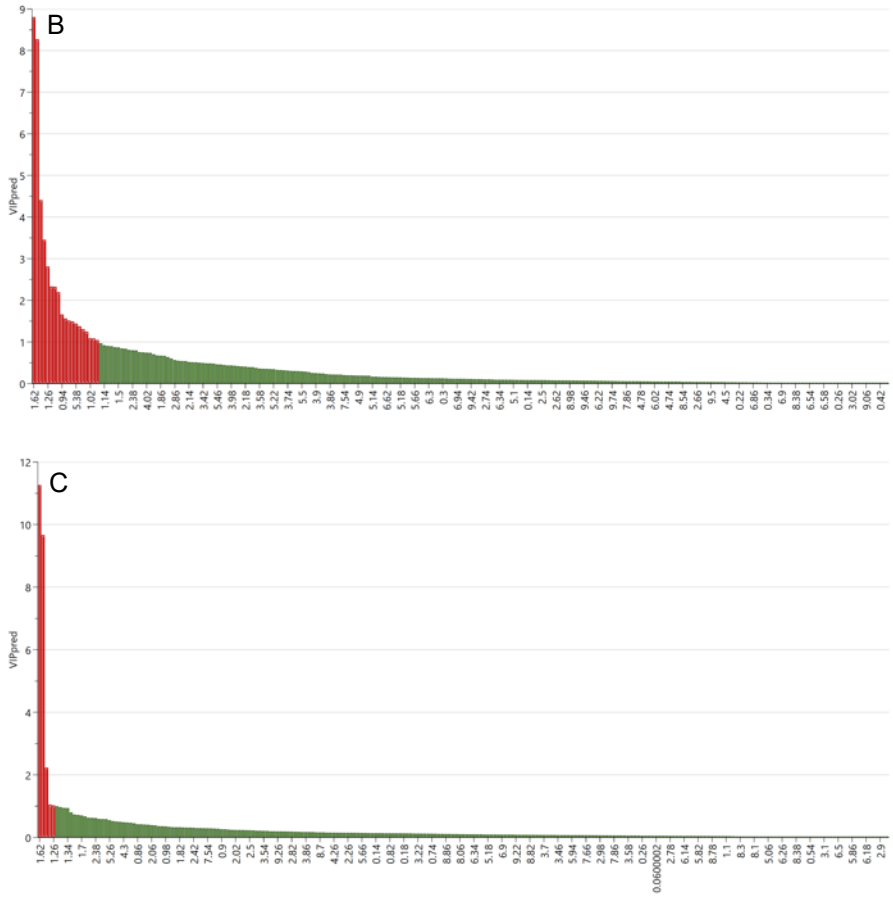

Figure 8.15 VIP predictive plots derived from OPLS-DA models of NMR spectra of organic extracts from HepG2 spheroids dosed with tetracycline at different concentrations. Spheroids were treated with either 0 (DMSO control), 100 or 600 µM tetracycline. Samples were collected and NMR analysis was carried out as described in Sections 2.10 and 2.13. A. Control vs 100 µM tetracycline. B. Control vs 600 µM tetracycline. C. 100 vs 600 µM tetracycline. Variables with a VIPpred value above 1 were selected as significant and were highlighted in red.

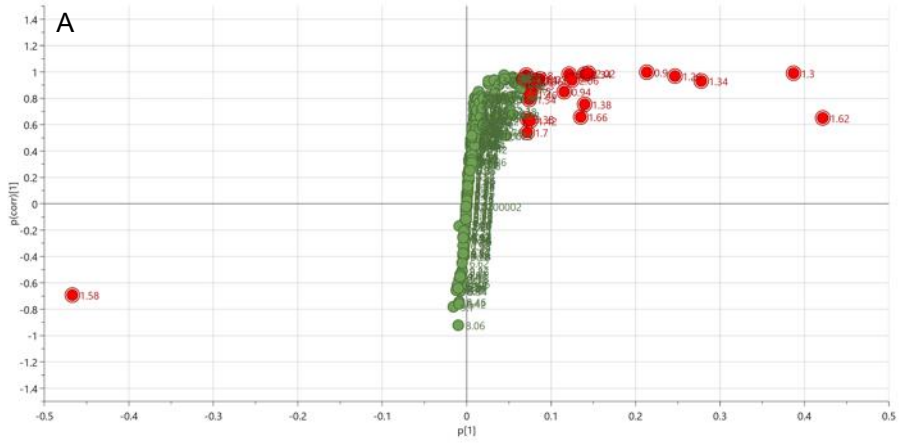

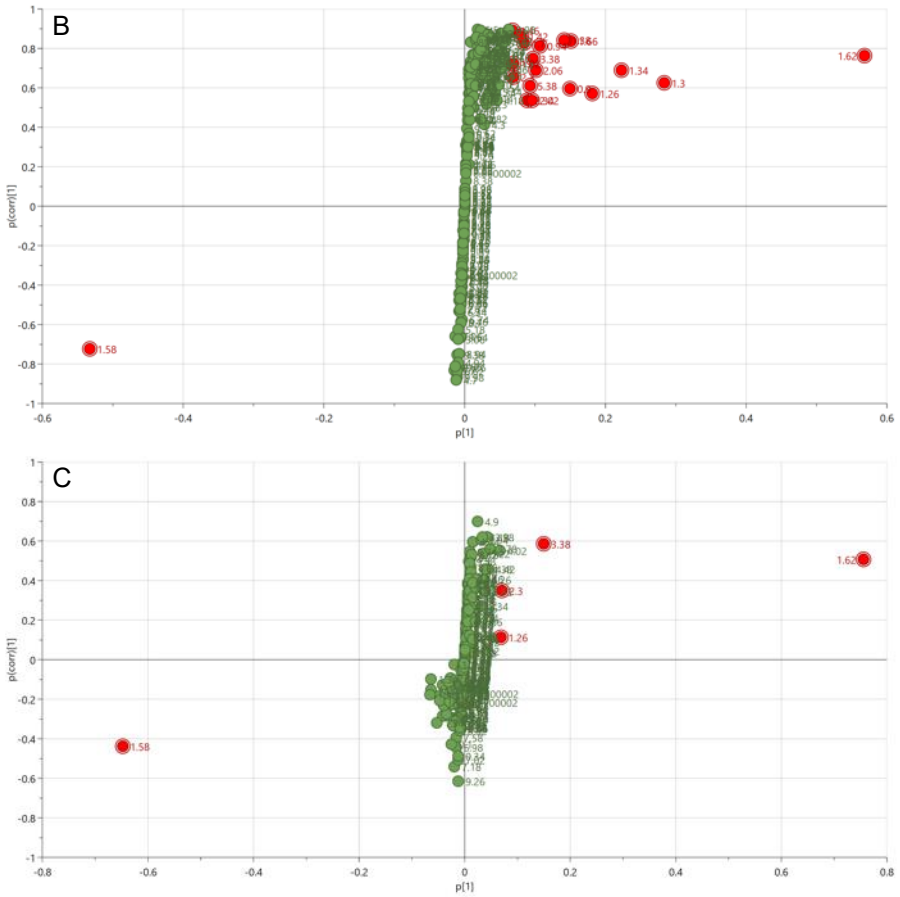

Figure 8.16 S-plots derived from OPLS-DA models of NMR spectra of organic extracts from HepG2 spheroids treated with tetracycline at different concentrations. Spheroids were treated with either 0 (DMSO control), 100 or 600 µM tetracycline. Samples were collected and NMR analysis was carried out as described in Sections 2.10 and 2.13. A. Control vs 100 µM tetracycline. B. Control vs 600 µM tetracycline. C. 100 vs 600 µM tetracycline.

8.1.6 Metabolomic analysis of aqueous monolayer extracts dosed with valproate

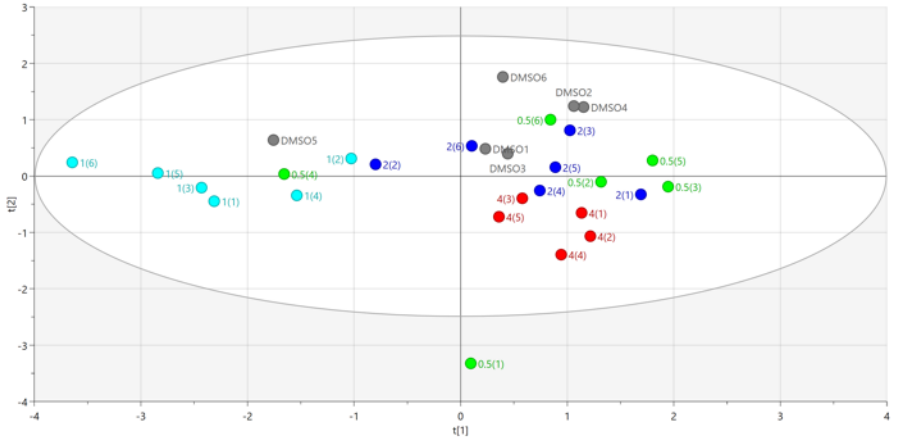

Figure 8.17 PCA scores plot derived from ^{1}H NMR spectra of aqueous extracts from HepG2 cells dosed with valproate at various dose levels. Cells were dosed with DMSO, 0.5, 1, 2 and 4 mM valproate and incubated for 24 hours. Aqueous cell extract samples were collected, and NMR analysis carried out as described in Sections 2.10 and 2.13. Each spot on the plot represents one sample. Grey = DMSO only control; green = 0.5 mM; light blue = 1 mM; blue = 2 mM; red = 4 mM.

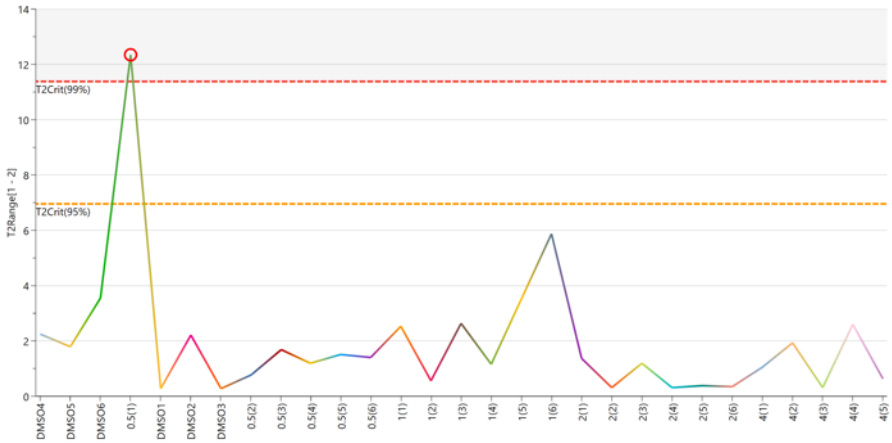

Figure 8.18 Hotelling's T2 plot created from PCA scores plot in Figure 8.13. Samples above the red line of the 99% confidence level are considered to be true outliers. Sample 0.5 (1) is circled in red.

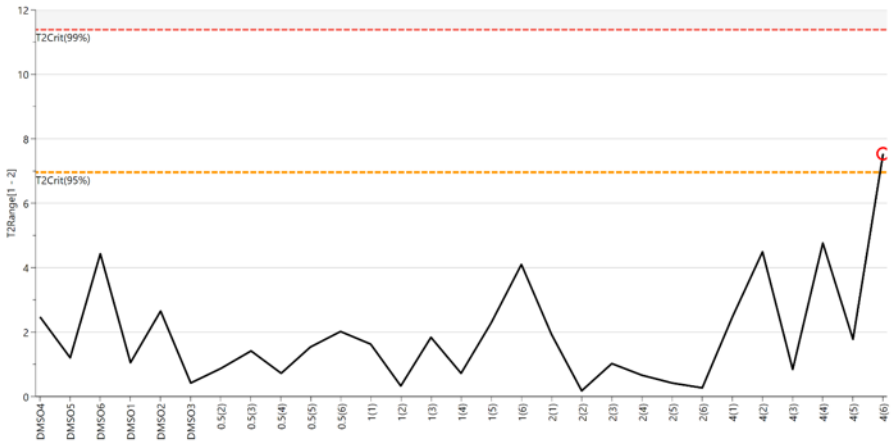

Figure 8.19 Hotelling's T2 plot created from PCA scores plots in Figure 5.5. Samples above the red line of the 99% confidence level are considered to be true outliers. Sample 4 (6) is circled in red.

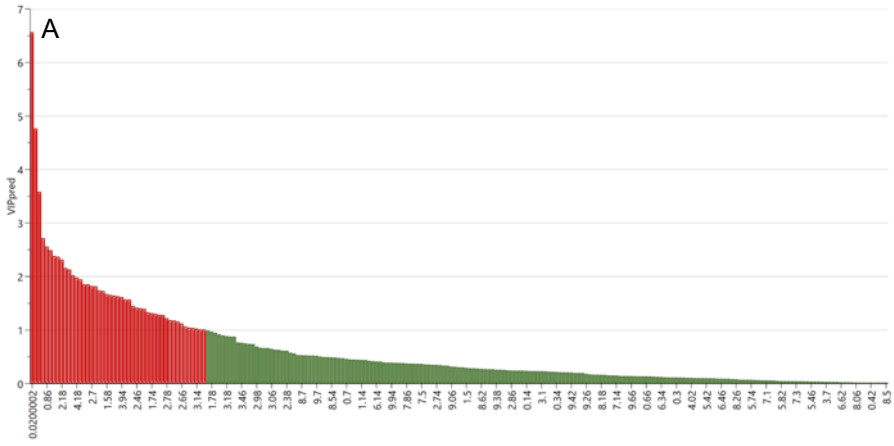

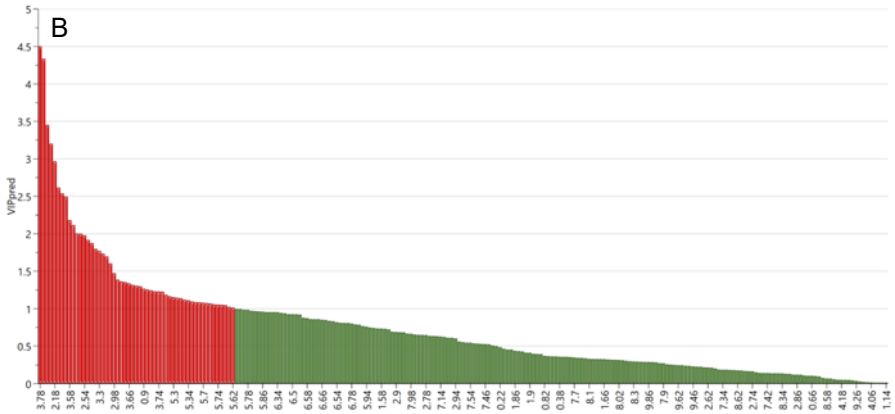
B
VIPpred

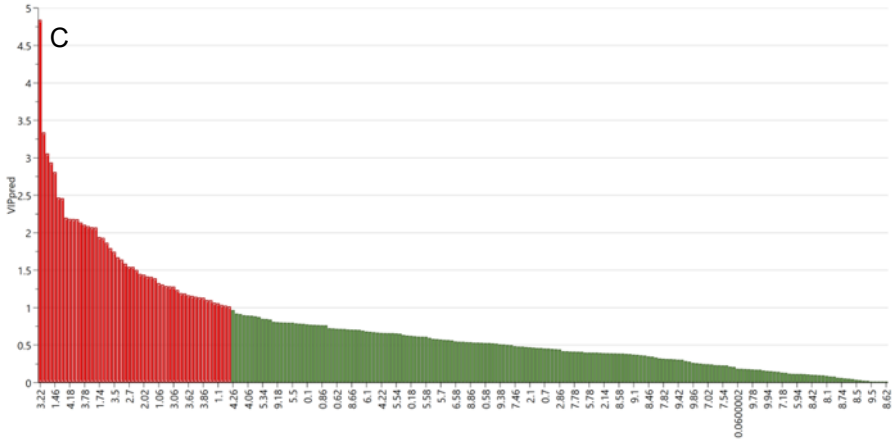
C
VIPpred

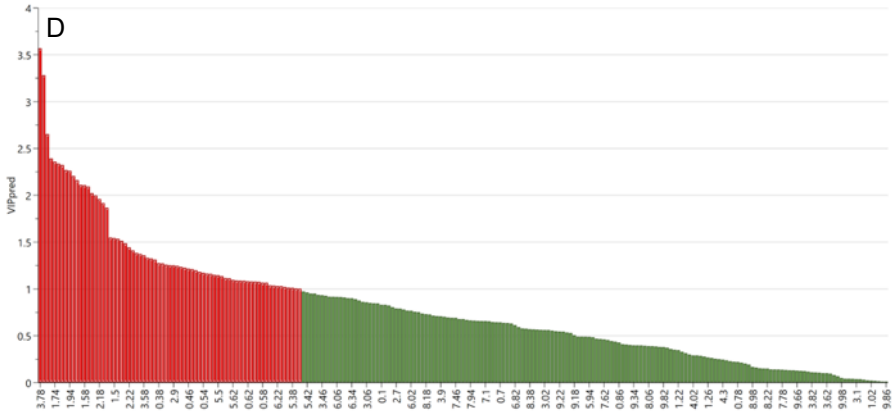
D
VIPpred

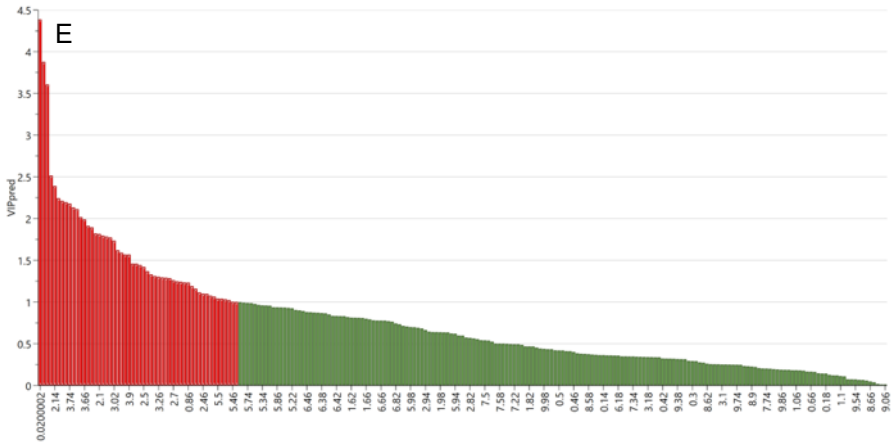
E
VIPpred

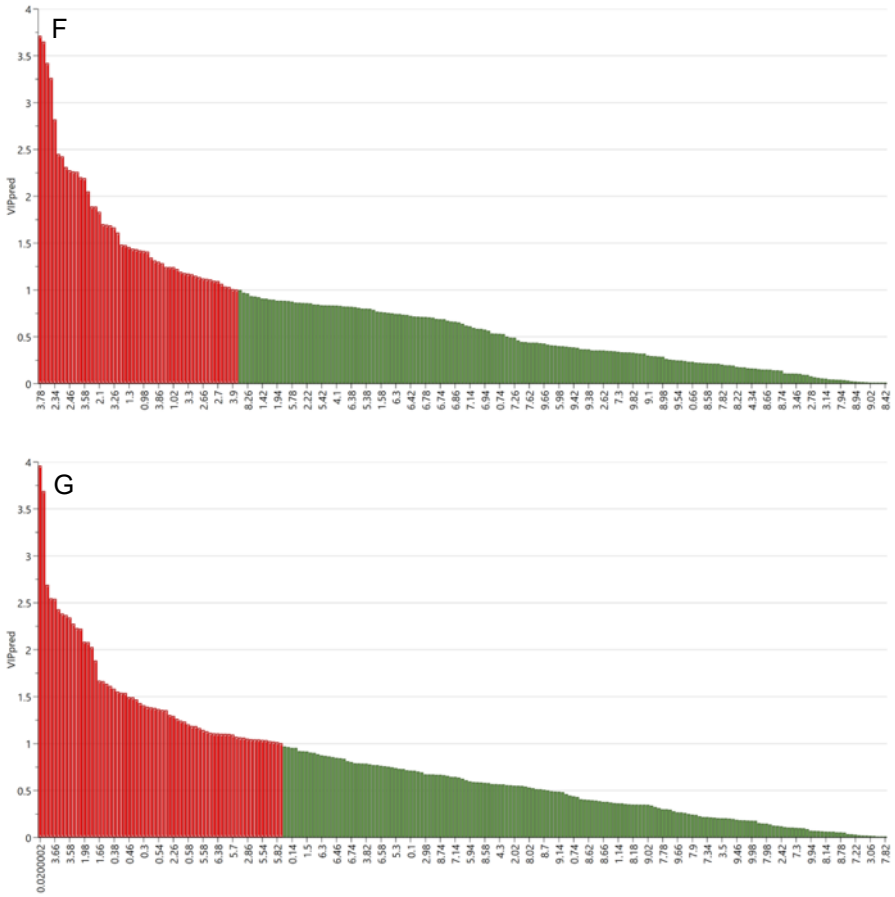

Figure 8.20 VIP predictive plots derived from OPLS-DA models of NMR spectra of aqueous extracts from HepG2 cells treated with different concentrations of valproate at 0, 0.5, 1, 2 and 4 mM. Samples were collected and NMR analysis was carried out as described in Sections 2.10 and 2.13. A. Control vs 0.5 mM valproate B. Control vs 1 mM valproate C. Control vs 2 mM valproate. D. control vs 4 mM valproate. E. 0.5 vs 1 mM valproate. F. 1 vs 2 mM valproate. G. 2 vs 4 mM valproate. Variables with a VIPpred value above 1 were selected as significant and are highlighted in red.

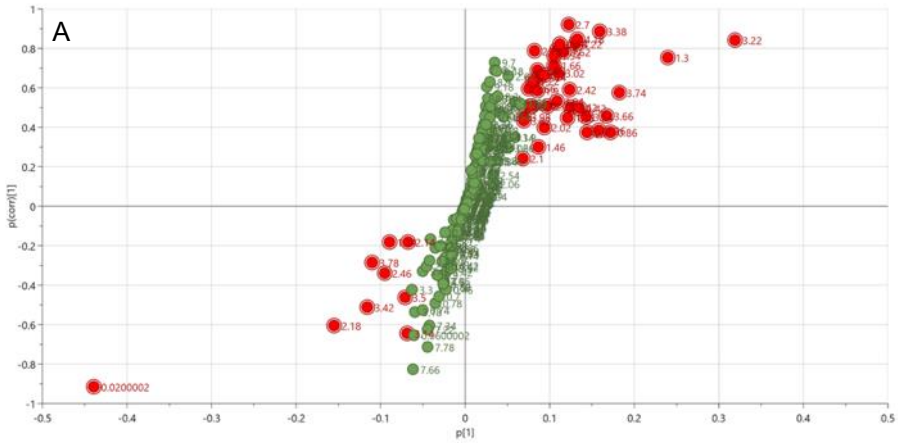

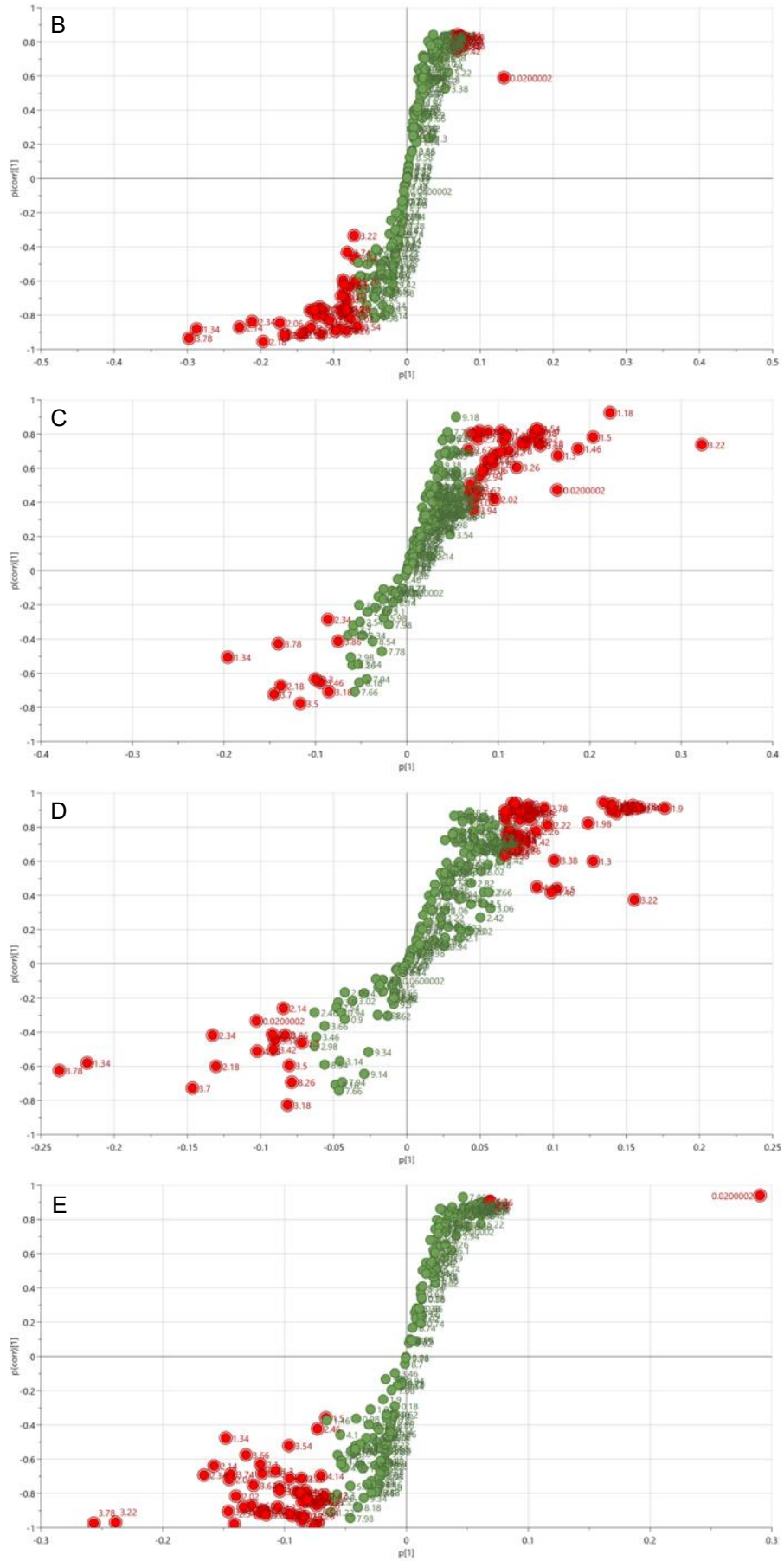
B
C
D
E
p(corr)[1]
p[1]

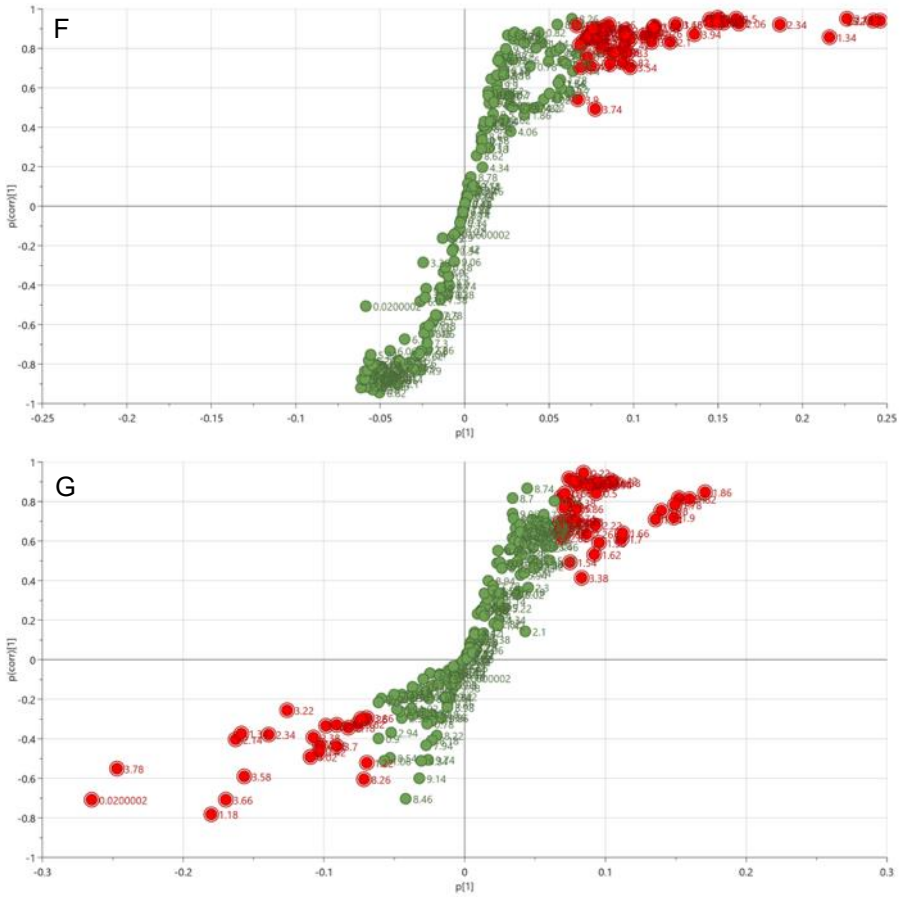

Figure 8.21 S-plots derived from OPLS-DA models of NMR spectra of aqueous extracts from HepG2 cells treated with different concentrations of valproate at 0, 0.5, 1, 2 and 4 mM. Samples were collected and NMR analysis was carried out as described in Sections 2.10 and 2.13. A. Control vs 0.5 mM valproate B. Control vs 1 mM valproate C. Control vs 2 mM valproate. D. control vs 4 mM valproate. E. 0.5 vs 1 mM valproate. F. 1 vs 2 mM valproate. G. 2 vs 4 mM valproate.

8.1.7 Metabolomic analysis of organic monolayer extracts dosed with valproate

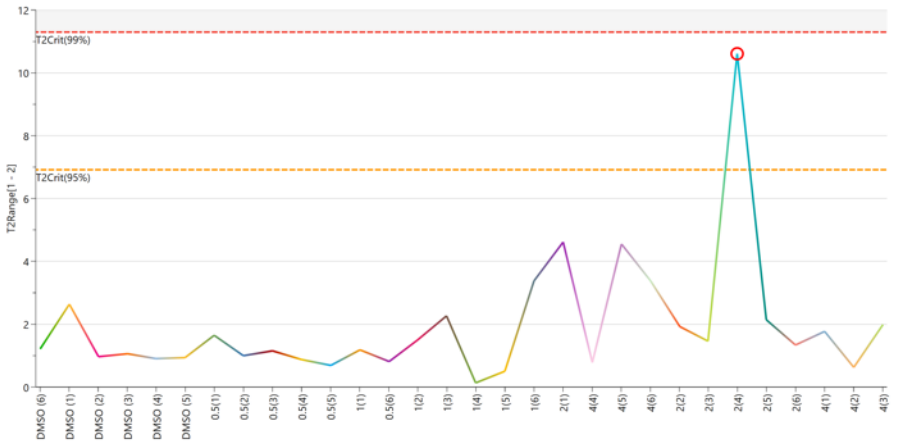

Figure 8.22 Hotelling's T2 plot created from PCA scores plots in Figure 5.8. Samples above the red line of the 99% confidence level are considered to be true outliers. Sample 2 (4) is circled in red.

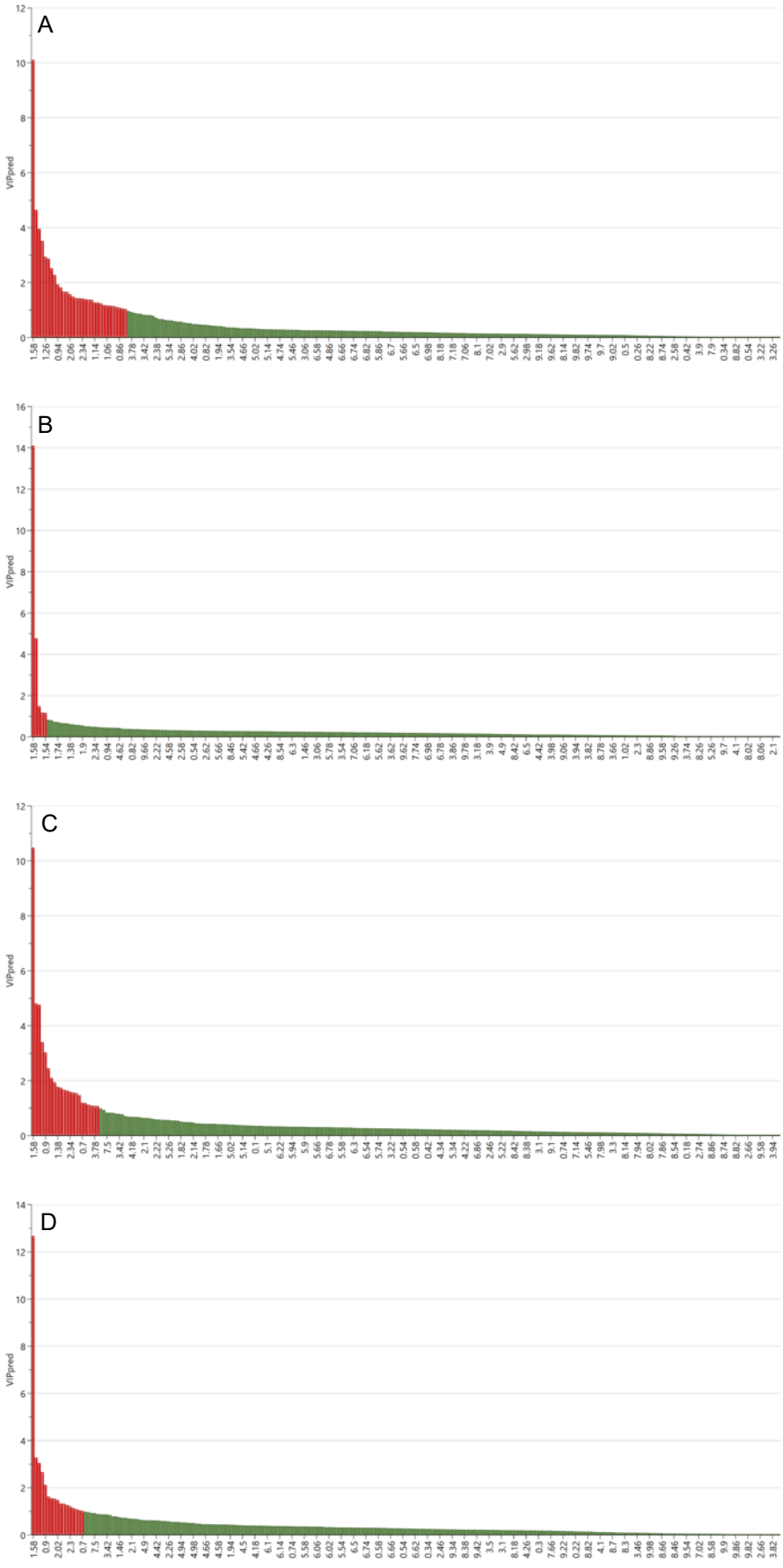
A
B
C
D
VIPpred

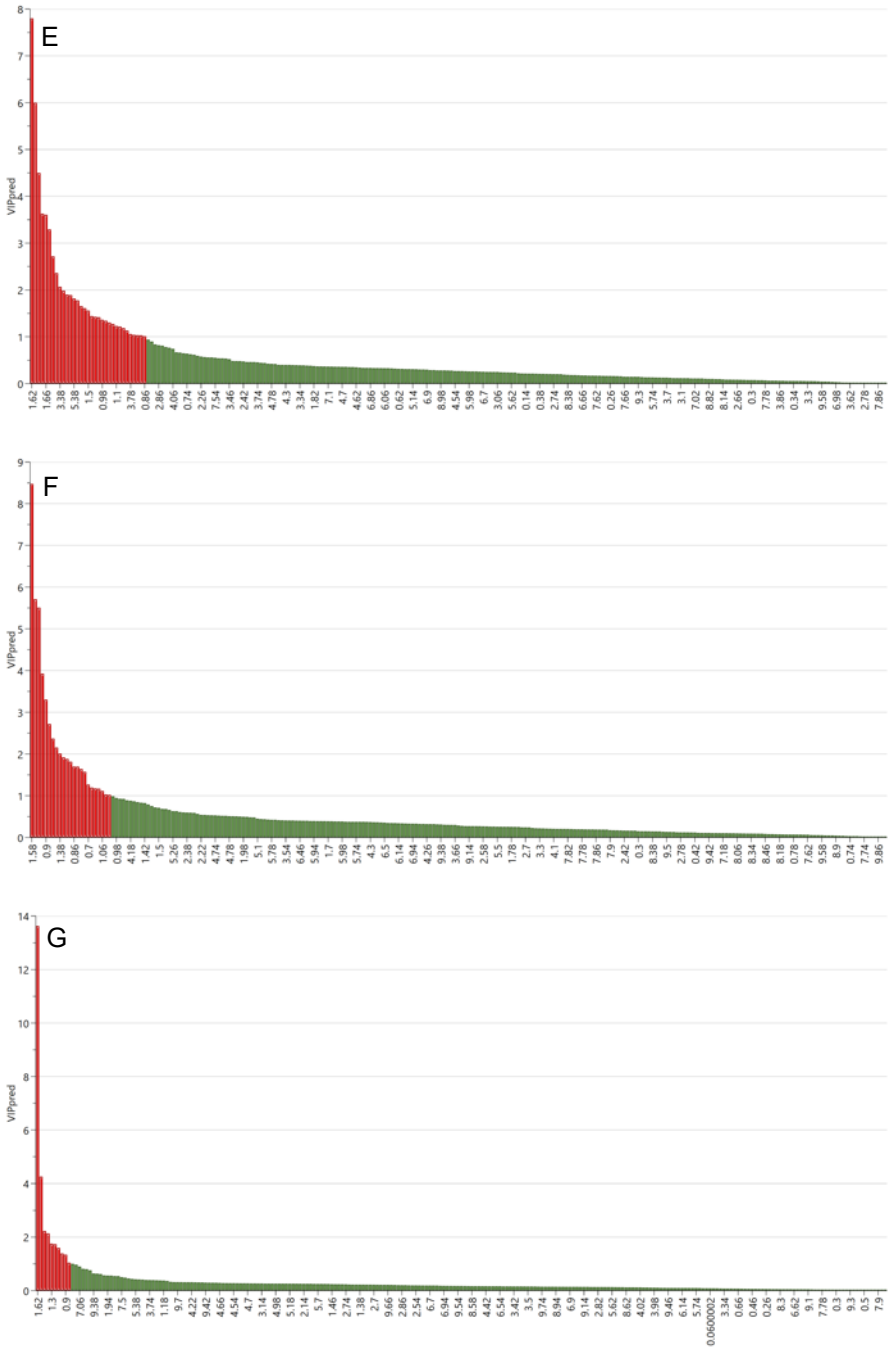

Figure 8.23 VIP predictive plots derived from OPLS-DA models of NMR spectra of organic extracts from HepG2 cells treated with different concentrations of valproate at 0, 0.5, 1, 2 and 4 mM. Samples were collected and NMR analysis was carried out as described in Sections 2.10 and 2.13. A. Control vs 0.5 mM valproate B. Control vs 1 mM valproate C. Control vs 2 mM valproate. D. control vs 4 mM valproate. E. 0.5 vs 1 mM valproate. F. 1 vs 2 mM valproate. G. 2 vs 4 mM valproate. Variables with a VIPpred value above 1 were selected as significant and are highlighted in red.

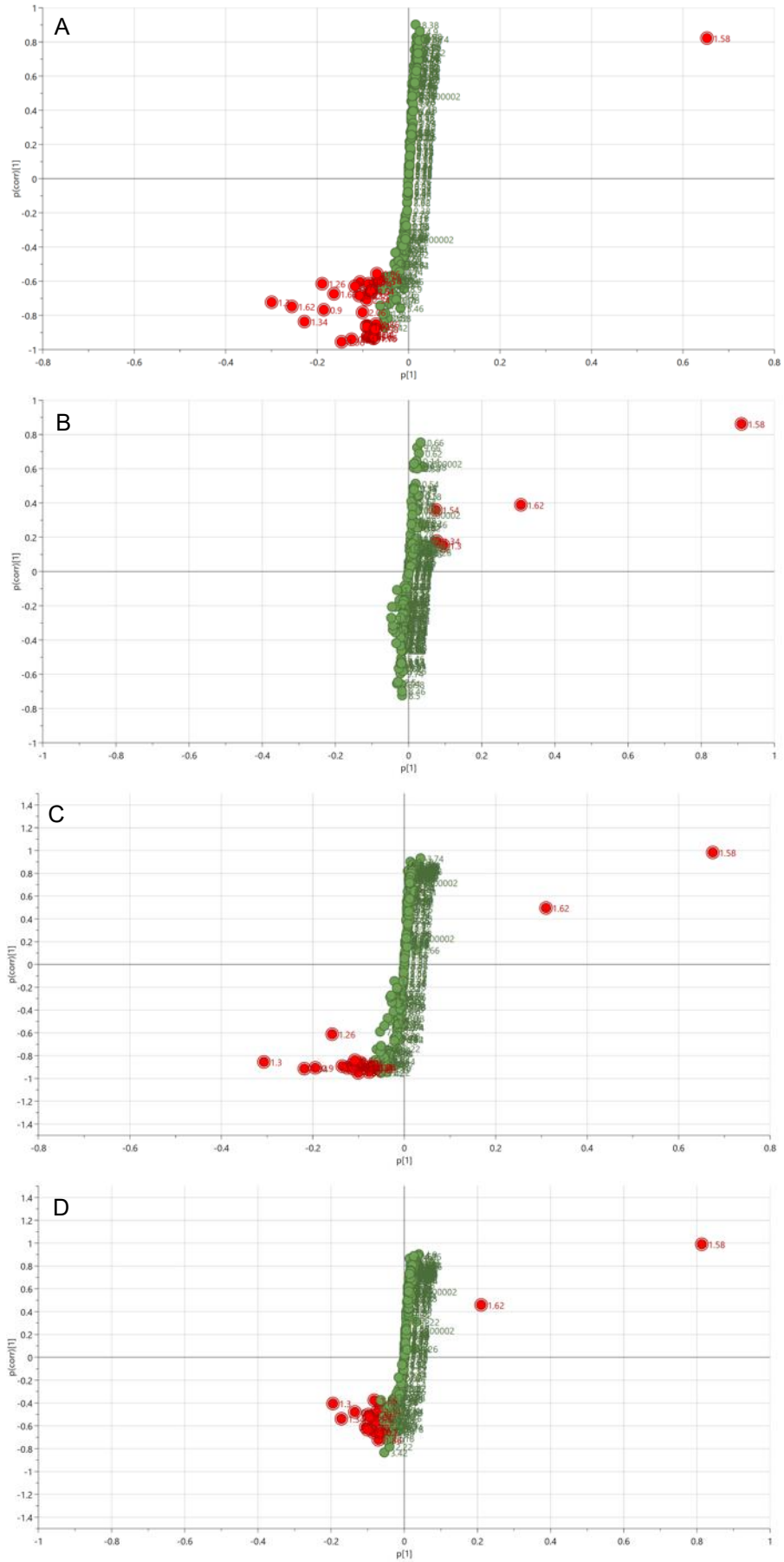
A
B
C
D
p[1]
p(corr)[1]
1.58
1.62
1.26
1.3
1.34
0.9

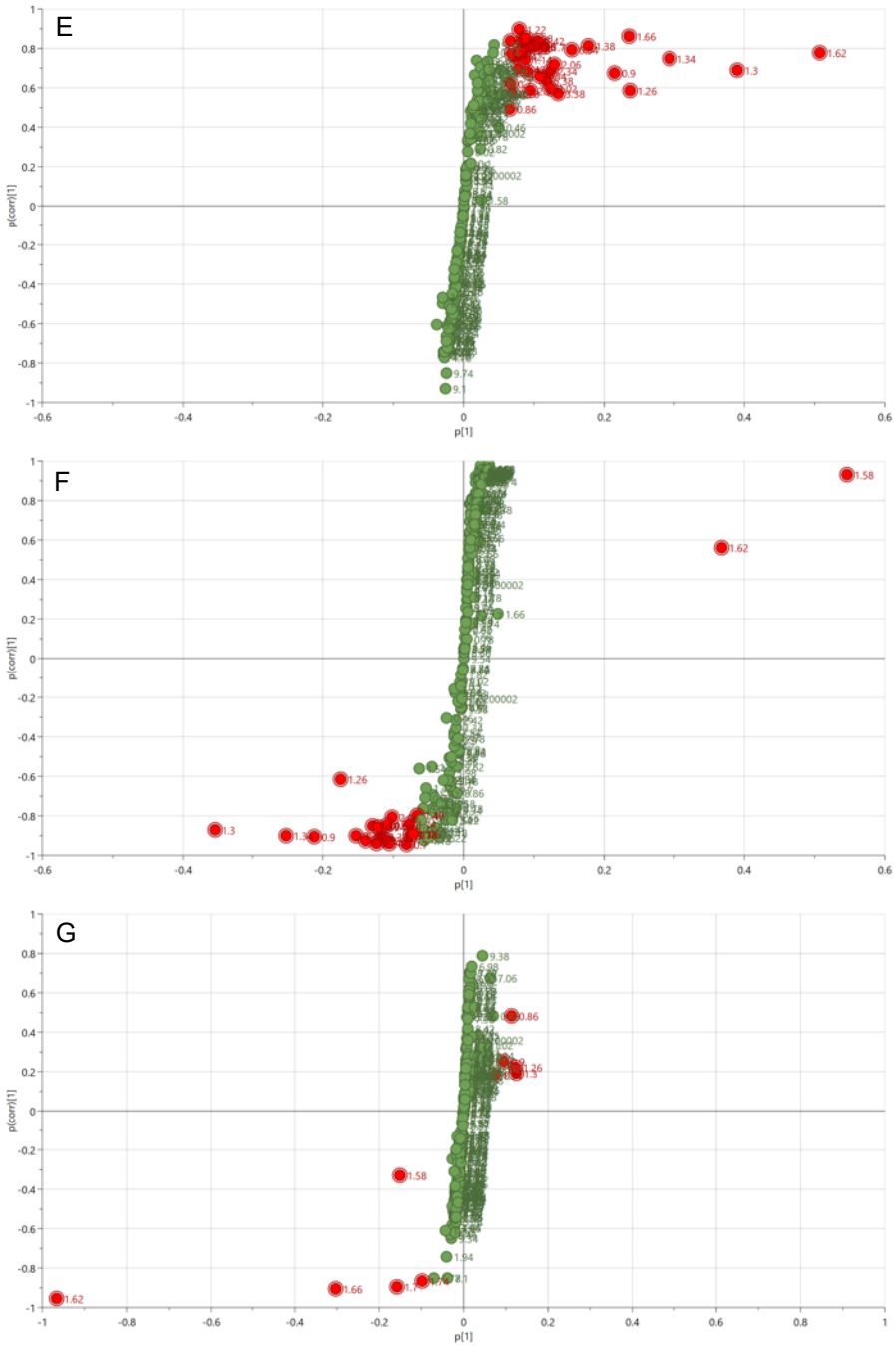

Figure 8.24 S-plots derived from OPLS-DA models of NMR spectra of organic extracts from HepG2 cells treated with different concentrations of valproate at 0, 0.5, 1, 2 and 4 mM. Samples were collected and NMR analysis was carried out as described in Sections 2.10 and 2.13. A. Control vs 0.5 mM valproate B. Control vs 1 mM valproate C. Control vs 2 mM valproate. D. control vs 4 mM valproate. E. 0.5 vs 1 mM valproate. F. 1 vs 2 mM valproate. G. 2 vs 4 mM valproate.

8.1.8 Metabolomic analysis of aqueous spheroid extracts dosed with valproate

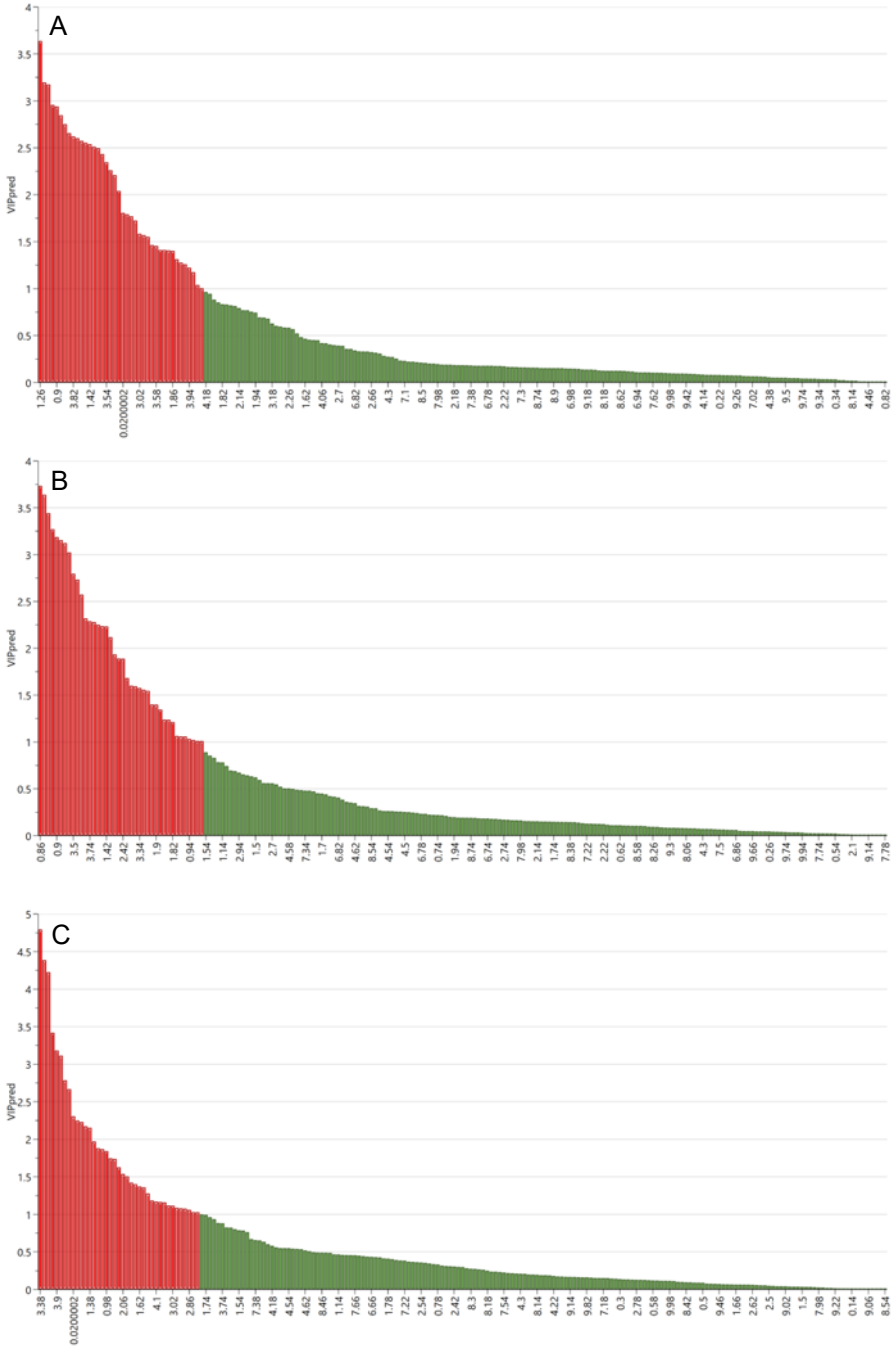

Figure 8.25 VIP predictive plots derived from OPLS-DA models of NMR spectra of aqueous extracts from HepG2 spheroids treated with valproate at different concentrations (0, 1 and 4 mM). Samples were collected and NMR analysis was carried out as described in Sections 2.10 and 2.13. A. Control vs 1 mM valproate; B. Control vs 4 mM valproate; C. 1 vs 4 mM valproate.

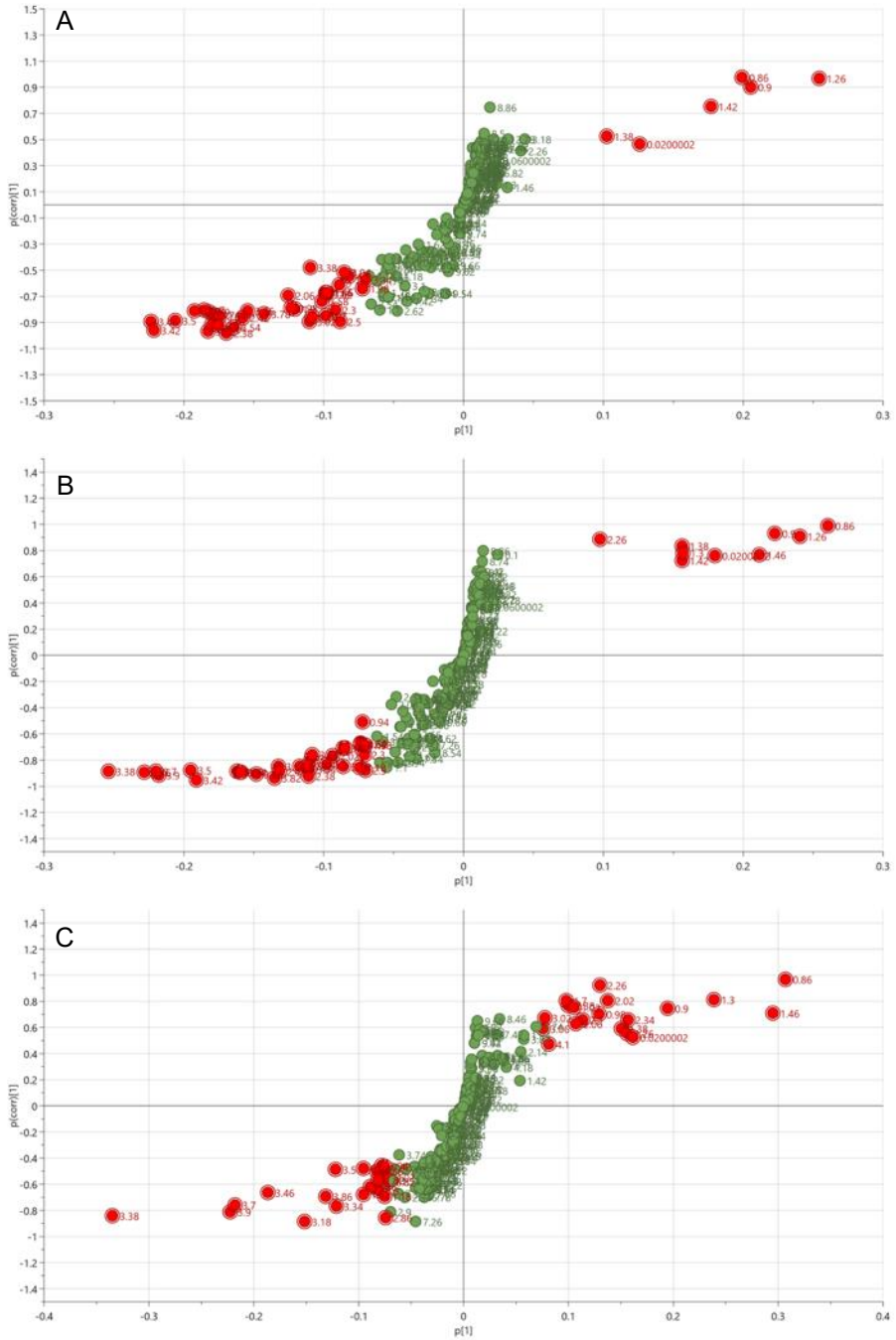

Figure 8.26 S-plots derived from OPLS-DA models of NMR spectra of aqueous extracts from HepG2 spheroids treated with valproate at different concentrations (0, 1 and 4 mM). Samples were collected and NMR analysis was carried out as described in Sections 2.10 and 2.13. A. Control vs 1 mM valproate; B. Control vs 4 mM valproate; C. 1 vs 4 mM valproate.

8.1.9 Metabolomic analysis of organic spheroid extracts dosed with valproate

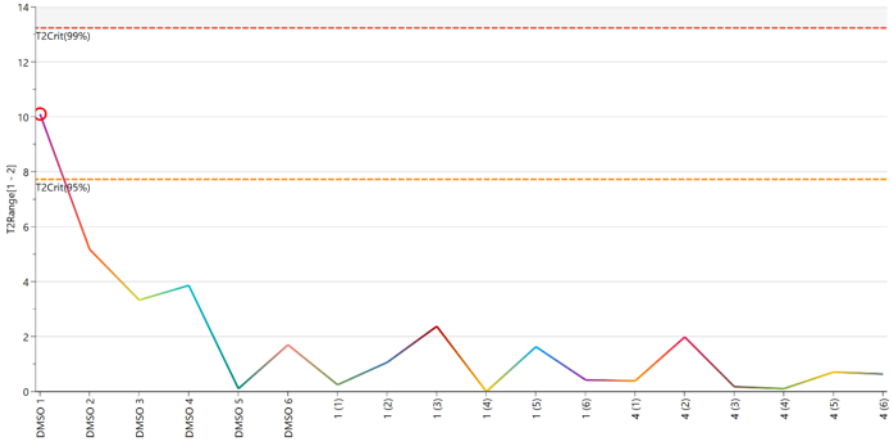

Figure 8.27 Hotelling's T2 plot created from PCA scores plots in Figure 5.18. Samples above the red line of the 99% confidence level are considered to be true outliers. Sample DMSO (1) is circled in red.

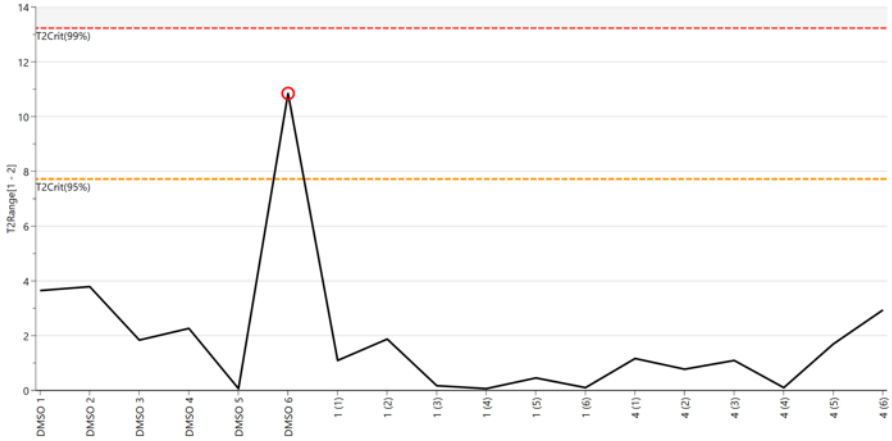

Figure 8.28 Hotelling's T2 plot created from PCA scores plots in Figure 5.19. Samples above the red line of the 99% confidence level are considered to be true outliers. Sample DMSO (6) is circled in red.

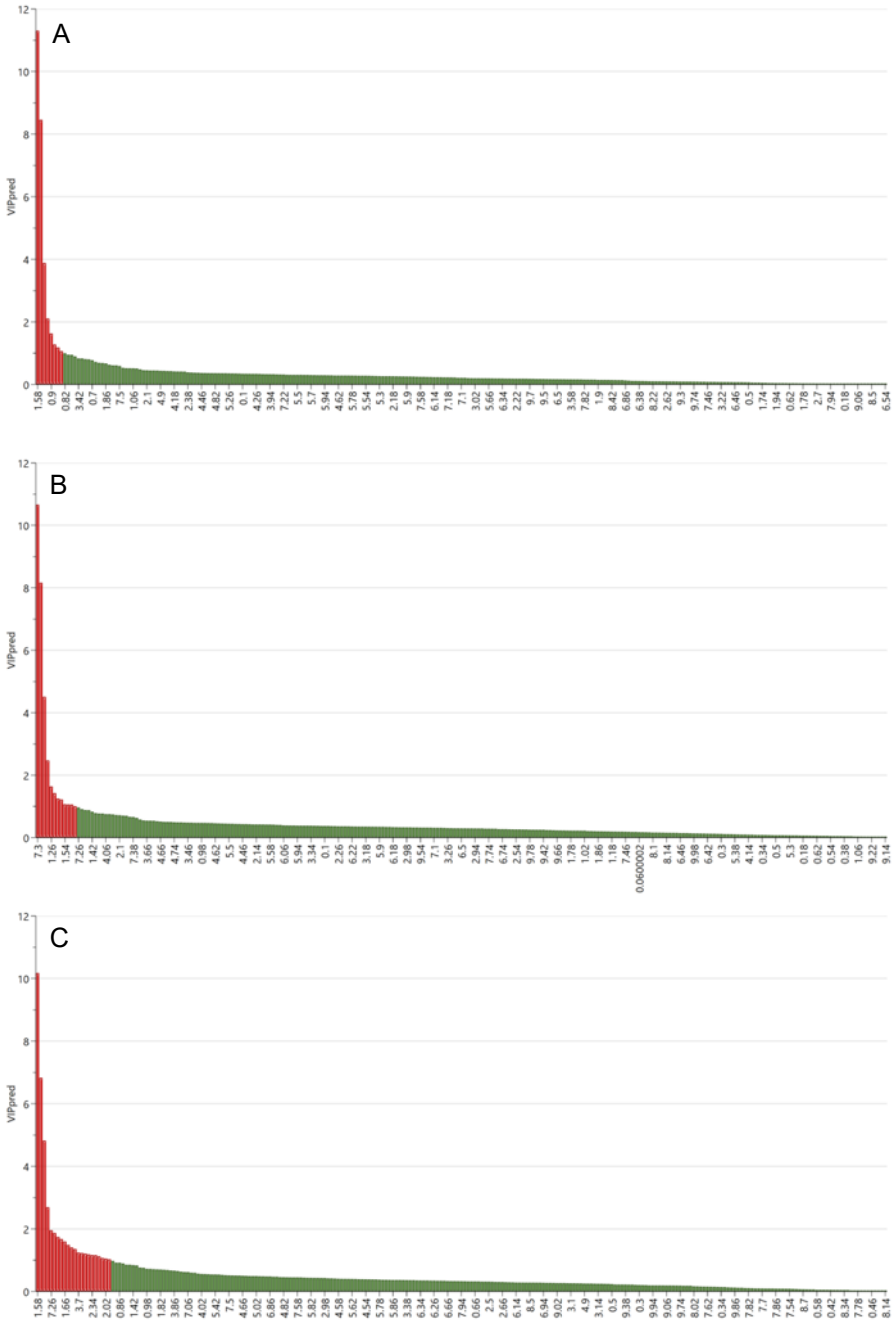

Figure 8.29 VIP predictive plots derived from OPLS-DA models of NMR spectra of organic extracts from HepG2 spheroids treated with valproate at different concentrations (0, 1 and 4 mM). Samples were collected and NMR analysis was carried out as described in Sections 2.10 and 2.13. A. Control vs 1 mM valproate; B. Control vs 4 mM valproate; C. 1 vs 4 mM valproate.

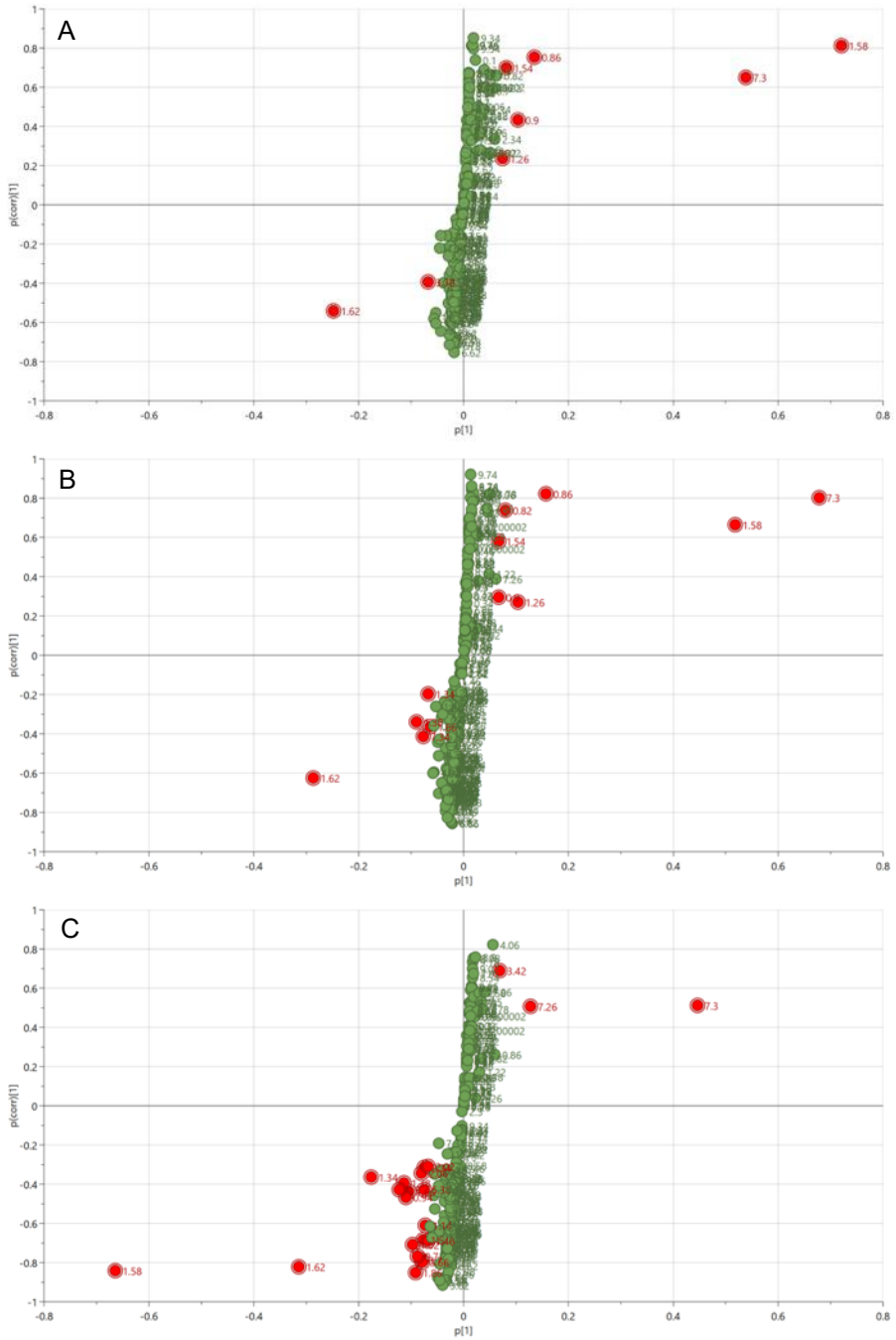

Figure 8.30 S-plots derived from OPLS-DA models of NMR spectra of organic extracts from HepG2 spheroids treated with valproate at different concentrations (0, 1 and 4 mM). Samples were collected and NMR analysis was carried out as described in Sections 2.10 and 2.13. A. Control vs 1 mM valproate; B. Control vs 4 mM valproate; C. 1 vs 4 mM valproate.

8.1.10 Validation of OPLS-DA models in Fatty acid treated groups

OPLS discriminate analysis was validated using the leave-one-out method. The scores plots below show an example of the results from this validation in the aqueous monolayer group treated with fatty acids.

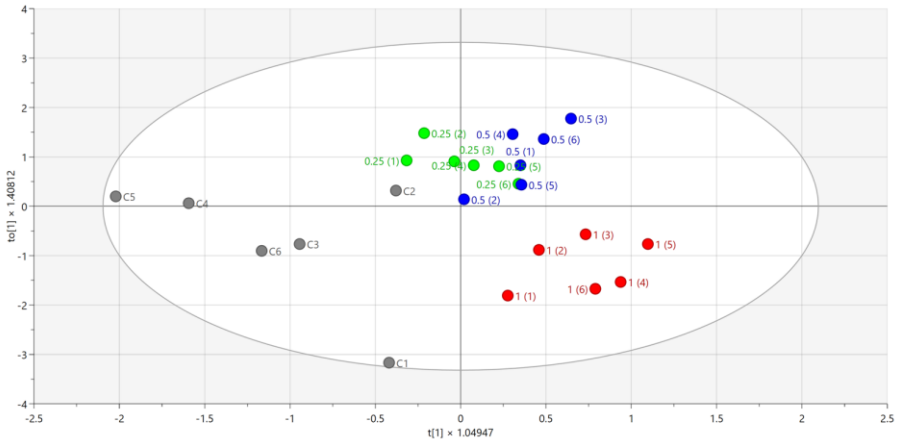

Figure 8.31 OPLS scores plot derived from NMR spectra of aqueous cell extracts from HepG2 cells treated with different dose levels of fatty acids. Cells were dosed with a 2:1 mixture of oleic acid and palmitate at 0, 0.1, 0.25, 0.5 and 1.0 mM and incubated for 24 hours. Samples were collected, and NMR analysis carried out as described in Sections 2.10 and 2.12. Each spot on the scores plot represents one sample. Grey = ethanol control; green = 0.25 mM; dark blue = 0.5 mM; red = 1.0 mM fatty acids.

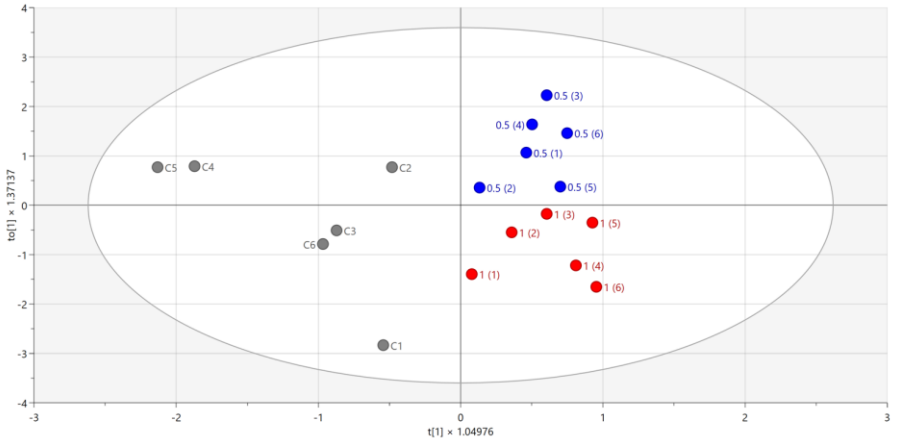

Figure 8.32 OPLS scores plot derived from NMR spectra of aqueous cell extracts from HepG2 cells treated with different dose levels of fatty acids. Cells were dosed with a 2:1 mixture of oleic acid and palmitate at 0, 0.1, 0.25, 0.5 and 1.0 mM and incubated for 24 hours. Samples were collected, and NMR analysis carried out as described in Sections 2.10 and 2.12. Each spot on the scores plot represents one sample. Grey = ethanol control; dark blue = 0.5 mM; red = 1.0 mM fatty acids.

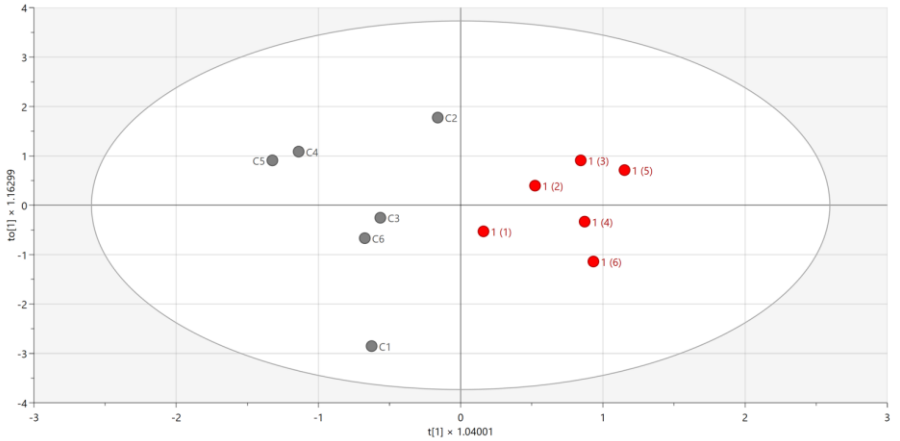

Figure 8.33 OPLS scores plot derived from NMR spectra of aqueous cell extracts from HepG2 cells treated with different dose levels of fatty acids. Cells were dosed with a 2:1 mixture of oleic acid and palmitate at 0, 0.1, 0.25, 0.5 and 1.0 mM and incubated for 24 hours. Samples were collected, and

NMR analysis carried out as described in Sections 2.10 and 2.12. Each spot on the scores plot represents one sample. Grey = ethanol control; red = 1.0 mM fatty acids.